Green Energy and Technology

Ashoke De · Ashwani K. Gupta · Suresh K. Aggarwal · Abhijit Kushari · Akshai K. Runchal *Editors*

Sustainable Development for Energy, Power, and Propulsion

Springer

Green Energy and Technology

Climate change, environmental impact and the limited natural resources urge scientific research and novel technical solutions. The monograph series Green Energy and Technology serves as a publishing platform for scientific and technological approaches to "green"—i.e. environmentally friendly and sustainable—technologies. While a focus lies on energy and power supply, it also covers "green" solutions in industrial engineering and engineering design. Green Energy and Technology addresses researchers, advanced students, technical consultants as well as decision makers in industries and politics. Hence, the level of presentation spans from instructional to highly technical.

Indexed in Scopus.

More information about this series at http://www.springer.com/series/8059

Ashoke De · Ashwani K. Gupta ·
Suresh K. Aggarwal · Abhijit Kushari ·
Akshai K. Runchal
Editors

Sustainable Development for Energy, Power, and Propulsion

Springer

Editors
Ashoke De
Department of Aerospace Engineering
Indian Institute of Technology Kanpur
Kanpur, Uttar Pradesh, India

Suresh K. Aggarwal
Department of Mechanical
and Industrial Engineering
University of Illinois at Chicago
Chicago, IL, USA

Akshai K. Runchal
Analytic and Computational
Research Inc. (ACRi)
Los Angeles, CA, USA

Ashwani K. Gupta
Department of Mechanical Engineering
University of Maryland
College Park, MD, USA

Abhijit Kushari
Department of Aerospace Engineering
Indian Institute of Technology Kanpur
Kanpur, Uttar Pradesh, India

ISSN 1865-3529 ISSN 1865-3537 (electronic)
Green Energy and Technology
ISBN 978-981-15-5666-1 ISBN 978-981-15-5667-8 (eBook)
https://doi.org/10.1007/978-981-15-5667-8

© Springer Nature Singapore Pte Ltd. 2021
This work is subject to copyright. All rights are reserved by the Publisher, whether the whole or part of the material is concerned, specifically the rights of translation, reprinting, reuse of illustrations, recitation, broadcasting, reproduction on microfilms or in any other physical way, and transmission or information storage and retrieval, electronic adaptation, computer software, or by similar or dissimilar methodology now known or hereafter developed.
The use of general descriptive names, registered names, trademarks, service marks, etc. in this publication does not imply, even in the absence of a specific statement, that such names are exempt from the relevant protective laws and regulations and therefore free for general use.
The publisher, the authors and the editors are safe to assume that the advice and information in this book are believed to be true and accurate at the date of publication. Neither the publisher nor the authors or the editors give a warranty, expressed or implied, with respect to the material contained herein or for any errors or omissions that may have been made. The publisher remains neutral with regard to jurisdictional claims in published maps and institutional affiliations.

This Springer imprint is published by the registered company Springer Nature Singapore Pte Ltd.
The registered company address is: 152 Beach Road, #21-01/04 Gateway East, Singapore 189721, Singapore

Local Organization Team and Message from the Director, NIT, Kurukshetra

Local Organization Team

Dr. Satish Kumar, Director, NIT, Kurukshetra
Dr. Pankaj Chandna
Dr. Vinod Mittal
Dr. Gulshan Sachdeva

Message from the Director, NIT, Kurukshetra

In my professional career which spans over three and a half decades, I was associated with the aerospace industry for a significant period in the fields of missiles, strategic systems, and hypersonic propulsion. Power and propulsion play a very important role in the fields of energy, aviation, and defense. There is a pressing need to amalgamate these areas using sustainable energy through the development of clean and green technologies, which would serve the present needs and also meet future requirements when the conventional sources of energy may be exhausted. I say it with extreme pride that the National Institute of Technology (NIT), Kurukshetra, organized this International Workshop on Energy, Power, and Environment (ISEPP-2019) which is the tenth in a series of workshops on the broad theme of energy, power, and propulsion that started in 2004. Over the years, this workshop has grown into a world-class forum in the field of sustainable developments in energy, power, and propulsion. This workshop was organized in collaboration with the Indian Institute of Technology (IIT), Kanpur; University of Maryland, College Park; University of Illinois at Chicago, and Analytic and Computational Research Inc., USA. The workshop was attended by over 200 participants from different academic and research organizations and representatives from governments and industries. Many world-renowned scientists and researchers from Australia, Brazil, Finland, India, Italy, Japan, Malaysia, Thailand, Saudi Arabia, the UK, and the USA presented their latest research and development findings and shared their ideas in formal talks and informal exchange forums. Poster competitions for students were organized to bring young talent into the limelight. This attempt at the sustainable developments in the areas of power and propulsion is definitely one of its kind.

I wish everyone associated with this workshop-rich learning experience, and I am very confident that we all moved a step closer toward our understanding to have a cleaner and sustainable environment.

Preface

The development of environmentally sustainable power sources that drive the society and industry is now recognized as an imperative and important challenge for the engineers. Though there is increasing emphasis on developing renewable and alternative energy sources in a sustainable manner, fossil fuels remain the mainstay of our economy. Current technologies using fossil fuels for energy have degraded the environment and burdened the economy with the cost of cleanup operations. Climate change, rising global temperatures, and the impact on the protective ozone layer that are related to greenhouse gas emissions are now empirically proven facts. The consequent increase in global average temperatures, melting of glaciers, and sea level rise are now being recognized as serious threats to the very core of the existence of human society. Yet our need for energy is growing due to the growth of the human population, increased standards of living, and emerging economies. These factors mean that the average per capita energy use will increase substantially in the coming decades. Fossil fuels will continue to remain important in energy usage in the coming decades. Unless more efficient and sustainable energy sources are developed, we are looking at an environmental disaster waiting to happen.

The world population has reached over 7.7 billion and is growing at a rate of 1.08% per year. The projections are 9 billion people by 2037 and 10 billion by 2057. The worldwide energy supply in 2019 stands at about 170,000 TWh or approximately 580 quadrillions BTU. This is expected to increase to 815 quadrillions BTU by the year 2040. Per IEA, if we continue along its present path, without any additional changes in policy, energy demand will rise by 1.3% each year to 2040. If the policy intentions and targets stated by major energy user nations are actually implemented, this rate of energy demand will decrease to 1% per year. In either scenario, it seems that the prime source of energy in the next two decades will be fossil fuels. While considerable progress is being made to shift to renewable energy sources, fossil fuels are expected to provide the major share, approximately 78%, of the world's energy by 2040. The environment is already under stress; either of these scenarios places a significant additional burden on the environment with a somewhat slower rise in emissions but still far short of sustainability. We, therefore, need a sustainable development scenario that maps out a way to meet energy

demand goals, requiring rapid and widespread changes across all parts of the energy system. The current and foreseeable clean energy technologies are not likely to provide the answer. We need new and innovative technologies with improved efficiency to meet the goals of the Paris Agreement by holding the rise in global temperatures to well below 2 °C and pursuing efforts to limit it to 1.5 °C, and also meet global objectives of cost-effective energy access and cleaner air. The breadth of the world's energy needs means that there are no simple or single solutions. Emission reduction (in particular CO_2) must be achieved from all kinds of gas, liquid, and solid fossil fuel use with technologies providing efficient and cost-effective energy services in all energy-using sectors.

An international forum to discuss the challenges outlined above was started in 2004, with the focus on combustion, power, and propulsion technologies using all kinds of fuels available. Over the years, it has evolved into annual international workshops on Sustainable Energy, Power, and Propulsion (ISEPP), which have the broad framework of international collaborations and share ideas about research and development related to cleaner and efficient fuel(s) utilization, and development of alternative and renewable technologies for sustainability. The tenth workshop in this series was held from March 17 to 19, 2019, at the National Institute of Technology (NIIT), Kurukshetra, India. The objectives of this workshop were to encourage international collaborations and dissemination of knowledge related to sustainable energy initiatives and technology. The workshop attracted over 200 participants from different academic and research organizations and representatives from governments, industries, and academia. Many world-renowned scientists and researchers from Australia, Brazil, Finland, India, Italy, Japan, Malaysia, Thailand, Saudi Arabia, the UK, and the USA presented their latest research and development findings and shared ideas in formal talks and informal technical exchanges. The TEQIP (Ministry of Human Resource Development, India), the Defense Research and Development Organization (DRDO), India, the National Science Foundation (NSF), USA, and the Office of Naval Research (ONR) Global sponsored the workshop. It was co-sponsored by several leading research organizations and universities in the USA and India, including NIT, Kurukshetra, Siemens, LPS Bossard (Pvt.) Ltd., TSI, Inc., ACRi Los Angeles, IIT Kanpur, University of Maryland, College Park, and the University of Illinois at Chicago. The editors wish to express their sincere thanks to the faculty, staff, and students at NIT, Kurukshetra, for their unconditional support and warm hospitality provided to host this international Workshop.

This research monograph provides a wealth of knowledge on the latest research and development presented by the eminent scientists and engineers at the workshop. The broad theme of the monograph is energy, power, propulsion, and sustainability. The chapters are grouped into six parts. These are, respectively, High-Speed Propulsion, Renewable Fuels, Flames and Reacting Systems, Combustion Systems, Transport Processes in Energy Systems, and Sustainable Energy Technologies. These chapters deal with experimental and prototype systems using state-of-the-art diagnostic and analytic techniques. A number of chapters deal with specific design aspects while others deal with novel concepts using alternative

energy sources for improved performance and for the next generation of power and propulsion systems. The contributions to the cutting-edge research and development technologies should be of pinnacle interest to researchers and engineers working on sustainable energy technologies.

Kanpur, India — Ashoke De
College Park, USA — Ashwani K. Gupta
Chicago, USA — Suresh K. Aggarwal
Kanpur, India — Abhijit Kushari
Los Angeles, USA — Akshai K. Runchal

Introduction

Keywords Energy • Propulsion • Power • Renewable and alternative fuels • Environmental sustainability • Novel energy-efficient technologies • Modeling and simulation

Demand for energy is increasing due to both population growth and increased use by emerging economies. Most of our energy generation today relies on fossil fuels and is expected to remain the same way for the next few decades. The manner in which this energy is generated today leads to serious environmental degradation. Further, at the projected rate of consumption, our supply of fossil fuels is likely to be exhausted in the next few decades. These pose a serious existential threat to our human endeavor. The need for cleaner and sustainable energy is the need of the hour. This research book contributes valuable new knowledge to the growing literature on energy generation with minimal environmental impact and quest of renewable resources. It deals with methodologies that improve the efficiency and performance of existing energy conversion systems from fossil fuels with much reduced environmental impact. It also deals with the latest research into renewable drop-in biofuels, solar, and wind that are emerging with a continuously increasing contribution to our energy supply. This book contains the latest research from internationally renowned scientists and engineers from around the globe on topics

related to energy security and energy sustainability. This book will serve as a reference source for practicing engineers, educators, research professionals, and students in all energy-using sectors.

Ashoke De
ashoke@iitk.ac.in
Ashwani K. Gupta
akgupta@umd.edu
Suresh K. Aggarwal
ska@uic.edu
Abhijit Kushari
akushari@iitk.ac.in
Akshai K. Runchal
runchal@gmail.com

Contents

Sustainable Energy Technologies

About the Editors

Ashoke De is an Associate Professor at the Department of Aerospace Engineering, Indian Institute of Technology Kanpur. He has been the recipient of the Humboldt Research fellowship for Experienced Researchers, IEI-Young Engineer's Award-2014, DST Young Scientist award-2015, and P K Kelkar Research Fellowship from IIT Kanpur. He is a member of ASME, SIAM, FMFP, ISHMT and Combustion Institute. He received his MS from IIT Kanpur, and PhD from Louisiana State University. He has authored over 90 peer reviewed papers. His research interests include combustion modeling, hybrid RANS/LES model development, supersonic flows and Fluid-Structure interactions (FSI) with focus on computational mechanics in combustion and turbulent flows.

Ashwani K. Gupta is a Distinguished University Professor at the University of Maryland (UMD). He obtained his PhD and higher doctorate (DSc) from the University of Sheffield, was awarded a DSc from Southampton University and has received honorary doctorates from the University of Wisconsin Milwaukee, King Mungkut University of Technology North Bangkok, and University of Derby, UK. He received many honors and awards from AIAA and ASME and the President Kirwan Research Award and College of Engineering Research Award at UMD. Prof. Gupta has authored over 750 papers, 3 books, and edited 12 books in the areas of combustion, swirl flows, high temperature air combustion (HiTAC), distributed combustion, waste to energy, acid gas treatment, fuel reforming, and air pollution. He is Honorary Fellow of ASME and Fellow of AIAA, SAE, AAAS and RAeS (UK).

Suresh K. Aggarwal received his Ph.D. from Georgia Institute of Technology. He was a member of research staff at Princeton University and Senior Research Engineer at CMU. He then joined the University of Illinois at Chicago was promoted to Professor in 1995. He served as Director of Graduate Studies, and was also Visiting Scientist at ANL, Visiting Professor at Ecole Centrale-Paris, France and Guest Professor at Jiangsu University, China. His research interests include

combustion, multiphase reacting flows, emissions, clean energy, and fire suppression. He has authored over 360 publications and is a Fellow of ASME, AAAS and Associate Fellow of AIAA.

Abhijit Kushari is a Professor at the Department of Aerospace Engineering, Indian Institute of Technology Kanpur. Dr. Kushari received his PhD from Georgia Institute of Technology, in 2000 and joined the IIT Kanpur as an Assistant Professor in 2001. He became a Professor in 2014. His research interests are aerospace propulsion, gas turbine engines, turbo-machinery, liquid atomization flow control and combustion dynamics. He has authored more than 130 technical papers.

Akshai K. Runchal is the founder and Director of CFD Virtual Reality Institute and ACRI group of companies. His expertise is in Computational Fluid Dynamics (CFD). He has consulted widely on flow, heat and mass transfer, combustion, environmental impact, hazardous and nuclear waste, ground water and decision analysis to over 200 clients in 20 countries. He is the principal author of PORFLOW®, TIDAL®, ANSWER® and RADM™ simulation models that are used worldwide. He received his PhD from Imperial College (London), and Bachelor's in Engineering from PEC. He has taught in the USA, India and the UK. He has authored 7 books and over 200 technical publications. He has received many honors and awards, and given many invited contributions at conferences.

High-Speed Propulsion

Towards Credible CFD Analysis of High-Speed Propulsion Systems

K. Kailasanath

1 Introduction

The potential role of computational fluid dynamics (CFD) in the design and analysis of high-speed air-breathing propulsion systems is discussed in this article. For such computations to be most useful, they must be believable or "credible". How to go about assessing and establishing the credibility of numerical simulations, as pertaining to emerging, high-speed propulsion system concepts is discussed. The examples chosen to illustrate the key concepts are primarily based on the author's own experience in the development of high-speed propulsion systems based on detonations [1–6]. It is hoped that the readers of this article will be able to use the ideas presented here not only for detonation-based systems but also adapt the ideas to help assess and develop other concepts in high-speed propulsion.

1.1 Role of CFD

In this article, the term, "CFD", is used in the broad sense of the term to connote not only fluid flow but chemical reactions, energy release, heat transfer and other aspects of physical sciences pertinent to high-speed propulsion. There are several common reasons that we do "CFD" or more generally numerical simulations. They provide detailed diagnostics, often complementary to experiments. They can be used to conduct parametric studies, often independently varying parameters, again sometimes very difficult in laboratory experiments. Simulations can also be used to "test" under conditions that are difficult or prohibitively expensive in the laboratory. All

K. Kailasanath (✉)
Lorton, VA 22079, USA
e-mail: kkailasanath@gmail.com

© Springer Nature Singapore Pte Ltd. 2021

A. De et al. (eds.), *Sustainable Development for Energy, Power, and Propulsion*, Green Energy and Technology,
https://doi.org/10.1007/978-981-15-5667-8_1

these three roles may be viewed as being complementary to physical experiments in the laboratory. There is another potentially important role for numerical simulations that has not received as much attention as the above roles. This is to explore promising new concepts before laboratory experiments are conducted. This is the role that is explored further in this chapter.

For numerical simulations to play an effective role in the exploration and early development of new propulsion concepts, they need to be credible, not just to the scientist or engineer conducting the simulations but especially the potential users of the results. How to go about developing such credible simulations is discussed next.

2 Verification and Validation of Numerical Simulations

These terms are sometimes used interchangeably but really are different and have distinct definitions [7] in the CFD community. "Verification" is formally defined as "the process of determining that a model implementation accurately represents the developer's conceptual description of the model and the solution to the model" [8]. It is important to note that the perspective here is that of the "developer" of the CFD model. Hence, one would hope that this process of "verification" is always done since it can be done by the developer alone, without required participation of the user, experimentalist or anyone else. The details of how this can be carried out will be discussed in the next subsection.

In contrast, "validation" is the process of determining the degree to which a model is an accurate representation of the real world from the perspective of the intended uses of the model. Here the perspective shifts to the user (as opposed to the developer) and what the user wants to use the model for. Basically, the essential physics of the real problem the user wants to solve needs to be "accurately" represented. Pedantically, one can argue that this is nearly impossible except for the most simple cases, because our knowledge of the real world and models to represent it are necessarily incomplete and are only approximations. For example, most fluid flows in practical engineering problems involve some levels of "turbulence". Our understanding of the science behind turbulence and our efforts to capture it are still incomplete and involve a number of simplifications and theoretical assumptions. The solution for this quandary is the word "accurately", which can be expressed in degrees or levels of accuracy or more commonly levels of uncertainty. Also, "the intended uses of the model" in the definition are an important term because the level of accuracy required usually depends on the particular use or application. For example, overall performance estimates do not require the same level of certainty or accuracy as "stability" or other key operational parameters.

A simple way to distinguish the two terms is to think of "verification" as the process of solving the equations accurately and "validation" as the process of solving the "correct" equations. Here the term "correct" equations are used to indicate equations that are a "correct" or good enough representation of the real-world problem that the user or application scientist is solving. The distinction between the two terms and their

importance in being able to do credible simulations is clarified further by examining the processes that are usually adopted to conduct verification and validation or, as is often termed "V&V".

2.1 Process of Verification

As discussed above, the process of verification can be carried out solely by the software developer or person conducting the numerical simulations. The objective is to ensure that the formulated equations are solved accurately. Hence, the process involves various steps such as varying the spatial resolution (or grid size for finite difference solvers) and for unsteady problems, the temporal resolution. Assessing the dependence of the solution on the boundary conditions is often done. When possible, the solution to a simplified problem representing an important aspect of the problem of interest is conducted and compared to analytical solution or solutions obtained using other mathematical processes such as the method of characteristics. The important factor to remember is that this process is trying to ensure that the equations formulated are solved accurately in a mathematical sense. Of course, the order of accuracy desired is dependent on the problem at hand and the developer's perspective. At the end of this process, usually no claim can be made that the physical problem under consideration has been solved to the desired level of accuracy or an acceptable level of uncertainty.

2.2 Process of Validation

The process of validation involves comparison with accurate experimental data for the system of interest. It is important that the uncertainty in the experimental measurements has already been quantified. Doing rigorous comparison is relatively straightforward for a well-established propulsion system. For high-speed propulsion systems, there is a paucity of experimental data because of difficulties in reproducing high-speed flight conditions in laboratory experiments. Sometimes, actual flight test experiments are needed, and these tend to be extremely expensive and not readily accessible.

Since many high-speed propulsion systems are still under development, there is very little experimental data that is available. Furthermore, when we consider emerging concepts, often there is a reluctance to develop test articles and conduct experiments when there is significant uncertainty in the value of the relatively new concept. This makes the task of validation very difficult to conduct. This issue is explored in further detail using examples of detonation-based high-speed propulsion systems.

3 Verification and Validation of the Pulse Detonation Engine (PDE) Concept

Detonation-based engines are devices that harness the explosive power of detonations to attain very high speeds at very good efficiencies. It has been well established that on a thermodynamic basis, the energy conversion efficiency of detonations is typically more than twenty-five per cent greater than the flaming or deflagrative combustion mode used in conventional propulsion systems. The challenge has been in harnessing the thermodynamic efficiency for propulsive power. At the turn of this century, several estimates were published on the propulsive power of an idealistic PDE concept. The device considered is deceptively simple, consisting of a straight tube closed at one end and open at the other. Of course, a flight capable propulsion system will be significantly more complicated but the key combustor component is likely to be this simple tube or some variant of that. Hence, let us consider applying the ideas discussed so far in evaluating the sea-level, static performance of this idealized PDE device.

Early CFD analysis of the straight tube PDE operating at 1 atm with a stoichiometric mixture of hydrogen and air as the propellant was conducted and reported by various researchers [2, 9]. Unfortunately, the quoted performance number for the specific impulse (Isp) ranged from 1000 to 8000s. The Isp is used as a representative measure of the device performance because it has the same units of "seconds" in various systems of measurement units used in science and engineering. Such a wide variation in estimates is clearly unacceptable and none of the estimates could be "validated", since the required experimental data did not exist. Furthermore, developing and conducting experiments to obtain the required data itself became a point of debate because if the lower end of the estimates was the "correct" one, it would not be worthwhile to invest in further exploring this concept. To resolve this uncertainty, it was decided to conduct basic research to try to understand the reasons for the differences in performance estimates and to get a better estimate of the performance of this idealized engine.

3.1 Verification of Idealized PDE Simulations

Initially, one-dimensional simulations of the idealized PDE operating on hydrogen and air were conducted. Both temporal and spatial resolutions were varied to obtain solutions that did not depend significantly on these parameters. Further verification studies identified the boundary conditions used at the open end of the tube to be a potential issue. The flow out of the tube is initially supersonic as the detonation wave leaves the tube as a non-reactive shock but the flow slows down to subsonic speeds as the products of detonation are exhausted from the tube. The processes are illustrated in Fig. 1. Specifying boundary conditions for the supersonic phase is unambiguous, but the subsonic phase is more complicated. When the outflow is

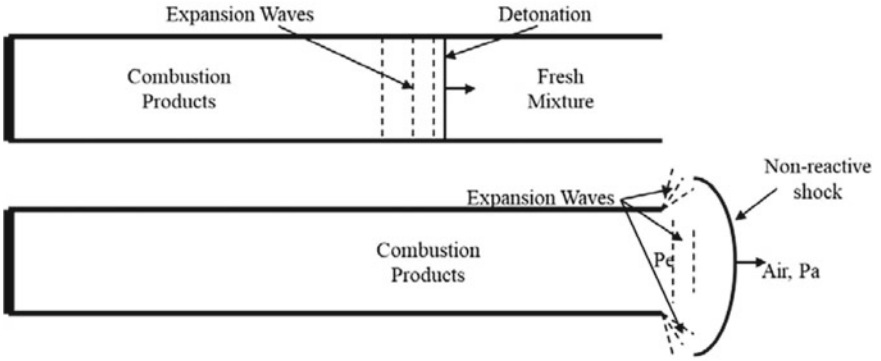

Fig. 1 Flow field inside and just outside an idealized PDE tube illustrating the difficulty of specifying boundary conditions at the open end of the tube

subsonic, any disturbance in the entire region outside the tube can communicate with the end of the tube and affect the outflow process. During subsonic flow, typical boundary conditions used have an expansion term which determines the rate at which the flow at the exit plane reaches the ambient conditions. By varying this expansion rate, various performances will be obtained [10]. Therefore, it appears that the wide variation in the estimated performance may be due to the different rates of expansion implied by the particular boundary conditions used. This point is further illustrated in Fig. 2, where the time variation of the head-end pressure is shown for three arbitrary choices of the boundary conditions. The areas under each of the curves are a measure of the performance. The impact of the three choices for the boundary conditions on the computed specific impulse (Isp) is illustrated in Fig. 3. While there are other factors that are different in the various performance estimates [10], the choice of parameters in the boundary condition alone can explain the wide variation in the reported performance. This example clearly illustrates the importance of

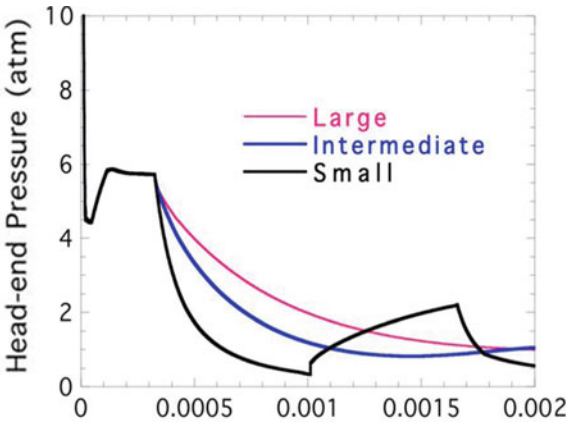

Fig. 2 Impact of choosing various boundary conditions on the time history of the head-end pressure

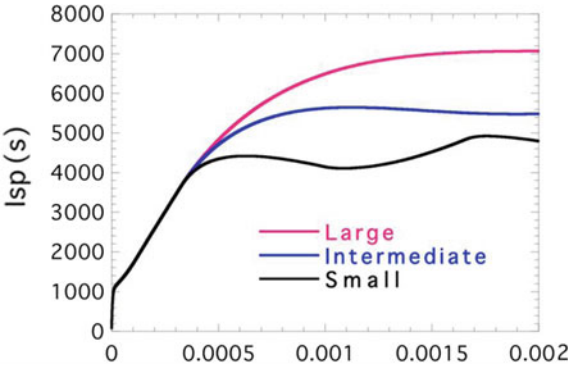

Fig. 3 Impact of choosing different boundary conditions on the computed specific impulse

systematically conducted verification studies that include testing the dependence of the solution on the boundary conditions used.

Reducing the Impact of Outflow Boundary Conditions The above discussion highlights the impact the choice of the open or outflow boundary condition can have on the computed performance but does not provide an answer to the "correct" choice. As mentioned earlier, verification involves solving the equations correctly. From the developer's point of view, each of the above solutions may be viewed as mathematically "correct" solutions to the specific set of formulated equations and the specific choice of the boundary conditions. In order to determine the solution desired by the user, we need to eliminate or reduce the impact of the choice of the outflow boundary condition.

One approach would be to avoid having to specify the outflow boundary conditions at the outflow of the tube, by making the tube exit interior to the computational domain and hence not a boundary. For the straight tube PDE, this can be done by extending the computational domain to include the exit plane of the tube as well as the regions around it as illustrated in Fig. 4. Of course, this requires multidimensional numerical simulations. The computational cost can be reduced by the judicious use of the grid points since not all regions outside the tube require the same amount of numerical resolution, as the region just near the exit of the tube. Such simulations have been carried out [11], and a closer examination of the flow just outside the tube highlights the complexity of the outflow and its strong temporal dependence. The computed performance estimate from such multidimensional simulations is 4161s for the PDE operating on a stoichiometric hydrogen–air mixture. Of course, this is still to be viewed as a good, "verified" theoretical estimate only. How well this estimate corresponds to physical reality can only be determined by conducting appropriate laboratory experiments. The physics (and chemistry) represented in the numerical model may not be a good enough representation of the "physical" reality. Hence, the importance of "validation studies" is following our verification studies.

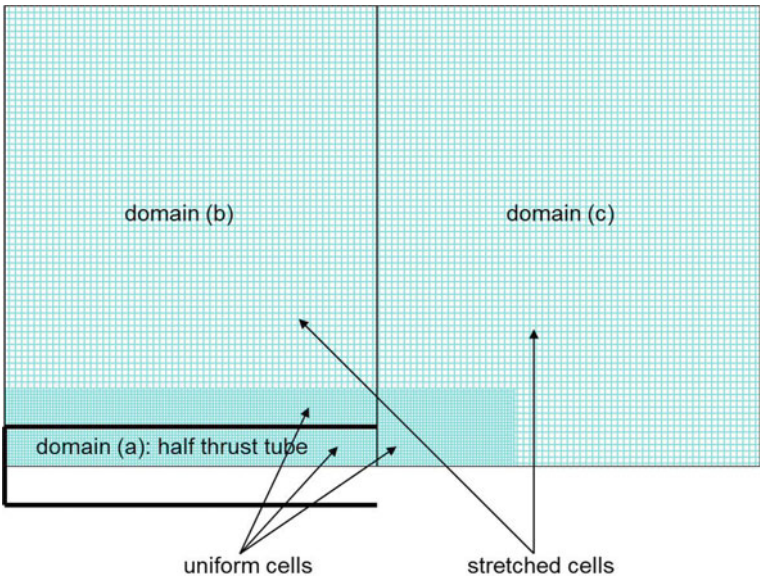

Fig. 4 Computational domain for multidimensional simulations where boundary conditions are not specified at the exit plane of the tube

3.2 Validation of Idealized PDE Simulations

Validation studies involve comparison of the results of numerical simulations to data from experimental measurements. Hence, they require external participation from scientists or engineers who have the skill and facilities to conduct the relevant experiments. It is important to remember that these validation experiments need to be conducted in a geometry as close to those used in the simulations, with similar initial conditions and boundary conditions. One may not think of "boundary conditions", when conducting experiments but it is important to keep that in mind. For example, for the idealized PDE discussed above, having a flat plate at some nearby distance away from the exit plane or connecting a flexible hose at the exit end of the tube to exhaust the products outside the laboratory facility will have some impact on the resulting measurements. Similarly, the method used to initiate detonations could also impact the measured performance. Ideally, there should be some coordination between the experimentalist and computational scientist for effective validation studies.

Such validation experiments [12, 13] were conducted at Stanford University in the USA. In their experimental set-up, the tube exhausted into a very large drum, thus mimicking the set-up used in the numerical simulations. Furthermore, initial validation experiments were conducted with easily detonable mixtures so that the impact of the initiation process can be minimized. The measured head-end pressure (pressure at the closed end wall of the tube) from which the other performance

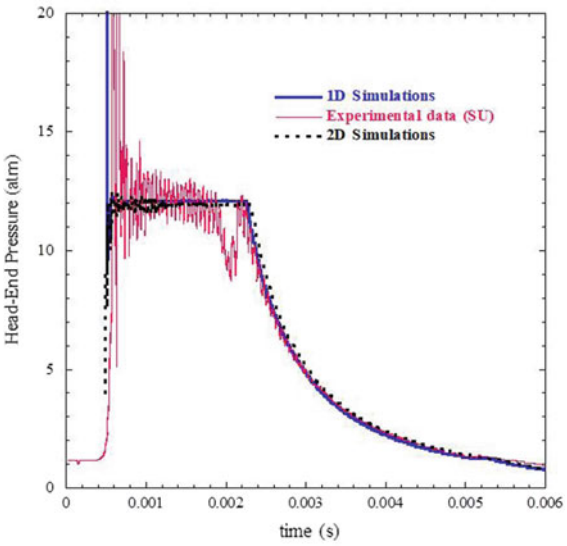

Fig. 5 Comparison of the measured head-end pressure with the predictions of one- and multidimensional simulations

measures are derived is compared in Fig. 5 to the head-end pressure predicted by the one- and multidimensional simulations.

In addition to the overall performance measures, detailed measurements of the pressure, temperature and velocity as a function of time were also made. Both the overall performance, as well as the basic physical parameters measured agreed well with the computational predictions [12, 13]. This gave confidence in the underlying physical models used in the simulations. Later, independent experiments [14] conducted at the U.S. Air Force Research Laboratory came up with a value for the Isp of 4100s for the idealized PDE operating on a stoichiometric hydrogen–air mixture, again in good agreement with the numerical predictions.

4 The Rotating Detonation Engine Concept

It is interesting and valuable to consider how the lessons learned from the verification and validation of the PDE concept can be used to evaluate another high-speed propulsion concept. Hence, the rotating detonation engine (RDE) concept is considered.

The geometry of an idealized RDE is shown in Fig. 6.

It is tempting to assume that the numerical model used for the PDE simulations can now be confidently used in RDE simulations since it has already undergone "verification and validation". But one must be cautious because the V&V process was specifically for the idealized PDE system. Yes, one can have some confidence since the underlying physics and chemistry are likely to be the same but the geometry

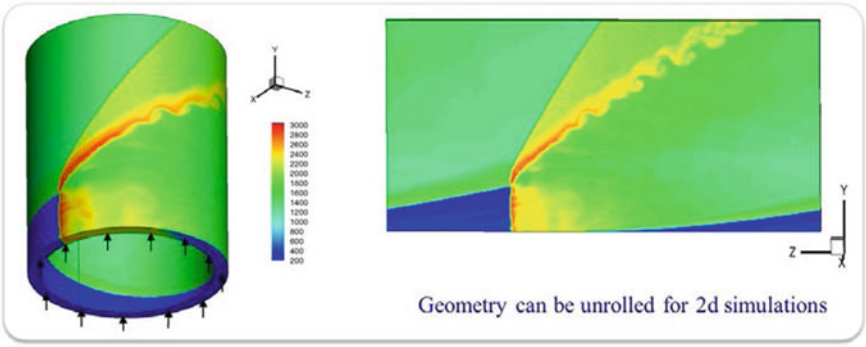

Fig. 6 Geometry of a rotating detonation engine (on the left) and the representative two-dimensional version typically used in numerical simulations

is quite different, and hence, additional verification and validation studies are needed. Indeed, further exploratory studies [15] showed that exhaust flow is quite complex and different in an RDE than in a PDE. The rotating detonation within the annular cylinder imparts a rotational component to the exhaust flow. Analogous to the PDE verification studies, the flow outside the exit of the cylindrical geometry must be captured accurately by including the domain outside the exit of the cylinder, as shown in Fig. 7. Such simulations have been carried out, and the results have been published [16]. A snapshot of the flow field identifying the key physics is shown in Fig. 8. It is anticipated that experiments to "validate" this predicted flow field will be conducted soon and published.

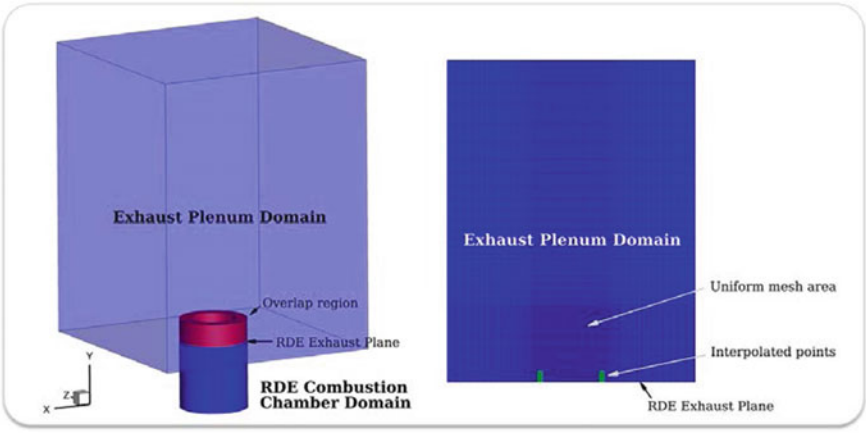

Fig. 7 Computational domain used in RDE simulations

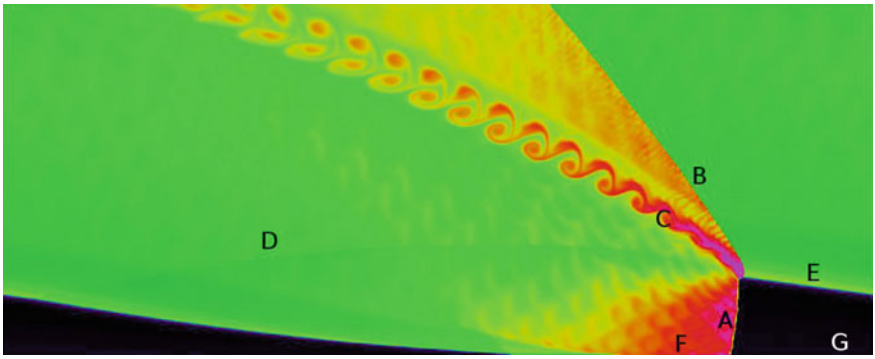

Fig. 8 Predicted flow field with the RDE. Various regions identified in the figure are **A** detonation wave, **B** oblique shock wave, **C** material slip line between freshly detonated products and older products, **D** secondary shock wave, **E** mixing region between fresh detonable mixture and detonated gases, **F** region with blocked injector nozzles and **G** fresh detonable mixture injected from below

5 Concluding Remarks

In this article, the basic concepts of verification and validation were introduced and applied to the development of a high-speed propulsion concept based on detonations, called the pulsed detonation engine (PDE). This process was taken to its logical conclusion, establishing the credibility of the simulations. Then, the concept of a related high-speed propulsion concept called the rotating detonation engine (RDE) was introduced. The lessons learned from the verification and validation of the PDE were applied to the RDE. The validation of this computed flow field is still incomplete, due to the lack of experimental data. This further highlights the role numerical simulations can play in the research and development of innovative concepts in high-speed propulsion or other disciplines. Both in the RDE as well as in other combustion or propulsion systems, heat transfer and wall effects could also play a significant role. Models representing these processes are still in their infancy and will require careful verification and validation before confident predictions can be made of the operation and performance of high-speed propulsion systems. The work discussed here can be viewed as a first but important step in achieving truly credible simulations of high-speed propulsion systems.

References

1. Kailasanath K (2000) Review of propulsion applications of detonation waves. AIAA J 38(9):1698–1708
2. Kailasanath K (2001) A review of PDE research—performance estimates. AIAA Paper 2001-0474, AIAA, Reston, VA

3. Kailasanath K (2001) A review of research on pulse detonation engine nozzles. AIAA Paper 2001-3932, AIAA, Reston, VA
4. Kailasanath K (2009) Research on pulse detonation combustion systems—a status report. AIAA Paper 2009-0631, AIAA, Reston, VA
5. Kailasanath K (2011) The rotating-detonation-wave engine concept: a brief status report. AIAA Paper 2011-0580, AIAA, Reston, VA
6. Kailasanath K (2020) Recent developments in the research on pressure-gain combustion devices. In: Gupta AK, De A, Aggarwal S, Kushari A, Runchal AK (eds) Green energy technology: innovations in sustainable energy and cleaner environment. Springer (last year's Meeting Paper) TBD, Singapore
7. AIAA (1998) Credible computational fluid dynamics simulations. AIAA J 36(5):665–764
8. AIAA Guide (1998) Guide for the verification and validation of computational fluid dynamics simulations. AIAA-G-077, AIAA, Reston, VA
9. Kailasanath K, Patnaik G, Li C (1999) Computational studies of pulse detonation engines: a status report. AIAA Paper 99-2634, AIAA, Reston, VA
10. Kailasanath K, Patnaik G (2000) Performance estimates of pulsed detonation engines. Proc Combust Inst 28:595–601
11. Li C, Kailasanath K, Patnaik G (2000) A numerical study of flow field evolution in a pulse detonation engine. AIAA Paper 2000-0314, AIAA, Reston, VA
12. Jenkins TP, Sanders ST, Kailasanath K, Li C, Hanson RK (2000) Diode laser-based measurements for model validation in pulse detonation flows. In: Proceedings of the 25th JANNAF Airbreathing Propulsion Meeting, Monterey, CA
13. Sanders ST, Mattison DW, Muruganandam TM, Hanson RK (2001) Multiplexed diode-laser absorption sensors for aeropropulsion flows. AIAA Paper 2001-0412, AIAA, Reston, VA
14. Schauer F, Stutrud J, Bradley R (2001) Detonation initiation studies and performance results for pulsed detonation engine applications. AIAA Paper 2001-1129, AIAA, Reston, VA
15. Schwer DA, Kailasanath K (2010) Numerical investigation of rotating detonation engines. AIAA 2010-6880, AIAA, Reston, VA
16. Schwer DA, Kailasanath K (2011) Numerical investigation of the physics of rotating-detonation-engines. In: Proceedings of the Combustion Institute, vol 33. The Combustion Institute, Pittsburgh, PA, pp 2195–2202

Numerical Study of Spherical and Cylindrical Shock Wave Focusing

V. S. Saranyamol, Nanda Soumya Ranjan, and Sugarno Mohammed Ibrahim

1 Introduction

1.1 Shock Focusing

Imagine a shock wave propagating from a point source. While propagating, it dissipates heat and a large amount of energy. Several reversible processes occur across a shock while propagating. Now, try to reverse the process by some means. A shock wave is developed and is getting converged to a confined point. The heat as well as energy increases rapidly while reversing the process of shock propagation. This process where a shock wave is getting focused to a point is termed as shock wave focusing (SWF). The same method is followed while doing an experiment of focussing sunlight on a paper to burn it. Compared to sunlight, there is a huge amount of energy associate with a shock.

The temperature at the focal point might increase in such a fashion that dissociation, ionization, etc. comes into picture. The gas in the high temperature region will start radiating. The radiating behaviour of the gas is of very much interest to the engineering and research world.

1.2 Application of Shock Wave Focusing

This phenomenon of shock waves converging to a point/region results in very high-energy concentration, high pressure/temperature, which is not only interesting from academic point of view but also finds practical application. A prominent application

V. S. Saranyamol · N. Soumya Ranjan · S. Mohammed Ibrahim (✉)
Indian Institute of Technology, Kanpur, India
e-mail: ibrahim@iitk.ac.in

© Springer Nature Singapore Pte Ltd. 2021

A. De et al. (eds.), *Sustainable Development for Energy, Power, and Propulsion*, Green Energy and Technology,
https://doi.org/10.1007/978-981-15-5667-8_2

is for the fusion reactions which demands high energy concentrations [1]. The high enthalpy region hitting the surface of a material can alter its molecular structural arrangement. This property is used widely for material synthesis [2], especially for diamond. The energy produced during SWF can be compared to a tiny gas bubble collapse to a huge supernova collapse [3]. When sound wave passes through a gas bubble, the bubble expands and then collapses. It radiates a large amount of energy while collapsing.

2 Experimental Methods for Shock Wave Focusing

There are several methods to obtain SWF experimentally. It includes the use of shock tubes, exploding wires, microexplosives, etc. The most reliable and stable method of SWF is with the help of shock tube. Several researchers have tried to focus cylindrical as well as spherical shock wave with the help of a shock tube. Other methods include the use of exploding wire [4] microexplosives [5], etc. Some of the experimental works done on the SWF are mentioned here.

Researches on SWF were started in the early 1940s. Guderly (1942) was the first to investigate the convergence of cylindrical and spherical shock waves analytically [6]

$$\frac{r}{r_0} = \left(1 - \frac{t}{t_0}\right)^{\alpha} \tag{1}$$

where r_0 is the initial radius at time t = 0 and t_0 is the instant of focusing when $r = 0$. α is the self-similarity exponent. It is governed by the acceleration of the shock front while converging. The value of α depends on the test gas as well as the shock properties. For air test gas, α for cylindrical shock is 0.834 and α for spherical shock is 0.717.

The first experimental study on SWF was done by Perry and Kantrowitz in 1951 [7]. They used a horizontal shock tube with a tear-drop insert in the test section to create cylindrical shocks as shown in Fig. 1. They studied converging and reflecting shocks, visualized by the schlieren technique, at two different shock Mach numbers (1.4 and 1.8). Also, a cylindrical obstacle was placed in the flow, and the result showed that the centre of convergence was displaced towards the disturbed side of

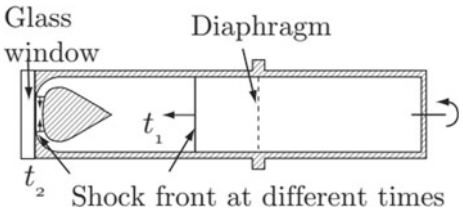

Fig. 1 Sketch of horizontal shock tube with a tear-drop insert

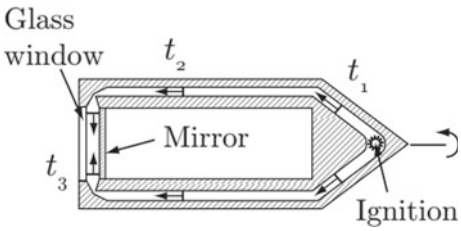

Fig. 2 Coaxial tube

the shock wave. Another interesting observation was the presence of light in the point of focusing. This was interpreted to be an indicator of the presence of high temperatures, as the radiation was believed to be caused by ionized gas.

The stability of cylindrical imploding detonation waves was further investigated by Knystautas and Lee in 1971 [8]. A coaxial tube was used and the detonation wave was initiated by a high-energy spark plug at the beginning of the tube. The setup is illustrated in Fig. 2. A cylindrical implosion chamber, with a diameter of 80 mm and a thickness of 10 mm, was mounted at the rear end of the coaxial tube. The implosion wave entered the cylindrical chamber through a converging-diverging section at the 90◦ bend to minimize the attenuation effects.

Sturtevant and Kulkarny in 1976 [9] performed experiments on plane shock waves which focused in a parabolic reflector mounted at the end of a shock tube. Different shapes of parabolic reflectors were used. Results showed that weak shock waves focused with crossed and looped fronts while strong shocks did not. It was concluded that the shock strength governed the behaviour during the focusing process and that nonlinear phenomena were important near the focal point.

Takayama et al. in 1987 [10] used horizontal annular shock tubes (Fig. 3) to investigate the stability and behaviour of converging cylindrical shock waves. The central body of the shock tube test section was given supports. These supports affected the stability of the shock wave. In order to investigate more on the effect of disturbances, they introduced cylindrical rods upstream of the test section. Takayama et al. concluded that the disturbances caused by the supports could not be suppressed by

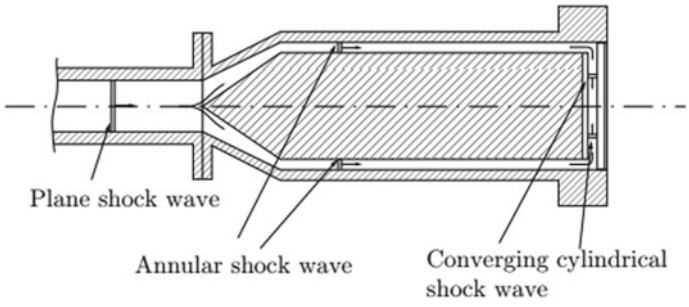

Fig. 3 Annular shock tube with 90° bend

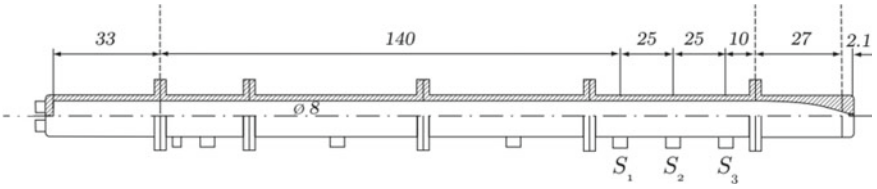

Fig. 4 Shock tube with attached converging section [11]

the cylindrical rods. Also, the instability, i.e., the deviation from a cylindrical shape, was found to be more significant for stronger shocks.

Malte [11] focused the shock wave with the help of a smooth converging transformation section attached to the shock tube. The converging section attached to the shock tube is shown in Fig. 4. There are three shock sensors (S_1, S_2 and S_3) flush mounted on the shock tube wall to obtain the shock strength. The shape of the transformation is parameterized as

$$\begin{aligned} x &= A \sin\theta \\ y &= B - R(1 - \cos\theta) \end{aligned} \tag{2}$$

where $0 \leq \theta \leq 0.35\pi$, $A = 300.7$ mm, $B = 40.0$ mm and $R = 57.3$ mm.

Investigations have reported that the shock waves accelerate, during convergence resulting in increased temperature and pressure while approaching the focal point. Due to increased temperature, light pulse was observed at the point of focusing. Photomultiplier signals were collected to study the radiations observed. Figure 5 shows a typical signal from the shock sensors and the photomultiplier. The coloured lines are of the shock sensors and black with inverted peak is from the photomultiplier.

Malte has also done numerical simulations to validate the experimental results. A detailed numerical study of converging shock is of research interest. In current work,

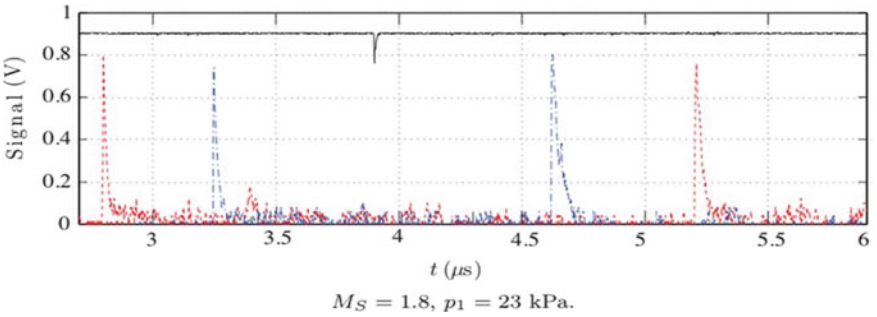

Fig. 5 Typical image from the pressure sensors and photomultiplier [11]

an attempt to study the detailed shock behaviour in a similar converging section is made. Cylindrical as well as spherical shock behaviour is analyzed with the help of CFD software ANSYS-Fluent.

3 Computational Method

Unsteady, density-based inviscid, two-dimensional simulations were carried out using commercially available CFD software ANSYS-Fluent. Simulations were carried out using explicit formulation and convective flux is calculated with AUSM. Two-dimensional planar simulations were performed to study the cylindrical shock convergence and two-dimensional axisymmetrical simulations to study the spherical shock convergence. The detailed discussion of the computational methodology is discussed in the following section.

3.1 Computational Domain

For the current simulations, a shock tube having 2 m driver section, 6 m driven section attached with a 296 mm converging segment has been used. The contoured converging test section for the present case is designed as per the geometric relations used by earlier researchers [10], with an intention to have minimum diffusion of the shock while focusing. Moreover, in order to have comparison with analytical solutions, 26 mm from the end of the converging part has been designed as a conical section having 21° semiapex angle. The exit diameter of the convergent section has been considered as 0.06 mm.

From the x-t diagram analysis, it was observed that the effect of the contact surface is not interrupting with the flow, and accordingly, the computational domain length was reduced. This helped to reduce the computational cost to a large extend. The modified computational domain is shown in Fig. 6. Here, a part of the driven section of the shock tube and the attached converging section is considered. Region 2 in figure corresponds to conditions across the incident shock of strength M_s. Region 1 corresponds to the conditions in the driver section of the shock tube, which is explained in Table 1.

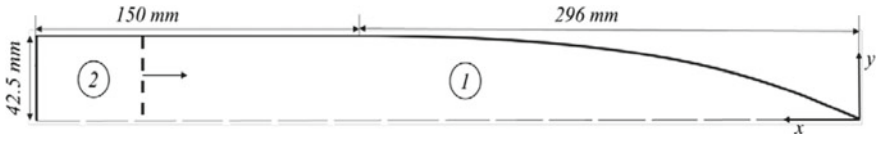

Fig. 6 Considered computational domain with dimensions

Table 1 Shock tube operating conditions

	Driver section	Driven section
Press (bar)	40	1/0.1
Temp (K)	293	293
Test gas	He/air	Air

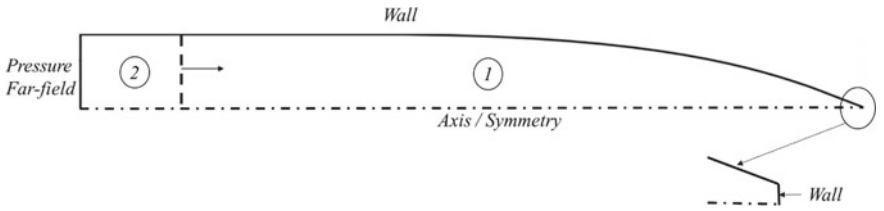

Fig. 7 Boundary conditions for the flow domain

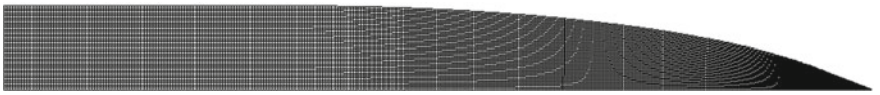

Fig. 8 Meshing of the computational zone

Simulations with spherical shock convergence were achieved with axis boundary condition to the bottom wall. Due to nature of existing domain, by assigning symmetry boundary condition to bottom wall, cylindrical SWF was obtained. The boundary condition given is illustrated in Fig. 7. Conditions behind the incident shock are given for the pressure farfield boundary at the inlet.

Meshing of the computational domain is carried out by quadrilateral mapped facing method with bias factor given to the zone of interest viz. converging section. As a result of the grid independence study, total number of cells is estimated to be 15,960. Meshing of the entire domain is presented in Fig. 8.

4 Test Conditions

Inviscid simulations were carried out for current work. Due to the transient nature of the problem, time step is also varied to arrive at an optimal value, which is set to 1e−7 for all the test cases. Different driver gas condition viz. air/helium at a pressure of 40 bar and driven gas condition with air at 1/0.1 bar pressure have been simulated for the present investigation. Corresponding to these conditions, Rankine–Hugoniot relation is used to obtain the flow properties associated with incident shock processed test gas. These properties are further used for initialization and providing

Table 2 Test cases for simulations

	He–air		Air–air	
	Case 1	Case 2	Case 3	Case 4
Driver gas pressure (P_1 bar)	0.1	1	0.1	1
Shock Mach number (M_s)	4.6881	2.9274	2.8464	2.0576
Pressure in region 2 (P_2 bar)	2.5475	9.8314	0.92853	4.7726
Temperature in region 2 (T_2 K)	1527.0	760.2143	733.2717	508.3088
Mach number in region 2 (M_2)	1.6334	1.3378	1.3143	0.9943
Velocity in region 2 (U_2 m/s)	1279.5	739.3612	713.3984	449.3561

inlet boundary condition for the domain marked as region 2 in Fig. 8. Table 1 shows the operating conditions used for the present work.

According to these conditions, four different test cases were simulated. Table 2 shows the various test cases and the shock strength of the initial planar shock produced in the shock tube.

4.1 Validation of Results

The unsteady flow parameters behind the spherical and cylindrical shock wave primarily depend upon the shock strength and temporal variation of shock location. Therefore, location of shock wave with respect to time for both the cases in the conical region is investigated, which is shown in Fig. 9. For comparison purpose, self-similar curves pertaining to Guderley's solution (Eq. 1) has also been plotted in this figure. Here, r_0 represents the starting location of the conical section where as

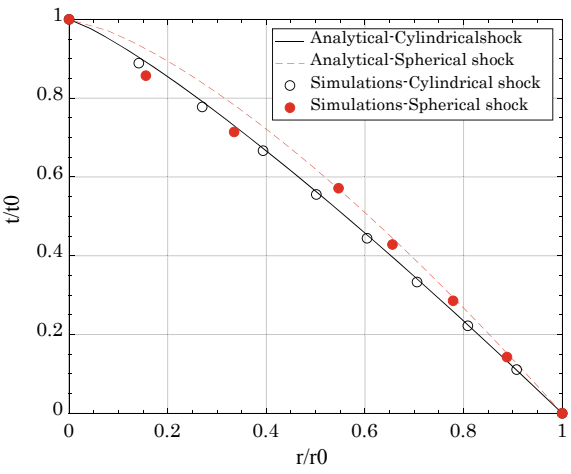

Fig. 9 Comparison of shock path of the focussing wave

t_0 corresponds to the time when shock wave reaches at this section. With respect to these reference values, for any value of $r < r_0$, corresponding 't' can be found out using Eq. 1. The value of self-similarity constant (α) for spherical shock and cylindrical shock propagation in air is considered to be 0.7171 and 0.8353, respectively [12]. Noticeable agreement between the analytical solution and simulation has been observed for the cylindrical SWF. Similarly, for spherical SWF also good match is perceived except for some discrepancy in the near end wall region.

5 Results and Discussion

As a result of the above mentioned simulations, transient variation of static temperature at specified points, Mach number distribution along the length of the converging section has been monitored. Perfect gas simulations were carried out with all the cases and real gas effects were added to a case of spherical convergence. Figure 10 depicts the variation in shock structure as it traverses along the convergent section. It can be perceived that the normal shock front starts curving as soon as it enters the converging section and becomes apparently circular with downstream propagation. This numerical schlieren image seems to be same irrespective of the nature of SWF. However, it has been observed that the shock speed is more in case of the axisymmetric simulation in comparison to the symmetry one.

Further, the temporal variation of temperature inside the convergent section is monitored at specified points viz. 85.9 and 22.5 mm from the end wall and as well as exactly at the end wall. It can be observed from Fig. 11 that, with propagation of spherical and cylindrical shock wave down the converging section, the magnitude of primary temperature rise due to incident shock is merely same for all the locations. However, upon reflection of the incident shock, the temperature rise becomes significant, which is around 7000 K near the end wall. The current simulation is 2D planar simulations for Case 3. The incident shock as well as the reflected shock can

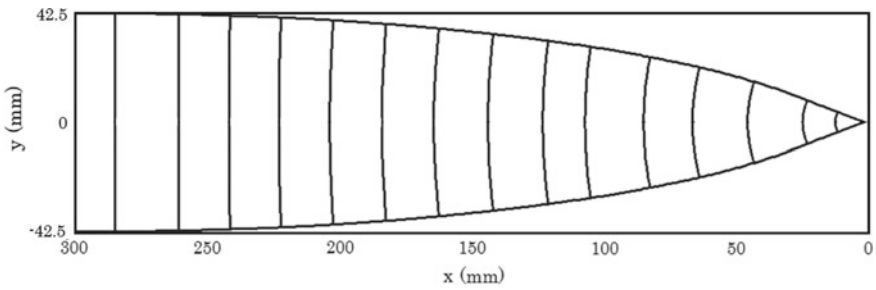

Fig. 10 Shock trajectory inside the converging section

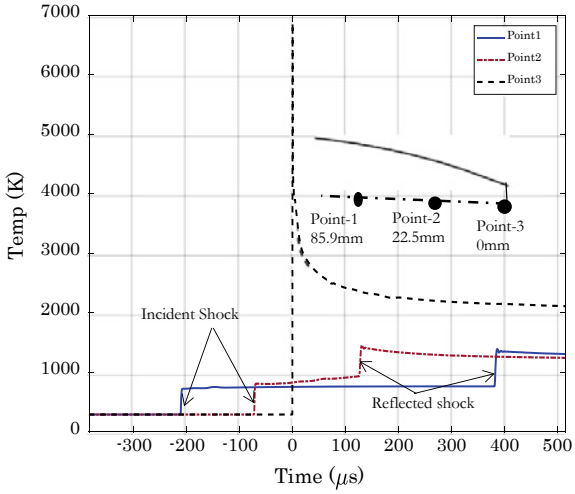

Fig. 11 Temporal variation of temperature in the convergent section

be observed from the figure at point 1 and 2. The cylindrical as well as spherical SWF was simulated for all the test cases as per Table 2, and the results are explained in the proceeding sections.

5.1 Cylindrical Shock Convergence

Results of cylindrical SWF are described in this section, which was achieved from 2D planar perfect gas simulations. Figure 12 shows the instantaneous density contour of the converging shock at two instances, −30 μs and −11 μs.

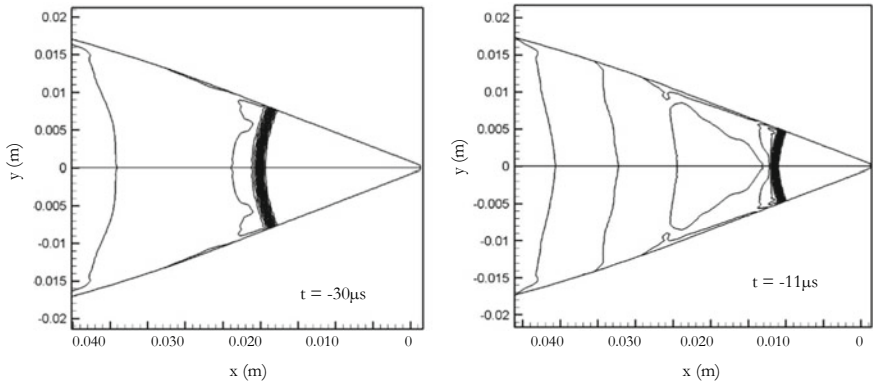

Fig. 12 Instantaneous density contour of cylindrical SWF

In this figure, t represents the time to reach focal point. $t = 0$ μs corresponds to the instant at which the shock reaches the end point of the converging section. The shape of the shock while propagating through the converging section can be traced from the figure. The temperature monitored at the end point of the converging section is shown in Fig. 13. The temperature is found to be maximum for case 1. This is expected since the strength of the shock for this case is larger when compared to the other cases, which can be observed from Table 2.

The acceleration of cylindrical shock front inside the convergent section is estimated for all the test cases. In view of this, Mach number along the central axis has been plotted in Fig. 14 for cylindrical SWF. It has been observed that irrespective of the driver gas and filling conditions in the driven section, most of the shock strengthening occurs in the conical section placed at the end. Nearly, circular shape of the incident shock at the end can be attributed for the rapid increase in Mach number. Trend of Mach number variation is found to be independent of operating parameters; however, the magnitude seems to be higher for helium as driver gas and driven section filling pressure of 0.1 bar.

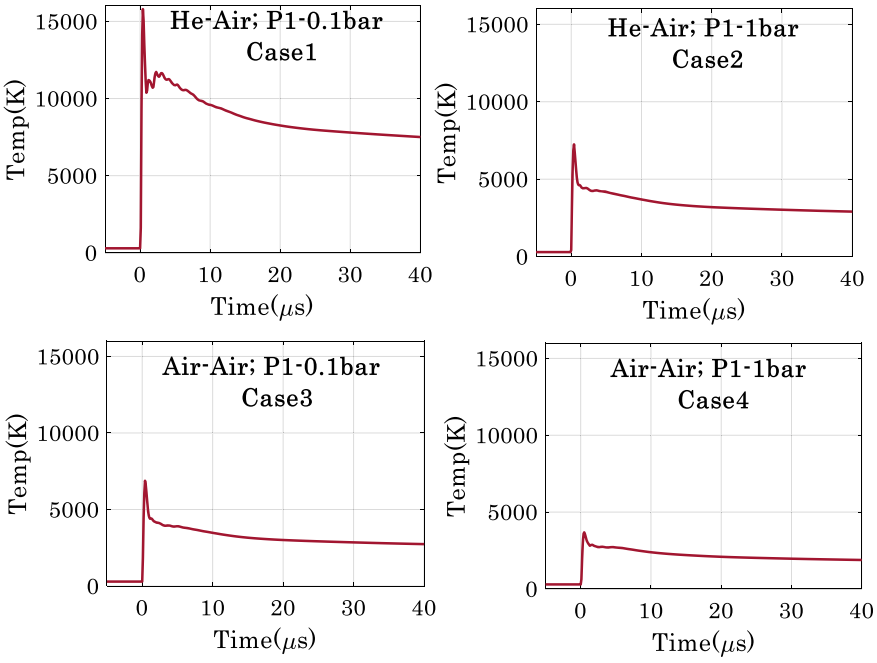

Fig. 13 Temperature distribution at the end point for cylindrical SWF

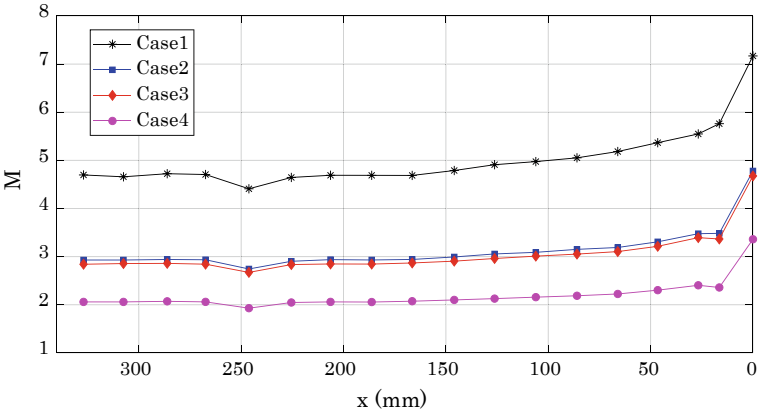

Fig. 14 Mach number variation within the converging section for cylindrical SWF

5.2 Spherical Shock Convergence

In order to obtain the spherical SWF, 2D axisymmetric simulations were carried out. The perfect gas simulation results of all the four cases are described in this section. Figure 15 shows the instantaneous density contour. Compared to Fig. 13, the shock moves much more faster while converging spherical shock. This can be observed from the time mentioned in the figure.

Figure 16 shows the temperature concentration at the converging section end wall. For most cases, more than 50% increment in maximum temperature is observed for spherical SWF. An increased temperature of 40,000 K is observed for incident shock strength of Ms 4.68.

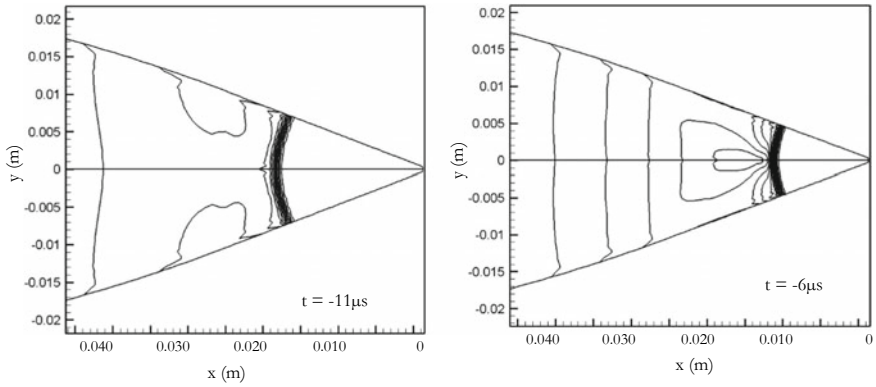

Fig. 15 Instantaneous density contour of spherical SWF

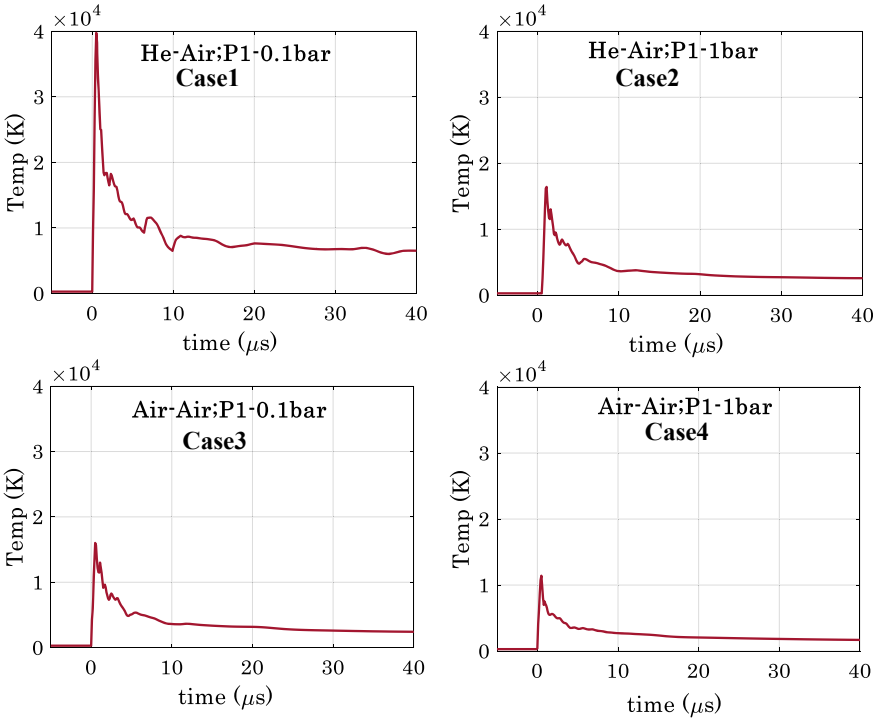

Fig. 16 Temperature distribution at the end point for spherical SWF

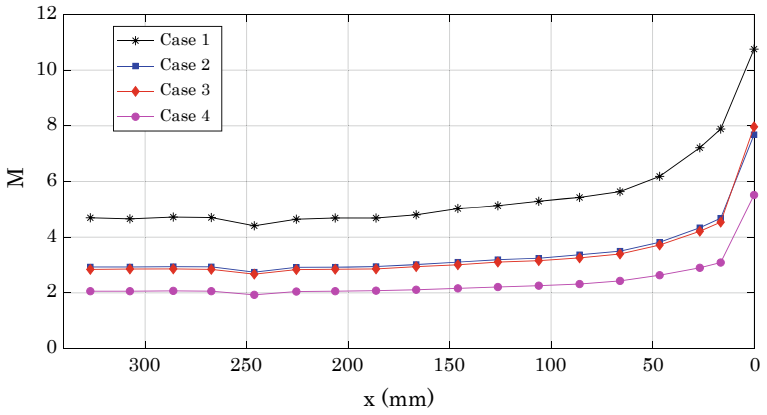

Fig. 17 Mach number variation within the converging section for spherical SWF. **a** Case 1. **b** Case 2

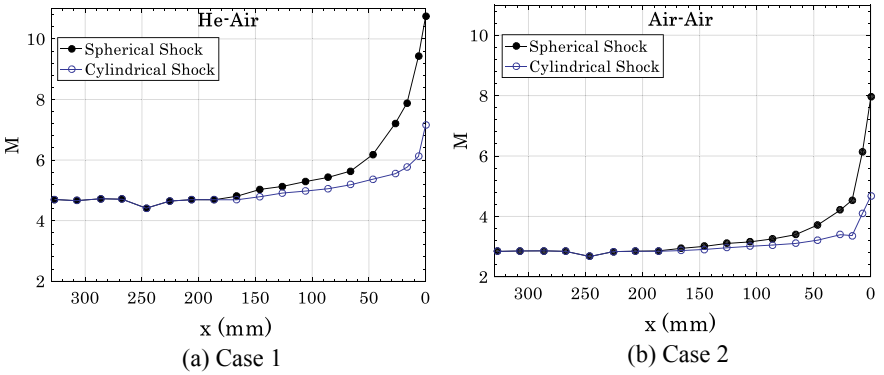

Fig. 18 Comparison of shock Mach number for cylindrical and spherical shock forms

Figure 17 shows the Mach number variation along the central line for all the cases. The Mach number of the shock, i.e., the shock strength, increases once it enters the converging section. This was same to that observed for the cylindrical shock case. While comparing spherical shock and cylindrical shock convergence together, the increased shock strength of the spherical shock is clearly distinguishable. This is depicted in Fig. 18.

The temperature the point of SWF is a large enough for ionization, dissociation, and other high temperature effects to occur. Hence, reaching a conclusion without considering real gas effects is difficult.

5.3 Real Gas Effects

All the above simulations have been performed with assumption of perfect gas, which will not be valid for actual experimental condition. Therefore, in view of accurate estimation of flow properties during focusing of shock fronts, real gas simulation in conjunction with high temperature effects is carried out and the results are shown in this section. The real gas simulations were carried out for spherical SWF for case 3. The variation of specific heat at constant pressure (C_p) was assumed to be piecewise-polynomial with respected to temperature [14]. The reaction parameters required for the simulations were taken from literatures [13]. Since the test gases for current simulations are air, oxygen, and nitrogen dissociation and combination reactions were considered, as mentioned in Table 3. All these considerations results in a reduction in the actual temperature obtained during SWF. Figure 19 shows the temperature comparison for both the simulations. 47% reduction in temperature is obtained with including the high temperature real gas effects. Figure 20 shows the Mach number comparison for the same test case. Due to the reduction in temperature, a reduction in shock strength is also achieved while the shock reached at the end wall of the converging section.

Table 3 Chemical reactions included

Reaction name	Reaction	Third bodies
O_2 dissociation	$O_2 + M = 2O + M$	O_2, N_2, NO, O, N
N_2 dissociation	$N_2 + M = 2N + M$	O_2, N_2, NO, O, N
NO dissociation	$NO + M = N + O + M$	O_2, N_2, NO, O, N
N_2–O exchange	$N_2 + O = NO + N$	–
NO–O exchange	$NO + O = N + O_2$	–
N_2–N exchange	$N_2 + N = 3N$	–
O_2–O exchange	$O_2 + O = 2O + O$	–
O_2–O_2 exchange	$O_2 + O_2 = 2O + O_2$	–
O_2–N_2 exchange	$O_2 + N_2 = 2O + N_2$	–
N_2–N_2 exchange	$N_2 + N_2 = 2N + N_2$	–

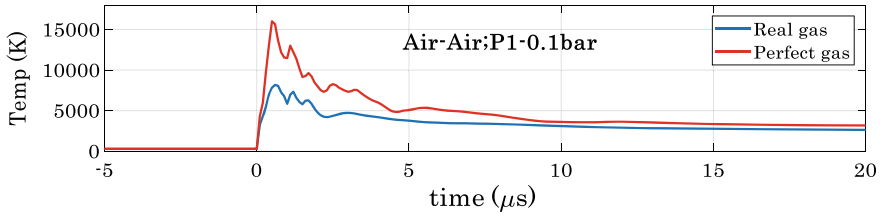

Fig. 19 Temperature comparison for real gas and perfect gas simulations

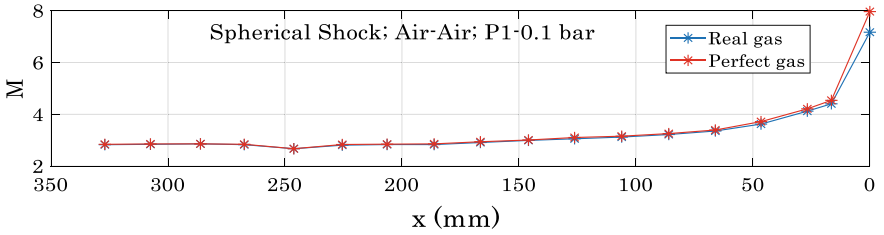

Fig. 20 Mach number comparison for real gas and perfect gas simulations

The initial mass fractions of nitrogen and oxygen were specified as per that present in air. The initial mass fractions of nitrogen atom, oxygen atom, and nitric oxide were set to zero during initialization of the flow domain. The reactions considered in Table 3 are having different activation energies. The rate of reaction mainly depends on its activation energy. At the time of focusing, the mass fraction of each species is varying due to variation in flow properties. The species mass fraction variation is given in Table 4. The mass fraction of nitrogen and oxygen has reduced by 15% and 64%, respectively during the time of focusing. At this instant, the mass fraction of N, O, and NO has increased. Presence of NO at the focusing region is considerable. This may be due to the higher activation energy required for NO dissociation.

Table 4 Mass fraction distribution of species during the focusing process

Species	Mass fraction before focusing	Mass fraction during focusing
N_2	0.78	0.6627
O_2	0.22	0.079
N	0	0.00101
O	0	0.01029
NO	0	0.249

6 Conclusion

During the current investigation, numerical simulation of a shock tube with attached converging section has been carried out successfully to create flow features which resembles spherical and cylindrical SWF. For both the SWF methods, numerical simulations were able to predict the accurate shock path in agreement with analytical solutions. It has been noticed that spherical SWF is having higher acceleration inside the convergent section. As a result, incident shock Mach number and static temperature magnitudes are found to be significantly higher for spherical SWF than the cylindrical one. With helium as driver gas and initial pressure of driven section as 0.1 bar seems to have higher magnitude of flow parameters among several other combinations. While considering the real gas effects, a reduction is maximum temperature is observed at the point of SWF. This also results in a reduction in the overall strength of the shock.

Acknowledgement The research was supported by Science and Engineering Research Board (SERB), India, through Early Career Research Grant, ECR/2018/000678.

References

1. Glass II, Sagie D (1981) Application of explosive-driven implosions to fusion. Phys Fluids 25:269
2. Glass II, Sharma SP (1976) Production of diamonds from graphite using explosive-driven implosions. AIAA J 14:402–404
3. Brenner MP, Hilgenfeldt S, Lohse D (2002) Single-bubble sonoluminescence. Rev Mod Phys 74
4. McGrath JR (1966) Exploding wire research 1774–1963. NRL Memorandum Report 1698, US Naval Research Laboratory
5. Hosseini SHR, Takayama K (2005) Implosion of a spherical shock wave reflected from a spherical wall. J Fluid Mech 530:223–239
6. Guderley G (1942) Starke kugelige und zylindrische Verdichtungsstöße in der Nähe des Kugelmittelpunktes bzw. der Zylinderachse. Luftfahrtforschung 19:302–313
7. Perry RW, Kantrowitz A (1951) The production and stability of converging shock waves. J Appl Phys 22:878–886
8. Knystautas R, Lee JHS (1971) Experiments on the stability of converging cylindrical detonations. Combust Flame 16:61–73

9. Sturtevant B, Kulkarny VA (1976) The focusing of weak shock waves. J Fluid Mech 73:651–671
10. Takayama K, Kleine H, Grönig H (1987) An experimental investigation of the stability of converging cylindrical shock waves in air. Exp Fluids 5:315–322
11. Malte K (20012) Energy concentration by converging shock waves in gases. Technical Report, KTH Mechanics, Royal Institute of Technology, Sweden
12. Ramsey SD, Kamm JR, Bolstad JH (2012) The Guderly problem revised. Int J Comput Fluid Dyn 26(2):79–99
13. Desai S, Kulkarni V, Gadgil H (2016) Delusive influence of nondimensional numbers in canonical hypersonic nonequilibrium flows. J Aerosp Eng 29(5)
14. See http://combustion.berkeley.edu/grimech/data/thermotable.html for information about temperature-dependent Cp of various gaseous species

Renewable Fuels

Renewable Energy Derived from Water Hyacinth Through Hydrothermal Gasification

Somrat Kerdsuwan and Krongkaew Laohalidanond

1 Introduction

Renewable energy is one of the alternative energy that can replace fossil energy such as coal, oil and natural gas whose resources are limited. The utilization of renewable energy has been increased every year. World Bioenergy Association reported that the share of renewable energy in total world energy consumption varied between 16.7 and 17.9% during 2000–2016, as listed in Table 1 [1]. Among all renewable energy sources, biomass had the highest share of 13% in global energy consumption in 2016 [1], as shown in Fig. 1.

Biomass is mostly used as renewable energy because it is clean and environmentally friendly, and carbon dioxide (CO_2) generated during its conversion process is absorbed by plant photosynthesis [2]. Therefore, biomass is considered to be CO_2 neutral.

As most of the countries in Asia and Africa are agricultural countries and there are a lot of forestry areas, these two continents have the largest share of primary energy supply from biomass compared to other renewable energy sources. In Africa, approximately 90% of renewable energy sources are derived from biomass and in Asia almost 70% of renewable energy sources in Asia came from biomass [1]. Biomass can be used for both heat and power production through thermal and biological process. In 2016, biomass is the third rank renewable energy sources used for electricity production, which has a share of 9% of global electricity from renewable energy, behind hydropower (68%) and wind energy (16%), while biomass has the largest share of 96% of global heat production from renewable energy [1].

S. Kerdsuwan (✉) · K. Laohalidanond
Department of Mechanical and Aerospace Engineering, King Mongkut's University of Technology North Bangkok, Bangkok, Thailand
e-mail: somrat_k@yahoo.com

© Springer Nature Singapore Pte Ltd. 2021

A. De et al. (eds.), *Sustainable Development for Energy, Power, and Propulsion*, Green Energy and Technology,
https://doi.org/10.1007/978-981-15-5667-8_3

Table 1 World final energy consumption from 2000 to 2016 (in EJ)

Year	Total	Coal	Oil	Gas	Nuclear	Renewables	Renewables (%)
2000	269	43.3	115	55.7	7.63	47.4	17.6
2005	302	57.3	15	61.1	8.20	50.6	16.7
2010	335	70.6	129	69.8	8.23	56.7	16.9
2015	358	74.6	138	73.3	7.68	63.4	17.7
2016	367	76.1	140	76.4	8.18	65.9	17.9

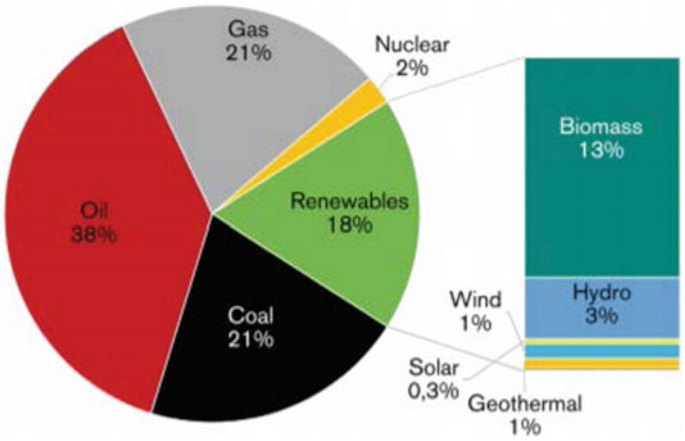

Fig. 1 World final energy consumption in 2016 by energy sources (in %) [1]

As Thailand is located in Asia and is an agricultural country, energy scenario is similar to other agricultural countries in Asia and Africa; biomass plays a prominent role among other renewable energy. Currently, Thailand has 175 biomass power plants with a total electricity capacity of 1119 MW [3], as shown in Fig. 2. Anyways, the total electricity capacity is still far from the target announced in Alternative Energy Development Plan 2015–2036 (AEDP2015), which states that the electricity produced from biomass should be increased to 5570 MW in 2036 [3]; see Table 2.

Most of the biomass fuel commercially used for power production in Thailand is rice husk, rice corncob, palm oil residues, sawdust, wood chip or bark [4], whose demand is high, leading to a very high fuel price. Therefore, many studies and researches focus on new biomass fuel which is still available and non-commercially used. Water hyacinth is one alternative to be used as bioenergy source for energy production since there are a substantial amount of water hyacinth in Thailand and South East Asia. Water hyacinth can grow rapidly in water sources resulting in excessive amounts which can obstruct drainage and water traffic or carry diseases [5]. The use of water hyacinth as bioenergy source can not only reduce its amount

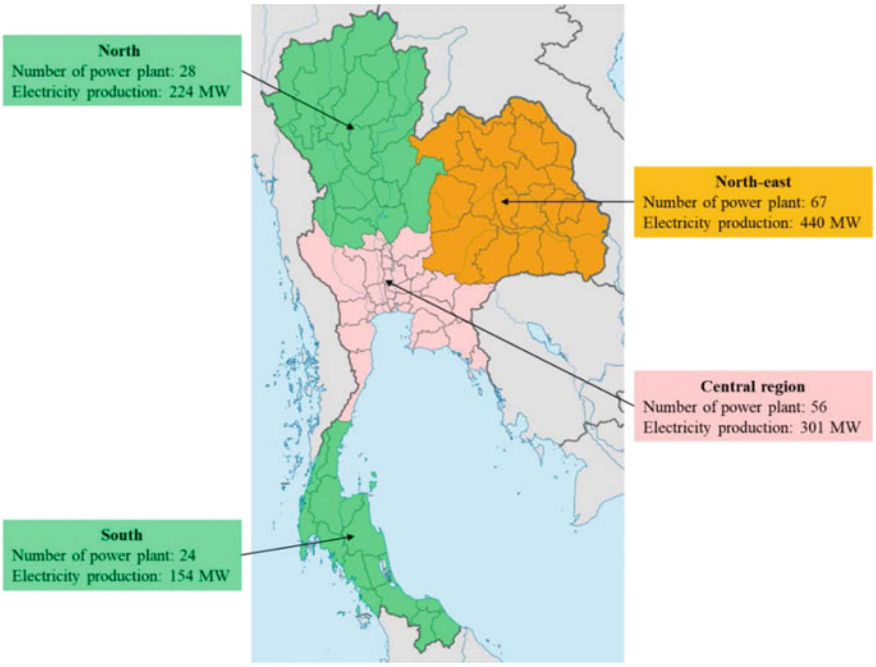

Fig. 2 Number of existing biomass power plant and capacity in Thailand by region [3]

Table 2 Renewable energy targets for electricity production of AEDP 2015 [3]

Renewable energy source	Electricity production (MW)
1. MSW	500
2. Industrial waste	50
3. Biomass	5570
4. Biogas (from wastewater)	600
5. Small hydropower	376
6. Biogas (from agricultural products)	680
7. Wind	3002
8. Solar	6000
9. Hydropower	2906.40

in water source but also convert it to energy, which can contribute to the decrease in fossil fuel import in the future.

Although water hyacinth is non-competitive bioenergy source, it has very high moisture content 86.51–92.28%wt. [6–8] which is not suitable for energy production by conventional combustion technology. This work emphasizes the hydrothermal

gasification process, which is considered to be more suitable for energy production from wet biomass. The objective of this work is to find the proper operating condition of hydrothermal gasification process for gaseous fuel production, including H_2, CO and CH_4.

2 Water Hyacinth

2.1 General

Water hyacinth (*Eichhornia crassipes*) is an aquatic plant originated from tropical or subtropical Amazon Basin. It can grow on the water surface, float and flow along the water stream. Its leaves look like a kidney or heart. There is a bouquet of light purple flowers, with the topmost petals being the largest and having yellow spots in the middle of the petals. When older, the roots of the water hyacinth have brown hair roots, brown, old and black, respectively, as shown in Fig. 3 [9, 10].

Water hyacinth can grow rapidly. It can be propagated by seeds, and one water hyacinth tree has up to 5000 seeds. When grown in water sources, these seeds can live up to 15 years and water hyacinth can reproduce up to double amount within 10 days in an appropriate environment. As it can grow very quickly, there is a substantial amount of water hyacinth on the water surface which can cause many problems. By ranking ten deadly weeds in the world, water hyacinth is in the eighth rank, as listed in Table 3.

Fig. 3 Water hyacinth

Table 3 List of the top ten deadly weeds in the world [11]

No.	Common name	Scientific name
1	Purple nutsedge	Cyperus rotundus
2	Bermuda grass	Cynodon dactylon
3	Barnyard grass	Echinochloa crus—galli
4	Jungll rice	Echinochloa colonum
5	Goose grass	Eluesine indica
6	Johnson grass	Sorghum halepense
7	Guinea grass	Panicum maximum
8	Water hyacinth	Eichhornia crassipes
9	Cogon grass	Imperata cylindrica
10	Lantana	Lantana camara

2.2 *Negative Impacts of Water Hyacinth*

As mentioned in Sect. 2.1, a large amount of water hyacinth can cause many negative impacts in a wide range, either transportation, irrigation, fishing, etc. The following will describe the negative impacts of water hyacinth [9, 12].

Transportation	Water hyacinth obstructs the waterway and can cause the accident in water traffic
Irrigation	Water hyacinth obstructs waterway, therefore water cannot drain simply resulting in flood. In addition, it also makes rivers, reservoirs or dams more shallows, resulting in less water retention
Fishing	Water hyacinth floating on the water surface can decrease light and oxygen to plunge into the water. As a result, the food of aquatic animals will decrease as well
Agriculture	Water hyacinth will be a habitat for various pests that can damage agricultural products
Public health	Water hyacinth will be a habitat for insects or other living things that carry diseases such as mosquitoes or vipers

2.3 *Use of Water Hyacinth*

Because of negative impacts of water hyacinth in various aspects, there are many attempts to get rid of them from water surface. One possibility is to make use of it. The followings are the use of water hyacinth for non-energetic purposes [9, 12].

Food and herb	Young leaves and young flowers of water hyacinth can be cooked with chili paste. In addition, it can be used as an herb for carminative, and if it was grounded into small pieces, it can be masked on ulcer to reduce inflammation
Animal food	Dried water hyacinths contain about 14–20% of protein, which has enough nutritional value to be used as animal feed such as pork and chicken
Handicraft	Wicker craft from water hyacinth, such as woven bags and woven baskets, is considered popular products. It is also an export product that generates revenue for the country
Agriculture	Water hyacinth is good water absorbent, and it has a sufficient amount of potassium, phosphorus and nitrogen. Thus, it can be mixed into manure for use as fertilizer
Wastewater treatment	Water hyacinth can be served as a bio-filter to adsorb waste or toxins in the water
Energy	Water hyacinth has also been used as fuel. Bio-charcoal produced from water hyacinth is commercially used for heating purpose

2.4 Fuel Properties of Water Hyacinth

Water hyacinth is an organic substance containing carbon and hydrogen, which can be considered as fuel. Table 4 shows the fuel properties of water hyacinth.

From Table 4, it can be seen that water hyacinth has a high amount of moisture. It contains high volatile matter (69.60–77.85%-wt.), but low fixed carbon and ash. Carbon content varies from 27.35 to 39.13%-wt., while hydrogen is amounted to 3.3–5.43%-wt. The heating value of water hyacinth is 13.26–15.54 MJ/kg. It has high potential to be used as fuel; however, it poses very high moisture content, which is not suitable to be used in thermal technology such as direct combustion technology for heat and power generation or gasification technology for producer gas production. In order to use water hyacinth for energy production, hydrothermal gasification is an alternative technology.

As water hyacinth is the lignocellulose material, it comprises three major components: hemicellulose, cellulose and lignin. Cellulose is a main component of water hyacinth which is amounted to 34.65–46.58%-wt. followed by hemicellulose, as shown in Table 5.

Table 4 Fuel properties of water hyacinth from various references

	Reference [10]	Reference [13]	Reference [14]
Proximate analysis			
Moisture[a]	92.12	8.53[b]	9.54[b]
Volatile matter[b]	69.60	76.85	77.85
Ash[b]	14.20	10.98	21.80
Fixed carbon[b]	16.20	12.17	0.35
Ultimate analysis[b]			
Carbon (C)	39.13	37.42	27.35
Hydrogen (H)	5.43	3.3	5.06
Nitrogen (N)	2.02	2.03	0.59
Sulfur (S)	0.07	–	1.15
Oxygen (O)	39.15	46.27	44.05
Ash[b]	14.20	10.98	21.80
High heating value (HHV, MJ/kg)	15.54	16.47	13.26

[a] %-wt. as received
[b] %-wt. as dry basis

Table 5 Composition of lignocellulose in water hyacinth [8]

Composition	Leaf (%-wt.)	Stem (%-wt.)
Hemicellulose	34.28	21.83
Cellulose	34.65	46.58
Lignin	1.26	1.52
Others	29.81	30.03

3 Hydrothermal Gasification

3.1 Theory

Hydrothermal gasification process is considered as a thermochemical process, in which wet biomass reacts with water under high temperature and high pressure close to its critical point (374.8 °C and at 22.1 MPa, Fig. 4).

The product of hydrothermal gasification process is mainly composed of carbon dioxide (CO_2), carbon monoxide (CO), methane (CH_4) and hydrogen (H_2) that can be used as synthetic fuel for heat and power generation or can be used for liquid or gaseous fuel production, e.g., Fischer–Tropsch fuel and dimethyl ether (DME), as shown in Fig. 5.

In the hydrothermal gasification process, water in biomass is used as reactant; therefore, no drying or dehumidification is required. Biomass is reacted with steam, called steam reforming reaction, which breaks down biomass into hydrogen and

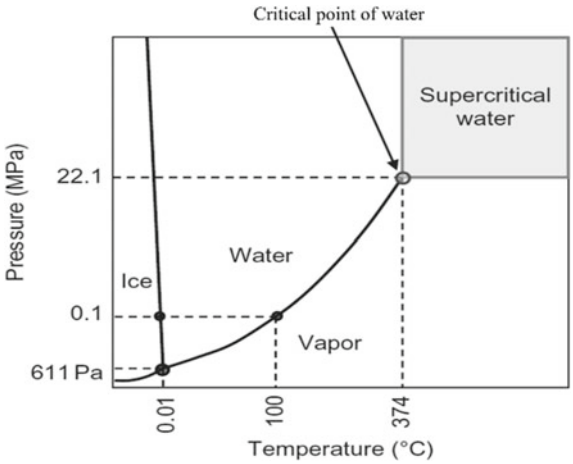

Fig. 4 Critical point of water phase diagram [15]

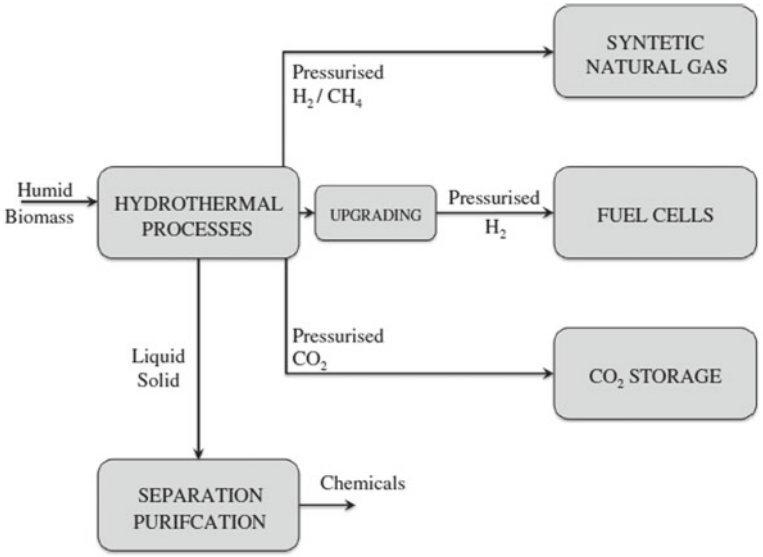

Fig. 5 Diagram for biofuel derived from hydrothermal gasification process [16]

carbon monoxide, as shown in Eq. (1). Besides steam reforming, biomass is thermally decomposed in pyrolysis reaction into gaseous products, as written in Eq. (2) [17–19].

$$C_xH_yO_z + (x - z)H_2O \rightarrow \left(x - z + \frac{y}{2}\right)H_2 + xCO \quad (1)$$

$$C_xH_yO_z \rightarrow CO + H_2 + C + C_mH_n + CO_2 + \text{other} \quad (2)$$

Further reactions relevant to the hydrothermal gasification process are water–gas shift, CO-methanation, CO_2-methanation and Boudouard reaction, which are described below.

Carbon monoxide is converted into carbon dioxide and hydrogen by reacting with water, called water–gas shift reaction, as shown in Eq. (3) [17–19].

$$CO + H_2O \rightarrow CO_2 + H_2 \quad \Delta H = -41.2\,\text{kJ/mol} \quad (3)$$

The reaction that carbon monoxide and carbon dioxide are converted into methane gas is called CO-methanation, as described by Eq. (4) and CO_2-Methanation, in Eq. (5) [17–19].

$$CO + 3H_2 \leftrightarrow CH_4 + H_2O \quad \Delta H = -206\,\text{kJ/mol} \quad (4)$$

$$CO_2 + 4H_2 \leftrightarrow CH_4 + 2H_2O \quad \Delta H = -165\,\text{kJ/mol} \quad (5)$$

The Boudouard reaction is a reversible reaction that will convert carbon monoxide into carbon and carbon dioxide as Eq. (6) [17–19].

$$2CO \leftrightarrow C + CO_2 \quad \Delta H = +172\,\text{kJ/mol} \quad (6)$$

Equations (3)–(6) are reversible reactions. The direction of the reaction depends on the operating conditions of the process.

3.2 Literature Review on Hydrothermal Gasification

Deniz et al. [17] studied the effect of biomass to water ratio and temperature on the hydrothermal gasification of sea grass (Posidonia oceanica). In the experiments, sea grass of 0.6, 0.9, 1.2, 1.5 and 1.8 g was mixed with deionized water of 15 ml and introduced into a batch-type vessel with a volume of 100 cm^3. The reaction time was 1 h at 400 °C without catalyst. The best ratio of biomass to water in order to achieve the highest molar fraction of hydrogen and the highest hydrogen yield was 0.08 g/ml (or 1.2 g seagrass).

Then the experiment was conducted using a biomass loading ratio of 0.08 g/ml at different temperatures. The amount of methane and hydrogen increased, and the amount of carbon dioxide decreased when the temperature raised from 300 to 600 °C. The maximum yield of hydrogen and methane was 10.37 and 6.34 mol/kg at 600 °C, respectively [18].

Cengiz et al. [20] studied the effect of temperature and pressure of hydrothermal gasification on the formation of hydrogen and methane gas by using sawdust from

pine and fir tree. The operating condition is at a temperature of 500 and 600 °C and a pressure ranging between 20.0 and 42.5 MPa without and with catalyst (K_2CO_3). Sawdust was fed into a stainless steel batch reactor with a volume of 100 ml for 1 h. It was found that when the pressure increased, methane and hydrocarbons increased while carbon dioxide, carbon monoxide and hydrogen gas decreased. The amount of gas yield from hydrothermal gasification at 600 °C was higher that its amount at 500 °C for all the pressure and the use of catalyst contributed to more gas yield.

Suraphong [21] studied the hydrothermal process of water hyacinth briquettes in an updraft and a downdraft gasifier. Twelve kg of water hyacinth briquettes was introduced into the gasifier for 120 min. Air flow rate was adjusted to 3.59×10^{-3} m^3/s, 4.31×10^{-3} m^3/s and 5.03×10^{-3} m^3/s for an updraft gasifier and 2.33×10^{-3} m^3/s, 3.42×10^{-3} m^3/s and 4.66×10^{-3} m^3/s for a downdraft gasifier. It can be seen that a maximum heating value of 4545.9 kJ/Nm^3 could be obtained by using the updraft gasifier at an air flow rate of 4.31×10^{-3} m^3/s. For the downdraft gasifier, the optimum air flow rate was 3.42×10^{-3} m^3/s, at which producer gas could reach the maximum heating value of 2135.76 kJ/Nm^3.

Madenoglu et al. [22, 23] conducted the hydrothermal gasification process in a 100 ml stainless steel batch furnace at a temperature of 300–600 °C with the utilization of trona ($Na_3(CO_3)(HCO_3) \cdot 2H_2O$), dolomite ($CaMg(CO_3)_2$) and borax ($Na_2B_4O_7 \cdot 10H_2O$) as catalysts for 1 h to compare the amount of hydrogen yield from cotton stalks, tobacco rods, hazelnuts shell, almond shell and walnut shell. It was found that trona was the optimum catalyst, and the optimum temperature was at 600 °C, at which condition the hydrogen gas yield varied from 39.9 to 82.4 mol H_2/kg C in biomass, depending on feedstock.

Onwudili and partner [24] studied the hydrothermal process of three algae species: spirulina or spirulina, brown algae (Saccharina) and chlorella. The hydrothermal gasification was carried out at 500 °C for 30 min in the presence/absence of NaOH and/or Ni–Al_2O_3 as catalyst. The experimental results showed that the presence of NaOH and NaOH + Ni–Al_2O_3 led to more than twice amount of hydrogen yield compared to its amount in the absence of NaOH. Anyway, amount of hydrogen yield decreased slightly with the used of NaOH + Ni–Al_2O_3.

In the presence of NaOH alone, the maximum hydrogen yield of 11.0–15.1 mol/kg feedstock was reached.

3.3 Summary

From a literature review, it can be summarized that temperature, pressure, biomass to water ratio, catalyst and retention time play important roles and operating parameters on the hydrothermal gasification, and consequently composition and amount of producer gas yield.

Effect of temperature and pressure
Temperature is the most important factor affecting the reaction rate occurring in hydrothermal gasification process. The raise in temperature leads to the higher producer gas yield and cold gas efficiency. Regarding producer gas composition, the higher temperature results in the higher content of methane, hydrogen and carbon dioxide, but lower content of carbon monoxide. In contrast to temperature, the increase in pressure decreases the producer gas yield.

Effect of biomass to water ratio
The increase in biomass to water ratio or the concentration of biomass in feedstock has negative effect on the hydrothermal gasification process because the higher biomass to water ratio decelerates the reaction rate.

Effect of retention time
The longer retention time for hydrothermal gasification can increase the producer gas yield. This statement can be evidenced by Mettanant et al. [25], who conducted the hydrothermal gasification of rice husk at 650 °C and 30 MPa for 10–60 min. It can be clearly seen that the concentration of hydrogen and carbon dioxide was sharply increased with increasing retention time, whereas the concentration of carbon monoxide decreased.

Effect of catalyst
The presence in catalysts contributes to the hydrothermal gasification reaction, especially the thermal decomposition of long-chain hydrocarbon into short-chain hydrocarbon. With the aid of catalyst, the reaction temperature is not too high. Contrary, the very high temperature is essential for hydrothermal gasification process in the absence of catalyst.

4 Experimental Study on the Hydrothermal Gasification of Water Hyacinth Without Catalyst

The experimental study on the non-catalytic hydrothermal gasification of water hyacinth will be discussed in this section. The objective of the experiment is to study the influence of biomass to water ratio and gasification temperature on the producer gas composition, which aims to produce high heating value gaseous fuel.

4.1 Designing of the Experiment's Conditions

From the literature review, it can be seen that the hydrothermal gasification process is an appropriate process to convert wet biomass into producer gas. But almost of studies have been done in super critical conditions where the reaction temperature for the hydrothermal gasification is quite high, resulting in the high-energy consumption. In order to reduce energy consumption, the experimental conditions of a non-catalytic hydrothermal gasification were designed at subcritical water (Fig. 6).

First, the experiments were conducted at the water hyacinth to water ratio (by mass) of 1:5, 1:10 and 1:15 at the reaction temperature of 300 °C and the reaction time of 60 min in order to investigate the appropriate water hyacinth to water ratio. The experimental conditions in this step are listed in Table 6.

Then, the appropriate water hyacinth to water ratio was used in further experiments to determine the effect of reaction temperature on the producer gas composition. The reaction temperature was varied from 240 to 320 °C, with the interval of 20 °C. The reaction pressure depended on the reaction temperature. Table 7 shows the experimental conditions to determine the optimum reaction temperature for hydrothermal gasification of water hyacinth.

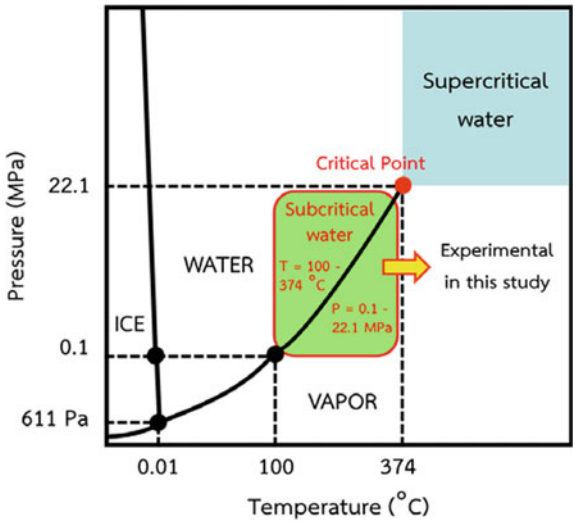

Fig. 6 Experimental conditions for subcritical hydrothermal gasification process

Table 6 Experimental conditions to investigate the appropriate water hyacinth to water ratio

Run No.	Water hyacinth: water	Reaction temperature (°C)	Reaction time (min)
1	1:5	300	60
2	1:10	300	60
3	1:15	300	60

Table 7 Experimental conditions to determine the optimum reaction temperature

Run No.	Water hyacinth: water	Reaction temperature (°C)	Reaction time (min)
4	Appropriate value resulted from run no. 1–3	240	60
5		260	60
6		280	60
7		300	60
8		320	60

4.2 Experiment Setup

Equipment used in this study was divided into three main parts: hydrothermal reactor, producer gas collection unit and gas analyzer.

Hydrothermal reactor

Batch-type autoclave reactor (Parr reactor model 4525 Bench Top Reactors) was used as the hydrothermal reactor (Fig. 7). The reaction temperature was automatically adjusted by heating element (230 V, 50/60 Hz and 5.5 A) to the maximum temperature of 350 °C with the maximum pressure of 13.1 MPa. The heating element covers at the outer surface of reactor and has the heating rate of 3 °C/min. One thermocouple type J and one pressure sensor are installed inside the reactor to measure the reaction temperature and pressure, respectively. Besides the aforementioned equipment, hydrothermal reactor is connected to control unit, coolant pipeline, cooling water pump, passages of fuel gas valves, etc., as shown in Fig. 8.

The control unit acts as an on/off device and serves to control the temperature as needed. The set value and actual value of temperature inside the reactor are shown on the display monitor

Cooling system has a function to cool the reactor. It consists of coolant pipe, made from a heat-resistant silicone rubber, and a small water pump. Cold water mixed with ice was used as coolant in the experiments to provide sufficient cooling capacity to exchange heat between reactor and environment.

Producer gas collection unit

Producer gas obtained from the hydrothermal gasification process is released from the reactor through the outlet gas valve and flows into the gas cleaning system, which consists of four impinger bottles filled with isopropanol in order to trap tars. One glass bottle containing silica gel is served to trap moisture before dry producer gas is flowing into the gas bag. Figure 9 presents the producer gas collection unit.

Gas analyzer

Hundred ml producer gas was suctioned from gas bag by glass syringe and injected into the gas chromatography (GC) model SHIMADZU GC-2014 for producer gas composition analysis (Fig. 10). The thermal conductivity detector (TCD) is a technique used to analyze the producer composition, in this study H_2, CO, CO_2 and CH_4.

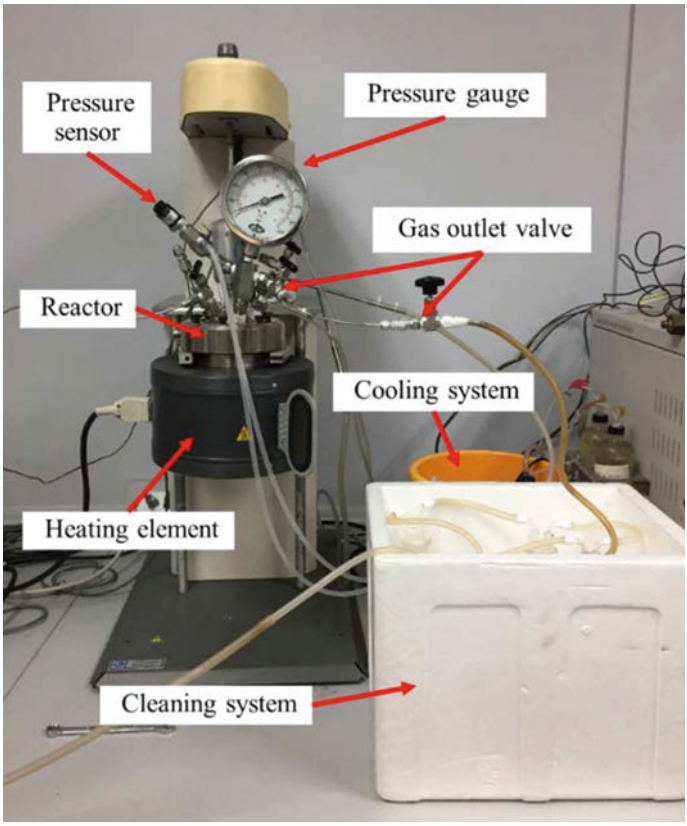

Fig. 7 Hydrothermal gasification reactor

4.3 Feedstock Preparation

Water hyacinths used in this study were collected from the Chao Phraya river, which is the major river in Thailand. The feedstock preparation process is present in Figs. 11 and 12.

4.4 Experimental Procedure

Water hyacinth was mixed with distilled water at the water hyacinth to water ratio of 1:5, 1:10 and 1:15 by mass and placed into the hydrothermal reactor. Then, nitrogen was fed into the reactor at a pressure of 2–3 bar for 30 min in order to purge the air out of the reactor. Thereafter, all valves were checked to be tightly closed, and the cooling system was connected to the reactor to dissipate heat occurring during the

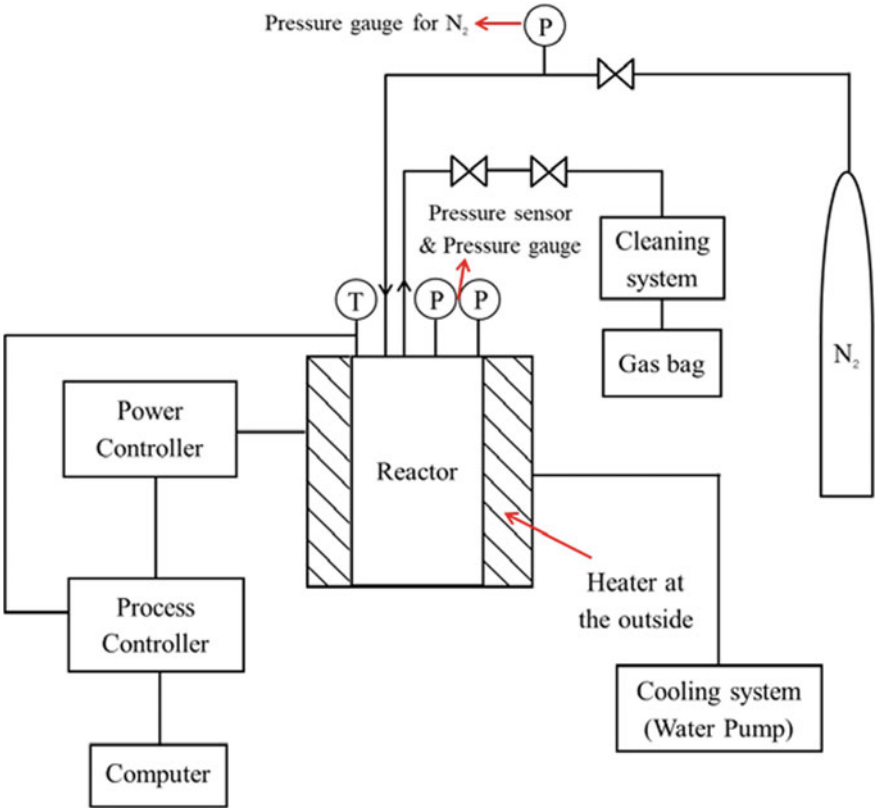

Fig. 8 Experimental setup

experiment. The reaction temperature and reaction time were set and controlled by control unit. The hydrothermal gasification was started and run for 60 min. During the experiments, reaction temperature and pressure were measured and displayed on monitor. After 60 min the experiment stopped, and the reactor was suddenly cooled down by replacing heating element with ice bath in order to prohibit the chemical reactions. At the end, the producer gas was suctioned into gas bag for producer gas composition analysis. Figure 13 shows the diagram of experimental procedure.

4.5 Determination of Lower Heating Value (LHV)

LHV of producer gas was calculated based on the composition of producer gas obtained from gas chromatography, as written in Eq. (8) [26].

$$\mathrm{LHV_{gas}} = [(30 \times \%\mathrm{CO}) + (25.7 \times \%\mathrm{H_2}) + (85.4 \times \%\mathrm{CH_4})] \times 0.0042 \quad (8)$$

Fig. 9 Producer gas collection unit

where

LHV_{gas} = Lower heating value of producer gas (MJ/Nm^3)
%CO = Concentration of CO in producer gas (%-Vol.)
$\%H_2$ = Concentration of H_2 in producer gas (%-Vol.)
$\%CH_4$ = Concentration of CH_4 in producer gas (%-Vol.)

4.6 Experimental Results

Ultimate and proximate analysis of water hyacinth
Table 8 shows the ultimate and proximate analysis of water hyacinth, as well as its heating value, both lower heating value (LHV) and higher heating value (HHV).

The results investigated in this study are corresponded to the proximate analysis and ultimate analysis of other studies which was mentioned in Table 4. From Table 8, it is remarkably seen that water hyacinth has very high moisture content and very

Fig. 10 Gas chromatography

high volatile matter content which can facilitate various reactions in the hydrothermal gasification process and can be converted into producer gas. Additionally, water hyacinth has high cellulose content but low percentage of lignin, therefore it can easily be decomposed at temperatures close to the critical temperature or above critical temperature [19].

Effect of water hyacinth to water ratio

Three different water hyacinths to water ratios of 1:5, 1:10 and 1:15 were used in this study. The reaction temperature of 300 °C and reaction time of 60 min were set as the experimental condition for all three ratios.

When using water hyacinth to water ratios of 1:5, it was found that the feedstock mixture was very dry which is not suitable for the experiment due to insufficient water content for the chemical reactions. Consequently, only water hyacinth to water ratios of 1:10 and 1:15 were experimented.

Table 9 and Fig. 14 present the results of the hydrothermal gasification process of water hyacinth to water ratio of 1:10 and 1:15 at 300 °C and 60 min. For the water hyacinth to water ratios of 1:10, H_2, CO and CH_4 yield was accounted for 0.596%-vol., 10.412%-vol. and 0.204%-vol., respectively. By increasing water hyacinth to

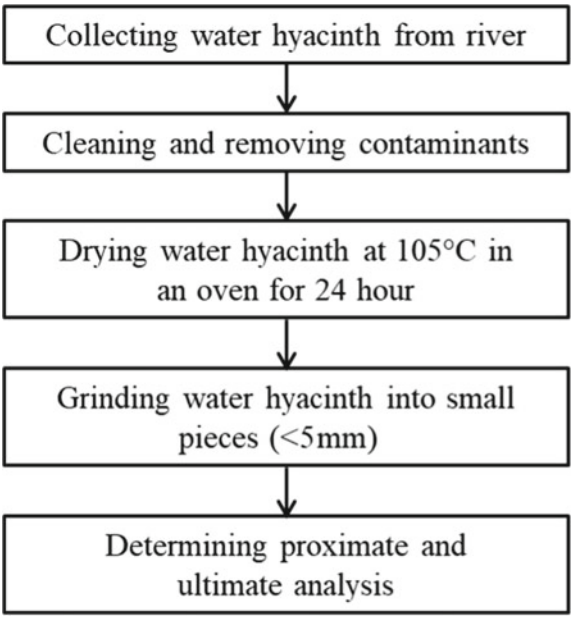

Fig. 11 Diagram for feedstock preparation

water ratio to 1:15, it was found that H_2, CO and CH_4 yield was decreased to 0.536%-vol., 9.484%-vol. and 0.159%-vol., respectively.

The lower heating value (LHV) of producer gas was calculated by Eq. (8) and presented in Fig. 15. Since the H_2, CO and CH_4 yielded from the hydrothermal gasification of water hyacinth to water ratio of 1:10 was higher than those from 1:15, the lower heating value of producer gas from 1:10 is also higher than its value from 1:15. LHV from the hydrothermal gasification of water hyacinth to water ratio of 1:10 and 1:15 was calculated to be 1.449 MJ/Nm^3 and 1.310 MJ/Nm^3, respectively. Since water hyacinth to water ratio of 1:10 can provide producer gas with higher LHV, water hyacinth to water ratio of 1:10 was the optimum ratio for further experiment to study the influence of reaction temperature on producer gas composition.

Effect of reaction temperature

To investigate the effect of reaction temperature on producer gas composition and lower heating value, water hyacinth to water ratio of 1:10 was placed in the reactor and the reaction temperature was varied to 260, 280, 300 and 320 °C. The reaction time was set to 60 min. Table 10 and Fig. 16 illustrate the producer gas composition depending on the reaction temperature.

The results reveal that reaction temperature plays a dominant role on producer gas composition. With increasing the reaction temperature from 260 to 320 °C, the amount of hydrogen and methane increased from 0.406 to 2.643%-vol. and 0.085 to 0.352%-vol., respectively, whereas the amount of carbon monoxide decreased from 11.165 to 6.952%-vol. Hydrogen content increased 6.5 times at 320 °C, compared to its amount at 260 °C. The enhancement of hydrogen and methane can be resulted from

Fig. 12 Preparation of feedstock

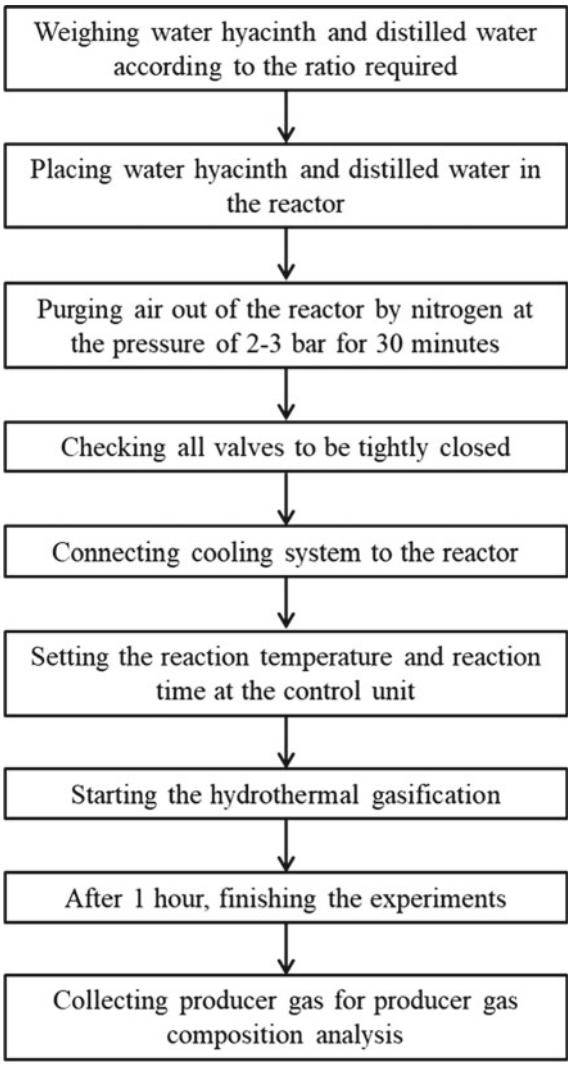

Fig. 13 Diagram of experimental procedure

steam reforming reaction (Eq. 1), water–gas shift reaction (Eq. 3) and methanation reaction (Eq. 4).

As presented in Fig. 17, LHV of producer gas increased from 1.481 MJ/Nm^3 at 260 °C to the maximum value of 1.505 MJ/Nm^3 at 280 °C. With further increase in reaction temperature, LHV tended to be decreased because the amount of carbon dioxide decreased, even amount of hydrogen and methane increased. The minimum LHV of 1.287 MJ/Nm^3 occurred at 320 °C. This meant that the decrease in carbon monoxide with increasing reaction temperature played a significant role on the lower heating value of producer gas.

Table 8 Chemical composition and heating value of water hyacinth

	Water hyacinth
Proximate analysis (%-wt.)	
Moisture[a]	89.84
Volatile matter[b]	19.26
Ash[b]	70.82
Fixed carbon[b]	9.92
Ultimate analysis (%-wt.)	
Carbon (C)	28.56
Hydrogen (H)	4.76
Nitrogen (N)	2.02
Sulfur (S)	44.38
Oxygen (O)	0.27
Ash[b]	0.75
Heating value (MJ/kg)	
Higher heating value (HHV)	11.67
Lower heating value (LHV)	10.64

[a]%-wt. as received
[b]%-wt. as dry basis

Table 9 Producer gas composition with different water hyacinth to water ratios

Temp. (°C)	Reaction pressure (MPa)	Water hyacinth to water ratio	Reaction time (min)	H_2 (%-vol.)	CO (%-vol.)	CH_4 (%-vol.)	CO_2 (%-vol.)
300	8.8	1:10	60	0.596	10.412	0.204	88.789
300	8.8	1:15	60	0.536	9.484	0.159	89.822

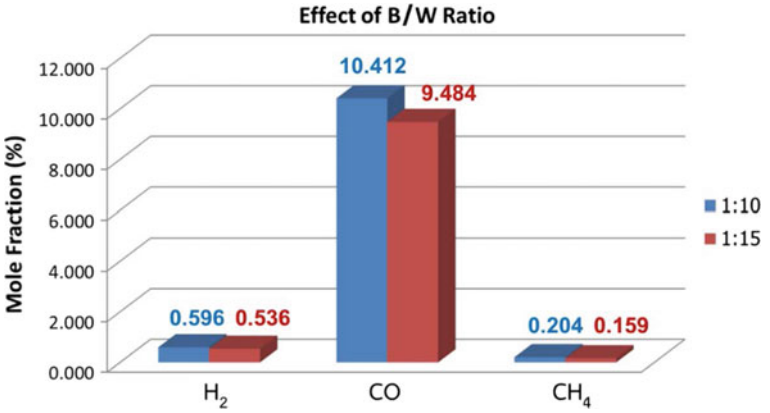

Fig. 14 Producer gas composition with different water hyacinth to water ratios

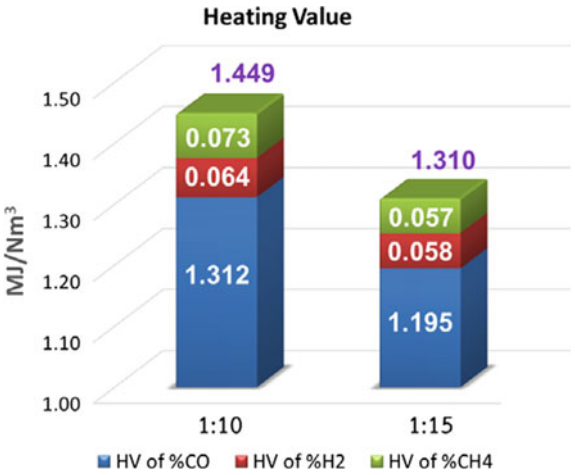

Fig. 15 LHV of producer gas with different water hyacinth to water ratios

Table 10 Producer gas composition with different reaction temperatures

Temp. (°C)	Reaction pressure (MPa)	Water hyacinth to water ratio	Reaction time (min)	H_2 (%-vol.)	CO (%-vol.)	CH_4 (%-vol.)	CO_2 (%-vol.)
260	4.9	1:10	1	0.406	11.165	0.085	88.344
280	6.6	1:10	1	0.492	11.219	0.106	88.183
300	8.8	1:10	1	0.596	10.412	0.204	88.789
320	11.5	1:10	1	2.643	6.952	0.352	90.053

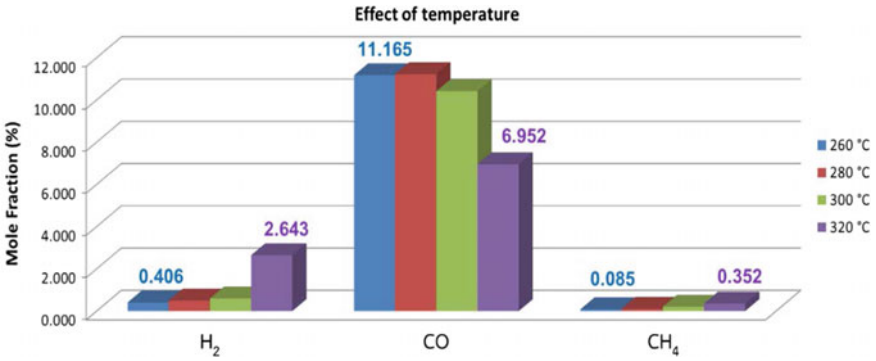

Fig. 16 Producer gas composition with different reaction temperatures

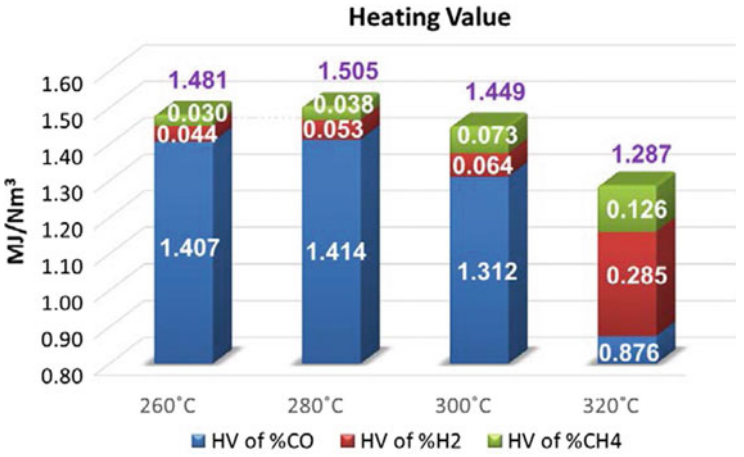

Fig. 17 LHV of producer gas with different reaction temperatures

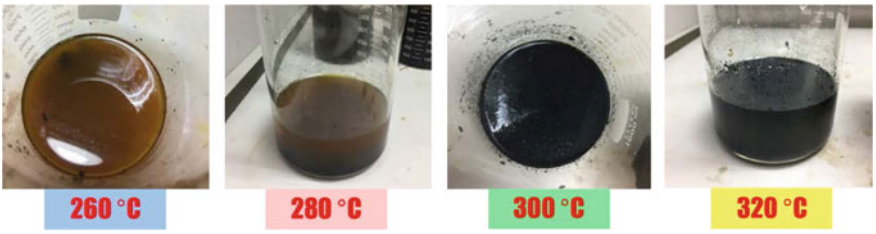

Fig. 18 Residue from the hydrothermal gasification

Residue from the hydrothermal gasification

After all experiments, there was the solid–liquid mixture remaining in the reactor. The mixture was non-viscous, light brown until black in color, depending on the reaction temperature, as shown in Fig. 22. When the reaction temperature increased, color of the mixture was changed from light brown to black. The change in color was the consequence of the hydrolysis reaction, by which water hyacinth was broken down into smaller molecules.

5 Summary

This study evidences that water hyacinth has a high potential to be used as bioenergy source for energy production. The advantages of water hyacinth are as follows:

- There is a substantial amount of water hyacinth.

- Its price is still cheap because it has not been used as commercial bioenergy sources.

However, because of its extremely high moisture content, it is not suitable to use as feedstock in conventional thermal conversion process; therefore, the hydrothermal gasification is considered as the proper conversion process to convert water hyacinth to gaseous fuel. Anyways, the quality of gaseous fuel obtained from the hydrothermal gasification depends on operating conditions, e.g., the water hyacinth to water ratio, the reaction temperature and the absence/presence of catalyst.

The optimum condition for the non-catalytic hydrothermal gasification from the experiments conducted in this study is the water hyacinth to water ratio of 1:10 and the reaction temperature of 280 °C, by which the producer gas posed the maximum LHV of 1.505 MJ/Nm^3. However, the optimum temperature is depended on the desired product. In case of the hydrogen-rich gas is the desired product, the optimum reaction temperature should be 320 °C, since the maximum hydrogen content in producer gas of 2.643%-vol. can be achieved.

As this study emphasized on non-catalytic hydrothermal gasification, the hydrogen content was rather low compared to other studies. In order to enhance the amount of hydrogen for further experimental studies in the future, catalytic hydrothermal gasification should be taken into consideration. The catalysts used are metal oxide catalyst such as ZnO, CuO and Cr_2O_3/Al_2O_3.

Acknowledgements The authors would like to express their grateful to the Waste Incineration Research Center (WIRC), Department of Mechanical and Aerospace Engineering, Faculty of Engineering and Science and Technology Research Center (STRI) of King Mongkut's University of Technology North Bangkok, for the facilities support.

References

1. World Bioenergy Association (2018) WBA global bioenergy statistics 2018. https://worldbioenergy.org/uploads/181203%20WBA%20GBS%202018_hq.pdf
2. Overend RP (2009) Direct combustion of biomass. Renewable energy sources charged with energy from the sun and originated from earth-moon interaction, vol 1, pp 74–100
3. Department of Alternative Energy Development and Efficiency (2015) Ministry of Energy, Alternative Energy Development Plan (AEDP2015) (in Thai)
4. National Science Technology and Innovation Policy Office (2015) and The Joint Graduate School of Energy and Environment, Manual for biomass combustion technology for industry (in Thai)
5. Regional Environmental Office 5 (2011) Ministry of Natural Resources and Environment, Manual for water hyacinth management (in Thai)
6. Barua VB, Goud VV, Kalamdhad AS (2018) Microbial pretreatment of water hyacinth for enhanced hydrolysis followed by biogas production. Renew Energy 126:21–29
7. Carlinia M, Castelluccia S, Mennunia A (2018) Water hyacinth biomass: chemical and thermal pre-treatment for energetic utilization in anaerobic digestion process. Energy Procedia 148:431–438

8. Ruen-ngam D, Jaruyanon P (2014) Hydrogen production from water hyacinth under hydrothermal treatment: experimental section. In: International conference on science, technology and innovation for sustainable well-being (STISWB), pp 148–153
9. Pollution Control Department (2007) Campaign and public relations project to solve the problem of the Chao Phraya River, Final report. http://ptech.pcd.go.th/pcd/document/001467/001467.pdf (in Thai)
10. Thailand Institute of Scientific and Technological Research (2016) Development and technology transfer for electricity production from biomass to establish a 1-MW pilot plant (in Thai)
11. Sucheera Chubundit (n.a.) Water hyacinth…National problems: Water hyacinth disposal law. http://web.senate.go.th/w3c/senate/pictures/comm/71/file_1408422840.pdf (in Thai)
12. Regional Environmental Office 6 (2011) Ministry of Natural Resources and Environment, Water hyacinth management http://reo06.mnre.go.th/home/images/upload/file/report/work2554/supareak01.pdf (in Thai)
13. Phichai K, Pragrobpondee P, Khumpart T, Hirunpraditkoon S (2013) Prediction heating values of lignocellulosics from biomass characteristics. Int J Chem Mol Eng 7:532–535
14. Singh R, Balagurumurthy B, Prakash A, Bhaskar T (2015) Catalytic hydrothermal liquefaction of water hyacinth. Bioresour Technol 178:157–165
15. Basu P (2013) Biomass gasification, pyrolysis and torrefaction, 2nd edn. Elsevier, London, pp 315–352
16. Molino A, Migliori M, Nanna F (2014) Glucose gasification in near critical water conditions for both syngas production and green chemicals with a continuous process. Fuel 115:41–45
17. Deniz I, Vardar-Sukan F, Yüksel M, Saglam M, Ballice L, Yesil-Celiktas O (2015) Hydrogen production from marine biomass by hydrothermal gasification. Energy Convers Manage 96:124–130
18. Jariyajirawatthana A (2007) Feasibility of black liquor gasification process in supercritical water. Master thesis, Faculty of Engineering, Chulalongkorn University. https://cuir.car.chula.ac.th/xmlui/bitstream/handle/123456789/15093/Asana_Ja.pdf?sequence=1&isAllowed=y (in Thai)
19. Reddy SN, Nanda S, Dalai AK, Kozinski JA (2014) Supercritical water gasification of biomass for hydrogen production. Int J Hydrogen Energy 39:6912–6926
20. Cengiz NÜ, Eren S, Saglam M, Yüksel M, Ballice L (2016) Influence of temperature and pressure on hydrogen and methane production in the hydrothermal gasification of wood residues. J Supercrit Fluids 107:243–249
21. Klaimukh S (2003) A comparison of producer gas from compressed hyacinth of up draft and down draft furnances. Master thesis, Energy Technology, King Mongkut's University of Technology Thonburi
22. Madenoglu TG, Kurt S, Saglam M, Yüksel M, Gökkaya D, Ballice L (2012) Hydrogen production from some agricultural residues by catalytic subcritical and supercritical water gasification. J Supercrit Fluids 67:22–28
23. Madenoglu TG, Yıldırır E, Saglam M, Yüksel M, Ballice L (2014) Improvement in hydrogen production from hard-shell nut residues by catalytic hydrothermal gasification. J Supercrit Fluids 95:339–347
24. Onwudili JA, Lea-Langton AR, Ross AB, Williams PT (2013) Catalytic hydrothermal gasification of algae for hydrogen production: composition of reaction products and potential for nutrient recycling. Bioresour Technol 127:72–80
25. Mettanant V, Basu P, Leon MA (2009) Gasification of rice husk in supercritical water. In: 8th World conference on chemical engineering, Montreal
26. Nanda S, Isen J, Dalai AK, Kozinski JA (2016) Gasification of fruit wastes and agro residues in supercritical water. Energy Convers Manage 110:296–306

Thermochemical Solutions for CO_2 Utilization to Fuels and Value-Added Products

K. G. Burra, P. Chandna, and Ashwani K. Gupta

1 Introduction

Improved lifestyle aided by energy utilization has been the goal since the Industrial Revolution. The outcome from these activities can be seen from the increased lifespan of humans, food security, and low infant mortality, increased efficiency of favorable substance production and advances in medical sciences, transportation and communication sectors. This rapid growth has been from the exploitation of fossil fuel resources including coal, petroleum and natural gas reserves to produce energy, fuels and synthetic chemicals such as oils and plastics. Fossil fuels are formed over a span of millions of years from the natural burial of dead organisms below the earth's crust followed by slow anaerobic decomposition that lead to carbon enrichment of these deposited materials. While usage of these resources, especially via combustion, has driven this revolutionary advancement, their rapid utilization led to imbalance in timescales. The consumption rate has been of the order of decades, while these reserves formed over a span of millions of years so that the natural carbon sequestration from atmosphere into biosphere via photosynthesis has been outpaced. Combustion of fossil fuels and their derivatives over this relatively short timescale has led to excessive carbon emissions from the earth's crust into the atmosphere. The consequences were not observed until investigation on CO_2 variation in the atmosphere that CO_2 showed its concentration to increase from 280 ppm (prior to the industrial era) to 400 ppm (or even 415 ppm recorded recently) [1]. The increased amounts of CO_2 in the atmosphere along with other gases such as CH_4 and water

K. G. Burra · A. K. Gupta (✉)
The Combustion Laboratory, Department of Mechanical Engineering, University of Maryland, College Park, MD 20742, USA
e-mail: akgupta@umd.edu

P. Chandna
Department of Mechanical Engineering, NIT Kurukshetra, Kurukshetra, India

© Springer Nature Singapore Pte Ltd. 2021

A. De et al. (eds.), *Sustainable Development for Energy, Power, and Propulsion*, Green Energy and Technology,
https://doi.org/10.1007/978-981-15-5667-8_4

vapor lead to increased trapping of sunlight radiation leading to steady rise in global temperature. The fossil fuel sources contributed to cumulative 37 Giga tons of CO_2 in the atmosphere in 2017. The CO_2 amount in the atmosphere is projected to increase to 63 Giga tons of CO_2 by 2050 at the current trajectory level [2, 3]. To understand this influence of anthropogenic carbon fluxes relative to natural carbon fluxes and their role in climate change, one requires an understanding of the working of natural carbon cycle, carbon fluxes and their feedback with the global climate parameters such as ice sheets, temperature over varying timescales [4].

2 Carbon Cycle and Its Impact on Climate

Understanding natural carbon cycle and its impact on the climate needs dwelling into the feedback mechanisms that relate the climate with the carbon cycle. These feedbacks between global climate conditions such as temperature and CO_2 content in the atmosphere are controlled by the carbon sinks that act over different timescales, of the order of 100,000 years down to 1000 years. These are described below.

2.1 Weathering-Metamorphism Feedback

Over a timescale of glacial cycles, i.e., of the order of 100,000 years, negative feedback exists to maintain stability between atmospheric CO_2 concentration and temperature given by a simplified representation given in Eq. (1).

$$CO_2 + CaSiO_3 \overset{\text{weathering}}{\Leftrightarrow} CaCO_3 + SiO_2 \tag{1}$$

Here, $CaSiO_3$ represents igneous rocks in mineral phase containing calcium oxide. These $CaSiO_3$ rocks react with CO_2 in the atmosphere via weathering until reaching equilibrium with the formation of sediments containing $CaCO_3$ over these rocks that inhibits their further reaction. Over these long timescales, any increase in atmospheric CO_2, from the equilibrium value, increases the global temperature, which enhances water cycle that increases the runoff of freshwater from land to sea. This increase in runoff causes rise in erosion of the sedimentary rocks into the ocean, leading to the exposure of fresh igneous rocks containing CaO that increases weathering. As weathering increases, atmospheric CO_2 decreases leading to decrease in temperature and thus rate of land–sea water runoff. This then decelerates the weathering process leading to equilibrium. Therefore, any variation in the atmospheric CO_2 or global temperature over these timescales is partially equilibrated via weathering feedback and thus stabilizing the global temperature and atmospheric CO_2 content [5].

2.2 Milankovitch Cycle and Albedo

The CO_2 and global temperature have been stable over time periods of 100,000 years owing to the weathering feedback, wherein earth's orbital wobbling (also called Milankovitch cycle) has led to varying solar intensity distribution to cause interglacial temperature cycles [6]. The temperature cycling is caused by cyclic melting and formation of polar ice sheets from Milankovitch cycle. As the ice sheets form, they increase the albedo (diffuse reflectance) of the earth's surface that increases the solar energy reflected from the earth. This leads to further cooling that accelerates the ice sheet formation. Similarly, when ice sheets melt due to rising temperature, earth's albedo effect decreases, which further accelerates global warming to promote ice sheet melting. Over the span of interglacial interval timescales, which span of the order of 10,000 years, the natural carbon cycle, due to albedo effect, has shown a positive feedback between the atmospheric CO_2 and global temperature [2, 4].

2.3 Oceanic Carbon Sink

Over timescales of 1000 years, another known phenomenon controls the feedback between atmospheric CO_2 and global temperature [2]. This corresponds to the equilibrium between CO_2 content in the oceans and atmospheric CO_2 at a given global temperature. The ocean–atmosphere carbon is significant over this timescale. The temperature and alkalinity of seawater and the flux of CO_2 between sea and air control the variation in solubility of CO_2 in seawater. It is proportional to the difference between the atmospheric CO_2 content and equilibrium CO_2 content based on Henry's law. But, actual CO_2 uptake by the ocean is more than the dissolution capability of CO_2 in water. This is made possible by the conversion of dissolved CO_2 into carbonic acid. As the CO_2 gets dissolved in water, a portion of it reacts with the water to form carbonic acid (H_2CO_3). This leads to low pH value (acidic) of the ocean. This acid reaches dissociative equilibrium with carbonate and bicarbonate ions that provides seawater buffer system. Equation (2) gives the overall reaction of dissolved CO_2 in this buffer. Higher CO_2 in the atmosphere leads to higher CO_2 absorption by the ocean and further leading to ocean acidification. It is also worth noting that the solubility of CO_2 in the water decreases with increase in temperature. As the CO_2 increases in the atmosphere, the rise in global temperature will lead to decreased solubility of CO_2 in sea water to accelerate the net CO_2 in the atmosphere.

$$CO_2 + H_2O + CO_3^{2-} \Leftrightarrow 2HCO_3^- \tag{2}$$

3 Anthropogenic Influence on Carbon Cycle

3.1 Impact of Anthropogenic Emissions on the Oceanic Sink

Isotopic studies have shown that, of the 10 Gton carbon/year emitted by human activity due to fossil fuels and deforestation, more than 2 Gton carbon/year is absorbed by the ocean; this net exchange occurs over ~100 years [7]. This suggests that the ocean is currently capable of absorbing the anthropogenic carbon emission and is yet to reach saturation. The anthropogenic emissions cause rise in atmospheric CO_2 to cause rise in global temperature and global warming that will decrease the solubility of CO_2 in the ocean. Coupled with that, as the atmospheric CO_2 content rises further, the ocean also loses buffer strength via consumption of CO_3^{2-} ions that leads to decline in the carbon sink capability. This falling buffer strength also increases the net time taken for CO_2 emission to be consumed by the ocean that further increases the net atmospheric CO_2.

At timescale of few 1000 years, this declining carbon sink gets slowly restored when the CO_3^{2-} concentration in the ocean falls below the saturation value of $CaCO_3$ dissolving reaction. This fall in CO_3^{2-} drives the equilibrium of Eq. (3) to dissolve the $CaCO_3$ from the ocean sediments to restore the oceanic carbon sink via replenishing the CO_3^{2-} [2]. The time taken will depend also on the atmospheric CO_2 residue when the ocean–air equilibrium is attained. While the dissolution of $CaCO_3$ increases CO_3^{2-} ions in the seawater and restores its carbon sinking capability, it takes few 1000 years and leads to a new ocean–air equilibrium value. Also, the new equilibrium point means the final ocean pH, atmospheric CO_2 and global temperature will equilibrate to a different value that could be uninhabitable or may lead to mass extinctions, especially in the marine ecosystem. The offset of this new equilibrium from the current habitable conditions is directly related to the CO_2 emission flux from fossil fuel consumption and other human activities.

$$CaCO_3 \Leftrightarrow Ca^{2+} + CO_3^{2-} \tag{3}$$

3.2 Duration of Global Warming

The last time earth's orbit was of similar eccentricity as of now, which is very close to being circular, interglacial interval (time between ice ages) lasted for about 50,000 years, while characteristic such interval lasts 10,000 years [2]. During this interval, the only degassing of carbon from land to air was from volcanic activities and hot springs, which correspond to a flux of 0.1 Giga ton/year [4]. This, after equilibrium with the ocean, then warms the earth that leads to melting of ice sheets followed by accelerated global warming. This was followed by gradual cooling driven by ice sheet formation leading to CO_2 uptake due to the Milankovitch cycle. However, now

the natural land–atmosphere carbon flux is supplemented by the fossil fuel combustion and deforestation-based CO_2 emission that are almost 100 times more than the natural degassing processes. If this interglacial interval can last as in the previous equivalent interval, then one can expect continuous global warming for the next ~50,000 years [2]. We expect that the anthropogenic emissions will lead to peaking of atmospheric CO_2 owing to ocean equilibrium followed by a long tail of additional atmospheric carbon. It is expected that the interaction of this tail with the orbital fluctuations will designate to the future climate on this earth. In this aspect, there is a possibility that this additional carbon tail, which is much higher than the natural degassing tail, can make it harder for the nucleation of ice sheets for the next ice age and thus delay the next ice age for a much longer time [2, 6].

3.3 Climate Change Accelerating Factors

The carbon cycle is currently acting in a negative feedback fashion via ocean and land uptake of CO_2. Currently, land uptake is 2 Giga ton carbon/year that represents intake to the biosphere and sequestration in the soil [2]. But with the anthropogenic emissions to persist, as of now, the global warming will only continue. Melting of ice sheets will continue, and albedo affect will begin to dominate in the future leading to accelerated global warming at the current level of activity. This accelerated rise in temperature will lower the ocean carbon intake to cause even a net CO_2 emission from the ocean into the atmosphere. As the temperature rises, the decomposition of carbon deposits in the soil will increase. This means that the land will decrease its activity to act as a carbon sink that will cause more release of CO_2 into the atmosphere than it can sink.

Permafrosts are the peat deposits in soil at northern latitudes where these deposits are preserved from degradation by being frozen. They are estimated to contain carbon of the order of 100 Giga tons [8]. As the temperature increases, these soils can melt, making the peat susceptible to degradation and release carbon to the atmosphere. Although permafrosts can take centuries to melt, this frozen soil meets with water near the lakes. It was found that under anoxic conditions of the lake sediments, the peat content undergoes anaerobic fermentation leading to CH_4 and CO_2 bubbling from around the lake periphery. Therefore, as the temperature rises and these permafrosts meet more liquid waterbodies, it can lead to released carbon, which further accelerates the feedback to result in higher temperature.

4 Need for Carbon Cycle Restoration

The concerns of delayed ice age, albedo effect, ocean acidification, permafrost melting and acceleration by CO_2 release from soil carbon and oceans in warmer conditions call for immediate action on restricting the net carbon emissions. Not

only is it necessary to decrease the rate of carbon emission, one must also decrease the atmospheric CO_2 via industrial scale CO_2 capture for sequestration or utilization. Deviation from fossil fuel dependency is essential to deviate away from the continuously increasing CO_2 emission to the environment. Our efforts on renewable energy to replace fossil fuels are growing. Current statistics show significant amounts of fossil fuel dependency and political support for the reserves, even in the developed countries such as the USA (see Fig. 1), [9]. Delayed action on the imminent warming to replace fossil fuels with renewable energy will only cause this earth uninhabitable. We are beyond the halfway mark of the maximum allowed CO_2 release to the atmosphere that will make the earth uninhabitable. Therefore, the development and implementation of industrial scale CO_2 capture and its conversion to valuable products are essential to avoid this imminent warming.

The problem of CO_2 emissions rose from fossil fuel consumption for energy, fuels and value-added chemicals. The CO_2 can be captured and recycled for use in energy, fuel and value-added chemicals production, which can provide sustainability to the anthropogenic contribution of natural carbon cycle [10]. In this chapter, we provide insights into the various techniques used for CO_2 capture and utilization. We start with state of the art of CO_2 capture techniques, their applicability along with drawbacks and challenges. This is followed by the pathways for utilization of this captured CO_2 focusing on thermochemical processes that utilizes CO_2, for example, in CO_2-assisted gasification, CO_2 splitting via chemical looping and other techniques to produce syngas, a precursor to produce energy, fuels and value-added chemicals. Note that CO_2 conversion can be significantly enhanced via CO_2-assisted gasification

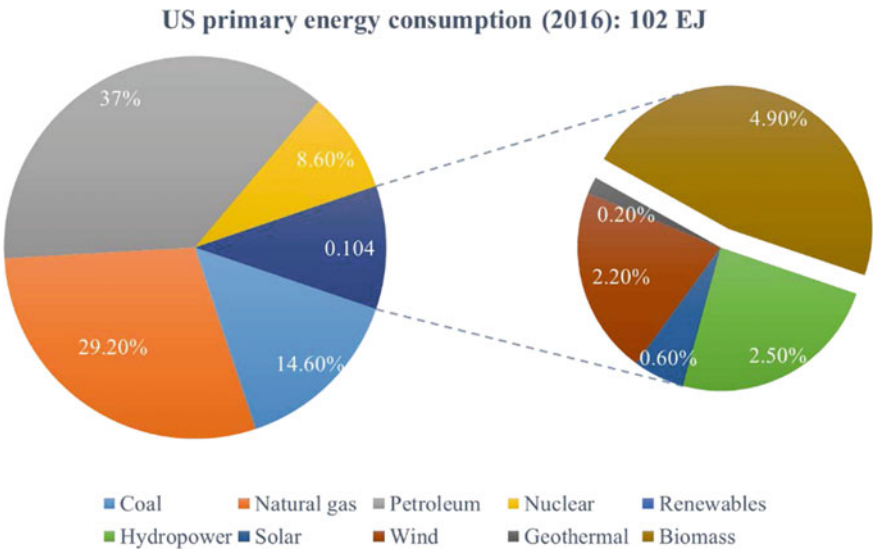

Fig. 1 Primary energy consumption in the USA in 2016 [9]

of biomass and solid wastes with special benefits on operation at relatively low temperatures compared to redox looping while providing higher conversion and performance.

5 Carbon Capture

In most large-scale CO_2 emission sources, the CO_2 concentration in the flue gas is less than 15% by vol. [11]. Direct utilization of this stream via most known techniques will yield low efficiency, high energy costs and extent of conversion due to the low CO_2 concentration. Thus, CO_2 capture techniques must convert the above low concentration CO_2 streams to high concentration stream or near pure CO_2 gas stream for its efficient transport and utilization. CO_2 capture typically involves separation of CO_2 from the gas stream via various well-known techniques followed by collection and compression for its efficient transportation. While CO_2 capture infrastructure already exists in some industrial applications such as natural gas pretreatment, ammonia production plants, they exist in the form of CO_2 removal to purify these industrial streams. CO_2 capture technologies are lacking to date in large size power plants. These strategies have significant potential to convert the existing fossil fuel applications for cleaner energy production with low-carbon or carbon neutral processes.

CO_2 capture technologies can be classified based on two different ideas. They are (i) based on the location of carbon separation in the industrial fossil fuel utilization chain and (ii) based on the methods used to separate out CO_2 from a given gas stream. First, we discuss the approaches of carbon capture from industrial and power plant processes which can be classified according to Fig. 2 [11]. In (a) **Post-combustion separation**, the separation of CO_2 from the exhaust gases produced by air combustion of carbonaceous fuels (coal, natural gas, oil or biomass) typically

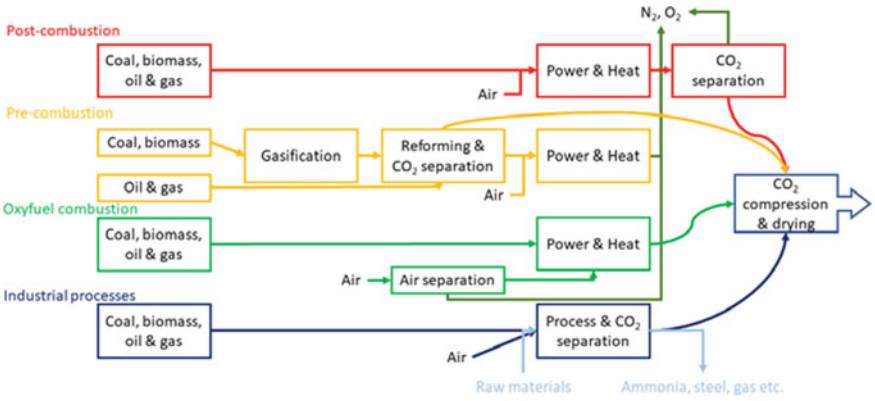

Fig. 2 Strategic pathways for carbon capture from CO_2 emitting plants [11]

uses chemical sorbent, while other techniques are still under development. In (b) **Pre-combustion separation**, the reforming of the carbonaceous fuels in the presence of H_2O or air/O_2 is used to yield syngas (H_2 and CO) followed by shift reaction to produce fuel steam containing H_2 and CO_2. The H_2 can be utilized as a fuel for clean energy production, while CO_2 is separated out from this fuel stream via physical or chemical absorption. In (c) **Oxy-fuel combustion**, direct capture of high-purity CO_2 is produced from the exhaust combustion gases of carbonaceous fuels (after water removal from the exhaust stream) using oxygen formed via cryogenic distillation of air or membrane/chemical looping techniques. In (d) **Industrial Processing**, separation of CO_2 from useful raw material and product streams occurs by first removing CO_2 and then purifies the reactants/products stream. Here, although the technology exists, but there is no focus on carbon capture. Presently, although the CO_2 is vented out into the atmosphere, there is potential for its easier capture.

Various CO_2 capture technologies described below can be classified based on the pathway used to separate out CO_2 from a given stream of gases.

5.1 Absorption-Based Capture

Solvent-based absorption processes are better suited for post-combustion carbon capture providing high capture efficiency with relatively low energy consumption. The flue gases after combustion are cooled and allowed to make contact with a solvent at ~313 to 333 K. The CO_2 reacts with the solvent and gets removed from the stream. This CO_2-rich solvent is moved to high temperature zone of 373–413 K, wherein CO_2 is stripped off the solvent using steam as the stripping gas. Significant amounts of CO_2 recovery are feasible but at a cost of increased reactor size and energy consumption; the purity of CO_2 obtained after stripping is almost 99.9%. The presence of contaminants, such as SO_x, NO_x and oxygen leads to side reactions of the solvent along with slow decomposition of the solvent causing solvent consumption and thus a need for fresh (added) solvent, which reduces the process efficiency [11]. Various amine-based solvents have been proposed and tested for this process with diluted aqueous mono ethanol amine (MEA) being the most common. With the amine-based absorption, contaminated flue gas leads to thermally stable nitrates and sulfates, which lowers the carbon capture capability of the solvent. This can be avoided by removal of these contaminants before carbon capture which increases the costs of the overall process. Amine solvent decomposition products and their impacts can be found in the literature [10]. A trade-off between the solvent consumption costs and contaminant removal costs is reached to achieve better overall economy of the carbon capture process while minimizing waste by-product streams. Various strategies were developed to integrate solvent absorption-based CO_2 capture with modifications to the power generation cycles depending on the steam utilization, energy requirements for solvent regeneration and other modifications [11]. Pathways to minimize the energy consumption from solvent regeneration were also developed by modifying the solvents and process design.

5.2 Adsorption-Based Capture

In this class of CO_2 capture, the high selectivity of special materials such as molecular sieves, activated carbons or other novel ceramic/perovskites are utilized for adsorbing CO_2 from the flue gas mixture depending on the temperature and partial pressure of CO_2 [10–13]. In the initial step, CO_2-rich flue gas is blown over these adsorbents, wherein the CO_2 is selectively adsorbed that lowers the CO_2 content in the exhaust flue gas. This is followed by a temperature/pressure swing, wherein the temperature is raised, or CO_2 partial pressure is lowered by passing a purge gas, or lowering the net pressure, which results in the desorption of pure CO_2 from the CO_2-rich adsorbent. Long time cycles in temperature swing make pressure swing operation a better pathway with more throughput and scalability. Studies into developing various kinds of novel adsorbent materials are currently being carried out with motivation to increase CO_2 selectivity, increase regeneration capability, increase resistance against flue gas contaminants, decrease energy consumption and increase scalability and operational efficiency.

5.3 Membrane-Based Capture

This method includes driving CO_2-rich gas stream alongside a CO_2 selective membrane for its separation from a given gas stream. As this process is significantly influenced by the pressure differential across the membrane and has inherently inferior selectivity compared to solvent absorbers, its efficiency is better at higher concentration of CO_2 in the input gas stream. Thus, it is currently used only for natural gas sweetening process. In the future, it is likely to be restricted to pre-combustion CO_2 capture pathways where the CO_2 concentration can be enhanced via shift reaction unlike the low concentration of CO_2 in post-combustion flue gases [14–16].

Novel membrane technologies are also being explored for flue gas separation. This includes membrane/solvent hybrid systems and facilitated transport membrane systems [11]. In the hybrid system, membrane acts as a gas permeable and liquid impermeable barrier between the input gas stream and an absorber solvent such as aqueous amines so that CO_2 in the input gas stream diffuses through pores or porous membrane or dissolves and diffuses through non-porous membranes into the solvent absorber, which captures the CO_2. This was developed to improve the control over operational conditions by avoiding direct solvent-gas contact, which can also enhance the scalability of solvent absorber systems. In the case of facilitated membranes, selective liquids such as amines and molten salt hydrates are supported on porous or ion exchange membranes so that CO_2 from the gas stream reversibly reacts with the solvent and gets transported through the membrane for desorption on the other side. Certain issues arise with these facilitated membranes including

decrease in selectivity with increase in CO_2 partial pressure and total input pressure due to saturation and other gas components entering the membrane.

5.4 Solid Sorbents Looping-Based Capture

Utilization of solid sorbents involves regenerable solids to react and remove CO_2 from the gas stream at a high temperature followed by regeneration of the solid to produce pure CO_2. Operation at higher temperatures compared to other techniques, such as solvent absorption, avoids the need for cooling the gas stream. This reduces the energy loss in cooling and reheating especially in post-combustion carbon capture systems. Typical sorbent cycling chosen for this purpose is carbonation and calcination of metal oxides, especially alkaline earth metals oxides with most common being CaO and its derivatives due to its ease of availability. Lithium oxides and mixed oxides such as Li_2ZrO_3, Li_4SiO4 and Na_2ZrO_3 oxides were also researched along with CaO [11, 17]. In this looping process, CaO reacts with CO_2 in the flue gas in post-combustion system or the syngas in pre-combustion setup to form $CaCO_3$ at relatively high temperature (700–800 °C). Then, either the solids are removed or the reactor is swung to higher temperature (>950 °C) without the input stream so that $CaCO_3$ is calcined to regenerate to CaO evolving CO_2, which can be pressurized, stored and utilized. Schematics of the post-combustion and pre-combustion carbon capture involving CaO looping are given in Fig. 3 [18, 19].

Carbonation reaction can be integrated either in situ or ex situ with respect to the fuel reforming or combustion processes. In the ex situ case of both pre-combustion and post-combustion systems, the shifted syngas stream and the flue gas stream are passed over the sorbent in a reactor separate from the reformer or combustor. But in the in situ setup, especially in the pre-combustion capture systems, carbonation can be incorporated into the reforming reactor so that simultaneous removal of CO_2 during

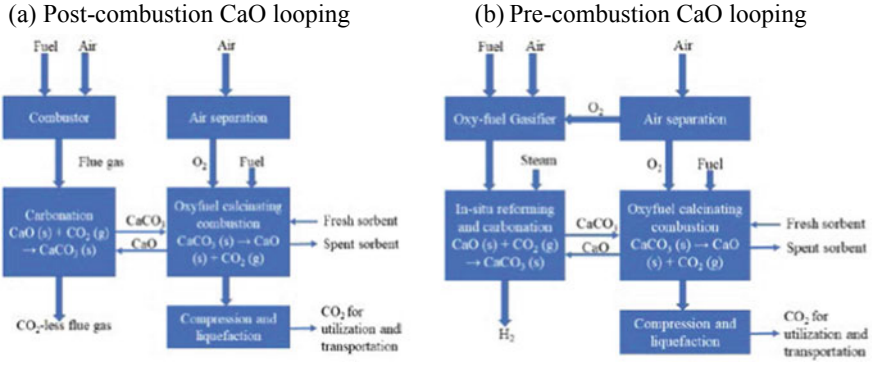

Fig. 3 Incorporation of CaO looping into **a** post-combustion and **b** pre-combustion carbon capture techniques [18, 19]

reforming of liquid/gaseous fuels or gasification of solid fuels such as coal/biomass can increase the thermodynamic equilibrium to drive toward product formation via Le Chatelier's principle [20–26]. This not only provides carbon capture but also improves the performance of steam reforming of natural gas, liquid fuels and steam gasification of coal/biomass allowing lower temperature operation and higher H_2 concentration in syngas yields as the carbonation reaction is exothermic. This then also provides additional energy for endothermic reforming reactions. In situ steam reforming of methane with Ca-looing was found to provide with H_2 concentration of more than 90% in the syngas yield, while integration with biomass and coal gasification yielded H_2 concentration between 70 and 80% by vol. [22, 24, 25].

Challenges associated with the utilization of CaO from natural minerals such as dolomite, limestone and calcites are their loss of carbonation capacity with repeated regeneration cycles. High temperature operation required for calcination results in significant sintering of CaO that occurs during the regeneration, and this leads to lowered reactivity during carbonation process and thus lowering the CO_2 capture capacity. Figure 4 shows the loss of porosity and thus surface area in limestone with temperature during calcination [27]. It was also found that carbonation kinetics involves two steps—fast carbonation on the surface of CaO with CO_2 followed by a slow diffusion-driven kinetics as the bulk CaO loses direct contact with CO_2 due to formation of $CaCO_3$ on the surface [20]. Some competing reactions due to contaminants also pose threat toward CaO carbonation kinetics such as formation of $CaSO_4$ formation from SO_x present in the flue gas. To improve the calcination reaction, steam purging has been tested to remove CO_2 out of the reactor, which would provide pure CO_2 unlike usage of N_2 or other permanent gases. However, steam addition

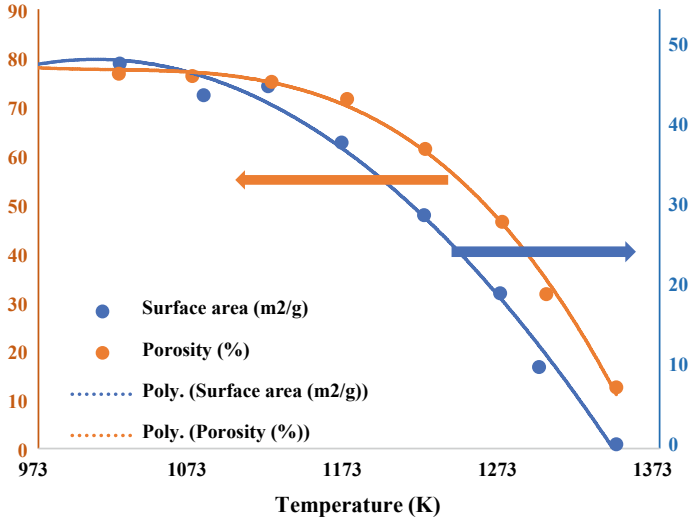

Fig. 4 Loss of surface area and porosity in nascent CaO with increase in calcination temperature [27]

Table 1 CO_2 capture capabilities of some natural and synthetic sorbents [16]

	Sorbent	Stoichiometric sorption capacity of calcined sorbent (mass CO_2/mass sorbent)	Calcination/Regeneration temperature (K)	Sorption capacity of calcined sorbent after 45 cycles (mass of CO_2/mass of sorbent)
Natural sorbents	Calcium carbonate ($CaCO_3$)	0.79	1173	0.316
	Dolomite ($CaCO_3.MgCO_3$)	0.46		0.16
	Huntite ($CaCO_3.3MgCO_3$)	0.25		0.2
	Hydrotalcite, promoted K_2CO_3/hydrotalcite	0.029	673	Stable
Synthetic sorbents	Lithium orthosilicate (Li_4SIO_4)	0.37	1023	Stable to 100 cycles
	Lithium zirconate (LI_2ZrO_3)	0.29	963	
	Sodium zirconate (Na_2ZrO_3)	0.24	1063	

causes increased tendency to sinter. Various novel sorbents were developed based on CaO looping with the goal to achieve sintering resistance, mechanical strength and faster kinetics especially in calcination along with lower temperature requirement for calcination. The novelty was obtained using varied pore structure, coating of CaO on stable metal oxides such as alumina or silica. Regenerative capability of some of these natural and novel sorbents is given in Table 1 [16]. Bi-functional materials that provide catalytic capability to hydrocarbon reforming along with CO_2 capture via carbonation have also been developed. This includes Fe/CaO-$Ca_{12}Al_{14}O_{33}$ which was actively tested for both tar reforming and water–gas shift reaction [28].

These processes were developed earlier for carbon capture. They can provide pure CO_2, which can be pressurized, transported and stored. Geological sequestration has been proposed as a carbon capture technique against fossil fuel consumption, along with its utilization for enhanced oil recovery and other industrial purposes. Conversion of CO_2 to CO for the production of energy, fuels and value-added chemicals can be the most useful strategy as this provides sustainable solution to the anthropogenic carbon cycle. This method can provide a sustainable pathway for the conversion of fossil or renewable energy into carbon-based energy, which can be utilized using the existing infrastructure with minimal overhaul.

6 Carbon Recycling by CO_2 Utilization

The CO_2 recovered from above-given carbon capture techniques can be split to form CO, which is a precursor to various syngas applications, such as liquid fuel productions via Fisher–Tropsch synthesis, methanol and other value-added chemical synthesis along with thermal energy production via combustion. Along with CO_2, splitting of H_2O has also been proposed to provide H_2, which along with CO provide active ingredients for syngas to produce liquid fuels and chemicals synthesis [29]. Equation (4) shows the overall splitting of CO_2 to CO along with the energy required to carry out such a process, while Eq. (5) shows the equation for splitting of H_2O and corresponding energy requirement. The energy required for splitting of H_2O or CO_2 is nearly the same. Splitting of H_2O has been examined more in the literature than CO_2 splitting and that some researchers propose splitting of CO_2 to be carried out indirectly by first splitting H_2O to H_2 and then using some of the energy evolved to convert CO_2 to CO via reverse water–gas shift reaction given in Eq. (6). Note that this pathway makes the H_2O splitting to be most limiting reaction. This pathway of utilizing H_2O splitting for indirect splitting of CO_2 is only useful if water is readily available in the form of steam, or if low temperature heat is available to produce steam. In case of lack of availability of low-cost steam, CO_2 splitting is efficient, if carried out directly (separate from H_2O splitting).

$$CO_2(g) \rightarrow CO\ (g) + \frac{1}{2}O_2(g) \quad \Delta H_R^0 = 283\ \text{kJ/mol} \tag{4}$$

$$H_2O\ (l) \rightarrow H_2(g) + \frac{1}{2}O_2(g) \quad \Delta H_R^0 = 286\ \text{kJ/mol} \tag{5}$$

$$H_2(g) + CO_2(g) \leftrightarrow H_2O\ (l) + CO\ (g) \quad \Delta H_R^0 = -3\ \text{kJ/mol} \tag{6}$$

Various sources can be used to fulfill the energy requirement of CO_2 splitting, but utilization of renewable energy resources such as solar, wind or geothermal energy makes overall process carbon neutral or even carbon negative. Alternatively, a replacement or supplement to fossil fuel needs to be made that will aid our quest to replace fossil fuels infrastructure with renewable energy for sustainable lifestyle and alleviate the growing concern on atmospheric CO_2 and its associated impact on the climate change [30]. While electrical energy can be used to drive Eqs. (4, 5), the easier and lower cost availability of heat (e.g., solar) makes such source a better choice for thermal splitting of CO_2. Various techniques have been devised to carry out CO_2 splitting to CO and its subsequent conversion to produce hydrocarbon fuels and chemicals by utilizing thermal energy from sources such as solar concentrators, geothermal energy and others. The status of these thermal routes along with their capabilities and challenges will be the focus here.

7 Thermolysis of CO_2

Thermolysis refers to direct splitting of CO_2 to CO or H_2O to H_2 by heating these gases to thermal dissociation temperatures. The temperatures required for such splitting exceed 3200–4200 K to obtain acceptable equilibrium constant [10, 29, 31]. There are significant challenges associated with direct utilization of thermal energy for high-temperature splitting. The temperature at which $\Delta G_R = 0$ (where ΔG_R represents Gibbs energy of reaction) for CO_2 splitting is ~3100 K and that for H_2O splitting is ~4100 K. The requirement of these very high temperatures calls for advanced ceramic reactor materials which will increase the investment and operational costs. Note that even zirconia ceramics can only be operated at temperatures below 2700 K. At such temperatures, the equilibrium conversion is very low. The products of such a reaction at high temperature are in atomic stage and not desired ratios of CO/O_2 or H_2/O_2. They must be rapidly quenched to avoid recombination of these products, which lowers the conversion efficiency. He gases then should be separated out at lower temperatures using gas separation techniques. This rapid quenching of high temperature introduces significant energy loss and thus loss of energy efficiency. Such high-temperature energy can be obtained from limited sources such as solar concentrators, electric and plasma furnaces [32].

CO_2 splitting using solar concentrators has been carried out and reported in the literature. While the conversion of CO_2 was relatively promising, the efficiency of energy utilization for CO_2 splitting was found to be low. Furthermore, it causes melting of zirconia reactor wall, energy losses in quenching and the possibility of thermal shock in the materials due to intermittency of solar radiation at such high temperature operation. Researchers agree that the possibility of development of this process is rather low [31, 33]. The above material limitations were avoided in the literature via plasma-assisted decomposition utilizing electrical energy where the high-temperature plasma zone is not in direct contact with the reactor surfaces. Such a pathway showed promising results with ~20% CO_2 conversion at electrical energy-to-fuel energy efficiency of 80%, and even higher conversion but at the cost of efficiency. Electrolysis of CO_2 is its direct competitor, and at present, it provides better performance along with the added benefit of inherently obtaining separated products [31]. The present state of the art reveals that direct splitting of CO_2 is only economically feasible using electrolysis. While the development of plasma reactors can make them compete with electrolysis, the requirement of electrical energy makes this whole process unattractive as there are many other better and efficient use of electrical energy. This form of energy is of relatively higher grade and is not available readily for CO_2 splitting especially when this energy is to be used for fuel and energy purposes.

8 Thermochemical Looping

As seen from Eqs. (4 and 5) in the previous section, the temperatures required to obtain reasonable thermodynamic equilibrium conversion are significantly higher than the operable temperatures of materials available or that can be developed soon. This high temperature requirement arises from the very high enthalpy (ΔH_R^0) of these reactions, which led researchers to alleviate this need of very high temperature by splitting these reactions to obtain multi-step operation each of which can operate efficiently at achievable temperatures. The multiple steps also simplified the product separation. Processes involving more than two steps were studied only for H_2O splitting such as three-step Sulfur–Iodine cycle and four-step Calcium–iron bromide cycle [34]. While the presence of multiple steps provided significantly low temperature operation compared to other thermochemical cycles, they pose multitude of technical challenges in their scalability to industrial operation. These cycles utilized corrosive chemicals which increase the development costs of reactors for seeking resistant to these streams [34]. Besides, increased number of steps increase losses associated with product handling, along with heat and material transfer during change between the steps. Apart from these issues, these chemical cycles are not applicable for CO_2 splitting as they are less robust so that their applicability is limited to converting readily available H_2O (steam).

Studies carried out to find two-step cycles with a maximum operation temperature less than 1373 K revealed no such cycle suggesting, minimum number of steps for this temperature range is 3 based on the entropy change [34, 35]. But two-step cycles can be found when the maximum operating temperature was raised. In the two-step cycles, most commonly studied method is the utilization of redox cycling of metal oxides for CO_2 and H_2O splitting. This is called redox looping in which the first step involves thermal reduction of metal oxide to a lower oxidation state or to a metallic state at high temperature with O_2 evolved during the reaction, see Eq. (7). In the second splitting step, this metal or low oxidation state metal oxide reacts with CO_2 or H_2O to split them and form CO or H_2 while simultaneously regenerating the high-oxidation state metal oxide, that is suitable for reaction in step 1, see Eq. (8 and 9). The second step usually operates at lower temperature compared to the first step. Equations (7, 8, and 9) are written to include cycling of both stoichiometric and non-stoichiometric metal-metal oxide redox pairs, and the deviation from stoichiometry during reduction is represented as δ, which is also known (in the literature) as oxygen storage capacity, a representative of maximum fuel yield [36].

$$\text{Reduction step at higher temperature: } M_xO_y \rightarrow M_xO_{y-\delta} + \frac{\delta}{2}O_2(g) \tag{7}$$

$$\text{Oxidation step at lower temperature: } M_xO_{y-\delta} + \delta CO_2(g) \rightarrow M_xO_y + \delta CO\ (g) \tag{8}$$

$$\text{Oxidation step at lower temperature: } M_xO_{y-\delta} + \delta H_2O(g) \rightarrow M_xO_y + \delta H_2(g) \tag{9}$$

Metal-metal oxide redox looping process significantly depends on metal properties and is classified based on the metal-metal oxide redox material pair used. This material pair or the metal oxides used for this purpose are referred to as oxygen carrier materials in the H_2O and CO_2 splitting and chemical looping literature [37, 38]. Based on the properties of these oxygen carrier materials during the reaction, the cycles are classified primarily into volatile cycles and non-volatile cycles. During volatile cycles, the oxygen carrier material undergoes solid–gas transition such as in the case of ZnO/Zn, while in non-volatile cycles, these materials maintain their solid state or do not vaporize during reduction. Due to the entropy rise corresponding to solid-gas transition, volatile cycles are thermodynamically more favorable compared to non-volatile cycles. Besides providing higher oxygen carrying capacity, they pose a major challenge in improving the efficiency of rapid quenching process that is needed at the end of reduction step to avoid recombination of O_2 and vapors of the oxygen carrier. This includes Zn vapors. Non-volatile metal oxide oxygen carriers, although inherently provide lower equilibrium conversion, they provide potentially better feasible pathway with the state of the art without the need for rapid quenching, such as Fe_3O_4/FeO-Fe_3O_4. Further details about these cycles, their challenges and novel materials are currently under development to combat the above issues.

8.1 Volatile Cycles

A variety of volatile oxygen carrier redox pairs have been examined and reported both thermodynamically and tested experimentally in the literature with ZnO/Zn being the most common pair [39, 40]. The high oxygen carrying capability is the main reason researchers have explored to improve these cycles. Volatile redox pairs examined in the literature include ZnO/Zn, CdO/Cd, SnO_2/SnO and GeO_2/GeO [32]. Zn was also proposed as an energy carrier due to its relatively low atomic mass and its reactivity with water. ZnO reduction to Zn can be carried out using solar concentrators or other accessible energy sources in appropriate locations (possibly remote) followed by transportation of the formed Zn to convenient energy and chemical production plants where Zn reacts with CO_2/H_2O to form syngas. The syngas produced can be utilized locally to produce fuels or various value-added chemicals or energy irrespective of the availability of any renewable energy at that site. At reduction temperatures of 2030 K to produce syngas of equimolar concentrations of CO and H_2 needed for Fisher–Tropsch synthesis along with incorporation of heat recovery from hot products, theoretical cycle efficiency beyond 50% can be achieved in ZnO/Zn cycle. In most cases, the H_2 to CO molar concentration of 2 is needed for liquid fuel production. The asymptotic conversion during Zn oxidation in the presence of CO_2 was found to increase to form ZnO [32]. Typical temperatures of Zn oxidation are ~650 to 700 K. For oxidation of Cd, Zn and some of these volatile metals, bubbling of H_2O or CO_2 through molten metals has been proposed for better kinetics. Redox temperatures of SnO_2/SnO were tested at 1873 and 873 K, respectively. SnO provided an advantage over Zn in reduction process due to its relatively

lower reactivity with O_2 compared to Zn which means lower recombination tendency and independence of reduction kinetics from quenching rate [41]. CO_2 conversion needed higher temperature and operated with slower kinetics than that of H_2O using SnO. Reduction reactions of oxides such as SnO_2 and GeO_2 resulted in disproportionation reaction during quenching zone to form Sn/SnO_2 from SnO and Ge/GeO_2 from GeO [32].

These cycles have been proposed with the help of thermodynamic cycle analysis and also demonstrated to some extent in lab-scale reactors. However, no successful and efficient demonstration of these cycles can be found in the literature. Inherent requirement of rapid quenching significantly reduced the energy efficiency and provided technical difficulties in reactor development. Furthermore, disproportionation of reactions showed limits on its attractiveness as a future endeavor for CO_2 conversion in the scope of energy, fuels and chemicals production.

8.2 Non-volatile Cycles

The need for the alleviation of quenching and handling of metal vapors makes non-volatile cycles very attractive. Due to a wide variety of oxygen carrier cycles, they can further be grouped into stoichiometric and non-stoichiometric redox pairs based on the extent of change in the oxidation state and crystallographic phase during the redox looping. During reduction, while stoichiometric pairs can form solid solutions and change their crystallographic phase, such as $Fe_3O_4/FeO\text{-}Fe_3O_4$, non-stoichiometric pairs allow for oxygen removal capability without major changes to the lattice structure, such as $CeO_2/CeO_{2-\delta}$ [36]. These categories are marked by their difference in the extent of their oxygen carrying capacity during redox looping. A cycle involving stoichiometric pairs is planned to completely change the oxidation state during redox cycling to accommodate higher oxygen storage capacity compared to cycles in non-stoichiometric pairs where only limited oxygen in the lattice is mobilized by creating anionic vacancies without complete change in oxidation state. While the non-stoichiometric pairs provide low oxygen storage capacities, they provide significantly faster redox kinetics and stability compared to the stoichiometric pairs. They slow down by the bulk diffusion-controlled reactions and the loss of surface area with continued cycling, which is due to sintering that lowers the surface kinetics. As oxygen carriers in each of these categories have corresponding challenges, researchers tried to address these by doping or substituting certain elements in the lattice structure, especially cationic species to improve their performance and alleviate these challenges. Before we discuss these cycles in detail, based on the oxygen carrier materials developed in the literature, classified by the basic components involved in the cycle, certain material design requirements need to be considered to provide some perspective into the feasibilities of these materials.

Oxygen carriers of non-volatile cycles remain in solid state during redox looping. Therefore, the morphological properties such as surface area, porosity, particle sizes

and grain boundaries are significantly more important than volatile cycles. Preparation of these oxygen carriers should focus on improving the above parameters and maintain them in real reactive condition such as high temperature operation especially in solar concentrator reactor operation. One must also consider thermal reduction from high-temperature operation in order to keep the enhanced properties after repeated redox cycling. This is important when discussing and considering novel materials and doped oxygen carriers for their improved kinetics and oxygen storage capacity [32]. This is especially important because phenomena such as thermal sintering, loss of oxygen capture capacity and transport limitations significantly influence the performance during repeated redox cycling. In the following, we discuss various novel oxygen carriers that are differentiated based on the material class and the phenomenon controlling oxygen mobility.

8.2.1 Iron Oxide-Based Cycles

The utilization of Fe_3O_4/FeO for redox cycling was first proposed by Nakamura for which the zero Gibbs energy point for reduction reaction was reached at ~2500 K [42]. While this cycle is not a volatile cycle, melting points of Fe_3O_4 (magnetite) and FeO (wüstite) are 2000 and 1643 K, respectively, which complicates the physicochemical characteristics and also significantly promotes sintering [36]. Based on thermodynamic stability of different phases of FeO, various oxidation states were found to be stable, and complete reduction to FeO was achieved at highest temperature. But at lower redox temperatures, lower redox extents can be explored, which will form a mixed phase of FeO-Fe_3O_4 instead of FeO [43]. At further lower temperature ranges, the lattice structure of Fe_3O_4 is stable and non-stoichiometric redox cycling favored. Therefore, the same starting material Fe_3O_4 can provide different levels of redox extent by varying stoichiometry depending on the reduction temperature. Due to this versatility, the iron oxides are significantly researched for the splitting of CO_2 and H_2O. Various doping and substitutions have been proposed and tested to alleviate the issue of sintering and increased oxygen storage capacity.

Inert materials such as ZrO_2, Al_2O_3, YSZ (Yttria-stabilized zirconia) have been proposed as the support or the base on which Fe_3O_4 can be supported on or dissolved in [44, 45]. When magnetite was supported on YSZ, it was found that the reduced form dissolved in the YSZ's thermally stable lattice that avoided melting and reduced sintering. It was also found to increase oxygen mobility (active metal assay basis), limited by the solubility of FeO in YSZ's cubic lattice, as oxygen transport occurred via rapid diffusion through stable YSZ instead of slow diffusion through solid solution of FeO-Fe_3O_4 [46]. Thermodynamic and lab-scale testing showed H_2O splitting to be more favorable compared to CO_2 in the case of Fe_3O_4/FeO. However, this relative selectivity could be varied using different doping agents. It was found that this cycle was kinetically feasible only at small grain sizes obtained either in the form of aerosolized nanoparticles or dissolved in inert but stable lattices. But a counteracting parameter to this was the rapid sintering which limits nanoparticle approach and the lowering of active phase, i.e., lowering redox active oxygen and thus oxygen

storage capacity with increase in inert material relative to iron oxides. While the presence of inert materials provides improved kinetic and conversion performance, cycle efficiencies could be lowered because of sensible energy requirement to heat the inert components and energy requirements for their transfer due to relative decrease in active oxygen per gram of solid [36].

The issue of lowering oxygen storage due to inert materials was alleviated when it was found that ferrite-based materials formed by substituting transition metal ions such as Ni and Co in Fe_3O_4 lattice increased the oxygen storage capacity as compared to pure Fe_3O_4 [34, 35, 47, 48]. Studies on the extent of reduction at 1473 K showed that increase in Co content in Co ferrite increased the oxygen yield, but this needs to be optimized because increase in the substituted ion more than certain extent affects the oxidation performance to directly impact the CO or H_2 yields. This was found to be the case with cobalt-substituted ferrite, where increase in Co content increased the thermodynamic barrier of oxidation reactions. In contrast, the extent reduction increased, see Fig. 5, that depicts the thermodynamics of oxidation with Co substitution [36, 49–51]. From Fig. 5a, thermodynamic barrier for oxidation of CoO using CO_2 or H_2O is high for oxidation temperatures compared to FeO. Figure 5b shows this influence which reveals that increase in Co ions in wustite decreased its extent of oxidation by increasing the Gibbs free energy required for oxidation. This was also proved experimentally for large Co concentrations. So, optimization on substitution is necessary to obtain improved understanding of redox performance, i.e., enhancement in both oxidation and reduction extents.

While the ferrite cycles via transition metal substitutions provided improved oxygen storage capacity compared to Fe_3O_4, sintering is still an issue to be resolved. This was proposed to be solved in the similar manner to that used to improve Fe_3O_4 performance. Supporting Ni- and Co-substituted ferrites over inert materials such as ZrO_2 or YSZ provided resistance to sintering [46, 47, 49, 50]. These composite materials provided both improved redox extents compared to Fe_3O_4 with the help of transition metal substitution and provided the ability to retain this performance over repeated redox cycles by alleviating sintering and by carrying out the processes

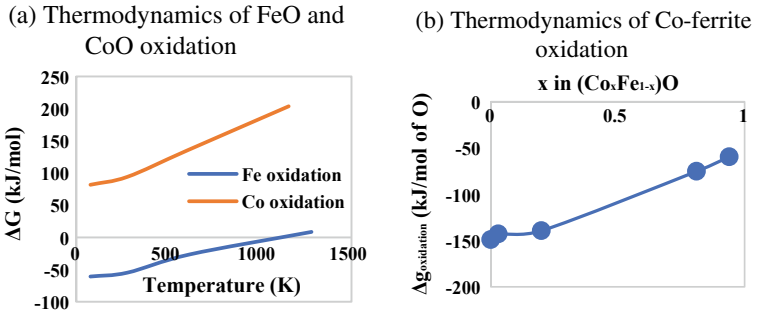

Fig. 5 Reaction for Gibbs free energy of oxidation in H_2O, for **a** FeO compared with CoO varying with temperature and **b** Co ferrite varying with Co content [35, 36]

over thermally stable and inert lattices. Oxidation analysis of Co-substituted ferrite dissolved in ZrO_2 using H_2O revealed that Fe oxidized simultaneously in dissolved state in ZrO_2 lattice and mixed lattice of Co-Fe [52].

Reduction barrier for Fe_3O_4-based materials was also found to decrease in the presence of Al_2O_3 according to thermodynamic analysis due to the formation of iron aluminate, which separate back when oxidized. This cycle is also called Hercynite cycle [36, 53]. This lowered the reduction temperature requirement compared to its counterparts in the absence of Al_2O_3. Equations (10 and 11) show a typical Hercynite cycle for Co ferrite with alumina modified for CO_2 splitting. Co ferrite in the presence of Al_2O_3 provided increase in oxidation yield by 4 times [53]. Improved kinetics was also demonstrated using Co ferrite deposited over high surface area of Al_2O_3.

$$CoFe_2O_4 + 3Al_2O_3 \rightarrow CoAl_2O_4 + 2FeAl_2O_4 + 0.5O_2 \tag{10}$$

$$CoAl_2O_4 + 2FeAl_2O_4 + CO_2 \rightarrow CoFe_2O_4 + 3Al_2O_3 + CO \tag{11}$$

Similar spinel structured iron-based alumina material was also developed by the current authors derived from layered double hydroxide (LDH) precursors. The authors focused on magnetite form of iron to first understand the reaction before proceeding to the ferrite forms. Fe_3O_4 stabilized on Mg-alumina (Mg/Al/Fe) was compared with Fe_3O_4 stabilized on MgO on their performance for CO_2 splitting. The oxygen carrier Mg/Al/Fe when cycled between 1673 and 1373 K provided CO yield that was 3 times higher with persistent performance over multiple redox cycles than CO yield obtained from other novel materials such as Zr-doped CeO_2 and other perovskite-based oxygen carriers. Figure 6 shows the redox cycling of Mg/Al/Fe carrier using thermogravimetric analysis [45]. While the alumina portion provided Hercynite cycle-assisted enhancement, presence of Mg provided enhanced thermal stability over multiple cycles. As these materials were prepared from novel precursors (layered double hydroxides in this case), the formed Mg/Al/Fe provided high surface area and increased oxygen exposed to surface. This resulted in fast surface

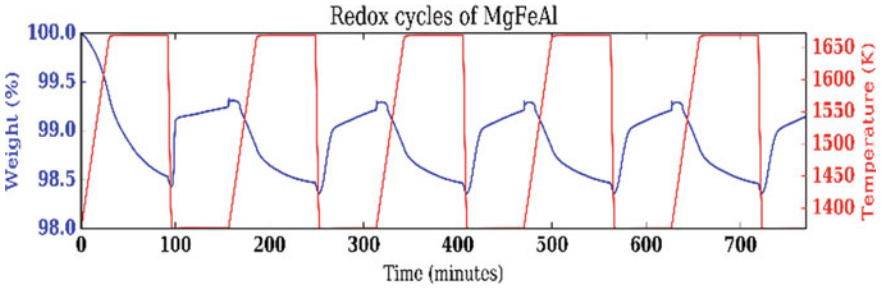

Fig. 6 Thermogravimetric analysis of redox cycling of Mg/Al/Fe between 1673 and 1373 K for CO_2 splitting

kinetics, which contributed to ~80% of the total oxidation conversion. The surface kinetics was sustainable to sintering over repeated redox cycles [45].

Further research into improvement and testing in pilot scale reactors such as solar concentrators-based reactors is necessary to obtain better and sustainable iron-based oxygen carriers. Added advantage gained by utilizing Fe-based oxygen carriers is from lower costs and increased material sustainability, compared to Ce oxides and perovskite-based oxygen carriers, and due to significantly more availability of iron oxides and ferrite minerals [45]. So, in the research involving ferrite and Hercynite cycles, researchers should also focus on limiting the doping agents to easily available oxides and lower the requirement of rare earth metal oxides and other materials that have low availability. Note that CO_2 and H_2O splitting will need to demonstrate using scale-up facility to significantly replace fossil fuel consumption and act as a bridge during our transition to complete renewable energy consumption and carbon neutral lifestyle. Since oxygen carrier materials will eventually be expended after multiple cycles and significant amounts of oxygen carrier materials will be required for large-scale operation, avoiding rare earth metal oxides and materials rarely available would help provide availability at not only certain regions but everywhere. This will be beneficial not only for sustainability in their utilization and ease in scaling but also avoid potential geo-political conflicts. We now discuss Ce-based oxygen carriers and their doped derivatives with focus on CO_2 and H_2O splitting in context with Fe-based oxygen carriers to determine the potential benefits and challenges they offer with this approach.

8.2.2 Cerium Oxide-Based Cycles

Redox cycling of CeO_2 revealed that reducing to stoichiometric levels (Ce_2O_3) should be avoided as they incur sublimation. So, reduction was limited to non-stoichiometric extents, $CeO_2/CeO_{2-\delta}$ (where $CeO_{2-\delta}$ is the reduced form of CeO_2 and δ represents its oxygen storage capacity), which not only avoided sublimation, but also avoided high temperatures required for complete reduction and provided fast oxidation kinetics and structural stability from non-stoichiometric kinetics [55]. Since CeO_2 is redox cycle to only non-stoichiometric extents, they inherently provide lower oxygen storage capacity compared to iron-based oxygen carriers. But this disadvantage is countered by fast kinetics and the lack of sintering issues in $CeO_2/CeO_{2-\delta}$ cycling which avoids the need for inert materials to effectively provide comparability in oxygen storage capacity with Fe-based alternatives. Sustained reduction extent over repeated cycling was found with storage capacity retention up to 86% even after 2000 cycles, see Fig. 7 [54], where δ represents extent of reduction as in $CeO_{2-\delta}$. Stable CeO_2 structure provided significant fast oxygen diffusion and also provided with the capability to use large-scale CeO_2 structures unlike Fe-based structures, which need to be limited to small scales for considerable kinetics. Due to this, the state-of-the-art reactor scale for CeO_2 is larger, i.e., it has been tested in many pilot scale solar concentrator reactors of larger scale than other oxygen carriers [34, 55, 56].

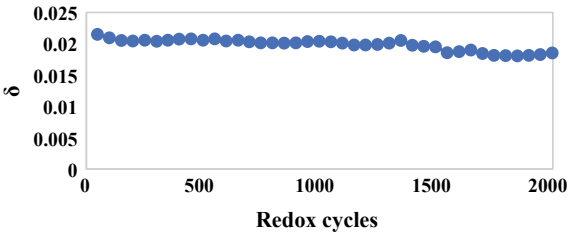

Fig. 7 Extent of reduction (δ) in CeO_2 after several redox cycles [54]

During CO_2 splitting, CeO_2 oxidation showed specific surface area dependency. Rate was significantly higher compared to typical iron-based oxygen carriers. It provided lower kinetics compared to H_2O splitting. But, at temperatures above 1100 K, CO_2 splitting was more favored as compared to H_2O splitting [32]. While CeO_2 cycling provides significant advantages over iron-based cycling, it required higher reduction temperatures, greater than 1800 K, along with relatively lower oxygen storage. This can be seen from Fig. 8 that compares thermodynamic oxygen yield under similar conditions with that from Co ferrite [57, 58]. This calls for improvement in its capabilities similar to ferrite improvement via doping and substitution.

A wide variety of dopants were incorporated into CeO_2's fluorite structure with rare earth metal, alkaline earth metal and transition metal oxides to improve its extent of reduction at lower temperatures and in some cases avoid sublimation when reduced at higher temperatures. Morphologically, variant derivatives were also tested including materials with multi-modal porosity to provide faster kinetics along with improved heat transfer when incorporated into solar concentrator reactors [54, 62]. Some sintering was found in the macroporous structures, but these materials maintained enhanced performance with reduced influence from sintering. Introduction of divalent and trivalent cations such as Ca^{2+}, Sr^{2+}, Y^{3+}, Pr^{3+} and Gd^{3+} increased oxidation rates by stabilizing intrinsic oxygen vacancies and thus mobilizing the oxygen within the lattice. However, they provided no enhancement to the extent

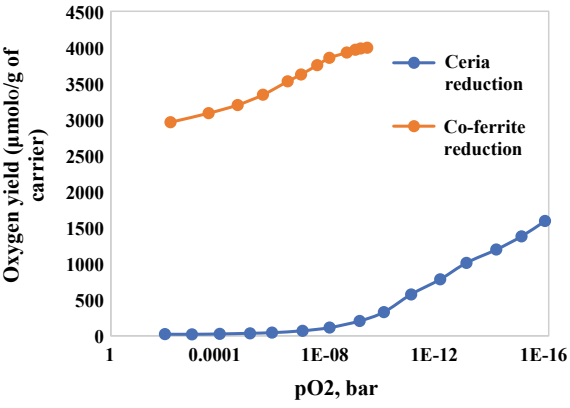

Fig. 8 Gaseous equilibrium oxygen yields from thermal reduction of CeO_2 and $Co_{2.4}Fe_{0.6}O_4$ at 1473 K [57, 58]

of reduction and thus did not improve the bottlenecking factors, see Fig. 9 [59]. Tetravalent ions such as Zr^{4+}, when added, provided with increased thermodynamic drive and enhanced the extent of net reduction of Ce^{4+} ions as seen from Fig. 10 that compares the reduction yield with pure CeO_2 [60, 63]. But addition of Zr^{4+} was found to decrease the extent of oxidation, so a trade-off is necessary to increase the overall performance and oxygen storage capacity so that further research is necessary to understand this behavior. Peak in solar energy-to-fuel conversion efficiency is presented in Fig. 11 that shows the effect of varying Zr content in CeO_2 [61]. Other rarer earth metals such as Hf^{4+}, Sm^{3+} were also screened but, as discussed in the previous sub-section, incorporation of these rare metals is a challenge or even detrimental especially when scaling up these processes [64]. Reference [55] provides an extensive review of doped ceria along with influence of preparation techniques and their performance in CO_2 and H_2O splitting. All of those tested for CO_2 splitting had oxygen storage significantly lower than that provided by LDH derived Mg/Al/Fe oxygen carrier with good stability even after 5 cycles [45]. Other class of materials was also developed, other than ferrite and ceria-based materials. We limit this section with our final class of materials called perovskite materials tested as oxygen carriers.

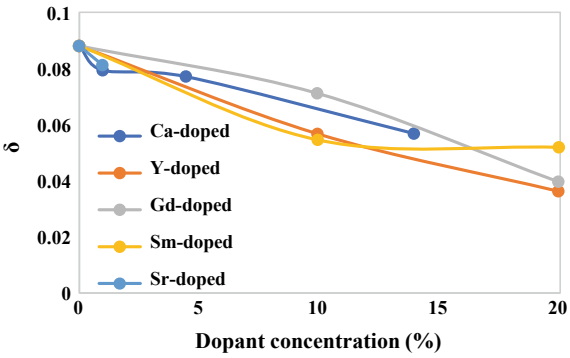

Fig. 9 Effect of dopant cation and its concentration on the extent of reduction at 1800 K [59]

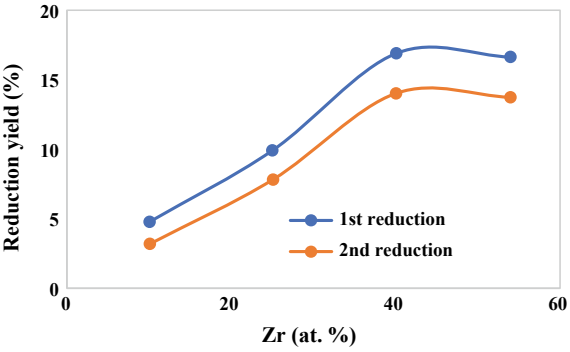

Fig. 10 Effect of Zr content in CeO_2 on the extent of reduction at 1573 K [60]

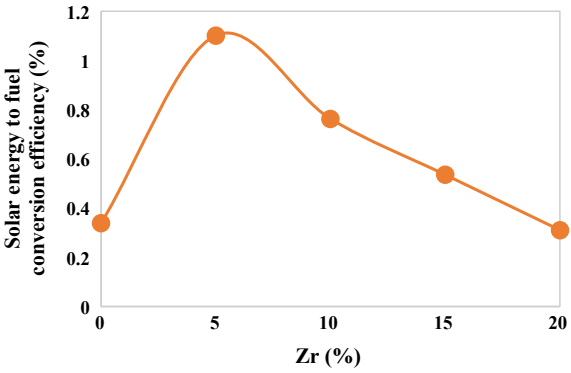

Fig. 11 Effect of Zr content in Zr-doped ceria on the solar energy-to-fuel conversion efficiency [61]

8.2.3 Perovskite-Based Cycles

These materials are mixed metal oxides, which are utilized for their non-stoichiometric redox behavior for CO_2 and H_2O splitting cycles. They are represented by the form $ABO_{3-\delta}$, where A and B are cationic vacancies that can be filled by a wide variety of dopants [65]. One of the common perovskites tested was LSM ($La_{1-x}Sr_xMnO_{3-\delta}$) which, by thermodynamic screening, was found to provide higher oxygen storage capacity compared to CeO_2 [51, 65–69]. While they provided enhanced extent of reduction, oxidation was less favorable, which often resulted in incomplete oxidation. Even with this inept performance, it was found to provide better performance compared to CeO_2. Addition of Mn ions to B sites and Sr ions to A sites in La-aluminate perovskites was found to provide significant increase in the extent of oxidation and yielded almost 6 times higher CO compared to pure CeO_2 [70]. This was carried out by redox cycling between 1573 and 1273 K and tested stability up to 80 cycles. Some research about incorporation of inert support was also carried out, which showed to affect its performance. While this class of materials is showing good promise, they are widely unexplored and could offer a good pathway for future investigation. But, as discussed in the previous sub-sections, doping of unreasonably rare cations, even though may provide an incremental increase, they should be avoided as we focus research efforts on sustainable and scalable materials. Incorporation of abundant transition metals and possible incorporation of Hercynite cycles into perovskite class materials could also provide fast kinetics, thermal stability along with significantly high oxygen storage capacity.

9 Biomass and Solid Wastes-Assisted Thermochemical Conversion

From above section, one can see the difficulty and practically of low CO_2 conversion along with issues of solar concentrator-based reactor and compatible material

development for realizing the thermochemical looping. These processes are necessary to bridge from existing infrastructure to a future of renewable and sustainable energy utilization with large replacement of fossil fuels. But, the current state of redox looping is not fully developed to be directly scaled which calls for additional improved development to transition from current state to the development of redox looping and possibly even beyond for efficiency and performance improvements. In the future, carbon neutral lifestyle and renewable energy production have been proposed using various sources such as wind, solar and geothermal. However, they require significant overhaul in the existing carbon-based infrastructure. Simultaneously, we need development of energy extraction techniques at larger scale, eventually reaching scales of fossil fuel energy. This need for infrastructure overhaul can be reduced by utilizing existing renewable carbon-based sources to produce fuels and chemicals that are similar in properties to the existing fossil fuel-based products and can be utilized in the existing infrastructure with minimal changes. Biomass, bio-wastes and municipal solid wastes, such as plastic, paper and rubber wastes, can be converted to syngas via thermochemical pathways such as gasification. This pathway is known to be a reliable precursor to various transportation fuels, value-added chemicals and a high-heating value fuel for direct combustion. Even though plastic and some rubber wastes are currently produced from fossil fuel-based sources and gasifying and utilizing them would mean carbon emissions, plastics production from syngas also needs to be considered along with energy applications. This means, as production of syngas is advantageous even for plastics production, gasification of plastic wastes to produce syngas can then be used to form ethylene and finally plastics. This would then offer an environmentally benign pathway for recycling the plastic wastes, which alleviates existing issues of waste management.

Gasification involves thermal decomposition of solid feedstocks in the presence of gasifying agents such as O_2/air/H_2O or CO_2 to form syngas and other by-products such as char, tar and some low molecular mass hydrocarbons. CO_2-assisted gasification can provide significant advantage from the perspective of carbon utilization as it converts CO_2 into valuable syngas. As this process is endothermic, the energy requirement can be obtained from various non-fossil energy sources. Utilization of renewable or waste heat to carry out this process can make significant improvement on the carbon cycling and energy efficiency. Unlike redox cycling, the temperatures required for this process with a good throughput are between 1173 and 1373 K. Renewable heat needed here for this purpose can be from solar concentrators that will enhance its efficiency. Equations (12 and 13) are the basic global reactions involved during CO_2-assisted gasification other than pyrolytic reactions. C_xH_y refers to pyrolytic intermediates, and C refers to solid state carbon content (which forms char at the end of reaction) [71]. During this process, the feedstock pyrolyzes at high temperature to form volatiles and char. These intermediates then react with CO_2 via dry reforming in the gas-phase and Boudouard reaction in the solid phase (with char) to form H_2 and CO, see Eq. (12 and 13). The syngas composition can be adjusted downstream using shift processes to desired values.

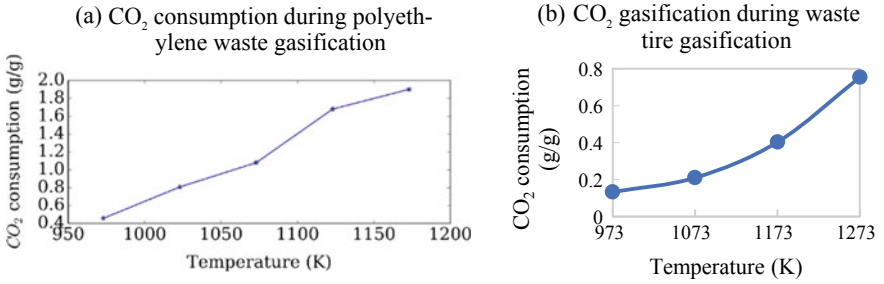

Fig. 12 Net CO_2 consumption per gram of **a** cross-linked polyethylene wastes and **b** waste tires gasified to form syngas [72, 74]

$$C_xH_y + xCO_2 \leftrightarrow \frac{y}{2}H_2 + 2xCO \tag{12}$$

$$C + CO_2 \leftrightarrow 2CO \tag{13}$$

Understanding the influence of CO_2 and the feasibility of this process for conversion of various feedstocks is essential to scrutinize feedstocks that offer more favorable possibilities on CO_2 utilization. The present authors and their predecessors have carried out series of CO_2-assisted gasification of various biomass wastes, plastic wastes and their mixtures to obtain the operable conditions, feasibility and extent of CO_2 utilization capability [72–75]. Some sample results are given in Fig. 12 which shows the net CO_2 consumed and converted to syngas per gram of feedstock utilized and the effect of temperature on CO_2 consumption [72]. Due to endothermic nature of these reactions, increase in temperature provided increased CO_2 conversion capability. But optimization is needed as increase in temperature increased energy requirement and thus decrease in cycle efficiency. Polyethylene wastes provided with CO_2 consumption as high as 2 grams per gram of polyethylene converted, while waste tires gasified consumed only ~0.5–0.7 grams of CO_2 per gram of tire feedstock. This is significantly high throughput compared to any other known CO_2 utilization pathways. Development of CO_2-assisted gasification for diverse feedstocks and scaling to appropriate levels is a necessary step toward renewable, sustainable and carbon neutral future.

10 Conclusions and Future Endeavors

Development of industrial processes for CO_2 utilization is of imminent importance as a bridge, while development of other carbon neutral energy and materials production techniques are being carried out for our quest to gradually replace fossil fuel consumption with renewables. CO_2 capture techniques showed that various efficient

techniques are available for capturing and transitioning to pure CO_2, but sustainability of the material, such as solvents and sorbents utilized for these processes, needs to be improved. Studies on incorporating these techniques into large-scale energy plants and other emitters are a future research pathway that is of pinnacle importance to screen and optimize these processes at pilot and industrial plant scale applications. Thermochemical redox looping was found to be promising in utilizing solar or other renewable energy to convert CO_2 to CO and H_2O to H_2. Their combination can be utilized and further explored to produce energy, transportation fuels and various other value-added chemicals. Due to faster reaction rates and relatively lower sintering tendency, CeO_2-based oxygen carrier materials for redox looping were the most extensively researched. While doping of CeO_2 was investigated to improve its performance, it needed higher reduction temperatures and provided with very low oxygen storage capacity and reduction extent compared to ferrite and Hercynite-based oxygen carriers. Some perovskite materials were also investigated in the literature, which provided significantly better redox activity and relatively similar kinetics of CeO_2, but they require rare earth metals and other rare metals which lowers its attractiveness as scaling this process would pose difficulties due to limited availability of these materials. The ferrite-based oxygen carriers provide a better option due to their ease of availability. They also provide higher availability of redox oxygen, but lacked in thermal stability, lost via sintering, and slower kinetics due to limited diffusion through FeO-Fe_3O_4 mixture. Incorporation of transition metals was found to enhance the redox oxygen storage capacity to some extent. Supporting or dissolving these materials over inert materials such as ZrO_2 was found to increase resistance toward sintering and improve the thermal stability and repeated cycle performance. Incorporation of alumina into these materials also provided with better performance at lower temperature due to the formation of aluminate. Layered double hydroxide (LDH) derived from mixed metal oxide of Mg/Al/Fe was developed, which provided with the highest and thermally stable CO yields and high oxygen storage capacity compared to any other CeO_2 derivatives, and also some novel perovskites. LDH provided thermal stability tested over 5 cycles. More oxygen corresponding to Fe on surface was active for redox looping which inherently improved kinetics compared to other iron-based oxygen carriers. Further research along these lines, including incorporation of other transition metals, requires detailed examination. This will help further improve its thermal performance and redox capability while maintaining reasonable scalability from wider availability of these materials. CO_2-assisted gasification of biomass, plastic and tire wastes was found to be most suitable and offered ease of scalability from the current state-of-the-art knowledge to convert CO_2 to a versatile product, syngas, which can be utilized to produce energy, fuels and value-added chemicals. Research into scaling this process for utilizing renewable energy needs to be addressed to develop a scalable version of this process. Development of a feed-flexible gasification reactor, which can provide with high CO_2 capture/utilization for varied feedstocks with minimal modification for operational conditions is much desired. This can help in scaling up of this process and provide a bridge toward carbon neutral energy future.

Acknowledgments This research work was supported by ONR and is gratefully acknowledged.

References

1. Keeling R (2018) Scripps Institute of Oceanography 2018. https://scripps.ucsd.edu/. Accessed 2 July 2018
2. Archer D (2010) The global carbon cycle. Princeton University Press, Princeton
3. Energy Information Administration U. Monthly Energy Rev (2019)
4. Falkowski P, Falkowski P, Scholes RJ, Boyle E, Canadell J, Canfield D et al (2000) The global carbon cycle: a test of our knowledge of earth as a system. Science 291:290–296. https://doi.org/10.1126/science.290.5490.291
5. Archer D (2005) Fate of fossil fuel CO_2 in geologic time. J Geophys Res 110:C09S05. https://doi.org/10.1029/2004jc002625
6. Hansen J, Sato M, Russell G, Kharecha P (2013) Climate sensitivity, sea level and atmospheric carbon dioxide. Philos Trans R Soc A Math Phys Eng Sci 371:20120294–20120294. https://doi.org/10.1098/rsta.2012.0294
7. Takahashi T (2004) Ocean science: enhanced: the fate of industrial carbon dioxide. Science 305:352–353. https://doi.org/10.1126/science.1100602
8. Zimov SA (2006) Climate change: permafrost and the global carbon budget. Science 312:1612–1613. https://doi.org/10.1126/science.1128908
9. Beiter P (2016) Renewable energy data book 2016. https://www.nrel.gov/docs/fy18osti/70231.pdf. Accessed 8 Aug 2018
10. Olah GA, Prakash GKS, Goeppert A (2011) Anthropogenic chemical carbon cycle for a sustainable future. J Am Chem Soc 133:12881–12898. https://doi.org/10.1021/ja202642y
11. Metz BOD, Coninck HC de, Loos M, Meyer LA (2005) IPCC, 2005: IPCC special report on carbon dioxide capture and storage. https://doi.org/10.1557/mrs2008.63
12. Wang D, Wang X, Ma X, Fillerup E, Song C (2014) Three-dimensional molecular basket sorbents for CO_2 capture: effects of pore structure of supports and loading level of polyethylenimine. Catal Today 233:100–107. https://doi.org/10.1016/j.cattod.2014.01.038
13. Ram Reddy MK, Xu ZP, Lu GQ, Diniz da Costa JC (2006) Layered double hydroxides for CO_2 capture: structure evolution and regeneration. Ind Eng Chem Res 45(22):7504–7509. https://doi.org/10.1021/ie060757k
14. Chen Z, Po F, Grace JR, Jim Lim C, Elnashaie S, Mahecha-Botero A et al (2008) Sorbent-enhanced/membrane-assisted steam-methane reforming. Chem Eng Sci 63:170–182. https://doi.org/10.1016/j.ces.2007.09.031
15. Patil CS, van Sint Annaland M, Kuipers JAM (2007) Fluidised bed membrane reactor for ultrapure hydrogen production via methane steam reforming: Experimental demonstration and model validation. Chem Eng Sci 62:2989–3007. https://doi.org/10.1016/j.ces.2007.02.022
16. Barelli L, Bidini G, Gallorini F, Servili S (2008) Hydrogen production through sorption-enhanced steam methane reforming and membrane technology: a review. Energy 33:554–570. https://doi.org/10.1016/j.energy.2007.10.018
17. Kumar S, Saxena SK (2014) A comparative study of CO_2 sorption properties for different oxides. Mater Renew Sustain Energy 3:30. https://doi.org/10.1007/s40243-014-0030-9
18. MacKenzie A, Granatstein DL, Anthony EJ, Abanades JC (2007) Economics of CO_2 capture using the calcium cycle with a pressurized fluidized bed combustor. Energy Fuels 21:920–926. https://doi.org/10.1021/ef0603378
19. Li F, Fan LS (2008) Clean coal conversion processes—progress and challenges. Energy Environ Sci 1:248–267. https://doi.org/10.1039/b809218b
20. Blamey J, Anthony EJ, Wang J, Fennell PS (2009) The calcium looping cycle for large-scale CO_2 capture. Prog Energy Combust Sci 36:260–279. https://doi.org/10.1016/j.pecs.2009.10.001

21. Charitos A, Hawthorne C, Bidwe AR, Korovesis L, Schuster A, Scheffknecht G (2010) Hydrodynamic analysis of a 10kWth Calcium Looping Dual Fluidized Bed for post-combustion CO_2 capture. Powder Technol 200:117–127. https://doi.org/10.1016/j.powtec.2010.02.012
22. Batini C, Burra KG, Gupta AK (2017) Sorption enhanced steam reforming of methane using CaO sorbent and Ni-based catalyst. In: 55th AIAA aerospace science meeting, AIAA. https://doi.org/10.2514/6.2017-1610
23. Xie M, Zhou Z, Qi Y, Cheng Z, Yuan W (2012) Sorption-enhanced steam methane reforming by in situ CO_2 capture on a CaO-Ca 9Al 6O 18 sorbent. Chem Eng J 207–208:142–150. https://doi.org/10.1016/j.cej.2012.06.032
24. Corella J, Toledo JM, Molina G (2006) Steam gasification of coal at low-medium (600–800 °C) temperature with simultaneous CO_2 capture in fluidized bed at atmospheric pressure: the effect of inorganic species. 1. literature review and comments. Ind Eng Chem Res 45:6137–6146. https://doi.org/10.1021/ie0602658
25. Koppatz S, Pfeifer C, Rauch R, Hofbauer H, Marquard-Moellenstedt T, Specht M (2009) H_2 rich product gas by steam gasification of biomass with in situ CO_2 absorption in a dual fluidized bed system of 8 MW fuel input. Fuel Process Technol. https://doi.org/10.1016/j.fuproc.2009.03.016
26. Udomsirichakorn J, Salam PA (2014) Review of hydrogen-enriched gas production from steam gasification of biomass: The prospect of CaO-based chemical looping gasification. Renew Sustain Energy Rev 30:565–579. https://doi.org/10.1016/j.rser.2013.10.013
27. Borgwardt H (1989) Sintering of nascent calcium oxide. Chem Eng Sci 44:53–60. https://doi.org/10.1016/0009-2509(89)85232-7
28. Zamboni I, Zimmermann Y, Kiennemann A, Courson C (2015) Improvement of steam reforming of toluene by CO_2 capture using Fe/CaO–Ca12Al14O33 bi-functional materials. Int J Hydrogen Energy 40:5297–5304. https://doi.org/10.1016/j.ijhydene.2015.01.065
29. Graves CR (2010) Recycling CO_2 into sustainable hydrocarbon fuels: electrolysis of CO_2 and H_2O. Columbia University
30. Marxer D, Furler P, Scheffe J, Geerlings H, Falter C, Batteiger V et al (2015) Demonstration of the entire production chain to renewable kerosene via solar thermochemical splitting of H_2O and CO_2. Energy Fuels 29:3241–3250. https://doi.org/10.1021/acs.energyfuels.5b00351
31. Graves C, Ebbesen SD, Mogensen M, Lackner KS (2011) Sustainable hydrocarbon fuels by recycling CO_2 and H_2O with renewable or nuclear energy. Renew Sustain Energy Rev 15:1–23. https://doi.org/10.1016/j.rser.2010.07.014
32. Agrafiotis C, Roeb M, Sattler C (2015) A review on solar thermal syngas production via redox pair-based water/carbon dioxide splitting thermochemical cycles. Renew Sustain Energy Rev 42:254–285. https://doi.org/10.1016/j.rser.2014.09.039
33. Perkins C, Weimer AW (2004) Likely near-term solar-thermal water splitting technologies. Int J Hydrogen Energy 29:1587–1599. https://doi.org/10.1016/j.ijhydene.2004.02.019
34. Yadav D, Banerjee R (2016) A review of solar thermochemical processes. Renew Sustain Energy Rev 54:497–532. https://doi.org/10.1016/j.rser.2015.10.026
35. Kodama T, Gokon N (2007) Thermochemical cycles for high-temperature solar hydrogen production. Chem Rev 107:4048–4077. https://doi.org/10.1021/cr050188a
36. Scheffe JR, Steinfeld A (2014) Oxygen exchange materials for solar thermochemical splitting of H_2O and CO_2: a review. Mater Today 17:341–348. https://doi.org/10.1016/j.mattod.2014.04.025
37. Yang W, Zhao H, Ma J, Mei D, Zheng C (2014) Copper-decorated hematite as an oxygen carrier for in-situ gasification chemical looping combustion of coal. Energy Fuels 28:3970–3981
38. Hossain MM, de Lasa HI (2008) Chemical-looping combustion (CLC) for inherent CO_2 separations-a review. Chem Eng Sci 63:4433–4451. https://doi.org/10.1016/j.ces.2008.05.028
39. Loutzenhiser PG, Meier A, Steinfeld A (2010) Review of the two-step H_2O/CO_2-splitting solar thermochemical cycle based on Zn/ZnO redox reactions. Materials (Basel) 3:4922–4938. https://doi.org/10.3390/ma3114922
40. Weibel D, Jovanovic ZR, Gaívez E, Steinfeld A, Mechanism of Zn particle oxidation by H_2O and CO_2 in the presence of ZnO n.d. https://doi.org/10.1021/cm503064f

41. Abanades S, Charvin P, Lemont F, Flamant G (2008) Novel two-step SnO2/SnO water-splitting cycle for solar thermochemical production of hydrogen. Int J Hydrogen Energy 33:6021–6030. https://doi.org/10.1016/j.ijhydene.2008.05.042
42. Nakamura T (1977) Hydrogen production from water utilizing solar heat at high temperatures. Sol Energy 19:467–475. https://doi.org/10.1016/0038-092X(77)90102-5
43. Nowotny J, Rekas M, Wierzbicka M (1982) Defect structure and electrical properties of the wustite phase. Zeitschrift Fur Phys Chemie 131:191–198. https://doi.org/10.1524/zpch.1982.131.2.191
44. Kodama T, Nakamuro Y, Mizuno T (2006) A two-step thermochemical water splitting by iron-oxide on stabilized zirconia. J Sol Energy Eng 128:3. https://doi.org/10.1115/1.1878852
45. Hussein AMA, Burra KG, Bassioni G, Hammouda RM, Gupta AK (2018) Production of CO from CO_2 over mixed-metal oxides derived from layered-double-hydroxides. Appl Energy 235:1183–1191. https://doi.org/10.1016/j.apenergy.2018.11.040
46. Coker EN, Ambrosini A, Rodriguez MA, Miller JE (2011) Ferrite-YSZ composites for solar thermochemical production of synthetic fuels: in operando characterization of CO_2 reduction. J Mater Chem 21:10767. https://doi.org/10.1039/c1jm11053e
47. KangG M, Zhang J, Zhao N, Wei W, Sun Y (2014) CO production via thermochemical CO_2 splitting over Ni ferrite-based catalysts. J Fuel Chem Technol 42:68–73. https://doi.org/10.1016/S1872-5813(14)60011-6
48. Lorentzou S, Karagiannakis G, Pagkoura C, Zygogianni A, Konstandopoulos AG (2014) Thermochemical CO_2 and CO_2/H_2O Splitting over $NiFe_2O_4$ for solar fuels synthesis. Energy Procedia 49:1999–2008. https://doi.org/10.1016/j.egypro.2014.03.212
49. Tong J, Jiang Q, Chen Z, Jiang Z, Li C (2015) Two-step thermochemical cycles for CO_2 splitting on Zr-doped cobalt ferrite supported on silica. Sol Energy 116:133–143. https://doi.org/10.1016/j.solener.2015.04.007
50. Chen Z, Jiang Q, Tong J, Yang M, Jiang Z, Li C (2017) Enhancement effects of dopants and SiO_2 support on mixed metal ferrites based two-step thermochemical water splitting. Sol Energy 144:643–659. https://doi.org/10.1016/j.solener.2017.01.049
51. Carrillo RJ, Scheffe JR (2017) Advances and trends in redox materials for solar thermochemical fuel production. https://doi.org/10.1016/j.solener.2017.05.032
52. Coker EN, Ohlhausen JA, Ambrosini A, Miller JE (2012) Oxygen transport and isotopic exchange in iron oxide/YSZ thermochemically-active materials via splitting of C(18 O) 2 at high temperature studied by thermogravimetric analysis and secondary ion mass spectrometry. J Mater Chem 22:6726–6732. https://doi.org/10.1039/c2jm15324f
53. Scheffe JR, Li J, Weimer AW (2010) A spinel ferrite/hercynite water-splitting redox cycle. Int J Hydrogen Energy 35:3333–3340. https://doi.org/10.1016/j.ijhydene.2010.01.140
54. Bonk A, Maier AC, Schlupp MVF, Burnat D, Remhof A, Delmelle R et al (2015) The effect of dopants on the redox performance, microstructure and phase formation of ceria. J Power Sources 300:261–271. https://doi.org/10.1016/j.jpowsour.2015.09.073
55. Bhosale RR, Takalkar G, Sutar P, Kumar A, Almomani F, Khraisheh M (2018) A decade of ceria based solar thermochemical H_2O/CO_2 splitting cycle. https://doi.org/10.1016/j.ijhydene.2018.04.080
56. Furler P, Steinfeld A (2016) Heat transfer and fluid flow analysis of a 4 kW solar thermochemical reactor for ceria redox cycling. Chem Eng Sci 137:373–383. https://doi.org/10.1016/j.ces.2015.05.056
57. Panlener RJ, Blumenthal RN, Garnier JE (1975) A thermodynamic study of nonstoichiometric cerium dioxide. J Phys Chem Solids 36:1213–1222. https://doi.org/10.1016/0022-3697(75)90192-4
58. Zhang WW, Chen M (2013) Thermodynamic modeling of the Co-Fe-O system. CALPHAD Comput Coupling Phase Diagrams Thermochem 41:76–88. https://doi.org/10.1016/j.calphad.2013.02.002
59. Scheffe JR, Steinfeld A (2012) Thermodynamic analysis of cerium-based oxides for solar thermochemical fuel production. Energy Fuels 26:1928–1936. https://doi.org/10.1021/ef201875v

60. Le Gal A, Abanades S, Bion N, Le Mercier T, Harlé V (2013) Reactivity of doped ceria-based mixed oxides for solar thermochemical hydrogen generation via two-step water-splitting cycles. Energy Fuels 27:6068–6078. https://doi.org/10.1021/ef4014373
61. Ganzoury MA, Fateen SEK, El Sheltawy ST, Radwan AM, Allam NK (2016) Thermodynamic and efficiency analysis of solar thermochemical water splitting using Ce-Zr mixtures. Sol Energy 135:154–162. https://doi.org/10.1016/j.solener.2016.05.053
62. Furler P, Scheffe J, Marxer D, Gorbar M, Bonk A, Vogt U et al (2014) Thermochemical CO_2 splitting via redox cycling of ceria reticulated foam structures with dual-scale porosities. Phys Chem Chem Phys 16:10503. https://doi.org/10.1039/c4cp01172d
63. Le Gal A, Abanades S (2012) Dopant incorporation in ceria for enhanced water-splitting activity during solar thermochemical hydrogen generation. J Phys Chem C 116:13516–13523. https://doi.org/10.1021/jp302146c
64. Scheffe JR, Jacot R, Patzke GR, Steinfeld A (2013) Synthesis, characterization, and thermochemical redox performance of Hf 4+ , Zr 4+, and Sc 3+ doped ceria for splitting CO_2. https://doi.org/10.1021/jp4050572
65. Orfila M, Linares M, Molina R, Botas JÁ, Sanz R, Marugán J (2016) Perovskite materials for hydrogen production by thermochemical water splitting. Int J Hydrogen Energy 41:19329–19338. https://doi.org/10.1016/j.ijhydene.2016.07.041
66. Scheffe JR, Weibel D, Steinfeld A (2013) Lanthanum–Strontium–Manganese perovskites as redox materials for solar thermochemical splitting of H_2O and CO_2. https://doi.org/10.1021/ef301923h
67. Dey S, Naidu BS, Govindaraj A, Rao CNR (2015) Noteworthy performance of La 1 − xCaxMnO3 perovskites in generating H_2 and CO by the thermochemical splitting of H_2O and CO_2. Phys Chem Chem Phys 17:122–125. https://doi.org/10.1039/C4CP04578E
68. Dey S, Naidu BS, Rao CNR (2015) Ln0.5A0.5MnO3 (Ln = Lanthanide, A = Ca, Sr) perovskites exhibiting remarkable performance in the thermochemical generation of CO and H_2 from CO_2 and H_2O. Chem A Eur J 21:7077–7081. https://doi.org/10.1002/chem.201500442
69. Yang C-K, Yamazaki Y, Aydin A, Haile SM (2014) Thermodynamic and kinetic assessments of strontium-doped lanthanum manganite perovskites for two-step thermochemical water splitting. J Mater Chem A 2:13612–13623. https://doi.org/10.1039/c4ta02694b
70. McDaniel AH, Miller EC, Arifin D, Ambrosini A, Coker EN, O'Hayre R et al (2013) Sr- and Mn-doped $LaAlO_3 - \delta$ for solar thermochemical H2 and CO production. Energy Environ Sci 6:2424. https://doi.org/10.1039/c3ee41372a
71. Burra KG, Gupta AK (2018) Thermochemical reforming of wastes to renewable fuels. In: Runchal AK, Gupta AK, Kushari A, De A, Aggarwal SK (eds) Energy for propulsion: a sustainable technologies approach. Singapore: Springer Singapore, pp 395–428. https://doi.org/10.1007/978-981-10-7473-8_17
72. Singh P, Déparrois N, Burra KG, Bhattacharya S, Gupta AK (2019) Energy recovery from cross-linked polyethylene wastes using pyrolysis and CO_2 assisted gasification. Appl Energy 254:113722. https://doi.org/10.1016/j.apenergy.2019.113722
73. Déparrois N, Singh P, Burra KG, Gupta AK (2019) Syngas production from co-pyrolysis and co-gasification of polystyrene and paper with CO_2. Appl Energy 246:1–10. https://doi.org/10.1016/j.apenergy.2019.04.013
74. Policella M, Wang Z, Burra KG, Gupta AK (2019) Characteristics of syngas from pyrolysis and CO_2-assisted gasification of waste tires. Appl Energy 254:113678. https://doi.org/10.1016/j.apenergy.2019.113678
75. Wang Z, Burra KG, Lei T, Gupta AK (2019) Co-gasification characteristics of waste tire and pine bark mixtures in CO_2 atmosphere. Fuel 257:116025. https://doi.org/10.1016/j.fuel.2019.116025

Performance and Controlling Regimes Analysis of Methane Steam Reforming on Ru/γ-Al_2O_3 Cordierite Monoliths

Carmen W. Moncada Quintero, Roman Z. Babar, and Stefania Specchia

Nomenclature

Fluid properties

$C_{CH_4,in}$; C_b	Methane concentration in feed mixture (bulk) (mol m^{-3})
Cp_f	Heat capacity of the gas mixture (J mol^{-1} K^{-1})
Cp_i	Heat capacity of *i* component (J mol^{-1} K^{-1})
C_s	Methane concentration at catalyst surface (mol·m^{-3})
$D_{CH_{4-mix}}$	Diffusivity of CH_4 in gas phase (m^2 s^{-1})
$D_{CH_{4,e}}$	Effective diffusivity of CH_4 in coated layer (m^2 s^{-1})
$D_{CH_{4-i}}$	Binary diffusion of CH_4 and i gas species (m^2 s^{-1})
D_k	Knudsen diffusion (m^2 s^{-1})
h_e	Heat transfer coefficient of gas mixture (W m^{-2} K^{-1})
$k_{m,e;}k_G$	Mass transfer coefficient of CH_4 (m s^{-1})
$k_{m,app}$	Apparent mass transfer coefficient (m s^{-1})
M_{CH_4}	Molecular weight of CH_4 (kg $kmol^{-1}$)
M_i	Molecular weight of *i* compound (kg $kmol^{-1}$)
M_{mix}	Molecular weight of gas mixture (kg $kmol^{-1}$)
P	Transverse Peclet number (m)
R_g	Universal gas constant (J mol^{-1} K^{-1})
u_o	Inlet gas velocity (m s^{-1})
v_{CH_4}	Molar volume of CH_4 (cm^3 mol^{-1})
v_i	Molar volume of *i* compound (cm^3 mol^{-1})
y_{CH_4}	Mole fraction of CH_4

C. W. Moncada Quintero · R. Z. Babar · S. Specchia (✉)
Department of Applied Science and Technology, Politecnico di Torino, Corso Duca degli Abruzzi 24, 10129 Torino, Italy
e-mail: stefania.specchia@polito.it

© Springer Nature Singapore Pte Ltd. 2021

A. De et al. (eds.), *Sustainable Development for Energy, Power, and Propulsion*, Green Energy and Technology,
https://doi.org/10.1007/978-981-15-5667-8_5

y_i	Viscosity of *i* compound (kg m^{-1} s^{-1})
μ_i	Viscosity of *i* compound (kg m^{-1} s^{-1})
μ_f	Viscosity of gas mixture (kg m^{-1} s^{-1})
λ_i	Thermal conductivity of i component (W m^{-1} K^{-1})
λ_{mix}	Thermal conductivity of gas mixture (W m^{-1} K^{-1})
ρ_f	Density of gas mixture (kg m^{-3})

Reaction Data

F_{tot}	Total gas flow rate (m^3 s^{-1})
k_{obs}	Observed first-order reaction rate constant (s^{-1})
k_s	Surface reaction rate constant
P	Reaction pressure (kPa)
r_{CH_4}	Reaction rate for CH_4 (kmol kg^{-1} s^{-1})
R_{CH_4}	Volumetric reaction rate for CH_4 (kmol m^{-3} s^{-1})
T	Reaction temperature (K)
T_b, T_s	Temperature in the bulk of the gas phase and surface of the catalyst layer (K)
$T_{b,c}$	Temperature in the bulk of the catalyst layer (K)
ϕ	Thiele modulus
H	Effectiveness factor
ΔH_r	Heat of MSR reaction (J mol^{-1})
λ_{cat}	Catalyst thermal conductivity (W m^{-1} K^{-1})
λ_e	Effective thermal conductivity (W m^{-1} K^{-1})

Monolith Properties

A_{ch}	Area of a single bare channel (m^2)
A_m	Monolith area (m^2)
$A_{\Omega,e}$	Cross-sectional area of fluid phase (m^2)
$A_{\Omega,i}$	Cross-sectional area of catalyst layer (m^2)
d_h	Hydraulic diameter (m)
d_f	Average channel dimension (m)
D	Inner length of the channel (m
D_m	Monolith diameter (m)
GSA	Geometric surface area (m^2 m^{-3})
l_w	Channel width (m)
L_m	Monolith length and diameter (m)
n	Cell density (N° cell m^{-2})
P_c	Interfacial perimeter (m
$R_{\Omega,e}$	Characteristic length for gas phase (m)

$R_{\Omega,i}$	Characteristic length for coated layer (m)
ε	Voidage of square channel
δ_w	Wall thickness (m)
ς	Cell density (cpsi)

Coated Layer Properties

$k_{m,I}$	Internal mass transfer coefficient (m)
r_p	Pore radius (m)
S_{BET}	Specific surface area ($\text{m}^2\ \text{g}^{-1}$)
V_{BJH}	Total pore volume ($\text{cm}^3\ \text{g}^{-1}$)
δ_c	Coated layer thickness (m)
ε_c	Coated layer porosity
ρ_c	Coated layer density (kg m^{-3})
τ_c	Tortuosity factor

Resistances

R_e	External mass transfer resistance (s m^{-1})
R_i	Internal mass transfer resistance (s m^{-1})
R_r	Reaction resistance (s m^{-1})
R_t	Overall resistance (s m^{-1})

Characteristic Times

t_c	Characteristic contact time (s)
t_d^e	Transverse diffusion time for the flow area (s)
t_d^i	Transverse diffusion time for the coated area (s)
t_r	Characteristic reaction time (s)
t_z	Longitudinal diffusion time (s)

Dimensionless Numbers

A	$D_{\text{CH}_4-\text{mix}}/D_{\text{CH}_4,e}$ ratio
B	$R_{\Omega,i}/R_{\Omega.e}$ ratio
Ca	Carberry number
Le	Lewis number

Pr	Prandtl number
Re	Reynold number
Sc	Schmidt number
Sh_i, Sh_e	Internal/external Sherwood number
$Sh_{i,\infty}$, $Sh_{e,\infty}$	Asymptotic internal/external Sherwood number
Sh_{app}	Apparent Sherwood number
$\beta_{in;}$ β_{ext}	Dimensionless internal/external Prater number
γ_b; γ_s	Arrhenuis number at the bulk and surface of the gas phase
χ	Damkholer for interphase heat transport
ψ	Damkholer for intraparticle heat
x	Radial coordinate

Abbreviations

BET	Brunauer–Emmet–Teller
EDX	Energy dispersive X-ray
FESEM	Field-emission scanning electron microscopy
ID	Internal diameter
MSR	Methane steam reforming
NDIR	Non-dispersive infrared
S_{BET}	Specific surface area calculated by BET method
SCS	Solution combustion synthesis
S/C	Steam-to-carbon ration
TOS	Time on stream
WGS	Water gas shift
WHSV	Weight hourly space velocity
XRD	X-ray diffraction

1 Introduction

Hydrogen (H_2) is one of the most abundant elements in the Earth's crust, and due to its capability to drive the generation of electricity without emitting harmful pollutants, H_2 is considered as a prominent clean, environmentally benign and safe-to-handle major energy carrier of the future [1, 2]. Nowadays, H_2 is used in several industrial processes such as refining, treating metals, and food processing. In addition, H_2 is an essential building block for the production of ammonia, and thus fertilizers, and of methanol, utilized as a part of the production of many polymers [3–7]. The most important source of H_2 today is natural gas (~97% of CH_4) with approximately 80% efficiency. In fact, more than 90% of the world's H_2 is produced by steam reforming (SR), being the most viable option for supporting a future hydrogen economy [8,

9]. Methane steam reforming (MSR) is a highly endothermic reaction (Reaction 1) accompanied mainly by the side reaction of the water gas shift (WGS), which is slightly exothermic (Reaction 2):

$$CH_4 + H_2O \rightarrow CO + 3H_2 \ \Delta H^0_{298} = +206.3 \text{ kJ mol}^{-1} \quad (1)$$

$$CO + H_2O \rightarrow CO_2 + H_2 \ \Delta H^0_{298} = -41.1 \text{ kJ mol}^{-1} \quad (2)$$

To be feasible at relatively low pressure and temperature ($T < 1000$ °C, P < 5 bars), these reactions are carried out in the presence of a catalyst. Nickel-based catalysts are actually the most widely used for industrial reforming processes because of their high availability and low cost [8–10]. However, the catalytic activity gradually decreases because of carbon deposition and sintering of Ni. Catalyst systems based on noble metals have been extensively studied by many researchers, giving rise to excellent catalytic performances toward MSR processes [11, 12]. Noble metals such as Ru, Rh, Pd, Pt, and Ir have a higher barrier for carbon formation during operation than Ni. Particularly, whiskers carbon formation (caused by carbon deposition) can be problematic at severe condition for an effective performance of the catalyst [13]. Moreover, the catalyst may eventually break down [14]. Among the noble metals, Ru and Rh are the most active metals with comparable performance, while Ru is the most promising candidate due to its lower price [11–15]. On the other hand, the nature of the support in MSR may also have a significant impact on the catalytic activity. Carrier materials for MRS catalysts require high specific surface area, wider pore structure easily accessible for gaseous transport, and thermal stability at high temperature (<1000 °C), even in the presence of steam [16]. Alumina (Al_2O_3) is widely used as catalyst carrier because it is inexpensive, reasonably thermally stable, and can provide a wide range of specific surface area and porosity through its different phases [17, 18]. Ferreira-Aparicio et al. [19] investigated the role of Al_2O_3 support on the catalytic activity of Ru catalysts during MSR. They found that surface hydroxyl groups play a main role in the catalyst's resistance to deactivation. In the same way, Berman et al. [20] reported that during 10 days of operation of 1 wt% Ru/γ-Al_2O_3 catalyst in the temperature range of 600–900 °C, the activity was stable without carbon depositions and change of mechanical properties of the catalyst.

Nowadays, research on MSR reaction is mainly devoted to improve the catalyst performance by producing as much H_2 as possible. Recently, the attention is focused on structured systems with active components supported on different configurations such as monoliths, foams, and honeycombs [16, 21–24]. In particular, monolith catalysts have been widely used in many applications due to for their excellent mechanical and chemical durability, high geometric surface area, rapid response to transient operation, low pressure drop and smaller sizes than reactors with traditional catalyst pellet materials. Furthermore, monolith reactors offer other advantages such as reduced capital cost, smaller footprints, and potentially easier transportation compared to fixed-bed reactors [25–27].

Several studies have shown that structured catalysts improve heat and mass transfer mechanisms between the fluid and solid phases. Especially, for endothermic process, high thermal conductive supports allow optimal thermal management in the catalytic volume maximizing heat transfer from the heating medium to the catalytic volume and reducing the temperature gradient due to the endothermicity of the reaction [28]. According to Tronconi et al. [28, 29], the effective thermal conductivity of a structured catalysts depends fundamentally on the conductivity of the substrate and that of the solid carrier deposited on the substrate. On the other hand, it is well known that in many heterogeneous catalytic reactions, the overall rate of reaction is often limited by mass transfer processes, which include both the internal diffusion (at intermediate temperatures) and external diffusion (at sufficiently high temperatures) of components into and out of the catalyst, especially for highly exothermic or endothermic reactions such as combustion or steam reforming [23, 24, 30, 31].

In the present work, we investigated the catalytic performance toward MSR of Ru and Rh on γ-Al_2O_3 catalysts supported on ceramic cordierite monoliths of square channel. Firstly, we compared the catalytic performance in terms of CH_4 conversion, H_2 production, CO selectivity, and H_2/CO molar ratio of Rh and Ru supported on γ-Al_2O_3. Secondly, we study the influence of the catalyst loading by varying the amount of carrier and active metal phase. Then, we evaluated the different controlling regimes (kinetic, intraparticle, or interphase diffusion control) and heat transfer effects for the best catalyst. All cordierite monoliths were coated by solution combustion synthesis. Finally, we evaluated the stability of the catalyst on the best-selected one.

2 Methods

2.1 Chemicals and Monoliths

Aluminum (III) nitrate nonahydrate, $Al(NO)_3$ $9H_2O$ ($\geq$98% purity), ruthenium (III) nitrosyl nitrate, $6Ru(NO)(NO_3)_3$ ($\geq$98% purity), rhodium(III) chloride, $RuCl_3$ ($\geq$98% purity), urea, CH_4N_2O ($\geq$99% purity) were purchased from Sigma–Aldrich. All aqueous solutions were prepared using ultrapure water (Millipore Milli-Q system with resistivity > 18 MΩ cm). For catalytic activity tests, pure CH_4, H_2, and N_2 gasses (purity 99.999%) were supplied in cylinders provided by SIAD S.p.A. (Italy) and used as received.

Ceramic monoliths of square channel (100 cell per $in.^2$) made of cordierite in dimensions of 40 mm diameter by 30 mm were provided by Chauger Honeycomb Ceramics Co. (Taiwan).

Table 1 List of catalyst prepared by varying metal and carrier load

Metal	Carrier	Catalyst	Abbreviation
1.5% Ru	5% Al_2O_3	1.5% Ru/5% Al_2O_3	1.5Ru5Al
3.0% Ru	5% Al_2O_3	3.0% Ru/5% Al_2O_3	3Ru5Al
1.5% Ru	10% Al_2O_3	1.5% Ru/10% Al_2O_3	1.5Ru10Al
1.5% Ru	20% Al_2O_3	1.5% Ru/20% Al_2O_3	1.5Ru20Al
1.5% Rh	10% Al_2O_3	1.5% Ru/10% Al_2O_3	1.5Rh10Al

2.2 Catalysts Preparation

Before the catalyst deposition, cordierite monoliths were cleaned in an ultrasonic bath with a water/acetone solution (50/50 vol.%) for 30 min and dried at 120 °C for 2 h. The catalytic layer based on Ru supported on γ-Al_2O_3 was coated by *in situ* solution combustion synthesis (SCS) following the detailed procedure discussed in our previous work [32]. Briefly, the necessary amounts of aluminum nitrate, ruthenium nitrosyl nitrate as precursors and urea as fuel were dissolved in aqueous solution (3 M) under vigorous stirring. The ratio between the amount of urea used and the stoichiometric amount (Φ) was equal to 1 [33, 34]. Then, each monoliths was dipped in the aqueous solution for 2–3 min and then introduced into a muffle furnace preheated at 600 °C for 10 min, where the combustion reaction occurred, letting the formation of the catalytic layer, and rapidly cooled down to room temperature in few minutes. The operation was repeated until the design weight of Ru/γ-Al_2O_3 was reached. Finally, the coated monoliths were calcined at 600 °C for 2 h in static air.

For comparison of the catalytic performance, Rh-based catalysts were also prepared with the same procedure by using the corresponding nitrate of the active metal. A set of X wt% ($X = 1.5$ and 3) of metal active phase (Ru, Rh) supported on γ-Al_2O_3 (with varying carrier loadings equal to 5, 10, and 20 wt% compared to the weight of the monolith) were prepared, according to Table 1.

2.3 Catalytic Tests

The catalytic activity of coated monoliths was evaluated toward MSR in a tubular reactor of AISI 310 (40 mm ID) placed in an electric oven, which provided sufficient heat to vaporize water. The entire plant was set to provide 3 kW of energy. The micro-reactor temperatures were measured by two K-type thermocouples located, respectively, at the inlet and outlet of the coated monolith. Before starting catalytic tests, the structured catalysts were reduced in situ sending a flow of 100 Nml min^{-1} of H_2 at 200 °C for 1 h. The catalytic tests were performed over a temperature range of 550–850 °C, at different steam-to-carbon molar ratios (S/C: 3-3.2) and weight hourly space velocities (WHSV 750–3000 Nl h^{-1} g_{cat}^{-1}). Mass flow controllers (Brooks Instrument Smart Mass Flow) were used to measure and control the flow

of gaseous reactants. The gas stream composition at the reactor outlet is monitored by an ABB gas analyzer (NDIR module Uras 14 for $CO/CO_2/CH_4$, paramagnetic module Magnos 106 for O_2 and H_2; water removed prior to entering the analyzer in a condenser at 3 °C). For all catalytic tests, measurements were repeated at least three times to assure their reproducibility and to check any possible aging phenomena on the structured catalysts.

The investigated catalysts were compared on the basis of CH_4 conversion, H_2 production, CO selectivity, and H_2/CO molar ratio. The CH_4 conversion is calculated to determine the amount of inlet CH_4 that has reacted and converted to products (Eq. 3).This value is based on the total dry outlet flow rate ($F_{\text{out,dry}}$), the inlet CH_4 flow rate ($CH_{4,\text{inlet}}$), and the CH_4 concentration in the product mixture ($CH_{4,\text{conc}}$).

$$\text{CH}_4\text{ conversion} = \left[1 - \frac{\left(\frac{\text{CH}_{4_{\text{conc}}} \times F_{\text{out}_{\text{dry}}}}{100}\right)}{\text{CH}_{4_{\text{inlet}}}}\right] \times 100 \tag{3}$$

The H_2 production is the H_2 concentration in the product mixture ($H_{2,\text{conc}}$). The H_2 selectivity (Eq. 4) is based on the molar volume of gas mixture (assuming it is an ideal gas mixture) and the CH_4 and H_2 outlet flowrates ($CH_{4,\text{outlet}}$ and $H_{2,\text{outlet}}$, respectively).

$$\text{H}_2\text{ Selectivity} = \left[\frac{\text{H}_{2_{\text{outlet}}}}{\left(\left(\frac{\text{CH}_{4_{\text{inlet}}}}{\text{Molecular Volume}}\right) - \text{CH}_{4_{\text{outlet}}}\right)}\right] \times 100 \tag{4}$$

The CO selectivity (Eq. 5) is based on the molar volume of gas mixture (assuming it is an ideal gas mixture) and the CH_4 and CO outlet flowrates ($CH_{4,\text{ outlet}}$ and CO_{outlet}, respectively).

$$\text{CO Selectivity} = \left[\frac{\text{CO}_{\text{outlet}}}{\left(\left(\frac{\text{CH}_{4_{\text{inlet}}}}{\text{Molecular Volume}}\right) - \text{CH}_{4_{\text{outlet}}}\right)}\right] \times 100 \tag{5}$$

Finally, the molar ratio of H_2/CO (Eq. 6) is monitored to analyze the product in syngas concentration.

$$\text{H}_2/_{\text{CO}}\,\text{Ratio} = \frac{\text{H}_{2_{\text{outlet}}}}{\text{CO}_{\text{outlet}}} \tag{6}$$

2.4 Characterization on the Best-Selected Catalyst

The specific surface area, textural properties of powder and structured samples were determined by N_2 physisorption at −196 °C using an ASAP 2020 instrument from Micromeritics. Prior to analysis, about 100 mg of each sample was outgassed overnight at 150 °C under high vacuum. The specific surface areas (S_{BET}) were determined by Brunauer–Emmet–Teller (BET) method in the relative pressure range of 0.05 and 0.30.

By using the same apparatus, the chemisorption analysis was carried out, in order to evaluate the active metals dispersion on supports. H_2 saturation was first performed by flowing 20 $Ncm^3\ min^{-1}$ of H_2 for 2 h at 350 °C, and at the end, a He flow rate of 20 $Ncm^3\ min^{-1}$ for 1.5 h was fed to the apparatus increasing the temperature to 370 °C. Then, at room temperature, a mixture of 10% CO in He was injected in pulses of 500 NμL each, until the fulfillment of constant outlet peaks. The amount of adsorbed gas was determined as the difference between the total injected volume and the residual escaped one. The metal dispersion on the carrier surface was determined as follows:

$$D_{\%} = 100 \cdot S_f \cdot \frac{V_{\text{ads}} \cdot M_{\text{me}}}{V_g \cdot F_{\text{me}}} \tag{7}$$

considering the stoichiometric factor S_f is equal to 1 (i.e., each Ru atom adsorbed one CO molecule), the total volume of CO chemisorbed refers to the mass of the carrier used for the analysis in $Ncm^3\ g^{-1}$ (V_{ads}), the metal atomic weight M_{me} (101.07 g mol^{-1} for Ru) and the total mass fraction of the metal on the catalyst (expressed as $g_{me}\ g^{-1}$ of carrier), and that one gas g_{mole}, V_g, occupies 22,414 cm^3 at normal conditions.

X-ray diffraction (XRD) patterns were collected using a Philips X-Pert MPD X-ray diffractometer equipped with copper Kα radiation at 40 kV and 30 mA to verify the effective composition of the samples and derive qualitative indications of the presence of comparatively large noble metals crystallite from its eventually visible peaks. All powder samples were scanned in the 2θ range of 20–70° over 1 h. The peaks were assigned according to the PCPFWIN database.

The surface morphology of the catalyst was examined by using a field-emission scanning electron microscopy (FESEM JEOL-JSM-6700F instrument). The elemental composition analysis was carried out by energy dispersive X-ray spectroscopy (Oxford Instruments Inca EDX apparatus).

The geometrical properties of monoliths for square channel are calculated by [35–39]:

$$n = \frac{1}{(D + \delta_W)^2} \tag{8}$$

$$\varepsilon = D^2 \cdot n \tag{9}$$

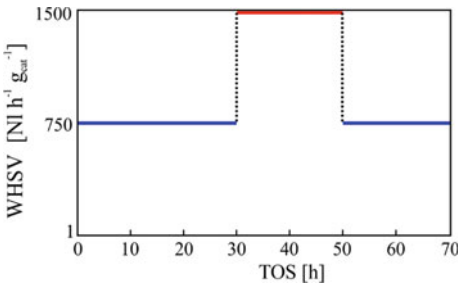

Fig. 1 Thermal cycling for stability tests: WHSV vs TOS at 800 °C and S/C of 3

$$\mathrm{GSA} = \frac{4\left(\sqrt{\varepsilon} - \varepsilon\right)}{\delta_w} \tag{10}$$

$$d_h = \frac{4 \cdot \varepsilon}{\mathrm{GSA}} \tag{11}$$

where n is the cell density (N° cell m^{-2}), D is the inner length of the channel (m), δ_w is the wall thickness (m), ε is the voidage for square channels, GSA is the geometric surface area (m^2 m^{-3}), and d_h is the hydraulic diameter (m).

2.5 Stability Measurements

Stability tests were performed over 70 h of time on stream (TOS) at 800 °C for the best-selected catalyst. The reactor was fed with a reactive mixture containing CH_4 and H_2O with a S/C equal to 3 and WHSV equal to 750 Nl h^{-1} g_{cat}^{-1}. At 30 h of TOS the WHSV was increased up to 1500 Nl h^{-1} g_{cat}^{-1}. At 50 h of TOS the WHSV was reported to 750 Nl h h^{-1} g_{cat}^{-1} till the end of the experiment (70 h of TOS), according to the thermal cycling shown in Fig. 1.

3 Results and Discussion

3.1 Ru/Rh Metal on γ-Al_2O_3 Carrier: Metal-Base Catalysts Comparison

In order to compare the catalytic performance of noble metals coated on monolith supports, Ru and Rh (active metal loading equal to 1.5 wt%) on γ-Al_2O_3 (10 wt% on the bare cordierite monolith) were tested toward the MSR reaction. The experiments were carried out in the temperature range of 550–850 °C, S/C equal to 3.0, and WHSV of 750 Nl h^{-1} g_{cat}^{-1}.

As can be seen from Fig. 2a, both noble metal-based catalysts do not reach complete methane conversion. However, the catalytic activity of the Ru-based one was found to be the most promising toward the MSR reaction in terms of CH_4 conversion, H_2 production, and CO selectivity. At temperatures higher than 750 °C, CH_4 conversion for 1.5Ru10Al catalyst remained slightly stable at 88.2%, reaching the maximum conversion (91.0%) at 800 °C, while for 1.5Rh10Al catalyst, CH_4 conversion increased for the entire temperature range studied achieving the maximum value of 87% at 850 °C. On the other hand, H_2 produced for both catalysts was nearly the same, except at temperatures between 600 and 700 °C, where H_2 production was slightly higher for 1.5Ru10Al catalyst (Fig. 2a). As far as the selectivity of CO is concerned, both catalysts showed an increase in CO selectivity at temperatures between 550 and 700 °C. At temperatures above 700 °C, CO selectivity for 1.5Rh10Al catalyst remained stable at approximately 42%, while for 1.5Ru10Al catalyst, it continued to increase up to 750 °C, where it reached the maximum selectivity value of 50.25% and then decreased due probably to the WGS reaction, which converts CO into CO_2 (Fig. 2b). In fact, as shown in Fig. 2c, at temperatures between 725 and 850 °C, the H_2/CO molar ratio was slightly higher for the Rh-based catalyst because of CO consumption (WGS reaction), which led to a higher CO_2 selectivity compared to that obtained for the 1.5Ru10Al catalyst (Fig. 2d). It is important to point out that the Ru-based catalyst produced a syngas richer in H_2 and selective to CO compared to the Rh-based catalyst one. For this reason, Ru was selected as the active metal phase for further investigations.

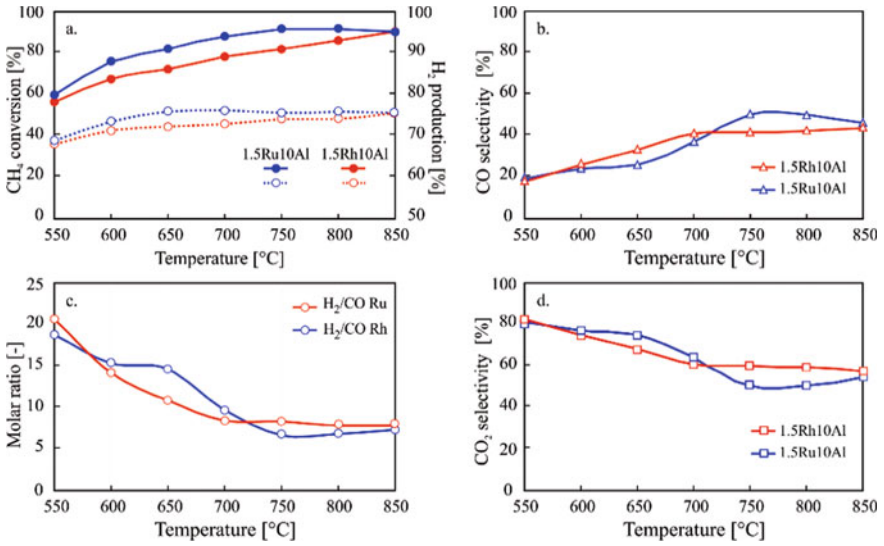

Fig. 2 MSR tests, performance comparison of monoliths 1.5% Ru and 1.5% Rh on 10% γ-Al_2O_3 at WHSV = 750 and S/C = 3. **a** CH_4 conversion and H_2 production; **b** CO selectivity; **c** H_2/CO molar ratio, and **d** CO_2 selectivity

3.2 *Ru/γ-Al_2O_3 Catalyst: Loading Comparison*

The effect of catalyst loading on catalytic performance of Ru/γ-Al_2O_3 for MSR was studied by varying the amount of both the carrier and the active metal phase. Three different loads of γ-Al_2O_3 (5, 10, and 20 wt%), corresponding to 3.20, 6.45, and 12.89 mg cm^{-2}, respectively, were studied. Ru, as the noble metal phase, was loaded on γ-Al_2O_3 with two different percentages of active phase (1.5 and 3.0 wt%, respectively) corresponding to a catalyst mass loading of 3.20 mg cm^{-2}. All experiments were carried out in the temperature range of 550–850 °C, with fixed S/C molar ratio of 3.0 and volumetric flow equal to 32.65 NL h^{-1}.

Figure 3a–d shows the effect of the carrier and active phase loading on the catalytic performance of the various catalytic monoliths. The results pointed out that the best catalytic performance was obtained with a load of 6.45 mg cm^{-2} (corresponding to 10 wt% of γ-Al_2O_3 and 1.5 wt% of Ru, sample 1.5Ru10Al), where the maximum CH_4 conversion achieved was 91% at 800 °C (Fig. 3a). On the other hand, H_2 concentration was quite stable for all catalyst at temperatures from 650 to 850 °C, with a H_2 production higher than 60%, except for 1.5Ru5Al catalyst (Fig. 3b), where the highest concentration of H_2 reached was 43.22%. Analyzing the selectivity of CO and the H_2/CO molar ratio (Fig. 3c, d), the highest concentration in dry reformate of CO was obtained for 1.5Ru10Al catalyst over the entire temperature range studied. Interestingly, for the catalysts with mass loading of 3.2 mg cm^{-2} (corresponding to

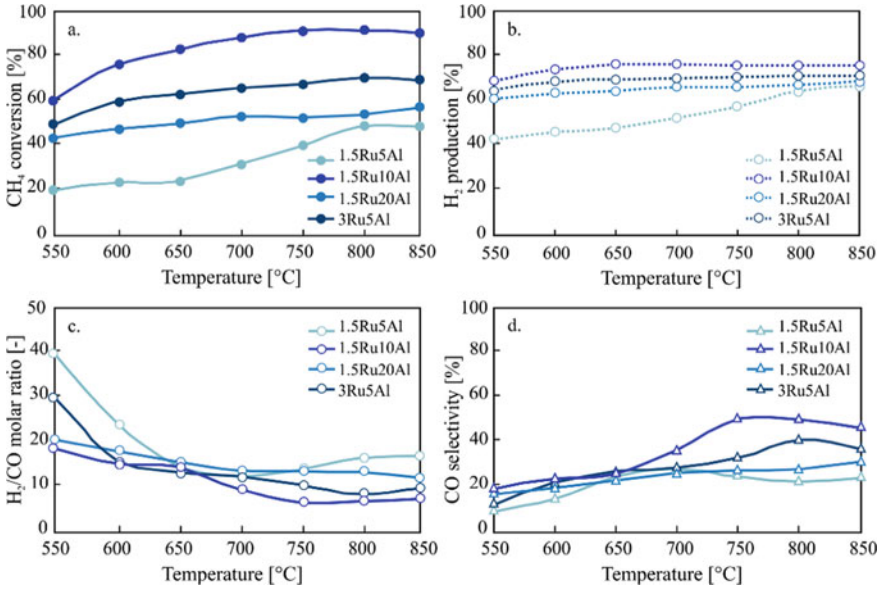

Fig. 3 MSR tests, performance comparison at WHSV = 750 and 3 S/C = 3 of Ru/γ-Al_2O_3 monoliths with different catalyst loadings: **a** CH_4 conversion; **b** H_2 production; **c** H_2/CO molar ratio; **d** CO selectivity

5 wt% of Al_2O_3 on the bare monolith), the catalytic performance was significantly improved with increasing metal loading (from 1.5 to 3 wt%). In fact, the maximum CH_4 conversions reached at 800 °C for 1.5Ru5Al and 3Ru5Al catalysts were 48.19% and 69.24%, respectively. Thus, the 3Ru5Al catalyst showed the second highest production of H_2 and CO selectivity after the 1.5Ru10Al one. It is also important to note that all catalysts studied showed similar CO selectivity (23.37-27.08%) at 650 °C. Comparing with the results obtained by Amjad et al. [21] for Ru/Al_2O_3 catalyst powder, similar results were reached in terms of CH_4 conversion, H_2 production, and CO selectivity in the temperature range of 550–650 °C. Thus, according to our previous work [39], it is possible to conclude that by increasing catalyst loading by more than 10 mg cm^{-2}, the catalytic performance toward the MSR reaction decreases. This result can be explained considering that an excess of Al_2O_3 carrier, which leads to a thicker layer covering the monolith walls, could not participate in the catalytic reaction and may even decrease both the dispersion of the noble metal and the number of active sites. Besides, it is well known that higher catalyst loadings lead to higher coating thickness and, therefore, a higher intraparticle mass transfer resistance, worsening the overall catalyst performance [40–42]. In the following section, we highlight in depth the mass transfer effects on structured monolith catalyst.

3.3 *Mass Transfer Effects on Ru/γ-Al_2O_3 Structured Monolith Catalyst*

It is well known that the performance of a catalytic monolith involves a combination of reaction and transport processes, where the reactants and products undergo a series of steps over the catalyst, including: (1) diffusion of the reactants from the bulk gas phase to the external surface of the structured catalyst (external or interphase diffusion); (2) diffusion of the reactants into the catalyst pores to the active sites (internal or intra-phase diffusion); (3) adsorption of the reactants onto active sites; (4) reaction at specific active sites on the catalyst surface; (5) desorption of products from catalyst sites; (6) diffusion of the products through the catalyst pores (internal or intra-phase diffusion), and (7) diffusion of the products across the boundary layer surrounding the structured catalyst (external or interphase diffusion) [43–45].

According to the literature, three main regimes of catalytic rate control can exist in a coated monolith: (i) external/interphase diffusion regime (Steps 1 and 7); (ii) internal/intra-phase diffusion regime (Steps 2 and 6); and kinetic regime (Steps 2 and 6) of the catalyst performance. Joshi et al. [46] developed a low-dimensional (LD) model to analyze catalytic reactions in washcoated monolith with channels of arbitrary shape. The LD model was derived directly by averaging the governing equations and using the concept of internal and external mass transfer coefficients, which were expressed in terms of three concentrations and two temperature modes and include washcoat diffusional effects without using the concept of effectiveness factor. Moreover, a practical criterion was developed to determine the transition

between various controlling regimes in terms of resistances or concentration ratios [47]. We used this criterion to quantify the relative importance of reaction, pore diffusion, and external mass transfer processes in a coated monolith by SCS. Firstly, we defined the characteristic length scales for transverse diffusion associated within gas phase ($R_{\Omega,e}$) and catalytic layer ($R_{\Omega,i}$) in a monolith of square channel and circular diameter with a coated layer for the case of first order reaction (Fig. 4). Then, we determined the external mass transfer coefficient ($k_{m,e}$) between the bulk of gas phase and the fluid-catalytic layer interface as [48]:

$$k_{m,e} = \frac{\mathrm{Sh}_e \cdot D_{\mathrm{CH_4-mix}}}{4 \cdot R_{\Omega,e}} \tag{12}$$

and the internal mass transfer coefficient ($k_{m,i}$) between the gas-catalytic layer interface and bulk of catalytic layer as:

$$k_{m,i} = \frac{\mathrm{Sh}_i \cdot D_e}{R_{\Omega,i}} \tag{13}$$

where D_f is the molecular diffusivity of the reactant in gas phase ($\mathrm{m^2\ s^{-1}}$), D_e is the effective diffusivity of CH_4 within coated layer ($\mathrm{m^2\ s^{-1}}$), Sh_e and Sh_i are the external and internal Sherwood numbers, respectively. To determine Sh_e, we considered the approximation proposed by Balakotaiah and West [49] used for any arbitrary geometry:

$$\mathrm{Sh}_e = \mathrm{Sh}_{e,\infty} + \frac{2.8}{\mathrm{Sc}^{\frac{1}{6}}}\sqrt{P} \tag{14}$$

where $\mathrm{Sh}_{e,\infty}$ is the asymptotic external Sherwood number ($\mathrm{Sh}_{e,\infty} = 2.98$ for square channel), Sc is the Schmidt number, and P is the transverse Peclet number calculated as [50, 51]:

$$P = \frac{R_{\Omega,e}^2 \cdot u}{L \cdot D_{\mathrm{CH_4-mix}}} \tag{15}$$

To estimate Sh_i we used the correlation proposed by Balakotaiah et al. [52]:

$$\mathrm{Sh}_i = \mathrm{Sh}_{i,\infty} + \frac{\Lambda\phi^2}{1 + \Lambda\phi} \tag{16}$$

where $\mathrm{Sh}_{i,\infty}$ is the asymptotic internal Sherwood number, ϕ is the Thiele modulus, and Λ is a constant that depends on the coated layer geometric and kinetic parameter [48]. Table 2 shows the effective diffusion lengths, asymptotic external and internal Sherwood numbers and Λ for the channel shape and flow area under consideration.

Thus, considering the following assumptions: (1) laminar and fully developed flow, (2) the hydraulic diameter of the channel much smaller than the length

Table 2 Effective diffusion lengths, asymptotic external and internal Sherwood numbers and Λ for square channel shape and circular flow area for the different catalyst studied

Catalyst	$R_{\Omega,e}$ [mm]	$R_{\Omega,i}$ [mm]	$\mathrm{Sh}_{e,\infty}$	$\mathrm{Sh}_{i,\infty}$	Λ
1.5Ru5Al	0.45	0.188	2.98	1.836	1.2
3Ru5Al	0.4508	0.1865	2.98	1.836	1.2
1.5Ru10Al	0.435	0.225	2.98	1.836	1.2
1.5Ru20Al	0.4	0.3182	2.98	2.533	0.73

of cordierite monolith, (3) isothermal conditions, and (4) first order kinetic; we expressed the overall resistance for mass transfer in a coated monolith by SCS according to Balakotaiah et al. [47] as:

$$R_t = R_e + R_i + R_r \tag{17}$$

$$\textbf{a}.\quad R_e = \frac{4 \cdot R_{\Omega,e}}{\mathrm{Sh}_e \cdot D_{\mathrm{CH_4-mix}}} \quad \textbf{b}.\quad R_i = \frac{R_{\Omega,i}}{\mathrm{Sh}_i \cdot D_e} \quad \textbf{c}.\quad R_r = \frac{1}{k_r \cdot R_{\Omega,i}} \tag{18}$$

with R_e resistance for external mass transfer (s m^{-1}), R_i resistance for internal mass transfer (s m^{-1}), R_r resistance for MSR reaction (s m^{-1}), and R_t overall resistance for MSR process (s m^{-1}).

To characterize the flow and the reactions, the following five characteristic times are used [49, 53, 54]:

$$t_c = \frac{L_m}{u_o};\ t_z = \frac{L_m^2}{D_{\mathrm{CH_4-mix}}};\ t_d^e = \frac{R_{\Omega,e}^2}{D_{\mathrm{CH_4-mix}}};\ t_d^i = \frac{\delta_c^2}{D_e};\ t_r = \frac{C_{\mathrm{CH_4,in}}}{r_{\mathrm{CH_4}} \cdot \rho_c} \tag{19}$$

where t_c is the convection (or residence) time, t_z is the longitudinal diffusion time for the flow area, t_d^e is the transverse diffusion time for the flow area, t_d^i is the transverse diffusion time for the coated area, and t_r is the reaction time.

In Fig. 5a–d, we show the effect of γ-Al_2O_3 amount on the controlling regimes toward MSR reaction on the prepared coated monolith catalysts. For all the catalysts studied, the resistances to mass transfer (inter-/intra-phase diffusion) are much less temperature sensitive, since the diffusivities of reacting species in the gas phase ($D_{\mathrm{CH_4-mix}}$) and in the coated layer (D_e) are much weaker functions of temperature

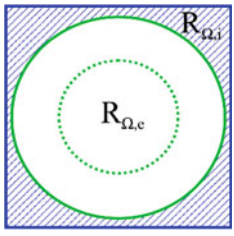

Fig. 4 Definition of the characteristic length scales for transverse diffusion associated within gas phase ($R_{\Omega,e}$) and catalytic layer ($R_{\Omega,i}$) in a monolith of square channel and circular diameter with a coated layer

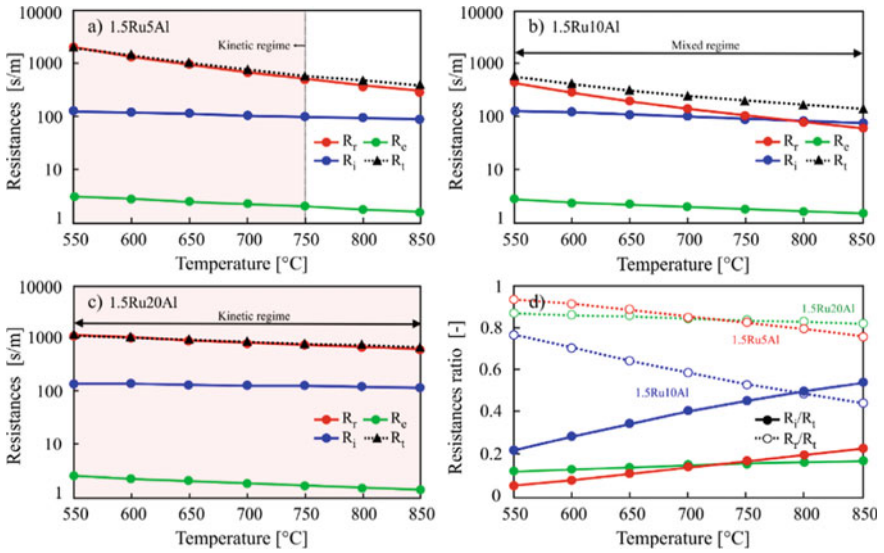

Fig. 5 Definition of the characteristic length scales for transverse diffusion associated within gas phase ($R_{\Omega,e}$) and catalytic layer ($R_{\Omega,i}$) in a monolith of square channel and circular diameter with different coating: **a** 1.5Ru5Al; **b** 1.5Ru10Al; **c** 1.5Ru20Al; **d** resistance ratios for all catalysts loading

in comparison to the reaction resistance, which is strongly dependent on Arrhenius equation. Thus, the interphase and intraparticle mass transfer rates increase only slightly with temperature. Therefore, as the catalyst temperature is increased, the reaction rate increases exponentially, the reaction resistance becomes less dominant and the mass transfer resistances become important.

When comparing the effect of γ-Al_2O_3 amount on the controlling regimes in catalytic monoliths, the 1.5Ru5Al monolith operates in a kinetic regime at temperatures lower than 750 °C (Fig. 5a). By increasing the γ-Al_2O_3 loading to 20 wt% (1.5Ru20Al catalyst), the process is completely controlled by the reaction for the entire temperature range studied (Fig. 5c). As a result, a nearly uniform concentration profile prevails in the transverse direction of the structure (Fig. 6). Thus, when the catalytic performance of MSR reaction is solely governed by the reaction kinetics, the total resistance (R_t) is practically equal to the reaction resistance and the R_r/R_t ratio is greater than 0.8 (Fig. 5d). Besides, as expected, when the monolith operates in a kinetic regime, the characteristic times for the MSR reaction are much larger than that for the external and internal mass transfer diffusion (see Tables 10, 11 and 12). On the other hand, for the 1.5Ru10Al catalyst (10 wt% of alumina, 6.45 mg cm^{-2}), the monolith operates in a mixed regime for all temperature range studied, in which both the kinetic and the intraparticle diffusion co-exist (Fig. 5a), with both R_r/R_t and R_i/R_t lower than 0.8. By observing the catalytic performance for the different loading of γ-Al_2O_3 (Fig. 3), it is worth noting that for the 1.5Ru20Al catalyst, the conversion of CH_4 increases slightly with temperature, being practically

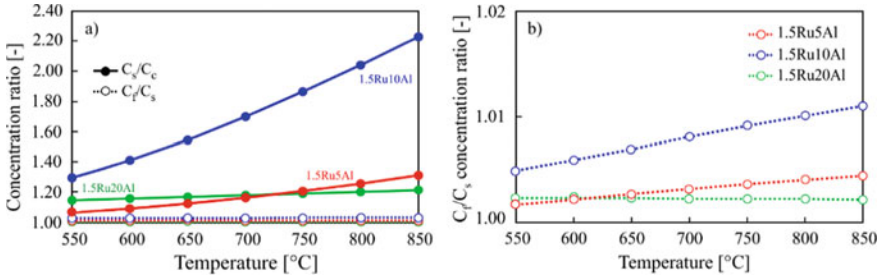

Fig. 6 Resistances (**a**) and concentration (**b**) ratios for the various catalysts tested

steady for the temperature range under consideration. This effect explains why the reaction resistance is practically independent with temperature. On the contrary, for the 1.5Ru10Al catalyst, CH_4 conversion increases more rapidly with temperature up to 750 °C, and then remains slightly stable.

To gain insight into the catalyst activity by varying the γ-Al_2O_3 content, we evaluated the Thiele modulus (ϕ) and the effectiveness factor (η) for a first-order kinetics reaction, according to the following equations [47, 48]:

$$\phi = \sqrt{\frac{k_r \cdot R_{\Omega i}^2}{D_e}} \quad \eta = \frac{1}{1 + \frac{\phi^2}{\mathrm{Sh}_i}} \tag{20}$$

where k_r is the observed first-order reaction rate constant (s^{-1}), $R_{\Omega,i}$ the effective transverse diffusion length in the coated catalyst layer for the internal resistance (m), D_e is the effective diffusivity of CH_4 ($m^2\ s^{-1}$), and Sh_i is the internal Sherwood number. All the correlations and physical parameters used for the calculations of ϕ and η are available in the Appendix. Figure 7 shows the effectiveness factor as a function of Thiele modulus for the different catalyst loadings. As expected, the effectiveness factor for the case of slow reaction $\phi \ll 1$ tends to unit. In particular, the 1.5Ru20Al catalyst showed a variation of ϕ much less sensitive to temperature

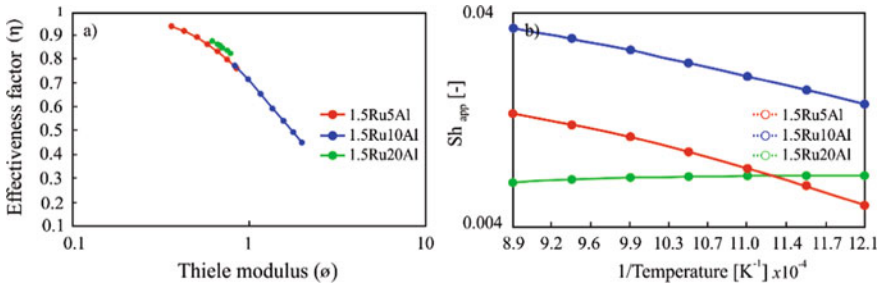

Fig. 7 Effectiveness factor (**a**) and apparent Sherwood number (**b**) for the various coated monoliths

($0.82 < \phi < 0.87$) than the other catalyst loadings, indicating that the process is rate-limited and the reaction rate is controlled by the intrinsic kinetics.

Additionally, we plot the experimentally observable overall Sherwood number (Sh_{app}) calculated using Eq. 21 as a function of reciprocal of temperature on a logarithmic scale (Fig. 7b). The theoretical upper limit for Sh_{app} ($Sh_{e,\infty}$) is 2.98 for the channel shape under consideration (square channel with circular flow area, Fig. 4) [50, 51].

$$\frac{1}{Sh_{app}} = \frac{1}{Sh_e} + \frac{\mu \cdot \lambda}{4} \cdot \frac{1}{Sh_i} + \frac{\mu \cdot \lambda}{4 \cdot \phi^2} \tag{21}$$

$$\mu = \frac{R_{\Omega,i}}{R_{\Omega,e}} \quad \lambda = \frac{D_f}{D_e} \tag{22}$$

It is evident from the results that the experimental conditions used lead to rather low values of Sh. Bennett et al. [55] reported a value of Sh_{app} as small as 0.05, which was attributed to the low activation energies and pre-exponential factors obtained for the catalytic oxidation of propane. Similar results were obtained by Joshi et al. [56] for the case of hydrogen oxidation on Pt, which presents a very low intrinsic activation energy (~9 kJ mol^{-1}), obtaining experimental Sherwood numbers (Sh_{app}) less than 0.55. In our study, the apparent activation energies obtained for the MSR reaction were determined from the conversion data ($X_{CH_4} < 5\%$) for the different catalyst loads ($Ea_{app} \approx 50$ kJ mol^{-1}). These values are low compared to other activation energies on supported Ru catalyst for MSR reaction [57, 58]. As shown in Fig. 7b, low Sh_{app} values (below 0.035) are obtained for the three catalysts studied, especially for 1.5Ru20Al catalyst.

On the other hand, it is interesting to note that the ratios of reactant diffusivities in the gas phase and the coated layer (μ) obtained in our study are greater than 225. Joshi et al. [48] studied the variation of Sh_{app} for the different controlling regimes by varying the values of μ for circular channel with circular flow area. They obtained that for values of diffusivity ratios higher than 200, the Sh_{app} for $\phi \ll 1$ (slow reaction) is much lower than 0.1 (~10^{-2} to 10^{-3}), as obtained in this study.

To study the effect of WHSV and S/C molar ratio on the controlling regimes in a coated monolith by SCS, we selected the 1.5Ru10Al catalyst according to the best results obtained in terms of CH_4 conversion, H_2 production, and CO selectivity. The 1.5Ru10Al catalyst was studied at space velocities of 750, 1500, and 3000 NL h^{-1} g_{cat}^{-1}, calculated on metal basis, and S/C molar ratio of 3 and 3.2, respectively. As visible in Fig. 8a, as the S/C molar ratio increases, both the mass transfer resistances and the reaction resistance increase. In particular, R_r for the S/C molar ratio of 3.2 is about 1.5 times higher than that obtained at S/C 3 for the entire temperature range studied. Since the catalytic performance decreased as the S/C molar ratio increased (Fig. 14), lower rate constants (k_r^{obs}) were obtained for S/C equal to 3.2, thus increasing the reaction resistance. Since a higher bulk reaction controlling is obtained either by increasing the S/C molar ratio as the WHSV, a concentration profile closer to the unit exists in the transverse direction of the monolith (Fig. 8b).

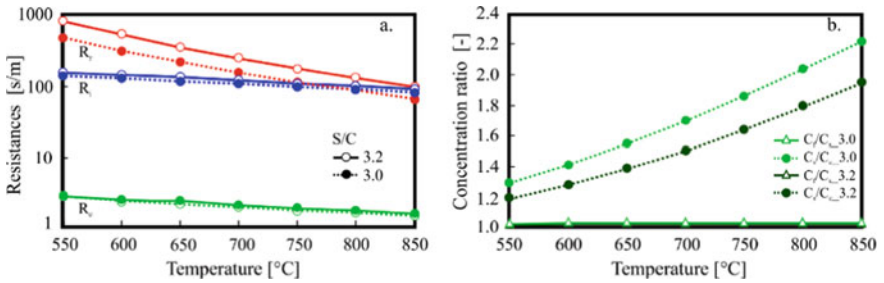

Fig. 8 Resistances (**a**) and concentration (**b**) ratios for different S/C values for the 1.5Ru10Al coated monolith

3.4 Heat Transfer Effects on Ru/γ-Al_2O_3 Structured Monolith Catalyst

For heterogeneous catalytic processes, heat management in chemical reactions is a very important aspect for both reactor design and overall performance of the process. In addition to mass transfer effects, heat transfer effects can also occur in heterogeneous catalysis for reactions with a significant heat of reaction, either exothermal or endothermal such as combustion or steam reforming [45, 59, 60]. External temperature gradients between the bulk of the fluid phase and the surface of the catalytic layer are originated from the reaction enthalpy associated with surface reaction. The external temperature difference can be large even when mass transfer limitations are negligible, which disguises the actual reaction kinetics occurring at surface temperature (T_s) and not at the bulk of the fluid phase temperature (T_b). The surface temperature can be determined by the heat balance at steady-state conditions, assuming that the outer surface of the catalyst layer is uniformly available for the reactants. In this way, each section of the outer surface behaves kinetically in the same way as all other parts, thus the steady-state analysis of that system is essentially one-dimensional [45, 59]. For more details of the heat balance, go to the supplementary information section. We report the final expression of the heat balance using the Chilton–Colburn analogies between mass and heat transfer:

$$(T_b - T_s) = \left(\frac{\Delta H_r \cdot C_b}{\rho_f \cdot c_{p,f}}\right) \cdot \mathrm{Le}^{-2/3} \cdot \mathrm{Ca} \tag{23}$$

$$\mathrm{Le} = \frac{\mathrm{Sc}}{\mathrm{Pr}};\ \mathrm{Ca} = \frac{\mathrm{C}_b - \mathrm{C}_s}{\mathrm{C}_b} \tag{24}$$

where T_b, T_s is the temperature in the bulk of the gas phase and surface of the catalyst layer (K), respectively, ΔH_r is the heat of MSR reaction (J mol^{-1}), C_b is the concentration in the bulk of the gas phase (mol m^{-3}), ρ_f is the density of the gas phase (Kg m^{-3}), $c_{p,f}$ is the heat capacity of the gas phase (J Kg^{-1} K^{-1}), Le is the fluid Lewis number, Pr is the Prandtl number, and Ca is the Carberry number.

Thus, by dividing Eq. 23 by T_b, it is possible to obtain the dimensionless external Prater number which represents the ratio of the maximum heat consumption and heat transfer rates:

$$\beta_{\text{ext}} = \frac{\Delta T_{\text{ad}}}{T_b} \cdot \text{Le}^{-2/3} = \left(\frac{\Delta \text{H}_r \cdot \text{C}_b}{\rho_f \cdot c_{p,f}} \right) \cdot \frac{1}{T_b} \cdot \text{Le}^{-2/3} \tag{25}$$

The interphase heat transfer limitations can be evaluated using the criterion derived by Mears [61] (Eq. 26) with the perturbation approach, in which the heat transfer resistance of the fluid phase is assumed to be lumped at the surface. We use this criterion to estimate the external heat transfer effects by varying the alumina content in the monolithic catalyst:

$$\chi = \frac{\left(\Delta H \cdot R^{\text{obs}} \cdot R_{\Omega e}\right)}{h_e \cdot T_b} < \frac{0.15}{\gamma_b}; \ \gamma_b = \frac{E_{\text{act}}}{R_g \cdot T_b} \tag{26}$$

where R^{obs} is the observed reaction rate (mol m^3 s^{-1}), h_e is the heat transfer coefficient associated for the gas phase (W m^{-2} K^{-1}), R_g is the gas constant (J mol^{-1} K^{-1}), E_{act} is the apparent activation energy of the reaction (J mol^{-1}), χ is the Damkholer for interphase heat transport and γ_b is the Arrhenuis number evaluated at the bulk of the gas phase.

As observed in Fig. 9, for the 1.5Ru5Al2O3 catalyst, external heat transfer limitations are presented for the complete temperature range studied, while for the

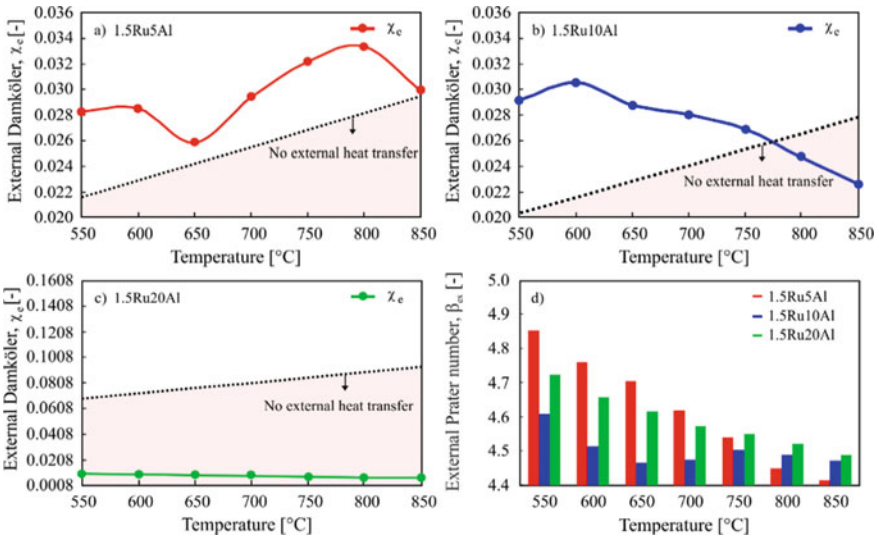

Fig. 9 External Damköhler numbers in a monolith of square channel and circular diameter with different coating: **a** 1.5Ru5Al; **b** 1.5Ru10Al; **c** 1.5Ru20Al. External Prater number for the various catalysts loading (**d**)

1.5Ru10Al catalyst the thermal effects are important a temperature below 725 °C. On the other hand, no interphase heat transfer limitations are observed for the higher catalyst loading. It is important to note that for the lower alumina content the temperature difference between the bulk of the gas phase and the surface of the catalytic layer increases considerably as the inlet gas temperature increases from 650 to 800 °C and then starts to decrease probably as mentioned above, and in this temperature range initiates the WGS reaction which is exothermic and leads to an increase in the T_s. For catalysts with 10 and 20 wt% of alumina, the ΔT is practically constant as the temperature of the reactant gas increases, approximately 70 and 25 K, respectively. It is also important to point out that the temperature difference between bulk and outer catalytic layer surface is directly proportional to the heat of MSR reaction per mol of diffusing reactant and the fractional drop in concentration between the bulk of the gas phase and the surface of the catalyst layer (see Eq. 23). Thus, the quotient of the heat consumed by complete reaction of unit volume of reacting gas mixture ($\Delta H_r \cdot C_b$) and the volumetric heat capacity of the reacting mixture ($\rho_f \cdot c_{p,f}$) gives the temperature rise equivalent to complete adiabatic conversion of the reacting mixture when C_s is zero. Eq. 23 also shows that heat transfer limitation and ΔT may be significant if ΔH_r values are large, even when concentration gradients are small as those obtained in Sect. 3.4 for all the alumina loading studied. Since the MSR reaction is highly endothermic, the temperature of the catalyst surface will be less than in the bulk-fluid phase, and the observed rate will be less than that corresponding to the bulk-fluid temperature.

In addition to the interphase heat transfer limitations, a large number of highly exothermic and endothermic catalytic reactions are accompanied by internal thermal effects, particularly for relatively fast intrinsic kinetics. Anderson in 1963 [62] applied the perturbation approach to derive a criterion for the lack of importance of temperature gradients in catalyst particles. The reaction is assumed to follow Arrhenius temperature dependence, and this criterion is valid regardless of whether there are diffusion limitations in the particle or not. Thus, we use this criterion to evaluate the intraparticle heat transfer effects by varying the alumina content in the structured catalyst:

$$\frac{\left(\Delta H \cdot R^{\text{obs}} \cdot R_{\Omega i}^2\right)}{\lambda_{\text{cat}} \cdot T_s} < \frac{0.75}{\gamma_s} \tag{27}$$

$$\psi = \frac{\left(\Delta H \cdot R^{\text{obs}} \cdot R_{\Omega i}^2\right)}{\lambda_{\text{cat}} \cdot T_s};\ \gamma_s = \frac{E_{\text{act}}}{R_g \cdot T_s} \tag{28}$$

where λ_{cat} is the thermal conductivity of the Ru/Al_2O_3 catalyst (W m^{-1} K^{-1}), ψ is the Damkohler for intraparticle heat transport and γ_s is the Arrhenuis number evaluated at the surface of the gas phase. As observed from the Fig. 10a–c, for all the catalyst loading studied $\psi \ll \frac{0.75}{\gamma_s}$ indicating that the absence of intraparticle heat transfer. This can also be observed by studying the temperature gradients within the catalytic layer using the relationship originally derived by Damköhler in 1943 [63], which is

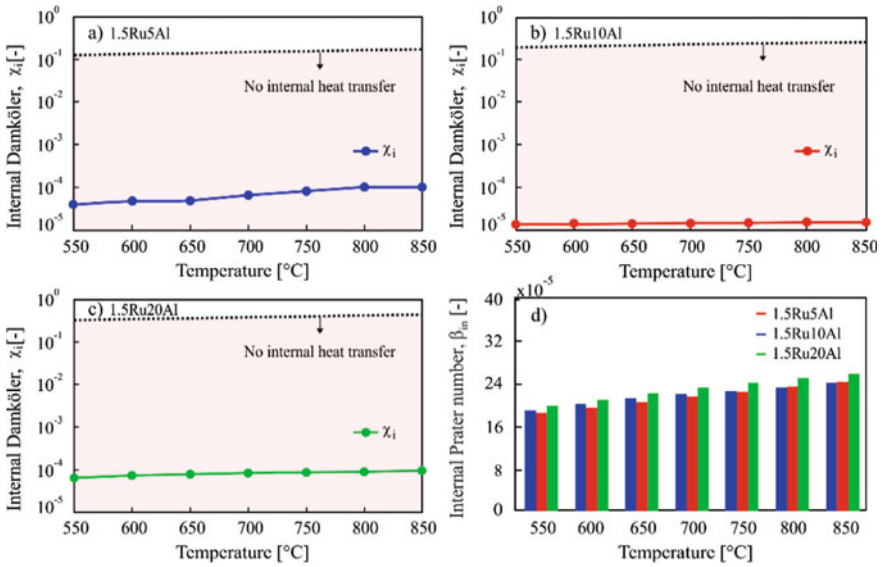

Fig. 10 Internal Damköhler numbers in a monolith of square channel and circular diameter with different coating: **a** 1.5Ru5Al; **b** 1.5Ru10Al; **c** 1.5Ru20Al. Internal Prater number for the various catalysts loading (**d**)

valid for all the kinetics and applies to all the particle geometries assuming that T_s and C_s are uniform over the entire boundary surface [45]:

$$\left(T_s - T_{b,c}\right) = (\Delta H_r) \cdot \frac{D_e}{\lambda_e} \cdot \left(C_s - C_{b,c}\right) \tag{29}$$

where $T_{b,c}$ is the temperature in the bulk of the catalyst layer (K), $C_{b,c}$ is the concentration within the catalyst layer, and λ_e is the effective thermal conductivity. It is worth noting the largest possible temperature difference into the catalyst layer is attained when the concentrations within the bulk of the catalyst layer becomes zero; hence, we can refer the maximum temperature difference ($\Delta T_{\max}$) to the surface temperature using the dimensionless internal Prater number (β_{in}) by [45, 59]:

$$\beta_{\text{in}} = \Delta T_{\max} T_s = \frac{(\Delta H_r) \cdot C_s}{T_s} \cdot \frac{D_e}{\lambda_e} \tag{30}$$

As shown in Fig. 10 d, all β_{in} values are much smaller than one, indicating the absence of temperature gradients within the catalytic layer, confirming in this way the results obtained by using the Anderson criterion.

In the following section, we will discuss the results obtained of the physicochemical characterization on the best catalyst selected.

3.5 Characterization of Powdered Catalyst and Coated Structured Supports

Table 3 shows the specific surface area (S_{BET}) of powder samples, bare and coated monoliths. Comparing with the pure powder of γ-Al_2O_3, the S_{BET} of 1.5 wt% Ru/γ-Al_2O_3 powder catalyst was decreased by 82.6%, to 191.5 $m^2\ g^{-1}$. Instead, considering the practically zero S_{BET} of the bare monolith, as expected, the deposition of γ-Al_2O_3 on the monolith, as carrier of Ru (the active metal) notably increased the S_{BET} of the bare monolith.

Ru metal dispersion and crystallite size obtained from H_2 chemisorption were 5.3% and 25 nm, respectively. Similar results were obtained in our previous work in terms of crystal size [33], while a greater dispersion of Ru is obtained when the catalyst is prepared in a single step by SCS.

Figure 11 shows the XRD diffraction patterns of the 1.5 wt% Ru/γ-Al_2O_3 catalyst, compared with the reference patterns of γ-Al_2O_3 and RuO_2. The diffractogram shows the peaks related to the Ru in its oxidized form (RuO_2 JCPDS database, ref. 00-002-1365) and the γ-Al_2O_3 in its amorphous structure (JCPDS database, ref. 00-001-1243).

Figure 12 shows FESEM images of the coated monolith. There is a good dispersion of the catalytic particles on the surface of the monolith. In particular, alumina particles on the surface of the monolith are well dispersed by providing sufficient specific surface area to host Ru. Furthermore, Ru particle size distribution on Al_2O_3 particles seems to be wider. Table 4 shows the EDX analysis coupled with FESEM, giving evidence of the presence of Ru particles and alumina.

Table 3 Specific surface area values of different types of catalysts

Catalyst	S_{BET} [$m^2\ g^{-1}$]
γ-Al_2O_3 powder	231.7 [39]
Ru/γ-Al_2O_3 powder	191.5 [21]
1.5 wt% Ru/γ-Al_2O_3 on cordierite monolith	23.8
Bare cordierite monolith	0.009

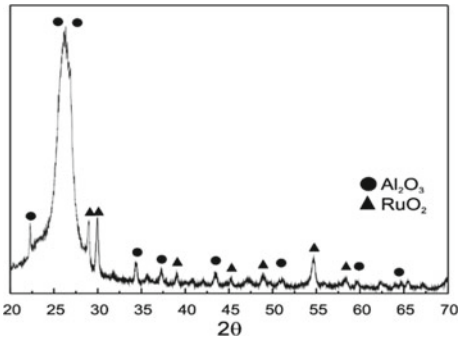

Fig. 11 XRD patterns of 1.5 wt% Ru/γ-Al_2O catalyst, with the reference peaks of RuO_2 (JCPDS database, ref. 00-002-1365) and γ-Al_2O_3 (JCPDS database, ref. 00-001-1243)

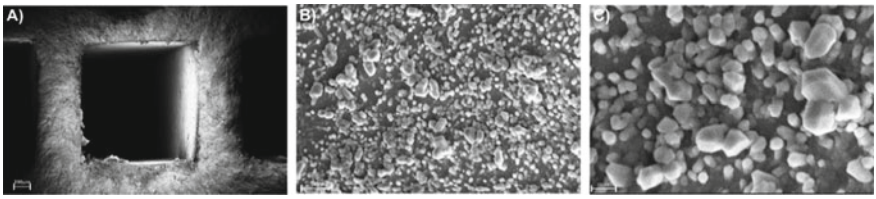

Fig. 12 FESEM images of 1.5% Ru on 10% alumina on 100 cpsi monolith at different magnifications. **a** 100X, **b** 50,000 kX, **c** 150,000 kX

Table 4 EDX analysis of the 100 cpsi monolith coated with 1.5% Ru on 10% alumina

Element	Weight %	Atomic %
O	53.45	68.56
Mg	1.09	0.92
Al	34.88	26.50
Si	5.54	2.58
Ru	7.04	1.44
Tot	100.00	100.00

3.6 Ageing Test on the Best Performing Coated Monolith

After performing various experiments, the catalyst 1.5Ru10Al performed best in all types of test. The conversion remained higher than the others, and it showed high productivity and higher CO selectivity at low WHSV for temperatures between 600 and 750 °C and S/C 3. The most competitive catalyst with the same experimental conditions was Rh, but it was clearly seen that the difference in performance was almost more than 8%.

Furthermore, a new cordierite monolith was coated with the best catalyst, 1.5%Ru/10%Al_2O_3, and its catalytic performance was evaluated with respect to time. Figure 13 shows methane conversion versus the time on stream (TOS), at two different WHSV. In the first 30 h, reaction conditions were fixed at 800 °C, WHSV = 750 and S/C = 3. Then, for the next 20 h, WHSV was increased to 1500, and finally

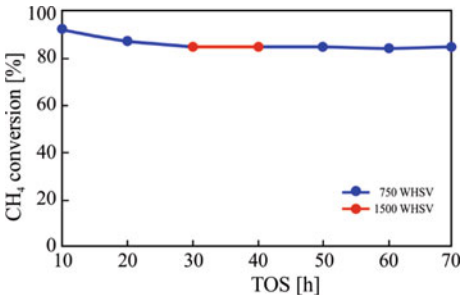

Fig. 13 Stability test of the cordierite monolith coated with 1.5%Ru/10%Al_2O_3 catalyst at 800 °C and S/C = 3. WHSV variable between 750 and 1500 Nl h^{-1} g_{cat}^{-1}

reduced again to 750 (being T and S/C always constant at 800 °C and 3, respectively). Clearly, the coated monolith kept methane conversion almost constant at its starting value, independent of the variation of WHSV.

Thus, this test confirms that overall at the temperature of 800 °C, even when varying the WHSV, no significant difference is recorded in methane conversion, which remained stable throughout the time period.

4 Conclusion

In this study, the catalytic performance and mass/heat transfer effects were evaluated for Ru/γ-Al_2O_3 catalyst supported on ceramic cordierite monolith toward MSR reaction. All the catalysts were prepared in a single step by solution combustion synthesis coated on over monolith of square channel with 100 cpsi. By comparing the catalytic performance of Ru and Rh as active metal phase, the Ru-based catalyst was found to be more active toward MSR reaction, showing a syngas richer in H_2 for the entire temperature range studied. The best catalyst loading of Ru/γ-Al_2O_3 catalyst was 6.45 mg cm^{-2}, where the excess of Al_2O_3 carrier could only lead to a thicker layer and not participate in the catalytic reaction, leading to the catalyst working in an entirely kinetic regime. The temperature dependence on the external and internal diffusion regimes is much weaker compared to the reaction resistance, which is strongly dependent of the Arrhenius equation. External heat transfer limitations were presented at lower carrier content, while that low values of internal Prater numbers confirmed the absence of internal heat limitation. An excellent stability of the 1.5% Ru on 10% Al_2O_3 catalyst (1.5Ru10Al sample) was observed over 70 h of TOS for MSR process.

Appendix

In the following, a detailed explanation of fluid and catalyst layer properties determination, characteristic time analysis, external and internal mass transfer calculations and heat transfer investigation is reported.

Estimation of Fluid Properties

Molecular weight (M_{mix}), density (ρ_f) and viscosity (μ_f) of gas mixture were calculated as:

$$M_{\text{mix}} = \sum_{i=1}^{n} y_i M_i \tag{31}$$

$$\rho_f = \frac{P M_{\text{mix}}}{R_g T} \tag{32}$$

$$\mu_f = \frac{\sum_{i=1}^{n} \mu_i y_i M_i^{1/2}}{\sum_{i=1}^{n} y_i M_i^{1/2}} \tag{33}$$

where y_i is the mole fraction of the compound, M_i is the molecular weight of the compound (kg kmol^{-1}), P is the pressure (kPa), T is the absolute temperature (K), R is the universal gas constant (J mol^{-1} K^{-1}), and μ_i is the viscosity of a single component (kg m^{-1} s^{-1}).

Gas viscosity (μ_i, μP) of a single component was calculated as:

$$\mu_i = A + BT + CT^2 \tag{34}$$

using the tabulated values of A, B, and C [64] (Table 5).

The diffusivity of CH_4 in gas mixture ($D_{CH_4-\text{mix}}$, cm^2 s^{-1}) was calculated from the binary diffusion of CH_4 and i gas species (D_{CH_4-i}) by:

$$D_{CH_4-\text{mix}} = \frac{1 - y_{CH_4}}{\sum_{i=1; i\neq CH_4}^{n} \frac{y_i}{D_{CH_4-i}}} \tag{35}$$

where D_{CH_4-i} was determined by Fuller equation (Eq. 36) [65], using tabulated values of v_i [66].

$$D_{CH_4-i} = \frac{10^{-3} T^{1.75} \left(\frac{1}{M_{CH_4}} + \frac{1}{M_i}\right)}{P\left(v_{CH_4}^{1/2} + v_i^{1/3}\right)^2} \tag{36}$$

where v_i is given in Table 6.

The effective diffusivity of methane ($D_{CH_4,e}$) in the catalytic layer was calculated using the following equation [67, 68]:

Table 5 Values of A, B, and C used in Eq. 34

	CH_4	H_2O	H_2	CO	CO_2
A	3.844	−36.826	27.758	23.811	11.811
B	0.40112	0.429	0.212	0.53944	0.49838
C	−0.00014303	−0.0000162	−0.0000328	−0.00015411	−0.00010851

Table 6 Values of v_i used in Eq. 36

	CH_4	H_2O	H_2	CO	CO_2
v_i ($cm^3 \cdot mol^{-1}$)	24.4	12.7	7.1	18.9	26.9

$$D_{CH_4,e} = \frac{\varepsilon_c}{\tau_c} \cdot \left(\frac{1}{D_{CH_4-mix}} + \frac{1}{D_k} \right)^{-1} \tag{37}$$

where ε_c is the coated layer porosity ($\varepsilon_c = \rho_c \cdot V_{BJH}$) [69], τ is the tortuosity factor ($\tau = 2 - \varepsilon_c$) [70] and the Knudsen diffusion (D_k) was determined by Eq. 38 [71]:

$$D_k = 9700 \cdot r_p \cdot \sqrt{\frac{T}{M_{CH_4}}} \tag{38}$$

where ρ_c(kg m^{-3}) is the bulk density of the catalyst (3500 kg m^{-3}), V_{BJH} is the total pore volume (cm^3 g^{-1}), r_p is the pore diameter (cm) and M_{CH_4} is the molecular weight of CH_4.

The mass transfer coefficient of CH_4 (k_G, m s^{-1}) was determined from the Sherwood number (Sh) by:

$$k_G = \frac{Sh \cdot D_{CH_4-mix}}{d_h} \tag{39}$$

where Sh is calculated from Reynold (Re) and Schmidt (Sc) numbers by Eqs. 40, 41 and 42 [60, 72, 73].

$$Sh = 2.976 \cdot \left(1 + 0.095 \cdot Re \cdot Sc \cdot \frac{d_h}{L_m} \right)^{0.45} \tag{40}$$

$$Re = \frac{d_h \cdot u_0 \cdot \rho_f}{\mu_f} \tag{41}$$

$$Sc = \frac{\mu_f}{\rho_f \cdot D_{CH_4-mix}} \tag{42}$$

where d_h is the hydraulic diameter of the bare monolith (m), L_m is the monolith length (m), u_0 is the inlet gas velocity at operative conditions (m s^{-1}), ρ_f is the density of gas mixture (kg m^{-3}), μ_f is the viscosity of gas mixture (kg m^{-1} $s^{-}1$) and D_{CH_4-mix} is the diffusivity of CH_4 in gas phase (m^2 s^{-1}).

The inlet gas velocity at operative conditions u_0 (m s^{-1}) was calculated as:

$$u_o = \frac{F_{ch}}{A_{ch} \cdot \varepsilon} \cdot \frac{T}{T_{St}} \cdot \frac{P}{P_{St}} \tag{43}$$

where F_{ch} is the total flow of the gas mixture for channel ($m^3\ s^{-1}$), ε is the coated monolith voidage, A_{ch} is the frontal area of the bare monolith for square channel (m^2), T_{St} (K) and P_{St} (Pa) are the standard temperature and pressure, T(K) and P (Pa) are the operative temperature and pressure.

The thermal conductivity of gas mixture (λ_{mix}, W m^{-1} K^{-1}) was calculated as:

$$\lambda_{mix} = \frac{\sum_{i=1}^{n} \lambda_i y_i M_i^{1/2}}{\sum_{i=1}^{n} y_i M_i^{1/2}} \tag{44}$$

where λ_i is the thermal conductivity of a single component (W m^{-1} K^{-1}) calculated as:

$$\lambda_i = A + BT + CT^2 \tag{45}$$

using the tabulated values of A, B, and C [64] (Table 7).

The heat capacity of the gas mixture (Cp_f J mol^{-1} K^{-1}) was calculated as:

$$Cp_f = \frac{\sum_{i=1}^{n} Cp_i y_i M_i^{1/2}}{\sum_{i=1}^{n} y_i M_i^{1/2}} \tag{46}$$

where Cp_i is the heat capacity of a single component (J mol^{-1} K^{-1}) calculated as [64] (Table 8).

$$Cp_i = A + BT + CT^2 + DT^3 + ET^4 \tag{47}$$

Table 7 Values of A, B, and C used in Eq. 45

	CH_4	H_2O	H_2	CO	CO_2
A	−0.00935	0.00053	0.03951	0.00158	−0.01200
B	1.4028E−04	4.7093E−05	4.5918E−04	8.2511E−05	1.0208E−04
C	3.3180E−08	4.9551E−08	−6.4933E−08	−1.9081E−08	−2.2403E−081

Table 8 Values of A, B, C, D, and E used in Eq. 47

	CH_4	H_2O	H_2	CO	CO_2
A	34.942	33.933	25.399	29.556	27.437
B	−3.9957E−02	−8.4186E−03	2.0178E−02	−6.5807E−03	4.2315E−02
C	1.9184E−04	2.9906E−08	−3.8549E−05	2.0130E−05	−1.9555E−05
D	−1.5303E−07	−1.7825E−08	3.188E−08	−1.2227E−08	3.9968E−09
E	3.9321E−11	3.6942E−12	−8.758E−12	2.2617E−12	−2.9872E−131

Estimation of Coated Layer Properties

Specific surface area (SA_{BET} = 23.79 m^2 g^{-1}) was determined from Brunauer-Emmett-Teller (BET) and Barrett-Joyner-Halenda (BJH) analytic methods for N_2 adsorption-desorption isotherms. Pore radius (r_p = 100 Å) was given by $2PV_{BJH}/SA_{BET}$ equation.

Characteristic Time Analysis

The characteristic contact time, or residence time (t_c, s) is determined by [73]:

$$t_c = \frac{L_m}{u_o} \tag{48}$$

where L_m is the monolith length (m) and u_o is the inlet gas velocity at operative conditions (m s^{-1}).

The transverse diffusion time for the flow area (t_d^e, s) is determined by [73]:

$$t_d^e = \frac{R_{\Omega e}^2}{D_{CH_4-mix}} \tag{49}$$

where $R_{\Omega e}$ is the characteristic length scale for the fluid phase (m) and D_{CH_4-mix} is the diffusivity of CH_4 in gas phase (m^2 s^{-1}).

The transverse diffusion time for the coated area (t_d^i, s) is determined by [73]:

$$t_d^i = \frac{\delta_c^2}{D_{CH_4,e}} \tag{50}$$

where $D_{CH_4,e}$ is the effective diffusivity of CH_4 in the coated layer (m^2 s^{-1}) and δc is the coated layer thickness (m) calculated as [47]:

$$\delta_c = \frac{l_w^2 - \frac{\pi}{4} \cdot d_f^2}{\pi \cdot d_f} \tag{51}$$

where l_w (m) is the channel width and d_f (m) is the average channel dimension estimated by SEM.

The characteristic reaction time t_r (s) is determined by [73]:

$$t_r = \frac{C_{CH_4,in}}{r_{CH_4} \cdot \rho_c} \tag{52}$$

where $C_{CH_4,in}$ is the concentration of CH_4 in the feed mixture (kmol m^{-3}), r_{CH_4} is the observed reaction rate for CH_4 (kmol m^{-3} s^{-1}), and ρ_c is the density of the catalytic layer (kg m^{-3}).

The longitudinal diffusion time t_z (s) is determined by [49]:

$$t_z = \frac{L_m^2}{D_{CH_4-mix}} \tag{53}$$

where L_m is the monolith length (m) and D_{CH_4-mix} is the diffusivity of CH_4 in gas phase (m^2 s^{-1}).

External and Internal Mass Transfer Analysis

Characteristic Dimensions for the External and Internal Mass Transfer Analysis

In order to study the external and internal mass transfer resistances, two different characteristic cross-sectional areas for a single channel of the monolith are defined: the cross-sectional area of gas phase or circular flow area $A_{\Omega,e}$ (m^2) and the cross-sectional area of coated catalyst layer $A_{\Omega i}$ (m^2).

The cross-sectional area of fluid phase $A_{\Omega,e}$ (m^2) is calculated as:

$$A_{\Omega,e} = \frac{\pi \cdot d_f^2}{4} \tag{54}$$

where d_f (m) is the average channel dimension estimated by SEM.

The cross-sectional area of coated catalyst layer $A_{\Omega,i}$ (m^2) is calculated as:

$$A_{\Omega i} = A_{ch} - A_c \tag{55}$$

where A_{ch} is the area of a single bare channel (m^2) and A_c is the area remaining available in the channel for the flow of reactants after catalyst deposition (m^2). For the channel shape under consideration (square channel with circular flow area, Fig. 4), A_c (m^2) corresponds with the circular flow area $A_{\Omega,e}$ (m^2).

The area of a single bare channel A_{ch} (m^2) is calculated as:

$$A_{ch} = l_w^2 \tag{56}$$

where l_w (m) is the channel width.

Thus, it is possible to define the characteristic length scales for the fluid phase $R_{\Omega,e}$ (m) and for the coated catalyst layer $R_{\Omega,i}$ (m).

The characteristic length scale for the fluid phase $R_{\Omega,e}$ (m) is defined as [47]:

$$R_{\Omega,e} = \frac{A_{\Omega,e}}{P_c} \tag{57}$$

where $A_{\Omega e}$ (m^2) is the flow area (or cross-sectional area of fluid phase) and P_c (m) is the fluid-coated catalyst layer interfacial perimeter.

The fluid-coated catalyst layer interfacial perimeter is calculated as:

$$P_c = \pi \cdot d_f \tag{58}$$

Thus, the characteristic length scale for the fluid phase $R_{\Omega e}$ (m) can be expressed as:

$$R_{\Omega,e} = \frac{\frac{\pi \cdot d_f^2}{4}}{\pi \cdot d_f} = \frac{d_f}{4} \tag{59}$$

The characteristic length scale for the coated catalyst layer $R_{\Omega,i}$ (m) is defined as [47]:

$$R_{\Omega,i} = \frac{A_{\Omega,i}}{P_c} \tag{60}$$

where $A_{\Omega i}$ (m^2) is the cross-sectional area of coated catalyst layer and P_c (m) is the fluid-coated catalyst layer interfacial perimeter.

Thus, the characteristic length scale for the coated catalyst layer $R_{\Omega i}$ (m) can be expressed as:

$$R_{\Omega,i} = \frac{l_w^2 - \frac{\pi \cdot d_f^2}{4}}{\pi \cdot d_f} \tag{61}$$

External and Internal Mass Transfer Coefficients

The external mass transfer coefficient $k_{m,e}$(m s^{-1}) between the bulk of fluid phase and the fluid-coated catalyst layer interface is calculated as [47]:

$$k_{m,e} = \frac{\mathrm{Sh}_e \cdot D_{\mathrm{CH_4-mix}}}{4 \cdot R_{\Omega e}} \tag{62}$$

where Sh_e is the external Sherwood number, $D_{\mathrm{CH_4-mix}}$ is the diffusivity of CH_4 in gas phase (m^2 s^{-1}) and $R_{\Omega,e}$ is the characteristic length scale for the fluid phase (m).

The internal mass transfer coefficient $k_{m,i}$(m s^{-1}) between the interior of the coated catalyst layer and fluid-coated catalyst layer interface is calculated as [47]:

$$k_{m,i} = \frac{\mathrm{Sh}_i \cdot D_{\mathrm{CH_4},e}}{R_{\Omega,i}} \tag{63}$$

where Sh_i is the internal Sherwood number, $D_{\mathrm{CH_4},e}$ is the effective diffusivity of CH_4 in the coated layer ($m^2\ s^{-1}$) and $R_{\Omega,i}$ is the characteristic length scale for the coated catalyst (m).

The external Sherwood number Sh_e is calculated by [47]:

$$\mathrm{Sh}_e = \mathrm{Sh}_{e,\infty} + \frac{2.8}{\mathrm{Sc}^{1/6}} \cdot \sqrt{P} \tag{64}$$

where $\mathrm{Sh}_{e,\infty}$ is the asymptotic external Sherwood number, Sc is the Schmidt (Sc) number and P is the transverse Peclet number. For square channel, $\mathrm{Sh}_{e,\infty} = 2.98$.

The transverse Peclet number is calculated as [47]:

$$P = \frac{R_{\Omega,e}^2 \cdot u_o}{L_m \cdot D_{\mathrm{CH_4-mix}}} \tag{65}$$

where $R_{\Omega,e}$ is the characteristic length scale for the fluid phase (m), u_o is the inlet gas velocity at operative conditions ($m\ s^{-1}$), L_m is the monolith length (m) and $D_{\mathrm{CH_4-mix}}$ is the diffusivity of CH_4 in gas phase ($m^2\ s^{-1}$).

The internal Sherwood number Sh_i is calculated by [47]:

$$\mathrm{Sh}_i = \mathrm{Sh}_{i,\infty} + \frac{\Lambda \cdot \phi^2}{1 + \Lambda \cdot \phi} \tag{66}$$

where $\mathrm{Sh}_{i,\infty}$ is the asymptotic internal Sherwood number, Λ is a constant that depends on the coated catalyst layer shape and kinetic parameters and ϕ is the Thiele modulus.

The Thiele modulus ϕ for a first order reaction is defined as:

$$\phi = \sqrt{\frac{k_{\mathrm{obs}} \cdot R_{\Omega,i}^2}{D_{\mathrm{CH_4},e}}} \tag{67}$$

where k_{obs} is the observed first-order reaction rate constant (s^{-1}), $R_{\Omega,i}$ is the effective transverse diffusion length in the coated catalyst layer (m) and $D_{\mathrm{CH_4},e}$ is the effective diffusivity of CH_4 ($m^2\ s^{-1}$).

The effectiveness factor η for a first order reaction can be expressed as [47]:

$$= \frac{1}{1 + \frac{\phi^2}{\mathrm{Sh}_i}} \tag{68}$$

where ϕ is the Thiele modulus for a first order reaction and Sh_i is the internal Sherwood number.

Multiple Resistances in Series Approach

The overall resistance for mass transfer R_t(s m^{-1}) is defined as [47]:

$$R_t = R_e + R_i + R_r \tag{69}$$

where R_e is the resistance for the external mass transfer (s m^{-1}), R_i is the resistance for the internal mass transfer (s m^{-1}) and R_r is the reaction resistance (s m^{-1}).

The resistance for the external mass transfer R_e(s m^{-1}) can be calculated as:

$$R_e = \frac{1}{k_{m,e}} \tag{70}$$

where $k_{m,e}$ is the external mass transfer coefficient between the bulk of fluid phase and the fluid-coated catalyst layer interface (m s^{-1}).

The resistance for the internal mass transfer R_i (s m^{-1}) can be calculated as:

$$R_i = \frac{1}{k_{m,i}} \tag{71}$$

where $k_{m,i}$ is the internal mass transfer coefficient between the interior of the coated catalyst layer and fluid-coated catalyst layer interface (m s^{-1}).

The reaction resistance R_r (s m^{-1}) can be calculated as:

$$R_t = \frac{1}{k_{\text{obs}} \cdot R_{\Omega i}} \tag{72}$$

where $R_{\Omega i}$ (m) is the characteristic length scale for the coated catalyst layer and k_{obs} (s^{-1}) is the observed first-order reaction rate constant.

Thus, the apparent (or overall experimentally observable) mass transfer coefficient $k_{m,\text{app}}$ (m s^{-1}) can be calculated as [47]:

$$\frac{1}{k_{m,\text{app}}} = \frac{1}{k_{m,e}} + \frac{1}{k_{m,i}} + \frac{1}{k_{\text{obs}} \cdot R_{\Omega i}} \tag{73}$$

where $k_{m,e}$ is the external mass transfer coefficient between the bulk of fluid phase and the fluid-coated catalyst layer interface (m s^{-1}), $k_{m,i}$ is the internal mass transfer coefficient between the interior of the coated catalyst layer and fluid-coated catalyst layer interface (m s^{-1}), k_{obs} is the observed first-order reaction rate constant (s^{-1}) and $R_{\Omega i}$ is the characteristic length scale for the coated catalyst layer (m).

Writing Eq. 73 in dimensionless form gives:

$$\frac{1}{k_{m,\text{app}}} \cdot \frac{D_{\text{CH}_4-\text{mix}}}{4 \cdot R_{\Omega,e}} = \left(\frac{1}{\text{Sh}_e} + \frac{R_{\Omega,i} \cdot D_{\text{CH}_4-\text{mix}}}{4 \cdot R_{\Omega,e} \cdot D_{\text{CH}_4,e} \cdot Sh_i} + \frac{D_{\text{CH}_4-\text{mix}}}{4 \cdot R_{\Omega,e} k_{\text{obs}} \cdot R_{\Omega i}} \right) \tag{74}$$

$$\frac{1}{\mathrm{Sh}_{\mathrm{app}}} = \left(\frac{1}{\mathrm{Sh}_e} + \frac{\alpha \cdot \beta}{4} \cdot \frac{1}{\mathrm{Sh}_i} + \frac{\alpha \cdot \beta}{4 \cdot \phi^2} \right) \tag{75}$$

where the various dimensionless groups appearing in Eq. 75 are defined as:

$$\beta = \frac{R_{\Omega,i}}{R_{\Omega,e}} \alpha = \frac{D_{\mathrm{CH_4-mix}}}{D_{\mathrm{CH_4},e}}, \phi^2 = \frac{k_{\mathrm{obs}} \cdot R_{\Omega,i}^2}{D_{\mathrm{CH_4},e}},$$
$$\phi^2 = \frac{k_{\mathrm{obs}} \cdot R_{\Omega i}^2}{D_{\mathrm{CH_4},e}}, \mathrm{Sh}_{\mathrm{app}} = \frac{4 \cdot k_{m,\mathrm{app}} \cdot R_{\Omega e}}{D_{\mathrm{CH_4-mix}}} \tag{76}$$

where $k_{m,\mathrm{app}}$ (m s^{-1}) is the apparent (or overall experimentally observable) mass transfer coefficient, $D_{\mathrm{CH_4},e}$ is the effective diffusivity of CH_4 (m^2 s^{-1}), $D_{\mathrm{CH_4-mix}}$ is the diffusivity of CH_4 in gas phase mixture (m^2 s^{-1}), $R_{\Omega i}$ is the characteristic length scale for the coated catalyst layer (m), $R_{\Omega e}$ is the characteristic length scale for the fluid phase (m), Sh_i is the internal Sherwood number, Sh_e is the external Sherwood number, k_{obs} is the observed first-order reaction rate constant (s^{-1}), ϕ is the Thiele modulus for a first order reaction and $\mathrm{Sh}_{\mathrm{app}}$ is the apparent (or experimentally observed) mass transfer coefficient.

In kinetic regime, the apparent mass transfer coefficient can be written as:

$$\mathrm{Sh}_{\mathrm{app,kin}} = \frac{4 * \phi^2}{\alpha \cdot \beta} \tag{77}$$

Heat Transfer Effects

For highly endothermic reactions such as methane steam reforming, temperature gradients between the gas phase and catalyst surface cannot be neglected. Under steady-state conditions, the rate of mass transfer of methane reactant from the gas phase mixture to the solid surface must be equal to the rate of methane reactant conversion by surface reaction:

$$k_{m,e} \cdot A_{\Omega,e} \cdot (C_b - C_s) = k_s \cdot A_{\Omega,e} \cdot C_s^n \tag{78}$$

where k_s is the surface reaction rate constant, C_b is the concentration in the bulk of the gas phase (mol m^{-3}), C_s is the concentration in the surface of the catalyst layer (mol m^{-3}).

Assuming that the outer surface of the catalyst particle is uniformly accessible to the reagents, that is, the thickness of the concentration and thermal boundary layers over the particle surface has constant values. Since each section of the outer surface behaves kinetically the same as all other parts, steady-state analysis of such a system is essentially one-dimensional [45, 59]. Thus, the heat generated by the

surface reaction can be calculated by multiplying the mass transfer rate with the heat of reaction per mol of reactant. At steady state, we can obtain:

$$k_{m,e} \cdot A_{\Omega,e} \cdot (C_b - C_s) \cdot (\Delta H_r) = h_e \cdot A_{\Omega,e} \cdot (T_b - T_s) \tag{79}$$

Solving the temperature difference, the final expression is given by:

$$\frac{k_{m,e}}{h_e} \cdot (C_b - C_s) \cdot (\Delta H_r) = (T_b - T_s) \tag{80}$$

where T_b,T_s is the temperature in the bulk of the gas phase and surface of the catalyst layer (K) respectively, ΔH_r is the heat of MSR reaction (J mol^{-1}) and h_e is the heat transfer coefficient associated for the gas phase (W m^{-2} K^{-1}).

Hence, using the Chilton–Colburn analogy between heat and mass transfer ($j_H \approx j_M$) for simple gas mixture, we can replace the ratio $\frac{k_{m,e}}{h_e}$ and obtain the following expression [45, 59]:

$$k_{m,e} = \frac{j_M \cdot G}{\rho_f \cdot \mathrm{Sc}^{\frac{2}{3}}} h_e = \frac{j_H \cdot G \cdot Cp_f}{\mathrm{Pr}^{\frac{2}{3}}} \tag{81}$$

$$(T_b - T_s) = \frac{\Delta H_r}{\rho_f \cdot Cp_f} \cdot \left(\frac{\mathrm{Pr}}{\mathrm{Sc}}\right)^{\frac{2}{3}} \cdot (C_b - C_s) \tag{82}$$

Considering the Lewis (Le) and Carberry (Ca) number, we can obtain the final expression as [45, 59]:

$$\mathrm{Le} = \frac{\mathrm{Sc}}{\mathrm{Pr}} \; \mathrm{Ca} = \frac{C_b - C_s}{C_b} \tag{83}$$

$$(T_b - T_s) = \left(\frac{\Delta H_r \cdot C_b}{\rho_f \cdot c_{p,f}}\right) \cdot \mathrm{Le}^{-2/3} \cdot \mathrm{Ca} \tag{84}$$

where ρ_f is the density of the gas phase (Kg m^{-3}), $c_{p,f}$ is the heat capacity of the gas phase (J Kg^{-1} K^{-1}) and Pr is the Prandtl number.

Thus, by dividing Eq. 83 by T_b, it is possible to obtain the dimensionless external Prater number (β_{ext}), which represents the ratio of the maximum heat consumption and heat transfer rates:

$$\frac{T_s}{T_b} = 1 - \left(\frac{\Delta H_r \cdot C_b}{\rho_f \cdot c_{p,f}}\right) \cdot \frac{1}{T_b} \cdot \mathrm{Le}^{-2/3} \cdot \mathrm{Ca} \tag{85}$$

$$\frac{T_s}{T_b} = 1 - \frac{\Delta T_{ad}}{T_b} \cdot \mathrm{Le}^{-2/3} \cdot \mathrm{Ca} \tag{86}$$

$$\frac{T_s}{T_b} = 1 - \beta_{\mathrm{ext}} \cdot \mathrm{Ca} \tag{87}$$

where ΔT_{ad} is the adiabatic temperature rise ($\Delta T_{ad} = \frac{\Delta H_r \cdot C_b}{\rho_f \cdot c_{p,f}}$; K) and β_{ext} is the dimensionless external Prater number ($\beta_{\text{ext}} = \frac{\Delta T_{\text{ad}}}{T_b} \cdot \text{Le}^{-2/3}$).

The interphase heat transfer limitations can be evaluated using the criterion derived by Mears [61] (Eq. 88) with the perturbation approach, in which the heat transfer resistance of the fluid phase is assumed to be lumped at the surface:

$$\chi = \frac{\left(\Delta H \cdot R^{\text{obs}} \cdot R_{\Omega e}\right)}{h_e \cdot T_b} < \frac{0.15}{\gamma_b}; \quad \gamma_b = \frac{E_{\text{act}}}{R_g \cdot T_b} \tag{88}$$

where R^{obs} is the observed reaction rate (mol m^3 s^{-1}), h_e is the heat transfer coefficient associated for the gas phase (W m^{-2} K^{-1}), R_g is the gas constant (J mol^{-1} K^{-1}), E_{act} is the apparent activation energy of the reaction (J mol^{-1}), χ is the Damkholer for interphase heat transport and γ_b is the Arrhenuis number evaluated at the bulk of the gas phase.

Anderson in 1963 [62] applied the perturbation approach to derive a criterion for the lack of importance of temperature gradients in catalyst particles. The reaction is assumed to follow Arrhenius temperature dependence and this criterion is valid regardless of whether there are diffusion limitations in the particle or not:

$$\frac{\left(\Delta H \cdot R^{\text{obs}} \cdot R_{\Omega,i}^2\right)}{\lambda_{\text{cat}} \cdot T_s} < \frac{0.75}{\gamma_s} \tag{89}$$

$$\psi = \frac{\left(\Delta H \cdot R^{\text{obs}} \cdot R_{\Omega,i}^2\right)}{\lambda_{\text{cat}} \cdot T_s}; \quad \gamma_s = \frac{E_{\text{act}}}{R_g \cdot T_s} \tag{90}$$

where λ_{cat} is the thermal conductivity of the Ru/Al_2O_3 catalyst (W m^{-1} K^{-1}), ψ is the Damkohler for intraparticle heat transport and γ_s is the Arrhenuis number evaluated at the surface of the gas phase.

In order to study the effects of mass and heat transfer, both balances must be solved simultaneously to estimate the concentration and temperature profile. From the mass balance, we can write the following expression:

$$D_e \cdot \frac{\mathrm{d}^2 c}{\mathrm{d}x^2} - (-R) = 0 \tag{91}$$

The heat balance can be written as:

$$\lambda_e \frac{\mathrm{d}^2 T}{\mathrm{d}x^2} - (-R) \cdot (\Delta H_r) = 0 \tag{92}$$

where λ_e is the effective thermal conductivity (W m^{-1} K^{-1}). Considering that the reaction rate (R) is the same in both balances, we can obtain the following expression:

Table 9 Properties of the bare monolith

Σ	[cpsi]	100
D_m	[m]	0.030
L_m	[m]	0.0019
δ_w	[m]	0.00063
N	[m]	0.1563
E	[–]	0.564
GSA	[$m^2\ m^{-3}$]	1187.333
d_h	[m]	0.0019
A_m	[m]	0.00126

$$\frac{D_e \cdot (\Delta H_r)}{\lambda_e} \cdot \frac{\mathrm{d}^2 c}{\mathrm{d}x^2} = \frac{\mathrm{d}^2 T}{\mathrm{d}x^2} \tag{93}$$

By integrating the Eq. 93 and considering the surface concentration and temperature (C_s, T_s), we can obtain the following linear expression between internal temperature and reactant concentration [15, 16]:

$$\left(T_s - T_{b,c}\right) = (\Delta H_r) \cdot \frac{D_e}{\lambda_e} \cdot \left(C_s - C_{b,c}\right) \tag{94}$$

where $T_{b,c}$ is the temperature in the bulk of the catalyst layer (K) and $C_{b,c}$ is the concentration within the catalyst layer (mol m^{-3}). It is worth noting the largest possible temperature difference into the catalyst layer is attained when the concentrations within the bulk of the catalyst layer becomes zero, hence we can refer the maximum temperature difference ($\Delta T_{\max}$) to the surface temperature using the dimensionless internal Prater number (β_{in}) by [15, 16] (Tables 9, 10, 11 and 12).

$$\beta_{\text{in}} = \frac{\Delta T_{\max}}{T_s} = \frac{(\Delta H_r) \cdot C_s}{T_s} \cdot \frac{D_e}{\lambda_e} \tag{95}$$

Table 10 Characteristic times for the 1.5Ru5Al catalyst

T [°C]	t_c [s]	t_d^i [s]	t_d^e [s]	t_r [s]	t_z [s]
550	0.3091	0.0456	0.0012	0.2238	5.1500
600	0.2914	0.0441	0.0010	0.1928	4.5926
650	0.2756	0.0428	0.0009	0.1883	4.1264
700	0.2615	0.0405	0.0008	0.1441	3.6903
750	0.2487	0.0394	0.0007	0.1151	3.3138
800	0.2371	0.0384	0.0007	0.0943	2.9217
850	0.2266	0.0384	0.0006	0.0939	2.6402

Table 11 Characteristic times for the 1.5Ru10Al catalyst

T [°C]	t_c [s]	t_d^i [s]	t_d^e [s]	t_r [s]	t_z [s]
550	0.3091	0.0714	0.0010	0.1521	4.5226
600	0.2914	0.0691	0.0008	0.1212	3.9330
650	0.2756	0.0670	0.0007	0.1113	3.4816
700	0.2614	0.0651	0.0007	0.1040	3.1674
750	0.2487	0.0634	0.0006	0.1001	2.9079
800	0.2371	0.0618	0.0006	0.1001	2.6688
850	0.2266	0.0604	0.0005	0.1014	2.4751

Table 12 Characteristic times for the 1.5Ru20Al catalyst

T [°C]	t_c [s]	t_d^i [s]	t_d^e [s]	t_r [s]	t_z [s]
550	0.3091	0.1319	0.0008	0.4222	4.7509
600	0.2914	0.1277	0.0008	0.3860	4.2279
650	0.2756	0.1239	0.0007	0.3713	3.8065
700	0.2614	0.1204	0.0006	0.3459	3.4299
750	0.2487	0.1172	0.0006	0.3495	3.1437
800	0.2371	0.1142	0.0005	0.3401	2.8716
850	0.2266	0.1115	0.0005	0.3195	2.6049

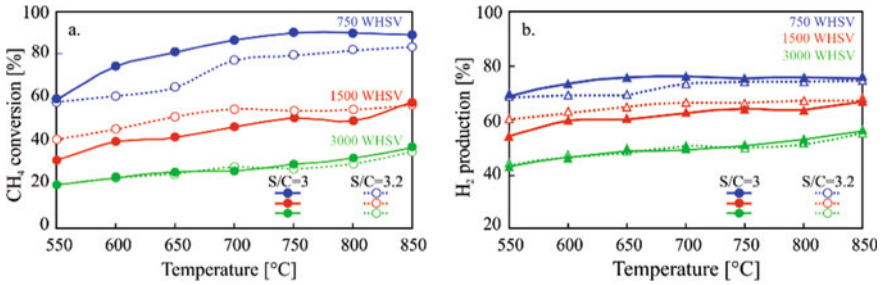

Fig. 14 MSR tests, performance comparison of monoliths 1.5% Ru on 10% γ-Al_2O_3 at various WHSV and S/C **a** CH_4 conversion; **b** H_2 production

References

1. Hosseini SE, Wahid MA (2016) Hydrogen production from renewable and sustainable energy resources: promising green energy carrier for clean development. Renew Sustain Energy Rev 57:850–866
2. IAEA (1999) IAEA-TECDOC-1085: hydrogen as an energy carrier and its production by nuclear power. Iaea-Tecdoc-1085
3. Alves JJ, Towler GP (2002) Analysis of refinery hydrogen distribution systems. Ind Eng Chem Res 41:5759–5769

4. Meyers RA (1996) Handbook of petroleum refining processes. Second. McGraw-Hill, New York
5. Yamaguchi D, Tang L, Burke N et al (2012) Small scale hydrogen production from metal-metal oxide redox cycles. Hydrog Energy Challenges Perspect 2:31–54
6. Karadag D, Köroğlu OE, Ozkaya B et al (2014) A review on fermentative hydrogen production from dairy industry wastewater. J Chem Technol Biotechnol 89:1627–1636
7. Holladay JD, Hu J, King DL, Wang Y (2009) An overview of hydrogen production technologies. Catal Today 139:244–260
8. Barreto L, Makihira A, Riahi K (2003) The hydrogen economy in the 21st century: A sustainable development scenario. Int J Hydrogen Energy 28:267–284
9. Hansen K, Ingerslev M, Felby C et al (2006) Bioenergy in the Nordic-baltic-NW Russian Region. 66
10. Abbas SZ, Dupont V, Mahmud T (2017) Kinetics study and modelling of steam methane reforming process over a NiO/Al_2O_3 catalyst in an adiabatic packed bed reactor. Int J Hydrogen Energy 42:2889–2903
11. De S, Zhan GJ, Luque R, Yan N (2016) Ni-based bimetallic heterogeneous catalysts for energy and environmental applications. Energy Environ Sci 9:3314–3347
12. Omoregbe O, Danh HT, Abidin SZ et al (2016) Influence of lanthanide promoters on Ni/SBA-15 catalysts for syngas production by methane dry reforming. Procedia Eng 148:1388–1395
13. Tsyganok AI, Inaba M, Tsunoda T et al (2003) Dry reforming of methane over supported noble metals: A novel approach to preparing catalysts. Catal Commun 4:493–498
14. Rass-Hansen J, Christensen CH, Sehested J et al (2007) Renewable hydrogen: Carbon formation on Ni and Ru catalysts during ethanol steam-reforming. Green Chem 9:1016–1021
15. Rostrup-Nielsen JR, Bak Hansen JH (1993) CO_2-reforming of methane over transition metals. J Catal 144:38–49
16. Ashraf MA, Sanz O, Italiano C et al (2018) Analysis of $Ru/La\text{-}Al_2O_3$ catalyst loading on alumina monoliths and controlling regimes in methane steam reforming. Chem Eng J 334:1792–1807
17. Tijburg IIM, Geus JW, Zandbergen HW (1991) Application of lanthanum to pseudo-boehmite and γ-Al_2O_3. J Mater Sci 26:6479–6486
18. Arai H, Machida M (1996) Thermal stabilization of catalyst supports and their application to high-temperature catalytic combustion. Appl Catal A Gen 138:161–176
19. Ferreira-Aparicio P, Rodríguez-Ramos I, Anderson JA, Guerrero-Ruiz A (2000) Mechanistic aspects of the dry reforming of methane over ruthenium catalysts. Appl Catal A Gen 202:183–196
20. Berman A, Karn RK, Epstein M (2007) Steam reforming of methane on a Ru/Al_2O_3 catalyst promoted with Mn oxides for solar hydrogen production. Green Chem 9:626–631
21. Amjad U, Vita A, Galletti C et al (2013) Comparative study on steam and oxidative steam reforming of methane with noble metal catalysts. Ind Eng Chem Res 52:15428–15436
22. Amjad U, Moncada Quintero CW, Ercolino G et al (2019) Methane steam reforming on the Pt/CeO_2 catalyst: effect of daily start-up and shut-down on long-term stability of the catalyst. Ind Eng Chem Res 58:16395–16406
23. Italiano C, Ashraf MA, Pino L et al (2018) Rh/CeO_2 thin catalytic layer deposition on alumina foams: Catalytic performance and controlling regimes in biogas reforming processes. Catalysts 8:1–25
24. Vita A, Italiano C, Ashraf MA et al (2018) Syngas production by steam and oxy-steam reforming of biogas on monolith-supported CeO_2-based catalysts. Int J Hydrogen Energy 43:11731–11744
25. Govender S, Friedrich HB (2017) Monoliths: a review of the basics, preparation methods and their relevance to oxidation. Catalysts 7
26. Roy S, Bauer T, Al-Dahhan M et al (2004) Monoliths as multiphase reactors: A review. AIChE J 50:2918–2938
27. Boger T, Heibel AK, Sorensen CM (2004) Monolithic catalysts for the chemical industry. Ind Eng Chem Res 43:4602–4611

28. Visconti CG, Tronconi E, Groppi G et al (2011) Monolithic catalysts with high thermal conductivity for the Fischer-Tropsch synthesis in tubular reactors. Chem Eng J 171:1294–1307
29. Tronconi E, Groppi G, Visconti CG (2014) Structured catalysts for non-adiabatic applications. Curr Opin Chem Eng 5:55–67
30. Ercolino G, Karimi S, Stelmachowski P, Specchia S (2017) Catalytic combustion of residual methane on alumina monoliths and open cell foams coated with Pd/Co_3O_4. Chem Eng J 326:339–349
31. Ercolino G, Stelmachowski P, Specchia S (2017) Catalytic performance of Pd/Co_3O_4 on SiC and ZrO_2 open cell foams for process intensification of methane combustion in lean conditions. Ind Eng Chem Res 56:6625–6636
32. Ercolino G, Grzybek G, Stelmachowski P et al (2015) Pd/Co_3O_4-based catalysts prepared by solution combustion synthesis for residual methane oxidation in lean conditions. Catal Today 257:66–71
33. Vita A, Cristiano G, Italiano C et al (2014) Methane oxy-steam reforming reaction: Performances of $Ru/\gamma\text{-}Al_2O_3$ catalysts loaded on structured cordierite monoliths. Int J Hydrogen Energy 39:18592–18603
34. Specchia S, Galletti C, Specchia V (2010) Solution Combustion Synthesis as intriguing technique to quickly produce performing catalysts for specific applications. Stud Surf Sci Catal 175:59–67
35. Nijhuis TA, Beers AEW, Vergunst T et al (2001) Preparation of monolithic catalysts. Catal Rev Sci Eng 43:345–380
36. Williams JL (2001) Monolith structures, materials, properties and uses. Catal Today 69:3–9
37. Plummer HK, Baird RJ, Hammerle RH et al (1999) Measurement of automotive catalyst washcoat loading parameters by microscopy techniques. Microsc Microanal 5:267–281
38. Cybulski A, Moulijn JA (1998) Structured catalysts and reactors. Marcel Dekker Inc, New York
39. Wójcik S, Ercolino G, Gajewska M et al (2018) Robust $Co_3O_4|\alpha\text{-}Al_2O_3|$ cordierite structured catalyst for N_2O abatement—validation of the SCS method for active phase synthesis and deposition. Chem Eng J 377:120088
40. Millington B, Whipple V, Pollet BG (2011) A novel method for preparing proton exchange membrane fuel cell electrodes by the ultrasonic-spray technique. J Power Sources 196:8500–8508
41. Arzamendi G, Die PM, Gandia LM (2013) Renewable hydrogen technologies. Luis Gandia Gurutze Arzamedi Pedro Dieguez. Elsevier Science, Amsterdam 472.
42. Spivey JJ, Dooley KM (2009) Catalysis. The Royal Society of Chemistry
43. Dumesic JA. Huber GW, Boudart M (2008) Principles of heterogeneous catalysis. In: Handbook of heterogeneous catalysis. Wiley-VCH Verlag GmbH & Co. KGa
44. Klaewkla R, Arend M, Hoelderich WF (2011) A review of mass transfer controlling the reaction rate in heterogeneous catalytic systems. Mass Trans Adv Aspects 667–684
45. Kashid MN, Renken A (2013) Microstructured devices for chemical microreactors. Wiley-VCH Verlag Gmbh & Co
46. Joshi SY, Harold MP, Balakotaiah V (2009) Low-Dimensional models for real time simulations of catalytic monoliths. AIChE J 55:1771–1783
47. Joshi SY, Harold MP, Balakotaiah V (2010) Overall mass transfer coefficients and controlling regimes in catalytic monoliths. Chem Eng Sci 65:1729–1747
48. Joshi SY, Harold MP, Balakotaiah V (2009) On the use of internal mass transfer coefficients in modeling of diffusion and reaction in catalytic monoliths. Chem Eng Sci 64:4976–4991
49. Balakotaiah V, West DH (2002) Shape normalization and analysis of the mass transfer controlled regime in catalytic monoliths. Chem Eng Sci 57:1269–1286
50. Young LC, Finlayson BA (1976) Mathematical models of the monolith catalytic converter: Part II. Application to automobile exhaust. AIChE J. 22:343–353
51. Bhattacharya M, Harold MP, Balakotaiah V (2004) Mass-transfer coefficients in washcoated monoliths. AIChE J 50:2939–2955

52. Balakotaiah V (2008) On the relationship between Aris and Sherwood numbers and friction and effectiveness factors. Chem Eng Sci 63:5802–5812
53. Laguna OH, Domínguez MI, Centeno MA, Odriozola JA (2016) Catalysts on metallic surfaces: monoliths and microreactors. New materials for catalytic applications. Elsevier B.V.
54. Kockmann N (2008) Transport phenomena in micro process engineering. Norbert Kockmann, Springer, Berlin
55. Bennett CJ, Hayes RE, Kolaczkowski ST, Thomas WJ (1992) An experimental and theoretical study of a catalytic monolith to control automobile exhaust emissions. Proc R Soc Lond A 439:465–483
56. Joshi SY, Ren Y, Harold MP, Balakotaiah V (2011) Determination of kinetics and controlling regimes for H_2 oxidation on Pt/Al_2O_3 monolithic catalyst using high space velocity experiments. Appl. Catal B Environ 102:484–495
57. Berman A, Karn RK, Epstein M (2005) Kinetics of steam reforming of methane on Ru/Al_2O_3 catalyst promoted with Mn oxides. Appl Catal A Gen 282:73–83
58. Choudhary TV, Goodman DW (2000) Methane activation on Ni and Ru model catalysts. J Mol Catal A: Chem 163:9–18
59. Onsan ZI, Avci AK (2016) Multiphase catalytic reactors. Wiley, Hoboken, N.J.
60. Shah RK, London AL (1978) laminar flow forced convection in ducts: a source book for compact heat exchanger analytical data. Academic, New York
61. Mears DE (1971) Diagnostic criteria for heat transport limitations in fixed bed reactors. J Catal 20:127–131
62. Anderson JE (1963) A criterion for isothermal behaviour of a catalyst pellet. Chem Eng Sci 18:147–148
63. Damköhler G (1943) The excess temperature in contact grains. Z Phys Chemie 193:16–28
64. Yaws CL (1999) Chemical properties Handbook. McGraw-Hill, New York
65. Fuller EN, Schettler PD, Giddings JC (1966) A new method for prediction of binary gas-phase diffusion coefficients. Ind Eng Chem 58:18–27
66. Green DW, Perry RH (2008) Perry's chemical engineers' handbook, 8th edn. McGraw-Hill
67. Cao C, Zhang N, Cheng Y (2016) Numerical analysis on steam methane reforming in a plate microchannel reactor: effect of washcoat properties. Int J Hydrogen Energy 41:18921–18941
68. Hayes RE, Kolaczkowski ST, Li PKC, Awdry S (2000) Evaluating the effective diffusivity of methane in the washcoat of a honeycomb monolith. Appl Catal B Environ 25:93–104
69. Talebian-Kiakalaieh A, Amin NAS (2016) Theoretical and experimental evaluation of mass transfer limitation in gas phase dehydration of glycerol to acrolein over supported HSiW catalyst. J Taiwan Inst Chem Eng 59:11–17
70. Kolitcheff S, Jolimaitre E, Hugon A et al (2017) Tortuosity of mesoporous alumina catalyst supports: Influence of the pore network organization. Microporous Mesoporous Mater 248:91–98
71. Satterfield CN (1970) Mass transfer in heterogeneous catalysis. Massachusetts Institute of Technology Press, Cambridge
72. Ertl G, Knözinger H, Weitkamp J (1997) Handbook of heterogeneous catalysis. VCH, Weinheim
73. Incera Garrido G, Patcas FC, Lang S, Kraushaar-Czarnetzki B (2008) Mass transfer and pressure drop in ceramic foams: a description for different pore sizes and porosities. Chem Eng Sci 63:5202–5217

Flames and Reacting Systems

Effect of Natural Gas Blend Enrichment with Hydrogen on Laminar Burning Velocity and Flame Stability

A. R. Khan, M. R. Ravi, and Anjan Ray

1 Introduction

The combustion of fossil fuels has approximately an 85% share in supplying the global energy requirement [1]. This massive amount of fossil fuel burning is a cause of environmental pollution and climate change. Therefore, the study of efficient and controlled combustion is significant for the development of human society as well as for providing a better environment for all. Natural gas (NG) is the most widely used gaseous fuel in the world [2], and it has a wide range of applicability in domestic, industrial, and automotive applications. NG is not only cheaper and abundantly available, but it is also the cleanest fossil fuel. Although the main combustible component of NG is methane (55.8–98.1%), its composition varies depending upon the field from which it is extracted, season, refineries, and processes through which it is produced [3]. Along with methane, natural gas also contains ethane (0.5–13.3%), propane (0–23.7%), non-combustible gases such as N_2 and CO_2, and relatively trace level of heavier hydrocarbons (HC). Hence, methane alone cannot be considered as the representative of an NG blend. Keeping in mind the variability in the composition of the NG blends, the fuel flexibility of any combustion appliance is an essential concern in their design stages. The variability in the composition of the NG alters its combustion and emission characteristics. Some characteristics of importance from the design point of view of a combustion device are listed below:

1. Unstretched adiabatic laminar burning velocity (LBV)
2. Ignition delay time
3. Regimes of flashback and lift-off
4. Flammability limits
5. Quenching distance

A. R. Khan · M. R. Ravi · A. Ray (✉)
Department of Mechanical Engineering, Indian Institute of Technology Delhi, New Delhi, India
e-mail: raya@mech.iitd.ac.in

© Springer Nature Singapore Pte Ltd. 2021

A. De et al. (eds.), *Sustainable Development for Energy, Power, and Propulsion*, Green Energy and Technology,
https://doi.org/10.1007/978-981-15-5667-8_6

Out of the above-discussed combustion characteristics, LBV is the most fundamental combustion characteristic of any fuel–air mixture. It is defined as follows: "*The burning velocity is defined as the relative velocity, normal to the flame front, with which the unburnt gas moves into this front and is transformed* [4]."

Effective and accurate design of combustion appliances requires an accurate value of laminar burning velocity. Laminar burning velocity is also an important input parameter for I.C. engine modeling and laminar flamelet modeling. A chemical kinetic scheme can also be validated using the measured values of laminar burning velocity. The other characteristics, such as flashback, blowoff, and quenching distance, are dependent on the LBV. Variation in the composition of a multicomponent fuel–air mixture will alter the LBV, and in turn, this will also affect other related phenomena (heat release rate, quenching distance, flashback, etc.). NG combustion chemistry can be best studied by considering methane, ethane, and propane as the combustible components of the NG blends [5].

As methane is the principal combustible component in an NG blend, the NG blend combustion has some drawbacks. The reason is high C–H bond dissociation energy of methane [6]. Eventually, the presence of methane in an NG blend is a source of some peculiar properties like reduced LBV, and higher ignition delay time compared to other hydrocarbon fuels (either pure or a blend of higher HC). Moreover, NG has a lower lean-burn limit, and hence, a fuel-lean operation decreases the thermal efficiency and increases the flame instability. The NG-fueled SI engine experiences cycle-to-cycle variation, which increases HC and CO emissions during the lean-burn operation of the engine. This hinders the drivability of the vehicle. The best remedy to the above problem could have a complete shift to the hydrogen combustion. But at present, we lack the required infrastructure for production, storage, and its safe distribution. Therefore, as of now, the best-suited remedy to the above issues is to blend NG with hydrogen. In addition to higher LBV and low lean-burn limit, hydrogen has zero carbon content, which enhances the engine performance and reduces the CO and CO_2 emission. Hence, it is the need of the hour to study the effect of enrichment with H_2 on the LBV and flame stability of multicomponent NG blends. This study summarizes our previous studies [7, 8], which deal with the effect of higher hydrocarbons and enrichment with H_2 on the LBV and flame stability of various NG blends.

1.1 Preferential Diffusion Instability

The response of the stretched flame, such as flame speed, may be significantly affected in the presence of preferential diffusion of heat or mass of the unburned fuel–air mixture [9]. The relative importance of the heat or mass diffusion can be quantified by a non-dimensional number termed as Lewis number (Le). Lewis number can be defined as the ratio of the thermal diffusivity (α) to the mass diffusivity (D) of the unburnt fuel–air mixture. If for a given fuel–air mixture Le > 1, the diffusion of the heat from the reaction zone to the preheat zone is predominant. On the other

hand, for Le < 1, mass diffusion of the unburned fuel–air mixture from the preheat zone to the reaction zone is higher, and it modifies the local fuel–air equivalence ratio. Kwon et al. [10] discussed two types of preferential diffusion. They termed preferential diffusion of mass with respect to heat as diffusive-thermal instability. The preferential diffusion of one of the species with respect to the other species of the reactant in the abundant inert is called as diffusive-diffusive instability. However, they were not able to identify which one of the two is responsible for flame instability. They referred to both of these mechanisms jointly as preferential diffusion instability.

Flame stability of fuel–air mixtures with respect to preferential diffusion of one of the components in the reaction zone can be quantified by calculating burned gas Markstein length (L_b). Burned gas Markstein length (L_b) is the slope of the straight line plot of stretch rate (K) versus stretched lame speed (S_b); steeper the slope, larger will be the effect of stretch on flame speed. Hence, it addresses the sensitivity of the flame speed to the flame stretch rate. Markstein length is independent of the flame stretch rate, and it depends on the type of the fuel and equivalence ratio of the fuel–air mixture. Markstein length can be non-dimensionalized by dividing it with the laminar flame thickness (δ). The positive value of Markstein length reduces the cell size and wrinkles on the flame surface and hence makes it stable and smooth. On the other hand, the negative value of Markstein length is a sign of an unstable flame in which the size of the cellular structures and wrinkles will grow. A positive (negative) value of L_b indicates stable (unstable) flame with respect to the preferential diffusion effect. A lean propane–air mixture has a Lewis number (Le) > 1, which increases L_b, while a lean methane–H_2–air mixture has Le < 1, which tends to decrease the L_b. Hence, the effect of the presence of higher hydrocarbons (HC), and H_2, on flame stability is essential to understand the sensitivity of the mixture to perturbations.

In view of the above discussion, the objectives of the present work have been formulated as follows:

1.2 Objectives of the Present Study

1. To study the effect of enrichment with hydrogen on the laminar burning velocity (LBV) and burned gas Markstein length (L_b) of NG blends at 0.1 MPa pressure and 300 ± 3 K temperature. This study also provides the opportunity to investigate the effect of the simultaneous inclusion of higher HC, viz. C_2H_6 and C_3H_8, and H_2, on the LBV and L_b of the blends. The experimental results of LBV and L_b are obtained at various levels (25, 50, and 75%) of H_2 addition in the fuel, for a broad range of equivalence ratios ($\Phi = 0.6$ to 1.4).
2. To assess and identify the best-suited chemical kinetic mechanism in terms of its capability to predict the LBV of the multicomponent NG–H_2 blends. CHEMKIN-PRO® [11] software package is used, and the LBV predictions of GRI-MECH 3.0 [12], UCS-MECH 2.0 [13], and San Diego mechanism [14] are compared. The appropriate chemical kinetic mechanism is adopted to analyze the oxidation chemistry of different NG–H_2 blends.

2 Methodology

2.1 Fuel Selection

It is decided to select three NG blends to investigate the effect of enrichment of the selected multicomponent NG blends with H_2. Out of the three NG blends, two NG blends are selected based on their compositions, and the remaining one will be chosen by its flame stability response to the preferential diffusion effect. The two NG blends based on compositions are NG6 and NG5 blends. NG6 blend belongs to the source of NG, which has the highest mole fraction of methane and the lowest mole fraction of higher HC. As per the outcome of our previous study [7], the NG blend which will have approximately constant burned gas Markstein length, (L_b), will be selected. Composition of the NG blends chosen for the present study is shown in Table 1.

The H_2 addition level, $\%_{H_2}$, is defined as per the expression of Eq. 1, which expresses the percentage of H_2 in the NG–H_2 blend.

$$\%_{H_2} = \left\{\chi_{H_2}/\left(\chi_{H_2} + \chi_{NG}\right)\right\} \times 100 \tag{1}$$

where χ_{H_2} and χ_{NG} are the mole fractions of H_2 and NG, respectively, present in the NG–H_2 blend. The three different $\%_{H_2}$ used in the present study are 25, 50, and 75. The gases used have purity levels as follows: CH_4–99.95, O_2–99.999, N_2–99.994, C_2H_6–99.9, C_3H_8–99.9, and H_2–99.999 pure.

Enrichment with H_2 is done by substituting some of the NG mole fraction with a similar amount of H_2. Therefore, the air requisite of this H_2-enriched NG blend will be different from that of the corresponding NG blend, and hence, fuel–air equivalence ratio is calculated as per the requirement of NG–H_2 blend. To fill the combustion chamber with each species, the partial pressure of each reactant species is calculated by using Eq. (2).

$$\left(\frac{100 - \%_{H_2}}{100}\right)\mathrm{NG} + \left(\frac{\%_{H_2}}{100}\right)\mathrm{H_2} + \left(\frac{\lambda}{\Phi}\right)(\mathrm{O_2} + 3.76\,\mathrm{N_2}) \tag{2}$$

where the first pair of parentheses in Eq. (2) denotes the number of moles of NG $\left(\chi_{CH_4} + \chi_{C_2H_6} + \chi_{C_3H_8}\right)$ in the NG–H_2 blend, and χ represents the mole fraction

Table 1 Composition (% volume) of different NG blends used in the present study

S. No.	NG blends	Final species composition		
		CH_4 %	C_2H_6 %	C_3H_8 %
1	NG2	62.00	30.40	7.60
2	NG5	56.82	21.59	21.59
3	NG6	92.18	3.91	3.91

Table 2 Test matrix for the experimental plan of the present study

S. No.	Fuel	Oxidizer	Equivalence ratio
1	75% NGi + 25% H_2	Lab air (21% O_2 and 79% N_2)	0.6–1.4
2	50% NGi + 50% H_2	Lab air (21% O_2 and 79% N_2)	0.6–1.4
3	25% NGi + 75% H_2	Lab air (21% O_2 and 79% N_2)	0.6–1.4

All the experiments are performed at 300 ± 3 K temperature and 0.1 MPa initial pressure where i = 5, 6…

of different constituent of NG blend. The second pair of parentheses represents the number of moles of H_2 in NG–H_2 blend, and λ is number of moles of O_2 required to completely burn a given NG–H_2 blend. Table 2 shows the test matrix for the experimental plan of the present study. The oxidizer used is termed as lab air. To ensure the repeatability of the experiments, lab air is prepared by mixing the pure O_2 (21%) and N_2 (79%) from respective cylinders.

2.2 Experimental Setup and Procedure

To systematically quantify and eliminate the effect of stretch on the LBV, constant pressure outwardly propagating spherical flame method is used in the present study. The overall layout of the experimental setup is shown schematically in Fig. 1. All the experiments are performed at an initial pressure of 0.1 MPa and a temperature of 300 ± 3 K. As shown in Fig. 1, the experimental setup consists of a 43-liter cylindrical combustion chamber with two quartz windows (GE 124) of 0.178 m diameter to provide the optical access through the two flat surfaces of the cylindrical vessel of the combustion chamber as shown in Fig. 1. First of all the combustion chamber is purged with the dry compressed air with the help of a compressor (make: ELGI, model: Dr. Vayu, capacity: 92 lpm, max. pressure: 8 bar) and dryer (make: TRIDENT, model: dryspell: 10 M2) to remove any leftover combustion product.

After purging the combustion chamber, it is evacuated with the help of a vacuum pump (make: Truvac, model: 2 TV-5B, capacity: 10 CFM, min. pressure: 0.3 Pa) to remove any atmospheric air and moisture present in it. Then, with the help of a digital static pressure gauge (make: Keller, model: LEO 2), the combustion chamber is filled with the reactants one by one as per their partial pressures for a specific equivalence ratio starting with the lowest partial pressure reactant. The combustion chamber is left as it is for approximately 5 min to prepare a quiescent premixed mixture. A Z-type configuration shadowgraph system, along with the high-speed motion camera (make: Photron, model: FASTCAM MINI UX 100), is used to capture the flame images. A trigger box is designed to synchronize the actuation of the camera and ignition coil. The camera captures this shadowgram at an operating frequency of 4000–20,000 frames/s depending on the combination of particular equivalence ratio and fuel–air mixture. For constant pressure outwardly propagating spherical flame method, it

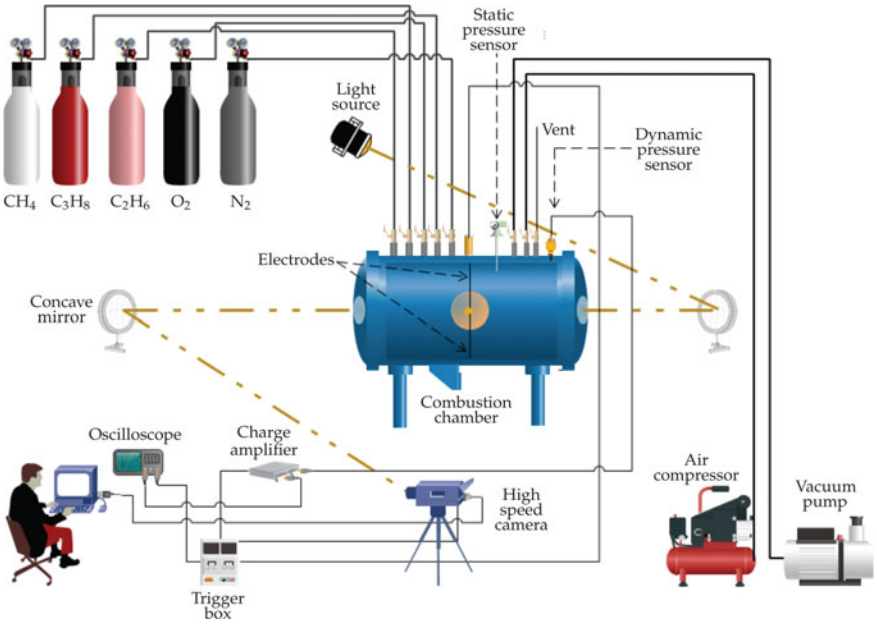

Fig. 1 Sketch of the layout of the experimental setup

is necessary to accurately trace the pressure versus time history in the combustion chamber. The pressure inside the combustion chamber remains constant for a small fraction of time, which is termed as pre-pressure period. The pressure variation as a function of time in the combustion chamber is measured using a piezo-electric dynamic pressure transducer (make: Kistler, model: Kistler 701A). Finally, with the help of a charge amplifier (make: Kistler, model: Kistler 5165 A), and oscilloscope (make: Teledyne Lecroy, model: WAVESURFER 3024) pressure versus time history is captured.

From pressure versus time plot, a constant pressure period is identified, and only this region is selected for further post-processing of the acquired flame images. The Canny edge detection program of the MATLAB® environment is used to extract the flame radius versus time data from flame images. Flame radius, r_f, versus time, t, data is used to calculate the slope between two consecutive radii versus time data with the help of a spreadsheet. This instantaneous slope represents the stretched flame speed, S_b, and expressed as follows:

$$S_b = \frac{\mathrm{d}r_f}{\mathrm{d}t} = \frac{r_{f2} - r_{f1}}{t_2 - t_1} \tag{3}$$

where r_{f2} and r_{f1} are instantaneous radii at time t_2 and t_1, respectively. The stretched flame speed data calculated in this manner was slightly scattered and oscillatory in nature. It was difficult to get a clear trend of the data. This observation was also

reported in the previous studies [15, 16]. Bradley et al. [15] have attributed this phenomenon to the acoustic disturbances excited by the flame propagation in a close combustion chamber wall. To smooth out the noisy data points from stretched flame speed data, a data smoothing, built-in algorithm LOWESS of SIGMA PLOT® [17] was used in the present work. "LOWESS" means locally weighted regression. The smooth curve of S_b values is obtained by the regression of the scattered data points. The smoothing factor in the present work is chosen to be 0.35 [18].

All the practical flames experience stretch owing to the flame motion and flame curvature. A parameter known as stretch rate (K) quantifies the flame stretch. The flame stretch rate is calculated as follows:

$$K = \frac{2}{r_f}\frac{\mathrm{d}r_f}{\mathrm{d}t} = \frac{2}{r_f}S_b \tag{4}$$

The stretched flame speed, S_b, is plotted as a function of the stretch rate, K, for the quasi-steady period, where it is free from initial ignition disturbances, and the effects of chamber confinement. Since the experiments are performed up to a finite stretch rate, which belongs to a pre-pressure period in the combustion chamber, the stretched flame speed, S_b, is extrapolated to the zero stretch rate, K, to get the unstretched flame speed, S_b°. Nonlinear model of extrapolation [19], shown in Eq. (5), has been used to obtain the unstretched flame speed, S_b°.

$$\left(\frac{S_b}{S_b^\circ}\right)^2 \ln\left(\frac{S_b}{S_b^\circ}\right)^2 = \left(\frac{2L_b}{S_b^\circ}\right)\left(\frac{\mathrm{d}S_b}{\mathrm{d}r_f} - K\right) \tag{5}$$

where $(\mathrm{d}S_b/\mathrm{d}r)$ is associated with flame acceleration. The flame acceleration term is also calculated in a similar way to stretched flame speed by performing the first-order finite difference of flame speed S_b with respect to the flame radius, r_f. To perform the nonlinear extrapolation, Eq. (5) is fitted to the experimental data of S_b versus K by least-square regression and unstretched flame speed, S_b°, and L_b is determined with the help of constants of fitting. Finally, by applying the mass conservation across the thin flame sheet, unstretched LBV, S_u°, is obtained by using the expression, $S_u^\circ = S_b^\circ\left(\rho_b^\circ/\rho_u\right)$. Where ρ_u is the density of the unburned fuel–air mixture and ρ_b° is the density of products at equilibrium.

The method suggested by Moffat [20] is used to calculate the total absolute uncertainty. The total uncertainty is a combined effect of random and systematic uncertainties in the measurement. Calculation of the random uncertainty is accomplished by repeating (3–5 times) the experimentations with similar initial operating conditions. For all experimental results, calculation of the random uncertainty is carried out at 95% confidence interval. Calculation of the systematic uncertainty is carried out by first estimating the uncertainties in the primary measurands (pressure, temperature, time, and radius), and then, estimating the uncertainty propagation into the derived quantities, which are based on these primary measurands. The systematic uncertainty in the LBV is considered as the function of systematic uncertainties in radius, time,

stretched flame speed (S_b), stretch rate (K), a term associated with the flame acceleration ($\mathrm{d}S_b/\mathrm{d}r$), and unstretched flame speed $\left(S_b^{\circ}\right)$. Finally, we can calculate the absolute uncertainty by using the following equation:

$$U = \sqrt{\left(U_R^2 + U_S^2\right)} \tag{6}$$

where U is total uncertainty, U_R is random uncertainty, and U_S is systematic uncertainty.

2.3 Numerical Simulation

Numerical modeling is performed by using PREMIX module of the CHEMKIN-PRO® [11] simulation software package. A premixed, freely propagating, and adiabatic, planar flame, which fixed in a reference point is simulated such that its LBV is defined as the normal velocity of the unburned fuel–air mixture moving into the flame front. Effect of Soret effect and multicomponent transport is considered. The adaptive grid parameters GRID and CURV are set at 0.025 and 0.1, respectively, for all the numerical simulations. Total of 1000 grid points are used for a simulation domain of 12 cm, which starts 2 cm before (upstream) the flame. The remaining 10 cm is in the post-flame zone. GRI-MECH 3.0 [12], USC-II [13], and San Diego mechanism [14] are used to predict the LBV of different NG–H_2 blends. Numerical simulations are performed to evaluate the suitability of these mechanisms in predicting the LBV of different NG–H_2 blends.

3 Results and Discussion

In the present study, experiments are performed at an initial pressure of 0.1 ± 0.0004 MPa and a temperature of 300 ± 3 K. Before studying the effect of enrichment of the NG blends, we will first discuss the effect of the composition of the NG blend on the LBV and L_b of the fuel–air mixture.

3.1 Effect of NG Composition on LBV

In the present study, we have used three representatives of the NG blend, which cover a wide range of the sources from which NG blends can be extracted. Figure 2 shows the LBV versus equivalence ratio plot for various NG blends without enrichment with H_2.

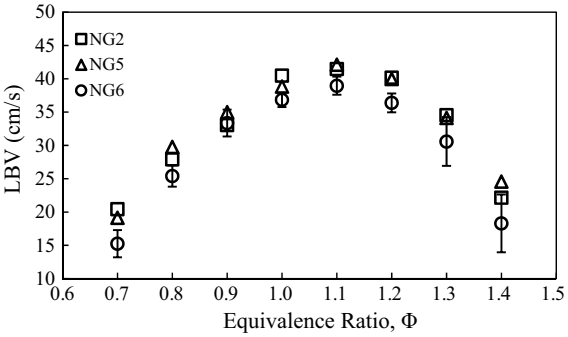

Fig. 2 Experimentally evaluated unstretched LBV as a function of equivalence ratio for various NG blends without enrichment with H_2 [8]

It is noticed that in comparison to NG2 and NG5, NG6 blend (highest methane fraction (92.18%)) has the lowest LBV at all equivalence ratios. However, if we compare NG2 and NG5, we cannot say which one is having a higher LBV. Increase in the higher hydrocarbons (ethane and propane) mole fraction increases the C_2H_5 radical concentration due to lower C–C bond dissociation energy of ethane and propane compared to methane, which has no C–C [6]. Consequently, as the mole fractions of the higher HCs in an NG blend are increased, the laminar burning velocity of the NG blend also increases, but this impact is more prominent for off-stoichiometric mixtures. It is also noticed that the variation in the composition of the NG blends has no effect on the location of equivalence ratio for peak LBV. For the present study, all the NG blends show peak LBV value at $\Phi = 1.1$. The average absolute uncertainty (U) for the entire range of experiments, at 95% confidence interval, is $\pm$ 2.2 cm/s ($\pm$ 9.0% relative uncertainty).

3.2 *Effect of NG Composition on Flame Stability*

Figure 3 compares the L_b values of different NG blends when it is not enriched with H_2 addition. Figure 3 shows the effect of the composition of a multicomponent NG blend on L_b, and hence, it assesses the effect of preferential diffusion on flame

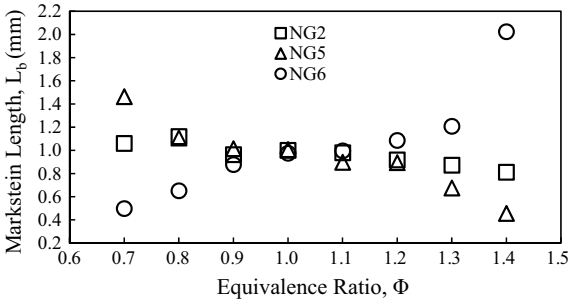

Fig. 3 Variation of burned gas Markstein length (L_b) as a function of equivalence ratio for different NG blends [8]

stability. It is observed that for the off-stoichiometric fuel–air mixtures, the trends of L_b values for NG5 and NG6 blends are contrasting to each other. This is because of the larger mole fractions of C_2H_6 and C_3H_8 in NG5 blend compared to NG6 blend, which show opposite trends of Le_{eff} to that of methane for off-stoichiometric fuel–air mixtures. All the NG blends of the present study have a stable flame (positive L_b values). It is important to notice that NG2 blend shows more or less constant values of L_b for the range of equivalence ratios investigated in the present study. Therefore, compared to NG5 and NG6 blends, the flame speed of NG2 blend is less sensitive to preferential diffusion and stretch effect. Summarizing the above observations, we can comprehend that methane reduces the flame stability (by reducing the values of L_b) of the lean fuel–air mixtures. In contrast to this, the presence of higher HCs increases the flame stability for lean fuel–air mixtures. Therefore, for off-stoichiometric fuel–air mixtures, the values L_b for an NG blend are hybrid of L_b of pure methane and higher hydrocarbons (C_2H_6 and C_3H_8).

3.3 Effect of Enrichment with H_2 on the LBV of NG Blend

Figure 4a-c show the effect of enrichment with H_2 on experimentally obtained unstretched LBV of different NG blends. It is noticed that when 25% H_2 is added, there is a small increase in the LBV of all the NG blends. Furthermore, as the H_2 mole fraction is increased to 50 and 75%, the increase in the LBV is sharper. From Fig. 4a, c, it is also noticed that as the mole fraction of H_2 in NG2 and NG6 blend is increased, the equivalence ratio for the peak LBV value shifts towards higher fuel–air equivalence ratio (from $\Phi = 1.1$ to $\Phi = 1.2$). While this trend is not observed in the case of NG5 blend, where the LBV peaks at $\Phi = 1.1$. This trend is only observed with 75% H_2 in the fuel.

For NG2–H_2 and NG5–H_2 blends, it is noticed that the relative increase in the LBV at 50% H_2 addition level is almost similar ($\approx$1.5 times of without H_2 addition). But, there is a slightly higher relative increase in the LBV of NG6–H_2 blend. At 75% H_2 addition level, the relative increase in the LBV for NG6–H_2 blend is the highest, and that of NG5–H_2 blend is the lowest. NG2–H_2 blend shows an intermediate effect on the relative increase in the LBV. From Fig. 4, it is observed that the relative increase in the LBV at $\Phi = 1.0$ is the lowest for all NG blends. On the other hand, the relative increase in LBV is the highest at $\Phi = 1.4$. Konnov [21], in his study, discussed the reason for this observation. He discussed that the adiabatic flame temperature peaks around $\Phi = 1.05$ to 1.1 for the methane–air flame. Therefore, the reaction rate of the important elementary reactions, which are highly sensitive to the temperature, also peaks around $\Phi = 1.05$ to 1.1. Eventually, it is observed that the effect of enrichment with the H_2 is the lowest around the point of peak adiabatic flame temperature.

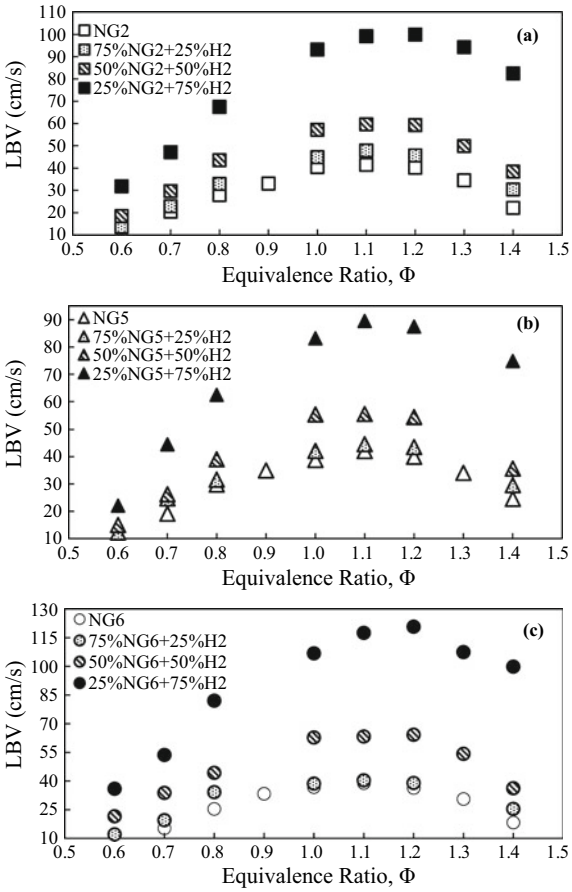

Fig. 4 Variation of experimentally evaluated LBV as a function of equivalence ratio for different levels of H_2 addition **(a)** NG2–H_2 blend in lab air, **(b)** NG5–H_2 blend in lab air, and **(c)** NG6–H_2 blend in lab air [8]

3.4 Analysis Based on the Expression Derived from Single-Step Global Reaction Asymptotics

Wu et al. [22] obtained an expression of LBV (S_u) as shown below:

$$S_u \sim (\alpha\, \mathrm{Le_{eff}})^{1/2} \exp(-T_a/2T_{ad}) \tag{7}$$

Equation 7 is based on the assumptions of the single-step global reaction asymptotics. In Eq. (7), the LBV is approximated as the function of transport and thermo-kinetic property. The addition of H_2 to enrich the NG blend alters the transport and thermo-kinetic properties, and hence, modifies the LBV of the NG–H_2 blend. Further, the quantities present in the first pair parentheses are termed as the diffusion factor, and it combines the two transport properties, i.e., thermal diffusivity (α) and effective Lewis number ($\mathrm{Le_{eff}}$). Similarly, constituents of the second pair of

parentheses are jointly termed as Arrhenius factor which is the function of activation temperature (T_a) and adiabatic flame temperature (T_{ad}). Colorado State Equilibrium calculator [23] is used to calculate the thermal diffusivity (α) of the fuel–air mixture. EQUIL code of CHEMKIN-PRO® is used to calculate the T_{ad} of the fuel–air mixture. Addabbo et al. [24] suggested a method to calculate the Le_{eff} of the multicomponent fuel–air mixture. In the present study, we have also used the same method to calculate the Le_{eff} of the multicomponent NG–H_2 blend. The single-step global reaction activation energy (E_a) is used to calculate the activation temperature (T_a), which is defined as $T_a = (E_a/R)$, where R is the universal gas constant. To calculate the activation temperature (T_a), first, we have to calculate the non-dimensional form of the E_a, which is termed as the Zeldovich number (Ze). We have used the following expression suggested by Muller et al. [25] to calculate the Ze.

$$\mathrm{Ze} = 4\frac{(T_{ad} - T_u)}{(T_{ad} - T^{\circ})} \tag{8}$$

where T° is termed as the inner layer temperature, and it corresponds to the temperature of the reaction zone where the slope of the temperature profile peaks. CHEMKIN-PRO® simulation software is used to calculate the slope of the temperature profile in the flame coordinate system. T_u is the initial temperature of the unburned fuel–air mixture (300 K in the present study). After calculating Ze by using Eq. (8), T_a can be calculated by using the following expression [26, 27]:

$$\mathrm{Ze} = \frac{E_a}{R}\frac{(T_{ad} - T_u)}{T_{ad}^2} \tag{9}$$

To study the effect of enrichment with H_2 on the LBV of various NG–H_2 blends, the values of diffusion and Arrhenius factors are normalized with their corresponding values at 0% H_2 addition level (denoted by a superscript #):

$$\text{Normalized Diffusion factor} = \frac{(\alpha\,\mathrm{Le}_{\mathrm{eff}})^{1/2}}{\left(\alpha^{\#}\,\mathrm{Le}_{\mathrm{eff}}^{\#}\right)^{1/2}} \tag{10}$$

$$\text{Normalized Arrhenius factor} = \exp\left[\frac{(-T_a/(2T_{ad}))}{\left(-T_a^{\#}/\left(2T_{ad}^{\#}\right)\right)}\right] \tag{11}$$

Analysis of Shift in Φ for Peak LBV Variations of diffusion and Arrhenius factors as a function of for NG6–H_2 blend at different levels of the H_2 addition have been shown in Fig. 5. The trends for other NG–H_2 blends are similar, and hence, for the brevity, they are not shown here. It is noticed that as the mole fraction of H_2 in and NG blend increases, the numerical value of the diffusion factor also increases. Similarly, there is a continuous increase in the value of the diffusion factor with the equivalence ratio, and this observation is true at each level of the H_2 addition. In contrast to this, at each level of the H_2 addition, the numerical value of the Arrhenius factor peaks

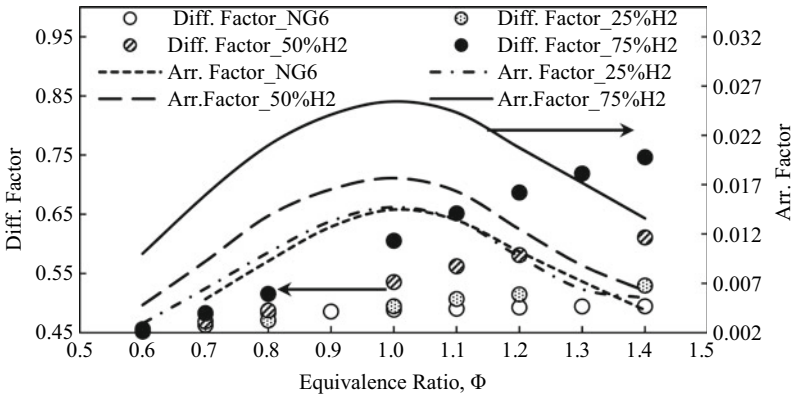

Fig. 5 Diffusion and Arrhenius factors variation as a function of Φ at different levels of the H_2 addition [8]

around $\Phi = 1.05$ to 1.1. As shown in Eq. (7), the LBV is approximated as a product of diffusion and Arrhenius factors. Hence, a continuous increase in the diffusion factor shifts the peak of the product of diffusion and Arrhenius factors toward a richer equivalence ratio. Eventually, the peak LBV value of an NG–H_2 blend shifts towards the fuel-rich equivalence ratio.

Analysis of the Influence of NG Composition and Enrichment with H_2 on LBV

Figure 6 shows the variations of normalized diffusion and normalized Arrhenius factors as a function of H_2 mole fraction in various NG–H_2 blends. From Fig. 6a, it is noticed that enrichment with H_2 on NG blend has a negative effect on the normalized diffusion factor of the lean fuel–air mixtures. Since diffusion factor is a function of Le_{eff} and α of the fuel–air mixture, the reason for this negative effect can be explained by demonstrating the effect of equivalence ratio and H_2 addition on Le_{eff}. Figure 7 shows the effect of enrichment with and variation of equivalence ratio (Φ) on Le_{eff} of NG2–H_2 blend. The trends for other NG2–H_2 blends are alike, and hence, they are not shown here. It is seen that the addition of H_2 in the lean fuel–air mixtures tends to reduce the values of Le_{eff}. Eventually, in Fig. 6a, for lean fuel–air mixtures, the addition of H_2 reduces the overall value of the normalized diffusion factor. From Fig. 6b, it is noticed that the normalized Arrhenius factor has a positive effect of enrichment with H_2. This observation is in contrast with the values of normalized diffusion factor for lean fuel–air mixtures. It is also noticed that with the increase of H_2 addition level, the value of normalized Arrhenius factor not only increases, but it is also significantly larger than the corresponding values of normalized diffusion factor. Therefore, from Eq. (7), the overall value of LBV, which is the product of diffusion and Arrhenius factors, increases irrespective of the equivalence ratio. As discussed above, from Fig. 6, it is also deduced that for all equivalence ratios, the effect of enrichment with H_2 on LBV is more pronounced via improvement in the Arrhenius factor (thermo-kinetic property). In the background of the above finding, it can be concluded that at stoichiometric fuel–air mixture, the effect of enrichment

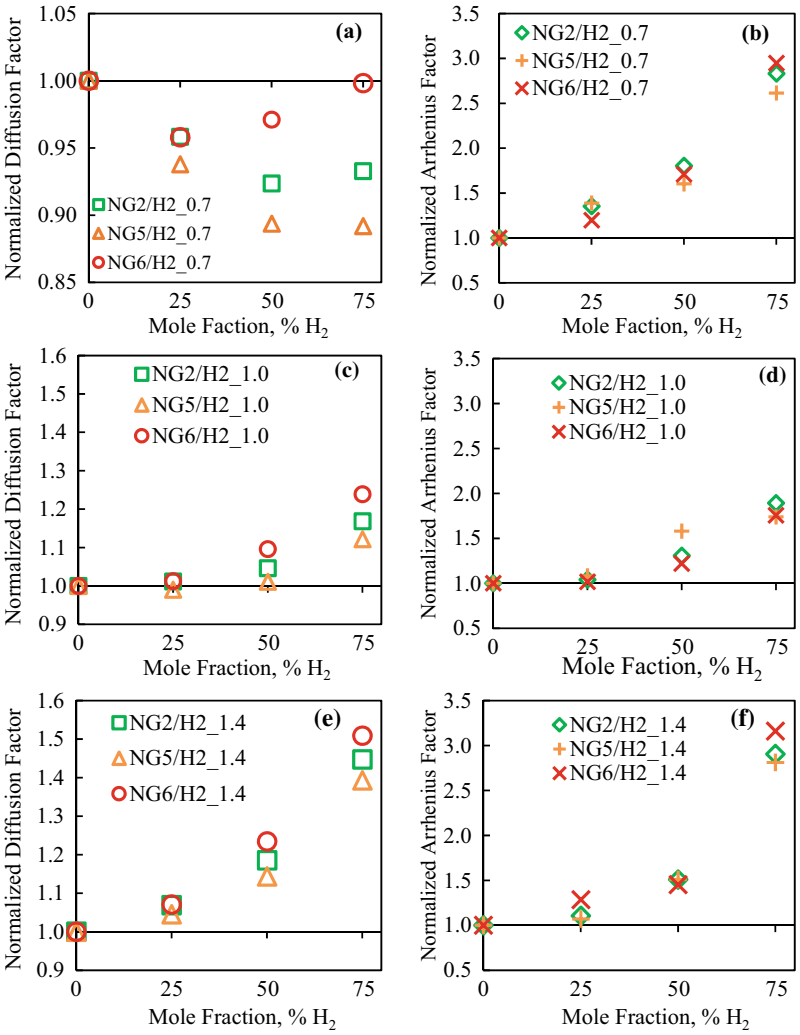

Fig. 6 Variation of normalized diffusion and Arrhenius factors as functions of mole fraction of H_2 (% H_2) in the various NG–H_2 blends; **(a)** and **(b)** $\Phi = 0.7$; **(c)** and **(d)** $\Phi = 1.0$; **(e)** and **(f)** $\Phi = 1.4$ [8]

with H_2 on LBV has the lowest effect compared to off-stoichiometric mixtures. This statement is supported by the observation of Fig. 6, where it is noticed that the values of normalized Arrhenius factors for all NG–H_2 blends are the lowest at $\Phi = 1.0$. For stoichiometric and the rich fuel–air mixtures, both transport and thermo-kinetic properties have a positive effect of the H_2 addition. This statement is evident in the observation of Fig. 6c–f. It is noticed that both normalized diffusion and normalized Arrhenius factors show an increasing trend in their values with the addition of H_2

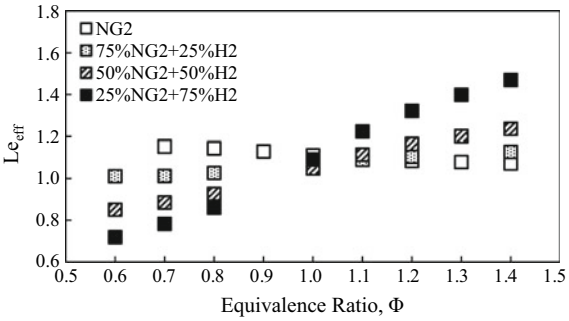

Fig. 7 Variation of Le_{eff} as a function of equivalence ratio for different NG2–H_2 blends [8]

in the fuel. Thus, from Eq. (7), for stoichiometric and the rich fuel–air mixtures, LBV of all NG–H_2 blends will increase with the addition of H_2. From Fig. 6, it is seen that the values of normalized diffusion and normalized Arrhenius factors are the highest compared to lean and stoichiometric fuel–air mixtures. Therefore, it can be concluded that the effect of enrichment with H_2 on the LBV of all NG–H_2 blends has the most positive effect on the rich fuel–air mixtures.

The plot of Fig. 6 can be further utilized to study the effect of NG composition on the LBV of various NG–H_2 blends. It is seen that for all equivalence ratios, the values of the normalized diffusion factor are the lowest for NG5 blend. The reason for this is due to the presence of higher HCs (C_2H_6 and C_3H_8) in the highest amount. Due to this, the diffusion coefficient of the NG5 blend is the lowest, and hence, the addition of H_2 has the least impact on the improvement of the normalized diffusion factor of NG5–H_2 blend. Similarly, the presence of higher HCs, which have lower C–C bond dissociation energy [6], makes the NG5 blend more reactive compared to NG2 and NG6 blends. Consequently, enrichment with the H_2 has the least effect on the normalized Arrhenius factor of NG5–H_2 blend. On the other hand, the blend which is having the highest mole fraction of CH_4—in present case NG6 blend—has larger C–H bond dissociation energy [6], and hence, it has the lowest reactivity. Thus, the addition of H_2 has the most positive impact on the LBV of NG6–H_2 blend.

Comparison of the Role of Thermal and Kinetic Effect As discussed above, improvement in the thermo-kinetic property (Arrhenius factor) is the main reason for the increment in the LBV when an NG blend is enriched with H_2. The thermal effect can be quantified by the modification in the adiabatic fuel temperature (T_{ad}) of the fuel–air mixture, and the kinetic effect can be quantified by the modification in Zeldovich number (Ze). The thermal effect can be considered as positive/negative if the Tad of the fuel–air mixture increases/decreases. In contrast to this, the kinetic effect is as positive/negative if the Ze decreases/increases. Now, the question arises is which one of these two effects is more dominant? To find the answer to this question, normalization of T_{ad} and Ze is done. To normalize these quantities, they are divided by values which correspond to the 0% H_2 addition level. The normalized quantities are denoted by # superscript.

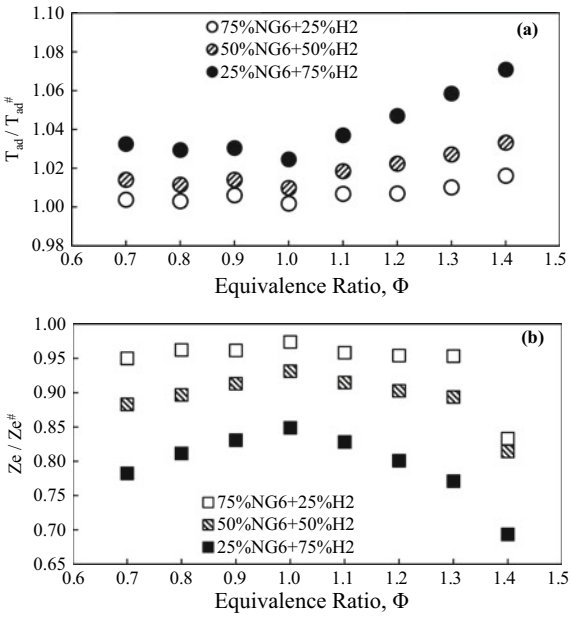

Fig. 8 Variation of **(a)** normalized adiabatic flame temperature and **(b)** normalized Zeldovich number as a function of equivalence ratio for different NG6–H_2 blends [8]

Figure 8a shows the variation of normalized adiabatic flame temperature as a function of equivalence ratio for various levels of H_2 addition. It is seen that the relative increase in the adiabatic flame temperature is the lowest at stoichiometric equivalence ratio, and the highest increase is noticed for the fuel-rich mixture ($\Phi = 1.4$). It is observed that the maximum relative increase in T_{ad} is ≈3.5% for 25 and 50% H_2 in the NG–H_2 blend. While, for 75% H_2 addition level, the relative increase in the T_{ad} is the highest (≈7.5%) for the rich ($\Phi = 1.4$) fuel–air mixture. The kinetic property, in terms of Zeldovich number (Ze) in Fig. 8b, shows that at 50% H_2 addition level, the reduction in the activation energy is ≈15%. While, at 75% H_2 addition level, for the rich fuel–air mixture ($\Phi = 1.4$), It is noticed that there is the largest drop (≈30%) in the activation energy. From the above discussion, we can say that the maximum percentage reduction in the activation energy is much larger (≈30%) compared to the maximum percentage increase (≈7.5%) in adiabatic flame temperature. Therefore, the effect of enrichment with H_2 primarily improves the chemical kinetics of the NG oxidation.

3.5 Effect of Enrichment with H_2 on the Flame Stability of NG–H_2 Blend

Flames are subjected to stretch by virtue of flame curvature, flame motion, and flow non-uniformities [28]. Under the influence of stretch, the flame speed may increase

or decrease on the basis of effective Lewis number (Le_{eff}) of the fuel–air mixture. This increase or decrease in the flame speed may cause flame surface instabilities. A flame may be subjected to three types of instabilities [29]:

a. Instability due to non-equi-diffusion of heat or mass ($Le_{eff} \neq 1$) is termed as the preferential diffusion instability.
b. Hydrodynamic instability.
c. Buoyancy instability if the flame speed is <10 cm/s [30].

Hydrodynamic instability causes flame surface distortion by generating cellular structures on the flame surface. These flames cannot be used for measuring the LBV. Every spherical flame, in the later stage of its expansion, is subjected to hydrodynamic instability. By visualizing the flame during its evolution inside the combustion chamber, the start of cellular structure on the flame surface can be identified. In this way, we can select the regime, of smooth, wrinkle-free flames having no sign of hydrodynamic instability. Similarly, by visual inspection of the flame, we can identify the buoyancy instability by observing a continuous upward shift in the center of the flame ball. Thus, the flame radius versus time data extracted in the present study is free from hydrodynamic and buoyancy instabilities and is only subjected to preferential diffusion instability.

Variation of the experimentally evaluated L_b values as a function of equivalence ratio is shown in Fig. 9. It helps to study the effect of enrichment with H_2 on the flame stability of various NG–H_2 blends at different levels of H_2 addition. Calculation of total relative uncertainty at various equivalence ratios shows that the maximum total uncertainty relative at 95% confidence interval is ±22%.

From Fig. 3, it is noticed that the NG blend, which has the largest mole fraction of CH_4–NG_6 blend—has the lowest values of L_b for the lean fuel–air mixtures. From Fig. 9a, it is noticed that the addition of H_2 even at 25% H_2 addition level makes the flame unstable ($L_b < 0$) against the preferential diffusion effect for $\Phi = 0.6$ and 0.7. By comparing Fig. 9a, b, we observed that for the rich fuel–air mixture irrespective of the NG blend composition, and increment of H_2 mol fraction from 25 to 50% in the fuel, the L_b values are positive and do not get affected significantly. In contrast to this, for 50% H_2 addition level, at $\Phi = 0.6$, all the NG blends become unstable ($L_b < 0$). However, at $\Phi = 0.7$, NG2 and NG5 blends, which have higher mole fractions of C_2H_6 and C_3H_8 compared to NG6 blend, maintain a positive value of L_b (stable flame). At 75% H_2 addition level, It is observed that only NG5 blend, which has the highest mole fraction of C_3H_8 compared to NG2 and NG6 blends, maintained a positive value of L_b (stable flame) at $\Phi = 0.7$. However, NG2 blend for a similar condition becomes unstable ($L_b < 0$) against the preferential diffusion effect. It is noticed that at 75% H_2 addition level, for the rich fuel–air mixtures, irrespective of their composition, all the NG blends show almost equal L_b values. Therefore, at 75% H_2 addition level, for the rich fuel–air mixture, L_b values, and hence, stability against the preferential diffusion effect is governed by H_2 only.

To get more insight, and to study the trends of L_b, it can be correlated with the expression of L_b, which is based on the single-step global reaction asymptotics [31, 32].

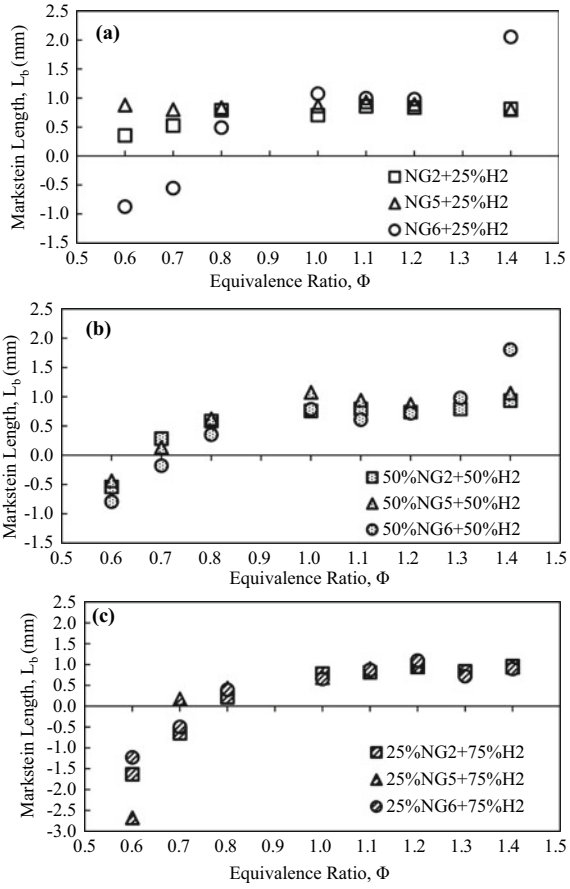

Fig. 9 Variation of experimental values of burned gas Markstein length (L_b) as a function of equivalence ratio (Φ) for various NG–H_2 blends. **(a)** at 25% H_2 addition, **(b)** at 50% H_2 addition, and **(c)** at 75% H_2 addition [8]

$$L_b \approx \left[\frac{\gamma_1}{\sigma} + \left\{\frac{\mathrm{Ze}}{2}\gamma_2(\mathrm{Le}_{\mathrm{eff}} - 1)\right\}\right]\delta \tag{12}$$

where δ is the laminar flame thickness, and $\sigma = \rho_u/\rho_b$ is thermal expansion ratio. ρ_u is the density of unburned fuel–air mixture, and ρ_b is the density of burned gas at equilibrium. γ_1 and γ_2 are functions of σ as given in reference [24, 31].

$$\gamma_1 = \frac{2\sigma}{\sqrt{\sigma} + 1} \tag{13}$$

$$\gamma_2 = \frac{4}{\sigma - 1}\left\{\sqrt{\sigma} - 1 - \ln\frac{\sqrt{\sigma} + 1}{2}\right\} \tag{14}$$

Following expression used by Jomaas et al. [32] has been adopted to calculate the value of laminar flame thickness (δ).

$$\delta = \frac{T_{\text{ad}} - T_u}{\left(\frac{\mathrm{d}T}{\mathrm{d}x}\right)_{\max}} \tag{15}$$

From Eq. (12), we observed that the overall numerical value and the sign of the burned gas Markstein length (L_b) vary as a response to the change in various parameters like Le_{eff}, δ, σ, and Ze. Besides individually, these parameters also affect L_b in combination.

It is noticed that if $\text{Le}_{\text{eff}} < 1$, the quantity inside the curly bracket will become negative, and it will reduce the value of L_b. Furthermore, if $\text{Le}_{\text{eff}} < 1$, it indicates the preferential diffusion of the mass into the reaction zone. Eventually, the local equivalence ratio will modify. If the fuel–air mixture is lean, the preferential diffusion will shift the local equivalence ratio toward the stoichiometric equivalence ratio side, and hence, the local flame speed will increase. Consequently, the bulge will form on the smooth flame surface, which will grow faster in the form of cellular structure, and in due course, this will make the flame unstable against the preferential diffusion effect.

Figure 10 shows the variation of the calculated values of laminar flame thickness (δ) as a function of equivalence ratio for various levels of H_2 addition in NG6–H_2 blend. The trend for other NG–H_2 blends are similar, and hence, not plotted here. It is observed that as the mole fraction of H_2 in the fuel is increased the value of δ is decreased. From Eq. (12), it is seen that L_b is proportional to δ. Therefore, any circumstances which decrease the value of δ will also decrease the value of L_b. From Fig. 10, it is noticed that at $\Phi = 1.4$, the reduction in δ with the addition of H_2 is the highest (42%) when the H_2 addition level is increased from 50 to 75% H_2 in NG6. This is also observed (not shown here) that the effect of the H_2 addition on the reduction of δ at $\Phi = 1.4$ is the highest for NG6 blend compared to NG2 and NG5 blends. This also explains the reason for the sudden decrease in the L_b for NG6–H_2 blend at $\Phi = 1.4$ when the H_2 addition level is increased from 50 to 75% (please see Fig. 9b, c).

The combined effect of Le_{eff} and Ze on the L_b can be studied by considering the variation of the term Ze ($\text{Le}_{\text{eff}} - 1$) present in Eq. (12). Let us consider that $\text{Le}_{\text{eff}} > 1$, and in this situation, if the value of Ze decreases, the value of the term Ze ($\text{Le}_{\text{eff}} - 1$) will also decrease, and hence, the overall value of L_b will also decrease. In contrast

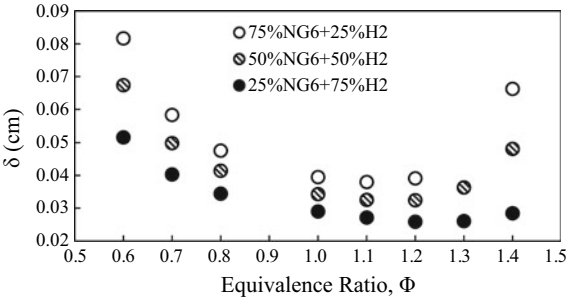

Fig. 10 Calculated values of laminar flame thickness (δ) versus equivalence ratio for various H addition levels [8]

Table 3 Effect of various parameters of Eq. (12) on L_b

S. No.	Parameter	Effect of increase in parameter on L_b	Effect of decrease in parameter on L_b
1	δ	$L_b \uparrow$	$L_b \downarrow$
2	$\sigma = \rho_u/\rho_b$	$L_b \downarrow$	$L_b \uparrow$
3	$\mathrm{Le_{eff}}$	$L_b \uparrow$	$L_b \downarrow$
4	Ze	If $\mathrm{Le_{eff}} > 1$, $L_b \uparrow$ If $\mathrm{Le_{eff}} < 1$, $L_b \downarrow$	If $\mathrm{Le_{eff}} > 1$, $L_b \downarrow$ If $\mathrm{Le_{eff}} < 1$, $L_b \uparrow$

to this, if $\mathrm{Le_{eff}} < 1$, and the value of Ze decreases then, the combined effect will increase the value of L_b when compared with the previous case ($\mathrm{Le_{eff}} > 1$, and Ze decreases). Therefore, while the addition of H_2 at $\Phi = 1.4$ will increase the value of $\mathrm{Le_{eff}}$, there will be a significant decrease in the δ and Ze of the fuel–air mixture. Consequently, at $\Phi = 1.4$, for NG6–H_2 blend, the combined effect of $\mathrm{Le_{eff}}$ and Ze will reduce the value of L_b.

As discussed earlier, NG5 blend is able to support a stable flame ($L_b > 0$) for a wider range of equivalence ratios at different levels of H_2 addition when compared to NG2 and NG6 blends. This behavior of NG5 blend is due to the presence of C_3H_8 in the largest proportion compared to NG2 and NG6 blends. Propane–air mixture has $\mathrm{Le_{eff}} > 1$ for the fuel-lean equivalence ratio. As opposed to this, H_2–air mixture has $\mathrm{Le_{eff}} < 1$ for the fuel-lean equivalence ratio. Therefore, the NG blend which contains both the species (C_3H_8 and H_2) in significant quantity, as present in NG5 blend, will have a $\mathrm{Le_{eff}}$ value hybrid of the pure propane and pure hydrogen. Ultimately, the larger proportion of propane present in NG5 blend will keep the $\mathrm{Le_{eff}} > 1$ for a wider range of the fuel-lean equivalence ratios (up to $\Phi = 0.7$), and hence, NG blend supports a stable flame ($L_b > 0$) for a wider range of equivalence ratios.

Table 3 summarizes the above discussion on the burned gas Markstein length (L_b). The upward arrow/downward arrow indicates an increase/decrease in the burned gas Markstein length, L_b.

3.6 Numerical Modeling of NG–H_2 Blends

In the analysis of Sect. 3.4, it discussed that the modification in the chemical kinetics is predominant in enhancing the oxidation of NG–H_2 blend. Therefore, to strengthen the conclusions based on the single-step global reaction asymptotic analysis, and to get a better insight of the chemical kinetics of NG–H_2 combustion chemistry, a detailed chemical kinetic analysis by using CHEMKIN-PRO® [11] is performed.

Variation of predicted LBV values by various chemical kinetic mechanisms as a function of equivalence ratio and their comparison with experimental results of NG2–H_2 blend is shown in Fig. 11. The trends for other NG–H_2 blends are similar, and hence, not shown here. It is seen in Fig. 11a that at 25% H_2 addition level, at

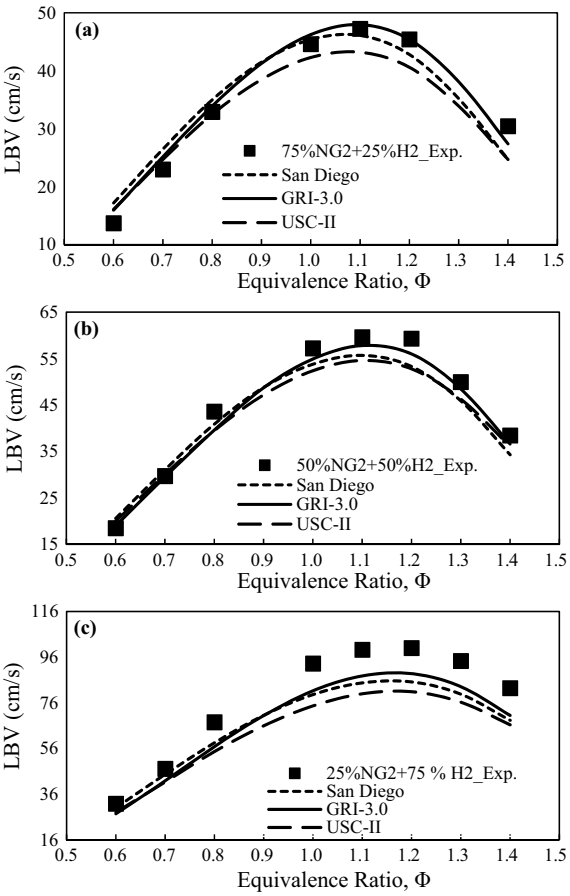

Fig. 11 Variation of predicted LBV values by various chemical kinetic mechanisms as a function of equivalence ratio, and their comparison with experimental results. **(a)** 75% NG2 + 25% H_2, **(b)** 50% NG2 + 50% H_2, and **(c)** 25% NG2 + 75% H_2 [8]

$\Phi = 0.6$, all the mechanisms overpredict the LBV values. However, the prediction of GRI-MECH 3.0 is within the maximum experimental uncertainty of ±8.08%. It is noticed that for the range of equivalence ratios varying between $\Phi = 0.7$ and 1.0, the LBV prediction of USC-II is within the experimental uncertainty. However, the underprediction is significant for the rich fuel–air mixtures. From Fig. 11a, it is also observed that the LBV prediction of San Diego mechanism is only acceptable near the stoichiometric equivalence ratio ($\Phi = 0.9$ to 1.1). Below $\Phi = 0.9$, it overpredicts the LBV, and beyond $\Phi = 1.1$, it underpredicts the LBV. Hence, from the above observations, it can be concluded that for 25% H_2 addition level, the predictions of LBV by GRI-MECH 3.0 are the closest to the experimental values.

From Fig. 11b, it is seen that at 50% H_2 addition level, from $\Phi = 1.0$ to 1.4, the predictions of GRI-MECH 3.0 are the best. On the other hand, USC-II and San Diego mechanisms underpredict the LBV. It is also to point out that at $\Phi = 1.4$, USC-II also performs equally well in predicting the LBV. At 75% H_2 addition level, as shown in Fig. 11c, for all values of $\Phi > 0.7$, all the mechanisms underpredict the

LBV. However, the prediction of GRI-MCH 3.0 is the closest to the experimental results. It is also noticed that the predictions of GRI-MECH 3.0 follow the trend of the experimental results, and it also predicts the shift in the point of peak LBV value. This trend is not predicted by the USC-II and Sandiego mechanisms. Excluding the values of $\Phi = 0.6$ and 0.7, for all fuel-lean equivalence ratios ($\Phi > 0.7$), every mechanism underpredicts the LBV. From the above discussion, it can be concluded that although at 75% H_2 addition level, GRI-MECH 3.0 underpredicts the LBV for most of the studied equivalence ratios, it has LBV predictions closest to the experimental results and it also follows the trend of experimental results. Hence, as per the suggestion of the Hu et al. [33], we can use GRI-MECH 3.0 for further combustion analysis without significantly affecting the interpretations of the results.

3.7 Effect of Enrichment with H_2 on Combustion Chemistry

Combustion chemistry of NG blends is governed by active radicals like H, O, and OH. The significance of these radicals in the oxidation of various HCs and H_2–air mixtures has been discussed by different research groups [29, 33–35]. Hence, the effect of enrichment with H_2 on the LBV of different NG–H_2 blend can be correlated with the relative increase in the mole fractions of these radicals in the active radical pool.

Variation in the relative increase in the mole fractions of H, O, and OH radicals as a function of equivalence ratio for different NG–H_2 blends at 50% H_2 addition level is shown in Fig. 12a–c, respectively. The overall trends for 25 and 75% H_2 addition are similar to 50% H_2 addition level, and hence, they are not shown here. The relative increase in the values of these radicals is calculated by considering the values of these radicals at 0% H_2 addition level as the baseline values. It is noticed that for each radical, the relative increase is the highest for NG6 blend. It is also observed that the relative increase in these radicals for NG5 blend is the lowest. This observation is in line with our previous discussion, where we have discussed that the effect of enrichment with H_2 on the LBV (combustion chemistry) of NG6 blend is the highest and the lowest for NG5 blend. The above discussion also infers that the increase in the LBV is proportional to the increase in H, O, and OH radicals. This can be used to identify that for which type of fuel–air mixture (equivalence ratio) the effect of the enrichment with H_2 is higher.

From Fig. 12, it is seen that for each radical, the relative increase in their mole fractions is higher for the rich fuel–air mixtures compared to stoichiometric and lean fuel–air mixtures. This observation further emphasizes the effect of enrichment with H_2 which is more effective for the rich fuel–air mixtures of NG blends.

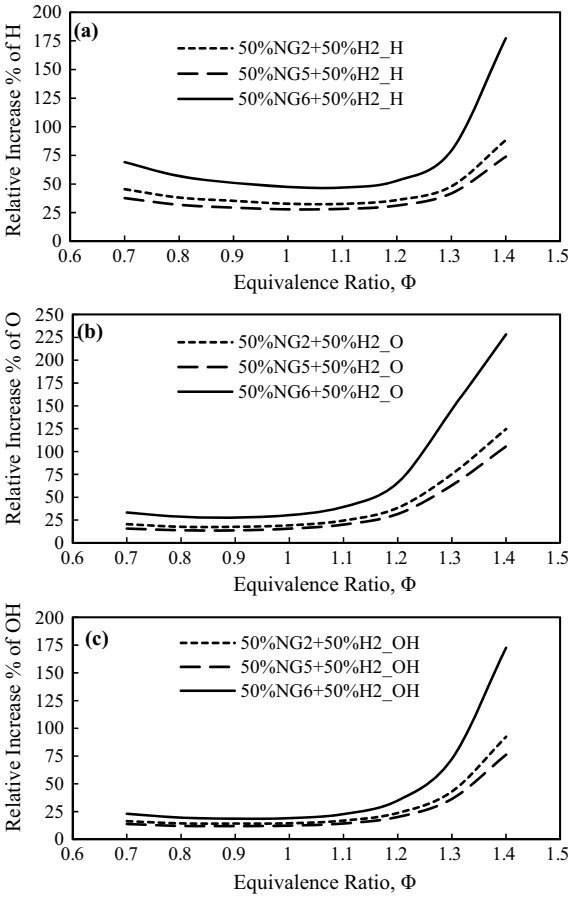

Fig. 12 Variation of the relative increase in the mole fraction of H, O, and OH radicals as a function of equivalence ratio for different NG–H_2 blends at 50% H_2 addition level. **(a)** Comparison for H radical, **(b)** comparison for O radical, and **(c)** comparison for OH radical [8]

3.8 Summary

The effect of enrichment with hydrogen on the NG blend is investigated by adding 25, 50, and 75% H_2 by volume to three different NG blends. The major outcomes of the experimental and chemical kinetic analysis of the present study are:

i. Enrichment with H_2 increases the LBV by enhancing the transport and thermo-kinetic properties of NG blends. However, the modification of thermo-kinetic property is more effective compared to transport property.
ii. Enrichment with H_2 is more effective on the rich fuel–air mixtures of NG blends compared to stoichiometric and lean fuel–air equivalence ratios.
iii. The impact H_2 addition on the enhancement of the thermo-kinetic property of CH_4 is more prominent compared to that of C_2H_6 and C_3H_8. Thus, the effect of enrichment with H_2 on LBV of NG6 blend is the highest, and NG5 blend has the least improvement in LBV.

iv. Because of steeper reduction in the activation energy of the fuel–air mixture, there is a significantly larger increase in the LBV beyond 50% H_2 addition level.
v. The addition of H_2 in NG–H_2 blend decreases the Le_{eff} of the lean fuel–air mixtures ($\Phi = 0.6$ and 0.7) and makes it less than unity. Hence, the flame becomes unstable against the preferential diffusion effect.
vi. The presence of higher HCs (C_2H_6 and C_3H_8) increases the Le_{eff} of the fuel–air mixture. Thus, due to the presence of C_3H_8 in a larger proportion in NG5–H_2, blend supports the stable flame for a wider range of equivalence ratios. In contrast to this, NG6–H_2 blend, which has the lowest proportion of C_3H_8, supports the most unstable flame against the preferential diffusion effect.
vii. Up to 50% H_2 addition level, GRI-MECH 3.0 is the best-suited chemical kinetic mechanism compared to USC-II and San Diego mechanisms.
viii. At 75% H_2 addition level, none of the mechanisms used in the present study performed well. However, the predictions of the GRI-MECH 3.0 are the closest to the experimental results, and they also follow the trends of experimental results.
ix. The relative increase in the mole fraction of H, O, and OH radicals are proportional to the increase in the LBV of the NG–H_2 blends. The relative increase in mole fractions of H, O, and OH radicals is the highest for NG6 blend and the lowest for NG5 blend. Similarly, the relative increase in the active radicals is also larger for the rich fuel–air mixture. Thus, the effect of H_2 addition on LBV is the highest for the rich fuel–air mixture of NG6 blend.

References

1. Law CK (2006) Combustion physics. Cambridge University Press, New York
2. U.S. Energy Information Agency (2013) International Energy Outlook 2013. Washington, DC 20585. https://doi.org/DOE/EIA-0484
3. Lowry W, de Vries J, Krejci M, Petersen E, Serinyel Z, Metcalfe W, Curran H, Bourque G (2011) Laminar flame speed measurements and modeling of pure Alkanes and Alkane blends at elevated pressures. J Eng Gas Turbines Power 133:091501. https://doi.org/10.1115/1.4002809
4. Rallis CJ, Garforth AM (1980) The determination of laminar burning velocity. Prog Energ Combust Sci 6:303–329
5. Lefort B, El Bakali A, Gasnot L, Pauwels JF (2017) Experimental and numerical investigation of low-pressure laminar premixed synthetic natural gas flames in rich conditions. Fuel 189:210–237. https://doi.org/10.1016/j.combustflame.2008.04.018
6. Luo Y-R (2002) Handbook of bond dissociation energies in organic compounds. CRC Press, Boca Raton, London, New York, Washington, DC
7. Khan AR, Ravi MR, Ray A (2019) Experimental and numerical study of the effect of higher hydrocarbon content on laminar burning velocity and flame stability of natural gas. Combust. Sci. Technol. 192, 359–390. https://doi.org/10.1080/00102202.2019.1565532
8. Khan AR, Ravi MR, Ray A (2019) Experimental and chemical kinetic studies of the effect of H2 enrichment on the laminar burning velocity and flame stability of various multicomponent

natural gas blends. Int J Hydrogen Energ 44:1192–1212. https://doi.org/10.1016/j.ijhydene.2018.10.207
9. Law CK (1989) Dynamics of stretched flames. Symp Int Combust 22:1381–1402. https://doi.org/10.1016/s0082-0784(89)80149-3
10. Kwon S, Tseng LK, Faeth GM (1992) Laminar burning velocities and transition to unstable flames in H2/O2/N2 and C3H8/O2/N2 mixtures. Combust Flame 90:230–246. https://doi.org/10.1016/0010-2180(92)90085-4
11. CHEMKIN-PRO (2016) CHEMKIN 17.0 (15151), ANSYS reaction design, San Diego
12. Smith GP, Golden DM, Frenklach M, Moriarty NW, Eiteneer B, Goldenberg M, Thomas Bowman C, Hanson RK, Song S, Gardiner WC, Lissianski VV, Qin Z (1999) GRI-Mech 3.0. http://www.me.berkeley.edu/gri_mech/
13. Wang H, You X, Joshi AV, Davis SG, Laskin A, Egolfopoulos F, Law CK (2007) USC mech version II. High-temperature combustion reaction model of H2/CO/C1-C4 compounds
14. San Diego mechanism (2016) Chemical-kinetic mechanisms for combustion applications. University of California at San Diego. http://combustion.ucsd.edu
15. Bradley D, Hicks RA, Lawes M, Sheppard CGW, Woolley R (1998) The measurement of laminar burning velocities and Markstein numbers for iso-octane–air and iso-octane–n-heptane–air mixtures at elevated temperatures and pressures in an explosion bomb. Combust Flame 115:126–144. https://doi.org/10.1016/s0010-2180(97)00349-0
16. Gu XJ, Haq MZ, Lawes M, Woolley R (2000) Laminar burning velocity and Markstein lengths of methane-air mixtures. Combust Flame 121:41–58. https://doi.org/10.1016/S0010-2180(99)00142-X
17. Systat Software, Inc. (2008) Sigma Plot, Version 11.0
18. Taylor SC (1991) Burning velocity and the influence of flame stretch
19. Kelley AP, Bechtold JK, Law CK (2011) Propagation of confined premixed flames. In: 7th US national technical meeting of the combustion institute. Combustion Institute, Georgia Institute of Technology, Charlottesville, VA, pp 1–24
20. Moffat RJ (1988) Describing the uncertainties in experimental results. Exp Therm Fluid Sci 1:3–17
21. Konnov AA (2010) The effect of temperature on the adiabatic laminar burning velocities of CH4-air and H2-air flames. Fuel 89:2211–2216. https://doi.org/10.1016/j.fuel.2009.11.038
22. Wu F, Kelley AP, Tang C, Zhu D, Law CK (2011) Measurement and correlation of laminar flame speeds of CO and C2 hydrocarbons with hydrogen addition at atmospheric and elevated pressures. Int J Hydrogen Energ 36:13171–13180. https://doi.org/10.1016/j.ijhydene.2011.07.021
23. Dandy DS (2018) Transport properties & chemical equilibrium calculator. http://navier.engr.colostate.edu/~dandy/code/code-4/
24. Addabbo R, Bechtold JK, Matalon M (2002) Wrinkling of spherically expanding flames. Proc Combust Inst 29:1527–1535. https://doi.org/10.1016/S1540-7489(02)80187-0
25. Müller UC, Bollig M, Peters N (1997) Approximations for burning velocities and Markstein numbers for lean hydrocarbon and methanol flames. Combust Flame 108:349–356. https://doi.org/10.1016/S0010-2180(96)00110-1
26. Seshadri K, Gottgens J (1991) Reduced kinetic mechanisms and asymptotic approximations for methane-air flames. Lect Notes Phys 111–136
27. Clavin P (1985) Dynamic behavior of premixed flame fronts in laminar and turbulent flows. Prog Energy Combust Sci 11:1–59. https://doi.org/10.1016/0360-1285(85)90012-7
28. Law CK, Sung CJ (2000) Structure, aerodynamics, and geometry of premixed flamelets. Prog Energy Combust Sci 26:459–505. https://doi.org/10.1016/S0360-1285(00)00018-6
29. Kwon OC, Faeth GM (2001) Flame/stretch interactions of premixed hydrogen-fueled flames: measurements and predictions. Combust Flame 124:590–610. https://doi.org/10.1016/S0010-2180(00)00229-7
30. Qiao L, Gu Y, Dahm WJA, Oran ES, Faeth GM (2007) Near-limit laminar burning velocities of microgravity premixed hydrogen flames with chemically-passive fire suppressants. Proc Combust Inst 31:2701–2709. https://doi.org/10.1016/j.proci.2006.07.012

31. Bechtold JK, Matalon M (2001) The dependence of the Markstein length on stoichiometry. Combust Flame 127:1906–1913. https://doi.org/10.1016/S0010-2180(01)00297-8
32. Jomaas G, Law CK, Bechtold JK (2007) On transition to cellularity in expanding spherical flames. J Fluid Mech 583:1–26. https://doi.org/10.1017/S0022112007005885
33. Hu E, Huang Z, He J, Jin C, Zheng J (2009) Experimental and numerical study on laminar burning characteristics of premixed methane-hydrogen-air flames. Int J Hydrogen Energ 34:4876–4888. https://doi.org/10.1016/j.ijhydene.2009.03.058
34. Tan Y, Dagaut P, Cathonnet M, Boettner JC, Bachman JS, Carlier P (1994) Natural gas and blends oxidation and ignition: experiments and modeling. Symp Int Combust 25:1563–1569. https://doi.org/10.1016/s0082-0784(06)80801-5
35. Cheng Y, Tang C, Huang Z (2015) Kinetic analysis of H2 addition effect on the laminar flame parameters of the C1–C4 n-alkane-air mixtures: from one step overall assumption to detailed reaction mechanism. Int J Hydrogen Energ 40:703–718. https://doi.org/10.1016/j.ijhydene.2014.11.010

Blowoff Characteristics of Laminar Partially Premixed Flames of Palm Methyl Ester/Jet A Blends

T. Maleta, R. N. Parthasarathy, and S. R. Gollahalli

Nomenclature

Da	Damköhler number
S_L	Laminar flame velocity
T	Absolute temperature of fuel/air mixture at exit
t_{flow}	Flow timescale (based on edge velocity gradient)
t_{chem}	Chemical timescale
α	Thermal diffusivity
Φ	Equivalence ratio

Abbreviations

PME	Palm methyl ester

1 Introduction

Flame extinction is one of the most fundamental phenomena studied in the combustion field [1]. It is governed by chemistry, mass transport and other combustion processes. The extinction of jet diffusion flames is described in terms of liftoff and blowout/blowoff. The blowoff characteristics are one of the important criteria in designing burners for various applications such as in boilers and gas turbines. It is

T. Maleta · R. N. Parthasarathy (✉) · S. R. Gollahalli
School of Aerospace and Mechanical Engineering, University of Oklahoma, Norman, OK, USA
e-mail: rparthasarathy@ou.edu

© Springer Nature Singapore Pte Ltd. 2021

A. De et al. (eds.), *Sustainable Development for Energy, Power, and Propulsion*, Green Energy and Technology,
https://doi.org/10.1007/978-981-15-5667-8_7

important to understand flame stabilization in order to control combustion in various applications.

Vanquickenbourne and van Tiggelen [2] were among the first to investigate the stabilization mechanisms of lifted, turbulent diffusion flames in still air. A majority of studies have focused on the flame stability mechanism in the turbulent regime [2–9]. Pitts [10] compared many competing theories which characterized the stabilization mechanism and blowout of lifted diffusion flames in the turbulent regime. Following Pitts' review [10], there was a large number of papers published which added to better understanding of this matter. Lawn [11] added the additional complexity of the matter when coflow was present. It was concluded that presence of coflow moved the stoichiometric contour and the contour of maximum flame velocity to a smaller radius at the same height in the jet. Thus, the flame stabilized further downstream.

A less number of studies have been conducted in the laminar regime—most of which dealt with blowout rather than blowoff [12]. Several studies reported that lifted flames blew out quickly after they were lifted from the burner without stabilizing at some liftoff height [13, 14]. Characteristics of reattachment and blowout of laminar lifted flames of propane fuel have been investigated experimentally in several studies [15–17]. It was reported that as the flow rate decreased from a lifted flame, the liftoff height decreased nonlinearly, and the flame reattached to a nozzle at a certain liftoff height [15]. Results showed that a lifted flame reattached quickly back to the burner when the jet velocity was decreased. However, hysteresis was observed as the liftoff velocities and reattachment velocities were significantly different [16, 17].

Typically, the Damköhler number has been used to characterize the blowoff/blowout of flames. The Damköhler number is the ratio of the flow timescale and the chemical reaction timescale. Studies have shown that the Damköhler number correlates well with the blowoff velocity and can be used for characterization of blowoff [1, 18]. As noted by Lewis and von Elbe [19], blowoff occurs when the gas velocity gradient at the jet edge becomes higher than the flame velocity gradient near the jet edge (which reduces to zero steeply). Thus, the gradient of velocity near the edge is an important factor in determining the flow timescale. The chemical timescale is inversely proportional to the square of laminar flame speed [1].

In recent years, the search for alternative fuels which are environmentally friendly and which could replace petroleum fuels has grown significantly. Biofuels are a renewable energy source produced from various feedstock which can be grown domestically. Biodiesels (a subcategory of biofuels) are produced by the transesterification of vegetable oils, residual fry oil or animal fats with alcohol and alkaline catalysts. Some of the biofuels have been suggested as a viable option for petroleum fuel replacement and have been experimentally investigated and are commercially available. Canola, palm and soy methyl esters (CME, PME, SME) are biodiesels which are produced by the transesterification of canola, palm and soy oil, respectively. These biodiesels are nearly carbon-neutral, and their physical properties are nearly similar to those of petroleum-based fuels; therefore, they can be blended with petroleum fuels and can be readily used in existing engines with little or no modifications [20]. There have been a number of studies which investigated emissions of biofuel (and blends of biofuel with petroleum fuel) combustion [21–23].

The performance of these fuels and their petroleum fuel blends in engines has also been well-documented [20, 24–26], but the fundamental knowledge of the stabilization mechanism and blowoff of the biofuels is still lacking, particularly in laminar regime. Thus, the motivation of this study was to improve our understanding of the stabilization mechanism and blowoff of laminar flames of these fuels.

2 Experimental Setup and Method

The details of the experimental setup, instrumentation and test conditions are presented in this section. A complete documentation of the setup and instrumentation is provided by Maleta [27].

2.1 Setup

All experiments were conducted in a steel test chamber with a cross section of 76 cm × 76 cm × 100 cm. The chamber was equipped with windows (20 cm × 90 cm) for optical access to the flames. The ambient pressure was atmospheric, and ambient temperature was room temperature. An exhaust duct (equipped with a fan) used to vent the combustion products from the test chamber was open to the atmosphere. The burner was located within the test chamber at the bottom center, and it was concentrically aligned within a circular tube of inner diameter 6.2 cm which was used to provide a coflow of air. A stainless steel circular tube 20.3 cm long (tapered 60° inward to provide more uniform flow as shown in Fig. 1) with 1.27 cm inner diameter served as a burner.

The liquid fuel was injected using a syringe pump into a heated stream of air at a location far enough upstream from the burner exit to ensure the fuel was completely vaporized before it was ignited (Fig. 1). High temperature heating tape wrapped around the 1.47 outer diameter circular tube was used to heat the air stream. The heating tape was connected to an automatic temperature controller which was used to obtain the temperature needed to completely vaporize the fuel, but not too high to cause coking. The inside section of the burner and tubes was regularly cleaned with a wire brush to remove any unburned fuel and debris. The exit temperature of the air–fuel mixture was measured with a K-type thermocouple. Another K-type thermocouple was used to measure the air temperature at the fuel injection port. The liquid fuel was injected through a high-temperature silica-based septum with a 50 ml syringe inserted into a syringe pump.

Two process heaters were used to heat the coflow of air. The exit temperature of the coflow air was about 20 °C lower than the exit temperature of the primary airflow. Three different coflow rates were used in this study: 1.985E−3 m^3/s (~2 L/s) with a bulk velocity of 1.1 m/s, 3.97E−3 m^3/s (~4 L/s) with a bulk velocity of 2.3 m/s and 5.95E−3 m^3/s (~6 L/s) with a bulk velocity of 3.5 m/s. Experiments

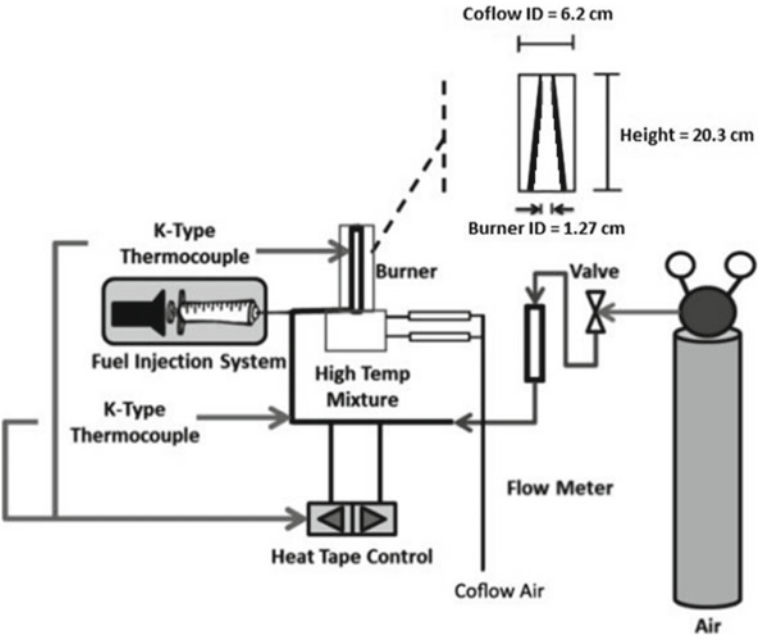

Fig. 1 Schematic diagram of the experimental setup

were also conducted with no coflow. Both primary airflow and coflow were metered using rotameters. Before the shop air reached the rotameters, it was passed through a purifier and an ice bath in order to prevent moisture and any particles entering the flow. The air–fuel mixture was ignited at the burner exit using a butane lighter with a flame length of approximately 1 cm.

The properties of the fuels studied are presented in Table 1. PME is heavier than Jet A and contains significant amount of oxygen (11.9%). It is also more viscous

Table 1 Properties of tested pure fuels

Fuel	Equivalent molecular formula	Molecular weight (kg/kmol)	Liquid density (kg/m^3)	Viscosity at 23 °C (cP)	$(A/F)_{Stoic}$ by mass	Lower heating value (MJ/kg)
JETA	$C_{13}H_{23}$	179	793	1.54	14.38	42.8
PME	$C_{17.05}H_{32.90}O_2$	269	867	5.61	11.17	39.4
PME25 JETA75	$C_{13.79}H_{24.93}O_{0.39}$	197	814	1.75	13.84	40.3
PME50 JETA50	$C_{14.70}H_{27.16}O_{0.84}$	217	830	2.40	13.33	41.1
PME75 JETA25	$C_{15.77}H_{29.78}O_{1.37}$	241	838	3.19	12.83	42.0

than Jet A. The energy content of PME is about 8% lower than that of Jet A. The stoichiometric air–fuel ratio for PME is lower than that of Jet A due to the presence of oxygen in the fuel molecule of PME. Three blends with volume concentrations of 25%, 50% and 75% of PME were used in the study. Their properties are in between those of the pure fuels, as seen from Table 1.

The experimental conditions are presented in Table 2. The exit Reynolds numbers were computed based on the bulk velocity of the fuel/air mixture, burner inner diameter and an estimated viscosity of the gases at the exit temperature. The flames were laminar and confirmed by visual inspection. A typical photograph of the Jet A flame is presented in Fig. 2 at an exit Reynolds number of 2600 and an equivalence ratio of 0.9.

Table 2 Experimental conditions

Fuel	Exit Reynolds number	Equivalence ratio at blowout	Fuel flow rate (ml/min)	Airflow rate at blowout (ml/min)	Primary flow bulk velocity at blowout (m/s)	Coflow bulk velocity (m/s)
Jet A	2400–3650	0.54–0.79	1.085–1.667	14,900–22,700	3.3–5.0	0, 1.1, 2.3
PME	2100–3100	0.53–0.81	1.085–1.667	14,500–20,450	3.3–4.7	0, 1.1, 2.3
PME25 JETA75	2200–3300	0.56–0.81	1.085–1.667	15,300–20,450	3.4–4.7	0, 1.1, 2.3
PME50 JETA50	2200–3200	0.57–0.82	1.085–1.667	14,500–20,500	3.5–4.7	0, 1.1, 2.3
PME75 JETA25	2200–3200	0.56–0.91	1.085–1.667	14,500–20,500	3.5–4.9	0, 0.69, 1.38

Fig. 2 Photograph of Jet A flame at an exit Reynolds number of 2600 and equivalence ratio of 0.9

2.2 Methodology

Blowoff measurements were taken at nine discrete fuel flow rates which ranged from 65.1 ml/h to 100 ml/h. The experiments were conducted in such way that after the fuel/air mixture was ignited (at approximately stoichiometric conditions), for a given fuel flow rate and a given coflow setting, the airflow rate was increased until the blowoff was reached.

As noted by von Lewis and Elbe [19], the gradient of velocity near the edge was an important factor in predicting the blowoff. A pitot static probe was used to obtain velocity values of exiting air at different conditions. The tip of pitot static probe was placed 6 mm above the burner, while the pitot static probe was mounted on a traverse and moved radially across the centerline of the burner in increments of 2 mm. A typical velocity profile (with no coflow) is presented in Fig. 3.

The velocity gradient at the burner edge was estimated by averaging the right and left side values of the gradients. These values were 1880, 1830 and 1350 s^{-1} for the three bulk velocities of 5.1, 4.3 and 3.5 m/s. With the presence of coflow, the values of these gradients decreased. Details of these measurements are documented by Maleta [27].

Inflame temperature profiles were measured at equivalence ratio of 0.9. A two-dimensional traverse was used to hold an R-type thermocouple (Platinum/Platinum-87%, Rhodium-13%) to collect data at three different flame heights while traversing radially through the flame in increments of 2 mm. The bead diameter of the thermocouple was 0.2 mm. The bead was coated with silica before every experiment to reduce the catalytic effects. A 1.6 mm outer diameter ceramic tube was used to provide structural support to very thin thermocouple wires (0.03 mm diameter). The collected temperature measurements were corrected for radiation and conduction losses according to procedures outlined by Jha et al. [28]. Temperature data from the thermocouple was collected using the LabVIEW data acquisition software and a

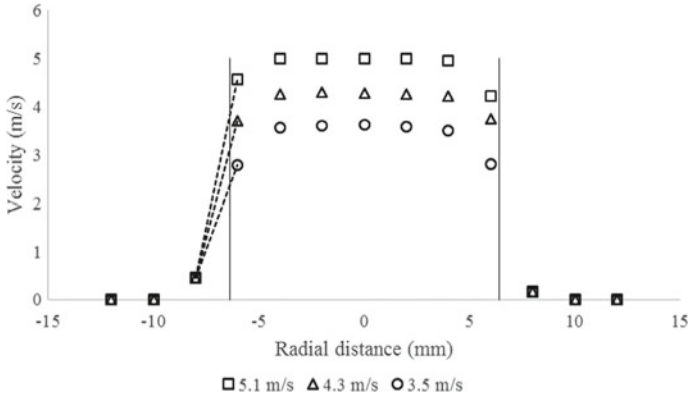

Fig. 3 Typical velocity profiles near the burner exit for three flow rates

personal computer. The readings were taken at 1 Hz at each point and averaged over 5 s as there was no noticeable difference when averaged over a longer time period.

2.3 Damköhler Number Calculations

The Damköhler number (Da) is the ratio of the flow timescale to that of the chemical reaction timescale.

$$\mathrm{Da} = \frac{t_{\mathrm{flow}}}{t_{\mathrm{chem}}} \tag{1}$$

where t_{flow} represents flow or residence timescale and t_{chem} represents the chemical reaction timescale. The flow timescale was taken as the inverse of the velocity gradient at the flame edge estimated using the measurements described in the previous section.

$$t_{\mathrm{flow}} = \frac{1}{\text{velocity gradient (at jet edge)}} \tag{2}$$

The chemical timescale was estimated using

$$t_{\mathrm{chem}} = \frac{\alpha}{S_{\mathrm{L}}^2} \tag{3}$$

where α represents the thermal diffusivity and S_{L} represents laminar flame speed. Lima et al. [29] reported that the thermal diffusivity of a fuel/air mixture decreased by 17% when the molar fraction of fuel in the mixture was 2.1%. Molar fractions of fuel in the fuel/air mixture in the present study were 1% or less. Thus, the thermal diffusivity of air was used as an estimate of the thermal diffusivity of the mixture.

The information on laminar flame speed at very low equivalence ratios (such as those reported in this study) is very limited. Therefore, the laminar flame speed of these fuels at low equivalence ratio was estimated assuming a parabolic correlation between laminar flame speed and equivalence ratio. Many studies reported laminar flame speed profiles which resembled a parabolic function [30–35]. Also, the laminar flame speed was assumed to vary with temperature as $T^{1.5}$ [34]. The parabolic correlations used to estimate the laminar flame speed (S_{L}) for various fuels are given in Eqs. 4 and 5. These equations were obtained by fitting a parabolic trend line to data points reported in the aforementioned studies [30, 35]. The units of laminar flame speed in these equations are cm/s.

$$\text{Jet A: } S_{\mathrm{L}} = -212.71\Phi^2 + 464.96\Phi - 165.13 \tag{4}$$

$$\text{PME: } S_{\mathrm{L}} = -133.64\Phi^2 + 336.46\Phi - 126.04 \tag{5}$$

3 Results and Discussion

3.1 Flame Blowoff Images

Sequences of blowoff images of the Jet A and PME flames are presented in Fig. 4a and b. The flames are blue in color (lean conditions) and laminar. As the air velocity is slowly increased, the attachment of the flame to the burner on one side begins to waver, and the flame is quickly blown off. Thus, the velocity gradient near the burner edge plays an important role in the blowoff phenomenon.

For the Jet A flame (Fig. 4a), the initial equivalence ratio, velocity and Reynolds number are 0.74, 3.8 m/s and 2800, respectively. The time interval between the images is 0.8 s. The flame is completely blown off the burner when the exit velocity is 4.1 m/s. A similar sequence is presented in Fig. 4b for the PME flame with an initial equivalence ratio, velocity and Reynolds number of 0.76, 3.7 m/s and 2550, respectively. The images are 0.3 s apart in this figure. The flame is completely blown off when the exit velocity reaches 3.9 m/s.

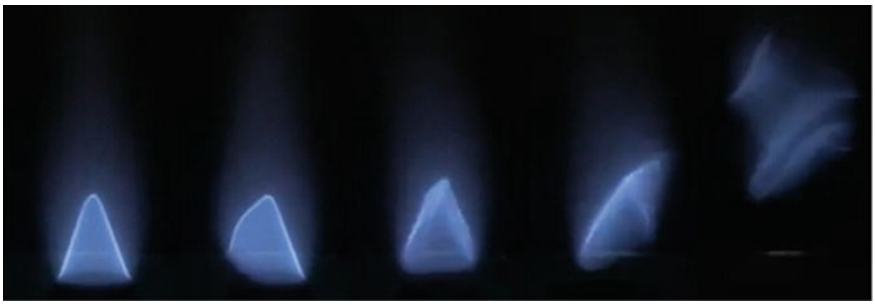

a

b

Fig. 4 **a** Sequence of Jet A flame blowoff images with no coflow; initial equivalence ratio of 0.74 and initial Reynolds number of 2800. **b** Sequence of PME flame blowoff images with no coflow; initial equivalence ratio of 0.76 and initial Reynolds number of 2550

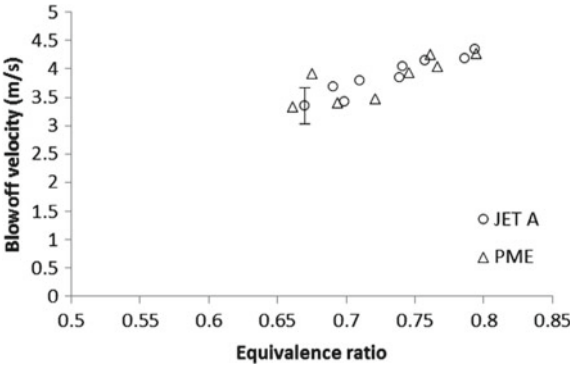

Fig. 5 Blowoff velocities of Jet A and PME flames with no coflow

3.2 Blowoff Velocity (No Coflow)

In this study, the blowoff conditions are reported for initial lean conditions (equivalence ratio of 0.5–0.8). The experiment was repeated at least three times for each flow condition, and the averages are displayed here. Uncertainties were computed following standard procedures and are presented as error bars in the figures.

The blowoff velocity of the Jet A and PME flames is plotted in Fig. 5 as a function of initial equivalence ratio. For Jet A flames, the blowoff velocity increased from 3.3 m/s at an initial equivalence ratio of 0.67–4.3 m/s at an equivalence ratio of 0.79. The variation is almost linear within this range. As the initial equivalence ratio is increased under lean conditions, the laminar flame velocity increases. For Jet A, the laminar flame velocity increases from 50.91 to 69.44 cm/s as the initial equivalence ratio is raised from 0.67 to 0.79 (as given by Eq. 4). Thus, a higher exit velocity is required for the flame to be blown off the burner.

The results for the PME flames are similar. The differences between the blowoff velocities of PME and Jet A flames were within experimental uncertainties.

3.3 Effects of Coflow on Blowoff Velocity

With the presence of coflow, a higher exit velocity is required to obtain the same velocity gradient as that achieved with no coflow. Therefore, the blowoff velocity is expected to increase as the coflow velocity is increased. The blowoff velocity of Jet A and PME flames is presented in Fig. 6a–c for coflow velocities of 1.1 m/s, 2.3 m/s and 3.5 m/s, respectively.

For a coflow velocity of 1.1 m/s, the blowoff velocity of Jet A flame increased from 3.4 m/s at an initial equivalence ratio of 0.66–4.5 m/s at an equivalence ratio of 0.77, as seen in Fig. 6a. The corresponding values for the PME flames were 3.4 m/s at an equivalence ratio of 0.65 and 4.5 m/s at an equivalence ratio of 0.76. As the coflow velocity was raised to 2.3 m/s, the value of blowoff velocity increased by 0.1 m/s

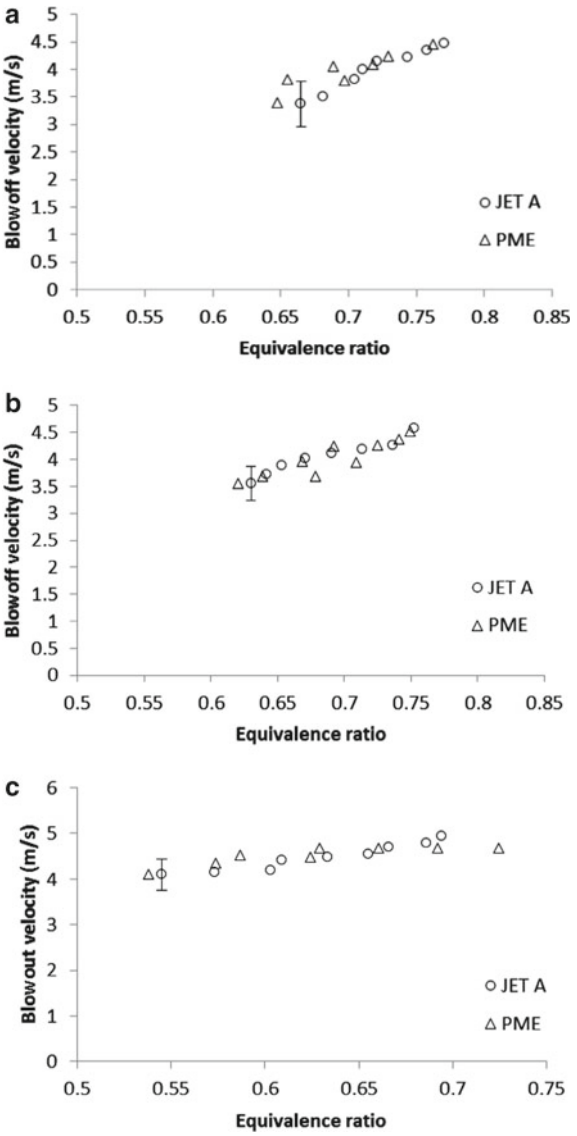

Fig. 6 **a** Blowoff velocities of Jet A and PME flames with a coflow of 1.1 m/s. **b** Blowoff velocities of Jet A and PME flames with a coflow of 2.3 m/s. **c** Blowoff velocities of Jet A and PME flames with a coflow of 3.5 m/s

(Fig. 6b). At the coflow velocity of 3.5 m/s, the blowoff velocity was flat at about 4.1 m/s. In this case, initial stable flames were achieved only for an equivalence ratio range of 0.55–0.75. The differences in blowoff velocities of Jet A and PME flames were within experimental uncertainties for all coflow conditions.

3.4 Damköhler Number

The Damköhler number was computed using Eqs. (1)–(5). The thermal diffusivity was assumed to be that of air at the exit temperature because the fuel mass fraction was small. The results are presented in Tables 3 and 4 for Jet A flames and PME flames, respectively. With no coflow, the average Damköhler number corresponding to blowoff was around 6 for the Jet A flames and 4 for the PME flames. With the presence of coflow velocities of 1.1 and 2.3 m/s, the average value of Damköhler number increased to 8 for Jet A flames but remained at 4 and 4.6 for the PME flames. Thus, it appears that the Damköhler number can be used effectively to estimate the blowoff velocity at lean conditions.

Table 3 Damköhler number for Jet A flames at blowoff

Coflow (m/s)	3.5		2.3		1.1		0	
	Φ	Da	Φ	Da	Φ	Da	Φ	Da
	0.55	2.3	0.63	6.5	0.66	7.8	0.67	5.0
	0.57	3.2	0.64	6.8	0.68	8.2	0.70	5.9
	0.60	4.6	0.65	7.1	0.71	9.4	0.69	5.2
	0.61	4.7	0.67	8.0	0.70	7.9	0.71	5.7
	0.63	5.6	0.69	8.8	0.71	7.6	0.74	6.5
	0.66	6.9	0.71	9.7	0.72	7.5	0.74	6.2
	0.67	7.1	0.74	10.6	0.74	8.0	0.76	6.6
	0.69	7.8	0.75	10.2	0.76	8.4	0.79	7.4
	0.69	7.5	0.75	9.0	0.77	8.4	0.79	7.1
Average Da		5.5		8.5		8.1		6.2

Table 4 Damköhler number for PME flames at blowoff

Coflow (m/s)	3.5		2.3		1.1		0	
	Φ	Da	Φ	Da	Φ	Da	Φ	Da
	0.54	1.2	0.62	2.8	0.65	3.5	0.66	3.0
	0.57	2.0	0.64	3.3	0.65	3.2	0.69	3.7
	0.57	1.7	0.68	4.7	0.65	3.0	0.72	4.3
	0.59	2.1	0.67	4.0	0.70	4.5	0.68	2.8
	0.62	3.0	0.71	5.3	0.69	3.8	0.76	4.9
	0.63	3.0	0.69	4.3	0.72	4.6	0.75	4.2
	0.66	3.6	0.73	5.5	0.73	4.6	0.77	4.5
	0.69	4.5	0.74	5.7	0.73	4.2	0.76	4.0
	0.72	5.1	0.75	5.8	0.76	5.0	0.79	4.6
Average Da		2.9		4.6		4.0		4.0

3.5 Blowoff Velocity of Blend Flames

The blowoff velocities of the blend flames for various coflow velocities are presented in Fig. 7a–d. The differences observed for the blend flames were within experimental uncertainties. As before, the blowoff velocity increased with initial equivalence ratio and with coflow. The Damköhler number could not be computed for the blend flames due to the lack of knowledge of laminar flame velocity of blend flames.

3.6 Flame Temperature

The measured flame temperature profiles at three heights from the burner are displayed in Fig. 8a–c. The measurements were conducted for a burner-exit equivalence ratio of 0.9. The temperature at half the inner cone height (Fig. 8a) shows the classical double-peak variation. The maximum temperature (close to 1740 K) was measured at the location of the flame front that was 5 mm from the center. At the tip of the inner cone, the maximum temperature was around 1710 K and was located at the center (Fig. 8b). The temperature variation was flat in the middle and decreased toward the edges. At twice the inner cone height, the maximum temperature was reduced to 1660 K due to mixing with entrained air (Fig. 8c); the temperature profile was flat, similar to that observed at the tip of the inner cone. There were no significant differences between the temperatures measured in the various flames. The adiabatic flame temperature of PME and Jet A was comparable at stoichiometric conditions [30].

4 Conclusions

The blowoff velocities of laminar partially premixed prevaporized laminar flames of Jet A, PME and blend flames of Jet A and PME were studied with and without heated coflow. The burner-exit equivalence ratio was in the range 0.53–0.83. The blowoff velocity was determined by increasing the primary airflow rate until the flame blew off, while the fuel flow rate and coflow rate were kept constant. Inflame temperature measurements were also made. The Damköhler number was used to characterize the blowoff of flames. Based on the results, the following conclusions were drawn:

(a) The blowoff velocity increased roughly linearly with equivalence ratio. The difference in flame blowoff velocity of all fuels was within experimental uncertainties.
(b) As the coflow velocity was increased, the blowoff velocities increased due to the reduction in the velocity gradient at the edge of the jet. The differences in the values of blowoff velocities became smaller as the coflow velocity was increased.

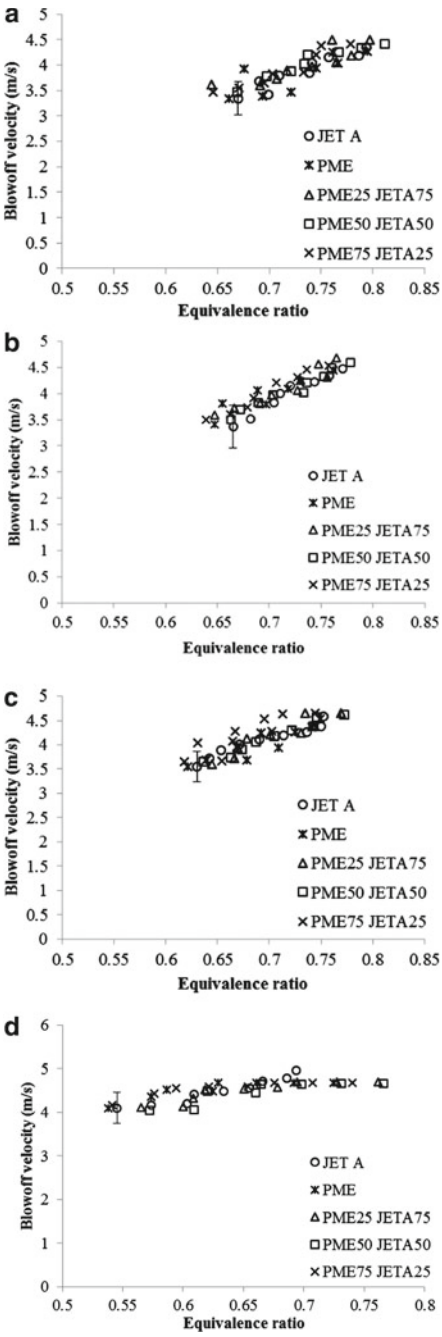

Fig. 7 **a** Blowoff velocities of blend flames with no coflow. **b** Blowoff velocities of blend flames with coflow velocity 1.1 m/s. **c** Blowoff velocities of blend flames with coflow velocity 2.3 m/s. **d** Blowoff velocities of blend flames with coflow velocity 3.5 m/s

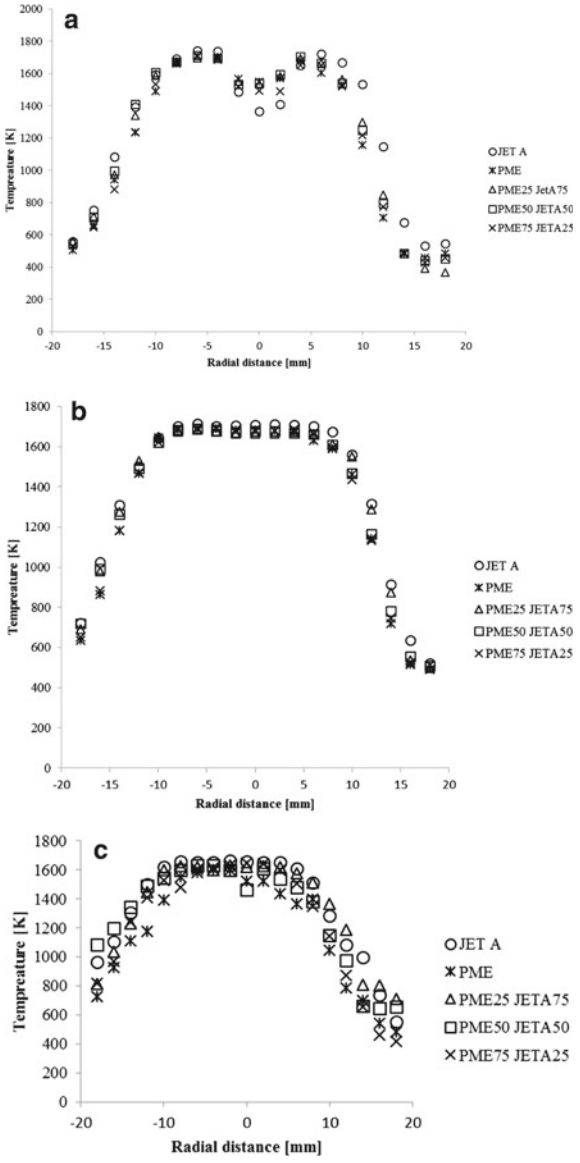

Fig. 8 **a** Temperature profiles at half the inner cone height (equivalence ratio of 0.9 and Reynolds number of 2600). **b** Temperature profiles at the tip of the inner cone (equivalence ratio of 0.9 and Reynolds number of 2600). **c** Temperature profiles at half the outer cone height (equivalence ratio of 0.9 and Reynolds number of 2600)

(c) A Damköhler number (based on the velocity gradient at the jet edge and the laminar flame speed and thermal diffusivity) value of 3–8 characterized the blowoff velocity. The laminar flame speed of the fuels at low equivalence ratio was estimated assuming a parabolic correlation between laminar flame speed and equivalence ratio and an absolute temperature variation of $T^{1.5}$. The

Damköhler number corresponding to the blend flames could not be determined due to the lack of knowledge of laminar flame velocity of blend flames.

(d) The temperature profiles in the various flames were similar, with peak temperatures of around 1740 K. The adiabatic flame temperature at stoichiometric conditions was comparable for PME and Jet A. The present measurements can be used to validate computational models of laminar PME and blend flames.

References

1. Glassman I, Yetter RA (1996) Combustion, 4th edn. Academic, Burlington
2. Vanquickenbourne L, van Tiggelen A (1966) The stabilization mechanism of lifted diffusion flames. Combust Flame 10:59–69
3. Kalghathi GT (1986) Lift-off heights and visible lengths of vertical turbulent jet diffusion flames in still air. Combust Sci Technol 41:17–29
4. Broadwell JE, Dahm WJA, Mungal MG (1985) Blow-out of turbulent diffusion flames. In: Twentieth symposium on combustion, pp 303–312
5. Tieszen SR, Stamps DW, O'Hern TJ (1996) A heuristic model of turbulent mixing applies to blowout of turbulent jet diffusion flames. Combust Flame 106:442–466
6. Brown CD, Watson KA, Lyons KM (1999) Studies on lifted jet flames in coflow: the stabilization mechanism in the near- and far-fields. Flow Turb Combust 62:249–273
7. Peters N, Williams FA (1983) Liftoff characteristics of turbulent jet diffusion flames. AIAA J 21:423–429
8. Rokke NA, Hustad JE, Sonju OK (1994) A study of partially premixed unconfined propane flames. Combust Flame 97:88–106
9. Choi BC, Chung SH (2013) An experimental study on turbulent lifted flames of methane in coflow jets at elevated temperatures. Fuel 103:956–962
10. Pitts WM (1988) Assessment of theories for the behavior and blowout of lifted turbulent jet diffusion flames. In: Twenty-second symposium (international) on combustion, vol 22, pp 809–816
11. Lawn CJ (2009) Lifted flames on fuel jets in co-flowing air. Prog Energy Combust Sci 35:1–30
12. Aggarwal SK (2009) Extinction of laminar partially premixed flames. Prog Energy Combust Sci 35:528–570
13. Lee BJ, Chung SH (1997) Stabilization of lifted tribrachial flames in laminar non-premixed jet. Combust Flame 109:163–172
14. Chung SH, Ko YS (1999) Propagation of unsteady tribrachial flames in laminar non-premixed jets. Combust Flame 118:151–163
15. Lee J, Chung SH (2001) Characteristics of reattachment and blowout of laminar lifted flames in partially premixed propane jets. Combust Flame 127:2194–2204
16. Savas O, Gollahalli SR (1986) Stability of lifted laminar round gas-jet flame. J Fluid Mech 165:297–318
17. Lee J, Jin SH, Chung SH (2003) Lifted flames in laminar jets of propane in coflow air. Combust Flame 135:449–462
18. Kedia KS, Ghoniem AF (2015) The blow-off mechanism of a bluff-body stabilized laminar premixed flame. Combust Flame 162:1304–1315
19. Lewis B, von Elbe G (1987) Combustion, flames and explosions of gases, 3rd edn. Academic, Burlington
20. Balakrishnan A, Parthasarathy RN, Gollahalli SR (2016) A review on the effects of biodiesel blends on compression ignition engine NOx emissions. J Energy Environ Sustain 1:67–76

21. Wang WG, Lyons DW, Clark NN, Gautam M, Norton PM (2000) Emissions from nine heavy trucks fueled by diesel and biodiesel blend without engine modification. Environ Sci Technol 34:933–939
22. Love N, Parthasarathy RN, Gollahalli SR (2009) Rapid characterization of radiation and pollutant emissions of biofuel and hydrocarbon liquid fuels. J Energy Resour Technol 131:1–9
23. Merchan-Merchan W, Sanmiguel SG, McCollam S (2012) Analysis of soot particles derived from biodiesels and diesel fuel air-flames. Fuel 102:525–535
24. Durbin T, Collins J, Norbeck J, Smith M (2000) Effects of biofuel, biofuel blends, and a synthetic diesel on emissions from light heavy-duty diesel vehicles. Environ Sci Technol 34:349–355
25. Labeckas G, Slavinskas S (2006) The effect of rapeseed oil methyl ester on direct injection diesel engine performance and exhaust emissions. Energy Convers Manag 47:1954–1967
26. Muralidharan K, Vasudevan D, Sheeba K (2001) Performance, emission and combustion characteristics of biodiesel fuelled variable compression ratio engine. Energy 36:5385–5393
27. Maleta T (2017) Blowoff characteristics of partially premixed flames of prevaporized blends of biofuels and petroleum fuels, MS thesis, School of Aerospace and Mechanical Engineering, University of Oklahoma, Norman, OK
28. Jha S, Fernando S, Filipto S (2008) Flame temperature analysis of biodiesel blends and components. Fuel 87:1982–1988
29. Lima JAP, Marín E, da Silva MG, Sthel MS, Cardoso SL, Takeuti DF, Gatts C, Vargas H, Rezende CE, Miranda LCM (2000) On the use of the thermal wave resonator cavity sensor for monitoring hydrocarbon vapors. Rev Sci Instr 71:2928–2932
30. Chong CT, Hochgreb S (2011) Measurements of laminar flame speeds of liquid fuels: Jet-A1, diesel and palm methyl esters and blends using particle imaging velocimetry. Proc Combust Inst 33:979–986
31. Wang YL, Feng Q, Egolfoupolos FN, Tostsis TT (2011) Studies of C4 and C10 methyl ester flames. Combust Flame 158:1507–1519
32. Liu W, Kelley AP, Law CK (2011) Non-premixed ignition, laminar flame propagation, and mechanism reduction of n-butanol, iso-butanol, and methyl butanoate. Proc Combust Inst 33:995–1002
33. Gomez-Meyer J, Gollahalli SR, Parthasarathy RN, Quiroga J (2012) Laminar flame speed of soy and canola biofuels. Ciencia Tecno Futuro 4:76–83
34. Zhang Z, Zhu S, Liang J, Tian L, Li G (2018) Experimental and kinetic studies of premixed laminar flame of acetone-butanol-ethanol (ABE)/air. Fuel 211:95–101
35. Kumar K, Sung C-J, Hui X (2011) Laminar flame speeds and extinction limits of conventional and alternative jet fuels. Fuel 90:1004–1011

Effect of Composition and Octane Sensitivity of Gasoline Surrogates on PAH Emissions

Krishna C. Kalvakala and Suresh K. Aggarwal

Nomenclature

ϕ	Equivalence Ratio
A1	Benzene (C_6H_6)
A2	Naphthalene ($C_{10}H_8$)
A3	Phenanthrene ($C_{14}H_{10}$)
A4	Pyrene ($C_{16}H_{10}$)
A5	Benzo[e]pyrene ($C_{20}H_{12}$)
EPRF	Ternary blend with ethanol
LPZ	Lean premixed zone
LTC	Low temperature combustion
MON	Motor octane number
NPZ	Non-premixed zone
PAH	Polycyclic aromatic hydrocarbons
PRF	Binary primary reference fuel
RON	Research octane number
RPZ	Rich premixed zone
OS (or S)	Fuel sensitivity

K. C. Kalvakala · S. K. Aggarwal (✉)
Department of Mechanical and Industrial Engineering,
University of Illinois at Chicago, Chicago, USA
e-mail: ska@uic.edu

© Springer Nature Singapore Pte Ltd. 2021

A. De et al. (eds.), *Sustainable Development for Energy, Power, and Propulsion*, Green Energy and Technology,
https://doi.org/10.1007/978-981-15-5667-8_8

1 Introduction

Transportation sector plays a crucial role in the increase in energy demand and currently accounts for nearly 20% (110 quadrillion BTUs) of global energy demand [1]. Moreover, this sector is almost entirely (99%) powered by internal combustion engines (ICE), with land and marine transport primarily by reciprocating ICE, and air transport by jet engines. While the combustion of fossil fuels is of critical importance, the issues related to adverse environmental and human health hazards caused by emissions from the combustion of fossil fuels need to be addressed [2–4]. It is critically important to develop novel technologies and combustion strategies that focus on high efficiency and cleaner engines. Low-temperature combustion (LTC) mode has been widely studied as a novel combustion mode. It offers the possibility to reduce both NOx and particulate matter via enhanced air-fuel mixing and intake charge dilution reducing peak combustion temperatures [5–7]. Variants of this engine technology include Homogeneous charge compression ignition (HCCI), dual-fuel reactivity-controlled compression ignition (RCCI), and partially premixed compression ignition (PPCI) and others.

Gasoline Compression Ignition (GCI) [8] is another variant of LTC mode engines, which has been gaining increasing attention due to its potential of achieving high thermal efficiencies and significantly low emissions under controlled combustion phasing. It combines the advantages of cleaner combustion of SI engine and high compression ratios of CI engine. Moreover, in order to control the autoignition event, the mixture (equivalence ratio) stratification within the cylinder is manipulated through late or early injection during the compression stroke. Further, compared to traditional gasoline fuels with high octane number, the low octane gasoline fuels are more suitable for GCI mode of combustion due to their higher resistance to autoignition. Low-octane fuels such as naphtha fuels are produced in a much simpler and eco-friendlier way compared to high octane gasoline fuels due to the absence of complicated refining processes and antiknock additives. Such fuels have longer ignition delays, higher volatility, and generally lower aromatic content compared to conventional diesel fuels. The longer ignition delay of naphtha fuel facilitates sufficient fuel-air mixing prior to ignition, hence increasing the possibility of cleaner combustion. Zhang et al. [9] investigated the combustion and emission characteristics of naphtha fuels with RON (research octane number) of 59 and 69 in a CI engine and demonstrated that these fuels could achieve enhanced premixed combustion resulting in reduced soot emissions. Chang et al. [10] observed that the use of naphtha fuel in PPCI mode increases the overall efficiency and reduces emissions. Moreover, since autoignition is the primary control mechanism for optimizing the engine performance at different operating conditions, the use of naphtha fuels in advanced LTC engines requires accurate modeling of ignition chemistry. It also requires the development of validated surrogate fuel mixtures for representing the atomization and ignition characteristics of these fuels under various operating conditions.

Primary reference fuel (PRF) surrogates are among the simplest surrogates employed to mimic gasoline combustion. A PRF is a binary mixture of n-heptane

and iso-octane. Several experimental and modeling efforts [11–15] are available in the literature describing ignition and soot characteristics of iso-octane and n-heptane as single components and also as PRF blends. However, commercial gasoline is a mixture of several hydrocarbons along with high aromatic content (20–30%) and other non-paraffinic species (5–10%). Consequently, such fuels tend to have a high Octane Sensitivity (S).[1] Thus, a PRF surrogate, which has zero octane sensitivity, has limited capability to emulate the ignition behavior of real gasoline fuel. Moreover, Kalghatgi and coworkers [14] demonstrated that real gasoline, due to high octane sensitivity, matches the behavior of different PRF blends at different operating conditions. Hence, PRF surrogates cannot be used to rate a gasoline-based on primitive RON and MON testing methods. Thus, there is a need to develop multi-component surrogates having high octane sensitivity (S), which will have the capability to represent the performance of real fuel for a broad range of operating conditions. In the process of developing multi-component surrogates, it becomes essential to identify the impact of each additional component (non-paraffinic) added to PRF fuel. For instance, Toluene primary reference fuel (TPRF), a ternary blend containing iso-octane/n-heptane/toluene as components, has been shown to be a better match to the composition and combustion properties (octane number, sensitivity) of gasoline compared to PRF mixtures [14, 16–20]. In this context, some recent studies have shown that the addition of toluene or other aromatic components to the surrogate can account for the effects of fuel sensitivity (S), and thus mimic the behavior of gasoline and naphtha type fuels [16, 21–23]. For instance, Gauthier et al. [16] evaluated the autoignition data of RD387 gasoline and a ternary surrogate (63% iso-octane, 17% n-heptane, 20% toluene) in a shock tube, and observed that the ternary surrogate adequately captures the autoignition characteristic of gasoline. A recent study by Jain et al. [19] confirmed the strong effect of octane sensitivity on transient ignition and flame evolution in homogeneous mixtures and diesel sprays. It was observed that in homogeneous mixtures, the fuel sensitivity has a strong influence on ignition at low ($T < 850$ K) to intermediate ($850\ \text{K} < T < 1100\ \text{K}$) temperatures, but a relatively small effect at higher ($T > 1100$ K) temperatures. At low temperatures, the effect of sensitivity was to reduce fuel ignitability, i.e., longer ignition delay. However, as the temperature was increased, the behavior was reversed, indicating shorter ignition delays for blends with higher sensitivity. This implied the existence of a 'transition temperature' at which the fuel ignitability is reversed. Results also indicated that the NTC behavior becomes increasingly less pronounced as the octane sensitivity is increased. Further, since fuel sensitivity provides a measure of aromatic content in the fuel, it implies that the presence of aromatic species can significantly affect the fuel sooting characteristics [24, 25]. Park et al. [24] considered nitrogen diluted gasoline opposed-jet flames and observed that the increase of either toluene or iso-octane content in the fuel leads to an increase in PAH concentration. An et al. [25] investigated the effect of toluene addition on particulate emissions in different combustion

[1]Fuel Octane Sensitivity (S) is defined as the difference between RON and MON. It is one such fuel property which directly relates to the composition of the fuel. It accounts for the non-paraffinic content present in the fuel.

modes, i.e., partially premixed combustion (PPC) and homogeneous charge compression ignition (HCCI) using a single-cylinder diesel engine. The results indicated higher soot emissions for the blend with toluene compared to that without toluene, in both the combustion modes. Further, a recent experimental study by Shao et al. [26] examined the formation of PAHs during the pyrolysis of two ternary surrogates (TPRF70 and TPRF97.5). They noticed that toluene consumption was promoted in TPRF mixtures relative to when it is a pure fuel while iso-octane remained to be the most reactive component. However, no direct correlation between the toluene content and PAH concentrations was observed. Despite higher toluene content in TPRF97.5, it produced lower amounts of benzene and naphthalene when compared to TPRF70. On the other hand, TPRF97.5 produced slightly higher amounts of phenanthrene and pyrene. Though these observations are for fuel pyrolysis, they help in understanding the complex behavior of multi-component fuels when compared to that of single-component fuels.

There have also been several experimental and computational studies dealing with the effect of using bio-derived fuels, such as ethanol, di-isobutylene, and butanol isomers on PAH and soot emissions [27–33]. However, the focus was mainly on binary mixtures. Inal et al. [34] have shown that the addition of alcohol, such as methanol, ethanol, and n-butanol, gasoline (n-heptane used as surrogate) has a clear inhibitory effect on PAHs formation. Yao et al. [35] concluded that alcohol addition can inhibit the formation of PAHs in laminar premixed n-heptane/toluene flames, especially at the later stages of the reaction zone, by inducing massive HO_2 and OH radicals. Maricq et al. [36] and Khosousi et al. [37] investigated the effect of ethanol addition on soot formation in coflow gasoline diffusion flames. Both observed that soot suppression is not significant until blending ratio of ethanol is more than 50%. The E85 flame produced significantly less soot than E0, E20, and E50 flames. Khosousi, with the help of simulations (assuming gasoline as TPRF blend), attributed this decrease in soot concentrations to lower aromatic content in the fuel stream (at higher ethanol dilution level) as opposed to the increased oxygen content of ethanol.

The studies mentioned above highlight the anomalous nature of fuel blends based on mixture composition. Further, the literature review indicates very few studies on PAHs and soot emissions from gasoline surrogates with more than two components, such as TPRFs and EPRFs (PRF with bio-derived fuel as the third component). Moreover, in order to further examine the fuel-engine interactions, it is important to relate fuel properties (physical and chemical properties) to engine performance and emissions. Octane sensitivity (S) is one such property that directly relates to the chemical nature of the fuel. Thus, in order to get a better insight into the effect of S on emissions, it is necessary to explore the sensitivity induced by various non-paraffinic sources. Motivated by these considerations, this chapter reviews research focusing on the effects of fuel composition and octane sensitivity on PAHs emissions in simplified laboratory-scale configurations. Three- and four-component blends, where S is induced due to toluene and/or ethanol in PRF mixtures, are considered. Some results are also presented for binary mixtures. The configurations considered include counterflow diffusion and partially premixed flames, and jet-stirred reactor and flow reactor focusing on pyrolysis behavior. The chapter mainly focuses on the

Table 1 PRF, TPRF, and ERPF blends (molar %) investigated in this work

Surrogate	ISO-Octane	n-Heptane	Toluene	Ethanol	RON	MON	Octane sensitivity (S)
PRF70-0	67.6	32.4	0	0	70	70	0
TPRF70-4	36.6	35	28.4	0	70[a]	66[a]	4[c]
TPRF70-5.7	23.6	36.6	39.8	0	70.05[b]	64.4[b]	5.7[c]
EPRF70-1.55	41.5	35.1	0	23.4	70[d]	68.44[d]	1.55[c]
EPRF70-4	22.7	37.4	0	39.9	70.04[d]	66[d]	4.04[c]
ETPRF70-4(1)	25.4	34.7	18.5	21.4	70[d]	66[d]	4[c]
ETPRF70-4(2)	38.0	34.2	23.0	4.8	70[d]	66[d]	4[c]
ETPRF70-5.7	12.5	35.1	32.0	20.3	70[d]	64.4[d]	5.6[c]

[a]RON and MON estimated by Javed et al. [39]
[b]RON and MON estimated using correlations developed by Kalghatgi et al. [14]
[c]Sensitivity OS = RON—MON (estimate)
[d]RON and MON estimated using correlations developed by Al Ramadan et al. [38]

results, rather than on the details of the computational model or experimental set-up. The compositions of the blends (PRF70, TPRF70-a, TPRF70-b, EPRF70-a, and EPRF70-b) used in this study are provided in Table 1. The correlations of Kalghatgi et al. [14] were used to formulate the PRF and TPRF blends, while EPRF and ETPRF blends were formulated using the correlations of Al Ramadan et al. [38]. They are formulated in such a way so as to maintain the RON = 70 while increasing the octane sensitivity. Thus, the blends contained different amounts of iso-octane, n-heptane and toluene or ethanol. For our study, four detailed or semi-detailed mechanisms were evaluated in terms of their predictive capabilities for PAHs emissions through comparison with LIF data in diffusion flames (details are not discussed in this review study). Based on this evaluation, a fairly detailed mechanism of Park et al. [26] involving 574 species and 3379 reactions was used for the study.

Format for name of blend—##PRF$$-, where ## is T(Toluene) or E(Ethanol) or TE (both Toluene and Ethanol) blended with PRF, $$–RON and *—Octane Sensitivity.*

2 Results and Discussion

Results discussed here are taken from previous publications dealing with the effects of surrogate composition and octane sensitivity (S) on PAH and soot emissions. As stated above, the results mainly focus on fuel mixtures having iso-octane/n-

heptane/toluene/ethanol components. The first part of the section discusses results for binary blends, followed by sections on ternary and quaternary blends. For the latter, the effects of fuel composition and S on the flame structure and PAH formation are discussed.

2.1 Binary Blends

As discussed earlier, binary blends consisting of any two of iso-octane, n-heptane or toluene have been of great interest in the context of developing a surrogate to capture the behavior of gasoline fuel under a wide range of operating conditions. Further, it has been observed in some studies that fuels behave very differently when part of a mixture rather than when used as a sole fuel, hence making it essential to understand the behavior of fuel mixtures. Choi et al. [11] performed experiments and computations in a counterflow configuration to examine the possible synergistic effect of PAHs and soot formation for binary mixtures. Flames of iso-octane/toluene (OT) and n-heptane/toluene (HT) were examined under two different conditions – soot formation/oxidation (SFO) and soot formation (SF). Note that in SFO flames, the soot zone is located on the fuel side of the flame, and thus the soot particles formed there migrate to the oxidizer side, where they get oxidized by species such as OH and O_2. On the other hand, the SF flame is located on the oxidizer side, and the soot particles are convected away from the flame and thus are not oxidized. The mole fractions of fuel mixture in fuel stream and oxygen content in oxidizer stream were $(X_F, X_O) = (0.30, 0.21)$ and $(0.07, 0.90)$ for SF and SFO flames, respectively, while the remaining portion of fuel and oxidizer streams is nitrogen.

Figure 1 presents the normalized maximum (normalized with respect to R_T[2] = 1 data) LII and LIF signals for iso-octane/toluene and n-heptane/toluene flames under SF and SFO conditions. Note that LIF and LII signals provide a measure of PAH concentration and soot volume fraction, respectively. In addition, LIF signals with longer detection wavelengths correspond to larger PAHs. As indicated in Fig. 1, the LII signals increase with toluene ratio monotonically, but their variation is far from linear. Further, the peak values of LIF signals for both OT and HT flames in SF condition occurs when $R_T \approx 0.7$, indicating a synergistic behavior with respect to toluene content on PAH formation for $R_T > 0.7$. This synergistic effect is relatively weak for flames under SFO condition. Numerical simulations further confirmed this synergistic behavior. Moreover, the formation of the first ring—benzene which is the starting point for the formation of higher PAHs shows a clear synergistic effect with R_T. The same was captured by both the mechanisms used in the study. The dominant reaction which produces benzene is $C_6H_5CH_3+H \rightarrow A1+CH_3$. Though the increase in R_T implies an increase in toluene content, there is decrease in H radicals, which are produced from i-C3H7 and t-C4H9, and thus originated from iso-octane. Thus, the decrease in H radical is related to reduced iso-octane content at higher RT.

[2] R_T—Toluene ratio, defined as the liquid volume ratio of toluene in the binary mixture.

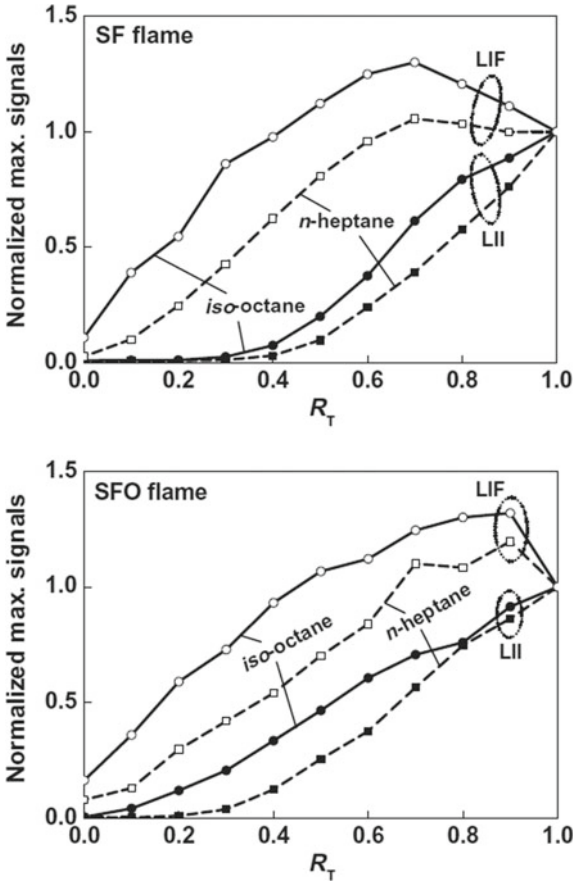

Fig. 1 Normalized maximum LII and LIF (400 nm) signals as a function of toluene ratio (R_T) in n-heptane/toluene (HT) and iso-octane/toluene (OT) in SF (top) and SFO flames. Adopted from [11]

Park et al. [24] reported a new set of experiments for OT and HT mixtures. As indicated in Fig. 2, toluene addition has a stronger effect on the formation of PAHs when added to n-heptane as compared to iso-octane (based on slopes), especially for smaller detection wavelength corresponding to smaller PAHs. They also developed a detailed mechanism with 574 species, which had the capability to predict PAHs species formed from multi-component blends. The mechanism was also able to capture the non-linear and synergistic effect on PAH formation in OT and HT flames. The cited study [24] also provided additional experimental data by measuring LII and LIF signals in flames burning PRF mixtures and TPRF mixtures. Results for the PRF flames are presented in Fig. 3, which plots the normalized maximum LIF and LII signals for PRF mixtures, in terms of octane ratio, R_i (defined as a molar ratio of iso-octane in the mixture). The experimental results indicate that PAH concentrations increase with increasing R_i, and the rate of increase is greater at higher wavelengths. The LIF data for shorter detection wavelength (330 nm) is nearly linear, while at a longer wavelength, the LIF data shows increasingly non-linear behavior with R_i.

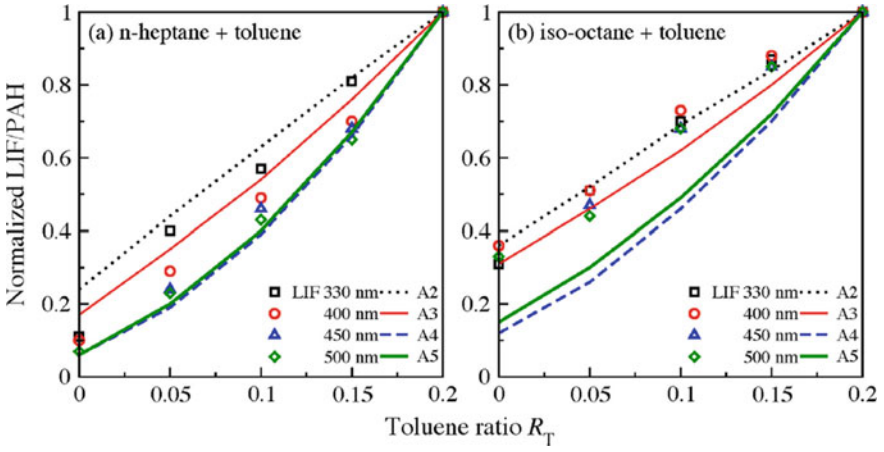

Fig. 2 Normalized maximum LII and LIF signals as a function of toluene ratio (R_T) in n-heptane/toluene and iso-octane/toluene mixture flames in SF condition. Values normalized with respect to $R_T = 0.2$. Adopted from [24]

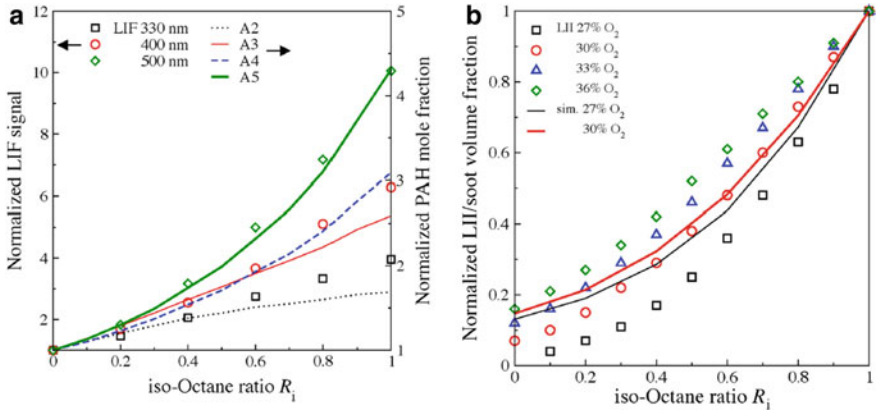

Fig. 3 Normalized maximum LII and LIF signals as a function of octane ratio (R_i) in n-heptane/iso-octane (PRF) mixture flames in SF condition. LII signals were captured at different oxygen molar concentrations in oxidizer stream. Values normalized with respect to $R_i = 0$ in (**a**) and $R_i = 1.0$ in (**b**). Adopted from [24]

Also, as indicated in Fig. 3b, LII signals, which correlate with soot show a non-linear increasing trend with R_i. Park et al. [24] performed simulations to calculate the soot volume fractions in flames burning iso-octane and n-heptane mixtures (Fig. 3b) by coupling the above mechanism with a detailed soot model. The results essentially captured the non-linear trend of soot volume fraction at different oxygen levels, thus confirming that the formation of PAHs and soot is related to the surrogate composition.

2.2 Ternary Blends

As stated in the preceding section, Park et al. [24] also performed flame experiments using TPRF ternary blends (iso-octane, n-heptane, and toluene) in order to examine the effect of fuel composition on PAH and soot emissions. A wide range of mixtures were considered with a fixed toluene fraction of 10% (T10PRF) and 20% (T20PRF), with the remaining comprised of iso-octane and n-heptane with varying iso-octane molar ratios (R_i). Figure 4 presents the normalized LIF signals and calculated peak PAHs mole fractions for T10PRF and T20PRF mixtures as a function of R_i. The experimental results indicate that the PAH formation trend for TPRF mixtures is similar to PRF mixtures, wherein PAHs increase at different rates at various detection wavelengths with varying Ri. However, the increase is fairly linear for both T10PRF and T20PRF mixtures, which is different from PRF mixtures. Moreover, the rate of increase (based on slope) is larger in T10PRF than the T20PRF mixtures. In addition, the mechanism can reasonably capture this trend of PAHs (A2-A5) formation for various TPRF mixtures. Figure 5 presents the normalized LII signals and calculated peak soot volume fractions for T10PRF and T20PRF mixtures as a function of R_i and at various oxygen levels in the oxidizer stream. LII signals increase linearly, in a fashion similar to LIF signals. The increase in LII signal at higher O_2 mole fraction is due to the higher flame temperature. Further, the results show that the rate of increase in soot volume fraction is smaller in higher O_2 concentration conditions than that in lower O_2 conditions. This indicates that the sensitivity of soot formation to octane ratio (R_i) diminishes as the O_2 mole Reactions R1303

fraction in the oxidizer stream increases. This is also true in T10PRF and T20PRF cases, where the sensitivity to R_i diminishes with the increase in toluene fraction. On the other hand, it is interesting to notice slightly higher soot formation in T20PRF flames when compared to T10PRF flames, while the PAH formation follows an opposite trend. In the cited study, a rate of production (ROP) analysis was performed to explain the effect of composition on PAHs formation. The results indicated that the odd-carbon number species (such as C_5H_5, $C_6H_5CH_2$, C_9H_7) and A1, which are responsible for the formation of higher PAH species, remain unaltered regardless of R_i, except for propargyl (C_3H_3) radical (which increases with increase in R_i). Benzene in TPRF mixtures is mainly produced from the reaction of toluene with H radical. The benzyl radical ($C_6H_5CH_2$) formed from toluene dehydrogenation, reacts with propargyl radicals and leads to the formation of A2 while the recombination of benzyl radicals forms A3 and the reaction of benzyl with indenyl (C_9H_7) radical leads to the formation of A4. Higher concentration of propargyl radicals enhances A2 formation, and also leads to another reaction ($A_2CH_2+C_3H_3 \rightarrow A_3 + 2H$) for A3 formation. More details on important reactions involved in formation of benzene and pyrene in ternary blends TPRF and EPRF, with regards to octane sensitivity are discussed in a later section.

The results for OT and HT binary mixtures have shown that toluene has a significant effect on PAHs and soot formation. However, details regarding the effect of toluene on PAH and soot formation in ternary mixtures (TPRF) are lacking in

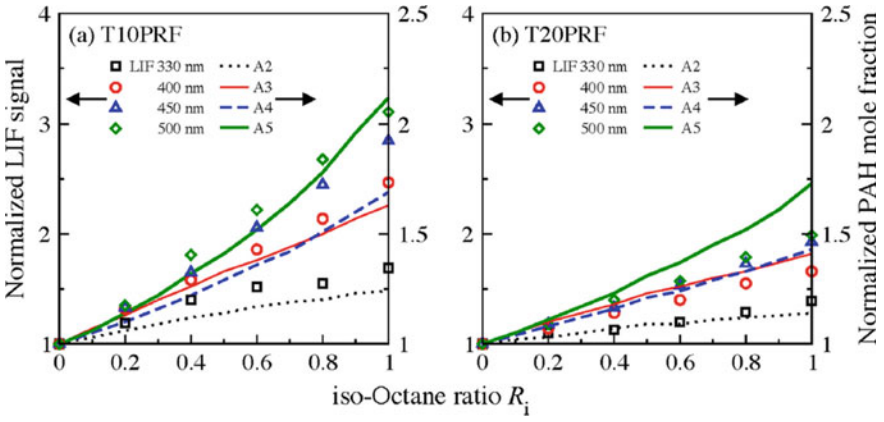

Fig. 4 Normalized maximum LIF signals (symbols) and calculated normalized peak PAH mole fractions as a function of octane ratio (R_i) in T10PRF and T20PRF counterflow diffusion flames. Normalized using values at $R_i = 0$. Adopted from [24]

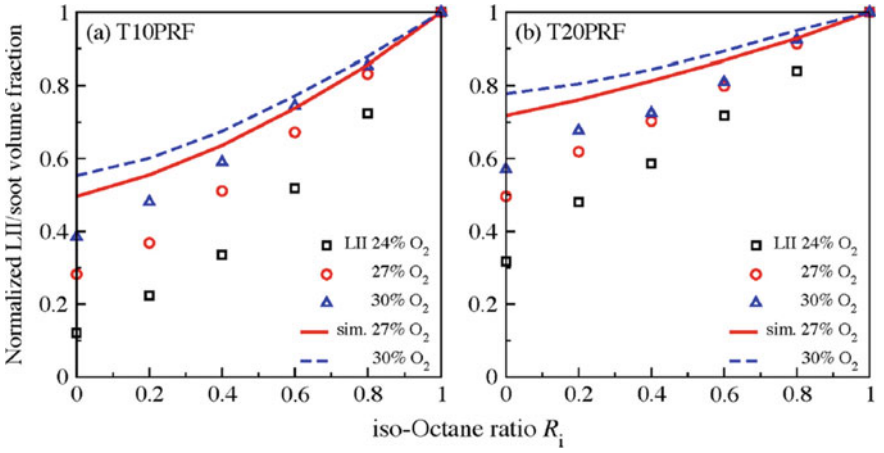

Fig. 5 Normalized maximum LII signals (symbols) and calculated normalized peak soot volume fraction as a function of octane ratio (R_i) in T10PRF and T20PRF counterflow diffusion flames. LII signals were captured for different oxygen mole fractions in oxidizer stream. Normalized using values at $R_i = 1$ Adopted from [24]

the literature. With this motivation, Shao et al. [26] performed experiments and elucidated the effect of fuel composition (with regards to toluene content) on PAH formation during pyrolysis in TPRF mixtures. Two ternary blends (TPRF70 and TPRF97.5), representing low octane (RON 70) and high octane (RON 97.5) gasoline, were examined in a jet-stirred reactor. The TPRF70 and TPRF97.5 blends have an octane sensitivity of $S = 4$ and 10.9, respectively. The molar compositions in the order toluene/is-octane/n-heptane were 0.285/0.365/0.35 and 0.775/0.08/0.145 for

TPRF70 and TPRF97.5, respectively. Thus, TPRF70 had significantly low toluene content when compared to TPRF97.5. Conventional knowledge would suggest that TPRF97.5 produces significantly more PAHs than TPRF70 due to higher toluene content in the former. However, experimental and numerical analysis carried by Shao et al. have shown that PAHs formation during pyrolysis is related to the mixture composition rather than on the concentration of single component of the mixture. It is noticed that, despite the significantly low toluene content in TPRF70, it produced slightly higher benzene and naphthalene (A2) compared to TPRF97.5, while the pyrolysis of TPRF97.5 produced slightly higher amounts of phenanthrene (A3) and pyrene (A4). This anomaly is explained with the help of rate of consumption of each component and the production of intermediates formed during pyrolysis of fuel. It is noticed that the rate of consumption of a fuel component is significantly different when part of a mixture compared to when used as a sole fuel.

Figure 6 compares the consumption of toluene, iso-octane, and n-heptane when part of the mixture (TPRF70 and TPRF97.5) and when used as sole fuels in JSR and flow reactor (FR) pyrolysis. It is noticed that toluene consumption is promoted in TPRF mixtures relative to when it is pure fuel. This is attributed to toluene consumption by radicals, such as H, CH_3, C_3H_3, C_3H_2, produced during the pyrolysis of iso-octane and n-heptane. While n-heptane is consumed at slightly lower temperatures when part of mixtures, there is not any significant effect on the consumption of iso-octane when part of mixture. Further, as mentioned by Park et al. [24], the main source of benzene formation is the reaction of toluene with H atoms in TPRF mixtures. However, due to the higher concentrations of iso-octane and n-heptane in TPRF70, there is increased production of smaller hydrocarbon intermediates, such

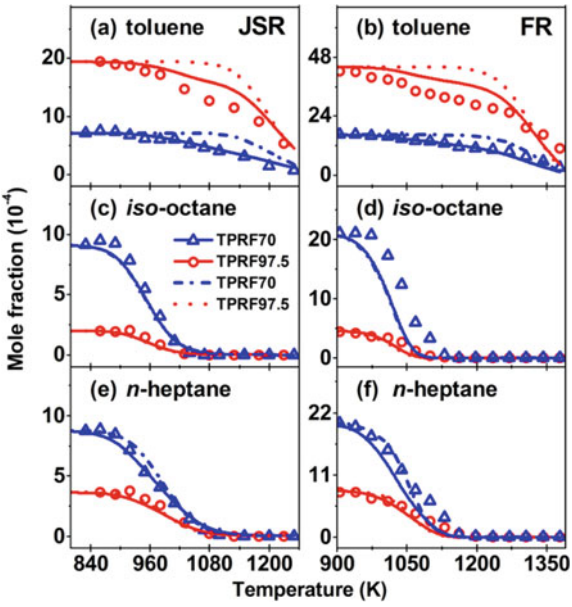

Fig. 6 Comparison of fuel component consumption when part of mixture (TPRF70 and TPRF97.5) (symbols and solid lines) and when used as sole fuel (dashed line) in JSR and FR pyrolysis. Symbols are experiment results while lines are simulation results. Adopted from [26]

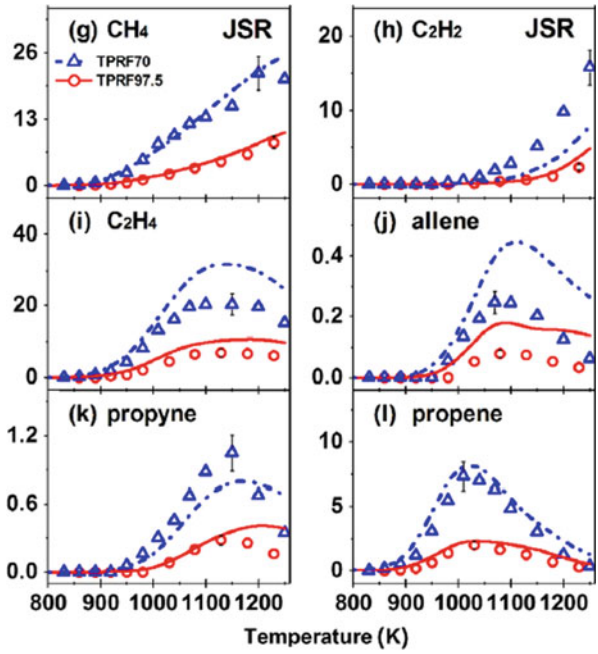

Fig. 7 Mole fraction of intermediates produced by TPRF70 (blue and dashed line) and TPRF97.5 (red and solid line) in JSR and FR pyrolysis. Symbols are experiment results while lines are simulation results. Adopted from [26]

as allene, acetylene, ethylene, propargyl, propene, and propyne in TPRF70 than in TPRF97.5. Figure 7 presents the mole fractions of the above-mentioned intermediates (except propargyl) produced during the pyrolysis of TPRF70 and TPRF97.5. Note that propargyl (C_3H_3) is mainly produced from allene and propyne. All these intermediates aide in the production of benzene through additional routes in TPRF70. For instance, the reaction of propargyl radical with allyl radical contributes nearly 28% of benzene formation in TPRF70, while its contribution is only 3% in TPRF97.5. Thus, the presence of other routes for benzene formation leads to comparable or slightly higher benzene production in TPRF70 compared to that in TPRF97.5, although TPRF97.5 has significantly high amounts of toluene. Further, propargyl also plays an important role in the production of naphthalene (A2). Dehydrogenation of 1,2-dihydronaphthalenyl radical ($C_{10}H_9$) leads to the formation of A2, where $C_{10}H_9$ is mainly produced from the reaction between benzyl and propargyl radicals. Further, the mole fractions of three and four ring structures A3 and A4 are slightly higher in TPRF97.5 than TPRF70. This is due to the increased amount of benzyl radicals produced from toluene dehydrogenation that leads to the formation of bibenzyl ($C_{14}H_{14}$), and this forms A3 and A4 through traditional HACA mechanism.

2.3 *Effect of Octane Sensitivity on PAHs—Ternary and Quaternary Mixtures*

Fuel Octane Sensitivity (S) as defined above is the difference between RON and MON. It is one such fuel property that is directly related to the fuel composition. It accounts for the non-paraffinic content in the fuel. Results in the preceding sections mainly focused on evaluating the effect of blend composition on PAHs and soot emissions. This section provides additional results and a more detailed discussion on the effect of blend composition and octane sensitivity on PAHs formation. Blends with a fixed RON of 70, but with different S values are considered, where the sensitivity is derived from toluene and/or ethanol. Results are presented for counterflow partially premixed flames (PPFs) with $\Phi = 2$. Table 1 provides the compositions of various binary, ternary, and quaternary blends under consideration. Jain et al. [31] evaluated four different mechanisms to identify a more suitable mechanism to examine the PAHs formation in flames burning TPRF mixtures. Based on this evaluation (details discussed in the cited study), the Park et al. mechanism [24] with 574 species and 3379 reactions was used for the investigation. Figure 8, which is a replica of Fig. 4, depicts the normalized maximum LIF signals and the computed normalized maximum PAHs (A2 to A5) mole fractions versus R_i in counterflow diffusion flames for T10PRF and T20PRF ternary blends containing 10% and 20% toluene by volume, respectively. Based on these results providing the validation for the mechanism, Jain et al. [31] performed a detailed investigation on the effects of blend composition and octane sensitivity on PAHs formation in Partially Premixed Flames (PPFs).

Figure 9a depicts the computed flame structures in terms of temperature and heat release rate (HRR) profiles for the four blends, namely PRF70, TPRF-4, EPRF-4, and ETPRF-4. The flame structure for all the four blends is characterized by two reaction zones, a rich premixed zone (RPZ) located on the fuel side, and a non-premixed

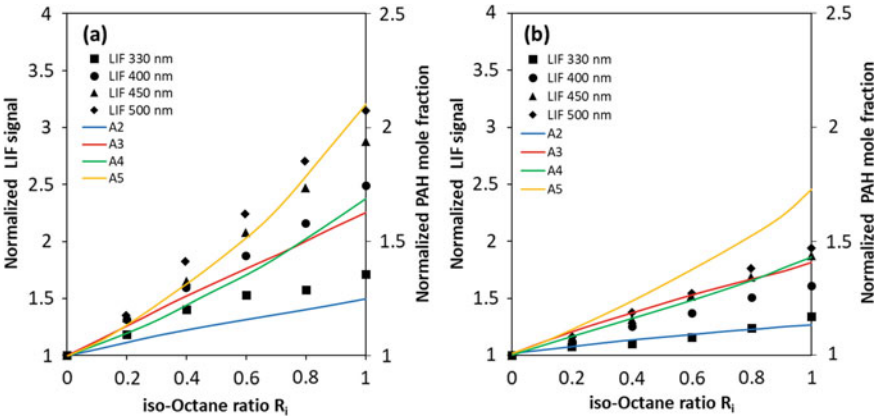

Fig. 8 Measured normalized maximum LIF signals [24] and computed PAHs for **a** T10PRF and **b** T20PRF blends using the Park et al. mechanism. Adopted from [31]

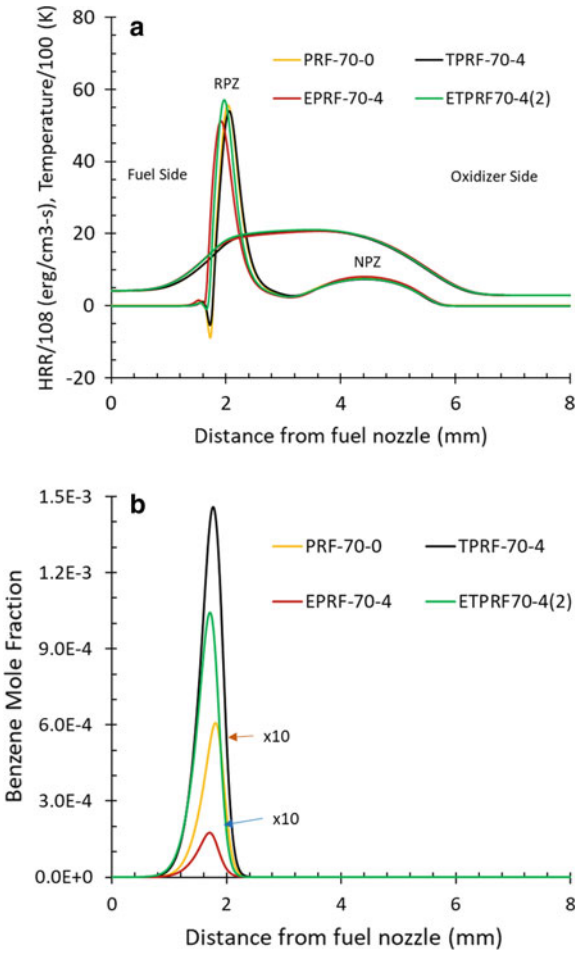

Fig. 9 Flame structure of various fuel mixtures under partially premixed flame at $\phi = 2$. **a** Temperature, HRR, and **b** benzene mole fractions. Adopted from [41]

zone (NPZ) located on the oxidizer side. As discussed in previous studies [39, 40], the heat release associated with the RPZ is mainly due to fuel pyrolysis/oxidation to produce CO, H_2, and intermediate hydrocarbons, whereas the heat release in NPZ is mainly due to the oxidation of CO and H_2. For these four blends, we observe only some minor quantitative differences in HHR profiles due to differences in fuel properties. Thus, the flame structures in terms of HHR and temperature profiles are essentially the same for the four blends. The HRR and temperature profiles for the other four blends (listed in Table 1) are also nearly the same, and therefore not shown. The peak temperatures for these blends are in the range 2070–2100 K. Figure 9b presents the benzene mole fraction profiles for the same four blends. As indicated, the formation of benzene occurs in the RPZ for all the blends. However, the amount of benzene formed depends strongly on the blend composition and octane sensitivity. To better comprehend the relative differences in the formation of PAHs

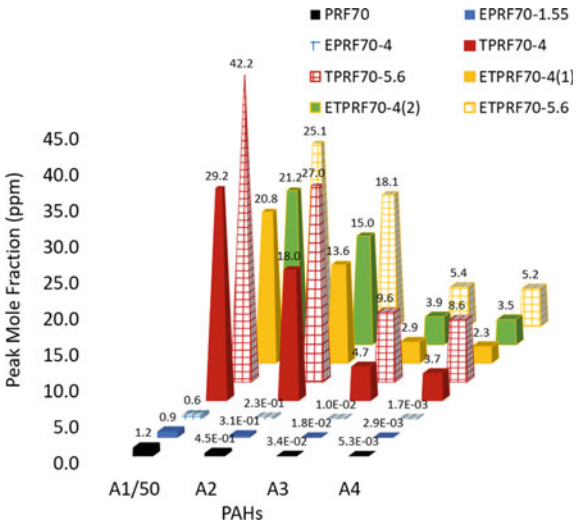

Fig. 10 Comparison of peak PAH mole fractions for various fuel mixtures

species for the various blends, the peak mole fractions of these PAH species for the eight surrogate fuels under consideration are plotted in a bar chart in Fig. 10. Note that in this figure, A1 mole fraction is scaled down by a factor of 50, while the other species indicate their true values. When an aromatic compound, such as toluene, is added to a binary blend (made of only paraffinic compounds), the concentrations of PAH species go up significantly, by nearly two orders of magnitude in general. Moreover, the higher octane sensitivity caused by increased toluene content further intensifies the formation of PAH species, as can be observed from the comparison of their concentrations for TPRF70-4 and TPRF70-5.7 blends. However, the results for EPRF blends indicate the opposite effect of octane sensitivity, i.e., the increase in octane sensitivity induced from ethanol content reduces the amounts of PAH species formed. Moreover, the reduction in PAH formation can be directly related to ethanol fraction in the blend. The EPRF70-4 blend also has much lower concentrations of PAHs when compared to EPRF70-1.55. Hence, the main observation here is that higher octane sensitivity is not always an indicator of increased PAH emissions. While TPRF70-4 and EPRF70-4 blends have the same RON (= 70) and octane sensitivity (S = 4), the TPRF70-4 blend tends to form significantly higher amounts of PAH species than EPRF70-4 due to the presence of toluene. Thus, for ternary blends, there does not seem to be any direct relation between octane sensitivity and PAHs emissions. Rather the amount of PAH species formed is related to the propensity of the third component. On the other hand, for four-component blends (ETPRFs), where sensitivity is induced from both toluene and ethanol, there seems to some link between S and PAH emissions. Figure 10 indicates that ETPRF70-4(1) and ETPRF70-4(2) blends produce similar amounts of PAHs. For instance, the maximum difference between peak mole fractions of PAHs is ± 1.4 ppm. ETPRF70-4(1) and ETPRF70-4(2) have the same RON and S values but significantly differ in their compositions. For instance, ETPRF70-4(1) contains 21% ethanol by volume, while

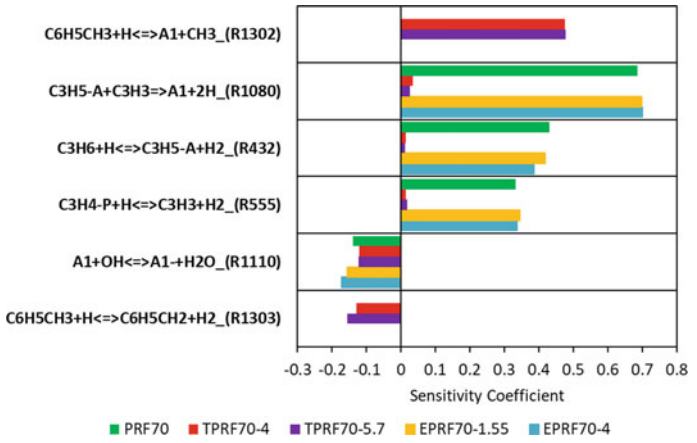

Fig. 11 Sensitivity coefficients of key reactions for benzene (A1) formation in PRF70, TPRF70-4, TPRF70-5.7, EPRF70-1.55, and EPRF70-4 partially premixed flames at $\phi = 2$. Adopted from [42]

ETPRF70-4(2) contains only 4.8% ethanol. Moreover, an increase in sensitivity to 5.6 (ETPRF70-5.7) leads to a significant increase in PAH formation, indicating some correlation between S and PAH emissions, when RON is fixed.

Figures 11 and 13 summarize the results of reaction sensitivity analysis for the formation of benzene (A1) and pyrene (A4), respectively, in PRF70 (S = 0), TPRF70-4, TPRF70-5.7, EPRF70-1.55 and EPRF70-4 flames. Benzene is known to be a key precursor for the formation of larger PAH species, such as pyrene. Moreover, since the soot particle inception models are often based on A1 and A4 concentrations, these species are also important for accurate soot predictions. Figure 11 presents the sensitivity coefficients for key reactions associated with benzene formation for the five blends under consideration. The reaction sensitivity analysis was done at a location in the flame corresponding to the peak A1 concentration. Note that a positive sensitivity coefficient for a given reaction implies that increasing the rate of that reaction promotes the production of species, while a negative value indicates that it retards the formation of that species. Figure 11 indicates that the reaction R1302 has high positive sensitivity for A1 production in TPRF70-4 and TPRF70-5.7 flames. This reaction provides a direct route for A1 formation and involves toluene reacting with hydrogen radical. Since PRF70 and EPRF70 blends do not contain toluene, this reaction is not relevant in these flames.

The analysis further shows that for PRF70 and EPRF70 (1.55 and 4) blends, the dominant path for A1 formation is through R1080, involving the reaction between propargyl (C_3H_3) and allyl (C_3H_5) radicals. As indicated in Fig. 11, the reaction R1080 has a much higher positive sensitivity for PRF70 and EPRF70 blends compared to that for TPRF70 blends. Similarly, reactions R432 and R555, which have high positive sensitivity for PRF70 and EPRF70 blends, lead to the formation of propargyl (C_3H_3) and allyl (C_3H_5) radicals, respectively, which then form A1

through R1080. Further, the A1 oxidation reaction (R1110) shows negative sensitivity for all the blends, since in this reaction A1 oxidizes to form benzene radical (A1-), which then reacts to form larger PAHs. Finally, R1303, which involves H-abstraction reaction for toluene forming toluene radical, has negative sensitivity, since toluene radical further reacts to form A4 directly.

Figure 12 presents the profiles of major and minor species that participate in the formation of benzene in partially premixed flames at $\phi = 2$ for the five fuel blends (PRF70, TPRF70-4, TPRF70-5.7, EPRF70-1.55, and EPRF70-4). As discussed above in the context of Fig. 10, the amount of benzene formed is the highest in TPRF70-5.7 flame due to high toluene content, and the lowest in EPRF70-4 flame due to the presence of ethanol. Thus, the amount of benzene formed in partially premixed flames for ternary blends depends on the propensity of the third component in the blend. PAH emissions increase with the amount of toluene present in the blend, while more ethanol in EPRF blends results in reduced PAH emissions. This is further confirmed by the benzene profiles shown in Fig. 12a, indicating significantly higher benzene peak for ternary blends with toluene compared to that for blends with ethanol or for binary blend. Also, propene represents an important intermediate

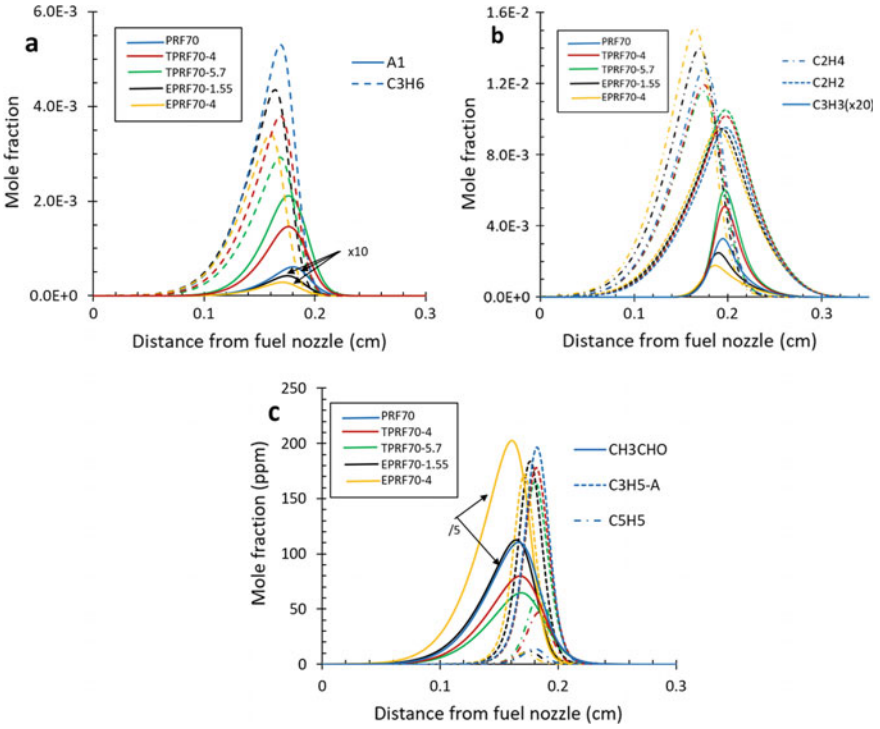

Fig. 12 Profiles of A1 (benzene) and intermediate species in PRF70, TPRF70, and EPRF70 partially premixed flames at $\phi = 2$; **a** A1 and C_3H_6, **b** C_2H_2, C_2H_4, C_3H_3 **c** CH_3CHO, C_3H_5-a, and C_5H_5. Adopted from [42]

species in the benzene formation route from iso-octane and n-heptane. As seen in Fig. 12a, the peak mole fractions of propene are the highest and lowest in PRF70 and EPRF70-4 flames, respectively. The mole fraction of propene formed nearly follows the iso-octane content in the fuel. Figure 12b plots the ethylene (C_2H_4), acetylene (C_2H_2), and propargyl (C_3H_3) profiles. As discussed earlier, these species play an important role in benzene formation. As indicated, there is a relatively small effect of toluene fuel sensitivity on the formation of ethylene since it is mostly formed directly through n-heptane and iso-octane. However, we notice higher amounts of ethylene in EPRF blends, since ethanol directly forms ethylene. Hence there is a direct correlation between ethanol and ethylene content, as indicated by the fact that EPRF70-4 flame has higher ethylene compared to EPRF70-1.55 flame. But interestingly, TPRF blends have higher acetylene and thus higher propargyl concentrations compared to EPRF blends. For all these blends, acetylene is formed mainly from ethylene, while propargyl is mainly produced from reactions involving propene, allyl, and acetylene. Further, TPRF blends have an additional route for the formation of acetylene and propargyl. This involves cyclopentadienyl (C_5H_5), which is mainly formed from the reduction of toluene. Thus, as shown in Fig. 12c, a higher concentration of toluene allows for increased formation of C_5H_5, which later reduces into acetylene and propargyl. Moreover, acetylene formed in EPRF blends tends to get oxidized, forming formaldehyde (CH_3CHO), as shown in Fig. 12c. Thus, we notice smaller amounts of acetylene and propargyl in EPRF blends. Hence, the presence of toluene in TPRF blends, apart from the direct route to form benzene, also plays an important role in the formation of acetylene and propargyl. These species are subsequently involved in the formation of benzene and higher PAHs, thus dramatically increasing PAH emissions.

Figure 13 presents the results of sensitivity analysis for pyrene (A4) formation in PRF70, TPRF70-4, TPRF70-5.7, EPRF70-1.55, and EPRF70-4 partially premixed

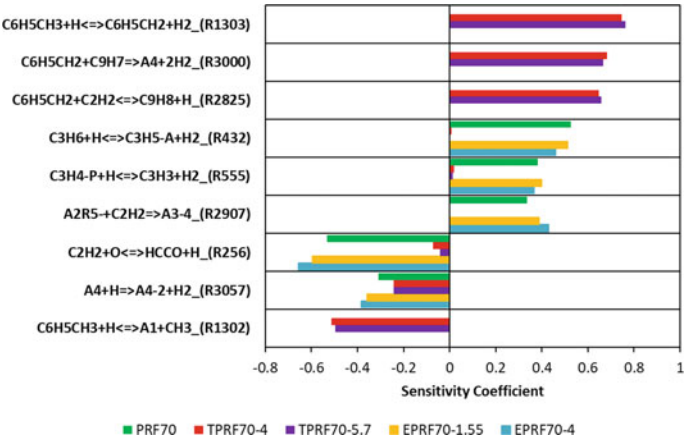

Fig. 13 Sensitivity coefficients of key reactions for pyrene (A4) formation in PRF70, TPRF70-4, TPRF70-5.7, EPRF70-4, and EPRF70-5.6 partially premixed flames ($\phi = 2$). Adopted from [42]

flames. Again, the sensitivity coefficients were calculated at a location corresponding to the peak A4 mole fraction. Reactions R1303, R3000, and R2825 show high positive sensitivity for A4 formation in TPRF70-4 and TPRF70-5.7 flames. All these reactions involve toluene or benzyl radical, which promote the formation of A4. The dominant A4 formation path for TPRF70-4 and TPRF70-5.7 is through reaction R3000, in which benzyl radical ($C_6H_5CH_2$) reacts with indenyl radical (C_9H_7) to form A4. Reactions R1303 and R2825 form these two radicals and thus promote the formation of A4. Note that the literature indicates significant variation in the reaction rate constant for R3000 [43], and thus requires further investigation. R432, R555, and R2907 are important reactions for the formation of A4 in PRF70 and EPRF70 (a and b) flames. As noted earlier, reactions R432 and R555 are also important for the formation of A1. Reaction R256 has negative sensitivity coefficient since it converts acetylene (C_2H_2), which is important for the production of PAHs, into oxygenated products, such as HCCO and CH_3CHO. Thus, this reaction (R256) has higher sensitivity in EPRF blends, thus reduces the amount of acetylene formed, and subsequently the amount of A4 formed. Reaction R3057 shows negative sensitivity coefficient since it involves the consumption of A4 through H-abstraction, while R1302 is an important reaction for the formation of A1, and thus reduces the formation of A4 through reactions R1303 and R3000.

3 Summary

In this chapter, we have discussed research dealing with the effects of fuel composition and octane sensitivity (S) on PAHs emissions in laboratory-scale configurations. The configurations include counterflow diffusion and partially premixed flames, and jet-stirred reactor and flow reactor focusing on fuel pyrolysis. Several surrogates with two, three, and four components, containing different amounts of n-heptane, iso-octane, toluene, and ethanol, are considered. Surrogates are formulated in such a way so as to maintain a RON = 70 and S = 0–5.6. Important observations are as follows:

1. Results for counterflow diffusion flames with binary n-heptane/toluene and iso-octane/toluene mixtures indicate a non-monotonic variation of PAHs emission with respect to toluene fraction in the mixture, implying a synergistic effect on PAHs emissions at higher toluene content ($R_T > 0.7$). This is due to the compositional effect on PAH chemistry, as confirmed by the computational study of Park et al. However, this synergistic behavior is not confirmed by the LII data or with respect to soot emissions. Results further indicate that the addition of toluene to iso-octane or n-heptane has a non-linear effect on PAHs and soot emissions with respect to the toluene content. For ternary blends (n-heptane, iso-octane, toluene), results indicate higher PAHs formation in T10PRF (10% toluene) flames compared to T20PRF (20% toluene) flames, while the soot formation follows an opposite trend.

2. Shao et al. [26] reported results on the pyrolysis of ternary blends in a jet-stirred reactor. An interesting observation was that the pyrolysis of TPRF70 and TPRF97.5 blends produced similar amounts of PAH species (A1–A4), although TPRF97.5 has significantly higher toluene (77.5%) compared to TPRF70 (28.5%). This anomaly was explained with the help of the rate of consumption of each component and the production of intermediates formed during pyrolysis. It was noted that the rate of consumption of an individual component is significantly modified when part of a blend. For instance, the rate of consumption of toluene was enhanced in TPRF blends mixtures relative to that when toluene is pure fuel. This is attributed to the toluene consumption by radicals, such as H, CH_3, C_3H_3, C_3H_2, produced during the pyrolysis of iso-octane and n-heptane.
3. For all eight blends (ternary and quaternary), the partially premixed flame structures are similar, characterized by a rich premixed zone (RPZ) on the fuel side, and a non-premixed zone (NPZ) on the oxidizer side. Most PAH species are produced close to RPZ for all the blends and consumed in the region between RPZ and the stagnation plane. However, PAHs emissions vary significantly depending upon the blend composition and octane sensitivity (S). For ternary blends with toluene, an increase in S results in higher PAHs emission. On the other hand, with ethanol as the third component, an increase in S reduces the amounts of PAHs formed. Thus, the PAHs emission is related to the propensity of the third component to form PAH species, rather than to S. For instance, TPRF70-a, and EPRF70-b blends have the same RON = 70 and S = 4, but TPRF70-a produces significantly higher amounts of PAHs. Thus, for these ternary blends, RON and S are not true indicators of PAHs emissions. PAHs emissions are more related to the blend composition.
4. Compared to ternary blends, results for quaternary blends indicate correlation between S and PAH emissions. For instance, ETPRF70-4(1) and ETPRF70-4(2) blends, which have the same RON and S values, but significantly different compositions, tend to produce a similar amount of PAHs. Moreover, an increase in S from 4.0 to 5.6 (ETPRF70-5.7) leads to a significant increase in PAHs formation, again indicating correlation between S and PAHs, when RON is fixed. Thus, further studies are warranted to examine different ternary and quaternary blends for a wider range of RON and S values. Future studies should also consider blends in which S is derived from various bio-derived fuels.

References

1. ExxonMobil. Outlook for energy; a view to 2040. https://corporate.exxonmobil.com/en/energy/energy-outlook/a-view-to-2040#/section/1-key-takeaways-at-a-glance
2. Wang H (2011) Formation of nascent soot and other condensed-phase materials in flames. Proc Combust Inst 33:41–67

3. Kennedy IM (2007) The health effects of combustion-generated aerosols. Proc Combust Inst 31(2):2557–2770
4. Oberdorster G, Sharp Z, Atudorei V, Elder A, Gelein R, Kreyling W, Cox C (2004) Translocation of inhaled ultrafine particles to the brain. Inhal Toxicol 16:437–445
5. Kukkadapu G, Kumar K, Sung CJ, Mehl M, Pitz WJ (2015) Autoignition of gasoline surrogates at low temperature combustion conditions. Combust Flame 162(5):2272–2285
6. Epping K, Aceves S, Bechtold R, Dec JE (2002) The potential of HCCI combustion for high efficiency and low emissions. SAE Technical Paper 2002-01-1923
7. Chang J, Kalghatgi G, Amer A, Viollet Y (2012) Enabling high efficiency direct injection engine with naphtha fuel through partially premixed charge compression ignition combustion. SAE Technical Paper 2012-01-0677
8. Putrasari Y, Lim O (2019) A review of gasoline compression ignition: a promising technology potentially fueled with mixtures of gasoline and biodiesel to meet future engine efficiency and emission targets. Energies 12:238. https://doi.org/10.3390/en12020238
9. Zhang Y, Kumar P, Traver M, Cleary D (2016) Conventional and low temperature combustion using naphtha fuels in a multi-cylinder heavy-duty diesel engine. SAE Int J Engines 9:1021–1035
10. Chang J, Viollet Y, Amer A, Kalghatgi G (2013) Fuel economy potential of partially premixed compression ignition (PPCI) combustion with naphtha fuel. SAE Technical Paper, paper 2013-01-2701
11. Choi BC, Choi SK, Chung SH (2011) Soot formation characteristics of gasoline surrogate fuels in counterflow diffusion flames. Proc Combust Inst 33:609–616
12. Inal F, Senkan SM (2002) Effects of equivalence ratio of species and soot concentrations in premixed n-heptane flames. Combust Flame 131:16–28
13. Edgar G (1927) Measurement of knock characteristics of gasoline in terms of a standard fuel. Ind Eng Chem 19(1):145–146
14. Kalghatgi G, Babiker H, Badra J (2015) A simple method to predict knock using toluene, n-heptane and iso-octane blends (TPRF) as gasoline surrogates. SAE Int J Engines 8:505–519
15. Shankar VSB, Sajid MB, Al-Qurashi K, Atef N, Alkhesho I, Ahmed A, Chung S, Roberts WL Morganti K (2016) Primary reference fuels (PRFs) as surrogates for low sensitivity gasoline fuels. In: SAE 2016 World congress and exhibition
16. Gauthier B, Davidson D, Hanson R (2004) Shock tube determination of ignition delay times in full-blend and surrogate fuel mixtures. Combust Flame 139:300–311
17. Sarathy SM, Farooq A, Kalghatgi GT (2018) Recent progress in gasoline surrogate fuels. Prog Energy Combust Sci 65:67–108
18. Jain SK, Aggarwal SK (2018) Compositional effects on the ignition and combustion of low octane fuels under diesel conditions. Fuel 220:654–670
19. Knop V, Pera C, Duffour F (2013) Validation of a ternary gasoline surrogate in a CAI engine. Combust Flame 160:2067–2082
20. Andrae JC, Björnbom P, Cracknell R, Kalghatgi GT (2007) Autoignition of toluene reference fuels at high pressures modeled with detailed chemical kinetics. Combust Flame 149:2–24
21. Knop V, Pera C, Duffour F (2013) Validation of a ternary gasoline surrogate in a CAI engine. Combust Flame 160(10):2067–2082
22. Rapp VH, Cannella WJ, Chen JY, Dibble RW (2013) Predicting fuel performance for future HCCI engines. Combust Sci Technol 185(5):735–748
23. Chaos M, Zhao Z, Kazakov A, Gokulakrishnan P, Angioletti M, Dryer FL (2007) A PRF+toluene surrogate fuel model for simulating gasoline kinetics. In: 5th US combustion meeting, pp 25–28
24. Park S, Wang Y, Chung SH, Sarathy SM (2017) Compositional effects on PAH and soot formation in counterflow diffusion flames of gasoline surrogate fuels. Combust Flame 178:46–60
25. Yanzhao A, Vedharaj S, Vallinayagam R, Dawood A, Masurier J, Najafabadi MI, Somers B, Chang J, Johansson B (2017) Effect of aromatics on combustion stratification and particulate emissions from low octane gasoline fuels in PPC and HCCI mode. SAE Technical Paper, Paper 2017-24-0086)

26. Shao C, Wang H, Atef N, Wang Z, Chen B, Almalki M, Zhang Y, Cao C, Yang J, Sarathy SM (2019) Polycyclic aromatic hydrocarbons in pyrolysis of gasoline surrogates (n-heptane/iso-octane/toluene). Proc Combust Inst 37:993–1001
27. Cancino LR, Fikri M, Oliveria AAM, Schulz C (2009) Autoignition of gasoline surrogate mixtures at intermediate temperatures and high pressures: Experimental and numerical approaches. Proc Combust Inst 32:501–508
28. Foong TM, Morganti KJ, Brear MJ, da Silva G, Yang Y, Dryer FL (2014) The octane numbers of ethanol blended with gasoline and its surrogates. Fuel 115:727–739
29. Solaka H, Tuner M, Johansson B, Cannella W (2013) Gasoline Surrogate Fuels for Partially Premixed Combustion of Toluene Ethanol Reference Fuels. SAE Technical Paper 2013-01-2540. https://doi.org/10.4271/2013-01-2540
30. Noh HK, No S-Y (2017) Effect of bioethanol on combustion and emissions in advanced CI engines: HCCI, PPC and GCI mode—a review. Appl Energy 208:782–802
31. Jain SK, Badhe AS, Aggarwal SK (2018) Effect of fuel sensitivity on PAH emissions in low-octane naphtha partially premixed flames. AIAA SciTech Forum, Kissimmee, FL, Jan 8–12
32. Liu F, Hua Y, Wu H, Lee C, He X (2019) An experimental study on soot distribution characteristics of ethanol-gasoline blends in laminar diffusion flames. J Energy Inst 91:997–1008
33. Cho J, Si W, Jang W, Jin D, Myung C, Park S (2015) Impact of intermediate ethanol blends on particulate matter emission from a spark ignition direct injection (SIDI) engine. Appl Energy 160:592–602
34. Inal F, Senkan SM (2002) Effects of oxygenate additives on polycyclic aromatic hydrocarbons (PAHs) and soot formation Combust Science Technol 174:(9)1–19. https://doi.org/10.1080/00102200290021353
35. Xu H, Yao C, Xu G, Wang Z, Jin H (2013) Experimental and modelling studies of the effects of methanol and ethanol addition on the laminar premixed low-pressure n-heptane/toluene flames. Combust Flame 160:1333–1344
36. Maricq MM (2012) Soot formation in ethanol/gasoline fuel blend diffusion flames. Combust Flame 159(1):170–180
37. Khosousi A, Liu F, Dworkin SB, Eaves NA, Thomson MJ, He X, Wang J et al (2015) Experimental and numerical study of soot formation in laminar coflow diffusion flames of gasoline/ethanol blends. Combust Flame 162(10):3925–3933
38. Al Ramadan AS, Sarathy SM, Khurshid M, Badra J (2016) A blending rule for octane numbers of PRFs and TPRFs with ethanol. Fuel 180:175–186
39. Javed T, Lee C, AlAbbad M, Djebbi K, Beshir M, Badra J, Curran H, Farooq A (2016) Ignition studies of n-heptane/iso-octane/toluene blends. Combust Flame 171:223–233
40. Berta P, Aggarwal SK, Puri IK (2006) An experimental and numerical investigation of n-heptane/air counterflow partially premixed flames and emission of NOx and PAH species. Combust Flame 145:740–764
41. Fu X, Han X, Brezinsky K, Aggarwal SK (2013) Effect of fuel molecular structure and premixing on soot emissions from n-heptane and 1-heptene flames. Energy Fuels 27:6262–6272
42. Jain SK, Badhe AS, Kalvakala KC, Aggarwal SK, Effect of fuel sensitivity on PAH emissions in partially premixed counterflow flames with low octane fuel. Submitted to Fuel journal
43. Sinha S, Rahman RK, Raj A (2017) On the role of resonantly stabilized radicals in polycyclic aromatic hydrocarbon (PAH) formation: pyrene and fluoranthene formation from benzyl–indenyl addition. Phys Chem Chem Phys 19:19262–19278

Hybrid RANS/LES Simulation of Methane–LO_x Combustion

Kisalaya Mishra, Malay K. Das, Ashoke De, and Kamal K. Kar

1 Background

The latest developments in rocket engine design have highlighted reusability issues of multi-stage orbit launch systems. Future space transportation solutions seek a reusable first phase using liquid oxygen and methane combination and a subsequent reusable or expendable phase using oxygen and hydrogen combination as propellants. Hence, liquid rocket engines operating with cryogenic conditions using oxygen–methane (Lo_x/CH_4) show superior performance and characteristics for the development of reusable launch vehicles (RLV). This particular fuel combination is promising [1] because compared to hydrogen, methane has a better thrust-to-weight ratio, lower diffusivity, and higher liquefaction temperature, which allows the design of lighter tanks and incorporation of higher payload carrying capacity. Methane has a higher specific impulse compared to kerosene, better cooling capacity [2], and reduced coking behavior [3]. Most of the liquid-propellant rocket engines operate at very high chamber pressures for superior performance. In such engines, fuel and oxidizer are injected as a spray of droplets or as gas streams. At supercritical conditions, the injected jets undergo a transcritical change of state; the liquid and gaseous phases are not easily distinguishable. The reacting flow properties resemble liquid-like densities, gas-like diffusivities, and pressure-dependent solubility, and processes like vaporization and atomization are replaced by turbulent-driven convection and diffusion mixing process. At such extreme conditions, surface tension and latent heat

K. Mishra · M. K. Das · K. K. Kar
Department of Mechanical Engineering, Indian Institute of Technology Kanpur, Kanpur 208016, India

A. De (✉)
Department of Aerospace Engineering, Indian Institute of Technology Kanpur, Kanpur 208016, India
e-mail: ashoke@iitk.ac.in

© Springer Nature Singapore Pte Ltd. 2021

A. De et al. (eds.), *Sustainable Development for Energy, Power, and Propulsion*, Green Energy and Technology,
https://doi.org/10.1007/978-981-15-5667-8_9

do not come into effect due to the absence of liquid–gas bonds [4]. Keeping this in mind, near the critical point, small changes of the state have a massive impact on transport properties. This leads to large gradients in density and other thermodynamics properties amid the mixing process. As the flame interacts with fluid dynamics, turbulence is modified by combustion through large fluctuations in kinematic viscosity and strong flow acceleration due to significant temperature changes induced by heat release. This mechanism is referred to as flame generated turbulence. Parallelly turbulence impacts the mixing process and can alter flame structure due to the fluctuating strain rates associated with turbulent eddies. This may enhance or even inhibit the processes involved in a chemical reaction.

To carry out CFD for reacting flows, turbulence modeling is an essential part. In terms of computational requirements, DNS is the most computationally expensive and can be applied realistically to simple geometries and low Reynolds numbers. LES can be used to deal with high Reynolds numbers on relatively coarser grids. The numerical accuracy of LES results is directly limited by the sub-grid-scale models used. RANS is computationally the least demanding method, but its accuracy is constrained by the closure models describing turbulence chemistry interactions. Combustion is usually dealt with in two regimes premixed combustion and non-premixed combustion. In non-premixed combustion, fuel and oxidizer are introduced separately, and combustion occurs at the interface of the two regions. Some of the salient features of non-premixed flames include diffusion flames, fast chemistry description, and jet flame-like structure. Molecular diffusion plays a crucial role in non-premixed combustion because the reacting species molecules need to reach the flame front for the reaction to happen. Diffusion flames do not feature a propagation speed, and the flame thickness is controlled by flow conditions. This results in difficulties while defining characteristic scales for non-premixed combustion. Coming to flame structure, a typical non-premixed flame consist of a thin flame post injector orifice, and the flame widens downstream into a conical shape comprising mainly of burnt gases. The flames are sensitive to stretch by turbulent fluctuations and more likely to be quenched as compared to turbulent premixed flames. Particularly for LO_X/CH_4 combustion, the chemical reaction temporal scales are typically much smaller compared to turbulent flow time scales, so the ratio represented by Damköhler number is very large. Hence, the chemistry can be assumed to be infinitely fast, existing in a chemical equilibrium condition. Many experimental difficulties are encountered while studying turbulent combustion due to high-temperature conditions inside the combustion chamber; hence, numerical modeling is the way forward. However, such complex behavior of injection, mixing, and combustion pose hindrances in choice of appropriate laws for the representation of liquid rocket engines and combustion chambers conditions. Therefore, a considerable amount of research has been dedicated to studying supercritical combustion regimes.

Extensive efforts have been carried out to establish an experimental framework to study the dynamics of supercritical fluid injection and mixing [5, 6]. Individual research groups have experimentally investigated high-pressure combustion of H_2/Lo_x and CH_4/Lo_x propellant combination. ONERA developed the Mascotte cryogenic test bench [7] studying flames in rocket engines with coaxial injection.

DLR, Germany, used an apparatus with M3 [8] burner to conduct similar experiments. In literature, there is a vast repository of works pertaining to different models to describe thermodynamic effects, combustion characteristics, turbulence closure, and chemical kinetics description. Minotti and Bruno [9] conducted an analysis of thermo-physical properties and compressibility factors of CH_4, O_2, CO_2, and H_2O at 15 MPa. They showcased the considerable differences of thermo-physical properties between ideal gas behavior and that obtained via experiments. Eddy dissipation model is used predominantly for non-premixed combustion [Poschner 2008, 10'], while Sozer et al. [11] extended the PDF approach to simplify the combustion description for the rocket engine simulation. Many works have established that the β-function pdf presents an excellent estimate of the sub-grid-scale mixture fraction distribution in turbulent reacting flows [12]. Modeling the injection phenomenon involves two significant strategies. Many authors have used a pure Eulerian approach with single gas phase approximation [13], but in literature, there is also some work that adopted the Eulerian–Lagrangian approach [14, 15] which considers oxidizer to be injected as liquid droplets coaxially with the fuel gas stream.

Extensive studies were carried out by Giorgi et al. [16–18] to numerically simulate 2D turbulent LO_x/CH_4 combustion. They analyzed the sensibility of different modeling approaches with the RANS model for turbulence. From the kinetics aspect, the reduced Jones–Lindstead model (modified by Frassoldati et al. [19]) and the full skeletal model from Grimech 3.0 were applied and compared. Similarly, Eddy dissipation concept (EDC) and probability density function chemical equilibrium approaches were contrasted for combustion modeling. To account for real gas effects, Soave-Redlich-Kwong and Peng-Robinson equations of state were enforced along with a comparison with Ideal gas approximation. For spray injection, they undertook both pure Eulerian treatment and the Lagrangian/Eulerian description for spray phase. Further, they concluded that the behavior of the LO_x spray and flame characteristics were sufficiently recreated with a pure Eulerian approximation in association with SRK equations of state and the PDF model.

Ierardo et al. [20] presented a large Eddy simulation of a coaxial CH_4/Lo_x injector, at near-critical conditions using the Lee-Kesler equations for real gas effects and EDC formulation for combustion modeling. Earlier investigations employing LES on the test cases of Singla et al. [21] in Mascotte chamber, Guézennec et al. [22] accounted for finite-rate chemistry implementing reduced chemical reaction mechanism, whereas Schmitt et al. [23] assumed infinitely fast chemistry and calculated the reaction rates based on the single-step reaction mechanism. In work by Muller and Pfitzner [24], the steady laminar flamelet model was employed. This was done in conjecture with a beta-shape probability density function, which is supposed to accurately represent *sgs* fluctuations. Zong et al. [25] conducted a study on combustion closure models for a splitter plate configuration at similar conditions and established that a steady laminar flamelet model coupled with a β-shaped PDF outperformed other alternative models.

In the present work, numerical analysis of cryogenic combustion involving methane and liquid oxygen propellant combustion. The combustion chamber geometry is adopted from the experimental works of Singla et al. [21] on the G2 case

of the MASCOTTE V04 test chamber. Detached eddy simulations (DES) are being carried out to investigate the complex integration between turbulence and combustion. DES is employed, keeping in mind that DES requires less computational effort while resolving sub-grid scales at the same time. For complete numerical modeling, appropriate models should be chosen to describe the combustion phenomenon, reaction mechanism, thermodynamic properties, and turbulence chemistry interactions. Non-premixed combustion is considered to represent combustion as fuel and oxidizer are injected as separate streams. To include the effects of turbulence on flame characteristics, a steady diffusion flamelet approach is used with β-shaped pdf accounting for the sub-grid scale (sgs) fluctuations. In regards to transcritical conditions existing in the combustion chamber under supercritical pressures and subcritical injection temperature of liquid oxygen, real gas effects need to be considered for calculating the thermodynamic properties of the mixture. To explain the chemical reactions involved, a modified model of reduced Jones–Linstedt chemkin mechanism is chosen over a detailed skeletal Grimech 3.0 mechanism. This is done keeping in mind that the former mechanism is computationally very cheap and produces an excellent agreement with experimental results. Further, the effect of chamber pressure is also studied by conducting simulations at a higher chamber pressure of 8 MPa and observing its impact on the turbulent flame structure. The primary objectives of this work are to investigate flame features, species mass fraction distributions and establish the viability of using DES to model turbulent combustion by comparing with experimental data and numerical results obtained using LES in literature.

2 Mathematical Formulation

Turbulent combustion involves two-way interaction between chemistry and turbulence. Combustion usually involves large mass fractions and density gradients. Turbulence itself has many unanswered questions pertaining to its structure and description. Coupling of various time and length scales results in an intrinsically complex phenomenon. Hence, modeling of turbulent combustion is a challenging task. It is governed by conservation equations for mass, momentum, energy, and species.

2.1 Turbulence Modeling

For high Reynolds number flows turbulent structures play a significant role in flow characteristics. Owing to multiple lengths and time scales, the nonlinear convection term becomes highly prone to numerical errors. This not only demands high resolution in time and space but also increases the stiffness of the Navier-Stokes equation. The detached Eddy simulation turbulence model is a compromise between RANS

and LES. In core flow regions with dominant large-scale unsteady turbulent scales, DES recovers sub-grid models like LES. Whereas in the near-wall region, where the grid needs fine resolution, DES approximates turbulence on the basis of Realisable k-ε RANS models [26] to save computational power.

The length scales for DES is

$$l_{\text{des}} = \min(l_{\text{rke}}, l_{\text{les}}) \tag{1}$$

where $l_{\text{rke}} = k^{3/2}/\varepsilon$, $l_{\text{des}} = C_{\text{des}}\Delta$.

The notations in the above equation are: k, ε, Δ, and C_{des} represent the turbulent kinetic energy, rate of dissipation, local grid spacing, and calibration constant, respectively. The Reynolds stress is modeled by calculating eddy viscosity using the Boussinesq hypothesis [27] in RANS and Smagorinsky–Lilly [28] model in LES.

$$\text{RANS: } \mu_t = \rho C_\mu \frac{k^2}{\varepsilon} \tag{2}$$

$$\text{LES: } \mu_t = \rho L_s^2 \left|\overline{S}\right| \tag{3}$$

where C_μ is calculated from flow parameters, L_s is sub-grid scales and $\left|\overline{S}\right| = \sqrt{2\overline{S}_{ij}\overline{S}_{ij}}$.

2.2 Combustion Modeling

Non-premixed combustion modeling includes solving transport equations for certain conserved scalars. The individual concentration of each species can be expressed in terms of the calculated mixture fraction fields. This helps in incorporating detailed reaction mechanisms as the formulation becomes independent of the number of species, and the need to solve conservation equations for individual species is avoided. So, the combustion process is simplified to a mixing problem, and in a way, the closure of terms involving reaction rates is circumvented. The mixture fraction and its variance are calculated from their equations for RANS regions [29, 30]

$$\frac{\partial}{\partial t}\left(\rho\overline{f}\right) + \nabla.\left(\rho\overrightarrow{v}\,\overline{f}\right) = \nabla.\left(\frac{\mu_t}{\sigma_t}\nabla\overline{f}\right) + S_m \tag{4}$$

$$\frac{\partial}{\partial t}\left(\rho\overline{f'^2}\right) + \nabla.\left(\rho\overrightarrow{v}\,\overline{f'^2}\right) = \nabla.\left(\frac{\mu_t}{\sigma_t}\nabla\overline{f'^2}\right) + C_g\mu_t\left(\nabla\overline{f}\right)^2 - C_d\rho\frac{\varepsilon}{k}\overline{f'^2} \tag{5}$$

The notations are $\overline{f}$, S_m mean mixture fraction and source term S_m which refers to mass transfer from the liquid phase into the dispersed phase in the medium. Also,

mixture fraction variance is given as $f' = f - \overline{f}$, and the constants in Eq. 5 σ_t, C_g, and C_d take the values 0.85, 2.86 & 2.0, respectively.

Similarly, the mixture fraction variance for the LES region is modeled as:

$$\overline{f'^2} = C_{\text{var}} L_s^2 \left|\nabla \overline{f}\right|^2 \tag{6}$$

where constant C_{var} equals 0.5.

As per the given conditions, fuel and oxidizer enter via separate inlets at different temperatures. So, the non-adiabatic assumption for energy treatment is considered in the non-premixed combustion model. The energy equation is expressed in the form of total enthalpy.

$$\frac{\partial}{\partial t}(\rho H) + \nabla.\left(\rho \overrightarrow{v} H\right) = \nabla.\left(\frac{k_t}{c_p}\nabla H\right) + S_h \tag{7}$$

Assuming Lewis number (Le) = 1, the contribution of diffusion and conduction terms is combined together into a single term in the RHS of Eq 7. The definition of enthalpy includes heat of formation from chemical reactions; hence, reaction sources are not included in S_h.

2.3 Flamelet Generation

A diffusion flame is assumed to account for flame stretching by turbulence. The steady diffusion flamelet approach envisions a turbulent flame brush to be an assemblage of thin, steady, laminar flamelets. These discrete structures are locally one-dimensional and are embedded in an inert turbulent flow field. A counterflow diffusion flame is usually selected to represent the flamelets [31, 32]. It consists of fuel and oxidizer jets, which are axisymmetric and opposed to each other. The flame increasingly departs from chemical equilibrium as jet velocities increase or distance between them diminishes. Eventually, the flame becomes excessively strained and is extinguished. In such a counterflow flame setup, mixture fraction varies between unity and zero, with value at fuel jet to be one and null at the oxidizer jet. The governing equations for energy conservation and species conservation can be transformed from physical space to mixture fraction space. The species mass fraction and temperature along the axis of laminar one-dimensional flamelets can then be uniquely determined using two parameters: mixture fraction and scalar dissipation [33].

$$\rho\frac{\partial T}{\partial t} = \frac{1}{2}\rho\chi\frac{\partial^2 T}{\partial f^2} - \frac{1}{c_p}\sum_i H_i S_i + \frac{1}{2c_p}\rho\chi\left[\frac{\partial c_p}{\partial f} + \sum_i c_{p,i}\frac{\partial Y_i}{\partial f}\right]\frac{\partial T}{\partial f} \tag{8}$$

$$\rho\frac{\partial Y_i}{\partial t} = \frac{1}{2}\rho\chi\frac{\partial^2 Y_i}{\partial f^2} + S_i \tag{9}$$

Here, Y_i, T, ρ, and f are the ith species mass fraction, temperature, density, and mixture fraction, respectively. $c_{p,i}$ and c_p are the ith species specific heat and averaged specific heat of mixture, respectively. S_i is the ith species reaction rate, and H_i is the specific enthalpy of the ith species. The below equation is responsible for modeling scalar dissipation across the flamelet, where a_s represents characteristic strain rate, and ρ_∞ denotes the density of oxidizer stream [34].

$$\chi(f) = \frac{a_s}{4\pi} \frac{3\left(\sqrt{\rho_\infty/\rho}+1\right)^2}{2\sqrt{\rho_\infty/\rho}+1} \exp\left(-2\left[\text{erfc}^{-1}(2f)\right]^2\right) \tag{10}$$

Based on statistical PDF methods, the laminar diffusion flamelets are embedded into the inert turbulent flow field to generate a turbulent flame. The probability density dunction (PDF), written as $p(f)$, characterizes the fraction of time the fluid spends in the proximity of the state f. The non-adiabatic standard PDF tables have the following dimensions: $\overline{T}(\overline{f}, \overline{f'^2}, \overline{H}, \overline{\chi})$, $\overline{\rho}(\overline{f}, \overline{f'^2}, \overline{H}, \overline{\chi})$, $\overline{Y_i}(\overline{f}, \overline{f'^2}, \overline{\chi})$ for $\chi \neq 0$ and $\overline{Y_i}(\overline{f}, \overline{f'^2}, \overline{H})$ for $\chi = 0$. Here, $\chi = 0$ it represents the equilibrium solution.

Modeling steady laminar flamelets for a broad range of enthalpies is computationally expensive. To circumvent this, mass fractions using adiabatic assumptions considering the fact that heat exchange onto the system bears a negligible effect on mass fraction distribution of species [35, 36]. The above approach is valid when mass fractions and temperature fields are obtained for a range of mean enthalpy gain/loss and tabulated for lookup during numerical simulations. Then, the species mass fraction and temperature, completely parameterized by f and χ_{st} in the localized flamelets, are augmented into the turbulent flame. Density-weighted averaging is subsequently carried out, and the β function PDF is incorporated using the below expression. Here, φ denotes temperature and mass fractions of individual species.

$$\overline{\phi} = \iint \phi(f, \chi_{st}) p(f, \chi_{st}) \, \mathrm{d}f \, \mathrm{d}\chi_{st} \tag{11}$$

For further simplification, statistical independence of f and χ_{st} is. Further, fluctuations in χ_{st} can also be ignored so that the PDF distribution of χ turns into a dirac delta function. The mean scalar dissipation can then be modeled as

$$\text{RANS: } \overline{\chi_{st}} = \frac{C_\chi \varepsilon \overline{f'^2}}{k} \text{ and LES: } \overline{\chi_{st}} = C_\chi \frac{(\mu_t + \mu)}{\rho \sigma_t} \left|\nabla \overline{f}\right|^2 \tag{12}$$

These integrals (Eq. 11) are computed and stored in a look-up table. The mean mixture fraction and mixture fraction variance are solved across the flow domain using Eqs. 4 and 5. The mean temperature and mean mass fraction fields can then be retrieved based on table interpolation. The chemistry is processed separately and tabulated beforehand. This offers significant computational savings while incorporating realistic chemical kinetics into the turbulent flames. There are certain restrictions within which this approach can be applied. Only a single mixture fraction can

be modeled, which follows a β-shaped PDF distribution. Further, it is limited to modeling relatively fast chemistry-based combustion, and fluctuations pertaining to scalar dissipation are also ignored.

The real combustion phenomenon includes numerous species and intermediate reactions. Reproducing the actual kinetics in full detail is computationally cumbersome. Studies have been made in this regard to develop a reduced model involving fewer species and reactions which predict the real phenomenon with good accuracy and are less heavy computationally. Andersen [37] modified the original multi-step Jones–Lindstedt reaction mechanism and applied it to oxy-fuel combustion. Later Frassoldati et al. [19] included the water–oxygen dissociation reactions to enhance accuracy. The resulting modified Jones–Lindstedt mechanism has six intermediate reactions and nine species in total. Giorgi et al. [18] compared the performance of this mechanism with a detailed Grimech 3.0 skeletal model and concluded that the reduced kinetics scheme provided an excellent depiction of the thermodynamic combustion phenomena.

2.4 Real Gas Equations of State

In the present study involving cryogenic combustion, oxygen is injected as liquid spray while methane enters as a gaseous stream. Two approaches can be adopted to model such injection, namely the Eulerian single-phase model or Eulerian–Langrangian discrete phase model. The first model assumes both fuel and oxidizer streams to be in the gaseous state. While in the Eulerian–Langrangian discrete phase model includes a Eulerian description of the gas phase and Langrangian equations for the dilute spray. The second model is more accurate but difficult to implement as modeling vaporization demands equations are specifying mass transport, energy transport, radiation, phase change, and interphase coupling. It often leads to stability issues along with longer computational time. Moreover, studies by Giorgi et al. [16–18] have shown that modeling with single-phase gives a good enough match with experimental results. To include real gas effects, the most widely used equations are the Soave-Redlich-Kwong equation (SRK) [38], Peng-Robinson equation (PR) [39] and Lee-Kesler equation (LK). The linear cubic Soave-Redlich-Kwong and Peng-Robinson are simple to solve and implement; instead, Lee-Kesler equations are nonlinear, require complex resolution, which makes the code heavier. In the present study, SRK equations are used which involves following equations

$$p = \frac{RT}{V - b + c} - \frac{\alpha(T)}{\left(V^2 + \delta V + \varepsilon\right)} \tag{13}$$

$$\alpha(T) = \alpha_0\left[1 + n\left(1 - (T/T_c)^{0.5}\right)\right]^2 \tag{14}$$

where $\alpha_0 = \frac{0.42747R^2T_c^2}{p_c}$, $b = \frac{0.08664RT_c}{p_c}$ and $n = 0.48 + 1.574\omega - 0.176\omega^2$. Here, p is the absolute pressure in Pascals, R is universal gas constant, V is specific molar volume (m^3/kmol), T is temperature (K). The constants α, b, c, δ are functions of critical temperature T_c, critical pressure p_c, acentric factor ω, and vary from model to model. The parameter δ equals b, whereas c and ϵ values are equated to 0 in the SRK model. Other thermodynamic properties such as enthalpy, internal energy, entropy, and specific heat capacities are expressed using appropriate ideal gas characteristics and departure functions. The mixture properties with corresponding mixture critical constants are evaluated using Van der Waals mixing rules.

2.5 Computational Details

In the present study, ANSYS FLUENT 18.0 [40] is used to simulate the flow. ICEM-CFD [41] is used for grid generation while post-processing is performed using multiple visualization tools. Experimental studies are from the Test bench RCM-03 Mascotte Single Injector [42]. The chamber pressure is maintained at 5.6 MPa, which far exceeds the critical pressures of both methane (1.3 MPa) and oxygen (5.04 MPa). The inlet conditions have been tabulated in Table 1. The methane stream is injected via an annular duct, which has an inner diameter of 0.0056 m and an outer diameter of 0.01 m. Liquid oxygen is injected via an inner, coaxial duct. It diverges from an initial diameter of 0.005 m to an exit diameter of 0.0054 m. The injector length is equal to 0.0072 m. The combustion chamber is 0.4 m long, consisting of a square cross-section throughout dimensions 0.05 m * 0.05 m. The domain length has been truncated to 0.32 m, which is sufficient in avoiding significant interactions between the reaction zone and chamber outlet and also allows for better grid resolution at similar computational costs. The multi-block grid consists of 2.7 million hexahedral cells with outer cylindrical block and inner O-grid type Butterfly block. The mesh has divisions of 450 nodes in the axial direction and 120 nodes in the radial direction. The smallest cell surface is about $5.2 * 10^{-9} m^2$, and the finest resolution is located at injector tip with a grid spacing of 15 μm. The grid division is higher in areas near injector inlet to account for large gradients of physical quantities and can be seen in Fig. 1b. This is to ensure the property values do not change by a considerable margin in-between adjacent cells. The resolved velocity spectrum obtained from time-series

Table 1 Inlet conditions for MascotteV04 G2 case [21]

	LO_2	CH_4
Mass flow rate (kg/s)	0.0444	0.1431
Velocity (m/s)	3.70	63.2
Temperature (K)	85	288
Density (kg/m^3)	1177.8	43.344

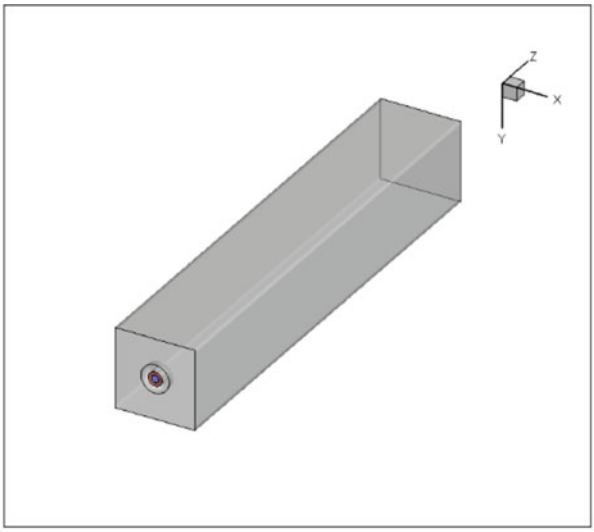

(a)

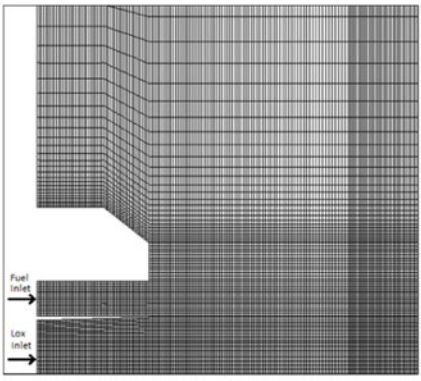

(b)

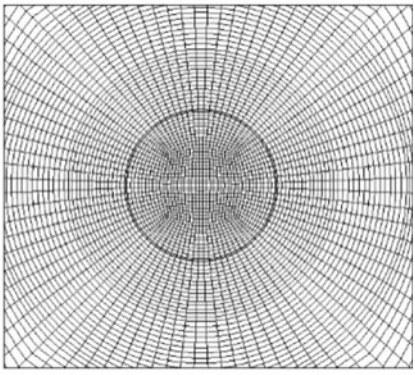

(c)

Fig. 1 Schematic illustrations of **a** computational domain, **b** near the injector field, **c** butterfly grid

data is shown in Fig. 2. The recovery of the −5/3 slope of the Kolmogorov spectrum is clearly demonstrated, which indicates sufficient resolution for the LES model in the core flow regions. The bounded second-order transient formulation is used, and the coupled algorithm is implemented to solve for coupling of pressure and velocity in discretized momentum equations. Bounded central differencing is used to spatially discretize momentum, and second-order upwind scheme is employed to discretize the diffusive and convective terms. Data sampling was initiated after the flow becomes statistically stationary to calculate mean quantities.

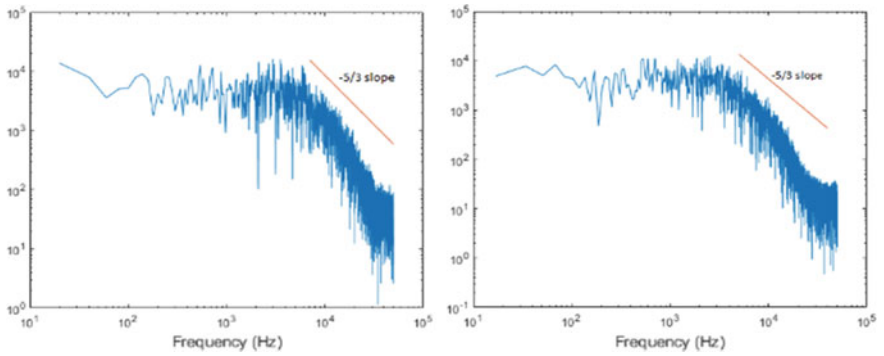

Fig. 2 Velocity spectrum at a chamber pressure of 5.6 MPa (left) and 8 MPa (right) showing resolution of Kolmogorov scales

3 Results and Discussion

The results obtained from the numerical simulation of turbulent non-premixed combustion at high pressures are given as per the following sequence:

I. Instantaneous flow visualization to understand the flame shape and turbulence effects.
II. Time-averaged temperature, velocity, and species mass fraction fields for validation with experimental findings.
III. The effect of chamber pressure on turbulent combustion phenomenon.

3.1 Instantaneous Flow Visualization

To illustrate turbulent flow features, Fig. 3 depicts the iso-contours of the Q criterion. Density iso-surface corresponding to $\rho = 150$ kg/s is represented in black color to highlight the dense oxygen core. Annular eddies are observed in the shear layers

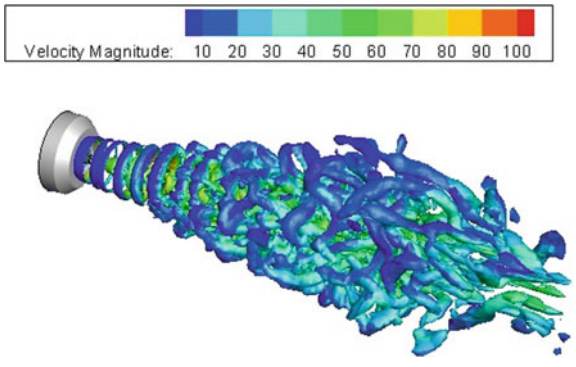

Fig. 3 Iso-contours of Q criterion (=10^7 s^{-2}) colored by velocity magnitude

existing in-between gaseous methane stream and quiescent combustion chamber environment. These roll up and grow in size to eventually wrinkle the oxygen core and cause turbulent mixing. Figure 4 gives the contour plots of instantaneous temperature, axial velocity, and other essential flow parameters along a central plane perpendicular to the injector with axial length plotted along the x-axis. The flame length, as well as flame shape, is highly variable. The OH species mass fraction distribution elucidates the flame outline, which is thin near injector post and then expands and gets wrinkled. The compressibility factor value for the gas mixture, in both axial and radial directions, is nearly 1 outside the flame boundary. However, inside the liquid oxygen core, the value is around 0.2, which shows that the real gas equation of state should be definitely used, and ideal gas assumptions would result in significant discrepancies in the flame field.

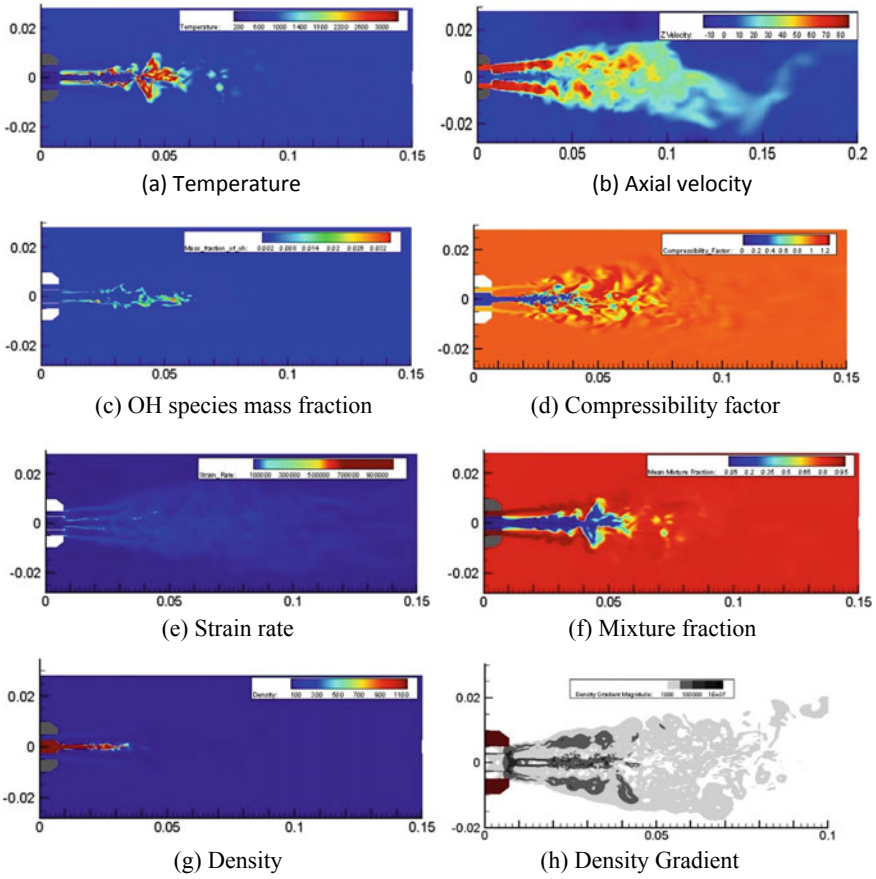

Fig. 4 Instantaneous contour plots of temperature, axial velocity, the mass fraction of OH, compressibility factor of the mixture, strain rate in shear layers, mixture fraction, density and its gradient in the injector near field

The contour plots of density and its gradient show some exciting features. Firstly, the conical shape of dense oxygen core can be observed. It extends roughly up to 30 mm (=6*D*) axially. The characteristic length used for non-dimensionalization is the hydraulic diameter of methane inlet denoted by $D = 0.005$ m. Next, strong density gradients are observed in the two coaxial shear layers one in-between methane stream and oxygen core while the other is in-between methane stream and combustor environment. The liquid oxygen core detaches from the Lo_x post, and this separation leads to an onset of turbulence. This is responsible for the tiny instability waves previously seen in the iso-contours of the *Q* criterion. Further, values of turbulent intensity and turbulent kinetic energy also showed peaks at the Lo_x post.

The phenomenon of flame quenching is quite common in non-premixed combustions. Under the action of turbulence, large fluctuations in the strain rate can cause the flame to blow off and become extinct. The maximum strain rate is observed in the shear layers (see Fig. 4e) and directly impacts flame instabilities. However, the maximum value of strain rate obtained from the simulations is $5 * 10^5$ s^{-1} for $P =$ 5.6 MPa and $4.3 * 10^5$ s^{-1} for $P = 8$ MPa, which is much less than the value for flame extinction. Pons et al. [43] evaluated the strain rate for flame extinction at 5.6 MPa to be 10^6 s^{-1}.

3.2 Averaged Flow Field Analysis

The ensemble average of certain critical flow variables like temperature, velocity, and species mass fraction of OH was calculated by averaging the data from instantaneous simulations over a considerable flow time. The mean temperature field clearly demarcates regions of thin thermal layers with large temperature gradients from broader regions of flame with nearly similar temperatures. The initial flame angle is around 5°, and there is an expansion post 20 mm to a flame angle of 15°. The average mass fraction of OH (Fig. 5c) recreates the average flame field observed from mean temperature contour plots. A thin flame front is followed by the thickening of the reaction zone gradually downstream. Giorgi et al. [16–18], in their work, deduced the position of maximum experimental temperature along the symmetry axis from backlight images and OH contour. Upon qualitative comparison of current results with the same given in Fig. 6, the flame geometry is successfully reproduced. However, it is observed that the flame length is slightly smaller, and abrupt flame end is also not reproduced in the time-averaged contour plots.

Due to gas expansion by combustion, the methane stream is deflected outwards, and the presence of the flame results in delaying the transition of two coaxial jets into a single jet. Negative velocities can be observed at two locations: one just downstream of the injector at the periphery of the oxygen jet and another due to weak recirculation near the walls at around 100 mm downstream of the injector. Looking at the streamlines, there exist two stable recirculation zones in the wake of the flame (Fig. 5d). Small recirculation bubbles are also seen some distance downstream of injector but of very weak strength. The backflow of hot gaseous products through

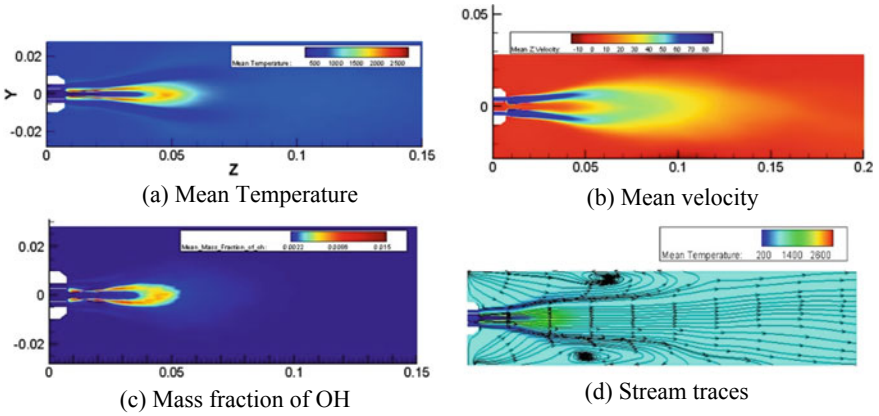

Fig. 5 Contour plots of mean temperature, mean velocity in the axial direction, the mass fraction of OH. **d** Streamtraces displayed over mean temperature

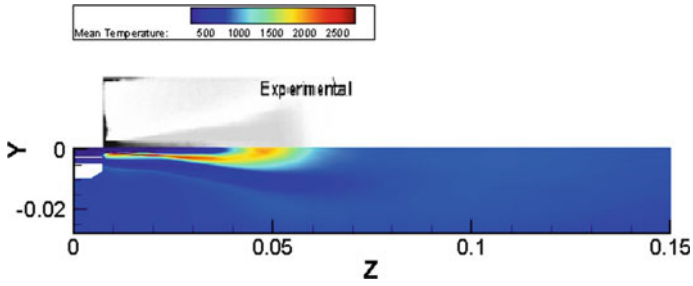

Fig. 6 Comparison with backlit experimental flame (Singla et al. [21])

recirculation stabilizes the flame, at the same time, promotes mixing and helps the flame to anchor at the injector tip wall (Fig. 7).

The location of the average temperature peak along the symmetry axis achieved from numerical simulations lies in close proximity of experimental data (Fig. 8). The

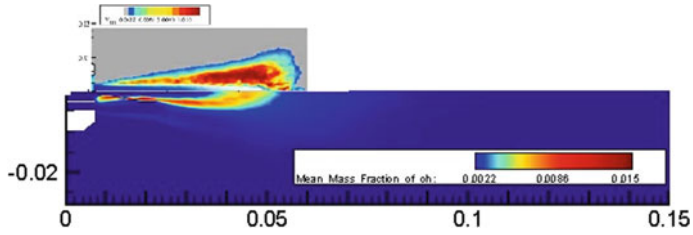

Fig. 7 OH contour comparisons with Abel transformed the image from experiments (Giorgi et al. [17])

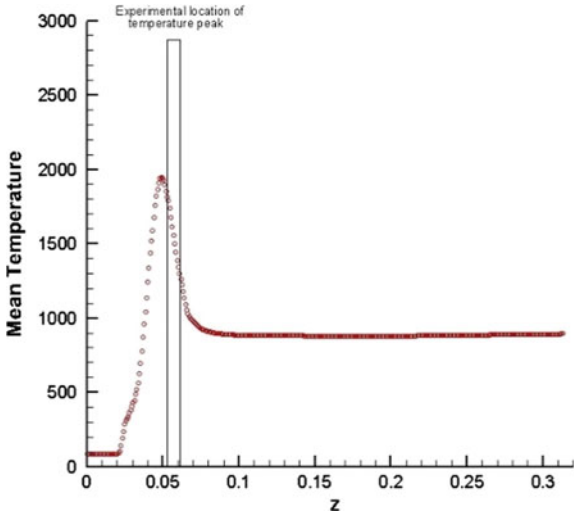

Fig. 8 Mean temperature along the symmetry axis

position of temperature peak along the axis of symmetry has been referred to as the flame length. Potential core length can be defined as the axial distance when the mass fraction of oxygen falls down to 0.9 is evaluated to be 30 mm = 6*D* from Fig. 9. The plot also provides another method to define flame length, i.e., distance of OH mean mass fraction peak value location from injector inlet. Looking onto the distribution of major reacting species CH_4, O_2, H_2O, CO_2, Fig. 10 plots the mass fraction of the above species in radial directions at axial locations varying from $z/D = 0.1$ to $z/D = 5$. The reaction zone can be visualized in the shear layer as the region where the mass fraction of O_2 decreases from peak value to its minimum. It is observed that the reaction zone thickens as we move downstream, increasing from 0.5 to 3 mm as we approach the rear part of the flame.

3.3 Effect of Chamber Pressure

At higher chamber pressure, a longer flame is observed. The temperature distribution and flame shapes are relatively similar. The central oxygen core is longer and rather undisturbed at higher pressure with a potential core length of around 40 mm = 8*D*. The mixing between methane stream and the quiescent environment is subdued at a higher pressure, and the methane jet stretches out for a longer distance in the higher-pressure case. The wrinkling of coherent eddies occurs relatively downstream and is less prominent as compared to lower chamber pressure. The number of annular eddies is also seen. The temperature distribution and peak values are similar and differ only marginally. On comparing the axial temperature plots (Fig. 12), it is established quantitatively that flame length for 8 MPa pressure cases is longer and approximately 55 mm, while for lower chamber pressure, it was around 48 mm. A

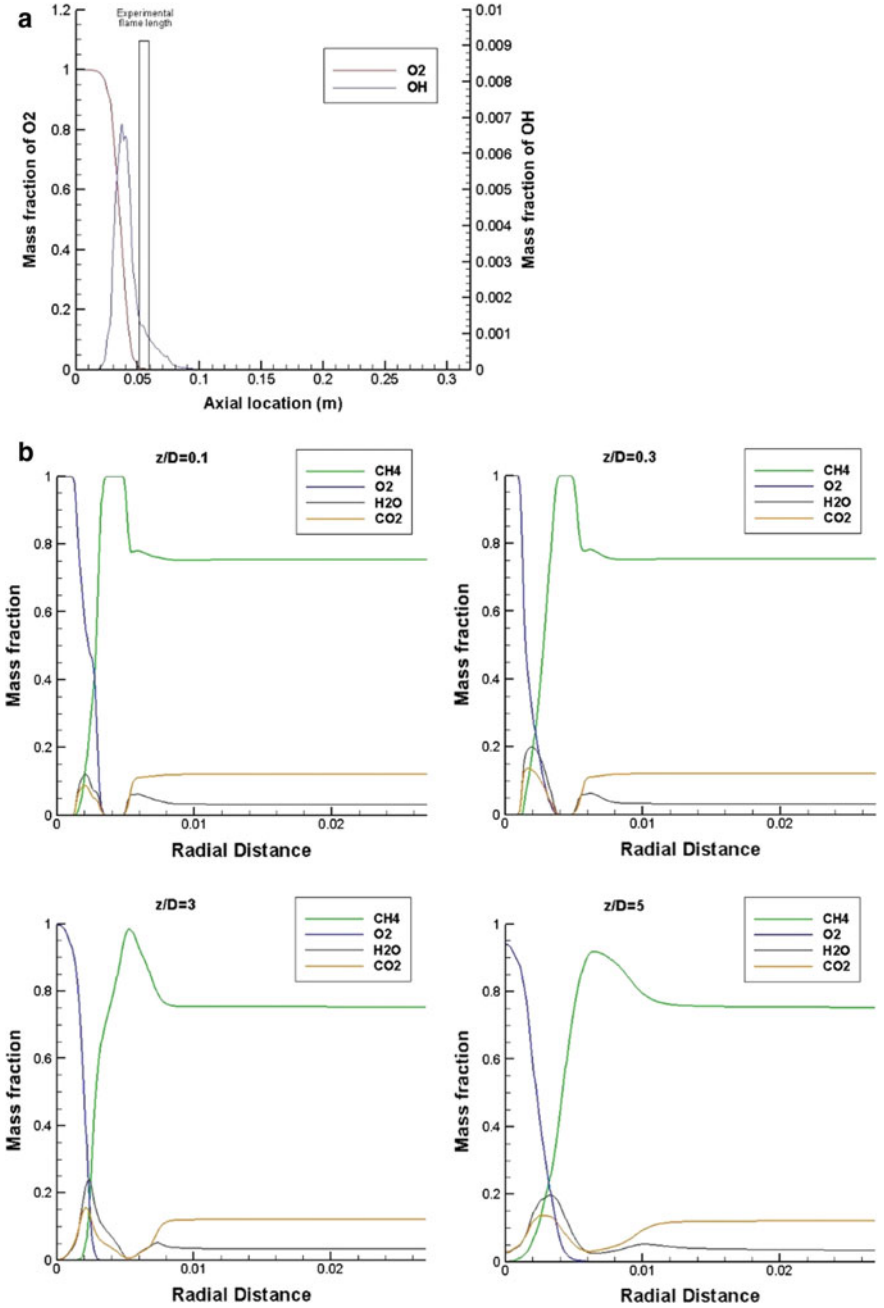

Fig. 9 **a** Mean species mass fractions of OH and O_2 along the symmetry axis. **b** Radial distribution of reactant and products mass fractions

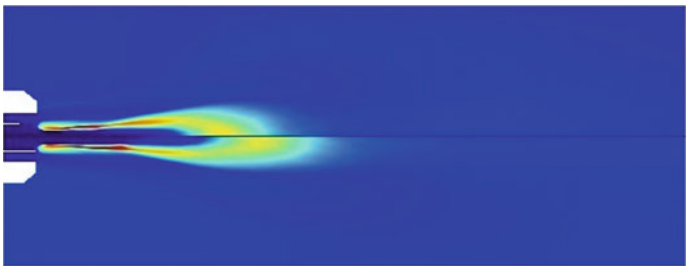

Fig. 10 Comparison of mean temperature contours at 5.6 MPa (top) and 8 MPa (bottom)

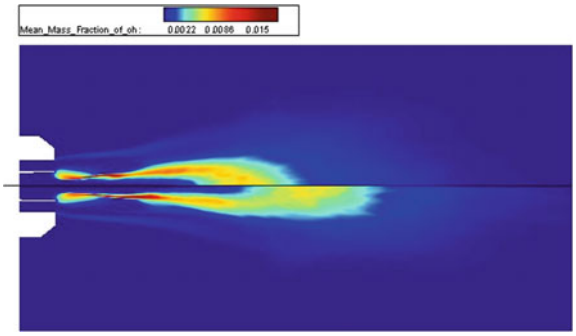

Fig. 11 Comparison of mean OH mass fraction contours at 5.6 MPa (top) and 8 MPa (bottom)

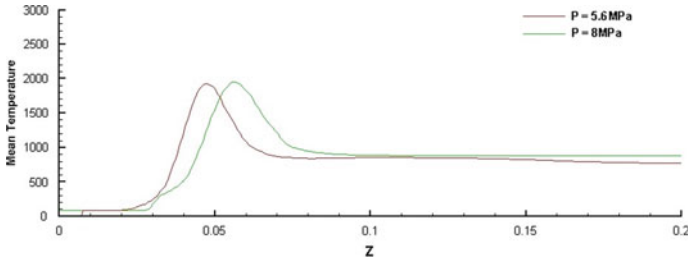

Fig. 12 Mean temperature distribution along the symmetry axis at 5.6 and 8 MPa

very slight change in flame spreading angle can be seen at a higher chamber pressure case in Fig. 11. This is also likely due to a reduction in the mixing process at higher pressure, which causes a decrease in the flame spreading angle. Axial distribution of species mass fraction plots given in Fig. 13 also provides a larger flame length at higher chamber pressure (Fig. 14).

It can be observed that DES simulates the turbulent flame approximately well near injector inlet but fails to predict sufficient expansion toward the rear part of flame along with the abrupt end reported in experiments. This may be due to eventual

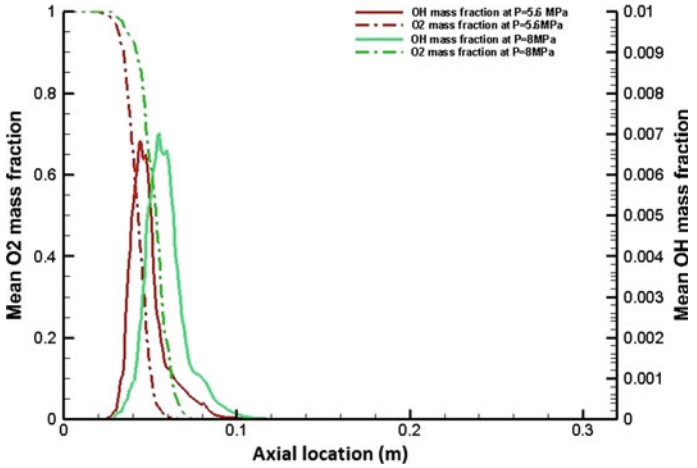

Fig. 13 Mean species mass fractions along the symmetry axis at 5.6 and 8 MPa

(a) 5.6MPa (b) 8MPa

Fig. 14 Temperature isocontour of $T = 1300$ K

break-up and mixing of vortical structures, which brings the small scales into the picture. These small scales are not adequately resolved by DES filtering, hence deviate from experimental observations. These can be addressed by resolving the grid further or employing LES to give better insights into the mixing of ring vortices and other turbulent structures. However, both of these approaches would require high computational costs.

4 Conclusion

In the present work, turbulent flames are numerically simulated through the means of Hybrid RANS/LES formulation. Non-premixed combustion model with a steady diffusion flamelet approach and β-shaped PDF functions is implemented to model turbulence chemistry interactions. SRK real gas equations are employed to simulate the transcritical conditions inside the combustion chamber. Keeping in mind the results and subsequent discussions presented in the previous section, one arrives at the following conclusions:

1. The instantaneous flame shape is highly variable with chemical reactions occurring in the shear layer. Annular eddies are observed which rollup and enhance mixing. The flame has a thin reaction zone post-injector tip, which gradually broadens downstream.
2. Upon comparison with experimental observations, the flame shape and characteristics match the experiments qualitatively. A slightly smaller flame length is noted, and the abrupt flame end is not reproduced in numerical results.
3. The flame is anchored at the Lo_x injector post and is stabilized by the presence of recirculation zones in the wake of flame. The dense oxygen core separates before the injector tip and leads to an onset of instability waves. The strain rates observed are well below the extinction rate, hence, prevents the flame from quenching.
4. Compressibility factor analysis reveals real gas effects inside the flame front. This is in agreement with experimental literature [9] in this regard, which states the existence of both liquids like properties and gas-like properties post-injection due to transcritical conditions.
5. The effect of increasing chamber pressure is a noticeably subdued mixing, larger flame length, smaller flame spreading angle, and a more extended undisturbed oxygen core.

DES is able to reasonably predict the experimental results at par with numerical simulations using LES formulation at meager computational costs. However, flame features toward the rear end are not reproduced enough due to the action of small, turbulent scales that DES fails to resolve.

Acknowledgements Financial support for this research is provided through IITK-Space Technology Cell (STC). The authors would like to acknowledge the IITK computer center (www.iitk.ac.in/cc) for providing the resources to perform the computation work, data analysis, and article preparation.

References

1. Ierardo N, Cuoco F, Accettura A, Congiunti C, Bruno C (2002) Lo_x-methane systems for high thrust lre. In: 4th International conference on launcher technology, Liege (Belgium)
2. Congiunti A, Bruno C, Ierardo N, Cuoco F (2002) Cooling potential of high pressure CH 4. In: Proceedings of the twenty-third international symposium on space technology and science (Selected papers), vol. I, pp 157–164
3. Liang K, Yang B, Zhang Z (1998) Investigation of heat transfer and coking characteristics of hydrocarbon fuels. J Propul Power 14(5):789–796
4. Chehroudi B, Talley D, Mayer W, Branam R, Smith JJ (2003) Understanding injection into high pressure supercritical environment, p 37
5. Chehroudi B, Talley D, Coy E (2002) Visual characteristics and initial growth rates of round cryogenic jets at subcritical and supercritical pressures. Phys Fluids 14(2):850–861
6. Oschwald M, Smith JJ, Branam R, Hussong J, Schik A, Chehroudi B, Talley D (2006) Injection of fluids into supercritical environments. Combust Sci Technol 78(1–3):49–100
7. Zurbach S, Thomas JL, Sion M, Kachler T, Vingert L, Habiballah M (2002) Recent advances on Lo_x/methane combustion for liquid rocket engine injector. In: 38th AIAA/ASME/SAE/ASEE joint propulsion conference & exhibit, p 4321

8. Yang B, Cuoco F, Oschwald M (2007) Atomization and flames in Lo_x/H_2-and Lox/Ch_4-spray combustion. J Propul Power 23(4):763–771
9. Minotti A, Bruno C (2007) Subtranscritical and supercritical properties for lo2-ch4 at 15mpa. J Thermophys Heat Transfer 21(4):796–810
10. Haworth DC (2000) A probability density function/flamelet method for partially premixed turbulent combustion. In: Proceedings of the summer program, pp 145–156
11. Sozer E, Hassan E, Yun S, Thakur S, Wright J, Ihme M, Shyy W (2010) Turbulence-chemistry interaction and heat transfer modeling of H_2/O_2 gaseous injector flows. In: 48th AIAA aerospace sciences meeting including the new horizons forum and aerospace exposition, p 1525
12. Cook AW, Riley JJ (1998) Subgrid-scale modeling for turbulent reacting flows. Combust Flame 112(4):593–606
13. Cutrone L, Ihme M, Herrmann M (2006) Modeling of high-pressure mixing and combustion in liquid rocket injectors. In: Proceedings of the summer program, p 269
14. Haidn OJ, Habiballah M (2003) Research on high pressure cryogenic combustion. Aerosp Sci Technol 7(6):473–491
15. Urzica D, Gutheil E (2009) Structures of laminar methane/nitrogen/oxygen, methane/oxygen and methane/liquid oxygen counterflow flames for cryogenic conditions and elevated pressures. Z Phys Chem 223(4–5):651–667
16. De Giorgi MG, Tarantino L, Ficarella A, Laforgia D (2010) Numerical modeling of high-pressure cryogenic sprays. In: 40th fluid dynamics conference and exhibit, p 5007
17. De Giorgi MG, Sciolti A, Ficarella A (2011) Different combustion models applied to high pressure Lo_x/Ch_4 jet flames. In: Proceedings of the 4th European conference for aerospace sciences, Saint Petersburg, Russia, pp 4–8
18. De Giorgi MG, Sciolti A, Campilongo S, Ficarella A (2012) Ultra lean combustion characterization in a pilot-scale gas turbine burner using image processing techniques. In: ASME turbo expo 2012: turbine technical conference and exposition. American Society of Mechanical Engineers, pp 1161–1176
19. Frassoldati A, Cuoci A, Faravelli T, Ranzi EL, Candusso C, Tolazzi D (2009) Simplified kinetic schemes for oxy-fuel combustion. In: 1st International conference on sustainable fossil fuels for future energy, pp 6–10
20. Ierardo N, Congiunti A, Bruno C (2004) Mixing and combustion in supercritical O_2/CH_4 liquid rocket injectors. In: 42nd AIAA aerospace sciences meeting and exhibit, p 1163
21. Singla G, Scouflaire P, Rolon C, Candel S (2005) Transcritical oxygen/transcritical or supercritical methane combustion. Proc Combust Inst 30(2):2921–2928
22. Guezennec N, Masquelet M, Menon S (2012) Large eddy simulation of flame-turbulence interactions in a Lo_x/Ch_4 shear coaxial injector. In: 50th AIAA aerospace sciences meeting including the new horizons forum and aerospace exposition, p 1267
23. Schmitt T, Méry Y, Boileau M, Candel S (2011) Large-eddy simulation of oxygen/methane flames under transcritical conditions. Proc Combust Inst 33(1):1383–1390
24. Müller H, Pfitzner M (2015) Large-eddy simulation of transcritical Lo_x/Ch_4 jet flames. In: 6th European conference for aeronautics and space sciences (EUCASS)
25. Zong N, Guillaume R, Yang V (2008) A flamelet approach for modeling of (Lo_x)/methane flames at supercritical pressures. In: 46th AIAA aerospace sciences meeting and exhibit, p 946
26. Tsan-Hsing S, Liou William W, Aamir S, Zhigang Y, Jiang Z (1995) A new k-ε eddy viscosity model for high reynolds number turbulent flows. Comput Fluids 24(3):227–238
27. Hinze JO (1975) Turbulence. Mcgraw-hill publishing co.
28. Smagorinsky J (1963) General circulation experiments with the primitive equations: I. the basic experiment. Monthly Weather Rev 91(3):99–164
29. Sivathanu YR, Faeth GM (1990) Generalized state relationships for scalar properties in nonpremixed hydrocarbon/air flames. Combustion and Flame 82(2):211–230
30. Jones WP, Whitelaw JH (1982) Calculation methods for reacting turbulent flows: a review. Combust flame 48:1–26

31. Peters N (1984) Laminar diffusion flamelet models in non-premixed turbulent combustion. Prog Energy Combust Sci 10(3):319–339
32. Peters N (1988) Laminar flamelet concepts in turbulent combustion. In: Symposium (international) on combustion, vol 21. Elsevier, pp 1231–1250
33. Pitsch H, Barths H, Peters N (1996) Three-dimensional modeling of NO_x and soot formation in di-diesel engines using detailed chemistry based on the interactive flamelet approach. Technical report, SAE technical paper
34. Kim JS, Williams FA (1997) Extinction of diffusion flames with nonunity lewis numbers. J Eng Math 31(2–3):101–118
35. Binniger B, Chan M, Paczkko G, Herrmann M (1998) Numerical simulation of turbulent partially premixed hydrogen flames with the flamelet model. Advanced Combustion GmbH, Internal Technical Report
36. Müller CM, Breitbach H, Peters N (1994) Partially premixed turbulent flame propagation in jet flames. In: Symposium (international) on combustion, vol 25. Elsevier, pp 1099–1106
37. Andersen J, Rasmussen CL, Giselsson T, Glarborg P (2009) Global combustion mechanisms for use in CFD modeling under oxy-fuel conditions. Energy Fuels 23(3):1379–1389
38. Soave G (1972) Equilibrium constants from a modified redlich-kwong equation of state. Chem Eng Sci 27(6):1197–1203
39. Peng D-Y, Robinson DB (1976) A new two-constant equation of state. Ind Eng Chem Fundam 15(1):59–64
40. Ansys Fluent Theory Guide. See also URL http://www.ansys.com
41. ANSYS (2017) ICEM CFD Realised 17.0ed. See also URL http://www.ansys.com
42. Depoutre A, Zurbach S, Saucereau D, Dumont JP, Bodele E, Gokalp I (2001) Rocket combustion modelling test case rcm-3. Numerical calculation of mascotte 60 bar case with thesee. Technical report, Society National D'etude Et De Construction De Moteurs D'aviation Moissy-Cramayel (France)
43. Pons L, Darabiha N, Candel S (2008) Pressure effects on nonpremixed strained flames. Combust Flame 152(1–2):218–229

Experimental and Numerical Studies on Combustion-Based Small-Scale Power Generators

B. Aravind, Karan Hiranandani, and Sudarshan Kumar

1 Introduction

The primary motivation behind the development of combustion-based portable sources of power can be attributed to the increasing demand of MEMS devices [1, 2]. Conventional electrochemical batteries are of limited use in military, aerospace, and stand-alone applications due to their long recharging periods, lack of portability due to heavy weight, and harmful effects towards the environment [3]. Hydrocarbon fuels have an energy density that is ~110 times that of a lithium-ion battery [4], which would cause a ~5% efficient combustion-based thermoelectric generator to be ~6 times more efficient than the conventional lithium-ion battery. The high energy density, relatively lighter weight, and compactness of the system make combustion-based power systems the preferred choice over conventional batteries [4]. Therefore, extensive research has been carried out in the field of combustion-based sources of power to realize the maximum possible efficiency from the system [5, 6]. However, due to the high surface area-to-volume ratio of microcombustors, flame stabilization poses a challenging obstacle for micropower generators [7]. The relatively low residence time of the flame in microcombustors along with the intense thermal-wall coupling leads to either radical or thermal quenching of the flame [8]. The problems regarding flame quenching have been resolved by excess enthalpy combustion [9–11], catalytic combustion [12, 13], and bluff body [14]. A thorough analysis of microcombustion with the assistance of porous media was carried out by Chou et al. [11]. They concluded that porous media enhanced the temperature distribution along

B. Aravind · S. Kumar (✉)
Department of Aerospace Engineering, Indian Institute of Technology Bombay, Powai, Mumbai 400076, India

K. Hiranandani
Department of Mechanical Engineering, Manipal Institute of Technology, Manipal Academy of Higher Education, Karnataka 576104, India

© Springer Nature Singapore Pte Ltd. 2021

A. De et al. (eds.), *Sustainable Development for Energy, Power, and Propulsion*, Green Energy and Technology,
https://doi.org/10.1007/978-981-15-5667-8_10

the wall, which increased the flame stability significantly. Vijayan et al. [12] used a Swiss-roll mesocombustor to study the effect of heat recirculation. Their study involved a detailed parametric analysis on variation of the inlet boundary conditions, combustor design, material, etc. Shirsat and Gupta analysed the problem of flame stabilization in Swiss-roll combustors [15] and, along with Wierzbicki et al. [16], concluded that Swiss-roll combustors improved the flame stability and enhanced the flame extinction limits. Based on the promising results obtained by their earlier study, Shirsat and Gupta used Swiss-roll combustors for generating thrust in micro-robotics and nanosatellites [17]. Flame dynamics have been studied in depth over the past decade through numerical simulations [18–22]. Wan and Zhao [19] designed a novel microcombustor with improved portability by preheating the incoming fuel–air mixture. They studied the flame dynamics in the microcombustor and reported an improved stability region accompanied by various regimes of instability due to the opposing effects of flow velocity and flame velocity. Numerical modelling of a curved microcombustor for the purpose of TPV power generation was carried out by Alipoor et al. [20] and Akhtar et al. [22]. Their studies showed an improved thermal output for the curved microcombustor due to enhanced flame stability limits and a higher wall temperature in the combustor. Zuo et al. [23] created a heat recirculation region by inserting a rectangular rib in a microcombustor for TPV applications. The recirculation region improves the heat transfer between the combustor wall and the gas, which improves the flame stability limits of the microcombustor. Due to the superior performance of hydrocarbon-based microcombustors over conventional chemical batteries and the promising results obtained from improved thermal management in the studies above, microcombustor-based sources of power like microgas turbines [24], micro-thermophotovoltaic generators [25, 26], fuel cells [27], and thermoelectric generators [28–32] were studied and analysed in depth. Heat engines were found to be impractical for microscale applications due to the large number of moving parts, which not only led to considerable heat loss through friction, but also produced a lot of noise with low conversion efficiencies. Thermoelectric and thermophotovoltaic sources of power, on the other hand, are less complex systems due to a lack of moving parts [33, 34]. This not only reduces maintenance costs and increases the overall lifespan of the system, but minimizes the noise produced as well. Cho et al. [35] analysed the different kinds of power sources on a microscale and provided valuable insights on the merits and demerits of different energy sources.

Extensive research has been carried out on thermophotovoltaic [25, 26] and fuel cell [27]-based micropower generators. A backward-stepped microcombustor, having a volume of 0.113 cm^2, was developed by Yang et al. for thermophotovoltaic power generation [25]. By using hydrogen as a fuel, a power rating of 1.02 W was reported by the TPV-based power generator. Ahn et al. proposed a power generation system which integrated a solid oxide fuel cell (SOFC) with a Swiss-roll combustor [27]. They obtained a peak power density of 420 mW/cm^2 and reported efficient performances at low Reynolds numbers as well. However, due to their bulky volume, high energy consumption, and short lifespans, thermoelectric power generators are preferred over fuel cells and TPV-based power generators. Researchers are currently investigating techniques to improve the relatively lower conversion efficiency of

TEGs [36, 37]. Yoshida et al. designed a thermoelectric generator by using a silicon-coated catalytic combustor and reported a peak output power of 0.184 W with a conversion efficiency of 2.8% [28]. Shimokuri et al. [30] integrated thermoelectric modules with a novel mesoscale combustor with a provision for vortex flow. They reported a significant rise in heat transfer rate due to the development of a vortex flow with a power output of 18.1 W and an efficiency of 3%. Yadav et al. [31] utilized a recirculation cup to heat thermoelectric modules by using a three-stepped combustor as the source of power. While an efficiency of 1.2% was obtained initially by using only one module, they reported an improved efficiency of 4.6% by utilizing all the surfaces of the cup and mounting four modules. Merotto et al. [32] used catalytic combustion to develop a TEG which produced a peak output power rating of 9.86 W with a conversion efficiency of 2.85%, which was later optimized and converted into a compact power generator with a power output of 1 W [38]. In addition to the experimental studies carried out on TEGs, a number of numerical models have been developed over the last decade to demonstrate the thermoelectric effect [39, 40]. In order to develop modules with high efficiency at a lower cost, factors like thermoelectric material properties, improved thermal management, etc., are analysed in great detail [41, 42]. Chen et al. [43] used custom functions to numerically model a three-dimensional thermoelectric module in a CFD environment. Zhou et al. [44] used a cylindrical shell and straight fins to model a novel TEG, while reporting an efficiency of 5.5%. Meng et al. [45] numerically integrated a microcombustor with a TEG module and a TPV cell while simultaneously accounting for the temperature-dependent properties of the thermoelectric materials. However, most of the aforementioned studies assume a constant temperature across the hot and cold sides of the module. In practical applications, such a scenario is not possible because the flame dynamics of the combustor produce a non-uniform temperature gradient across the hot side of the module. A numerical study which accounts for the variable temperature profile across the hot end of the module is not only lacking but would also be of great interest from a practical viewpoint.

In the present study, detailed experimental and numerical investigations on different thermoelectric micropower generators are carried out. The effect of different microcombustors and heat sinks on the performance of the micropower generator is analysed. In order to further optimize the system, a self-aspirating combustor is developed. The self-aspirating combustor eliminates the need for artificial supply of air and thus eliminates a portion of the auxiliary power requirement. Based on the above results, a stand-alone micropower generator for portable applications is developed. The present study also discusses the three-dimensional numerical modelling of a combustion-based thermoelectric micropower generator. The novelty of this aspect of the study lies in the development of an optimized combustor by analysing the flame dynamics in detail, while simultaneously integrating the thermoelectric model into a CFD environment. The accuracy of the thermoelectric model is validated by comparing the numerically obtained values with the values specified by the manufacturer. After establishing the accuracy of the thermoelectric model, the

thermoelectric performance of the integrated system is studied in depth by analysing parameters like the output power rating, open-circuit voltage, conversion efficiency, etc.

2 Experimental Details

The experimental set-up, which is similar to our previous studies [46, 47], consists of high-pressure air supply system, fuel tanks, electronic mass flow controllers (MFCs), the integrated thermoelectric power generator unit, and power-measuring instruments. The mass flow rates of propane and air are controlled separately through two MFCs of capacity 0–0.5 LPM and 0–2 LPM, respectively, by using a command module connected to a personal computer. The fuel is thoroughly mixed with air by injecting it as a high-velocity jet into the airflow. This ensures the preparation of a proper mixture for premixed combustion. A pilot flame (by using a butane torch) is used to ignite the fuel–air mixture at the ignition port of the combustor. After the proper stabilization of flame inside the combustor, the ignition port is closed which allows for the exhaust gas recirculation. The MFCs have an accuracy of $\pm 1\%$, and the thermocouples used to measure the temperature of the walls have an accuracy of 2%. The thermocouples are of k-type with a 0.5-mm bead diameter.

2.1 Microcombustor Details

In the present study, two modes of combustion systems were analysed: (I) artificial premixing and (II) self-aspirating mode. In order to study mode I, two types of combustors based on the multiple backward-facing step concept are fabricated and tested. Furthermore, an ejector system is developed to entrain the air in a self-aspirating mode, which theoretically could prepare a proper premixed mixture for combustion. A detailed analysis of the combustion characteristics of these combustors are presented in this section.

2.1.1 Multicombustors

Figure 1 shows the schematic diagram of the single and dual microcombustor configurations, which consist of one and two sets of microcombustors, respectively, in a rectangular chamber of size $32 \times 32 \times 10$ mm^3 fabricated using aluminium. Each microcombustor consists of three cylindrical backward-facing steps and two recirculating holes of 4-mm diameter [46]. The inlet diameter of the microcombustor is 2 mm and is increased to 6 mm along the inlet to outlet direction. The dimensions of the combustor are the same as that of the author's previous studies [46]. The purpose

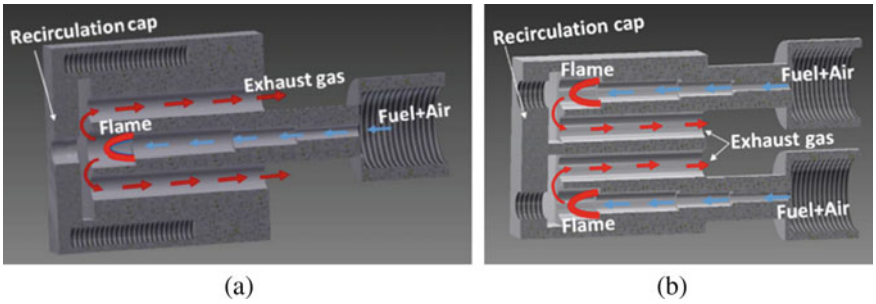

Fig. 1 Schematic of **a** single and **b** dual microcombustor

behind designing a backward-stepped facing combustor is to produce local recirculation in the region around the steps by allowing the mixture to undergo sudden free expansion. Along with these combustors, two 4-mm diameter holes are provided to expel the combustion products. These holes also help in the extraction of excess enthalpy from exhaust gases, preheat the fresh incoming mixture and concurrently transfer excess heat to thermoelectric modules.

2.1.2 Self-aspirating Combustors

The applications of self-aspirating combustors to obtain proper premixed flames for portable power generation are very limited [48, 49]. The present study investigates the viability of a self-aspirating microcombustor for thermoelectric power generation. The self-aspirating mode is achieved through an ejector system as shown in Fig. 2, which consists of a nozzle and converging–diverging (C-D) tube. The smaller diameter of the nozzle ($d = 0.3$ mm) causes the fuel to enter the ejector with a high-velocity jet, leading to a significant pressure drop in the ejector chamber. This low pressure causes air to be entrained into the 8-mm diameter-wide chamber through the annular inlet of the ejector. The difference between the velocities of the fuel flow and the airflow leads to viscous dragging, which enhances the mixing process between the air and the fuel. The ejector consists of a C-D tube which has a throat diameter of

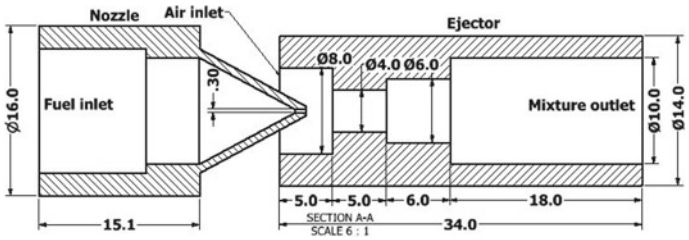

Fig. 2 Schematic of ejector system

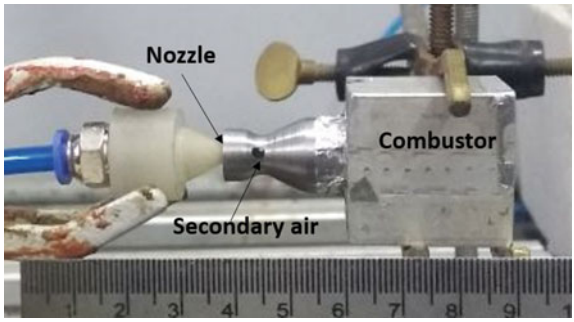

Fig. 3 Real photograph of self-aspirating microcombustor developed

4 mm. Furthermore, two 2-mm holes are drilled at the throat section for secondary air entrainment as shown in Fig. 3. The outlet of the ejector is then connected to a square heating block (which acts as combustor) of dimensions $32 \times 32 \times 32$ mm^3 fabricated from aluminium. The heating cup consists of a single backward-facing step of 1 mm at the inlet to stabilize the flame. A through-hole of 27-mm diameter is provided within to expel the exhaust gases.

On the perspective of power generation, self-aspirating combustors can reduce the input power significantly by eliminating the requirement of manually pumping the air into the combustor. Therefore, this system could lead to a significant rise in the overall system efficiency.

2.2 Micropower Generator Details

The power generator prototyped in the present study is based on the Seebeck effect, and consists of two Bi_2Te_3-based TEGs, mounted on to the bare faces of the microcombustor (as a heating source) along with the cooling jackets. The microcombustor will act as the heat source, and various active and passive cooling methods are tested to maintain a lower temperature across the cold side of the module. The effect of water-cooled and air-cooled sinks on the performance of the power generator is analysed and compared. Finally, an optimum sink is chosen to develop the stand-alone portable power generator. The water-cooled sink is made up of copper which consists of three passes, as shown in Fig. 4a. It is used as a heat sink for both the combustor configurations [46]. Multiple passes ensure sufficient cooling of the TEGs due to the enhanced residence time of the coolant within the jacket. The total volume of the cooling jacket is $32 \times 32 \times 10$ mm^3, and it maintains the water at a constant temperature of 303 K. The air-cooled sink, shown in Fig. 4b, consists of aluminium fins with a cooling fan to improve the output power and conversion efficiency by maintaining a lower temperature across the cold end of the module. The fin thickness, spacing, and height are 1.5 mm, 2 mm, and 17 mm, respectively. However, it is obvious that the air-cooled jackets are less efficient than the water-cooled jackets due to the low specific heat capacity of air. An auxiliary power source (powered by a DC supply

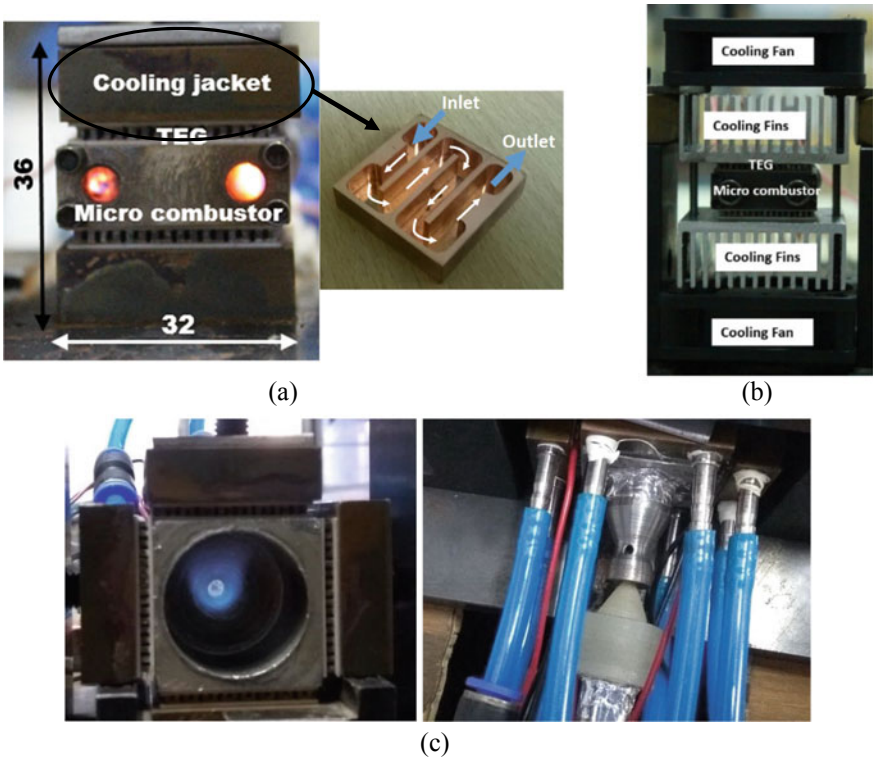

Fig. 4 **a** Water-cooled micropower generator, **b** air-cooled micropower generator, **c** self-aspirating mode micropower generator (left) front view and (right) top view

system TESTRONIX 92B) supplies power to the cooling fan. A tachometer is used to measure the speed of the cooling fan. The thermal characteristics of the system are measured for different fan speeds of 500 RPM, 1500 RPM, and 3000 RPM, which corresponds to auxiliary power ratings of 0.07 W, 0.19 W, and 0.38 W, respectively.

To develop the self-aspirating micropower generator, four thermoelectric modules are mounted on the bare faces of the combustor along with the cooling jacket as shown in Fig. 4c. The working of a self-aspirating combustor has already been discussed in detail in the previous section. The water-cooled sink has been adopted to extract the maximum power from the modules.

3 Result and Discussion

In this section, thermal characteristics of the microcombustor and power characteristics of the micropower generators are discussed in detail. The thermal performances of the single and the dual combustors are compared, and the more efficient combustor

is chosen for analysing the effect of different heat sinks on the power characteristics. Furthermore, the performance of the self-aspirating combustor has been analysed and a stand-alone micropower generator has been prototyped and studied.

3.1 Thermal Characteristics of the Combustors

The variation of fuel mass flow rates ($\dot{m}_f$) and input power (P_{in}) with different mixture velocities for $\phi = 0.9$ and 1.0 is shown in Fig. 5a. The proposed micropower generator is operated for $\dot{m}_f$ ranging from 6.44×10^{-7} kg/s to 2.15×10^{-6} kg/s and 7.14×10^{-7} kg/s to 2.38×10^{-6} kg/s, respectively, for $\phi = 0.9$ and 1.0, respectively. These fuel flow rates correspond to the minimum and maximum mixture flow rates of 118×10^{-7} kg/s ($v_{\text{in}} = 3$ m/s) and 390×10^{-7} kg/s ($v_{\text{in}} = 10$ m/s), respectively.

Since the thermoelectric output depends on the temperature difference across the module, it is important to analyse the amount of heat transferred by the gases to the combustor wall and the amount of heat lost through the exhaust gases. The thermal performance of the single and dual combustors is analysed. Variation of the average wall temperature and average exhaust gas temperature with the total mixture flow rates for the single and dual combustors is shown in Fig. 5b. Even though the average surface temperature is reported to be as high as 673 K for 234×10^{-7} kg/s ($v_{\text{in}} = 6$ m/s), mounting the modules on the combustor wall results in a significant temperature drop, causing it to fall below the temperature limit of the modules (<523 K). It can also be noted that the heat transferred to the combustor wall from the exhaust gases is significantly higher in case of the dual combustor configuration than for the single combustor [46]. The average surface temperature is observed to be almost 15 K higher in case of the dual combustor because of the enhanced wall–flame interaction and efficient heat recirculation. Conclusively, the

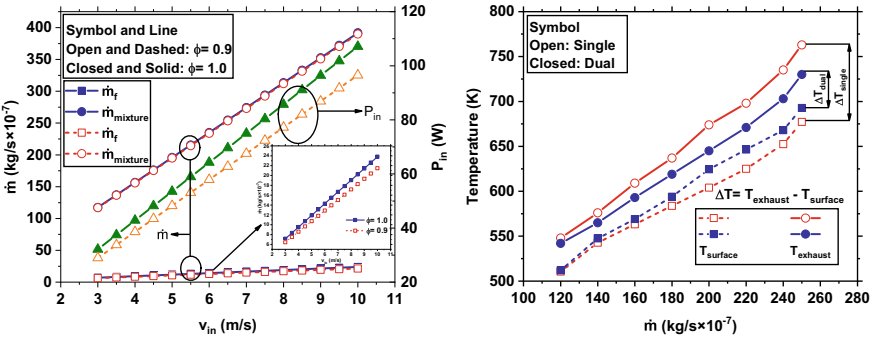

Fig. 5 **a** Variation of mass flow rates and input power with mixture velocity and **b** variation of thermal characteristics with total mixture flow rate

micropower generator is observed to be more efficient with a higher power output for the dual combustor case.

3.2 Power Characteristics of the Power Generator

3.2.1 Water-Cooled-Based Power Generator

A three-pass cooling jacket, made up of copper, is used as the water-cooled sink for the TEG. Initially, the output characteristics are measured for different cooling flow rates, ranging from 0.5 to 1.5 LPM. It is found that there is no significant difference in the output characteristics that are observed for cooling flow rates of 1.0 and 1.5 LPM. Therefore, the present experiments are carried out for coolant flow rate of 1.5 LPM. The heat transfer to the combustor wall is enhanced by increasing the residence time of the reacting mixture within the combustor, which is evident by ΔT $(T_H - T_C)$ of the dual combustor as demonstrated in Fig. 6b. It is observed that there is an increase of 10–20 K in the temperature difference between the dual and single combustor configurations, which corresponds to an increase in the η_{con} of the dual combustor case by 0.2–0.6%. Similar observations were reported in numerical studies which investigated the difference in the thermal output of multichannel microcombustors and single-channel microcombustors [50–52]. Figure 6b shows the output power comparison between single combustor- and dual combustor-based power generators for different mixture flow rates. It is observed that the power output increases with an increase in the mixture velocity. For a mixture flow rate of 390 $\times$ 10^{-7} kg/s ($v_{\text{in}} = 10$ m/s) and a power input of ~97 W, maximum power outputs of 3.89 and 4.6 W are achieved for the single combustor and dual combustor cases, respectively. It is observed from Fig. 6b that the trend for conversion efficiency is similar to the

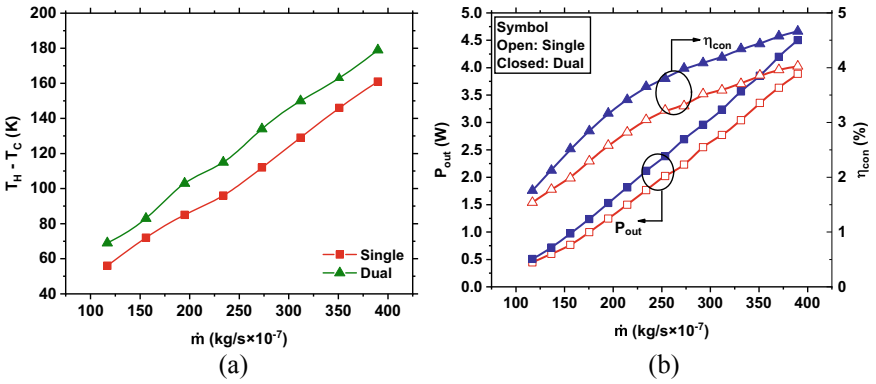

Fig. 6 Variation of **a** $T_H - T_C$ and **b** output power and conversion efficiency with total mixture flow rate at $\phi = 0.9$

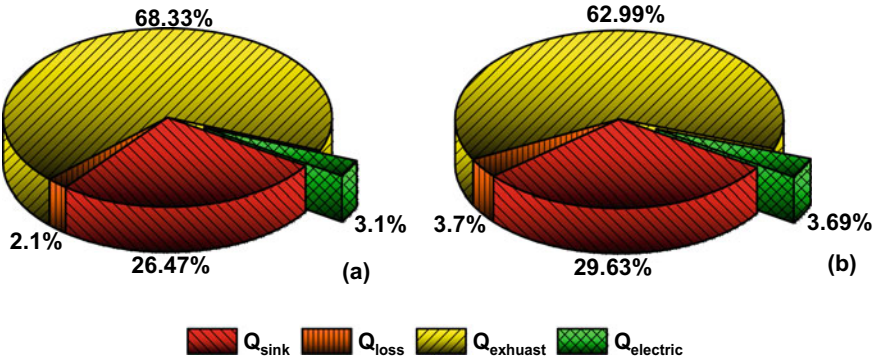

Fig. 7 Heat balance sheet for **a** single combustor and **b** dual combustor

trend observed for the output power for both combustor configurations. Since the electric power generated by the module is primarily dependent upon the temperature difference across the module, the conversion efficiency η_{con} is greatly dependent upon the wall temperature of the combustor.

The rate of heat transferred to the combustor wall is further analysed with the help of a detailed energy balance sheet. The energy balance analysis was carried for 273 $\times$ 10^{-5} kg/s ($v_{\text{in}} = 7$ m/s) at $\phi = 1.0$. The total heat energy supplied to the system is equal to the chemical energy of the supplied fuel, which is equal to the product of the mass flow rate of the fuel and its calorific value. To calculate the heat loss from the TEG to the heat sink, the contributions of the Peltier effect, heat loss through conduction, and Joule's heating effect are calculated. The heat balance sheet is shown in Fig. 7a, b. These values are obtained by assuming a uniform temperature across the lateral walls of the heating medium. This is then used to evaluate the convective heat losses from the combustor. Thus, the heat lost from the exhaust gases can be represented by $Q_{\text{exhuast}} = Q_{\text{input}} - (Q_{\sin k} + Q_{\text{loss}})$. It can be seen from Fig. 7 that the amount of heat lost to the ambient through exhaust gases is almost equal to 60%. The heat loss from the thermoelectric modules is found to increase with a rise in the power output from the modules and is presently reported to be 20–30% of the total heat loss. While the heat lost from the microcombustor is found to increase with increasing input power, the overall contribution of the input power is significant enough to lead to a reduction in the total contribution of the heat rejection from 4.4 to 3.54%. While the dual configuration leads to an increase in the surface area exposed to the ambient which leads to a higher heat loss of ~1.5%, its ability to transfer a greater amount of heat to the sink (~3.0%) through the combustor walls allows it to generate a power output higher than that of the single combustor by ~0.6%.

3.2.2 Air-Cooled-Based Power Generator

The difficulties in transporting a water-cooled sink due to its bulky volume and weight has limited the usage of water-cooled power generators for portable power applications. Although the air-cooled power generator is less efficient than the water-cooled power generator, air-cooled systems would be a better substitute in real-life portable power applications. Therefore, it is necessary to understand the comparative study between the performances of air-cooled power generators and water-cooled power generators. There are only a few studies [48, 53, 54] reported on the development of air-cooled microcombustor-based power generators, and some other recent studies are based on mimicking the microcombustor using an external electric heater [55–57]. In this section, the effect of different air-cooling methods on the dual combustor-based power generator is analysed. Figure 8a shows the variation of the output power with mixture flow rates for different auxiliary power input values. A value of 0 W for auxiliary input power refers to natural convection (only fins), while the other values represent forced convection (using CPU fan). Although the output power and conversion efficiencies are reported to increase with increasing mixture velocity for the fin-fan case, a significant drop in the output power values is observed for the case having only fins. This behaviour is attributed to the poor cooling capacity of the fin system. For auxiliary power inputs of 0.07, 0.19, and 0.38 W, conversion efficiencies of 1.2, 2.1, and 2.5% with power outputs of 1.3, 2.0, and 2.4 W are reported, respectively.

The auxiliary components of the system, like the fan, micro-blower, valves, etc., usually last for 8–10 years, which makes the system economically favourable from a manufacturing viewpoint. Besides being easily available, these components are relatively inexpensive and easy to assemble. The air required to produce the fuel–air mixture can be provided by a small micro-blower, while 180 g of fuel from a butane

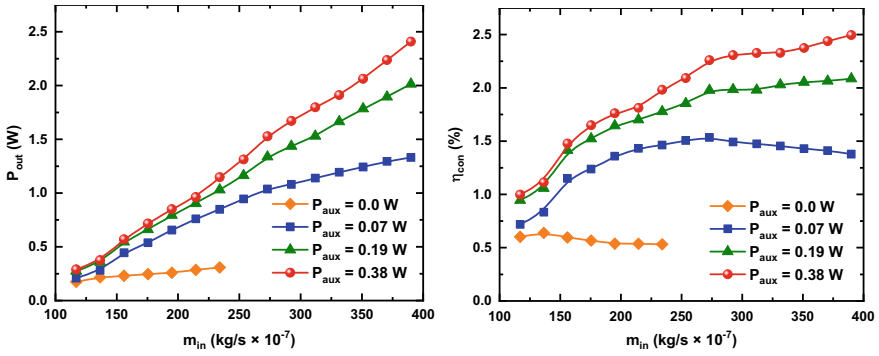

(a) (b)

Fig. 8 Variation of **a** output power and **b** conversion efficiency with mixture flow rates for different auxiliary powers

cartridge can produce a constant power output from the system for 24 h. Recharging of the entire system only requires replenishment of the butane cartridge.

3.3 Self-aspirating Power Generator

The dimensional details of the self-aspirating microcombustors are explained in the previous sections. The self-aspirating combustor uses the Venturi effect to entrain the air through the annular gap provided between nozzle exit and ejector entrance. To study the air entrainment, contours of the axial velocity of the propane fuel are plotted and shown in Fig. 9a. There is a sharp rise in the inlet velocity as the fuel enters the ejector, with a maximum velocity in excess of 110 m/s being reported. As the area of the chamber increases, a significant drop in the velocity of the fuel jet is observed. This sudden rise in the velocity leads to a pressure drop in the ejector chamber, leading to air being entrained through the air inlet.

One of the major obstacles regarding self-aspirating combustors is the inability to analyse and regulate the equivalence ratio of the fuel–air mixture created in the ejector chamber. Figure 9b shows the contours of the equivalence ratio of the mixture across the ejector chamber. Due to improper mixing of fuel and air, variation of equivalence ratio is observed along the axial line of ejector. The mixture is richest around the

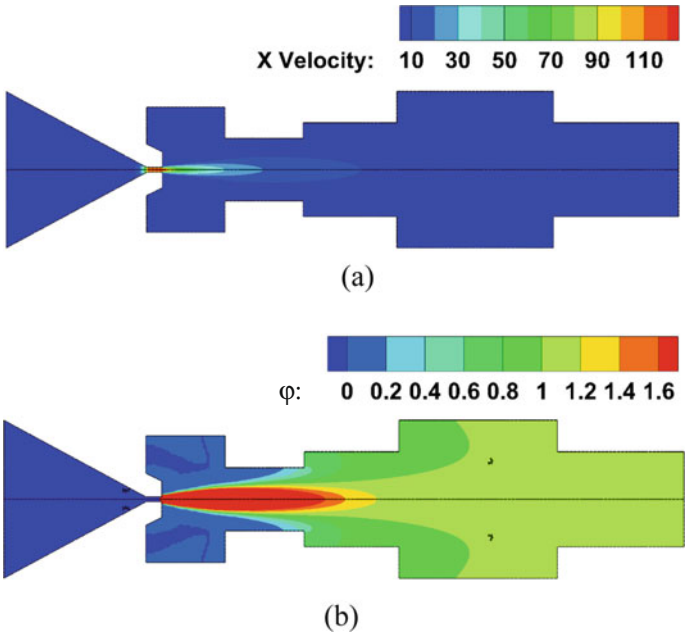

Fig. 9 Contours of **a** axial velocity and **b** equivalence ratio

fuel jet ($\phi \gg 1$), while the outlet equivalence ratio is observed to be in the range of 0.9–1.0. The backward-facing steps are provided to create zones of local turbulence in the ejector chamber, which enhances the mixing process between the air and the fuel. Therefore, it is concluded that employing secondary air entrainment would definitely improve the equivalence ratio, which would result in a zero auxiliary power consumption. With aid of the aforementioned numerical observations, a detailed experimental investigation on the performance of the self-aspirating microcombustor and power generator was carried out. The effect of secondary air entrainment on flame stabilization has been compared with the primary air case and shown in Fig. 10. In case of no secondary flow, diffusion flames were obtained for power inputs of 65 and 128 W. This is indicated by the appearance of the distinct orange colour in the flame, which points towards insufficient air for the combustion. This problem is rectified in the second case (*d-f*) through the provision of secondary airflow. This provides sufficient air for complete combustion of the fuel, evident by the blue premixed flame obtained for all three different power inputs.

Further, a power generator, based on the self-aspirating combustor, is prototyped. A premixed flame is found to be stabilized on the backward-facing step, which heats the combustor wall. This acts like the hot side of a thermoelectric generator. The temperature on the combustor surface is nearly 423 K at an input power of 128 W. However, a significant drop in the surface temperature is reported after mounting the modules on the combustor. The hot side temperature drops by almost 60 K, and a power output of nearly 0.5 W is achieved for a power input of 128 W. This

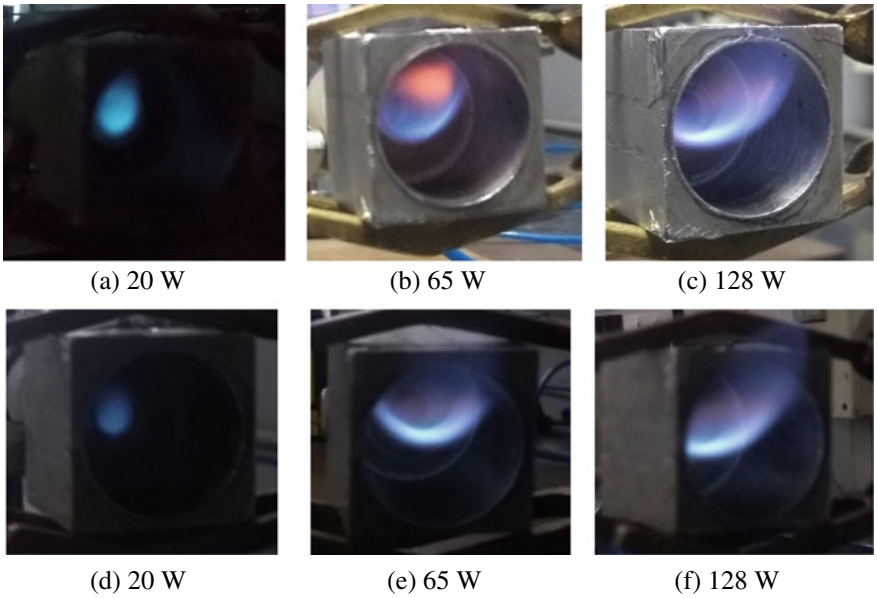

Fig. 10 **a** is no secondary air and **b** is secondary air

lower output power indicates improper combustion, which results in the poor thermal characteristics of the combustor. It is also observed that a further increase of input power beyond 128 W partially shifts the flame outside the combustion chamber and most of the heat is lost unused. Also, the combustor can be further modified to use the enthalpy of exhaust gases, which would certainly improve the power output and conversion efficiency of the system.

3.3.1 Development of a Stand-alone Micropower Generator

A stand-alone power generator on a microscale, having the capacity to deliver a constant power output of 1 W, is designed as shown in Fig. 12a, b. The outer body is constructed by using acrylic. It occupies a total volume of 120 × 95 × 75 mm^3 and weighs ~400 g. The system is slightly bulky, but there is potential for further optimizations. The power supply unit of the thermoelectric generator comprises two thermoelectric modules mounted on the microcombustor. Aluminium fins, along with an additional cooling fan, perpendicular to the fins, are used as a heat sink. A micro-air blower is used in conjunction with a butane cartridge to supply the premixed fuel–air mixture. The mass flow rate and equivalence ratio of fuel–air mixture are varied with the help of a potentiometer. Although the water-cooled sink produces a better thermoelectric output, the portability of the system is reduced with a water-cooled sink. Thus, an air-cooled sink is used in the integrated system.

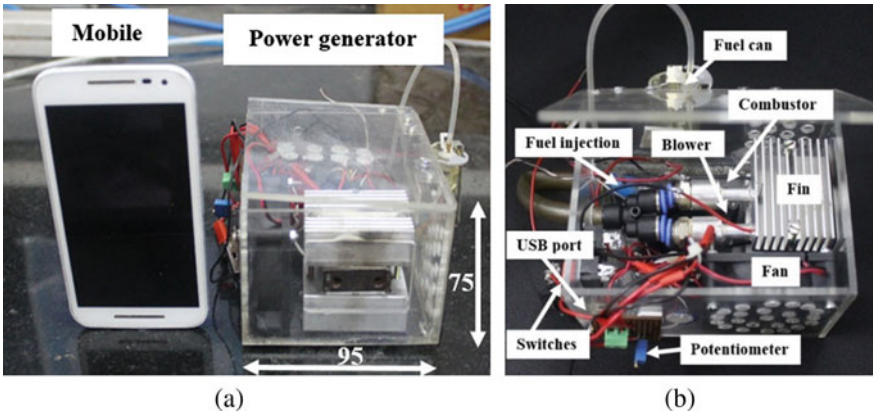

Fig. 12 **a** Size comparison of the micropower generator prototype and **b** inside view

4 Numerical Modelling of Micropower Generator

In this section, three-dimensional modelling of a combustor-based thermoelectric power generator has been carried out. Although numerous studies can be found on the numerical modelling of microcombustors and TEGs exclusively, designing an integrated system numerically is of great challenge and interest for optimizing the real micropower generator systems. The study derives its novelty from being the first such model to simulate an integrated microcombustor–thermoelectric power generator in a CFD environment and analysing the thermal output of the combustor in 3D.

4.1 Computational Domain and Governing Equations

The computational domain of the integrated system is shown in Fig. 13. The steel combustor has two rectangular backward-facing steps at combustor widths of 4 mm and 6 mm at distances of 5 mm and 25 mm from the inlet, respectively. The steps produce local eddies which lead to increased turbulence in the region around the steps. In order to preheat the incoming reactant mixture, a 2-mm-thick recirculating steel cup is placed at a distance of 3 mm from the combustor exit. It allows the recirculating exhaust gases to heat the outer combustor wall, which conducts the heat to the incoming unburnt mixture, while simultaneously providing a housing for the thermoelectric module. The thermoelectric module is modelled as a $40 \times 40 \times 3.5$ mm^3 rectangular block with three different layers. The central layer is a Bi_2Te_3 layer, which serves as the semiconductor, and is sandwiched between two ceramic

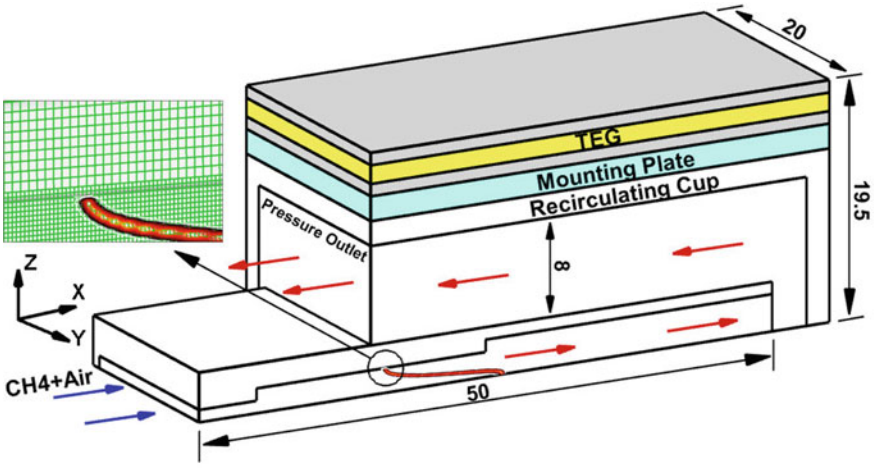

Fig. 13 Computational domain of the integrated thermoelectric generator

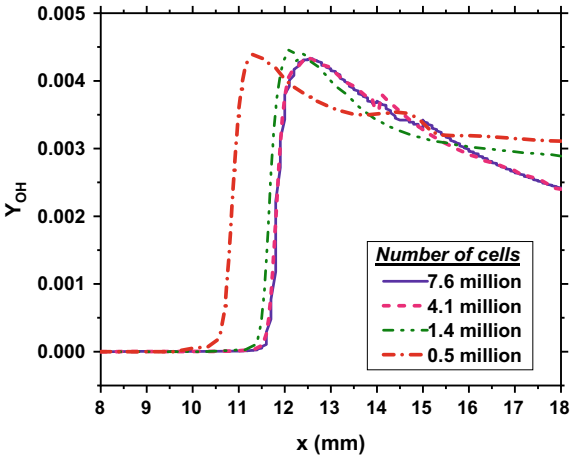

Fig. 14 Grid independence study for the present computation

layers. A premixed CH_4–air mixture is passed through the 2-mm inlet and ignited at the combustor exit.

In order to establish the independence of the obtained results on the computational grid, a mesh independence study is carried out. Simulations are carried out for four different grids ranging from 0.5 million cells to 7.6 million cells. The mass fraction of the OH species is measured along the inner wall of the combustor for all four grids as shown in Fig. 14. Since negligible difference is obtained between the readings obtained for the grids having 7.6 million cells and 4.1 million cells, the grid having 4.1 million cells is used for the present computation.

The 3D Navier–Stokes equations are used as the governing equations for the combustion reactions. Due to a low Knudsen number (<1), the fluid medium is treated as a continuum. In order to reduce the complexity of the reactions, the following assumptions are made: (a) Dufour effects are neglected, (b) radiation effects are neglected, (c) work done by the pressure and viscous forces is considered to be negligible, (d) steady-state combustion, and (e) due to a low Mach number, the flow is assumed to be incompressible. As a result, the governing equations are reduced to the following forms (Eqs. 1–4).

$$s\frac{\partial \rho_f}{\partial t} + \nabla.\rho_f \vec{v} = 0 \tag{1}$$

$$\frac{\partial \rho_f u_i}{\partial x} + \nabla.\rho_f \vec{v} = -\nabla p + \nabla.(\mu \nabla u_i) \tag{2}$$

$$\frac{\partial \rho_f h}{\delta t} + \nabla.\rho_f \vec{v} h = \nabla.\left(k\nabla T - \sum_{j=1}^{n} h_j \overrightarrow{J_j}\right) - \sum_{j=1}^{n} \frac{h_j^o}{M_j} R_j \tag{3}$$

$$\frac{\partial Y_j}{\partial t} + \nabla.\left(\rho_f \vec{v} Y_j\right) = -\nabla.\left(\overrightarrow{J_j}\right) + R_j \tag{4}$$

where ρ, p, μ, h, k, M_j, and Y_j represent fluid density, pressure, viscosity, enthalpy, thermal conductivity, molecular weight, and mass fraction of jth species. $\vec{v}$ denotes the two-dimensional velocity vector. $\overrightarrow{J_j}$ is the diffusion flux, and R_j is the volumetric rate of jth species determined from the Maxwell–Stefan equation and the Arrhenius equation, respectively.

To account for the thermoelectric effect simultaneously, the governing equations for the TEG model need to be integrated into the CFD model. Chen et al. [43] adopted the following equations to integrate the thermoelectric model:

$$\nabla J_c = 0 \tag{5}$$

$$\nabla q = -\nabla[k\nabla T] = mc\frac{\partial T}{\partial t} + J_c^2\rho_c + [\nabla\alpha]TJ_c \tag{6}$$

$$\nabla V = -\alpha\nabla T - \rho_c J_c \tag{7}$$

Before integrating these equations, they are modified to account for the non-uniform temperature profile across the hot side of the module. Equation 5 conserves the electric flux J_c flowing through a unit cell of the domain, while Eq. 6 provides a solution for the thermal field generated, where the second term on the RHS of Eq. 6 represents the temperature-dependent Joule's electric energy and the third term accounts for the Peltier and Thomson effects. Equation 7 gives the value of the electric field generated.

4.2 Boundary Conditions and Reaction Modelling

The GRI 3.0 mechanism [58] is used to simulate the flow of the premixed CH_4–air mixture through the inlet at the ambient temperature $T_a = 300$ K. Different mixture velocities ranging from $v_{in} = 1$ to $v_{in} = 7$ m/s are simulated for $\phi = 0.8$ and $\phi = 1$. A no-slip condition is applied on the inner walls of the microcombustor. To account for the heat loss from the walls of the combustor exposed to the ambient, a mixed boundary condition was applied on the external walls with a standard heat transfer coefficient (20 W/m^{2}K) and emissivity (0.9). A Neumann boundary condition with constant pressure is assigned at the outlet. To account for possible turbulence, the k-ε turbulence model is adopted. The polynomial relations of the semiconductor material [45] are applied to integrate the temperature-dependent nature of the semiconductor material (Table 1).

Table 1 Material specifications

Material	Cell zone	ρ_c (kg/m^3)	K (W/m K)	c_p (J/kg K)
Bi_2Te_3	Semiconductor material TEG	10,922	Variable [45]	200
Ceramic	Ceramic walls of module	4300	18	419
Steel	Combustor and cup walls	8030	16.27	502.48

Table 2 Details of the User-Defined Scalars used in the 3-D modelling of the TEG

Scalar	Mathematical formula	Source term	Diffusivity
UDS_A	$\nabla \text{UDS\_}A = -\rho J$	0	$\frac{1}{\rho}$
UDS_B	$\nabla \text{UDS\_}B = \alpha$	0	1
UDS_C	$\nabla \text{UDS\_}C = -\alpha \nabla T$	$\frac{\partial \alpha \left(\frac{\partial T}{\partial x}\right)}{dx} + \frac{\partial \alpha \left(\frac{\partial T}{\partial y}\right)}{\mathrm{d}y}$	1
UDS_D	$\nabla \text{UDS\_}D = \frac{\partial \alpha \left(\frac{\partial T}{\partial x}\right)}{\mathrm{d}x}$	0	1
UDS_E	$\nabla \text{UDS\_}E = \frac{\partial \alpha \left(\frac{\partial T}{\partial y}\right)}{\mathrm{d}y}$	0	1
UDS_F	$\nabla \text{UDS\_}F = \frac{\partial \alpha \left(\frac{\partial T}{\partial z}\right)}{\mathrm{d}z}$	0	1
Energy	–	$\frac{1}{\rho}(\text{UDS\_}A)^2 - \nabla \text{UDS\_}B \frac{T}{\rho} \nabla \text{UDS\_}A$	k

4.3 Numerical Methodology

A general-purpose CFD software FLUENT 16.2 [59] is used to carry out the simulations. Spatial integration was used to carry out the steady-state simulations. Unlike earlier studies that simulated the thermoelectric effect on FEM solvers, the present study integrates the combustion process with the thermoelectric effect while accounting for the non-uniform temperature profile across the hot side of the module as well. ANSI C coding is used to integrate the thermoelectric equations into the CFD software [43]. The Joule, Peltier, and Thomson terms are defined as source terms with the help of user-defined scalars and user-defined functions. The terms are then hooked to the CFD software after interpreting the code in the solver. The additional terms in the governing equations for the thermoelectric effect are defined in Table 2.

4.4 Results and Discussion

A detailed analysis of the thermal characteristics of the microcombustor is carried out, with parameters like exhaust gas temperature, combustion efficiency, flame position, etc., being studied thoroughly. This is followed by an investigation into the thermoelectric characteristics of the integrated system such as the open-circuit voltage,

output load power, conversion efficiency where the obtained results are compared with known values.

4.4.1 Thermal Characteristics of the Combustor

Since the thermoelectric output of the integrated system depends primarily on the temperature difference across the module, it is crucial to analyse the average temperature of the hot side of the module. Variation of the average temperature of the hot side of the module with the mixture velocity is shown in Fig. 15a. There is a steady rise in the average temperature of the hot side with increasing inlet velocity, with the temperature profile for the $\phi = 1$ case being greater than the $\phi = 0.8$ case. A maximum temperature of 551 K is obtained for $v_{in} = 9$ m/s at $\phi = 1$. The higher temperature profile for $\phi = 1$ can be attributed to the fact that the combustion reaction at stoichiometric ratio has a greater combustion intensity than the reaction occurring at $\phi = 0.8$.

The temperature difference between the $\phi = 1$ and the $\phi = 0.8$ cases decreases with increasing mixture velocity. This trend can be explained by the position of the flame in the combustor for different mixture velocities. Figure 15b shows the position of the flame along the axial length of the combustor for different mixture velocities. The flame is observed to move further downstream with increasing mixture velocity. It is noted that the axial position of the flame in case of $\phi = 0.8$ and $\phi = 1$ coincides for $v_{in} = 1$ and $v_{in} = 3$ m/s, but the flame moves further downstream for $v_{in} = 5$ and $v_{in} = 7$ m/s in case of $\phi = 0.8$. This causes the flame in case of $\phi = 0.8$ to be in closer proximity with the module than in case of $\phi = 1$. As a result, the difference between the average temperatures of the hot side of the module decreases with increasing mixture velocities.

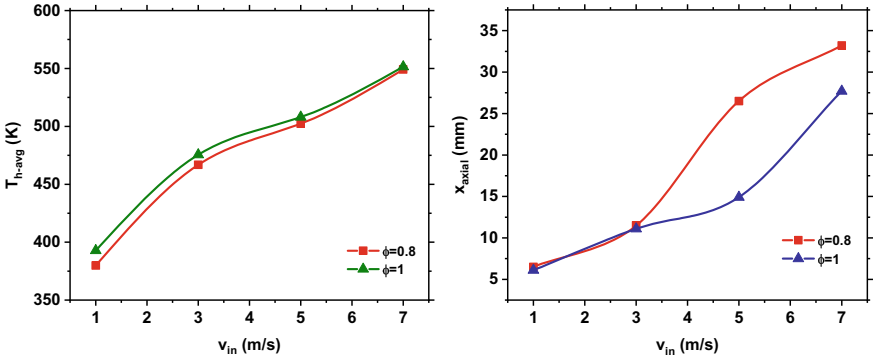

Fig. 15 Variation of **a** average temperature of hot side of the module and **b** flame position along the axial length of the combustor with mixture velocity

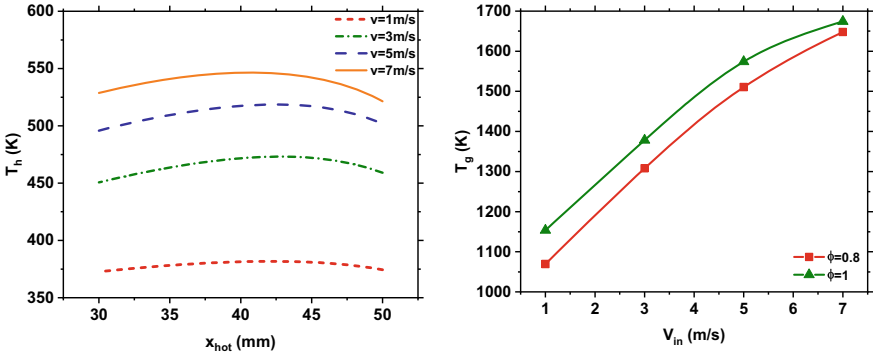

Fig. 16 **a** Temperature distribution along hot side of the module and **b** variation of average gas temperature with mixture velocity

In case of an integrated thermoelectric power generator with a combustor power source, a non-uniform temperature distribution is obtained along the hot side of the module instead of a constant, uniform temperature. The temperature distribution along the hot side of the module in the direction of flow of exhaust gas is studied in Fig. 16a. Higher temperature profiles are obtained for greater mixture velocities. The peak temperature is reported in the central portion of the module, with a maximum temperature of ~545 K obtained for $v_{\text{in}} = 7$ m/s. The primary reason for obtaining the temperature peak in the central portion is because of the additional heat loss taking place from the lateral ends of the hot side of the module. The central portion loses heat only through conduction, while the lateral ends are exposed to ambient conditions and lose heat through convection and radiation as well. Consequently, temperatures at the ends of the horizontal wall of the module are lower than the temperatures obtained in the central portion of the hot wall. It is also noteworthy that simulations have not been carried out for mixture velocities greater than 7 m/s. This is mainly because velocities in excess of 7 m/s lead to temperature hotspots in excess of 573 K being formed along the hot side of the module, which leads to thermal breakdown of the module.

The temperature of the exhaust gases is also a metric to measure the intensity of the combustion reaction. Exhaust gas temperature for different mixture velocities is shown in Fig. 16b. Increasing inlet velocities lead to a rise in the exhaust gas temperature as well. Since the combustion reaction taking place at stoichiometric ratio has the highest combustion intensity, a maximum exhaust gas temperature of ~1675 K is obtained for $v_{\text{in}} = 7$ m/s at $\phi = 1$.

In order to improve the efficiency of the integrated system, it is desirable to obtain the maximum possible combustion intensity. Figure 17 shows the combustion intensity for different mixture velocities and equivalence ratios. Variation of the Nusselt number for $\phi = 1$ is shown along the inner combustor wall in Fig. 17a. The maximum Nusselt number obtained is equal to ~3100 for $v_{\text{in}} = 7$ m/s, with

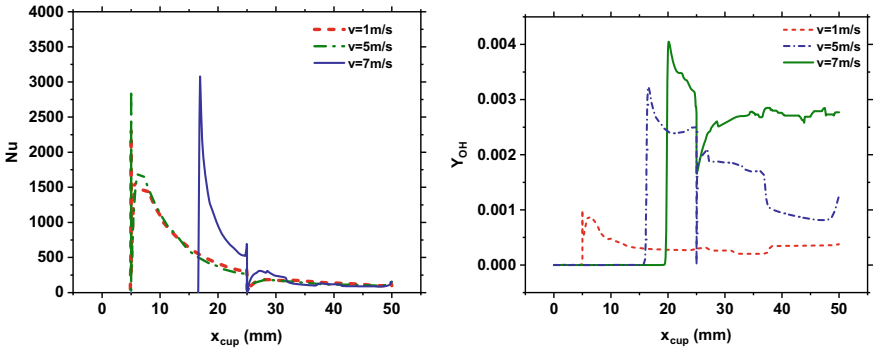

Fig. 17 Variation of **a** Nusselt number at $\phi = 1$ and **b** mass fraction of OH $\phi = 0.8$ along the inner combustor wall

the peak being located further downstream with increasing velocity. Since Nusselt number is a measure of the amount of heat transferred to the combustor wall, the maximum Nusselt number is an indicator of the fact that more heat is transferred to the combustor wall with increasing mixture velocity. Greater the heat transferred to the wall, greater is the intensity of combustion. Figure 17b shows the variation of the mass fraction of OH along the inner combustor wall at $\phi = 0.8$. A trend similar to that of the Nusselt number is obtained for Y_{OH}, with the maximum value of ~0.04 obtained at $v_{in} = 7$ m/s. OH concentration is a direct metric of the combustion intensity [60]. A higher OH combustion indicates a higher combustion intensity. These readings confirm the observations made in Fig. 17a as well.

The maximum values of Nusselt number and Y_{OH} can be used to predict the exact location on the combustor wall where the flame is anchored. Since the point of contact between the flame and the combustor wall will have the maximum amount of heat transfer and highest combustion intensity, the Nu and Y_{OH} peaks indicate the anchoring point for the flame on the inner combustor wall. However, since the flame location in Fig. 15b is plotted along the axial wall of the combustor and in Fig. 17 is plotted along the inner combustor wall, the difference between the distances at which the maximum Nu and Y_{OH-} are obtained in Fig. 17 and the distances at which the flame tip is located in Fig. 15b gives an approximate measure of the length of the flame.

The three-dimensional contours of temperature (upper half) and velocity (lower half) for different mixture velocities are shown in Fig. 18. The flame shifts downstream with increasing mixture velocities and has a tendency to stabilize at the steps due to enhanced local turbulence. A significant jump in velocity is reported after combustion, with velocities as high as 19 m/s obtained for $v_{in} = 7$ m/s. In order to point the exact location of the flame front, contours of the mass fraction of HCO are overlapped with the velocity contours in the lower half of the figures.

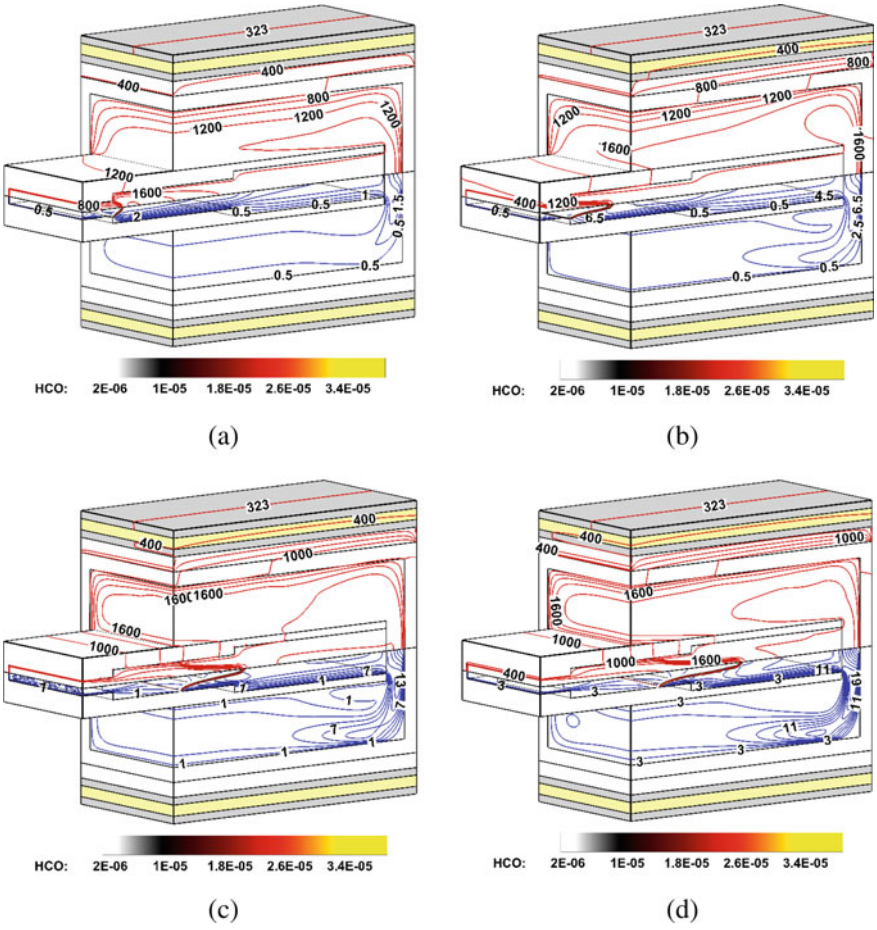

Fig. 18 Contours of temperature (upper half) and velocity and mass fraction of HCO (lower half) for **a** $v_{in} = 1$ m/s, **b** $v_{in} = 3$ m/s, **c** $v_{in} = 5$ m/s, **d** $v_{in} = 7$ m/s

4.4.2 Validation of TEG Simulation

Before studying the thermoelectric characteristics of the system, it is important to verify the accuracy of numerical model of thermoelectric generator developed. For validation purposes, the numerical results obtained are compared with the values specified by the manufacturer [61]. The module is designed independently, and constant temperature values are applied as boundary conditions on both ends of the module. A comparison between the standard values of the open-circuit voltage and output power, as specified by the manufacturer, and the numerically obtained results for the same boundary conditions and material properties is shown in Fig. 19. There is a steady rise in the open-circuit voltage and the output power with a rise in the temperature of the hot side of the module, which leads to a rise in the temperature

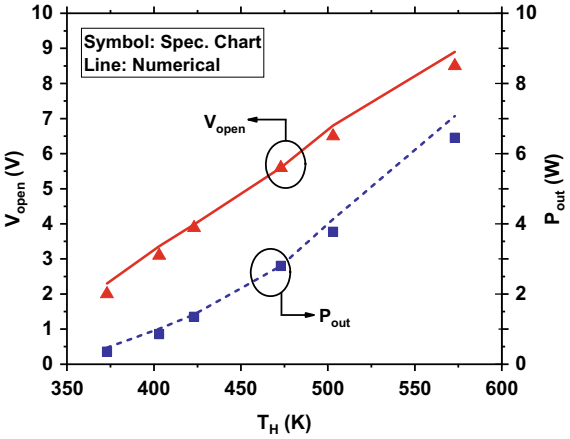

Fig. 19 Verification of the TEG module

difference across the hot and cold ends of the module since the cold end of the module is kept at 323 K. It is interesting to note that while the specified and numerical values almost coincide, there is a slightly greater difference between the readings obtained at 573 K. This can be attributed to the fact that the manufacturer specifies 573 K as the thermal breakdown temperature of the module and the optimum operating temperature at 525 K. As a result, the module may malfunction at temperatures equal to or greater than 573 K. Thus, simulations for mixture velocities that may exceed the breakdown temperature of the module are not carried out.

4.4.3 Integration of TEG with Combustor

The validated model of TEG is integrated into the microcombustor for the power generation. The thermoelectric performance is measured in terms of the voltage obtained due to the temperature difference across the walls of the module and its conversion efficiency. Figure 20a shows the variation of the open-circuit voltage and output current with the average temperature of the hot side of the module. Comparisons are drawn between the specified values of the two quantities. There is a rise in the open-circuit voltage with increasing temperature, and a corresponding rise in the output current as well. A maximum open-circuit voltage of 7 V and output current of 1.2 A are obtained for an average temperature of ~550 K. The rise in the voltage and the current can be attributed to the increasing temperature difference between the two walls of the module, since the cold side is maintained at a constant temperature of 323 K. The deviation between the numerical and specified values is due to the presence of a non-uniform temperature gradient in the numerical model of the integrated system. These values have been extracted at average temperatures for the sake of comparison. The specified values have been calculated with constant temperature values at the boundaries. This leads to a slight difference between the specified and numerical values.

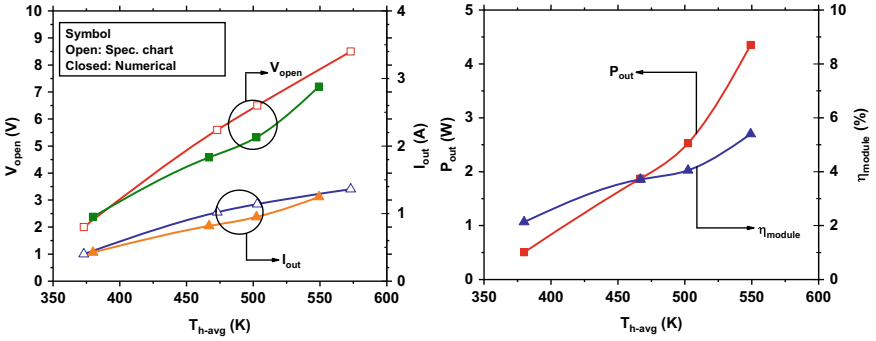

Fig. 20 Variation of **a** open-circuit voltage and output current and **b** output power and conversion efficiency of the module with average temperature of the hot side of the module

Figure 20b shows the variation of the output power and conversion efficiency of the module with the average temperature of the hot side of the module. The output power increases with a rise in the average temperature of the hot side of the module with a maximum output power of ~4.5 W at ~550 K. The trend can be attributed to the increasing voltage with a rise in temperature. The conversion efficiency of the module also increases with rise in temperature. A maximum conversion efficiency of 5.3% is obtained for a temperature of ~550 K.

5 Conclusion

Experimental and numerical investigations on microcombustor-based thermoelectric generators are carried out in the present study. In the experimental analysis, the performance of the single and dual microcombustors was compared, where the surface temperature of the dual combustor is reported to be greater than that of the single combustor by 15 K. Further, the effect of different cooling sinks on power generation is studied. Maximum power outputs of 4.5 and 2.4 W with conversion efficiencies of 4.66 and 2.5% are achieved for water-cooled and air-cooled power generators, respectively. The air-cooled power generator is shown prominently due to its decent power output and portability. To explore the possibility of improving the system further, self-aspirating combustors are analysed numerically and experimentally as well. The power generator based on the self-aspirating combustor was able to deliver 0.5 W of electric power without any auxiliary power. Based on these results, a stand-alone micropower generator capable of delivering a power output of 1 W is designed. Further, the experimental analysis is complemented with a three-dimensional numerical analysis of the thermoelectric generator in a CFD environment. After successful verification of the code, the thermoelectric performance of

the integrated system is evaluated. The numerical model reports a maximum output power of 4.35 W and a conversion efficiency of 5.39%.

References

1. Riffat SB, Ma X (2003) Thermoelectrics: a review of present and potential applications. Appl Therm Eng 23(8):913–935
2. Rowe D, Min G (1998) Evaluation of thermoelectric modules for power generation. J Power Sources 73(2):193–198
3. Fernandez-Pello AC (2002) Micropower generation using combustion: issues and approaches. Proc Combust Inst 29(1):883–899
4. Walther DC, Ahn J (2011) Advances and challenges in the development of power-generation systems at small scales. Prog Energy Combust Sci 37(5):583–610
5. Kaisare NS, Vlachos DG (2012) A review on microcombustion: fundamentals, devices and applications. Prog Energy Combust Sci 38(3):321–359
6. Cho J-H et al (2009) Demonstration of an external combustion micro-heat engine. Proc Combust Inst 32(2):3099–3105
7. Maruta K (2011) Micro and mesoscale combustion. Proc Combust Inst 33(1):125–150
8. Norton DG, Vlachos DG (2003) Combustion characteristics and flame stability at the microscale: a CFD study of premixed methane/air mixtures. Chem Eng Sci 58(21):4871–4882
9. Kim NI et al (2007) Development and scale effects of small Swiss-roll combustors. Proc Combust Inst 31(2):3243–3250
10. Shirsat V, Gupta A (2011) Performance characteristics of methanol and kerosene fuelled meso-scale heat-recirculating combustors. Appl Energy 88(12):5069–5082
11. Chou S et al (2010) Porous media combustion for micro thermophotovoltaic system applications. Appl Energy 87(9):2862–2867
12. Vijayan V, Gupta A (2010) Combustion and heat transfer at meso-scale with thermal recuperation. Appl Energy 87(8):2628–2639
13. Vijayan V, Gupta A (2010) Flame dynamics of a meso-scale heat recirculating combustor. Appl Energy 87(12):3718–3728
14. Fan A, Zhang H, Wan J (2017) Numerical investigation on flame blow-off limit of a novel microscale swiss-roll combustor with a bluff-body. Energy 123:252–259
15. Shirsat V, Gupta A (2011) A review of progress in heat recirculating meso-scale combustors. Appl Energy 88(12):4294–4309
16. Wierzbicki TA, Lee IC, Gupta AK (2014) Combustion of propane with Pt and Rh catalysts in a meso-scale heat recirculating combustor. Appl Energy 130:350–356
17. Shirsat V, Gupta A (2013) Extinction, discharge, and thrust characteristics of methanol fueled meso-scale thrust chamber. Appl Energy 103:375–392
18. Aravind B et al (2016) Investigations on flame dynamics of premixed H_2-air mixtures in microscale tubes. RSC Adv 6(55):50358–50367
19. Wan J, Zhao H (2017) Dynamics of premixed CH_4/air flames in a micro combustor with a plate flame holder and preheating channels. Energy 139:366–379
20. Alipoor A, Saidi MH (2017) Numerical study of hydrogen-air combustion characteristics in a novel micro-thermophotovoltaic power generator. Appl Energy 199:382–399
21. Akhtar S, Kurnia JC, Shamim T (2015) A three-dimensional computational model of H_2-air premixed combustion in non-circular micro-channels for a thermo-photovoltaic (TPV) application. Appl Energy 152:47–57
22. Akhtar S et al (2017) Investigation of energy conversion and flame stability in a curved micro-combustor for thermo-photovoltaic (TPV) applications. Appl Energy 192:134–145
23. Zuo W et al (2016) Numerical investigations on an improved micro-cylindrical combustor with rectangular rib for enhancing heat transfer. Appl Energy 184:77–87

24. Waitz IA, Gauba G, Tzeng Y-S (1998) Combustors for micro-gas turbine engines. J Fluids Eng 120(1):109–117
25. Yang W et al (2004) A prototype microthermophotovoltaic power generator. Appl phys Lett 84(19):3864–3866
26. Lee S, Um D, Kwon O (2013) Performance of a micro-thermophotovoltaic power system using an ammonia-hydrogen blend-fueled micro-emitter. Int J Hydrogen Energ 38(22):9330–9342
27. Ahn J et al (2009) A thermally self-sustaining miniature solid oxide fuel cell. J Fuel Cell Sci Tech 6(4):041004
28. Yoshida K et al (2006) High-energy density miniature thermoelectric generator using catalytic combustion. J Microelectromech Syst 15(1):195–203
29. Jiang L et al (2011) Experimental study of a plat-flame micro combustor burning DME for thermoelectric power generation. Energy Convers Manage 52(1):596–602
30. Shimokuri D, Taomoto Y, Matsumoto R (2017) Development of a powerful miniature power system with a meso-scale vortex combustor. Proc Combust Inst 36(3):4253–4260
31. Yadav S, Yamasani P, Kumar S (2015) Experimental studies on a micro power generator using thermo-electric modules mounted on a micro-combustor. Energ Convers Manage 99:1–7
32. Merotto L et al (2016) Study of a thermoelectric generator based on a catalytic premixed meso-scale combustor. Appl Energy 162:346–353
33. Hsu C-T et al (2011) Experiments and simulations on low-temperature waste heat harvesting system by thermoelectric power generators. Appl Energy 88(4):1291–1297
34. Aranguren P et al (2015) Experimental investigation of the applicability of a thermoelectric generator to recover waste heat from a combustion chamber. Appl Energy 152:121–130
35. Chou S et al (2011) Development of micro power generators—a review. Appl Energy 88(1):1–16
36. Ali H, Yilbas BS, Al-Sharafi A (2017) Innovative design of a thermoelectric generator with extended and segmented pin configurations. Appl Energy 187:367–379
37. He W et al (2015) Recent development and application of thermoelectric generator and cooler. Appl Energy 143:1–25
38. Fanciulli C et al (2018) Portable thermoelectric power generation based on catalytic combustor for low power electronic equipment. Appl Energy 215:300–308
39. Chen M et al (2009) Numerical modeling of thermoelectric generators with varing material properties in a circuit simulator. IEEE Trans Energy Convers 24(1):112–124
40. Gao X et al (2012) Numerical model of a thermoelectric generator with compact plate-fin heat exchanger for high temperature PEM fuel cell exhaust heat recovery. Int J Hydrogen Energy 37(10):8490–8498
41. Bjørk R et al (2014) Analysis of the internal heat losses in a thermoelectric generator. Int J Therm Sci 85:12–20
42. Fraisse G et al (2013) Comparison of different modeling approaches for thermoelectric elements. Energy Convers Manage 65:351–356
43. Chen M, Rosendahl LA, Condra T (2011) A three-dimensional numerical model of thermoelectric generators in fluid power systems. Int J Heat Mass Transf 54(1–3):345–355
44. Zhou M, He Y, Chen Y (2014) A heat transfer numerical model for thermoelectric generator with cylindrical shell and straight fins under steady-state conditions. Appl Therm Eng 68(1–2):80–91
45. Meng L, Li J, Li Q (2017) A miniaturized power generation system cascade utilizing thermal energy of a micro-combustor: design and modelling. Int J Hydrogen Energy 42(27):17275–17283
46. Aravind B et al (2018) Compact design of planar stepped micro combustor for portable thermoelectric power generation. Energy Convers Manage 156:224–234
47. Aravind B, Khandelwal B, Kumar S (2018) Experimental investigations on a new high intensity dual microcombustor based thermoelectric micropower generator. Appl Energy 228:1173–1181
48. Singh T, Marsh R, Min G (2016) Development and investigation of a non-catalytic self-aspirating meso-scale premixed burner integrated thermoelectric power generator. Energy Convers Manage 117:431–441

49. Satoh D et al (2005) Micro-ejector to supply fuel–air mixture to a micro-combustor. Sens Actuators A 119(2):528–536
50. Su Y et al (2016) Numerical study on a multiple-channel micro combustor for a micro-thermophotovoltaic system. Energy Convers Manage 120:197–205
51. Yilmaz H, Cam O, Yilmaz I (2017) Effect of micro combustor geometry on combustion and emission behavior of premixed hydrogen/air flames. Energy 135:585–597
52. Zuo W et al (2017) Numerical investigations on a comparison between counterflow and coflow double-channel micro combustors for micro-thermophotovoltaic system. Energy 122:408–419
53. Shimokuri D, Hara T, Ishizuka S (2014) Development of a portable power system with meso-scale vortex combustor and thermo-electric device. J Phys Conf Ser
54. Vican J et al (2002) Development of a microreactor as a thermal source for microelectromechanical systems power generation. Proc Combust Inst 29(1):909–916
55. Zhao D, Tan G (2014) A review of thermoelectric cooling: materials, modeling and applications. Appl Therm Eng 66(1–2):15–24
56. Lv S et al (2018) Study of different heat exchange technologies influence on the performance of thermoelectric generators. Energy Convers Manage 156:167–177
57. Alghoul M et al (2018) A review of thermoelectric power generation systems: roles of existing test rigs/prototypes and their associated cooling units on output performance. Energy Convers Manage 174:138–156
58. Smith GP (1999) GRI-Mech 3.0. http://www.me.berkley.edu/gri_mech/
59. Fluent A (2015) Theory guide. Ansys Inc, Pennsylvania
60. Zhang Y et al (2019) Effects of inlet parameters on combustion characteristics of premixed CH_4/air in micro channels. J Energy Inst 92(3):824–834
61. Thermonamic Electronics (Jiangxi) Corp Ltd. Product Specification Sheet (2015). http://www.thermonamic.com/TEP1-1264-1.5-English.pdf

Combustion Systems

Fundamental Combustion Research Challenged to Meet Designers' Expectations

Hukam C. Mongia, Kumud Ajmani, and Chih-Jen Sung

1 Introduction

When Mongia sold his senior management leaders, Dr. Monte Steel, Carl Paul, and Dr. John Mason, in 1973 for making a long-term resource commitment, he had very clear long-term objectives in mind but shared with them an achievable objective, namely empirical/analytical combustion technology and product development methodology that will result in reduction of resources requirement including manpower, facilities, dollar and time. Empirical/analytical methodology has worked very well for rich-dome combustors in addition to providing insight for lean combustion concepts; some examples are given in [1–3]. A total of 29 combustors' development activities used this methodology as summarized in Table 1. It should be pointed out that combustion modeling capabilities improved considerably during the technology development activities of the first five combustors listed in Table 1. Afterward, the only change during application was increasing the number of nodes starting from approximately 20,000 in the beginning to 150,000 by the end of 1993. We got good qualitative guidance from CFD and did not encounter unreasonable surprises during the development of these 29 combustors.

Motivated by continuously improving CFD capability and increasing emphasis on improving combustion design development combined with challenges for developing 40 pressure ratio gas turbine combustors led us to formulate and calibrate an anchored design methodology that worked well for rich-dome combustors starting with its first

H. C. Mongia (✉)
CSTI Associates, LLC, Yardley, PA, USA
e-mail: hmongia43@hotmail.com

K. Ajmani
CFD Nexus, LLC, Cleveland, OH, USA

C.-J. Sung
University of Connecticut, Storrs, CT, USA

© Springer Nature Singapore Pte Ltd. 2021

A. De et al. (eds.), *Sustainable Development for Energy, Power, and Propulsion*, Green Energy and Technology,
https://doi.org/10.1007/978-981-15-5667-8_11

Table 1 Status of modeling capabilities during application of the first five combustion technology programs. Subsequent 24 technology and product development programs used qualitative guidance from 2-step or 4-step eddy breakup spray combustion models. seven rich-dome combustion products used anchored CFD code

#	Programs	Status of CFD during preliminary design phase
1	Army combustor design criteria ACDC concept I	2-step gaseous fuel combustion model not calibrated
2	ACDC concept II	Same as above. models calibrated at end of programs 1 and 2
3	NASA pollution reduction technology concept 3 (premix and LDI)	CFD with spray combustion was phased in after calibration with data; no NO_x emissions prediction capability.
4	ACDC 2200 °F ΔT concept I	Two-step spray combustion model calibrated
5	NASA counter-flow film-cooled combustor	Above along with idle CO, HC and LBO calibrated

The modeling capability described in Row 5 was used in (6) ATF-3 combustor, (7) Low Smoke TFE 731, (8) Advanced Cruise Missile Engine Combustor, (9) Garrett's first ATEGG Combustor, (10) F109 combustor and (11) TFE1042 combustor

The following programs used COM3D, a code provided by NASA GRC, with increasingly more grids approaching 150,000 by 1993: (12) Army Low Pattern Factor Combustor, (13) NASA/Army Compliant Matrix Cooling Combustor, (14) 501 K 9 PPM NO_x Combustor, (15) 501 K 25 PPM NO_x Combustor, (16) NASA High-Speed Ultra-low NO_x Combustion Conceptual Design Feasibility, (17) 501 K Effusion Combustor, (18) 501 K 80 PPM NO_x Combustor, (19) T406/GMA 2100 Combustor, (20) GMA 3007 Combustor, (21) T56-A427 Nozzle Carboning, (22) Model 150 combustor, (23) Model 120 Combustor, (24) T800 + Lamilloy Combustor, (25) T800 + Effusion-Cooled Combustor, (26) Low Smoke 570 combustor, (27) Expendable Turbine Engine Combustor, (28) Limited Life Turbine Combustor, and (29) ATEGG XTC 16/1

Anchored CFD [4] was used in (1) GE90 Dual Annular Combustor (DACII), (2) GP7200, (3) AF and NAVSEA Trapped Vortex Combustor, (4) GE90-110/115B, (5) CF34-10, (6) LMS100 SAC and (7) CFM56 Tech Insertion

application in 1995 for the GE90DACII [4]. Subsequently, an additional five rich-dome combustion products and one technology combustor were developed by using the anchored design methodology which used the number of nodes approaching one million, as summarized in Table 1.

The anchored modeling approach's limitations for application to lean combustion systems investigated in [5, 6] motivated us to initiate in 2001, a new modeling approach known as comprehensive combustion System Analysis (CSA). The CSA modeling approach intended for use in both rich- and lean-dome combustors did not require any input other than compressor exit profiles of total and static pressures and accompanying velocity and turbulence kinetic energy profiles. The pressure and airflow distributions across the combustor were calculated by CSA in addition to spray characteristics. Other details of this approach are provided in [7] and the references therefrom. References [8, 9] provided a synopsis of the modeling capabilities prior to CSA. The CSA modeling activities initially started at a reasonable speed went into high gear because of the good results on new lean-dome technology,

known popularly as TAPS, see [10], and its intended transition to GEnx. All this motivated us to set a long-term accuracy target as summarized in Sect. 2.

Section 3 shares some recent data on lean-dome product combustors and swirl-venturi lean direct injection (SV-LDI) technology and describes two examples that could be or may not be considered technology setbacks depending upon one's perspective. As discussed extensively in [11], in spite of all the effort that has been expended in improving gas turbine combustion modeling and CFD simulations, the designer has to rely considerably on his ingenuity and "seeing through the fog" for making many of the combustor modifications. Therefore, a concerted joint effort was pulled together between the authors to illustrate formulation and application of modern CFD tools to help develop SV-LDI technology complemented by properly defined fundamental diagnostics and simulation of an SV-LDI single-element mixer relevant for low-power operation as described in Sects. 4 and 5 followed by a summary in Sect. 6.

2 Accuracy Goals and Current Status

As expected, we wanted CFD prediction capabilities as good as experimental data which means comparable to standard deviation σ_{exp} of design variables considered most important for gas turbine combustors, namely gaseous and particulate emissions; combustor durability represented through the capability of predicting liner and dome wall temperature for the regions considered critical for determining the mean-time between shop visits for repair and overhaul; idle lean blowout fuel/air ratio; and combustor exit temperature characteristics expressed through two commonly used terms, namely average radial profile expressed as radial profile factor and nonuniformity via pattern factor.

Reference [11] provided an extensive discussion on the capabilities of the three popular modeling approaches, namely, semi-analytical, anchored CFD, and CSA in addition to an overview status of the latter given in [7]. The authors have been involved in model validation efforts for several years for idealized test rig hardware as well as "real" engine hardware mixers, see for example [12–14]. The only TAPS reacting flow validation effort shared with limited details for pilot operation in lean-dome combustors for two mixers was given in [15] from where we have reproduced Fig. 1 on the CSA predictability for NO_x and CO. Figure 1 shows that NO_xEI at idle through approach operation can be predicted within $\pm$1.0EI error band of data. From the normalized values of NO_xEI for a rich-dome combustor's simulation summarized in [16], the authors' predicted average errors for the takeoff NO_xEI of 11%; whereas for a development combustor, the CSA predicted NO_xEI with test rig data falling within 2.0EI (Table 2).

Table 3 provides more recent engine emissions σ_{exp} values recommended in [11] that CFD simulations should aspire to achieve. From here, we can set our long-term CFD accuracy goals comparable with experimental error, namely 5% for LTO NO_x, 20% for LTO HC, 10% for LTO CO, and 20% for maximum SAE smoke number.

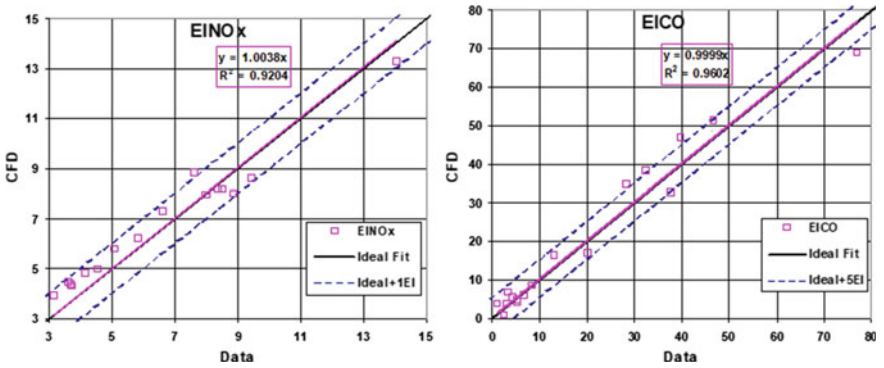

Fig. 1 Typical CSA capability for predicting NO_xEI and COEI characteristics of two TAPS combustors in pilot only operation mode showing approximately error band of ±10% for NO_xEI and COEI

Table 2 Long-term CFD prediction capabilities should be comparable with standard deviation of experimental data σ_{exp}; typical σ_{exp} values are

Design parameters	Typical σ_{exp} values
Landing and takeoff NO_xEI	Maximum (5% NO_xEI, 0.69)
Idle HCEI	Minimum (20% Idle HCEI, 1.25)
Idle COEI	Minimum (10% Idle COEI, 4.4)
Maximum SAE smoke number	Maximum (20% max smoke number, 1.35)
Dome and liner wall temperature, °F	Maximum [10% (T_{max}-T_3), 25]
Idle lean blowout (LBO) fuel/air ratio	Maximum (10% Idle LBO, 0.0005)
Radial profile factor (RPF)	Maximum (10% RPF, 0.01)
Pattern factor (PF)	Maximum (20% PF, 0.03)

Table 3 Current status of engine emissions measurement standard deviation σ for HC, CO, NO_x and smoke number (SN)

LTO HC	Range of σ %		LTO CO	Range of σ %		LTO NOx	Range of σ %		SN	Range of σ %	
<0.24	25	100	<5	25	75				<5	29%	57%
<1	17%	25	<10	8.2%	25				<10	7%	29%
>1	8%	17%	>10	5.1%	8.2%	>30	1.7%	5.9%	>10	7%	14%

Refer to Figs. 2, 3, and 4 for representative values of LTO NO_x, CO, and HC values compared to the three subgroups defined in Table 3.

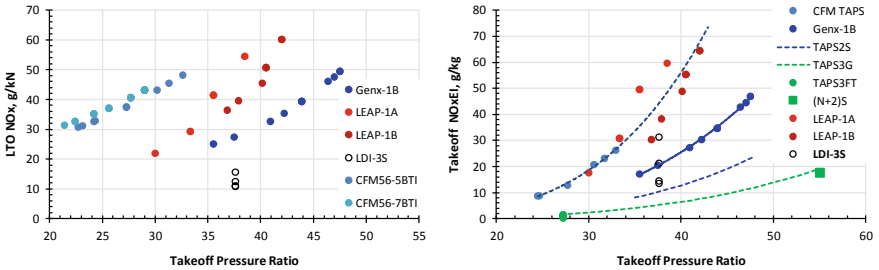

Fig. 2 Lean-dome combustion products (GEnx-1B, LEAP-1A, LEAP-1B) compared with two rich-dome combustion products (CFM56-5BTI, CFM56-7BTI) and promising LDI-3 technology sector rig test results from [17] shown on the left-hand side in terms of LTO NO_x. The same lean-dome data set plus more (TAPS2 in a sector, TAPS3 in flame tube and $N + 2$ in sector rig) in terms of takeoff NO_xEI is shown on the right-hand side

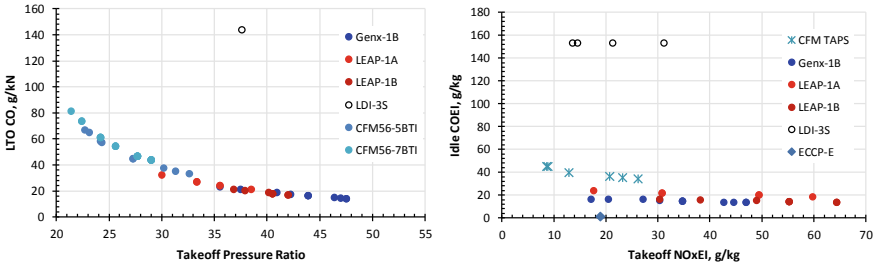

Fig. 3 Lean-dome combustion products and LDI-3 compared with rich-dome products, LTO CO on the left-hand side, idle COEI versus takeoff NO_xEI on the right-hand side

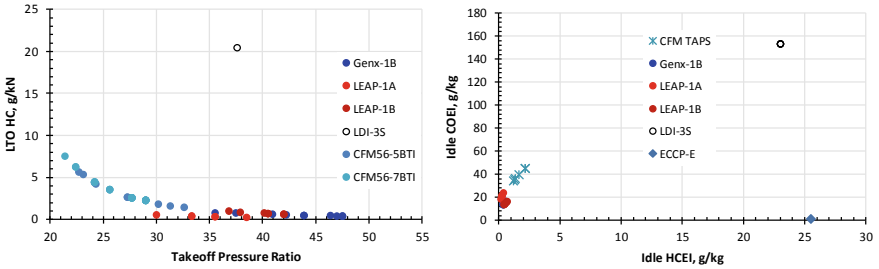

Fig. 4 Lean-dome combustion products and LDI-3 compared with rich-dome products, LTO HC on the left-hand side, idle COEI versus idle HCEI on the right-hand side

3 Challenges for Fundamental Research Dealing with Surprises

There are many challenges combustion technologists face during technology and product development processes; and many of the setbacks may not be viewed as setbacks by some. Figure 2 illustrates two recent examples, one for a lean-dome combustion product, LEAP-X, and the second for the ongoing LDI-3 technology development effort. Propulsion engine emissions performance is judged by its landing takeoff emissions values as shown in the left-hand side of Fig. 2 for NO_x, Fig. 3 for CO and Fig. 4 for HC. The LEAP-1A and LEAP-1B engines have lower LTO NO_x values compared to their predecessor engines, the CFM56-5B and CFM56-7B Tech Insertion engines, demonstrating approximately 40% reduction at a pressure ratio of 33. But compared to the GEnx at a pressure ratio of 35, LEAP-X's LTO NO_x is 67% higher. However, this increase in LTO NO_x can be dismissed easily as large versus medium engine size engines issue. The ongoing LDI-3 technology has demonstrated considerably lower (approximately 70%) LTO NO_x compared to the LEAP-X it might one day replace.

However, if one wants to believe in the applicability in the right-hand side of Fig. 2, where takeoff NO_xEI versus pressure ratio is used for comparing high-power NO_x technologies of different combustors, then LEAP-1B's NO_xEI at a pressure ratio of 42 is approximately 110% higher than the GEnx. Again, some may simply dismiss it by interpreting the LDI-3 data in regard to its impact on LTO NO_x. There is a big uncertainty in the reported LDI-3 NO_xEI which was estimated by extrapolating sector rig data to the design takeoff pressure and temperature levels. Even when the calculated NO_xEI covers a broad range of 13.6 and 31.2, it has an insignificant effect on its LTO NO_x values as shown in the left-hand side of Fig. 2. But this variation in takeoff NO_xEI for the LDI-3 and LEAP-X has serious consequences for assessing how good TAPS and LDI technologies are. Is LDI-3 better than that of the GEnx or worst? Should we worry about higher values of takeoff NO_xEI of the LEAP-X? Fundamentally, LDI's mixedness should be expected to be lower than that of a partially-premixing TAPS which has already shown potentials for achieving TAPS3 levels, approximately ¼ of GEnx. Finally, seeing LEAP-1B approach NO_xEI levels of the lean-dome DAC of the GE90 is a bad omen when one realizes that it was this setback of the lean DAC that led to the development of TAPS technology. In conclusion, there may not be any setback in TAPS technology. LTO NO_x of LEAP-X is considerably smaller than its predecessor rich-dome combustion products, and its higher value of takeoff NO_xEI is simply a verification of the concern Mongia had in 2005 during the GEnx preliminary design phase that TAPS technology may turn out to have a large swath of takeoff NO_xEI determined by its degree of partial mixedness and complex tradeoff on operability and dynamics.

The engine operability data are generally cloaked in secrecy by the original equipment manufacturers (OEM's) in spite of the fact that all OEM's face essentially the same design requirements when looked from "30,000 feet altitude." All OEM's engines have to meet customers' requirements in regard to cold-day ground-start

requirements, fuel/air ratio, no flame shooting out, no white smoke, ignition time, acceleration times to idle and to full power and deceleration time back to idle thrust; altitude ignition, especially for two-engine airplanes where ignition is required at the cruise altitude for engines in thermal equilibrium with its surroundings; and many more operability requirements we do not need to list in a manuscript limited by page count.

However, one can make a fairly broad level assessment of engines' operability by comparing publicly available data on LTO CO and HC and the corresponding idle emissions as summarized in Figs. 3 and 4. Similar to Fig. 2, the left-hand side of these figures show LTO CO and HC values from where we can see no setback for the LEAP-1A and LEAP-1B engines compared to both rich-dome CFM56-5B and CFM56-7B Tech Insertion and GEnx with TAPS combustion system. Recognizing that LDI-3 is an ongoing technology development effort, it should take into consideration that unless its future activities do not care of its low-power, LDI-3 may turn out worse than the first DAC demo engine tested in 1978 [18], identified as ECCP-E in the right-hand side of Figs. 3 and 4.

As summarized succinctly very well in [17], "the evolution of the single venturi lean-direct injection (SV-LDI) family of combustor concepts is described in Fig. 5. SV-LDI designs successfully reduced NO_x emissions at high-power conditions. However, the original SV-LDI designs (SV-LDI-1) had two major disadvantages: poor low-power operability and a complex, multi-branch fuel stem [19]. The second-generation of SV-LDI designs (SV-LDI-2) improved the low-power operability by better isolating the pilot fuel-air mixer [20, 21]. However, SV-LDI-2 still had a complex, multi-branched fuel stem that would make the thermal management of the fuel difficult. The third-generation of SV-LDI, SV-LDI-3, replaces the complex, multi-branched fuel stem with a single, multi-injection-point fuel stem. This both simplifies fuel stem design and improves the thermal management of the fuel."

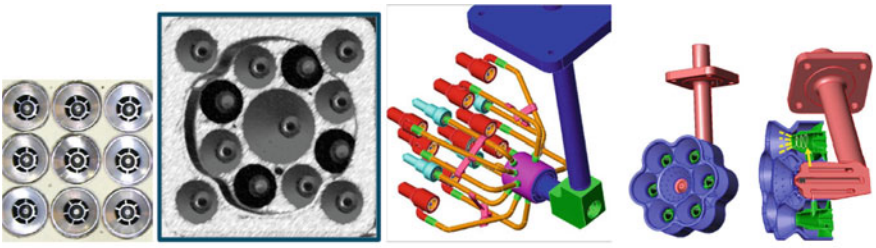

Fig. 5 Evolution of swirl-venturi (SV−) LDI. Shown are: **a** the dome face of first-generation SV-LDI, with all fuel-air mixers identical except for swirler-vane angle and orientation; **b** the dome face of a second-generation SV-LDI configuration, featuring a larger, recessed pilot fuel-air mixer for improved low-power operability; **c** the multi-branched fuel stem used in second-generation SV-LDI configurations; **d** the dome face of a third-generation SV-LDI configuration; and **e** a cut-out side view of a third-generation SV-LDI configuration showing the single, multi-injection-point fuel stem

Authors are impressed with the [17] team's capability, but we dare to suggest that the team forgot the importance of the effect of the yellow-highlighted material in Fig. 5 which could be postulated for the poorer idle performance of LDI-3 v4 (which uses pre-filming airblast nozzle for the pilot) compared to the pressure atomizers used in LDI-2 and v3 of LDI-3, as summarized in Fig. 6. Had the technology process been properly conducted by combination of boxes 5 and 6 shown in Fig. 7, maybe the idle COEI and HCEI values could be closer to 40 and 6, respectively, instead of 120 and 24 shown in Fig. 6. Readers may want to refer to [11] for discussion on hypothesis-driven technology and product development process.

Getting good-quality representative emissions measurement on test rigs is much harder than engines, especially in a fuel staged combustor, ca. v3 and v4 of LDI-3 shown in Fig. 8 reproduced here from [17]. Thus, emissions data taken at simulated approach conditions provide only a qualitative assessment of the LDI-3 configurations as summarized in Fig. 9. In conclusion, a better pilot arrangement is required for turning LDI-3 into a viable next-generation propulsion engine combustion system.

GE Aviation was granted US patent a generic TAPS pilot based LDI combustion system shown in Fig. 10. It may be worth noticing that patent application was submitted on September 29, 2000, and this patent was granted on June 2, 2002, well

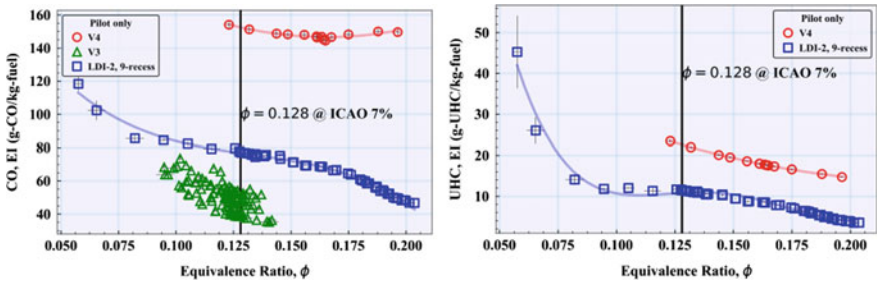

Fig. 6 Idle emissions, CO and HC of the two LDI-3 configurations, v3 and v4, compared with the LDI-2 recessed configuration

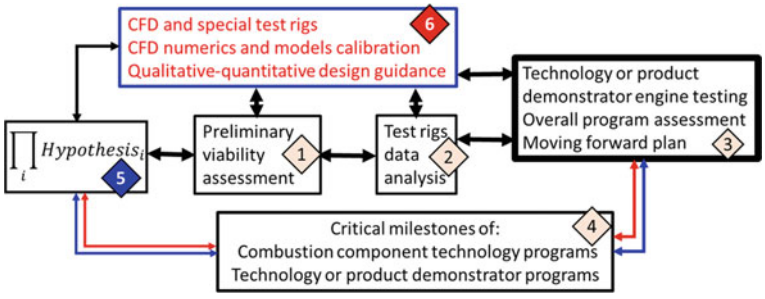

Fig. 7 Conventional combustion technology or product development process comprised of boxes 1 through 4 has been complemented by boxes 5 and 6 starting early 1970s; reproduced from [11]

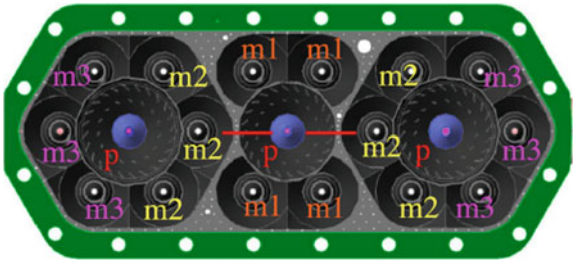

Fig. 8 The 19-point V4 SV-LDI configuration. The labels indicate the stage of each fuel-air mixer: p = pilot, $m1$ = main 1, $m2$ = main 2, and $m3$ = main3. The location of the slit is indicated by the red lines

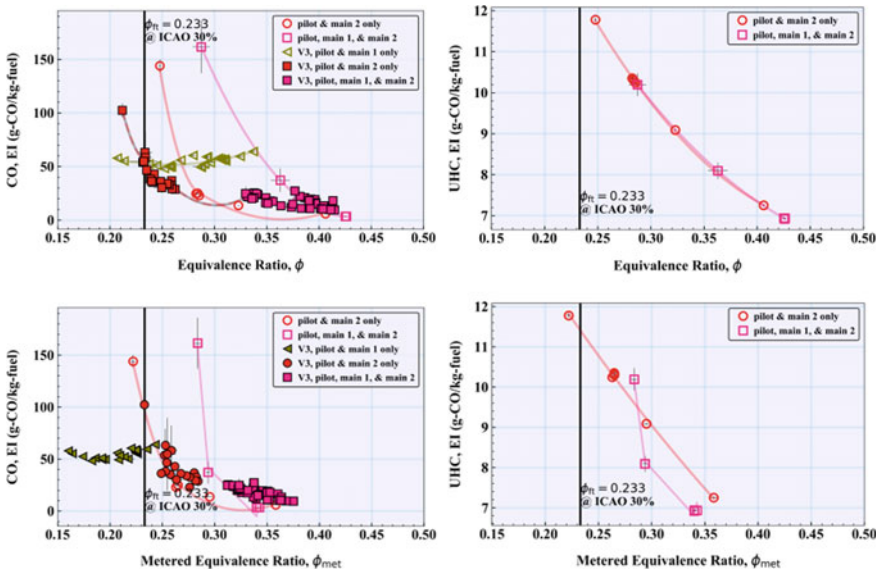

Fig. 9 CO and HC emissions indices of v3 and v4 LDI-3 measured at simulated approach conditions

before the publication of LDI-1 data in 2005 as reported in [19]. Two of the three LDI-2 configurations reported in [20, 21] shown in Fig. 11 were intended to investigate their low-power performance in order to verify whether 5-recess design is good for idle and approach or 9-recess design is required for idle, approach, and beyond. This strategy was apparently not pursued during LDI-3 design and testing phase.

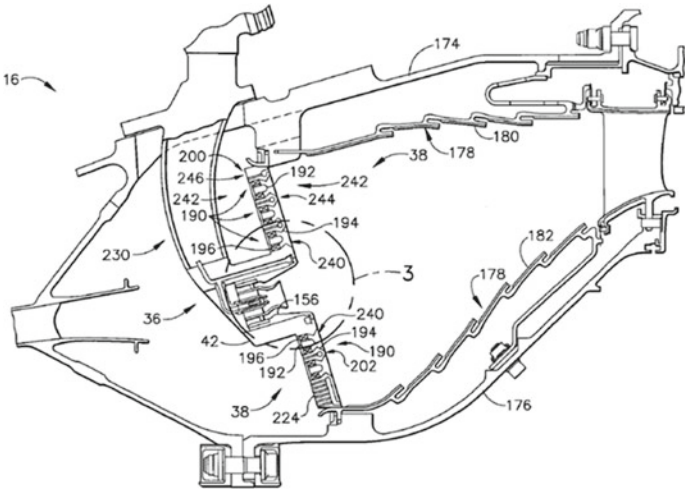

Fig. 10 TAPS pilot stabilized LDI concept, US Patent 6405, 52, June 2, 2002

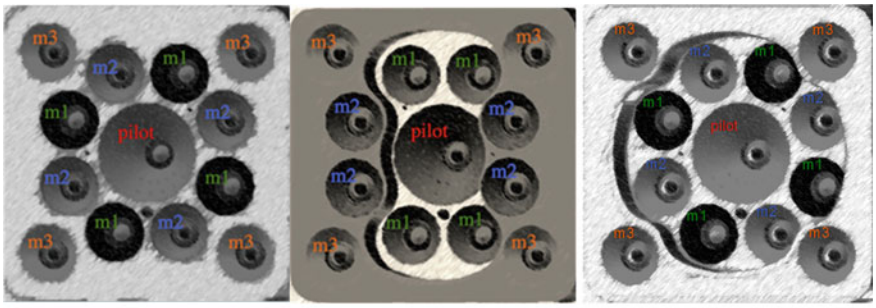

Fig. 11 LDI-2 configuration without shielded pilot (**a**), shielded pilot for idle (**b**), and shielded 9-mixers for idle through approach operation (**c**)

4 RANS and TFNS Simulations for Supporting SV-LDI-2 and LDI-3 Technology Development

A CFD analysis of SV-LDI-2 and LDI-3 technology has been underway since 2012, with the National Combustion Code (OpenNCC) developed by NASA Glenn Research Center (GRC). The CFD analysis has included RANS and Time-Filtered Navier–Stokes (TFNS), a type of Very Large Eddy Simulation (VLES) approach to obtain steady-state and time-accurate CFD solutions for several LDI-2 and LDI-3 configurations. The OpenNCC software has also been used extensively for optimization of the aerodynamic flow features of several iterations of the LDI-2 and LDI-3 hardware.

NASA GRC's CFD development and analysis to support LDI injector design used many of the best practices developed for OpenNCC using single-element and nine-element LDI-1 designs [22, 23]. Details of the CFD efforts using NASA's OpenNCC code for the ERA program's LDI-2 configurations were reported by Ajmani et al. [24] (Woodward FST's LDI-2) and [25], Goodrich's multipoint LDI. For LDI-3 designs, OpenNCC has served as a useful tool to help screen fuel-filming injectors [26] and provide CFD-based optimization of air-swirler designs for Woodward FST's LDI-3 configurations. A detailed analysis of the aerodynamic performance, fuel-air mixing, and combustion characteristics of a five-element module (four mains, one pilot) of Woodward FST's LDI-3 design was reported in [27]. A CFD evaluation of the 'medium-power (7%) and low-power (30%) combustion characteristics of Woodward FST's nineteen-element, three-cup flametube LDI-3 design was reported in [28] and [29], respectively.

4.1 OpenNCC Computational Approaches and Methods

The OpenNCC code is a state of the art computational tool that is capable of solving the time-dependent, Navier–Stokes equations with chemical reactions. The code is being developed primarily at the NASA GRC in order to support combustion simulations for a wide range of applications and has been extensively validated and tested for low-speed chemically reacting flows. Several "best practices" for the use of OpenNCC for LDI injector design were achieved by extensive "anchoring" [22] with available LDI-1 data [19]. The anchoring work enabled the use of OpenNCC in the evaluation of LDI-2 designs [24] and advanced CFD screening of LDI-3 designs [27] at NASA GRC.

OpenNCC uses second-order accurate central-differences for the convective and diffusion flux discretization, and a Jameson operator (a blend of second and fourth-order dissipation terms) for numerical stability. The second and fourth-order dissipation parameters are typically set to 10^{-4} and 0.05, respectively [30]. The value of k_2, the constant that scales the second-order dissipation gradient switch, is typically set to 0.25. In order to enhance convergence acceleration in pseudo-time, implicit residual smoothing is used to smooth the computed residuals in OpenNCC RANS. Turbulence closure is obtained by using a two-equation, cubic k-ε model with variable $C\mu$ [31] and dynamic wall functions with pressure gradient effects [32]. Time-integration of the flow equations is performed by a steady-state RANS approach to obtain initial non-reacting flow solutions, followed by a time-accurate TFNS/VLES [33] approach for detailed, time-resolved non-reacting, and reacting flow solutions.

In the TFNS approach, the filtered Navier–Stokes equations are established by applying a temporal filter to the exact form of the governing equations. The eddy viscosity contains a filtering-control parameter (FCP), which is defined as the ratio of a (conceptual) temporal filter width to a characteristic integral time scale of the turbulent flow. In contrast to a typical LES approach, where the (spatial) filter width is formally linked to the grid spacing, the (temporal) filter width for TFNS does not

relate to the time-step of the numerical solution. Hence, unlike LES, the sub-filter field of TFNS is not the subgrid field. In principle, TFNS grids must numerically support the spatial gradients of the filtered variables under investigation. In practice, the content of the sub-filter turbulent kinetic energy is regulated by the (specified) FCP. All the TFNS solutions presented in this paper use an FCP value of 0.25. This value of FCP was established by studying the sensitivity of the time-averaged, non-reacting flow TFNS solution for a chosen mesh resolution, as reported in [22].

4.1.1 Chemical Kinetics and Ignition Modeling

A computationally affordable kinetics mechanism (of fewer than 20 species) with liquid spray simulations of Jet-A fuel which can provide emissions predictions (NO_x, CO), and model various flight conditions of interest (idle, LBO, takeoff, cruise, approach), remains an open challenge for the chemical kinetics community. In the current work, a 14-species, 18-reactions reduced-kinetics model was used to compute the species source terms for Jet-A/air combustion using finite-rate. Jet-A fuel was modeled as a surrogate mixture of decane/benzene/hexane (72.7/18.2/9.1% by mass). The kinetics mechanism was validated by matching adiabatic flame temperature, flame-speed, and ignition-delay with experimental shock-tube data and LDI-1 emissions data, in the equivalence ratio range of 0.5–1.0 [34]. The reduced-kinetics mechanism used for the current LDI-3 analysis was also validated against NASA GRC's LDI-2 experimental emissions data for a second-generation, thirteen-element flame-tube array [24]. Many research groups use flamelet-modeling, which allows for use of detailed kinetics models at much lower computational cost, than the reduced-kinetics approach chosen here. The work reported here used reduced finite-rate chemical kinetics due to enhanced robustness and accuracy experienced with OpenNCC, particularly for NO_x emissions predictions of non-premixed, liquid-fueled gas turbine engine combustor conditions.

4.1.2 Liquid Phase and Spray Modeling

The liquid spray (Jet-A fuel) was modeled by tracking spray particles in a Lagrangian framework, where each particle represents a group of actual spray droplets [35]. The governing equations for the liquid phase are based on a Lagrangian formulation where the spray particle position and velocity are described by a set of ordinary differential equations. The Lagrangian solution process used for this study employed a best-practice unsteady spray model such that droplet groups are only integrated for a fraction of their lifetime (but restarted at this point for the next iteration), rather than to a completely steady-state solution. The typical spray integration time-steps were 10^{-7} s (local time-step) and 10^{-6} s (global time-step), which is also the gas-phase physical time-step. This translates to 10 local time-steps for each global time-step for the spray solver. In order to save computational time, spray particles were injected into the flow field at every 10th time-step (injection time-step).

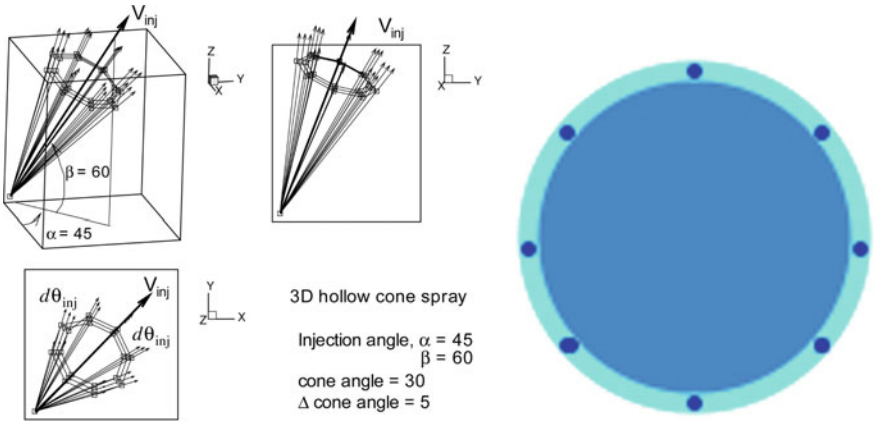

Fig. 12 OpenNCC computational setup for spray modeling of simplex injectors (left-hand side) and airblast injectors (right-hand side)

The current spray computations with OpenNCC assumed that the fuel sheet that is shed from the trailing edge of each pre-filming injector's surface breaks up into streams of uniform liquid mass and momentum, as shown in Fig. 12. This assumption was made because OpenNCC's physical spray models are not yet fully validated for comprehensive liquid modeling of the liquid fuel flow within the pre-filming passages of the current injector designs. Each annular sheet of liquid fuel film exiting each pre-filming injector was thus approximated as a set of eight discrete fuel streams, located 22.5° apart in the circumferential direction. The flow for each of the eight fuel streams was initialized 1 mm downstream of the trailing edge of each pre-filming injector. Each stream was computationally modeled as a 5°-solid cone containing spray particles injected in eight stochastically varying directions at an initial injection velocity of 5 m/s and temperature of 300 K. This "sheet breakup" approach followed the best-practice modeling method for airblast injectors reported for LDI-2 configurations in [23].

The droplet size distribution for injected particles was prescribed by the following correlation equation [36]:

$$\frac{\delta n}{n} = 4.21 \times 10^6 \left[\frac{d}{d_{32}}\right]^{3.5} e^{-16.98\left[\frac{d}{d_{32}}\right]^{0.4}} \frac{\delta d}{d_{32}}$$

Here, δn is the number of droplets in the size range between d and $d + \delta d$, n is the total number of droplets, and d_{32} is the Sauter mean diameter (SMD). A user-specified number of "droplet groups" is used to represent the drop size distribution among a finite number of droplet classes. An SMD of 10 μm with eight droplet groups was used for modeling each of the eight fuel streams for each pre-filming injector. The net result was that 64 new droplets were injected into the computational domain for each of the eight fuel streams of each pre-filming injector at each injection time-step.

Each pressure-atomizing simplex injection element (pilot) located at the center of each multi-element module was modeled as a 60° hollow cone of 10° thickness, each containing spray particles injected in 32 stochastically varying directions, at an injection velocity of 28 m/s. An SMD of 8 μm and eight droplet groups were also used to model each simplex injector. The net result was that 256 new droplets were injected into the computational domain for each simplex injector (pilot) at each injection time-step of the computation.

4.1.3 Turbulence-Chemistry Interaction Modeling

A variation of the "Eulerian PDF (EUPDF)" model of [37] was used with the OpenNCC TFNS solver to study the impact of turbulence-chemistry interaction modeling on the reacting flow field CFD predictions. The TFNS/PDF approach used here is similar to the FDF/PDF filtering method developed by James et al. [38] for LES simulations. The energy and the species mass fractions over the entire computational domain are obtained by solving the time-filtered conservation equations. The EUPDF model is used as a subgrid model for mixing and combustion to provide an estimation of the filtered reaction source terms and is referred to herein as the "PDF-like" model. More specifically, (i) instead of using the EUPDF model to directly establish the entire species field (without actually solving the filtered conservation equations of species), the EUPDF model is used locally (both in space and time) to only provide approximations of filtered reaction source terms in the filtered equations (which are now being solved), (ii) instead of solving the unfiltered quantities using the EUPDF equations, the same mathematical forms of the EUPDF equations for the unfiltered quantities are adopted as a subgrid model for mixing and combustion of time-filtered scalars, with the molecular transport coefficients substituted by the "effective" transport coefficients; see [39] for details of the "PDF-like" model.

In computational practice, the combined TFNS and "PDF-like" (TFNS/PDF) method utilizes a hybrid algorithm. The velocity and the density over the entire computational domain are obtained by solving the time-filtered Navier–Stokes equations in OpenNCC. The scalars (i.e., the energy and the species mass fractions) over the entire computational domain are obtained by solving the PDF transport equation using stochastic elements (Monte-Carlo particles), i.e., the filtered conservation equations for the scalars are not employed. In the current work, the "PDF-like" solver used 25 Monte-Carlo particles per computational cell to model the turbulence-chemistry interactions at each physical time-step. A converged time-accurate TFNS solution computed with laminar chemistry is first obtained and then used to advance the computations with the "PDF-like" solver. This approach provides considerable savings in overall computational time and allows for a comparison of the effect of the "PDF-like" solver on the predicted NO_x emissions, flame position and shape, and reacting flowfield in the combustor.

4.2 LDI-2 Configurations, Operating Conditions, and Results

Figure 13 shows the two LDI-2 configurations investigated here.

1. Five-point recess (left-hand side of Fig. 13): Central Pilot Injector, One Main Stage (Four Injectors) are recessed from the main dome. Three flametube configurations, Config 3, Config 7, Config 9 of Table 4, were computed with OpenNCC, and emissions were compared with Woodward FST's data.
2. "Baseline" or "Flat Dome" (right-hand side of Fig. 13): Exit plane of the venturi for all thirteen injectors is flush with the main combustor dome. A single flametube configuration, Config 10 of Table 4, was computed with OpenNCC, and emissions were compared with Woodward FST's data.

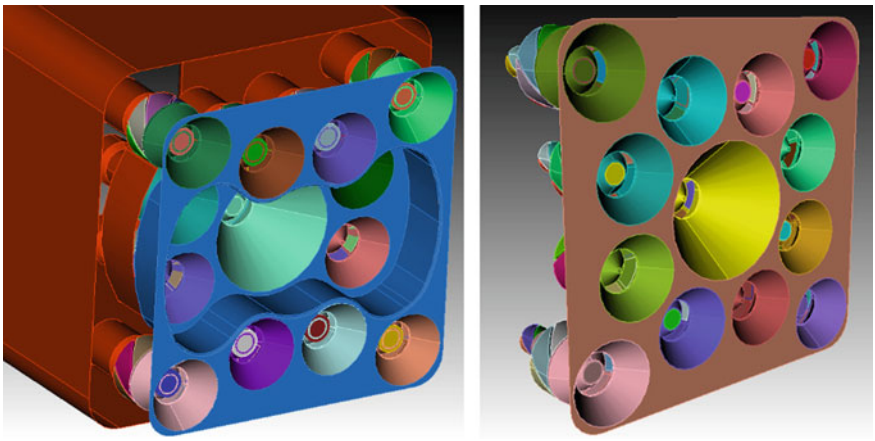

Fig. 13 Two LDI-2 flametube configurations [21]. Five-point recess on the left-hand side, "baseline" or "flat dome" on the right-hand side

Table 4 Details of SV-LDI swirler angles for four different LDI-2 configurations. OAS/IAS: Outer/Inner Air Swirlers. CW/CCW: Clockwise/Counter-Clockwise swirler orientation

Configuration	Pilot (airblast) (OAS/IAS)	Main 1 (simplex)	Main 2 (airblast) (OAS/IAS)	Main 3 (airblast) (OAS/IAS)
5pt recess config 3	57CCW/57CW	45CW	45CW/57CCW	45CW/57CCW
5pt recess config 7	57CCW/57CW	55CCW	45CW/57CCW	45CW/57CW
5pt recess config 9	57CCW/57CW	45CW	45CCW/45CW	45CCW/45CW
"Basline" config 10	Simplex 55CCW	45CCW	45CW/45CW	45CW/45CW

A comparison of the experimental NO_xEI for "medium" (simulated cruise) and "high" (simulated takeoff) power operating points of a typical N + 2 engine cycle, and the corresponding CFD emissions predictions are summarized in Fig. 14. OpenNCC RANS predicts NO_xEI values to within 25% of experimental data for twelve different medium-power (cruise) and high-power (sea-level takeoff or SLTO) conditions, for four different LDI-2 geometry configurations. It may be desirable to use a better reduced-kinetics mechanism optimized for further improving the CFD predictions for NO_xEI.

A second set of experimental test conditions which included "low" power, along with "medium" and "high" power operating points of a typical N + 2 engine cycle [24] are summarized in Table 5.

The CFD results with OpenNCC for representative "low", "medium", and "high" power operating points of a typical N + 2 engine cycle condition, and the corresponding emissions results are summarized in Table 6.

Summary of LDI-2 CFD analysis with OpenNCC is listed below.

- Computed effective area with OpenNCC RANS agrees very well with measurements (within 10%).

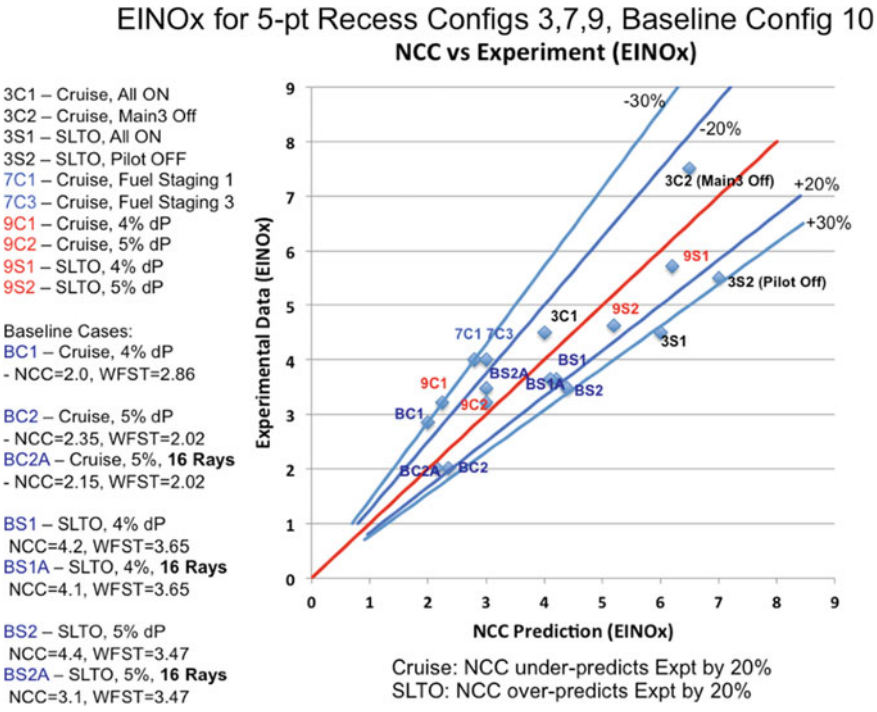

Fig. 14 OpenNCC RANS predictions of NO_xEI compared with experimental data for four different LDI-2 configurations at "medium" (simulated cruise) and "high" (simulated takeoff) power cycle conditions

Table 5 Experimental test conditions and emissions data at three different power conditions (5-pt recess, Config 3)

Power	$T_{3\ avg}$ (F)	P_{3avg} (psi)	dP (psi)	AC_d (in^2)	P_4 (psi)	NO_xEI (g/kg fuel)	HCEI (g/kg fuel)	COEI (g/kg fuel)	Tad_farga (F)
Low	425	83	2.8	1.91	79	2.8	11.2	94.3	1637
Medium	1001	264	10.4	2.06	253	3.8	0.0	0.0	2512
High	1085	234	7.3	2.04	226	11.9	0.0	1.0	2989

Table 6 OpenNCC CFD AC_d, NO_xEI, and T4 predictions at three different power conditions (5-pt recess, Config 3)

Power	AC_d (in^2)	AC_d(NCC) (in^2)	NO_xEI(Expt) (g/kg Fuel)	NO_xEI(NCC) (g/kg Fuel)	T_4(Expt) (K)	T_4(NCC) (K)
Low	1.91	1.90	2.8	1.87	1165	1082
Medium	2.06	1.87	3.8	5.4	1651	1698
High	2.04	1.90	11.9	13.1	1916	1922

- Average exit temperature (T4) predicted by OpenNCC matches experimental data to within 10% for low-power. Excellent match at medium, high-power.
- NO_xEI prediction by OpenNCC is best for high-power cases; medium-power (+42%) and low-power (−33%) (poor combustion efficiency) cases show a larger error.
- For the low-power case, OpenNCC predicts COEI and HCEI of 1.7 and 22.8, respectively with resulting poor agreement with measured values of 94.3 and 11.2, respectively.
- OpenNCC RANS prediction of COEI and HCEI is poor for low-power (low-combustion efficiency) conditions. Use OpenNCC VLES/TFNS and/or turbulence-chemistry interaction models for improving predictability.

Recommendations and future work are as follows.

- Better spray data (droplet size, velocity, and temperature) needed for more accurate CFD modeling.
- Diagnostics at engine-relevant P_3, T_3 conditions needed to assist in validation/calibration of CFD models.
- RANS can serve as an effective tool to produce qualitative NO_xEI predictions for industry-relevant SV-LDI configurations, but only at medium-power conditions with high combustion efficiency.
- Prediction of low-combustion efficiency flows has too many challenges to be adequately resolved with RANS approach. Need higher-fidelity physics models and/or turbulence-chemistry interaction. Availability of better diagnostic data for spray at these conditions is also critical to better CFD accuracy.

4.3 LDI-3 Configurations, Operating Conditions, and Results

OpenNCC was used to perform simulations of a nineteen-element flametube configuration of an LDI-3 combustor proposed by Woodward FST [17, 29]. The nineteen elements are grouped into three modules, with a 7-5-7 element dome layout. Each module comprises a central pilot injector and four (or six) surrounding main injection elements as shown in Fig. 15. The candidate LDI-3 arrangement with a minimally recessed five-element central module is designated as the "baseline" configuration for the CFD simulations reported in this paper. The venturi exits of the two seven-element modules are in-line with the combustor dome plate hot side.

A summary of the CFD-optimized LDI-3 geometry design parameters [27] fabricated by Woodward FST for flametube testing is given below.

1. Pilot Injector with axial fuel injection: Integrated multi-element injector with circumferential slots for air injection—45% offset (w.r.t. axial centerline) for the pilot air-swirler inflow passages. All three pilots have a clockwise swirl when viewed from the downstream direction.
2. Main Injectors with pre-filming fuel injection and axial bladed air swirlers: Co-axial, counter-rotating, 48° outer (six blades), and 60° inner (four blades) axial

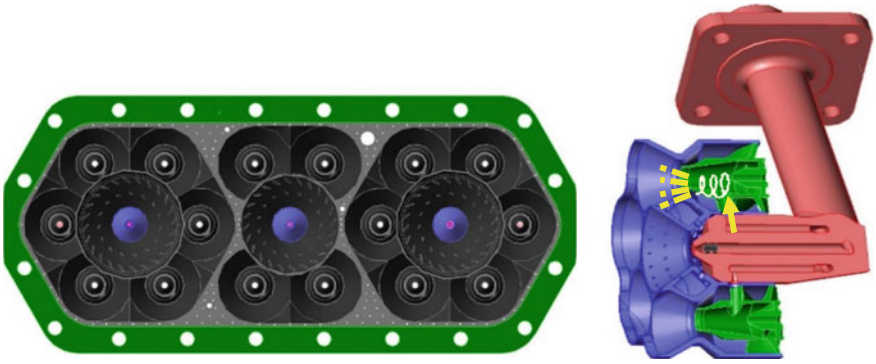

Fig. 15 Dome-layout and CAD for a LDI-3 combustor with one five- and two seven-injection element arrays

venturi swirl-passages. In addition, each adjacent main injector reverses the swirl orientation of the outer air swirlters w.r.t. the pilot swirlers.

The nineteen-element LDI-3 geometry consisting of a central "five-element" module surrounded by two "seven-element" modules CAD supplied by Woodward FST (Fig. 15) was imported into the CUBIT mesh generation software to create a fully tetrahedral mesh with 22 M elements, as shown in Fig. 16. Each blade passage and venturi was meshed as an individual block, and these blocks were then merged with adjacent volumes at their respective common surfaces. This ensured consistency of meshing across similar geometric elements, and also allowed for potential "drop-in" replacement of the axial air swirlers for the main injectors, and/or the radial air-swirler for the pilot, without needing to regenerate the complete mesh for the entire configuration.

OpenNCC RANS computations were performed for the third-generation LDI (LDI-3) combustor assembly. The non-reacting flow results were primarily used to perform a baseline comparison of effective area prediction with measured experimental results. The initial conditions were based on inflow conditions of $P_3 =$ 130 psi, $T_3 = 811$ K, and an overall 3% pressure drop (Δp). Adiabatic, no-slip boundary conditions were imposed at all solid walls. Fixed total-pressure (Pt_3) and total-temperature (Tt_3) conditions were imposed at all inflow faces (based on given P_3 and T_3) for all the upstream boundaries, mains, pilots, cooling holes. The static pressure at the downstream outflow plane (P_4) was fixed at a value computed from the desired pressure drop ($P_3 - \Delta p$). At convergence, the CFD computed mass flow rate that satisfied the desired P_3, T_3 and Δp were used to calculate the effective area (AC_d) of the various components (injectors, cooling holes) of the combustor assembly.

Axial velocity contours for four cross-sections along the length of the combustor are shown in Fig. 17. The combustor face is shown at the 0 mm plane, and two additional planes near the face are shown at the 12.7 mm (0.5″) and 25 mm (1.0″) axial locations. The 150 mm plane downstream of the face represents the location

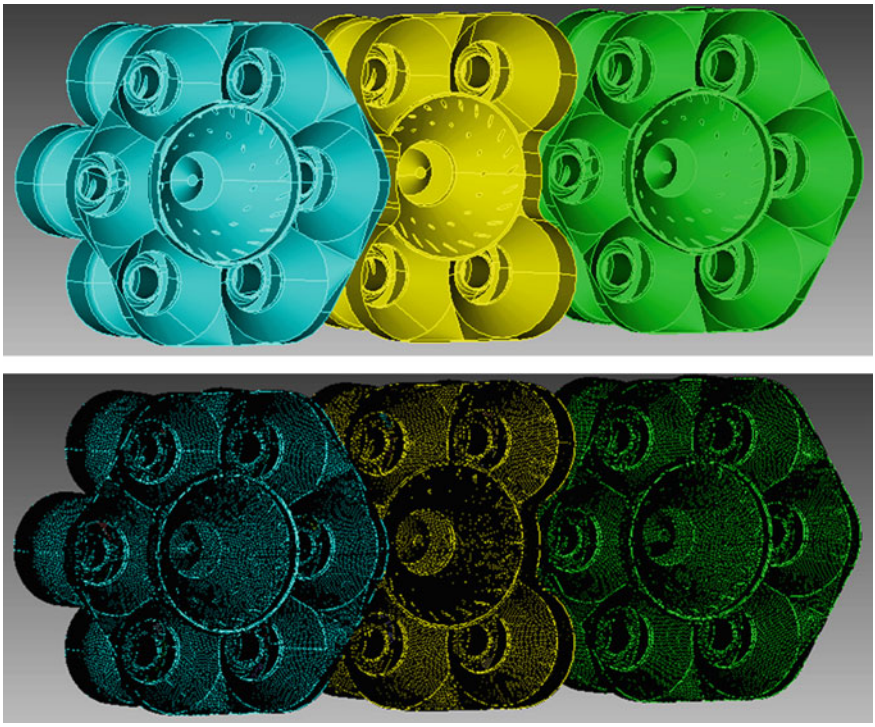

Fig. 16 Dome-layout (top) and surface mesh (bottom) for a three-cup LDI-3 combustor with five- and seven-injection element arrays

of experimental measurements of emissions data. The 0 mm plane shows the central recirculation zones (CTRZ) for the central pilots and some scattered regions of recirculation generated by the swirlers for the main injection elements. At 12.7 mm, the CTRZ behind all three pilots is considerably weakened, and very little CTRZ remains in the flow at the 25.4 mm location. The flow is fairly mixed out and uniforms at the 150 mm plane.

The RANS non-reacting flow predictions were used as an initial condition for the OpenNCC TFNS solver. The TFNS solver uses a time-accurate form of the Navier–Stokes equations with dual time-stepping and time-filtering [33]. The advantage of using a TFNS approach, as compared to an LES approach is that the relatively coarse RANS-like mesh can be used to obtain VLES-like fidelity.

Figure 18 shows the axial velocity contours for the non-reacting OpenNCC TFNS solution in four cross-sections along the combustor length. The individual central recirculation zones behind each injector are much more well-defined at the 0 mm plane, as compared to OpenNCC RANS (cf. Figure 17). In addition, the pilot recirculation zones exist beyond the 25.4 mm plane for OpenNCC TFNS, which suggests a

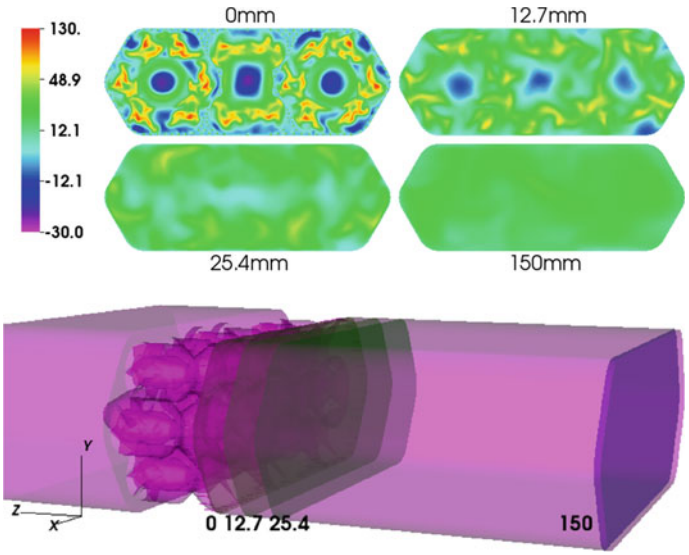

Fig. 17 Contours of axial velocity (m/s) (RANS non-reacting flow). Transverse cuts at combustor dome face (0 mm), two downstream planes and exit plane (150 mm) (top); locations of transverse planes along combustor (bottom)

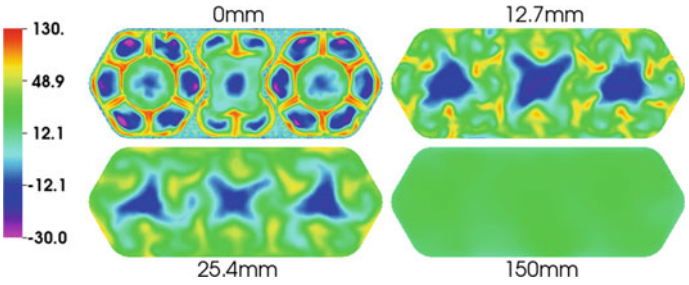

Fig. 18 Contours of axial velocity (m/s) (TFNS non-reacting flow). Transverse cuts at combustor dome face (0 mm), two downstream planes, exit plane (150 mm)

longer mixing region as compared to OpenNCC RANS. OpenNCC TFNS does indicate that the non-reacting flow is very well mixed out at the experimental emissions probe location of 150 mm.

The CFD-predicted mass flow rates at the inlet planes of the 16 main injectors, the three pilot injectors, and the various cooling holes, were used to compute the total AC_d of the nineteen-injector configuration. A comparison of the computed (RANS, TFNS) and experimentally measured AC_d values are shown in Table 7.

The reacting flow TFNS results for an overall furl-air ratio (FAR) of 0.03 are shown in the left-hand side of Fig. 19. The CFD predictions can be used to qualitatively compare the flame structure in the near dome-region (0, 12.7 mm) with an

Table 7 RANS compared to TFNS: effective area (AC_d) prediction

Effective area (AC_d)	Total (in^2)	Mains + Cooling (in^2)	Pilot (in^2)
Experiment	2.6717	2.3613	0.3104
CFD (RANS)	2.8522	2.5174	0.3348
CFD (TFNS)	2.7377	2.3915	0.3462

Computed $AC_d = \dot{m}/\sqrt{2\rho\Delta p}$ using the measured value of $\Delta p =$ 26,882 Pa

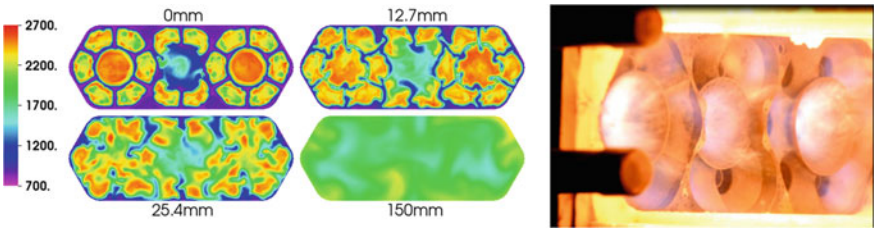

Fig. 19 Left: contours of temperature (K) (TFNS reacting flow). Transverse cuts at combustor dome face (0 mm), two downstream planes, exit plane (150 mm). Right: snapshot of reacting flow field

experimental snapshot of the flame structure shown in the right-hand side of Fig. 19. There seems to be a reasonable qualitative agreement between the CFD and the experiment for the flame structure, except for the prediction of the weak flame for the pilot element of the five-element module.

A comparison of experimental and CFD predictions of NO_xEI for the LDI-3 flametube using OpenNCC TFNS is shown in Fig. 20. The CFD predictions represent a range of "medium" power conditions where the experimental NO_xEI varies from 5 (actually measured) to 30 (extrapolated from actual measurements) for subsonic and supersonic cycles, respectively. Figure 20 can be used to evaluate the "progress" made from RANS/LDI-2 CFD predictions in 2014 (shown earlier in Fig. 14) and 2019 "state of the art" TFNS/LDI-3 capabilities of OpenNCC CFD.

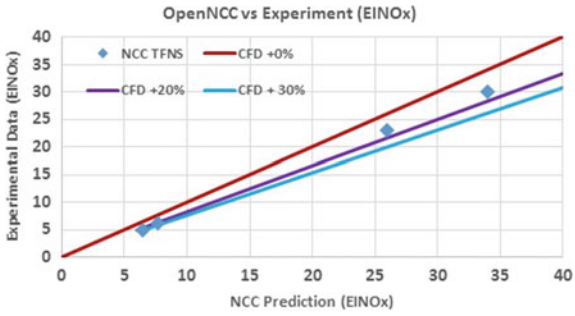

Fig. 20 OpenNCC TFNS predictions of NO_xEI compared with experimental data for LDI-3 at "medium" power cycle conditions

5 Fundamental Diagnostics and Model Validation of LDI-2 Pilot

In order to provide the fundamental understanding critical for undertaking the development of next-generation LDI technology, we have selected several candidate mixers for an integrated diagnostics and comprehensive simulation study. The objectives of the present fundamental investigation are as follows. With single-mixer experiments, we aim to collect benchmark quality engineering and advanced diagnostic data on various LDI pilot mixers with emphasis on operability and providing direction for improving low-power combustion efficiency data supported by accompanying simulations. These experimental datasets will be used to develop, calibrate, and validate advanced turbulent combustion models capable of predicting emissions and operability for lean-dome combustor strategies in general and LDI concepts in particular.

It has to be pointed out that the current study is not a matter of conducting benchmark quality experiments and supporting modeling. Our emphasis is more on integrating combustion design and/or technology effort with relevant supporting simple element testing and associated modeling effort. Moreover, it will be of interest to show whether commercial codes widely adopted in industry, academia, and research professionals, e.g., ANSYS Fluent, Converge CFD Software, etc., are equally satisfactory as compared to OpenNCC.

Furthermore, the fundamental research to develop a suite of design tools involving turbulent combustion and spray dynamics will require extensive computational and experimental work. Simulations must be conducted to verify that the tools accurately predict combustor emissions and performance parameters. These simulations will require validation with high-quality experimental data for LDI concepts. Therefore, detailed fundamental single-element experiments for various LDI-2 swirler/injector combinations have been conducted to collect high fidelity experimental data. With newly acquired diagnostics data on single-element LDI, the current commercial CFD model capabilities in reproducing the experimental results are assessed.

Recognizing that spray modeling capabilities remain the weakest link for accurate predictions of combustor performance and emissions, gaseous fuel was first used to circumvent the complications due to jet fuel atomization, transport, evaporation, mixing, and combustion. The RANS and LES solvers available in commercial CFD software are used to model the LDI experimental data collected herein. This will provide valuable feedback on the accuracy of the integrated advanced techniques to model flow in LDI environments. It is expected that the state of the art models for turbulence and chemical kinetics will need to be adopted for further improvement.

5.1 Experimental Specifications

The present experimental efforts focus on several pilot mixers of LDI-2 summarized in Fig. 21 and Table 8. These single-element LDI-2 mixers were provided by Woodward FST. Each mixer consists of a fuel tip with two concentric axial air swirlers, an IAS contained within the airblast-type fuel tip, and an OAS, located inside a converging-diverging venturi-flare body. Helical 45°/60° OAS vanes are installed with both clockwise and counter-clockwise rotation directions, while the IAS vanes are fixed at a 60° counter-clockwise rotation. The venturi throat diameter is $D_t = 0.52$ in, and its axial location is denoted as $x = 0$. In addition, the LDI flare exit has a diameter of $D_f = 1$ in, a full-included angle of 110°, and a length of $x_f = 0.37$ in.

Single-element experiments were conducted with the setup shown in Fig. 22. From upstream to downstream, the setup consists of an air supply system, flow control, test rig, and exhaust. The air supply system provides sufficient air to run under STP conditions (9.5 g/s) for 47 min. The current setup uses choked orifices to control the mass flow rate of air and gaseous fuel. A high-pressure/large volume syringe pump can provide up to 450 ml/min of liquid fuel when used in a follow-up program. The test rig, shown in Fig. 22, includes three parts: upstream chambers, injector/swirler assembly, and confinement chamber. Two upstream chambers, with layers of mesh between them, help to provide a uniform inlet flow. In the second upstream chamber, an extended tube provides access for inlet temperature and pressure measurement. A quartz chamber, with 304.8 mm length and 50.8 mm × 50.8 mm inner dimensions was used for confinement and to facilitate experiments with optical diagnostics, including Time-Resolved Particle Image Velocimetry (TR-PIV), Planar Laser-Induced Fluorescence (PLIF), and chemiluminescence imaging. Accurate three-dimensional traverse of the test setup is achieved by mounting the test

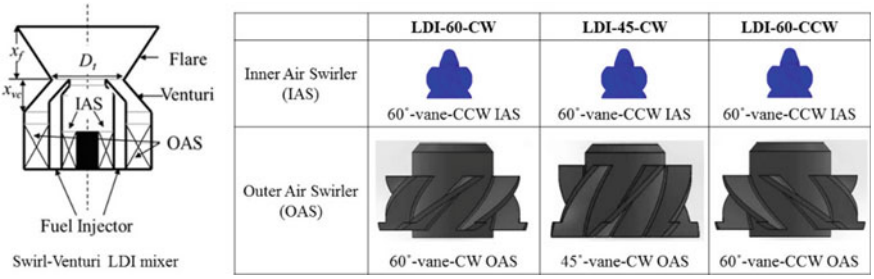

Fig. 21 Schematic of LDI-2 pilot mixers

Table 8 Specifications of swirlers used in the present fundamental research

Configuration	Swirler (IAS/OAS)
LDI-60-CW	60°CCW/60°CW
LDI-45-CW	60°CCW/45°CW
LDI-60-CCW	60°CCW/60°CCW

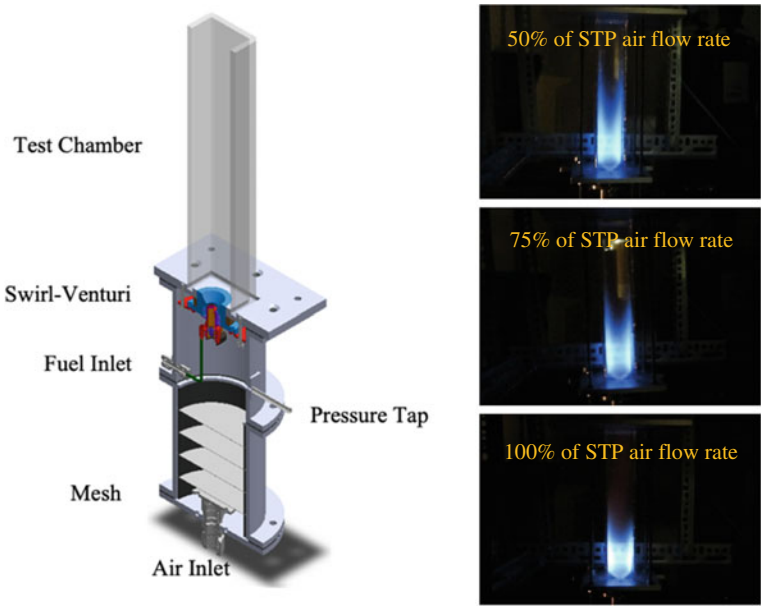

Fig. 22 Test rig design and flame images

rig on the worktable of a milling machine. Fueled by methane, the raw flame images at 50, 75, and 100% STP airflow rates using the LDI-60-CW mixer are also shown in Fig. 22 for demonstration purposes. Details of this test rig have been documented in [40–42].

Non-reacting and reacting flow field measurements were conducted using a TR-PIV system (up to 7500 Hz) to obtain time-correlated turbulence information. OH-PLIF was used to obtain spatially-resolved two-dimensional distributions of OH that can map the temperature field and flame structure. Along with the chemiluminescence measurements of CH*, OH*, and NO_2*, these imaging results provide insight into the flame/emissions characteristics of the selected LDI-2 mixers. When presenting the current experimental results in the following, the axial distance (x) and radial distance (y) are in units of D_t, while all velocity components are normalized by the mean axial velocity based on the venturi throat area, U_t.

Since, the LBO generally characterizes the operability limits of the combustor, LBO FAR as a function of pressure drop was measured to ensure that the combustor can operate over a range of conditions from start to maximum power. LBO is especially important for lean-front-end combustor concepts such as LDI due to the fuel-lean mixture in the combustor and the accompanying effects on flame stability. During the LBO process, OH*/CH* chemiluminescence imaging was also used to characterize the flame structure.

5.2 Experimental Results

Figure 23 demonstrates the diagnostics results, including TR-PIV, OH-PLIF, OH*/CH* chemiluminescence imaging, and direct flame imaging, of methane-fueled flame characteristics with an overall equivalence ratio of $\varphi = 0.60$ for the LDI-60-CW configuration at pressure drop conditions of $\Delta p = 1\%$ and 3%. Figure 24 further shows the flame response variation of the LDI-60-CW configuration with overall equivalence ratio at varying pressure drop conditions. At $\Delta p = 1\%$, it is seen from Fig. 24 that as φ is reduced after establishing a vigorously-burning flame anchored at the venturi exit (e.g., $\varphi = 0.7$), the flame gradually weakens and extends further downstream until flame lift-off is observed ($\varphi = 0.55$). Similar flame structure variation with φ is also observed for other Δp conditions. For a given pressure drop, the critical equivalence ratio below which the flame loses the anchor point near the venturi exit and moves downstream is determined as the flame lift-off limit. Further reducing φ leads to lean blowout. Figure 24 shows the flame lift-off limit and the LBO limit as a function of Δp for the LDI-60-CW configuration.

The methane-fueled flame structure variation with overall equivalence ratio for the LDI-45-CW configuration is illustrated in Fig. 25. In contrast, the LDI-45-CW flame is generally longer than the LDI-60-CW flame shown in Fig. 24 and extends in both the upstream and downstream directions. As φ is reduced, the LDI-45-CW flame weakens and gradually moves downstream until it extinguishes when reaching the LBO limit.

Figure 26 plots and compares the TR-PIV-measured mean axial velocity contours for the LDI-60-CW and LDI-45-CW configurations with $\varphi = 0.65$ and 0.85 at $\Delta p = 3\%$. It can be clearly seen that the resulting reacting flow field in the LDI-60-CW configuration exhibits a CTRZ near the venturi exit. For the LDI-45-CW configuration, on the other hand, no such CTRZ is observed in the resulting reacting flow

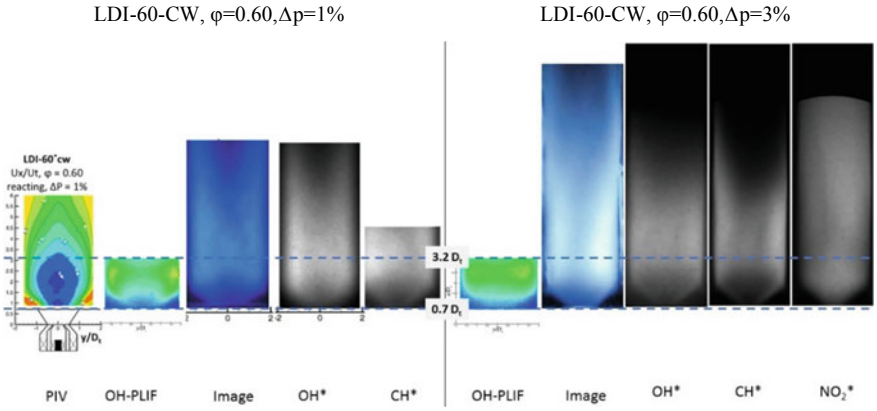

Fig. 23 Diagnostics results for the LDI-60-CW mixer with $\varphi = 0.60$ at $\Delta p = 1\%$ (left) and 3% (right)

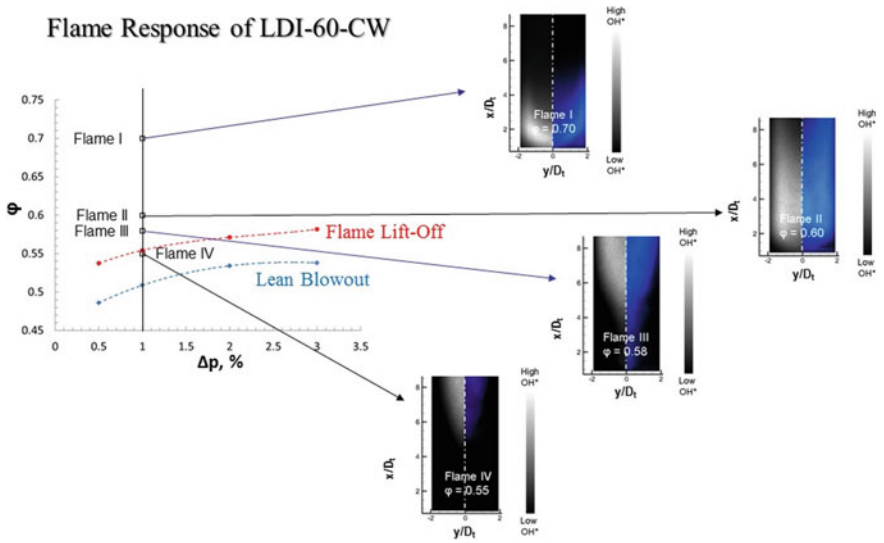

Fig. 24 Flame response of the LDI-60-CW mixer

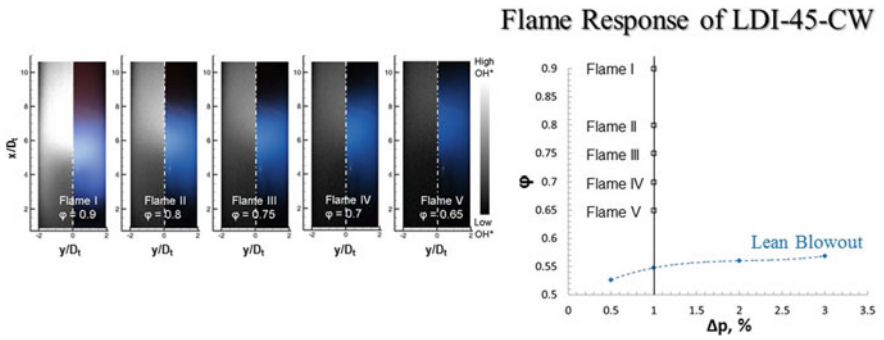

Fig. 25 Flame response of the LDI-45-CW mixer

field and the axial velocity at the exit of the venturi is strongly positive with smaller corner recirculation zones (CNRZ) being observed along each side of the combustion chamber. It is expected that with increasing vane angle the ratio of tangential velocity to axial velocity increases, thereby leading to higher swirl strength, which, in turn, creates an adverse pressure gradient and a CTRZ.

The differences in flame response observed in Figs. 24 and 25 are caused by the effect of OAS vane angle on the flow field. The flame of the LDI-60-CW configuration resides near the venturi exit because of the CTRZ, while the combustion zone of the LDI-45-CW configuration is located far downstream due to the positive axial velocities in the center region near the venturi exit. Tacina et al. [19] noted that NO_x emissions decrease with decreasing swirl strength. The present TR-PIV results

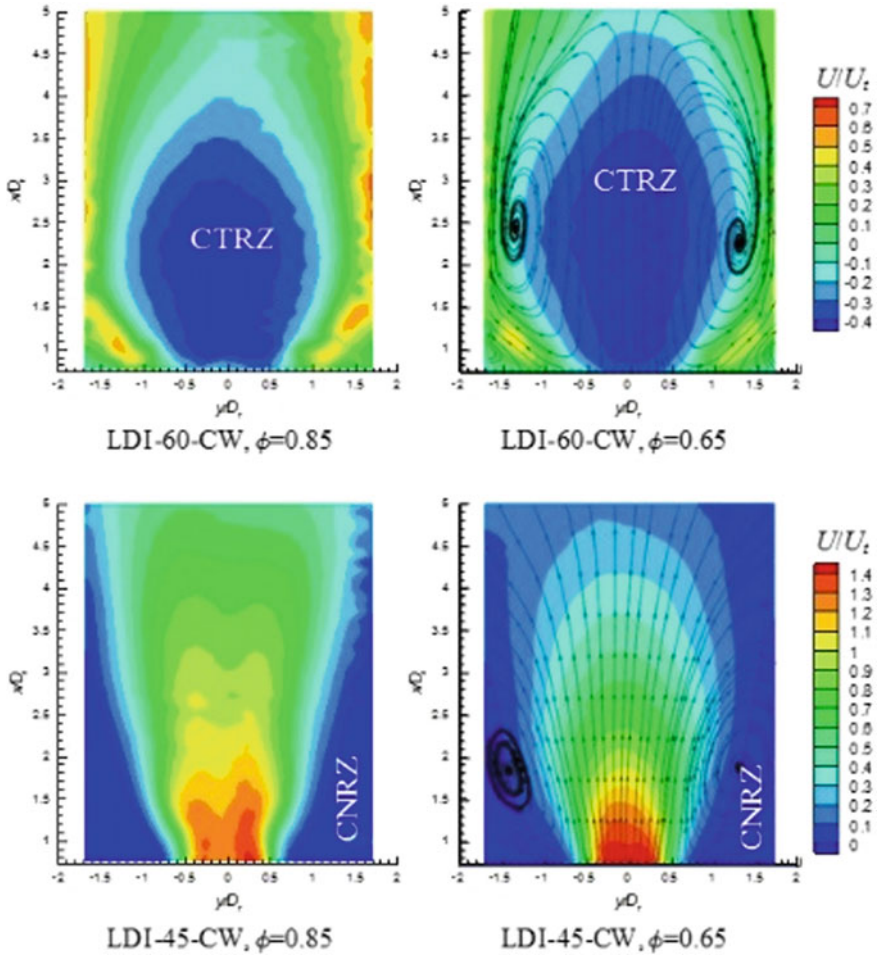

Fig. 26 Effect of OAS vane angle on mean axial reacting flow field at pressure drop of 3% and two overall equivalence ratios of 0.65 and 0.85

indicate that the lack of CTRZ and large positive axial velocities at the venturi exit in the LDI-45-CW configuration would reduce the average residence time within the combustion zone, and hence results in reduced NO_x emissions. However, the flame stability and operability range of the LDI-45-CW configuration will be impacted owing to the lack of flame stabilization near the venturi exit.

As the relative rotation directions between the IAS and OAS, co- or counter-rotating, can impact the air and fuel mixing process and the resulting flow field, Fig. 27 compares the non-reacting flow fields, in terms of mean axial velocity contours, of LDI-60-CW and LDI-60-CCW at $\Delta p = 3\%$. In particular, the co-rotating configuration should enhance swirling strength as the two streams reinforce each other. On the other hand, the counter-rotating configuration should have enhanced shear between

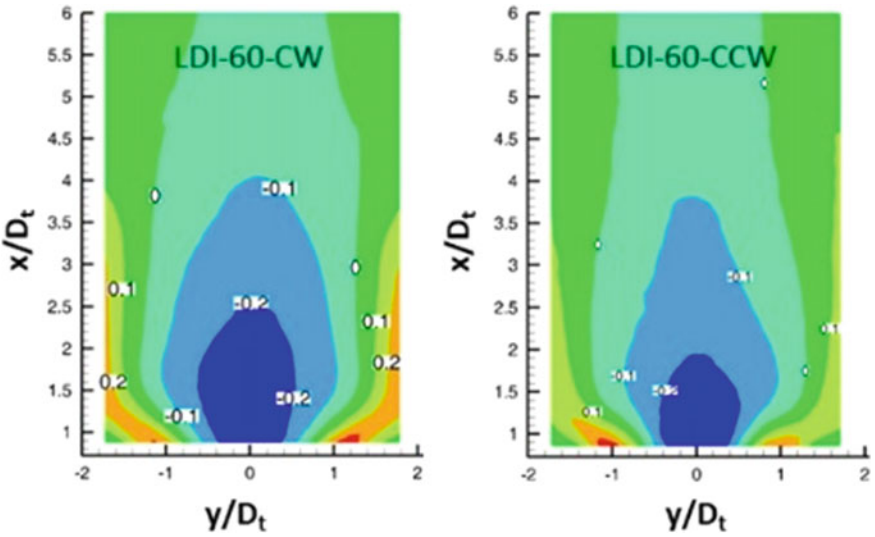

Fig. 27 Effect of air-swirler rotation direction on mean axial non-reacting flow field at pressure drop of 3%

the IAS and OAS flows, which potentially can improve fuel-air mixing. By keeping the IAS vanes at 60° CCW, it is seen from Fig. 27 that the change in OAS rotation direction does not fundamentally alter the general flow features, CTRZ or CNRZ, while LDI-60-CCW has a narrower CTRZ than LDI-60-CW.

5.3 CFD Results

In general practice, RANS is used initially for simplicity in determining the required mesh size to achieve accuracy ineffective area predictions for the main sub-elements of the combustion system, namely mixers, cooling, and swirlers. The developed meshes will then be refined and used in the benchmark element tests. Subsequently, the state of the art models for turbulence (TFNS, hybrid LES/RANS, or LES), spray, and chemical kinetics will need to be adopted for further improvement.

In order to achieve good agreement with non-reacting velocity and scalar profiles for LES and hybrid LES/RANS approaches, a solution-driven adaptive mesh generation methodology needs to be used. This approach will ensure that the subgrid modeling is maintained at minimally acceptable levels for applications across different types of LDI mixers.

Current status of an ongoing model simulation effort is presented next starting with Fig. 28 that gives an example of benchmark non-reacting TR-PIV data, including mean and fluctuating components of axial (U, u) and radial (V, v) velocities, for model validation using ANSYS Fluent. RANS simulations were conducted with the

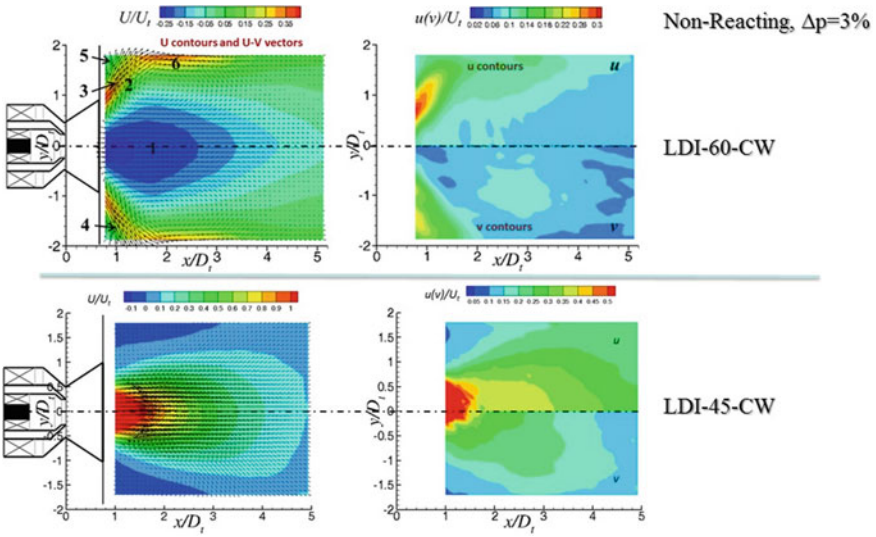

Fig. 28 TR-PIV-measured mean and fluctuating components of axial (U, u) and radial (V, v) velocities at pressure drop of 3% for the LDI-60-CW and LDI-45-CW configurations

standard k-ε (SKE), realizable k-ε (RKE), and Reynolds stress turbulence (RSM) models. Figure 29 demonstrates the mesh adaptation based on velocity gradients, as well as summaries and compares the RANS results of effective area, pressure contours at the venturi throat, and radial profile of mean axial velocities at $1D_t$ downstream the venturi exit. Figure 30 further compares the TR-PIV data and the

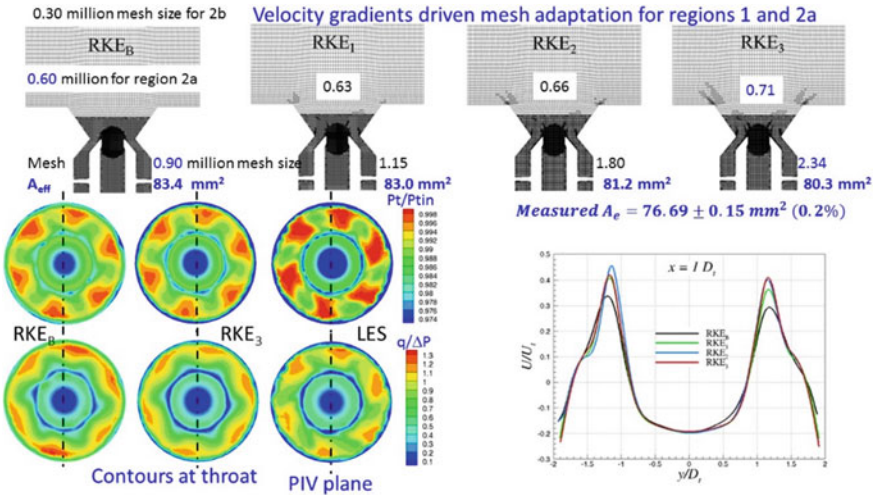

Fig. 29 RANS results of non-reacting flow field using various turbulence models

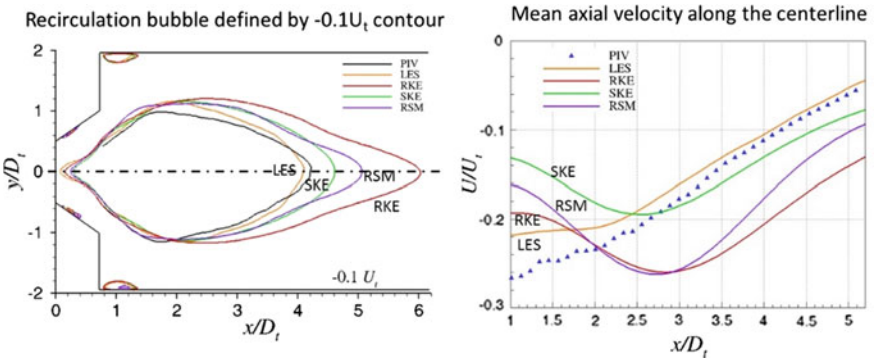

Fig. 30 Comparison of TR-PIV data and CFD results of RANS and LES for the recirculation bubble (left) and mean axial velocity along the centerline (right) using the LDI-60-CW configuration

CFD results of RANS and LES for recirculation bubble (left plot) and mean axial velocity along the centerline (right plot).

Based on the comparison of experimental and CFD results shown in Fig. 30, a number of criteria can be used to assess the performance of various models, such as forward/rear stagnation points, maximum width of recirculation zone and its axial location, recirculated mass, recirculation area/volume and residence time, zero axial velocity location, near-/far-stream velocity behavior, etc. It appears that best to worst performance seems to be LES, SKE, RSM, and RKE. Further improvements on LES are required to make it qualitatively predictive, while it is noted that in the present non-reacting flow simulations LES took a factor of 55 more CPU time compared to the two-equation turbulence model.

Furthermore, the ongoing CFD efforts are to assess the performance of the RANS and LES models for predicting flame shapes and LBO. Of particular interest is to evaluate whether the Flamelet Generated Manifold (FGM) approach can capture the flame characteristics from high-power FAR down to LBO for various LDI configurations. It is also of importance to conduct comprehensive simulations with scalar PDF and LES using affordable accurate kinetic schemes and compare the results with those of FGM. It is a nontrivial task to answer the above fundamental questions. Future publications will establish a state of the art modeling capabilities followed by more advanced models to be completed in the next five years.

In summary, we have collected good-quality diagnostics data on several practical pilot LDI configurations; and the resulting inferences are consistent with hypotheses-based LDI technology development approach described in Sect. 3. Preliminary non-reacting simulations show superior performance of LES over eddy viscosity-based RANS simulations, albeit the former requires 50 times more computational resources. Consistent with past experience, it requires considerably more resources to collect good-quality diagnostics data coupled with simulations, maybe by a factor of 5 or 10 compared to estimated level of effort. The planned completion of integrated

diagnostics/simulation effort will provide the insight needed for improving the further TFNS modeling capability described in Sect. 4.

6 Summary

The hypotheses-based combustion technology and product development approach backed properly by empirical/CFD models has worked well for 29 combustors since the middle of the 1970s. The "anchored CFD approach" has worked well for successfully completing the product introduction of seven rich-dome combustors. However, we have encountered several challenges for developing lean-dome combustion products (ca. DAC and TAPS) and next-generation partially-premixing or lean-direct injection technology concepts, and the supporting diagnostics and modeling activities which are needed for fully realizing benefits of lean combustion over rich-quench-lean approach backed by 50 plus years of development experience.

In spite of the simulation's accuracy limitations summarized in Sect. 4, OpenNCC's usefulness for guiding LDI-2 and LDI-3 technology development [17, 21, 22] is undisputed as summarized in [22–29]. In parallel, fundamental investigation comprised of integrated diagnostics/simulation was kicked off in 2014 under the premise: complexity of the stabilizing pilot flame structure at simulated low-power operation from moderately high equivalence ratio to flameout condition. Our diagnostic investigation has identified five flame structures that need to be properly predicted with advanced modeling efforts planned for the next five years. In the meantime, similar to past practice followed since the middle 1970s, "smart" combustion technologists will continue to make the best use of hypotheses-based lean-combustion technology development approach.

References

1. Mongia HC, Smith KF (1978) An empirical/analytical design methodology for gas turbine combustor. AIAA 1978-998
2. Mongia HC, Reynolds RS, Srinivasan R (1986) Multidimensional gas turbine combustion modeling: applications and limitations. AIAA J 24(6):890–904
3. Mongia HC (1993) Application of CFD in combustor design technology. AGARD CP-536, pp 12–1/12–18
4. Danis AM, Burrus DL, Mongia HC (1996) Anchored CCD for gas turbine combustor design and data correlation. ASME 1996-GT-143
5. Hura HS, Joshi ND, Mongia HC (1998) Dry low emissions premixer CCD modeling and validation. ASME 1998-GT-444
6. Hura HS, Mongia HC (1998) Prediction of NO emissions from a lean dome gas turbine combustor. AIAA 1998-3375
7. Mongia HC (2008) Recent progress in comprehensive modeling of gas turbine combustion. AIAA 2008–1445
8. Mongia HC (2001) A synopsis of gas turbine combustor design methodology evolution of last 25 Years. In: 15th international symposium on air breathing engines, ISABE-2001-1086

9. Mongia HC (2001) Gas turbine combustor liner wall temperature calculation methodology. AIAA 2001-3267
10. Mongia, HC (2003) TAPS –A fourth generation propulsion combustor technology for low emissions. AIAA 2003–2657
11. Mongia HC, Ajmani K, Sung CJ (2019) Hypotheses driven combustion technology and design development approach pursued since early 1970s. 50 years of CFD in engineering sciences: a commemorative volume in memory of D. Brian Spalding. Runchal A (ed)
12. Kim WW, Menon S, Mongia HC (1999) Large eddy simulations of reacting flow in a dump combustor. Comb Sci Tech 143:25–62
13. Grinstein FF, Young G, Gutmark EJ, Hsiao G, Mongia H (2002) Flow dynamics in a swirl combustor. J Turbul 3(30):1–19
14. Wang S, Yang V, Hsiao G, Hsieh SY, Mongia HC (2007) Large eddy simulations of gas-turbine swirl injector flow dynamics. J Fluid Mech 583:99–122
15. Mongia H, Krishnaswami S, Sreedhar PSVS (2007) Comprehensive gas turbine combustion modeling methodology. In: Fluent's Int aerospace CFD Conference, Paris
16. Sripathi M, Krishnaswami S, Danis AM, Hsieh SY (2014) Laminar flamelet based NO_x predictions for gas turbine combustors. GT2014-27258
17. Tacina KM, Podboy DP, Lee FP, Dam B (2019) A third-generation swirl-venturi lean direct injection combustor with a prefilming pilot injector. GT2019-90484
18. Gleason CC, Bahr DW (1979) Experimental clean combustor program. Phase III—final report. NASA CR-135384
19. Tacina R, Lee P, Wey C (2005) A lean-direct-injection combustor using a 9-point swirl-venturi fuel injector. ISABE 2005-1106
20. Tacina, KM, Chang, CT, He, ZJ, Lee, P, Dam, B, Mongia, HC (2014) A second-generation swirl-venturi lean direct injection combustion concept. AIAA 2014-3434
21. Tacina KM, Podboy DP, He ZJ, Lee P, Dam B, Mongia HC (2016) A comparison of three second-generation swirl-venturi lean direct injection combustor concepts. AIAA 2016-4891
22. Ajmani K, Mongia HC, Lee P (2013) Evaluation of CFD best practices for combustor design: Part I—nonreacting flows. AIAA 2013-1144
23. Ajmani K, Mongia HC, Lee P (2013) Evaluation of CFD best practices for combustor design: Part II—reacting flows. AIAA 2013-1143
24. Ajmani K, Mongia HC, Lee P (2014) CFD computations of emissions for LDI-2 combustors with simplex and airblast injectors. AIAA 2014-3529
25. Ajmani K, Breisacher K (2014) Simulations of NO_x emissions from low emissions discrete jet injector combustor tests. AIAA 2014-3524
26. Ajmani K, Mongia HC, Lee P (2015) Parametric design of injectors for LDI-3 combustors. AIAA2015-3785
27. Ajmani K, Mongia HC, Lee P (2016) CFD based design of a filming injector for $N + 3$ combustors. AIAA2016-4783
28. Ajmani K, Mongia HC, Lee P (2017) CFD evaluation of a 3rd generation LDI combustor. AIAA2017-5017
29. Ajmani K, Mongia HC, Lee P, Tacina KM (2018) CFD predictions of $N + 3$ cycle emissions for a three-cup gas-turbine combustor. AIAA2018-4957
30. Swanson RC, Turkel E (1997) Multistage schemes with multigrid for Euler and Navier-Stokes equations. NASA TP-3631
31. Shih T-H, Chen K-H, Liu N-S, Lumley JL (1998) Modeling of turbulent swirling flows. NASA-TM 1998-113112
32. Shih T-H, Povinelli LA, Liu N-S, Chen K-H (2000) Generalized wall function for complex turbulent flows. NASA TM 2000-209936
33. Liu N-S, Shih T-H, Wey CT (2011) Numerical simulations of two-phase reacting flow in a single-element lean direct injection (LDI) combustor using NCC. NASA/TM-2011-217031
34. Ajmani K, Kundu K, Yungster S (2014) Evaluation of reduced mechanisms for combustion of Jet-A in LDI combustor CFD calculations. AIAA 2014-3662
35. Raju MS (2012) LSPRAY-IV: a lagrangian spray module. NASA CR-2012-217294

36. Banhawy YEl, Whitelaw JH (1980) Calculation of the flow properties of a confined kerosene-spray flame. AIAA J 18:1503–1510
37. Raju MS (2004) Current status of the overall spray solution procedure (combined CFD/scalar-Monte-Carlo-PDF/spray computations) developed under NCC. AIAA 2004-0327
38. James S, Zhu J, Anand MS (2007) Large eddy simulations of turbulent flames using the filtered density function model. Proc Combust Inst 31:1737–1745
39. Liu N-S, Wey CT (2014) On the TFNS subgrid models for liquid-fueled turbulent combustion. AIAA 2014-3569
40. Ren X, Xue X, Sung CJ, Brady KB, Mongia HC, Lee P (2016) The impact of venturi geometry on reacting flows in a swirl-venturi lean direct injection airblast injector. AIAA 2016-4650
41. Ren X, Xue X, Sung CJ, Brady KB, Mongia HC (2018) Fundamental investigations for lowering emissions and improving operability. Propul Power Re 7(3):197–204
42. Ren X, Xue X, Brady KB, Sung CJ, Sung Mongia HC (2019) The impact of swirling flow strength on lean-dome LDI pilot mixers' operability and emissions. Expe Therm Fluid Sci 109:109840

Mitigation of Thermoacoustic Instability Through Amplitude Death: Model and Experiments

Sirshendu Mondal and Nevin Thomas

1 Introduction

1.1 Amplitude Death in Coupled Oscillators

When nonlinear oscillators are coupled, a range of emergent phenomena such as synchronization and oscillation quenching are exhibited, depending on the dynamics of the systems and the way in which the coupling is structured [1]. Generally, synchronization or phase locking [2, 3] is exhibited due to weak coupling, while strong coupling affects the amplitude, leading to oscillation quenching [4, 5]. The oscillation quenching phenomenon has two structurally different manifestations, namely amplitude death (AD) and oscillation death (OD). When the parameter values of a system of coupled oscillators are appropriate to bring about AD, the oscillations of the individual oscillators cease, and subsequently all the oscillators return to the same steady state of the system [6]. On the contrary, oscillation death (OD) results from the symmetry breaking of the system and the individual oscillators occupy altered steady states which can be different from the original steady state of the system [7]. Although both phenomena have been widely observed in nature and have many useful applications, in this paper, we restrict our study to the occurrence of AD in coupled thermoacoustic oscillators exhibiting limit cycle behaviour.

The first instance of AD was reported by Rayleigh in a system of two organ pipes positioned side by side [8]. He observed that, when the two pipes were kept close by, their effect on each other caused the sound from both to die down, whereas each

S. Mondal (✉)
National Institute of Technology, Durgapur 713209, India
e-mail: sirshendumondal13@gmail.com

N. Thomas
Indian Institute of Technology Madras, Chennai 600032, India
e-mail: nevinth1729@gmail.com

© Springer Nature Singapore Pte Ltd. 2021

A. De et al. (eds.), *Sustainable Development for Energy, Power, and Propulsion*, Green Energy and Technology,
https://doi.org/10.1007/978-981-15-5667-8_12

of them sounded with its own frequency when kept far away, free from the influence of the other pipe. Recent studies by Abel et al. [9, 10] made use of experiments and mathematical models to explain this phenomenon based on synchronization theory. Subsequently, AD has been experimentally observed in a variety of systems such as electrically coupled chemical oscillators [11], thermo-kinetic oscillators [12] and many coupled electronic circuits [5, 13]. Different types of couplings including dissipative, time-delay, dynamic, conjugate and nonlinear are experimentally found capable of leading coupled oscillatory systems to a state of AD [14]. With proper control strategies, we can avoid unwanted oscillations in certain systems by inducing AD; while in other instances where oscillations have to be maintained (e.g. pulse combustors [15, 16]), we can ensure that the system never reaches the AD state. AD phenomenon finds applications in fields such as neuronal disorders, laser applications and meteorological phenomena [14]. From all these studies, we can infer that AD is a general outcome in coupled nonlinear oscillator systems with many important applications.

1.2 Thermoacoustic Instability and Existing Control Mechanisms

Generally, a thermoacoustic system consists of a heat source (or flame) confined in a duct. Thermoacoustic instabilities aoscillations do not rise from a positive interplay between the acoustic field of the duct and the heat release rate fluctuations from the flame, resulting in the system reaching a state of very high-amplitude oscillations [17]. The importance of thermoacoustic instability can be inferred from the fact that it has been observed in systems ranging from high performance propulsive systems to power generation units. Examples include rockets, aircraft engines, gas turbine engines, boilers [18, 19].

Modern gas turbine engines use lean premixed combustion technology to meet the NO_x and CO emission standards [20, 21], which very often makes them susceptible to the onset of thermoacoustic instabilities. On the other hand, a nonpremixed mode may also result in instabilities as in the case of aero-combustors. Near-stoichiometric air–fuel condition in afterburners is another instance where thermoacoustic instability occurs; however in case of rockets, it occurs even in rich fuel-oxidizer conditions. Very often, adverse effects such as flame flashback and blowout of the flame [22] happen due to thermoacoustic instability. In addition to this, high-amplitude pressure oscillations cause large levels of vibrations which can lead to a reduction in the lifetime of engines or cause serious structural damage [23]. Therefore, prediction and control of these high-amplitude oscillations are of primary importance in real engines [24, 25].

Hitherto, the high-amplitude pressure oscillations observed during thermoacoustic instability were suppressed using passive controls such as the installation of acoustic dampers, liners, baffles, and changing the flame anchoring position [23, 26].

Despite the simplicity of these passive control approaches, they are effective only over a limited range of operating conditions. A different approach involves active control strategies such as feedback control [27] and adaptive control [28] which could suppress the undesired thermoacoustic instabilities using actively functioning electro-mechanical devices. However, in active control, analysing the pressure fluctuations and actively taking the necessary steps to stop thermoacoustic instability requires complicated electro-mechanical feedback systems, which limits the practical applicability of such control methods in actual gas turbine engines [29]. Another approach for damping these thermoacoustic oscillations is to use external periodic forcing [30, 31] (open-loop control), which also falls short of practicality because of the difficulty in installing the actuators in real combustors. Recently, Biwa *et al.* [32] made use of a simple approach based on AD phenomenon to suppress the pressure oscillations in coupled thermoacoustic engines, wherein they coupled two such systems using a needle valve (dissipative coupling) and a vinyl tube (time-delay coupling). For appropriate values of coupling parameters, they observed complete suppression of oscillations or AD in both the engines.

1.3 A Novel Approach to Mitigate Thermoacoustic Oscillations

Almost all of the previous studies on thermoacoustic instabilities considered the suppression of oscillations in isolated systems. Suppression of these oscillations in coupled systems is not a much explored field which can be of significance in many practical systems, for instance, can and can-annular type combustors [33]. Although Biwa et al. [32] provide experimental evidence of AD in thermoacoustic engines, the system they studied does not involve mean flow and physically has very little in common with thermoacoustic instability observed in practical combustors. Further, their modelling was based on simple equations of coupled Van der Pol oscillators, which do not adequately capture the dynamics of a practical thermoacoustic system. Further, in majority of the previous studies [14], the focus was on symmetric coupling; however, in practice, such an ideal scenario is unlikely to exist. Therefore, we study the effect of asymmetrical coupling on AD behaviour of thermoacoustic systems. Also, the oscillations inside similar (dimensionally) practical combustors operating at the same conditions may not be identical owing to the inhomogeneities involved in real systems. Hence, we further investigate the prospect of achieving AD or at least suppressing the oscillations to a good extent in such systems.

To that end, we adopt a prototypical model of a thermoacoustic oscillator, known as horizontal Rijke tube [34], and perform the first systematic theoretical investigation on the effects of the two different types of couplings (time-delay and dissipative) applied separately and simultaneously on such systems. We observe the response of the system to varying coupling parameters and note the bifurcation points where the dynamics of both the oscillators transition from limit cycle to AD. While dissipa-

tive coupling can lead to AD only if there is a sufficient difference in the natural frequencies (detuning) of the two oscillators [35], time-delay coupling of sufficient strength with appropriate delay can bring about AD even in a system of two identical oscillators [5]. Simultaneous application of the two couplings leads the coupled thermoacoustic oscillators to reach AD state more easily (with a lesser coupling strength). We also establish that the increased heater power or equivalently increased amplitude of oscillations requires higher coupling strength for achieving AD in the same system. Further, the effect of asymmetry on the coupling parameters required to achieve AD is noted. Results from the model also indicate that AD or at least a significant reduction in amplitude is possible even in a system of two Rijke tube oscillators with considerably different amplitudes.

However, the oscillations cannot be completely cut short in practical systems. Combustion processes and turbulent incoming flows are bound to create noisy fluctuations in practical thermoacoustic systems [36]. Further, it has been shown in the past that the sources of these turbulent fluctuations are additive [37] and parametric [38, 39]. How different kinds of noise (white, pink, blue, etc.) affect the dynamics of an individual thermoacoustic oscillator has been studied in the past [36, 40]. In the present study, our focus is on the effect of white noise on coupled thermoacoustic oscillators. White noise is defined as a random signal with a constant power spectral density. We add white noise individually to the two self-sustained thermoacoustic oscillators, which are then subjected to coupling.

While in the deterministic case, an appropriate coupling can completely suppress the unwanted oscillations, the amplitude of oscillations does not go to zero in the presence of noise. However, a significant suppression can be achieved even in the noisy setting under appropriate coupling conditions. Since the noisy case lacks a well defined indicator of the transition to AD, we make use of the changes in the pressure amplitude distribution in a histogram, towards this purpose. The bifurcation from LCO to AD can be discerned from the change in the distribution from bimodal to unimodal. Further, we observe from one-parameter bifurcation plots that, as the noise intensity increases, the subcritical nature of transitions are completely lost. We also observe the area of amplitude suppression zones shrinks with noise intensity in the two-parameter bifurcation plots. Additionally, these figure point to the fact that it is easier to achieve suppression when the time-delay coupled thermoacoustic oscillators are non-identical (different natural frequencies). An additional weak dissipative coupling on the system makes the amplitude suppression a further easy task.

2 Model for Coupled Rijke Tube Oscillators

The prototypical thermoacoustic system we use here is the horizontal Rijke tube. It is a horizontal duct with a concentrated heat source (a heated cylinder in the model used here). The Rijke tube oscillator was often chosen to study the intricacies of thermoacoustic instabilities in the past [25, 34, 41, 42], because of its analytical tractability.

In the present study, we build on the model developed by Balasubramanian and Sujith [34]. The linearized momentum (Eq. 1) and energy (Eq. 2) equations for the acoustic field, neglecting the effect of mean flow ($M = 0$) and mean temperature gradient in the duct, are given as [34],

$$\bar{\rho}\frac{\partial \tilde{u}'}{\partial \tilde{t}} + \frac{\partial \tilde{p}'}{\partial \tilde{x}} = 0, \tag{1}$$

$$\frac{\partial \tilde{p}'}{\partial \tilde{t}} + \gamma \bar{p}\frac{\partial \tilde{u}'}{\partial \tilde{x}} = (\gamma - 1)\dot{\tilde{Q}}'\delta(\tilde{x} - \tilde{x}_f). \tag{2}$$

Here, $\tilde{x}$ is the axial distance, $\tilde{x}_f$ is the location of the heat source, $\tilde{t}$ is time, $\tilde{u}'$ is the acoustic velocity, $\tilde{p}'$ is the acoustic pressure, $\bar{\rho}$ and γ are the mean density and the ratio of specific heats of the medium, respectively, and $\dot{\tilde{Q}}'$ is the heat release rate fluctuations per unit area due to the heated cylinder. Dirac delta (δ) function is used to capture the compactness of the heat source.

The pressure ($\tilde{p}$) at both ends of the duct are equal to the ambient pressure ($\bar{p}$). Therefore, the acoustic pressure fluctuations ($\tilde{p}'$) at the boundaries are negligible, as $\tilde{p}' = \tilde{p} - \bar{p} = 0$. As a consequence, we can impose the boundary conditions as $\tilde{p}' = 0$ at both ends of the duct. Variables in Eqs. (1) and (2) are non-dimensionalized as follows,

$$x = \frac{\tilde{x}}{l}; t = \frac{\tilde{t}}{l/c_0}; u' = \frac{\tilde{u}'}{u_0}; p' = \frac{\tilde{p}'}{\bar{p}}; \dot{Q}' = \frac{\dot{\tilde{Q}}'}{c_0\bar{p}}; M = \frac{u_0}{c_0}. \tag{3}$$

Tilde is used to represent dimensional variables and those without tilde are non-dimensional. Here, l is the length of the duct, u_0, and $\bar{p}$ are the steady-state velocity, pressure, and temperature of the flow, respectively, c_0 is the speed of sound, and M is the Mach number corresponding to the mean flow.

After non-dimensionalizing and adding a damping term ($\zeta p'$ in Eq. (2), where ζ is the damping coefficient), the governing equations take the following form [42],

$$\gamma M\frac{\partial u'}{\partial t} + \frac{\partial p'}{\partial x} = 0, \tag{4}$$

$$\frac{\partial p'}{\partial t} + \gamma M\frac{\partial u'}{\partial x} + \zeta p' = (\gamma - 1)\dot{Q}'\delta(x - x_f). \tag{5}$$

The heat release rate in the duct is modelled using a modified form of King's law [43, 44]. This correlation quantifies the quasi-steady heat transfer from a heated cylinder to the flow around it. We use the parameter time lag (τ_1) to capture the thermal inertia of the heat transfer in the medium. Therefore, an empirical model was suggested in which the heat release rate fluctuations are written as a function of

the acoustic velocity fluctuations (i.e. $u'_f(t-\tau_1)$ observed at the heater location, x_f, and with a delay τ_1) as [42, 44],

$$\dot{Q}'(t) = \frac{2L_w(T_w - \bar{T})}{S\sqrt{3}c_0\bar{p}}\sqrt{\pi\lambda C_v u_0 \bar{\rho} l_c}\left[\sqrt{\left|\frac{1}{3} + u'_f(t-\tau_1)\right|} - \sqrt{\frac{1}{3}}\right], \tag{6}$$

where l_c, L_w, T_w are the radius, length, and temperature of the heater wire, respectively, S is the cross-sectional area of the duct, $\bar{T}$ is the steady-state temperature of the flow, λ, C_v are thermal conductivity and specific heat at constant volume, respectively, of the medium within the duct.

Substituting Eq. (6) in the energy equation, Eq. (5), we obtain [42],

$$\begin{aligned}&\frac{\partial p'}{\partial t} + \gamma M \frac{\partial u'}{\partial x} + \zeta p' \\ &= \quad (\gamma - 1)\frac{2L_w(T_w - \bar{T})}{S\sqrt{3}c_0\bar{p}}\sqrt{\pi\lambda C_v u_0 \bar{\rho} l_c}\left[\sqrt{\left|\frac{1}{3} + u'_f(t-\tau_1)\right|} - \sqrt{\frac{1}{3}}\right]\delta(x - x_f).\end{aligned} \tag{7}$$

The set of partial differential equations (PDE) given by Eqs. (4) and (7) can be reduced to ordinary differential equations (ODE) using the Galerkin technique [45]. To that end, velocity (u') and pressure (p') fluctuations in the duct are written in terms of basis functions or the Galerkin modes [34]. These basis functions represent the natural acoustic modes of the duct in the absence of heat release. These functions form a complete basis and also satisfy the boundary conditions ($p'(0, t) = 0; p'(1, t) = 0$). The basis functions for u' and p' can be written as follows:

$$u' = \sum_{j=1}^{N} \eta_j \cos(j\pi x), \tag{8}$$

$$p' = -\sum_{j=1}^{N} \dot{\eta}_j \frac{\gamma M}{j\pi} \sin(j\pi x). \tag{9}$$

Here, η_j and $\dot{\eta}_j$ are the time-varying coefficients of the acoustic velocity (u') and the acoustic pressure (p') in the Galerkin expansion, respectively, and N represents the number of Galerkin modes considered. In the present study, we choose first ten modes, since addition of further modes brought about only negligible improvement to the solution [42].

The following ODEs are obtained by substituting the expansions for u' (Eq. 8) and p' (Eq. 9) into the PDEs given in Eqs. (4) and (7) and then projecting along the basis functions [34]:

$$\frac{\mathrm{d}\eta_j}{\mathrm{d}t} = \dot{\eta}_j, \tag{10}$$

$$\frac{\mathrm{d}\dot{\eta}_j}{\mathrm{d}t} + 2\zeta_j\omega_j\dot{\eta}_j + \omega_j^2\eta_j = -j\pi K\left[\sqrt{\left|\frac{1}{3} + u_f'(t-\tau_1)\right|} - \sqrt{\frac{1}{3}}\right]\sin(j\pi x_f), \tag{11}$$

where

$$u_f'(t-\tau_1) = \sum_{j=1}^{N}\eta_j(t-\tau_1)\cos(j\pi x), \tag{12}$$

and $\omega_j = j\pi$ is the non-dimensional angular frequency of the jth duct mode. The coefficient of the second term on the left-hand side of Eq. (11), $2\zeta_j\omega_j\dot{\eta}_j$, represents the frequency dependent damping [41, 46, 47], where ζ_j can be written as,

$$\zeta_j = \frac{1}{2\pi}\left[c_1\frac{\omega_j}{\omega_1} + c_2\sqrt{\frac{\omega_1}{\omega_j}}\right]. \tag{13}$$

Here, c_1 and c_2 are the damping coefficients, values of which determine the amount of damping in the system. The values of c_1 and c_2 are chosen as 0.1 and 0.06, respectively, for all the simulations in this study. These values are chosen such that it conforms with the cold decay rate calculated from experiments [48]. The value of x_f is chosen to be 0.25 (=$l/4$), as it is the most favourable location for the onset of thermoacoustic instability [41].

In Eq. (11), K is the non-dimensional heater power which is specified as,

$$K = \frac{4(\gamma-1)L_w(T_w-\bar{T})}{\gamma M c_0\bar{p}S\sqrt{3}}\sqrt{\pi\lambda C_v u_0\bar{\rho}l_c}. \tag{14}$$

When the value of K is increased beyond a critical value ($K_{\mathrm{Hopf}} = 0.62$), the system undergoes a Hopf bifurcation, wherein the oscillations in the system grow and saturate at a high-amplitude value (Fig. 1a). This is the state of limit cycle oscillations (LCO). The waveform and amplitude spectrum of the acoustic pressure signal corresponding to $K = 0.75$ are shown in Fig. 1b, c, respectively. At LCO, the system oscillates with a constant amplitude (Fig. 1b) and frequency ($\omega = 3.25$ in Fig. 1c). When the value of K is reduced in the reverse path, a fold bifurcation happens at a lower value of K ($K_{\mathrm{fold}} = 0.52$) than K_{Hopf}. This results in a bistable (hysteresis) region, which is the characteristic of subcritical Hopf bifurcation [42], as can be seen from Fig. 1a.

The study by Balasubramanian et al. [34] is taken as the reference for choosing the values of constants involved in Eq. (14). The resulting set of equations Eqs. (10) and(11) along with Eqs. (13) and (14), gives the time evolution equations of the system dynamics.

Let the superscripts 'a' and 'b' denote the first and second Rijke tubes, which are coupled through both time-delay and dissipative couplings as shown in Fig. 2. Now, the modified governing equations for the first Rijke tube oscillator are as shown below:

$$\frac{\mathrm{d}\eta_j^a}{\mathrm{d}t} = \dot{\eta}_j^a, \tag{15}$$

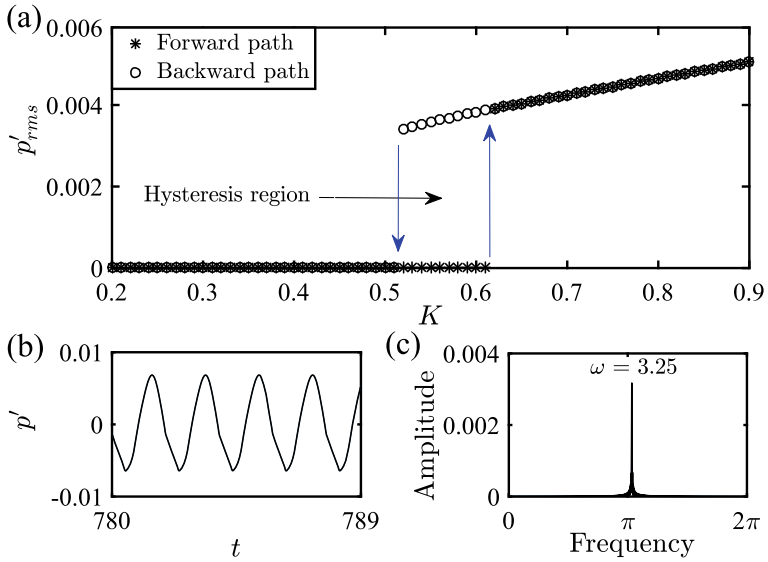

Fig. 1 **a** Bifurcation diagram showing the variation p'_{rms} with heater power (K). In the forward path, we observe a Hopf bifurcation point around $K_{\text{Hopf}} = 0.62$. However, in the reverse path, the bifurcation happens through fold point around $K_{\text{fold}} = 0.52$. **b** The waveform and **c** amplitude spectrum of the acoustic pressure signal corresponding to $K = 0.75$ (a state of limit cycle oscillation) are shown. For the given set of parameter values, we observe a dominant peak in non-dimensional frequency around $\omega = 3.25$. Reproduced with permission from [49]

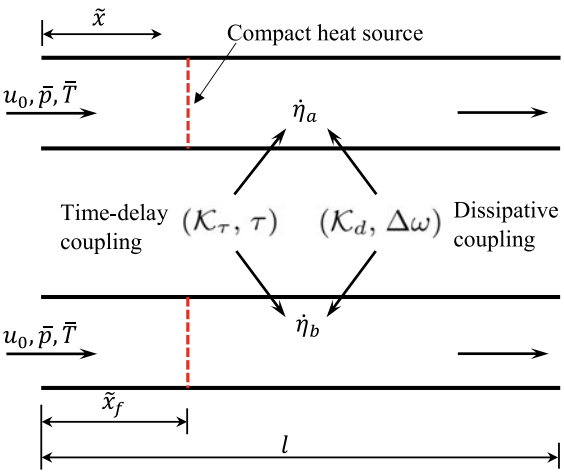

Fig. 2 A simplified illustration of the two coupled Rijke tube oscillators (named as 'a' and 'b') subjected to both dissipative ($\mathcal{K}_d$, $\Delta\omega$) and time-delay ($\mathcal{K}_\tau$, τ) couplings. The time-varying coefficient, $\dot{\eta}$, of the acoustic pressure term is the variable being coupled. The flow direction is from left to right and the compact heat source is a single cylindrical wire, shown by red dashed lines. Reproduced with permission from [49]

$$\frac{\mathrm{d}\dot{\eta}_j^a}{\mathrm{d}t} + 2\zeta_j\omega_j\dot{\eta}_j^a + \omega_j^2\eta_j^a = -j\pi K^a\left[\sqrt{\left|\frac{1}{3} + u_f'^a(t-\tau_1)\right|} - \sqrt{\frac{1}{3}}\right]\sin(j\pi x_f) + \underbrace{\mathcal{K}_d(\dot{\eta}_j^b - \dot{\eta}_j^a)}_{\text{Dissipative coupling}} + \underbrace{\mathcal{K}_\tau(\dot{\eta}_j^b(t-\tau) - \dot{\eta}_j^a(t))}_{\text{Time-delay coupling}}. \quad (16)$$

The governing equations for the second Rijke tube oscillator can be obtained by flipping the superscripts 'a' and 'b' in the above differential equations. The second and third terms on the right-hand side of Eq. (16) are the dissipative and time-delay coupling terms, respectively. Inserting $\mathcal{K}_\tau = 0$ reduces the dynamical system to dissipatively coupled oscillators, while $\mathcal{K}_d = 0$ yields time-delay coupled ones. The four parameters which are varied in the model to study their effect on AD are dissipative coupling strength ($\mathcal{K}_d$), time-delay coupling strength ($\mathcal{K}_\tau$), detuning ($\Delta\omega = |\omega_a - \omega_b|$) and delay time ($\tau$). In all the simulations performed in this study, the quantities ω_b/ω_a (ω_a and ω_b being the natural frequencies of the first and the second Rijke tube oscillators, respectively, where $\omega = 2\pi f, f$ being the frequency) and $\Delta\omega$ are varied by keeping ω_a constant at 3.25 (determined from the fast Fourier transform of the pressure time series, Fig. 1c) and varying ω_b.

The ODEs given in Eqs. (15) and (16) are solved numerically using the fourth-order Runge–Kutta scheme, and p' and u' are calculated from Eqs. (8) and (9), respectively.

Finally, after adding the stochastic component, Eq. (16) is given as,

$$\frac{d\dot{\eta}_j^a}{dt} + 2\zeta_j\omega_j\dot{\eta}_j^a + \omega_j^2\eta_j^a = -j\pi K^a\left[\sqrt{\left|\frac{1}{3} + u_f'^a(t-\tau_1)\right|} - \sqrt{\frac{1}{3}}\right]\sin(j\pi x_f) + \underbrace{\mathcal{K}_d(\dot{\eta}_j^b - \dot{\eta}_j^a)}_{\text{Dissipative coupling}} + \underbrace{\mathcal{K}_\tau(\dot{\eta}_j^b(t-\tau) - \dot{\eta}_j^a(t))}_{\text{Time-delay coupling}} + \underbrace{\sigma\epsilon(t)}_{\text{Noise}} \quad (17)$$

In the last term of Eq. (17), σ and $\epsilon(t)$ are respectively, the strength of the additive noise and the Gaussian white noise with zero mean and a variance proportional to the square root of the time step used [48]. The non-dimensional noise intensity is defined as,

$$\beta = \frac{I}{P} \quad (18)$$

where I is the root-mean-square value of the applied white noise (calculated by taking the rms of $\sigma\epsilon$ over a period of time) and P is the root-mean-square value of the acoustic pressure oscillations in the deterministic case.

3 Model Results and Discussions

We devote this section to demonstrate the effect of two types of couplings, namely time-delay and dissipative coupling, on the occurrence of AD in the system of two coupled thermoacoustic oscillators. We first demonstrate the effect of individual coupling on the occurrence of AD in both the oscillators and then study the case where they are applied simultaneously. The results are summarized in the bifurcation plots. In the one-parameter bifurcation plot, an rms value of the acoustic pressure oscillations (p'_{rms}) is plotted as a function of one of the parameters (e.g. time-delay, τ) which is varied. The value of p'_{rms} is calculated when the transients are over and the acoustic pressure oscillations achieve an asymptotic state after the application of coupling.

In the two-parameter bifurcation plot, the variation of the coupling strength required to achieve AD is plotted as a function of the corresponding coupling parameter—delay time or detuning. While the one-parameter bifurcation plot helps in detecting the transition points of both oscillators from limit cycle oscillations (LCO) to AD state, the two-parameter bifurcation plot aids in depicting the regions of AD in the system dynamics for a given range of the parameter values.

3.1 Effect of Time-Delay Coupling

3.1.1 Deterministic Case

First, we analyse the effect of time-delay coupling alone, i.e., when $\mathcal{K}_d = 0$, on the system of two identical ($\Delta\omega = 0$) thermoacoustic oscillators (Fig. 3). Coupling in majority of the physical systems involves time-delay, due to the finite time a signal needs to travel from one system to the other. When two conservative systems are coupled through the first time-derivative of the variable involved in the governing equations ($\dot{\eta}$ or equivalently acoustic pressure in the case of Rijke tube oscillators) with delay, they can exhibit AD [14]. Physically, in the system considered here, the coupling strength and delay time may be varied by changing the diameter and length, respectively, of the tube that couples the two Rijke tube oscillators. Ideally, if the length of the connecting tube is zero, there will be no delay between the signals from the two oscillators. In such a case, the oscillators are said to be dissipatively coupled.

Figure 3a, b is two representative plots showing the effect of time-delay coupling on the amplitude of acoustic pressure signal acquired from one of the oscillators. Since the thermoacoustic oscillators considered in this case are identical, and the coupling between them is symmetric, the variation of acoustic pressure exhibited by these oscillators is also identical. In both the cases (Fig. 3a, b), the non-dimensional heater power in both Rijke tubes ($K^a = K^b = K$) is maintained constant at 0.92. This value of K is chosen because it is sufficiently higher than the K value corresponding to the Hopf point ($K_{\text{Hopf}} = 0.62$) for the individual Rijke tube oscillators [42]. In

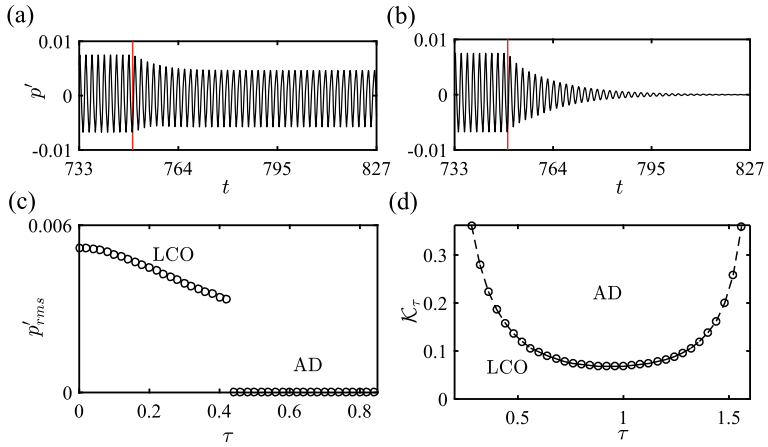

Fig. 3 Temporal variation of non-dimensional acoustic pressure (p'), when time-delay coupling between the two oscillators is **a** not strong enough ($\mathcal{K}_\tau = 0.04$, $\tau = 0.5$) and **b** strong enough ($\mathcal{K}_\tau = 0.2$, $\tau = 0.5$) to achieve AD. The vertical line (shown in red) indicates the instant at which coupling is applied. **c** One-parameter bifurcation plot showing the variation of p'_{rms} with τ ($\mathcal{K}_\tau = 0.16$). **d** Two-parameter bifurcation diagram in the parameter plane of time-delay coupling strength ($\mathcal{K}_\tau$) and delay time (τ) showing the region of AD. For all plots, $\mathcal{K}_d = 0$, $\Delta\omega = 0$ and $K^a = K^b = 0.92$. Reproduced with permission from [49]

these two figures, the time-delay coupling strength ($\mathcal{K}_\tau$) is the sole parameter varied across the two cases, other parameters being kept constant: non-dimensional delay time ($\tau = 0.5$), dissipative coupling constant ($\mathcal{K}_d = 0$) and detuning ($\Delta\omega = 0$).

Figure 3a shows the case where the coupling strength between the two Rijke tube oscillators is not strong enough ($\mathcal{K}_\tau = 0.04$) to achieve AD. We observe that the amplitude of the LCO shows a small decrease from the instant where the coupling is applied, before saturating to another steady-state value. On the other hand, when the coupling is strong enough ($\mathcal{K}_\tau = 0.2$) to achieve AD (Fig. 3b), the amplitude of LCO of the acoustic pressure (p') decays exponentially to a zero value, once the coupling is applied. We show a one-parameter bifurcation plot in Fig. 3c that shows the variation of p'_{rms} with τ for one of the Rijke tube oscillators while the time-delay coupling strength is held constant ($\mathcal{K}_\tau = 0.24$). We observe that the bifurcation of LCO to AD happens around $\tau = 0.4$, where the p'_{rms} value of LCO suddenly falls to zero. We further notice that, prior to the bifurcation, when the delay is not sufficient to achieve AD for the given value of $\mathcal{K}_\tau$, the amplitude of LCO continuously reduces by a small value with increase in τ. A qualitatively similar bifurcation plot is obtained when τ is kept constant and the value of $\mathcal{K}_\tau$ is varied (shown in supplementary material, Fig. S1a).

The effect of time-delay coupling on AD characteristics of two identical thermoacoustic oscillators is further studied using a two-parameter bifurcation plot (Fig. 3d) in which the time-delay coupling strength ($\mathcal{K}_\tau$) required to achieve AD is plotted against delay time (τ). The bifurcation diagram turns out to be a U-shaped plot in

the range of parameter values considered. The $\mathcal{K}_\tau$–τ combinations which lie inside the U-shaped plot exhibit AD, while those lying outside do not. The points indicated by the markers along the U-shape are the points where bifurcation occurs from LCO to AD. These points correspond to the smallest coupling strength, at a particular τ, for which AD occurs in the dynamics of both the oscillators.

From Fig. 3d, we observe that AD most easily occurs around $\tau = 0.94$. This corresponds to a value of $\omega\tau$ close to π. Although in most of the previous studies [14, 50] on mutually coupled oscillators, AD was most favoured around $\omega\tau = \pi/2$, this is not the same in the present study. Achieving AD near $\omega\tau = \pi$ might be a characteristic of the specific system we study. Furthermore, in other studies on closed-loop forcing of thermoacoustic oscillations, a phase delay of π has been implemented as a strategy of active control in thermoacoustic systems [27]. In such cases, reduction in the amplitude has been found due to the negative feedback between self-sustained oscillations and phase-lagged oscillations of the feedback signal. This might be a reason behind the observation of AD region around the phase delay of π when time-delay coupling alone is implemented in our system. However, the precise reason behind achieving AD around $\omega\tau = \pi$ in coupled Rijke tube oscillators needs further investigation.

3.1.2 Stochastic Case

We next compare the time series of acoustic pressure signals obtained in the stochastic and deterministic cases in the coupled thermoacoustic oscillator system. We observe that the addition of white noise results in random fluctuations in the amplitude of the signal compared to the noiseless case (Fig. 4d–f). The non-dimensional heater power value, K is kept constant at 0.8 ($K_{\text{Hopf}} = 0.62$) in all the sub-figures in Fig. 4 and the time-delay coupling strength ($\mathcal{K}_\tau$) is increased from Fig. 4a–c (without noise) and Fig. 4d–f (with noise). In Fig. 4, the only variable altered across the three figures (Fig. 4a–f) is the time-delay coupling strength ($\mathcal{K}_\tau$). We observe that there is a decrease in the magnitude of LCO once the coupling is applied in both the cases as shown in Fig. 4b, e. However, a complete termination of oscillations (or AD) is observed in the deterministic case (Fig. 4c) when the coupling strength is further increased, while small-scale aperiodic oscillations persisted in the noisy case (Fig. 4f) post-transition to AD.

Since even the strong coupling could not bring down the pressure oscillations to zero value in the stochastic case (Fig. 4d–f), determining the transition point to AD is hard. We found that histograms provide a feasible way to detect the bifurcations from LCO to AD in the stochastic case. In Fig. 5, we present six histograms corresponding to the cases presented in Fig. 4. The ordinate value, N represents the number of data points in the pressure time series with a particular non-dimensional acoustic pressure value p'. We note that the amplitude distribution of p' is bimodal with two distinct peaks seen away from the mean, in the absence of noise (Fig. 5a), in line with the past literature [48, 52]. As we introduce a time-delay coupling between the two oscillators, the two peaks come closer to the mean value (Fig. 5b). When we further

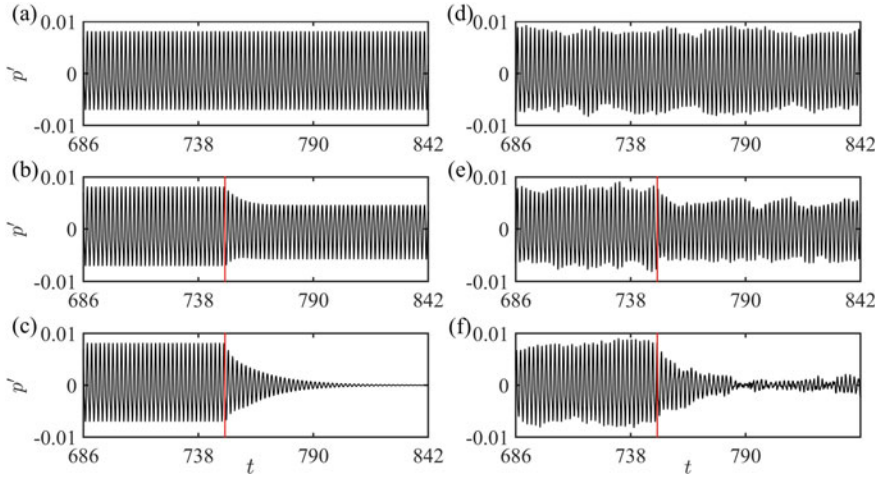

Fig. 4 Temporal variation of non-dimensional acoustic pressure (p') obtained from the thermoacoustic oscillator 'a' in the absence of noise **a**–**c** and in the presence of noise **d**–**f** respectively. **a** In the absence of coupling ($\mathcal{K}_\tau = 0$, $\beta = 0$), **b** relatively weak time-delay coupling ($\mathcal{K}_\tau = 0.06$, $\beta = 0$) is applied, and **c** relatively strong time-delay coupling ($\mathcal{K}_\tau = 0.12$, β=0) which can lead to AD state is applied. The corresponding cases in the presence of noise are shown in (**d**) $\mathcal{K}_\tau = 0$, $\beta = 0.012$, **e** $\mathcal{K}_\tau = 0.06$, $\beta = 0.012$, and **f** $\mathcal{K}_\tau = 0.12$, $\beta = 0.012$. The red vertical line indicates the time instant at which coupling is applied. For all the plots, the non-dimensional heater powers of the two Rijke tubes, $K^a = K^b = 0.8$, and delay time, $\tau = 0.5$, are fixed. Reproduced with permission from [51]

increase the $\mathcal{K}_\tau$ value so as to reach the state of AD, we see that pressure distribution is essentially the mean value (the spike seen in Fig. 5c), which is zero in this case. On the other hand, when we add external noise to the uncoupled system, the peaks become shorter and the spread of distribution increases (Fig. 5d). Also, the smoother peaks are observed in the stochastic case in contrast to the sharp peaks in the deterministic case. The increase in the spread conforms with increase in the variance (ψ^2) value of the pressure time series when noise is added. Similar to the noise-free scenario, these two peaks come closer to the mean value when we introduce a coupling in the system, as depicted in Fig. 5e. When we further increase the $\mathcal{K}_\tau$ value in Fig. 5f, we see that a single peak is formed by the merging of the two peaks which existed before. We can characterize this transition in the distribution from bimodal to unimodal as an indicator of the bifurcation to AD, in the stochastic case. However, it is difficult to assign a critical parameter value at which the distribution becomes unimodal from bimodal as this transition from LCO to AD is a smooth process [53].

Now, we study the effect of varying noise intensity on the one-parameter bifurcation plots. Figure 6 corresponds to the case where a system of two identical ($\omega_b/\omega_a = 1$) thermoacoustic oscillators is subjected to time-delay coupling alone. As shown in Fig. 6a–f, when we increase β there is a change in the nature of the transition. We notice that, when $\beta = 0$, a subcritical Hopf bifurcation happens at a critical $\mathcal{K}_\tau$ value (the $\mathcal{K}_\tau$ value at which a sudden drop in the p'_{rms} happens in

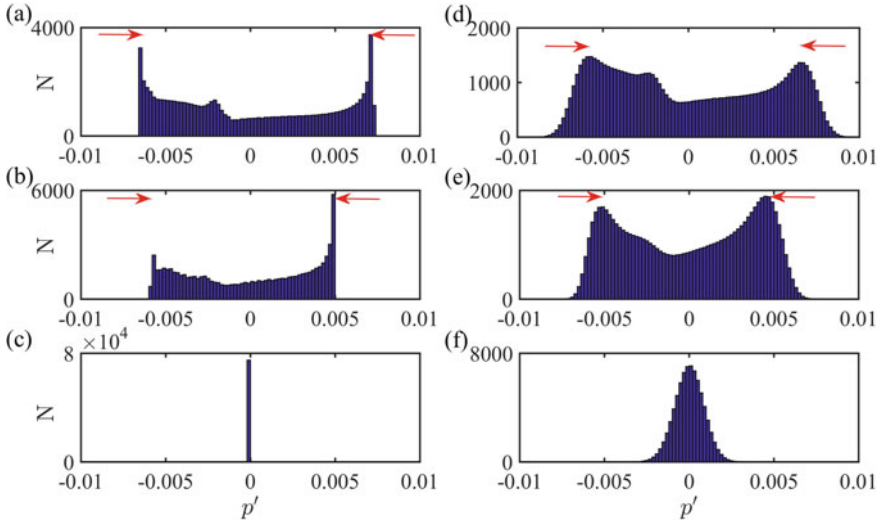

Fig. 5 Histograms plotted for the time series data of acoustic pressure obtained from the thermoacoustic oscillator 'a' for the two cases: in the absence of noise (**a–c**) and in the presence of noise (**d–f**). ψ^2 represents the variance in the pressure time series : **a** $\mathcal{K}_\tau = 0$, $\beta = 0$, $\psi^2 = 2.164 \times 10^{-5}$; **b** $\mathcal{K}_\tau = 0.06$, $\beta = 0$, $\psi^2 = 1.324 \times 10^{-5}$; **c** $\mathcal{K}_\tau = 0.12$, $\beta = 0$, $\psi^2 = 0$; **d** $\mathcal{K}_\tau = 0$, $\beta = 0.012$, $\psi^2 = 2.215 \times 10^{-5}$; **e** $\mathcal{K}_\tau = 0.06$, $\beta = 0.012$, $\psi^2 = 1.437 \times 10^{-5}$; **f** $\mathcal{K}_\tau = 0.12$, $\beta = 0.012$, $\psi^2 = 7.023 \times 10^{-7}$. The transients in the time series are not included in the data used for plotting histograms. We see that the acoustic pressure amplitude distribution changes from bimodal to unimodal with increasing $\mathcal{K}_\tau$ which can be ascribed to the transition from LCO to AD. Reproduced with permission from [51]

Fig. 6a). Figure 6b, where $\beta = 0.0068$, exhibits an almost similar behaviour although the p'_{rms} values do not reach zero after bifurcation. However, as we further increase β, the drop in p'_{rms} becomes smoother, as seen in Fig. 6c–f, which can no longer be called subcritical. Therefore, noise induces a change in the criticality of the Hopf bifurcation in the context of the transition to AD. This is in agreement with the past studies of nonlinear oscillator models in the presence of noise, which theoretically predicted a suppression of the subcritical nature of the transition [48, 52–55]. In contrast to the noise-free case (Fig. 6a), a complete cessation of oscillations as in amplitude death (AD) is impossible in the stochastic case (Fig. 6b–f). Furthermore, from Fig. 6b we can see that, with the addition of low-amplitude external noise, the bifurcation to AD happens at a lower value of $\mathcal{K}_\tau$ than the noise-free case (Fig. 6a). Similar instances where the presence of noise induces an early bifurcation are found in the past literature [53].

Further, to demonstrate the suppression zones achieved by coupling two Rijke tube oscillators, we use two-parameter diagrams. The bifurcation plot in the time-delay coupling constant ($\mathcal{K}_\tau$) and delay time (τ) parameter space is shown in Fig. 7. The points in Fig. 7b, c are the points where the oscillation amplitude in the Rijke tube oscillators becomes 20% of their initial value (in the stochastic case, when the

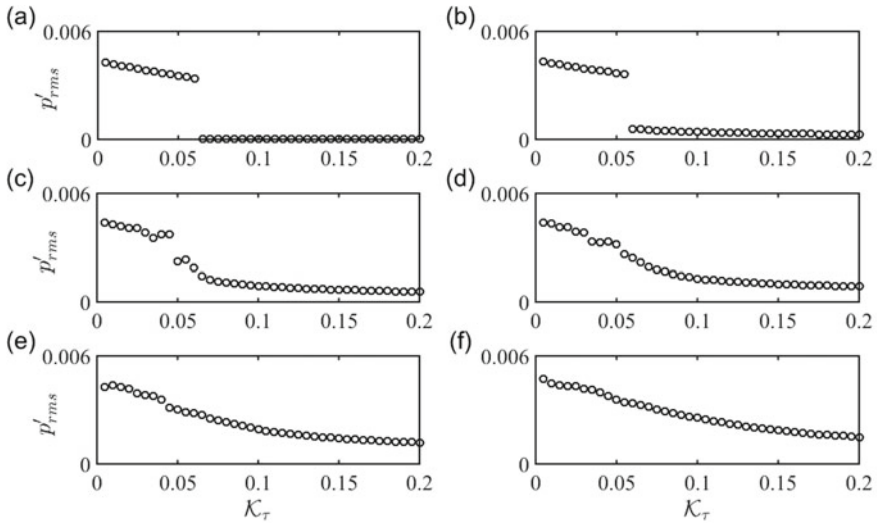

Fig. 6 Bifurcation diagrams depicting the variation of root-mean-square value of the non-dimensionalized acoustic pressure (p'_{rms}) with increase in the time-delay coupling strength ($\mathcal{K}_\tau$) between the two thermoacoustic oscillators for different values of noise intensity, β. **a** $\beta = 0$, **b** $\beta = 0.0068$, **c** $\beta = 1.37 \times 10^{-2}$, **d** $\beta = 0.0204$, **e** $\beta = 0.0273$, **f** $\beta = 0.0341$. For all the figures, $K^a = K^b = 0.72$ and $\tau = 0.5$. We observe a departure from the subcritical nature of the transition from LCO to AD with increase in β. Reproduced with permission from [51]

oscillation amplitude goes below 20% of its initial value, we refer to it as noisy AD and LCO otherwise). We chose 20% as a good enough suppression from the initial oscillatory state, as the p'_{rms} value deviates from the base noise level to higher amplitudes because noise incites a nontrivial response from the thermoacoustic system [56]. This is in contrast to the deterministic case where a complete cessation of oscillations to zero value is observed. We observe a U-shaped plot which is centred around the $\omega\tau$ (here ω value is set at 3.26 for both the Rijke tube oscillators) value of π for the noiseless case (see Fig. 7a). However, achieving such an ideal scenario in real systems is near to impossible. In the range of $\mathcal{K}_\tau$ and τ values considered, we see that the plot breaks into two-independent U-shaped parts centred around $\omega\tau$ value of $\pi/2$ and $3\pi/2$, as we add noise into the system. When we further increase the noise intensity, we observe that the coupling strength needed to achieve the 80

3.2 Effect of Dissipative Coupling

3.2.1 Deterministic Case

Now, we study the effect of dissipative coupling alone (for $\mathcal{K}_\tau = 0$) on the coupled behaviour of the system of two non-identical ($\Delta\omega \neq 0$) Rijke tube oscillators (Fig. 8). We observe that, when $\mathcal{K}_d$ is not high enough ($\mathcal{K}_d = 0.1$) to reach AD state,

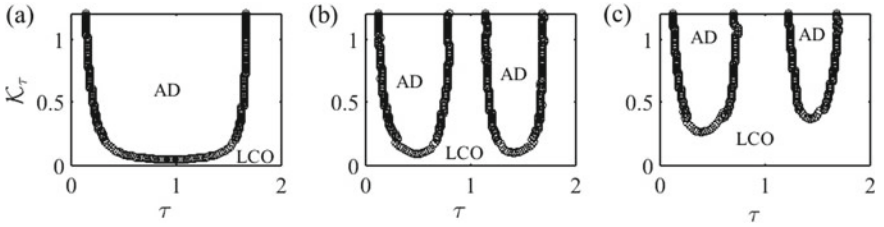

Fig. 7 Two-parameter bifurcation diagram in the parameter plane of time-delay coupling strength ($\mathcal{K}_\tau$) and delay time (τ) for different values of noise intensities: **a** $\beta = 0$, **b** $\beta = 1.37 \times 10^{-2}$ and, **c** $\beta = 0.0273$. The markers in (**a**) correspond to the points in the parameter plane where bifurcation from LCO to AD occurs. In (**b**) and (**c**), the markers correspond to the points where the time-delay coupling between the two thermoacoustic oscillators leads to the suppression of LCO amplitude to 20% of its original value (without coupling, i.e., when $\mathcal{K}_\tau = 0$). For all the plots, $K^a = K^b = 0.8$, and $\omega_b/\omega_a = 1$. LCO marked in the plots refers to the stochastic limit cycle oscillations. We observe that, introduction of noise results in a qualitative change as well as a reduction in the size of amplitude suppression zones. Reproduced with permission from [51]

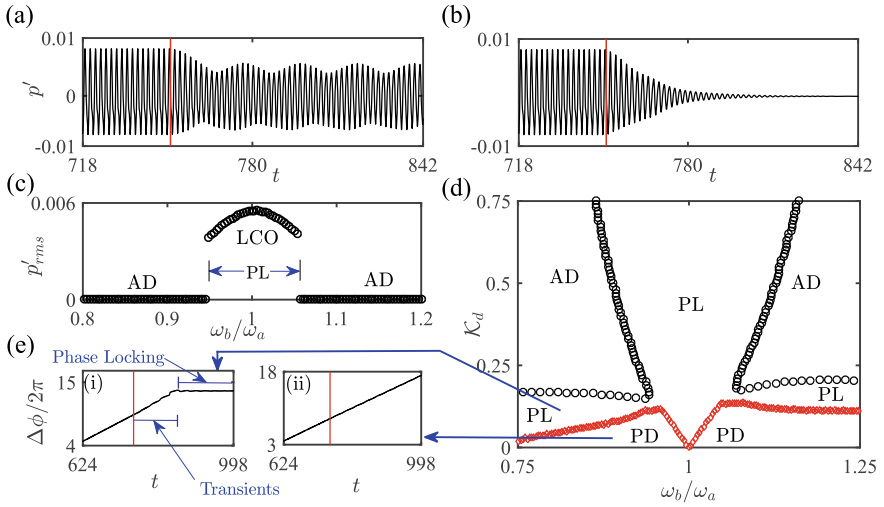

Fig. 8 Temporal variation of non-dimensional acoustic pressure (p'), when the dissipative coupling between the two oscillators is **a** not strong enough ($\mathcal{K}_d = 0.1$, $\Delta\omega = 0.24$) and **b** strong enough ($\mathcal{K}_d = 0.3$, $\Delta\omega = 0.24$) to achieve AD, respectively. **c** One-parameter bifurcation plot showing the variation of p'_{rms} with ω_b/ω_a ($\mathcal{K}_d = 0.18$). **d** Two-parameter bifurcation diagram in the parameter plane of dissipative coupling strength ($\mathcal{K}_d$) and ratio of natural frequencies (ω_b/ω_a), showing regions of AD, phase locking (PL) and phase drifting (PD). Circles (in black) indicate the boundary between AD and PL region, while diamonds (in red) mark the boundary between PL and PD. **e** Phase plots showing the variation of relative phase ($\Delta\phi$) between the two oscillators for (i) PL region, and (ii) PD region. Note that phase locking in (**e**-i) follows a small interval of transients wherein the signals show phase drifting behaviour. The vertical lines (shown in red) in (**a**), (**b**) and (**e**) indicate the instant at which coupling is applied. For all the plots, $\mathcal{K}_\tau = 0$ and $K^a = K^b = 1.02$. Reproduced with permission from [49]

the amplitude of LCO of both the oscillators reduces a bit and oscillates around this reduced value once the coupling is applied (see Fig. 8a). At this state, the oscillations of both oscillators show a beat like behaviour, because of the interaction between the two oscillators with two different but close by frequencies. However, when the $\mathcal{K}_d$ value is high enough ($\mathcal{K}_d = 0.3$) to achieve AD, amplitude of both the oscillators dies down after the application of coupling (Fig. 8b). In Fig. 8c, we plot a one-parameter bifurcation plot that shows the variation of p'_{rms} with ω_b/ω_a for both the Rijke tube oscillators, while the dissipative coupling strength ($\mathcal{K}_d$) between them is kept constant at 0.18. We observe from Fig. 8c that it is impossible to achieve AD through dissipative coupling alone, when the natural frequencies of the two oscillators are very close by. In the current case with the given dissipative coupling strength ($\mathcal{K}_d = 0.18$), oscillations were observed in the range of ω_b/ω_a values from 0.95 to 1.05, and AD on either sides. We obtain a second one-parameter bifurcation plot (shown in supplementary material, Fig. S1b), qualitatively similar to that in Fig. 16c, when ω_b/ω_a is kept constant at 0.93 (or $\Delta\omega = 0.24$) and the value of $\mathcal{K}_d$ is varied.

Further, we illustrate the regions of AD in the parameter plane of $\mathcal{K}_d$ and ω_b/ω_a, when time-delay coupling is absent in the system of two Rijke tube oscillations, i.e., $\mathcal{K}_\tau = 0$ (Fig. 8d). In Fig. 8d, the circular (in black) and diamond (in red) markers correspond to the points where bifurcation from phase locking (PL) to AD, and phase drifting (PD) to PL occur, respectively. Phase drifting is said to occur between two oscillators, when the relative phase between them is unbounded and exhibit an increase with time. On the other hand, phase locking is the scenario where the relative phase between the oscillators is bounded. For those combinations of $\mathcal{K}_d$ and ω_b/ω_a values which are segregated solely by the curve with circular markers, AD will occur, and for other combinations of $\mathcal{K}_d$ and ω_b/ω_a values, AD is not observed. In the region amidst the curves with circular and diamond markers, the relative phase between the two oscillators will become locked after the coupling is applied (Fig. 8d).

The relative phase dynamics with one such combination of $\mathcal{K}_d$ and ω_b/ω_a in the PL region is shown in Fig. 8e(i). However, this phase locking follows a small interval of phase drifting after the application of coupling, owing to the transients [Fig. 8e(i)]. In contrast, phase drifting happens in the region below the curve with diamond markers (Fig. 8d). The relative phase dynamics with a combination of $\mathcal{K}_d$ and ω_b/ω_a in the PD region is shown in Fig. 8e(i).

Therefore, we infer that, as the coupling strength between the two oscillators is increased, the system moves from phase drifting to phase locking (or synchronization) and then to AD. However, when the natural frequencies of the two oscillators are very close by, even very high values of coupling strength are not sufficient to achieve AD, as can be seen from the range of ω_b/ω_a values around 1 (0.93–1.08) in Fig. 8d. This is in accordance with the earlier literature on AD [32, 35], which states that there should be a sufficient difference between the frequencies of the two oscillators for a purely dissipative coupling to bring about AD. However, phase locking easily happens in the region of ω_b/ω_a values around 1 as the frequency values of the two oscillators are already very close. Furthermore, the zone of phase locking in the range of ω_b/ω_a values around 1 becomes wider as we increase the coupling strength, which is similar to the experimental observation reported by Biwa et al. [32].

Further, we note that the bifurcations observed in Fig. 8d are different from the ones plotted in the space of ϕ (analogous to dissipative coupling strength) and Δf (frequency detuning, corresponding to $\Delta\omega$ in the present study) by Biwa et al. [32] In their study, the transitions are (i) from phase drifting (PD) to phase locking (PL) through AD when Δf is sufficiently large, and (ii) a direct transition from PD to PL when Δf is small. In contrast, we observe the transitions (i) from phase drifting (PD) to amplitude death (AD) through phase locking (PL) when the value of ω_b/ω_a is away from 1, and (ii) direct transition from PD to PL when the value of ω_b/ω_a is close to 1. We believe that this dissimilarity in the first transition could be due to the difference in the underlying mechanisms which lead to the onset of self-sustained oscillations in the two systems.

3.2.2 Stochastic Case

We now examine how noise affects the one-parameter bifurcation plot of a dissipatively coupled thermoacoustic system. We know that dissipative will not be able to bring about AD in a system of two identical ($\omega_b/\omega_a = 1$) oscillators [35]. So, we consider two thermoacoustic oscillators which possess non-identical natural frequencies ($\omega_b/\omega_a \neq 1$) in this case. Figure 9 depicts the variation of p'_{rms} with the ratio of natural frequencies of both the thermoacoustic oscillators. The deterministic case (Fig. 9a) points to the fact that, AD is not possible with dissipative coupling alone if the detuning between the two thermoacoustic oscillators is not sufficient. We observe that p'_{rms} drops to zero on either side of $\omega_b/\omega_a = 1$, when the bifurcation to AD happens. We can observe a change in the nature of the transition as the noise intensity increases from Fig. 9a–f, similar to the cases in Fig. 6. The abrupt drop in the p'_{rms} value at a critical ω_b/ω_a value is not observed anymore with increasing β. We also see that a total stoppage of oscillations as in amplitude death (AD) is impossible in the presence of noise (Fig. 9b–f). However, when there is sufficient detuning between the two thermoacoustic oscillators, a significant amount of suppression is attainable with dissipative coupling.

We continue by studying the effect of noise on the two-parameter bifurcation plot when only dissipative coupling is applied. Figure 10 is bifurcation diagram produced in the two-parameter space of dissipative coupling strength ($\mathcal{K}_d$) and the ratio of natural frequencies (ω_b/ω_a). The points in Fig. 10 carry the same meanings as in Fig. 7. We observe that, a considerable reduction in the oscillation amplitudes in two dissimilar ($\omega_b/\omega_a \neq 1$) noisy ($\beta \neq 0$) thermoacoustic oscillators can be attained by applying appropriately strong dissipative coupling. The bifurcation diagrams in the two-parameter space in the noisy case (Fig. 10b, c) are qualitatively similar to the noise-free case (Fig. 10a) as can be seen from the figure. As in the previous case, the size of suppression zones was reduced as a result of increase in the noise intensity. Also, we note that as the β value is increased from 1.07×10^{-2} in Fig. 10b to 2.13×10^{-2} in Fig. 10c, the plot shifts up and the gap around $\omega_b/\omega_a = 1$ widens. Therefore, we can conclude that, a higher coupling strength and higher detuning is needed to achieve the same amount of suppression with increased β, i. e., noise levels.

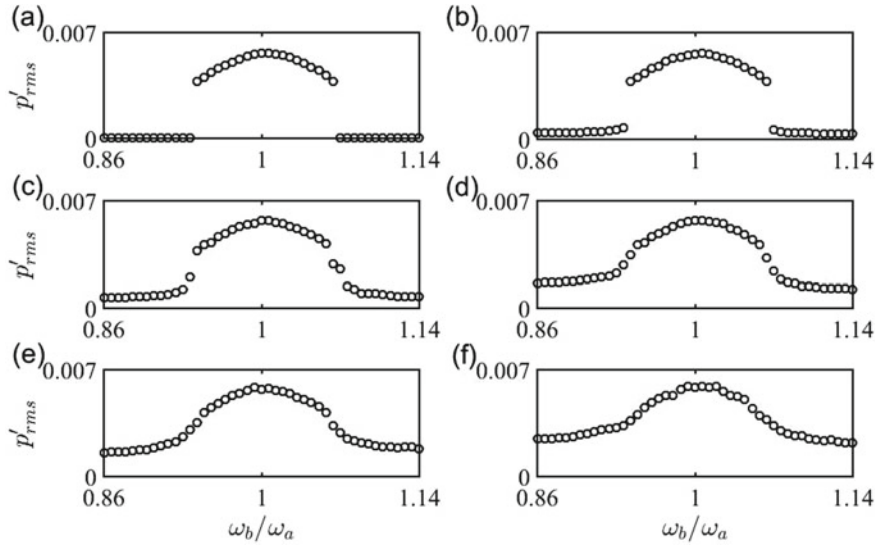

Fig. 9 One-parameter bifurcation diagrams depicting the variation of p'_{rms} with ω_b/ω_a for different values of noise intensity: **a** $\beta = 0$, **b** $\beta = 5.3 \times 10^{-3}$, **c** $\beta = 1.07 \times 10^{-2}$, **d** $\beta = 1.59 \times 10^{-2}$, **e** $\beta = 2.13 \times 10^{-2}$, **f** $\beta = 2.66 \times 10^{-2}$. For all the figures, $K^a = K^b = 1.02$ and $\mathcal{K}_d = 0.16$. We observe that similar to Fig. 6, the transition from LCO to AD becomes smoother and loses its subcritical nature with increasing β. Reproduced with permission from [51]

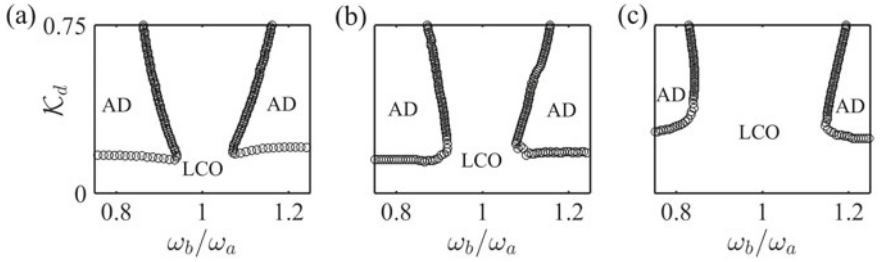

Fig. 10 Two-parameter bifurcation diagram in the parameter plane of dissipative coupling strength ($\mathcal{K}_d$) and ratio of natural frequencies (ω_b/ω_a) of the two coupled thermoacoustic oscillators for different values of noise intensities: **a** $\beta = 0$, **b** $\beta = 1.07 \times 10^{-2}$ and, **c** $\beta = 2.13 \times 10^{-2}$. We observe that with an increase in β, the amplitude suppression zones become smaller in the region considered. Reproduced with permission from [51]

3.3 *Effect of Simultaneous Application of Time-Delay and Dissipative Coupling*

3.3.1 Deterministic Case

We now consider the effect of applying both time-delay and dissipative couplings together on the regions of AD in the two-parameter bifurcation plots. Here, the non-dimensional heater power for both the Rijke tube oscillators ($K^a = K^b = K$) is kept constant. The bifurcation diagrams in the parameter plane constituted by $\mathcal{K}_\tau$ and τ shown in Fig. 11a represent the case where dissipative coupling is applied to a system which is already coupled through time-delay. The bifurcation plot corresponding to the case when the system of two identical oscillators was subjected to time-delay coupling alone is shown in Fig. 11a(i) for comparison, while in Fig. 11a(ii)–(iv), the oscillators are non-identical. We see that the introduction of detuning ($\Delta\omega = 0.24$) between the oscillators results in the splitting of the AD region into 3 unequal regions, even when $\mathcal{K}_d = 0$, as shown in Fig. 11a(ii). This change in regions of

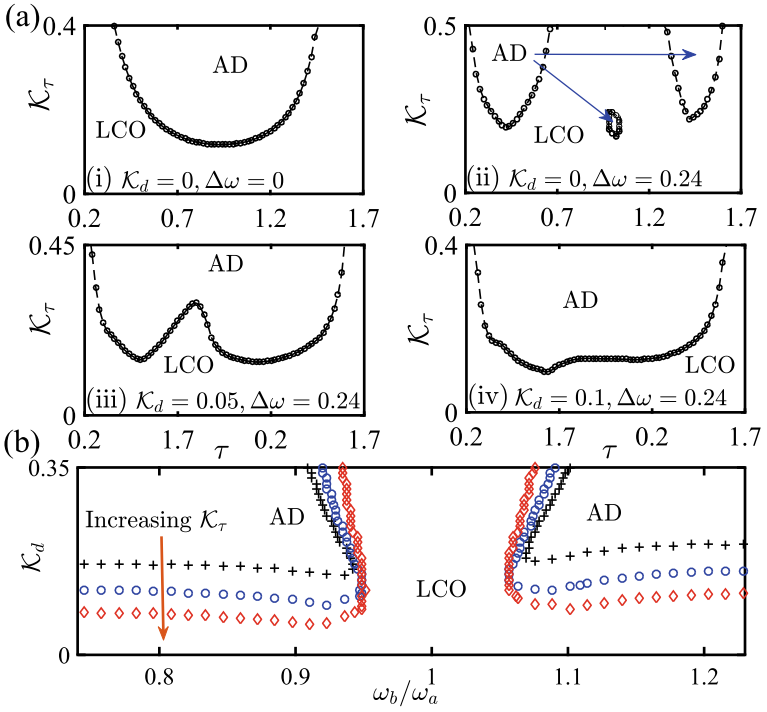

Fig. 11 Two-parameter bifurcation diagram in the parameter plane of: **a** $\mathcal{K}_\tau$ and τ, when (i) $\mathcal{K}_d = 0$, $\Delta\omega = 0$ (ii) $\mathcal{K}_d = 0$, $\Delta\omega = 0.24$ (iii) $\mathcal{K}_d = 0.05$, $\Delta\omega = 0.24$, and (iv) $\mathcal{K}_d = 0.1$, $\Delta\omega = 0.24$. **b** $\mathcal{K}_d$ and ω_b/ω_a for three different $\mathcal{K}_\tau$ values keeping the value of τ constant at 0.5: Plus—$\mathcal{K}_\tau = 0$; Circle—$\mathcal{K}_\tau = 0.04$; Diamond—$\mathcal{K}_\tau = 0.08$. Reproduced with permission from [49]

AD can have practical implications. In practice, for a set of seemingly identical oscillators, we expect them to give rise to AD for a certain set of parameter values, as indicated in Fig. 11a(i). However, we may not achieve AD in such cases with the given set of parameter values, because of the inherent detuning ($\Delta\omega \neq 0$) between the oscillators [Fig. 11a(ii)]. At this detuning ($\Delta\omega = 0.24$) when dissipative coupling is introduced ($\mathcal{K}_d = 0.05$), we notice the merging of these separated AD zones into a single W-shaped region as seen in Fig. 11a(iii). Finally, with further increase in $\mathcal{K}_d$, the central W-shaped region becomes more flattened, resulting in the appearance of a single unsymmetric U-shaped region in the two-parameter plane, as can be seen from Fig. 11a(iv).

We further show the effect of applying time-delay coupling to a system which is already coupled through dissipative coupling in Fig. 11b. The regions of AD in the two-parameter bifurcation plot in the parameter plane of $\mathcal{K}_d$ and ω_b/ω_a are affected as a consequence of adding time-delay coupling. The circular markers correspond to the case where dissipative coupling alone is applied to the system. As the time-delay coupling strength applied on the oscillators is increased, the graphs shift downward and the region near the ω_b/ω_a value of 1, where AD is unattainable, narrows down. The values of $\tau = 0.5$ and $\mathcal{K}_\tau = 0.04, 0.08$ are chosen such that the system does not exhibit AD with time-delay coupling alone. We can conclude that the $\mathcal{K}_d$ value needed for the bifurcation of LCO to AD is smaller in the presence of a small value of time-delay coupling, which alone is not sufficient to bring about AD, than in the case where dissipative coupling alone is applied. These trends from Fig. 11b make it evident that simultaneous application of both the couplings makes it easier to achieve AD. Please note that we focus on the occurrence of AD from Fig. 11 onward. Therefore, unlike Fig. 12, we do not distinguish PL and PD so as not to clutter the plots.

3.3.2 Stochastic Case

We also looked into the case where both the couplings (time-delay and dissipative) are applied simultaneously on the thermoacoustic system in the presence of noise (Fig. 12). Since dissipative coupling has its effect only on non-identical ($\omega_b/\omega_a \neq 1$) oscillators, we first introduced a detuning ($\omega_b/\omega_a = 0.923$) between the two Rijke tube oscillators.

From Fig. 12b, we note that the introduction of a detuning by itself caused a very significant reduction in the time-delay coupling strength ($\mathcal{K}_\tau$) needed to achieve the 80% suppression in the thermoacoustic oscillations. This is in contrast with the deterministic case [49], where the change in the suppression zones introduced by detuning alone in a time-delay coupled thermoacoustic system was not so drastic. In the deterministic case, applying a detuning resulted in the initial bifurcation plot (Fig. 5b in Thomas et. al. [49]) breaking into two U-shaped plots in the regions considered, while there was no significant decrease in the ($\mathcal{K}_\tau$) values required to achieve AD. Further, in the stochastic case that we discuss here, addition of a weak dissipative coupling ($\mathcal{K}_d = 0.05$) between the two non-identical thermoacoustic oscillators, further increases the ease of achieving suppression.

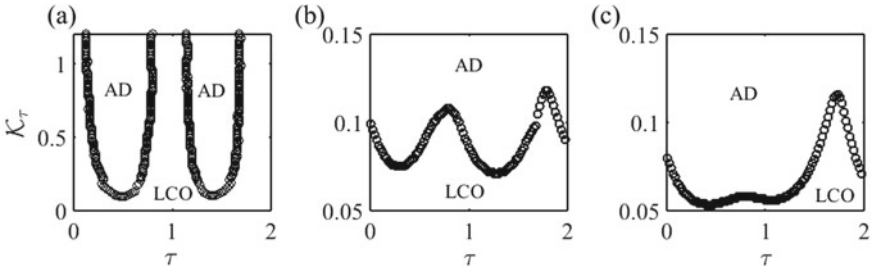

Fig. 12 Two-parameter bifurcation diagram in the parameter plane of time-delay coupling strength ($\mathcal{K}_\tau$) and delay time (τ), when **a** $\omega_b/\omega_a = 1$, $\mathcal{K}_d = 0$; **b** $\omega_b/\omega_a = 0.923$, $\mathcal{K}_d = 0$; **c** $\omega_b/\omega_a = 0.923$, $\mathcal{K}_d = 0.05$. For all the three cases, β=1.37 $\times$ 10^{-2}. Note that the ordinates are not the same for all the plots. We notice that introduction of a detuning and further application of a dissipative coupling can significantly increase the ease of achieving suppression. Reproduced with permission from [51]

3.4 *Effect of Asymmetrical Coupling on AD Phenomenon*

Further, we try to understand the effect of asymmetrical coupling on the coupled dynamics of the two Rijke tube oscillators. A system of two oscillators is said to be asymmetrically coupled when the coupling strength as perceived by the two oscillators is different, which may be the case in many practical systems. We use symmetry parameters n ($0 \leq n \leq 1$) and m ($0 \leq m \leq 1$) to bring in asymmetry to the coupled Rijke tube oscillator model as shown below:

$$\mathcal{K}_d^a = n\mathcal{K}_d; \qquad \mathcal{K}_d^b = (1-n)\mathcal{K}_d, \tag{19}$$

$$\mathcal{K}_\tau^a = m\mathcal{K}_\tau; \qquad \mathcal{K}_\tau^b = (1-m)\mathcal{K}_\tau. \tag{20}$$

Two-parameter bifurcation diagram in which $\mathcal{K}_\tau$ required to attain AD is plotted against m, in the range of m values from 0 to 0.5 is shown in Fig. 13a.

We observe that, the $\mathcal{K}_\tau$ value needed to attain AD increases with an increase in the asymmetry in the coupling. This increase is very marginal when asymmetry is less (in the range of m values from 0.5 to 0.25), but becomes very sharp as m approaches zero. When the variation of $\mathcal{K}_\tau$ with m is plotted in the log-log scale, we obtained a straight line, which indicates that there exists a power law relation between the smallest $\mathcal{K}_\tau$ value required to achieve AD and the asymmetry parameter (m). This implies that the oscillatory behaviour of the system is not affected gradually, but in an exponential manner when the asymmetry in the time-delay coupling is varied. Further studies need to be done to understand the physics behind this power law relation. Figure 13a will be symmetrical about $m = 0.5$, as increasing the m value beyond 0.5 is equivalent to interchanging the two identical oscillators. In other words, the degree of asymmetry for the identical oscillators essentially increases in the same manner, as we move away from 0.5 in either directions. The combinations of $\mathcal{K}_\tau$ and m values for an asymmetrically coupled system which can lead to AD are those

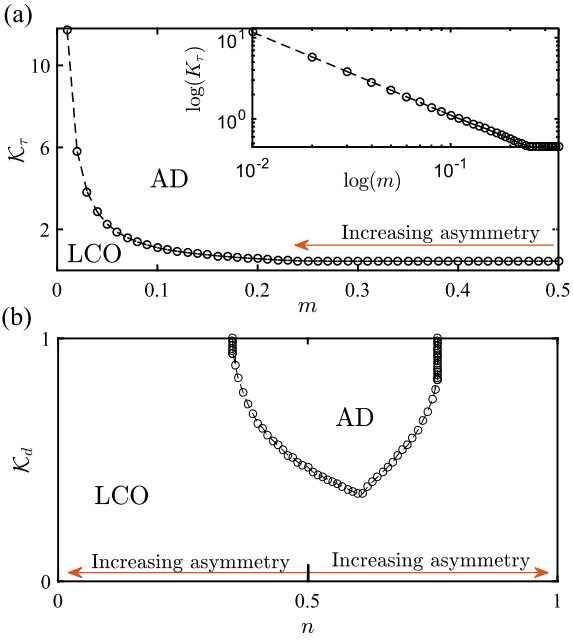

Fig. 13 Two-parameter bifurcation diagram in the parameter plane of: **a** $\mathcal{K}_\tau$ and m, where the upper right inset shows the fit in the log-log plot, which turns out to be a straight line—indicating a power law relation. The parameters that are held fixed are $\tau = 0.5$, $\Delta\omega = 0$ and $\mathcal{K}_d = 0$. **b** $\mathcal{K}_d$ and n, where $\mathcal{K}_\tau$ value is fixed at 0 and $\Delta\omega = 0.55$. Reproduced with permission from [49]

which lie above the curve. We see that, there is only negligible increase in the $\mathcal{K}_\tau$ values required to attain AD around m = 0.5–0.2 (Fig. 13a). Therefore, the model for symmetrical coupling is sufficient to predict the time-delay coupling strength required to attain AD even in practical coupled oscillators, where slight asymmetry is bound to occur.

We also analyse the effect of asymmetry in dissipative coupling alone on the system of two coupled Rijke tube oscillators. Figure 13b represents the two-parameter bifurcation diagram in parameter plane of $\mathcal{K}_d$ and n. However, we notice that, asymmetry in dissipative coupling does not seem to exhibit a power law behaviour as in the case of time-delay coupling (Fig. 13a). Further, AD is attained only in the range of n values around 0.35–0.76 (for, $\Delta\omega = 0.55$). Also, it is important to note that this plot is not symmetrical about $n = 0.5$, as the two coupled oscillators are non-identical. Since there are two different frequencies associated with the two oscillators, increasing the m value beyond 0.5 is not equivalent to interchanging the oscillators. Now, we turn our attention to achieving amplitude death in experiments with a system of coupled Rijke tubes.

4 Experimental Set-Up and Data Analysis

The experimental set-up (Fig. 14a) used to study the amplitude quenching behaviour of limit cycle oscillations consists of a pair of horizontal Rijke tubes (named as A and B). In these systems, an electrically heated wire mesh acts as the heating source [41].

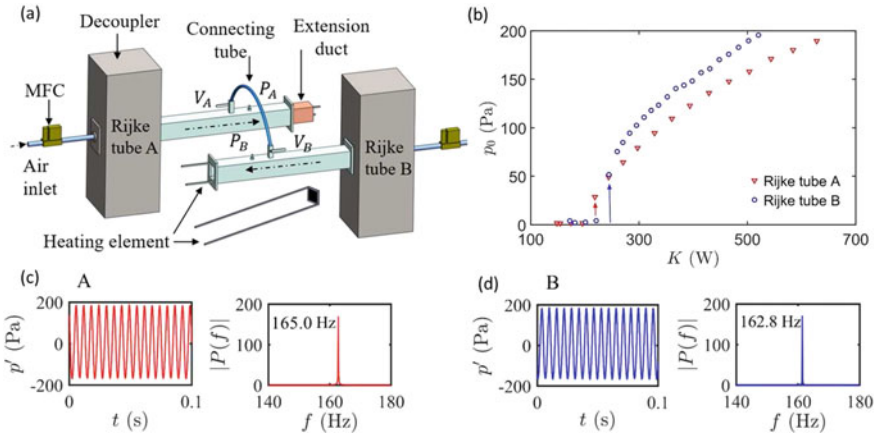

Fig. 14 **a** Schematic of the experimental set-up having two horizontal Rijke tube oscillators A and B, which are coupled using a connecting tube. **b** Variation of root-mean-square amplitude, p_0, with heater power (K) for the isolated Rijke tube oscillators A (red triangles) and B (blue circles). **c**, **d** The time series of limit cycle oscillations and the corresponding amplitude spectrum of Rijke tube oscillators A and B, respectively, prior to coupling. The uncoupled natural frequency of oscillator A is $f_{0A} = 165.0 \pm 1.1$ Hz and oscillator B is $f_{0B} = 162.8 \pm 1.1$ Hz. Reproduced with permission from [57]

The detailed characteristics of a single horizontal Rijke tube system can be obtained from refs. [41, 58]. Here, Rijke tube A (Fig. 14a) has a cross section of $9.3 \times 9.4\,\text{cm}^2$ and is 102.0 cm long, while Rijke tube B has a cross section of $9.3 \times 9.5\,\text{cm}^2$ and a length of 104.0 cm. Separate decouplers of dimensions $120.0 \times 45.0 \times 45.0\,\text{cm}^3$ are attached to the inlet of both the Rijke tubes to ensure that the flow entering the systems is immune from the upstream disturbances. The dimensions of the decoupler being much bigger than the cross section of the duct, the pressure is maintained at ambient conditions (acoustic pressure fluctuations, $p' = 0$ Pa) at both ends. Separate heating elements are located at a distance of 27.5 cm from the decoupler in each system. A mean air flow rate of 40 SLPM is supplied to each system through separate mass flow controllers (Alicat Scientific, with an uncertainty of ± 0.52 SLPM). The decay rates of each system are experimentally measured in the absence of flow by subjecting the systems to external sinusoidal perturbations using a loudspeaker (Ahuja AU60). The acoustic decay rate values for Rijke tube A and Rijke tube B are measured to be $14.5 \pm 0.5\,\text{s}^{-1}$ and $12.7 \pm 0.6\,\text{s}^{-1}$, respectively. We maintain the acoustic decay rate within bounds to ensure consistency in the experimental conditions and the repeatability of the experimental results.

The characterization of the individual Rijke tube oscillators is performed by analysing their amplitude and frequency response with a change in the heater power (K). Figure 1b shows the variation of root-mean-square value, henceforth referred to as amplitude, of acoustic pressure oscillations (p_0) of the uncoupled oscillators A and B with the heater power (K). We observe that both the systems exhibit Hopf

bifurcation, i.e., the transition from a steady state to stable limit cycle oscillations (shown in Fig. 14c, d), at different critical values of K, owing to the difference in decay rates of each oscillator. We also observe a small difference in the frequency of oscillator A (165.0 Hz) and B (162.8 Hz) due to the difference in their lengths. In order to study the dynamics of identical oscillators, the amplitude and frequency of oscillator A are adjusted by varying the heater power and the length of the oscillator, respectively, such that the resultant uncoupled amplitude and frequency values of oscillator A are equal to that of oscillator B.

The position of a square extension duct of side 9.0 and length 12.0 cm is manually changed to vary the natural frequency of Rijke tube A initially from 165.0 to 162.8 Hz to make both Rijke tubes oscillators identical. Although identical conditions cannot be attained in practice and the oscillators are only nearly identical, the uncertainty being small, we refer to these oscillators having nearly equal amplitude and frequency as identical in the subsequent sections. The limit cycle dynamics of these systems are coupled by connecting them using a vinyl tube, whose length and diameter are varied as control parameters (see Fig. 14a). The length (L') of the connecting tube is varied from 72.0 to 132.0 cm in steps of 5.0 cm, while the diameter (D) is varied from 0.4 to 1.2 cm in steps of 0.2 cm. Here, the length of the connecting tube (L') is normalized with the wavelength ($L = L'/\lambda$, where $\lambda = c/f_{0B}$ and c is the speed of sound at ambient conditions) of acoustic standing wave developed in oscillator B (the oscillator whose length remains constant throughout the study). The coupling ports for the vinyl tube, indicated as V_A and V_B, are located at a distance of 46.5 cm from the outlet of both the Rijke tubes and are equipped with ball-type valves which are manually opened to initiate the coupling between the systems.

Simultaneous measurements of acoustic pressure fluctuations are performed prior to and after the initiation of coupling using pressure transducers (PCB 103B02, with an uncertainty of ± 0.2 Pa) located at positions P_A and P_B, at a distance of 31.5 cm from the outlet of the tubes, as shown in Fig. 14a. The data are acquired from each oscillator at a sampling rate of 10 kHz for a duration of 25 s for each set of experiments using a DAQ system (NI USB 6343). All experiments conducted to study the synchronization and the suppression of oscillation after coupling are carried out at values sufficiently away from the Hopf point of both the oscillators.

Further analysis on the coupled dynamics of these oscillators is performed after an introduction of frequency and amplitude mismatch in the system. The amplitude mismatch (Δp_0) and frequency detuning (Δf) in the system are defined as $\Delta p_0 = |p_{0A} - p_{0B}|$ and $\Delta f = |f_{0A} - f_{0B}|$, where $\{p_{0A}, f_{0A}\}$ and $\{p_{0B}, f_{0B}\}$ are the amplitudes and frequency of oscillator A and B, respectively, in their uncoupled state. Since the frequency of acoustic oscillations in the duct is directly dependent on its length, the frequencies of oscillator A are varied from 147.8 to 162.8 Hz by varying its effective length using an extension duct. This frequency variation in oscillator A corresponds to 0 to 15 Hz of frequency detuning in the system. The frequency of limit cycle oscillations in oscillator B (f_{0B}) is maintained constant throughout the study. The normalized frequency detuning ($\Delta f/f_{0B}$) corresponding to this frequency change in

oscillator A with respect to oscillator B is nearly 0 to 0.092. Similarly, the amplitude mismatch between the acoustic oscillations in both the oscillators is introduced by varying the heater power (K) of oscillator A with respect to that of oscillator B.

5 Experimental Results and Discussions

5.1 *Effect of Variation in Coupling Parameters on Identical Oscillators*

The primary methodology adopted to quench thermoacoustic oscillations in identical Rijke tube systems is to vary the length (L) of the connecting tube having a diameter of 1.0 cm. Towards this purpose, the amplitude and frequency in the uncoupled state of the Rijke tube oscillators A and B are maintained at nearly equal values, and the acoustic response of the systems is measured for each length (L) of the connecting tube. The synchronization analysis of the acoustic pressure data is performed by extracting the instantaneous phases of both the oscillators using the Hilbert transform [2], which helps in extending the signal from the real plane to a complex plane. Hence, we obtain the analytic signal, $\zeta(t) = p(t) + p_H(t)$, where $p(t)$ is the acquired pressure signal and $p_H(t)$ is its corresponding Hilbert transformed signal given by,

$$p_H(t) = \frac{1}{\pi} P.V. \int_{-\infty}^{\infty} \frac{p(\tau)}{t-\tau} \mathrm{d}\tau, \tag{21}$$

where $P.V.$ is the Cauchy Principal value. The instantaneous phases of each signal, $\Phi(t)$, is obtained from the analytic signal as $\zeta(t) = A(t)\exp(i\Phi(t))$. The relative phase between the signals of oscillators A and B is obtained from the difference of their instantaneous phases ($\Phi_A(t)$ and $\Phi_B(t)$, respectively) as $\Delta\Phi(t) = \Phi_A(t) - \Phi_B(t)$. When the coupled oscillators are synchronized, the temporal variation of relative phase between them fluctuates around a constant value. This constant value of relative phase is computed in terms of mean phase difference between the two signals ($\overline{|\Delta\Phi|}$) as follows:

$$\overline{|\Delta\Phi|} = \frac{1}{N} \sum_{t=1}^{N} |\Delta\Phi(t)|, \tag{22}$$

where N is the total number of samples in the signal and $\Delta\Phi(t)$ is the instantaneous phase difference (wrapped in the interval of 0° and 180°) between two oscillators.

Figure 15a shows the two-parameter bifurcation plot between the uncoupled amplitude (p_0) of the oscillators and the length (L) of the connecting tube used for coupling the identical oscillators. We observe that for lower values of p_0, the coupled

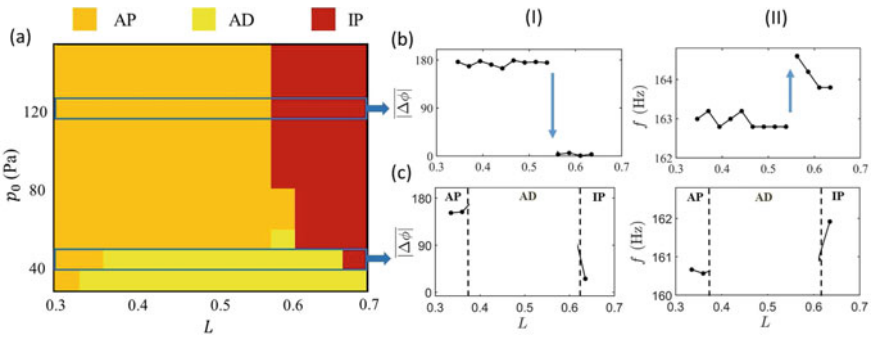

Fig. 15 **a** Two-parameter bifurcation plot between the uncoupled amplitude of pressure oscillation (p_0) and the length (L) of the connecting tube, displaying the coexistence of amplitude death and phase-flip bifurcation in a system of identical oscillators. Depending on the value of the uncoupled amplitude of the oscillators, the coupled dynamics of the system exhibits either; **b** phase-flip bifurcation for higher values, or **c** transition from anti-phase (AP) to in-phase synchronization (IP) via amplitude death (AD) for lower values. Reproduced with permission from [57]

dynamics exhibited by the system transition from a state of anti-phase synchronization to in-phase synchronization via an intermediate state of amplitude death (AD) as L is increased (as shown in Fig. 15c). The state of anti-phase synchronization is characterized by a phase shift of nearly 180° between the oscillators, whereas, during the state of in-phase synchronization, both oscillators exhibit nearly 0° of phase shift. The dominant frequency of the oscillators is observed to be lower during anti-phase synchronization and higher during in-phase synchronization, as compared to their uncoupled value. In the intermediate state between anti-phase and in-phase synchronization, we observe complete quenching of oscillations in both the oscillators due to coupling, and thus, the system behaviour converges to a homogeneous steady state. Such a state of coupled dynamics is termed as amplitude death [59]. The instantaneous phase calculated using the Hilbert transform is undefined due to the lack of oscillations during this state and hence is not discussed in Fig. 15c.

When the amplitude of acoustic pressure oscillations in the uncoupled state of the oscillators is sufficiently high, we observe an abrupt transition from anti-phase synchronization to in-phase synchronization, as the length of the connecting tube is increased (see Fig. 15b). During this transition, the mean value of the phase difference between the oscillators abruptly changes from nearly 180° to 0° [Fig. 15b(I)], which is accompanied by a corresponding jump in their dominant frequency [(Fig. 15b(II)]. Such a sudden switching of phase difference between the oscillators at a critical value of the coupling parameter is commonly referred to as phase-flip bifurcation, PFB [60]. The direction of jump in the frequencies of oscillators during the PFB observed in our system is opposite to what is usually reported in the literature [60, 61], where such a synchronization transition is associated with a decrease in the frequency of oscillators. From Fig. 15b, we observe that the critical value of L at which the PFB happens is around 0.53. Previous theoretical studies by [49, 51] on similar Rijke tube

oscillators have reported the existence of AD in identical oscillators. They showed that, when the oscillators are only time-delay coupled, the increase in amplitude of limit cycle oscillations reduces the region for which AD is observed in the parameter space of coupling constants (i.e. delay and coupling strength) in the system. However, their study did not report the existence of PFB in the model of coupled Rijke tube oscillators. We, here, report the first experimental evidence of phase-flip bifurcation in coupled thermoacoustic systems. We also conclude that a connecting tube of appropriate length (in the range shown in the Fig. 15a) is sufficient to quench the undesired thermoacoustic oscillations with low amplitude and is insufficient to do so for the high-amplitude oscillations in coupled Rijke tube oscillators.

Now, let us take a closer look at the suppression behaviour of acoustic oscillations in coupled identical Rijke tubes when the amplitude of their oscillations in the uncoupled state is low ($p_0 = 40\,\text{Pa}$) and high ($p_0 = 120\,\text{Pa}$). We study this behaviour of oscillators when the dimensions (L and D) of the connecting tube are varied. Here, the suppression in the amplitude is quantified as $\Delta p = p_0 - p$, where p_0 and p are the amplitudes of acoustic pressure oscillations before and after the initiation of coupling, respectively. The suppression is normalized with the uncoupled amplitude (p_0) such that $\Delta p/p_0 = 1$ corresponds to complete suppression (or amplitude death) and $\Delta p/p_0 = 0$ points towards the lack of suppression in the amplitudes of Rijke tube oscillators.

When the amplitude of pressure oscillations is low ($p_0 = 40\,\text{Pa}$), we observe that the relative suppression of coupled oscillations varies significantly with the diameter of the connecting tube (Fig. 16a). For smaller diameters of the connecting tube ($D = 0.4$ and $0.6\,\text{cm}$), we observe the presence of weak coupling between the oscillators A and B when $L < 0.48$, which, in turn, is projected as the lack of suppression in the oscillations in Fig. 16a. In contrast, we observe a complete suppression in oscillations for $L \geq 0.48$ until the system dynamics transition to in-phase synchronization at $L = 0.58$. Such an interaction among the oscillators leading to changes in the amplitude of coupled oscillations for $L \geq 0.48$ suggests the existence of stronger coupling between them. When the diameter of the connecting tube is larger, $D \geq 0.8\,\text{cm}$, we observe an increase in the suppression of acoustic pressure oscillations in coupled Rijke tubes, in the entire range of L considered in our study. Furthermore, the system dynamics exhibits the state of amplitude death ($\Delta p/p_0 \to 1$) for L ranging from 0.39 to 0.58, irrespective of the value of D used for the connecting tube. These observations further suggests that, the occurrence of AD is possible only for certain combinations of dimensions (L and D) of the connecting tube when low-amplitude identical Rijke tube oscillators are coupled.

For the case shown in Fig. 16b with $p_0 = 120\,\text{Pa}$, we see that the variation in the relative suppression ($\Delta p/p_0$) of acoustic pressure oscillations with the length of the connecting tube remains nearly the same, irrespective of the diameter of the connecting tube used. Hence, we can conclude that any combination of length and diameter of the connecting tube considered in the current study proves ineffective in suppressing high-amplitude pressure oscillations of identical Rijke tube oscillators.

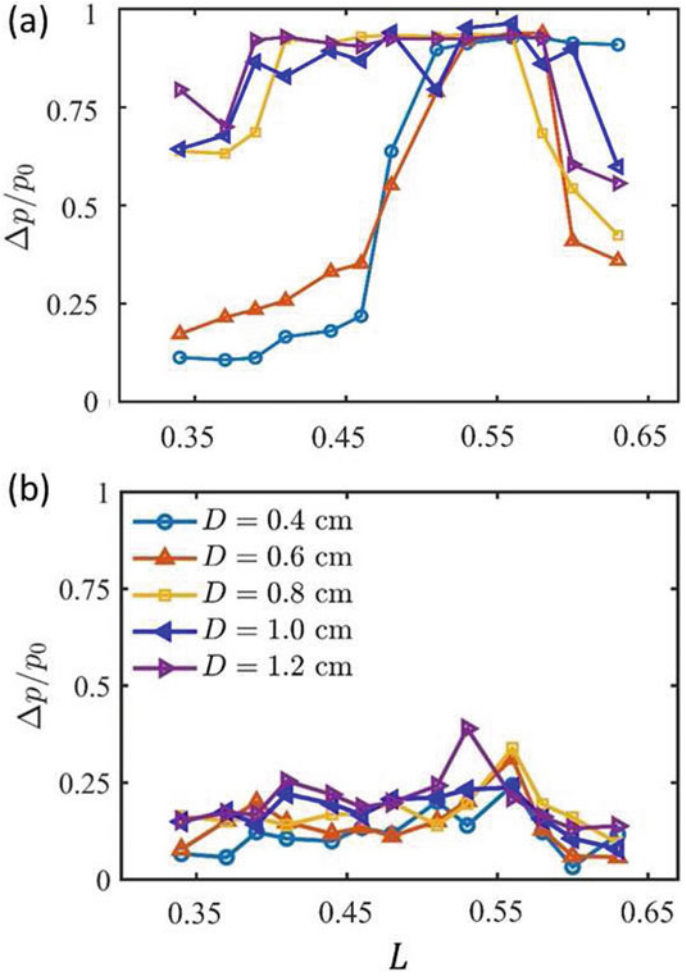

Fig. 16 Variation of relative suppression in the amplitude of acoustic pressure oscillations ($\Delta p/p_0$) in oscillator A is plotted with respect to the length of the connecting tube (L); for various values of diameter (D). The amplitude of uncoupled oscillations, p_0, is 40 Pa in (**a**) and 120 Pa in (**b**). A similar trend can be observed in the case of oscillator B. Reproduced with permission from [57]

5.2 *Effect of Frequency Detuning on the Amplitude Suppression Behaviour of Coupled Oscillators*

Having discussed the insufficiency of variation in the dimensions (i.e. length and diameter) of the connecting tube in complete suppression of high-amplitude acoustic pressure oscillations ($p_0 > 60$ Pa), we introduce frequency detuning in the system to suppress them. The amplitudes of limit cycle oscillations in the uncoupled state,

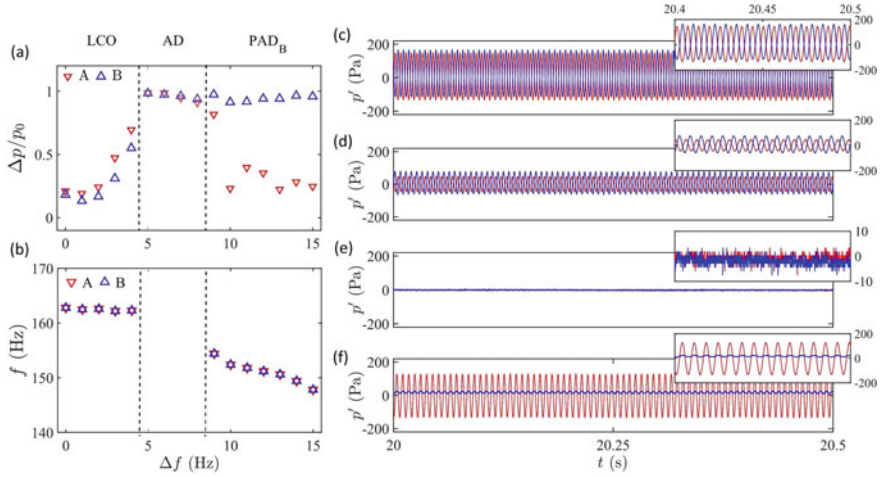

Fig. 17 Variation of **a** relative suppression in the response amplitudes and **b** dominant frequencies of oscillators A and B after coupling for different values of frequency detuning, Δf, when $L = 0.48$, $D = 1.0$ cm and $p_0 = 120$ Pa. The time series corresponding to various states of coupled dynamics observed for frequency detuning of **c** 0 Hz—no suppression, **d** 4.0 Hz—significant suppression, **e** 7.0 Hz—amplitude death, and **f** 15.0 Hz—partial amplitude death. Reproduced with permission from [57]

p_0, of both the oscillators are kept nearly constant at 120 Pa. The dimensions of the connecting tube ($L = 0.48$ and $D = 1.0$ cm) are fixed such that they correspond to maximum suppression of limit cycle oscillations after coupling (as observed in Fig. 16a, b). The introduction of frequency detuning in coupled Rijke tubes engendered an increase in the suppression of pressure oscillations in both the systems (Fig. 17a). For low values of detuning (say 0–5.0 Hz), we observe that the suppression in the amplitude of coupled oscillations increases monotonically with detuning. We observe nearly 10% reduction in the amplitude of limit cycle oscillations in both the Rijke tubes for $\Delta f = 0$ Hz (Fig. 17c), which increases to nearly 60% for $\Delta f = 4.0$ Hz (Fig. 17d). In addition to the reduction in amplitude, we also note that coupling these detuned oscillators causes mutual synchronization between them, leading both the oscillators to stabilize at identical frequencies (as shown in Fig. 17b). With further increase in the value of frequency detuning, $4.0\,\text{Hz} < \Delta f < 9.0\,\text{Hz}$, we observe complete quenching of pressure oscillations (i.e. $\Delta p/p_0 \approx 1$) in both the systems, which is also referred to as the state of amplitude death. Figure 17e represents such a case of amplitude death, with simultaneous quenching of oscillations in both the oscillators, leading to the absence of periodic behaviour in their dynamics, for $\Delta f = 7.0$ Hz.

When the frequency detuning in the system is sufficiently large, $\Delta f > 9.0$ Hz, we observe that one among the oscillators regains its periodic oscillations while the other oscillator remains in a nearly quenched state. Such a phenomenon of oscillation quenching, where limit cycle oscillations of one oscillator coexists with a nearly

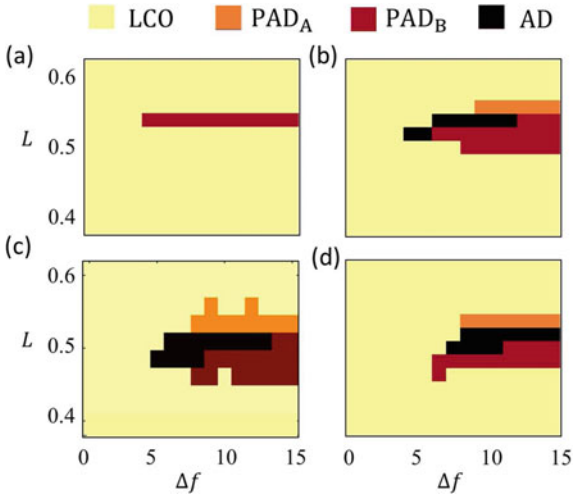

Fig. 18 Two-parameter bifurcation plots between frequency detuning in the system (Δf) and length of the connecting tube (L) for diameter values of **a** 0.6 cm, **b** 0.8 cm, **c** 1.0 cm, and **d** 1.2 cm when p_0 is fixed at 120 Pa in both the oscillators. Various states of coupled dynamics namely limit cycle oscillations (LCO), partial amplitude death in oscillator A (PAD$_A$), partial amplitude death in oscillator B (PAD$_B$), and amplitude death (AD) are depicted in the plots. Reproduced with permission from [57]

quenched state of another due to coupling, is referred to as partial amplitude death [62, 63]. For the frequency detuning of $\Delta f = 15.0$ Hz, we notice that the oscillations in Rijke tube B are nearly quenched (i.e., minimal fluctuations) while that in Rijke tube A retain the state of large amplitude limit cycle oscillations (see Fig. 17f). We also note that during the state of partial amplitude death, both the oscillators exhibit identical frequencies (see Fig. 17b), whose value tends to be closer to that of the oscillator with higher amplitude. In other words, in Fig. 17f, where oscillator A exhibits higher amplitude oscillations compared to oscillator B, both the oscillators oscillate with a frequency near the uncoupled frequency value of oscillator A (see Fig. 17b). This also suggests that the oscillator which regains its oscillations during the state of partial amplitude death drives the oscillations in the other oscillator which is oscillating at significantly lower amplitudes.

In Fig. 18, we show the coupled dynamics of limit cycle oscillations (LCO) developed in detuned Rijke tube oscillators for various dimensions (L and D) of the connecting tube. The amplitudes of both LCO are fixed at 120 Pa in their uncoupled state. Two-parameter bifurcation plots between the length of the connecting tube (L) and the frequency detuning between oscillators (Δf) are plotted for various values of connecting tube diameters (D). For a lower value of the tube diameter, $D = 0.6$ cm (Fig. 18a), we notice the existence of only LCO and PAD dynamics for the range of L and Δf investigated in this study. The coupling induced by smaller diameter tube being weak and hence is insufficient to simultaneously quench the oscillations

in both the oscillators. The effect of finite detuning ($\Delta f > 3.0$ Hz) for $L = 0.56$ is noticed only in oscillator B, where the LCO is quenched while they are retained in oscillator A, indicated as PAD_B in Fig. 18a. On the other hand, when the tube diameter is sufficiently large, $D = 0.8$, 1.0 and 1.2 cm, we see the existence of all LCO, AD and PAD states in the coupled dynamics of both the Rijke tubes (see in Fig. 18b–d). For lower values of frequency detuning ($\Delta f < 4.0$ Hz), we observe LCO in both the oscillators, irrespective of the value of L for all these diameters. When the frequency detuning is relatively high ($\Delta f > 5.0$ Hz), oscillation quenching is observed for a specific range of L in either one or both the Rijke tube oscillators, depending on the dimensions of the tube as is explained subsequently.

For the case of $D = 0.8$ cm, shown in Fig. 18b, we observe that the AD region is limited to $L \approx 0.5$ at $\Delta f = 3.0$ to 10.0 Hz. For larger values of detuning ($\Delta f = 8.0$ to 13.0 Hz), we observe the occurrence of PAD along with the states of LCO and AD in our system. Here, the oscillation quenching states (PAD and AD) are limited over the range of L from 0.46 to 0.55. At very high values of frequency detuning ($\Delta f > 13.0$ Hz), the occurrence of PAD states alone is witnessed for this range of L in the system. A similar scenario is observed in the case of $D = 1.0$ cm as shown in Fig. 18c; however, we observe that the overall zone of suppression (region covered by AD and PAD states) is increased. For larger values of diameter, $D = 1.2$ cm (see Fig. 18d), the value of Δf corresponding to the occurrence of PAD is lower than that corresponding to the state of AD. Further we observe that for Δf ranging from 6 to 15 Hz, we observe the existence of AD, PAD and LCO for varying values of L. This is in contrast with the behaviour shown by smaller diameters such as 0.8 and 1.0 cm, where we observe the state of PAD and LCO alone at frequency detuning values of $\Delta f > 13.0$ Hz (Fig. 18b,c). Thus, we can conclude that the amplitude suppression zone of LCOs in coupled Rijke tubes is increased due to the addition of frequency mismatch between the systems, and the suppression is maximum for a finite range of L around 0.5 and $D = 1.0$ cm.

6 Summary

We explored the effect of time-delay and dissipative couplings on the occurrence of amplitude death phenomenon in a system of two coupled thermoacoustic oscillators known as horizontal Rijke tubes. Bifurcation plots obtained from the mathematical model give us an idea about the combination of coupling parameters that need to be set to achieve AD in the thermoacoustic oscillators considered. The results indicate that AD is more easily achieved when both the couplings are applied together. The fact that, theoretically AD is possible under asymmetric coupling and in coupled oscillators with dissimilar amplitudes is also demonstrated. This phenomenon of AD in the Rijke tube oscillator model, if found experimentally feasible, can be extended to real combustion systems where the unwanted high-amplitude oscillations which may lead to a serious structural damage can be inhibited. The theoretical finding that

AD can occur even in oscillators with considerably dissimilar amplitudes also needs experimental verification in practical thermoacoustic systems.

Further, with the use of a single connecting tube of appropriate length and diameter, we showed that limit cycle oscillations having low amplitudes can be completely quenched in both the oscillators. However, in order to quench the limit cycle oscillations with high amplitude in either one or both the oscillators, we need to have a finite frequency detuning in the system. We observe that, when oscillators of nearly equal amplitude and frequency are coupled, we observe the coexistence of amplitude death (AD) and phase-flip bifurcation (PFB) in the system. In coupled identical oscillators, the dynamics of low-amplitude limit cycle oscillations transition from anti-phase to in-phase state of synchronization via an intermediate state of AD. However, for high-amplitude oscillations, the system displays PFB. Hence, we conjecture that the amplitude of limit cycle oscillations in identical oscillators determines the coupling requisites (length and diameter of the tube) necessary for affecting the amplitude of each oscillator. For a given length and diameter of the connecting tube, when the amplitude of limit cycles is low, the oscillators are weak, and hence, the coupling induced due to a given tube diameter is sufficient to cause AD in the system. On the other hand, when the amplitude of limit cycles is sufficiently large, the oscillators are considerably strong that AD is not achievable with the same diameter of the tube.

Our study finds applications in controlling and suppressing undesirable thermoacoustic oscillations produced in various physical systems such as multiple can and can-annular combustors. Moreover, the systematic investigation of oscillation quenching behaviour of coupled highly turbulent combustors and systems that exhibit thermoacoustic instabilities with several natural frequencies requires further investigation.

Acknowledgements Discussions with Prof. R. I. Sujith, IIT Madras, are gratefully acknowledged.

References

1. Matthews PC, Strogatz SH (1990) Phase diagram for the collective behavior of limit-cycle oscillators. Phys Rev Lett 65(14):1701
2. Pikovsky A, Rosenblum M, Kurths J (2003) Synchronization: a universal concept in nonlinear sciences, vol 12. Cambridge University Press, Cambridge
3. Kuramoto Y (1984) Cooperative dynamics of oscillator communitya study based on lattice of rings. Prog Theor Phys Suppl 79:223–240
4. Herrero R, Figueras M, Rius J, Pi F, Orriols G (2000) Experimental observation of the amplitude death effect in two coupled nonlinear oscillators. Phys Rev Lett 84(23):5312
5. Reddy DR, Sen A, Johnston GL (1998) Time delay induced death in coupled limit cycle oscillators. Phys Rev Lett 80(23):5109
6. Mirollo RE, Strogatz SH (1990) Amplitude death in an array of limit-cycle oscillators. J Stat Phys 60(1–2):245–262
7. Koseska A, Volkov E, Kurths J (2013) Transition from amplitude to oscillation death via Turing bifurcation. Phys Rev Lett 111(2):024103
8. Rayleigh JWS (1945) The theory of sound. Dover

9. Abel M, Bergweiler S, Gerhard-Multhaupt R (2006) Synchronization of organ pipes: experimental observations and modeling. J Acoust Soc Am 119(4):2467–2475
10. Abel M, Ahnert K, Bergweiler S (2009) Synchronization of sound sources. Phys Rev Lett 103(11):114301
11. Crowley MF, Field RJ (1981) Nonlinear phenomena in chemical dynamics. Springer, pp 147–153
12. Zeyer KP, Mangold M, Gilles E (2001) Experimentally coupled thermokinetic oscillators: phase death and rhythmogenesis. J Phys Chem A 105(30):7216–7224
13. Setou Y, Nishio Y, Ushida A (1996) Synchronization phenomena in resistively coupled oscillators with different frequencies. IEICE Trans Fundam Electron Commun Comput Sci 79(10):1575–1580
14. Saxena G, Prasad A, Ramaswamy R (2012) Amplitude death: The emergence of stationarity in coupled nonlinear systems. Phys Rep 521(5):205–228
15. Mondal S, Mukhopadhyay A, Sen S (2012) Effects of inlet conditions on dynamics of a thermal pulse combustor. Combust Theor Model 16(1):59–74
16. Mondal S, Mukhopadhyay A, Sen S (2017) Bifurcation analysis of steady states and limit cycles in a thermal pulse combustor model. Combust Theor Model 21(3):487–502
17. Rayleigh L (1878) The explanation of certain acoustical phenomena. Roy Inst Proc 8:536–542
18. Sujith RI, Juniper MP, Schmid PJ (2016) Non-normality and nonlinearity in thermoacoustic instabilities. Int J Spray Combust Dyn 8(2):119–146
19. Fisher SC, Rahman SA (2009) Remembering the giants: apollo rocket propulsion development. NASA Stennis Space Center
20. Polifke W, Döbbeling K, Sattelmayer T, Nicol DG, Malte PC (1995) In: ASME 1995 international gas turbine and aeroengine congress and exposition. American Society of Mechanical Engineers, pp V003T06A019–V003T06A019
21. Docquier N, Candel S (2002) Combustion control and sensors: a review. Prog Energy Combust Sci 28(2):107–150
22. Shanbhogue SJ, Husain S, Lieuwen T (2009) Lean blowoff of bluff body stabilized flames: Scaling and dynamics. Prog Energy Combust Sci 35(1):98–120
23. Putnam AA (1971) Combustion driven oscillations in industry. Elsevier Publishing Company
24. Poinsot T (2017) Prediction and control of combustion instabilities in real engines. Proc Combust Inst 36(1):1–28
25. Juniper MP, Sujith RI (2017) Sensitivity and nonlinearity of thermoacoustic oscillations. Annu Rev Fluid Mech 50:661–689
26. Bicen AF, Tse D, Whitelaw JH (1988) Flow and combustion characteristics of an annular combustor. Combust Flame 72(2):175–192
27. McManus KR, Poinsot T, Candel SM (1993) A review of active control of combustion instabilities. Prog Energy Combust Sci 19(1):1–29
28. Kablar NA, Hayakawa T, Haddad WM (2001) In: Proceedings of the 2001 American control conference, vol 3. IEEE, pp 2468–2473
29. Biwa T, Sawada Y, Hyodo H, Kato S (2016) Suppression of spontaneous gas oscillations by acoustic self-feedback. Phys Rev Appl 6(4):044020
30. Bellows BD, Neumeier Y, Lieuwen T (2006) Forced response of a swirling, premixed flame to flow disturbances. J Propul Power 22(5):1075–1084
31. Balusamy S, Li LKB, Han Z, Juniper MP, Hochgreb S (2015) Nonlinear dynamics of a self-excited thermoacoustic system subjected to acoustic forcing. Proc Combust Inst 35(3):3229–3236
32. Biwa T, Tozuka S, Yazaki T (2015) Amplitude death in coupled thermoacoustic oscillators. Phys Rev Appl 3(3):034006
33. Ghirardo G, Juniper MP (2013) Azimuthal instabilities in annular combustors: standing and spinning modes. Proc R Soc A 469(2157):20130232
34. Balasubramanian K, Sujith RI (2008) Thermoacoustic instability in a Rijke tube: Non-normality and nonlinearity. Phys Fluids 20(4):044103

35. Aronson DG, Ermentrout GB, Kopell N (1990) Amplitude response of coupled oscillators. Phys D Nonlinear Phenom 41(3):403–449
36. Waugh IC, Juniper MP (2011) Triggering in a thermoacoustic system with stochastic noise. Int J Spray Combust Dyn 3(3):225–241
37. Noiray N, Schuermans B (2013) Deterministic quantities characterizing noise driven Hopf bifurcations in gas turbine combustors. Int J Non-Linear Mech 50:152–163
38. Clavin P, Kim JS, Williams FA (1994) Turbulence-induced noise effects on high-frequency combustion instabilities. Combust Sci Technol 96(1–3):61–84
39. Lieuwen T, Banaszuk A (2005) Background noise effects on combustor stability. J Propul Power 21(1):25–31
40. Waugh I, Geuß M, Juniper M (2011) Triggering, bypass transition and the effect of noise on a linearly stable thermoacoustic system. Proc Combust Inst 33(2):2945–2952
41. K.I. Matveev, Thermoacoustic instabilities in the rijke tube: Experiments and modeling. Ph.D. thesis, California Institute of Technology (2003)
42. Subramanian P, Sujith RI, Wahi P (2013) Subcritical bifurcation and bistability in thermoacoustic systems. J Fluid Mech 715:210–238
43. King LV (1914) XII. On the convection of heat from small cylinders in a stream of fluid: Determination of the convection constants of small platinum wires with applications to hot-wire anemometry. Philos Trans R Soc Lond Ser A 214(509-522):373–432
44. Heckl MA (1990) Non-linear acoustic effects in the Rijke tube. Acta Acustica United Acustica 72(1):63–71
45. Lores ME, Zinn BT (1973) Nonlinear longitudinal combustion instability in rocket motors. Combust Sci Technol 7(6):245–256
46. Matveev KI, Culick FEC (2003) A model for combustion instability involving vortex shedding. Combust Sci Technol 175(6):1059–1083
47. Sterling JD, Zukoski EE (1991) Nonlinear dynamics of laboratory combustor pressure oscillations. Combust Sci Technol 77(4–6):225–238
48. Gopalakrishnan EA, Sujith RI (2015) Effect of external noise on the hysteresis characteristics of a thermoacoustic system. J Fluid Mech 776:334–353
49. Thomas N, Mondal S, Pawar SA, Sujith RI (2018) Effect of time-delay and dissipative coupling on amplitude death in coupled thermoacoustic oscillators. Chaos Interdisc J Nonlinear Sci 28(3):033119
50. Reddy DR, Sen A, Johnston GL (2000) Experimental evidence of time-delay-induced death in coupled limit-cycle oscillators. Phys Rev Lett 85(16):3381
51. Thomas N, Mondal S, Pawar SA, Sujith RI (2018) Effect of noise amplification during the transition to amplitude death in coupled thermoacoustic oscillators. Chaos Interdisc J Nonlinear Sci 28(9):093116
52. Gopalakrishnan EA, Tony J, Sreelekha E, Sujith RI (2016) Stochastic bifurcations in a prototypical thermoacoustic system. Phys Rev E 94(2):022203
53. Juel A, Darbyshire AG, Mullin T (1997) The effect of noise on pitchfork and Hopf bifurcations. Proc R Soc London A Math Phys Eng Sci 453:2627–2647 (The Royal Society)
54. Sastry S, Hijab O (1981) Bifurcation in the presence of small noise. Syst Control Lett 1(3):159–167
55. Zakharova A, Vadivasova T, Anishchenko V, Koseska A, Kurths J (2010) Stochastic bifurcations and coherencelike resonance in a self-sustained bistable noisy oscillator. Phys Rev E 81(1):011106
56. Kabiraj L, Steinert R, Saurabh A, Paschereit CO (2015) Coherence resonance in a thermoacoustic system. Phys Rev E 92(4):042909
57. Dange S, Manoj K, Banerjee S, Pawar SA, Mondal S, Sujith RI (2019) Oscillation quenching and phase-flip bifurcation in coupled thermoacoustic systems. Chaos Interdisc J Nonlinear Sci 29(9):093135
58. Gopalakrishnan EA, Sujith RI (2014) Influence of system parameters on the hysteresis characteristics of a horizontal Rijke tube. Int J Spray Combust Dyn 6(3):293–316

59. Koseska A, Volkov E, Kurths J (2013) Oscillation quenching mechanisms: Amplitude vs. oscillation death. Phys Rep 531(4):173–199
60. Prasad A, Kurths J, Dana SK, Ramaswamy R (2006) Phase-flip bifurcation induced by time delay. Phys Rev E 74(3):035204
61. Manoj K, Pawar SA, Sujith RI (2018) Experimental evidence of amplitude death and phase-flip bifurcation between in-phase and anti-phase synchronization. Sci Rep 8(1):1–7
62. Atay FM (2003) Total and partial amplitude death in networks of diffusively coupled oscillators. Phys D Nonlinear Phenom 183(1–2):1–18
63. Yang J (2007) Transitions to amplitude death in a regular array of nonlinear oscillators. Phys Rev E 76(1):016204

Emission Characteristics and Flame Stability in HEFA Fueled Gas Turbine Combustors

H. Fujiwara, P. Salman, S. Ando, H. Ishikawa, S. Nakaya, M. Tsue, and K. Okai

Nomenclature

ASTM	American Society for Testing and Materials
CO	Carbon monoxide
CO_2	Carbon dioxide
EI	Emission Index
FAME	Fatty and methyl-ester fuel
FT-SPK	Fischer-Tropsch Synthetic Paraffin Kerosene
HEFA	Hydro-treated Ester and Fatty Acid
ILIDS	Interferometric Laser Imaging Droplet Sizing
JAXA	Japan Aerospace Exploration Agency
KAKENHI	Grants-in-Aid for Scientific Research
LBO	Lean Blow Out
MHPS	Mitsubishi-Hitachi Power Systems
NEDO	New Energy Industrial Technology Development Organization
NO_x	Nitrogen oxides
nvPM	Non-volatile particulate matter
PASS	Photo acoustic soot sensor
Re	Reynolds number
RQL	Rich burn Quick quench and Lean burn
SPK	Synthetic Paraffin Kerosene

H. Fujiwara (✉) · K. Okai
Propulsion Research Unit, Aeronautical Research Directorate, Japan Aerospace Exploration Agency, 7-44-1 Jindaiji-Higashi, Chofu, Tokyo 182-8522, Japan
e-mail: fujiwara.hitoshi@jaxa.jp

P. Salman · S. Ando · H. Ishikawa · S. Nakaya · M. Tsue
Department of Aeronautics and Astronautics, Graduate School of Engineering, The University of Tokyo, 7-3-1 Hongo, Bunkyo, Tokyo 113-8656, Japan

© Springer Nature Singapore Pte Ltd. 2021

A. De et al. (eds.), *Sustainable Development for Energy, Power, and Propulsion*, Green Energy and Technology,
https://doi.org/10.1007/978-981-15-5667-8_13

TEC	Toyo Engineering Cooperation
THC	Total hydrocarbons
UOP	Universal Oil Products

1 Introduction

Global climate change due to the rapid increase in CO_2 emissions especially caused by aviation is one of the critical issues that can be solved through international collaborations. Although the amount of CO_2 emissions from aviation consists of only around 2% of the total CO_2 emissions, it is of crucial importance to start suppressing emissions caused by air traffic as early as possible. Recent rapid growth of aviation transportation has caused many activities that could curtail CO_2 reduction form aviation. Much efforts are in progress in other fields, such as electric and hybrid vehicles in the automotive sector and carbon dioxide capture and storage (CCS) installations in power generation plants. It should be noted that more than 90% of CO_2 emissions from commercial aircraft operations are generated by large aircraft, indicating of pursuing research to reduce commercial aircraft emissions with a focus on technology applicable to large commercial aircraft [1].

In aviation, alternative fuels are considered one of the important options to suppress CO_2 emission, while their specifications are strictly defined in ASTM D7566 "Standard Specification for Aviation Turbine Fuel Containing Synthesized Hydrocarbons" [2]. Its Annexes define not only the chemical and physical properties but also the manufacturing process of those fuels, which is of prime importance from the aviation safety point of view.

In our joint research group between JAXA and the University of Tokyo, discussions and investigations of bio-derived aviation alternative fuels started in 2010. At JAXA, the impact of introducing biofuels in turbofan jet engines has been investigated [3] and combustion testing begun with available (not-certified and general) bio-fuel (Fatty acid methyl-ester, FAME fuel) in 2011 [4]. As expected, the fuel had higher CO emissions at low load conditions due to low flame temperature [5].

In 2017, Mitsubishi-Hitachi Power System (MHPS) with partners (Toyo Engineering Cooperation (TEC), Chubu Electric Power and JAXA) started a project to conduct a pilot-scale plant testing on a Fischer-Tropsch Synthetic Paraffin Kerosene (FT-SPK) fuel production derived from lignocellulosic biomass supported by NEDO [6]. For this project, JAXA participated to conduct the final combustion tests of the product. In addition, the University of Tokyo and JAXA conducted fundamental research on biofuels combustion supported by KAKENHI.

This article presents the results of investigations on aviation certified biofuels to understand the limitations and potentials of bio-derived aviation fuels as a contribution towards more environmentally friendly aviation. It further focuses on emission characteristics and flame stability with Jet A1 and HEFA fuels using the same configurations.

The alternative turbine fuel used in this study was hydro-treated ester and fatty acid (HEFA) made from tallow fat, provided by Honeywell UOP/Nikki Universal. The manufacturing process is specified in Annex 2 of ASTM D7566. The HEFA fuel was available for commercial flights if the blending ratio did not exceed 50 vol.% as specified in Annex 2.

Specifications for HEFA are provided in ASTM D7566 Annex 2 [7]. To understand the similarities and differences of HEFA fuel compared to the baseline Jet A1 fuel, the properties of HEFA fuel were analyzed. Table 1 summarizes the result.

2 Combustor Tests and Conditions

2.1 Basic Combustion Tests

Several basic tests were conducted to understand the overall combustion characteristics of the mentioned fuels, including instabilities. Obtained data were analyzed to evaluate important structures of combustion, as well as air and fuel conditions.

Figure 1 shows a schematic and a photograph of one of the tested injectors. Figure 2 shows the experimental apparatus for the measurement of spray droplet diameter distribution, in which spray testing with swirled flow was realized. For the droplet measurement, Interferometric Laser Imaging for Droplet Sizing (ILIDS) was used [8–10].

Test conditions are shown in Table 2.

Single droplet evaporation tests were conducted using an apparatus shown in Fig. 3. The droplet diameter measurement was conducted with the method introduced by Nakaya and co-workers [11] both in normal and microgravity conditions.

Test conditions are shown in Table 3.

Combustion instability experiments with a fuel nozzle configuration such as for droplet diameter measurement were investigated at the University of Tokyo hypersonic and high-temperature wind tunnel. Figure 4 shows a schematic of the test apparatus. High-temperature air from the heater was injected into the experimental apparatus and high pressure was reached due to the choked nozzle further downstream. The flow was exhausted to the building's environment through the silencer tower (not shown in the schematics). CH* Chemiluminescence of the flame and Mie scattering of the spray were taken using high-speed cameras (Vision Research Inc., Micro LC 310, and MiroEx2) at 2000 and 1000 fps, respectively.

Test conditions are shown in Table 4.

Table 1 Chemical and physical analysis of the fuels

Properties	HEFA	D7566 Table A2.1-2	Jet A1	Jet A1: HEFA = 50:50	D7566 Table 1	Test method
Freezing point (°C)	−58.5	<−40	−48.0	−51.5	<−47	JIS K 2276
Dynamic viscosity (mm^2/s) @15 °C	1.963	N/A	1.655	1.786	<8 (−20 °C)	JIS K2283
Surface tension (mN/m)	22.5	N/A	23.6	23.1	N/A	JIS K 2241
Density (g/cm^3) @15 °C	0.7554	0.73–0.77	0.7886	**0.7732**	0.775–0.840	JIS K 2249-1
Net heat of combustion (MJ/kg)	44.14	N/A	43.38	43.73	>42.8	JIS K 2279
Physical distillation						JIS K 2254
Initial boiling point (°C)	146.5	N/A	148.5	148.5	N/A	
10% recovered temp. (°C)	165.0	<205	164.5	165.0	<205	
50% recovered temp. (°C)	208.0	Report	193.5	198.5	Report	
90% recovered temp. (°C)	253.5	Report	237.5	247.0	Report	
Final boiling point (°C)	269.0	<300	259.0	262.0	<300	
Lubricity (mm)	1.04	N/A	0.83	**0.87**	<0.85	ASTM D5001
Carbon (mass%)	84.7	N/A	86.1	85.4	N/A	JPI-5S-65
Hydrogen (mass%)	15.2	N/A	13.8	14.5	N/A	
Sulfur (mass%)	<0.0001	<0.0015	0.0006	0.0003	<0.3	JIS K 2541-6
Composition						ASTM D1319
Paraffin (vol.%)	98.4	Report	79.1	89.1	N/A	

(continued)

Table 1 (continued)

Properties	HEFA	D7566 Table A2.1-2	Jet A1	Jet A1: HEFA = 50:50	D7566 Table 1	Test method
Olefin (vol. %)	0.9	N/A	3.0	1.6	N/A	
Total aromatics (vol.%)	0.7	N/A	17.9	9.3	8-25	
Aromatics						ASTM D6379
Benzenes (vol.%)	<0.1	N/A	19.1	10.2	N/A	
(mass%)	<0.1	N/A	21.3	11.6	N/A	
Naphthalene (vol.%)	<0.1	N/A	0.1	0.1	N/A	
(mass%)	<0.1	N/A	0.2	0.1	N/A	
Total aromatics (vol.%)	<0.1	N/A	19.2	10.3	8.4–26.5	
(mass%)	0.1	N/A	21.5	11.8	N/A	

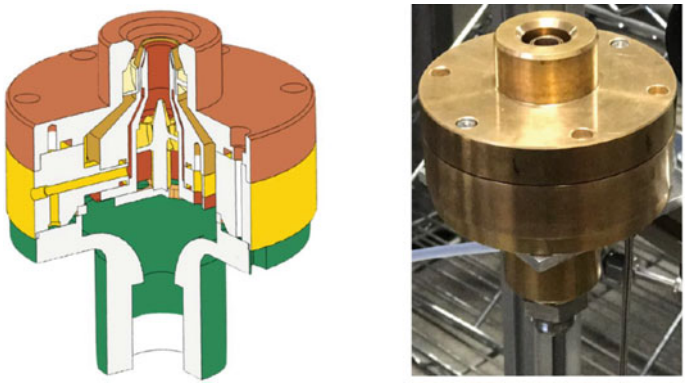

(a) Schematic view (b) Photograph

Fig. 1 Double-swirl air-blast fuel nozzle

2.2 *Single Sector Combustor Testing at JAXA Combustion Test Rig*

Two types of single-injector combustors were used for testing at JAXA AP7 medium-pressure test rig, with the maximum inlet temperature, pressure, and air-mass flow of 1000 K, 10 bar and 2 kg/s, respectively. Figure 5 shows the schematic of the test facility showing especially the air supply system.

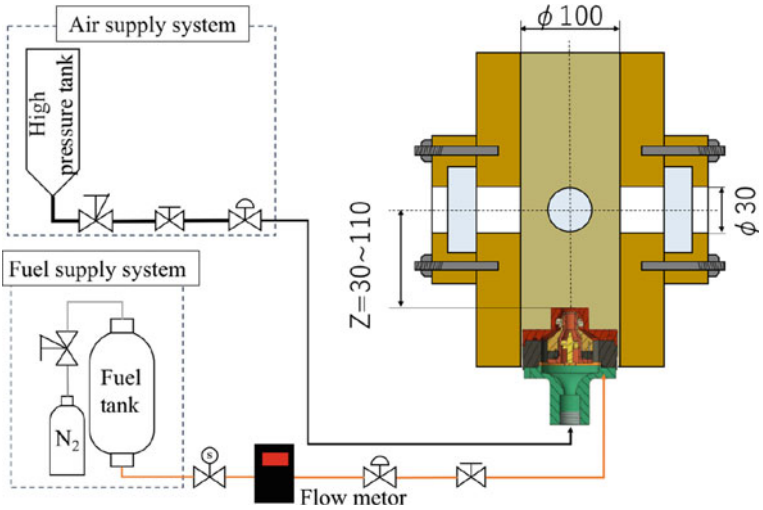

Fig. 2 Schematic of the experimental apparatus for droplet size measurement of a double-swirl injector at atmospheric condition

Table 2 Droplet diameter measurement test condition

Case	Air flow rate	Swirl number	Equivalence ratio	Fuel
B1	15 (g/s)	0.13	0.71	Jet A1, HEFA

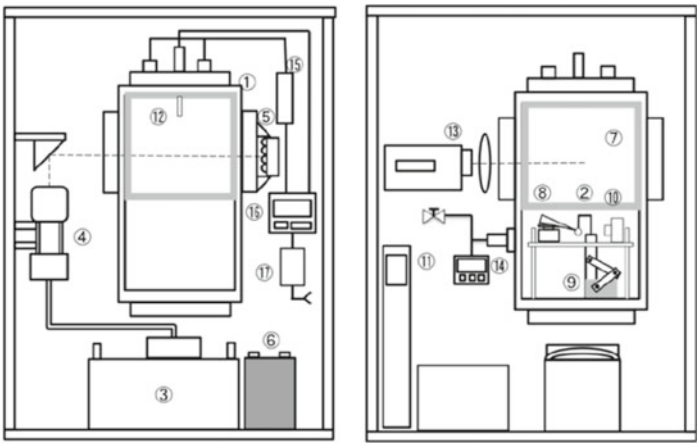

① Combustion chamber, ② Silica fiber, ③ High-speed camera, ④ Camera head, ⑤ LED back light, ⑥ 12V battery, ⑦ Electric furnace, ⑧ Glass tube, ⑨ Servomotor, ⑩ Camera, ⑪ UPS, ⑫ Thermocouple, ⑬ Video camera, ⑭ Pressure measurement, 1⑮ Solid state relay, ⑯ Temperature controller, ⑰ Circuit breaker

Fig. 3 Droplet evaporation test apparatus

Table 3 Single droplet evaporation test condition

Case	Temperature	Pressure	Gas composition	Fuel
B2	750 °C	Ambient pressure	Nitrogen 100%	Jet A1, HEFA

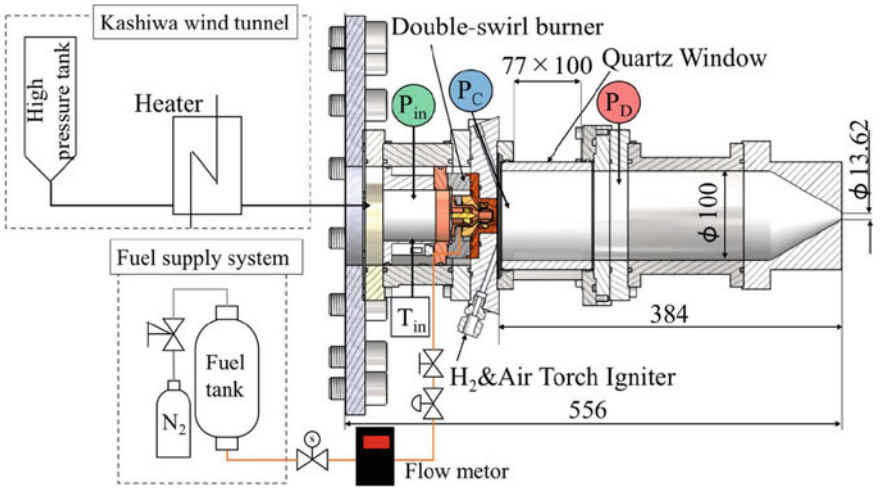

Fig. 4 Schematic of the experimental apparatus for double-swirl injector combustion testing at high pressure and temperature condition

Table 4 Test condition for high-temperature and pressure combustion at University of Tokyo combustion wind tunnel

Case	Air temperature	Air pressure	Equivalence ratio	Fuel
B3	600 K	500 kPa	0.71	Jet A1, HEFA

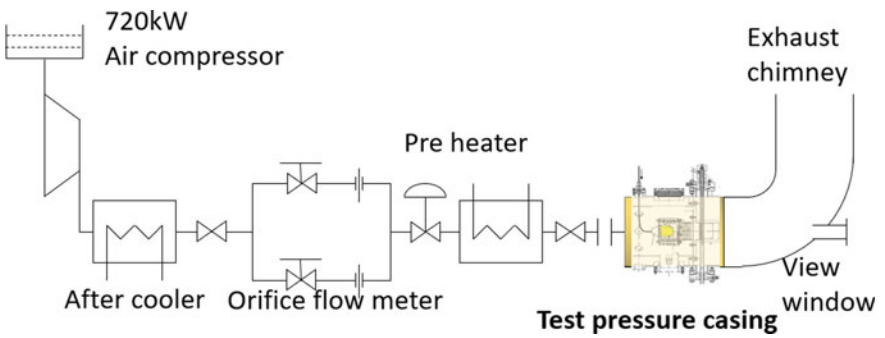

Fig. 5 Schematic of JAXA AP7 medium-pressure test rig (air supply system)

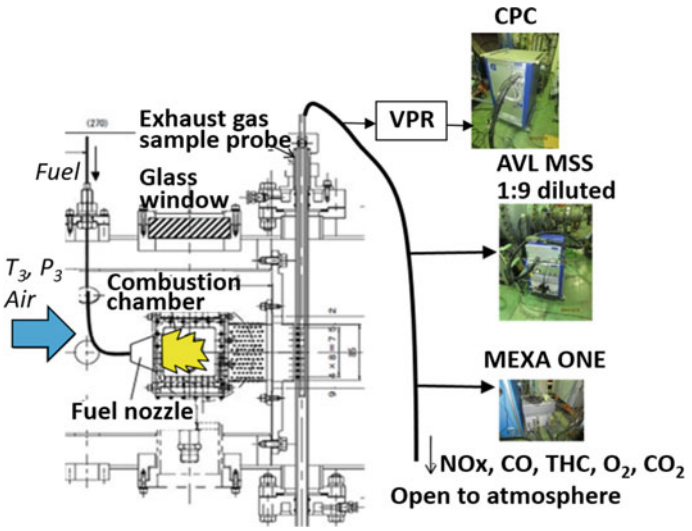

Fig. 6 Combustion test pressure casing overview

Whole test chambers are installed in a test pressure casing retractable from the facility to hold several different types of combustion chambers. Figure 6 shows an enlarged image of the pressure casing portion. The tested combustion chamber is installed in a pressure casing and connected to the fuel supply system. Cables from the measurement equipment are connected via the pressure casing.

This test rig is usually used for the demonstration of new combustor concepts and for the development of innovative measurement technologies. Crystal glass windows were installed in both the facility pressure casing and the combustor liner so that the high-pressure combustion phenomena can directly be observed from outside of the casing (see Fig. 7). An exhaust gas sample probe with eight ψ0.8 mm sampling holes was located at the exit of the combustor liner (Fig. 7).

The samples from the exhaust gas were led to the measurement instruments through a stainless-steel tube connected to a valve to control the mass flow and temperature of the sample gas. NO_x concentration was measured using a chemiluminescence detector (CLD), CO, and CO_2 concentrations were measured through nondispersive infrared detectors (NDIR), and total hydrocarbon (THC) concentration was measured using a flame ionization detector (FID), Horiba MEXA ONE. Nonvolatile particle matter (nvPM) mass concentration was measured using a photoacoustic soot sensor (PASS), AVL MSS 483. The number of nvPM was also measured through a condensation particle counter (CPC) with a particle remover (VPR). A condensation particle counter (CPC) is a particle counter that detects and counts aerosol particles by first enlarging them and using the particles as nucleation centers to create droplets in a supersaturated gas (see Fig. 8). In this study, nucleation is accomplished through thermal diffusion (working gas is n-butanol).

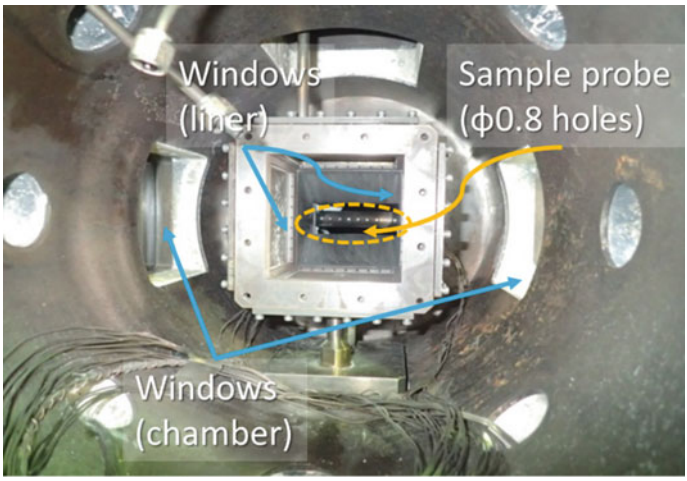

Fig. 7 View inside the pressure casing (viewed from upstream)

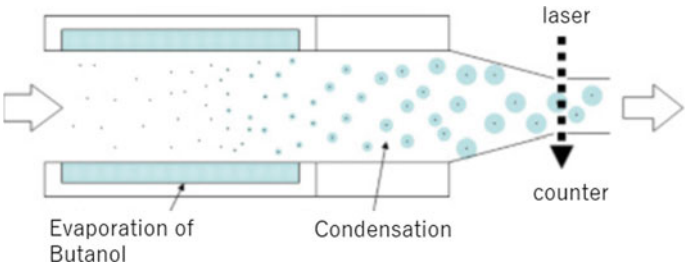

Fig. 8 Schematic of a condensation particle counter (CPC)

Spatial distribution of soot concentration was estimated using Hottel and Broughton two-color radiometry [12].

One of the tested combustors (case 1) was a RQL combustor [13] as shown in Fig. 9, wherein 10% of total air flow entered through the upstream Parker-Hannifin type air-blast fuel nozzle [5] (Fig. 10), while the remaining 90% of total air entered through the air holes located on the combustor liner (seen in Fig. 9 as combustion/dilution air holes). The other combustor (case 2) was a concentric lean-burn burner [14] as seen in Fig. 11, which consisted of a pilot diffusion burner located at the center and a lean premix main burner surrounding it. Only the pilot burner was fueled at low load inlet air condition, while at high load conditions both pilot and main burner were fueled.

Combustion tests were performed for the conditions shown in Table 5.

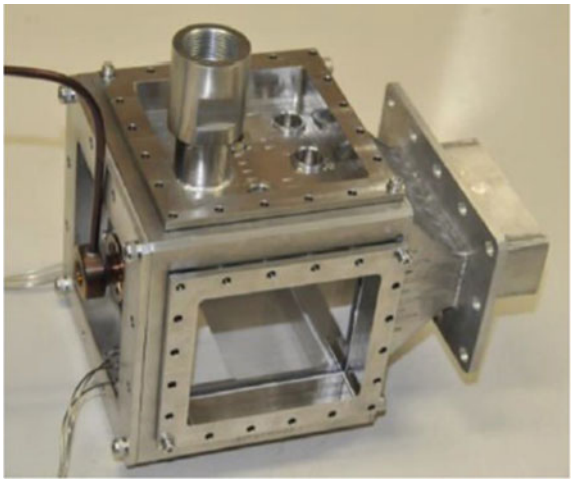

Fig. 9 Test chamber for RQL combustor

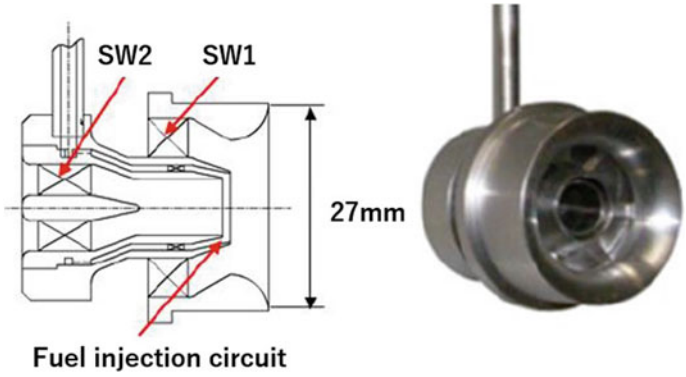

Fig. 10 Parker-Hannifin type air-blast fuel nozzle [13]

3 Results

3.1 Results of Basic Combustion Testing

To investigate the spray shape and structure in measurement locations, Mie scattering image was taken in the atmospheric pressure combustion test apparatus. Figure 12 shows the Mie scattering image for the same condition as droplet diameter distribution measurement shown in Table 2 (fuel was Jet A1). Time-averaged CH* chemiluminescence images for the two fuel were shown in Fig. 13. Squares in Figs. 12 and 13 indicate the locations of the ILIDS measurements.

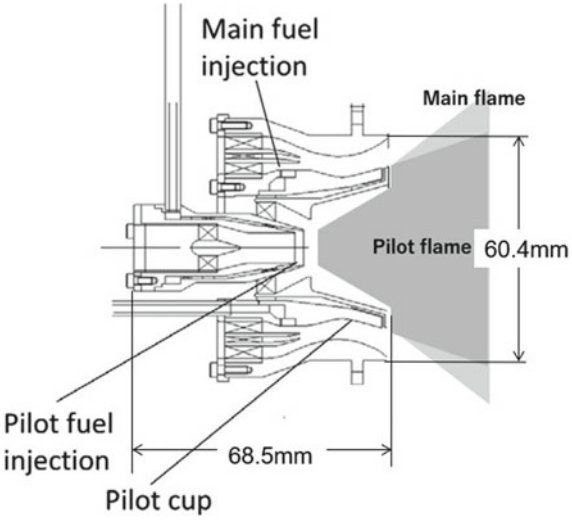

Fig. 11 Concentric lean burn burner

Table 5 JAXA combustion rig test conditions

Case	Combustor	Inlet temperature (K)	Inlet pressure (kPa)	Pressure loss ratio (%)	Fuel injection type
1-1	RQL	450	350	4.0	N/A
1-2		500	500	4.0	N/A
1-3		550	800	4.0	N/A
2-1	Lean burn	450	360	4.0	Pilot only
2-2		760	700	4.0	Pilot + main (pilot = 20%)
2-3		760	700	4.0	Pilot + main (pilot = 15%)

Mie scattering image shown in Fig. 12 suggests that spray flame relatively distributes near the center line from the injector exit. The density of the spray decreases with the distance downstream from the injector exit, and most of the spray droplets evaporate around $Z = 50$–70 mm. The location is close to the lifted flame position as seen in Fig. 13. These observations suggest that the spray distribution in the test configuration and condition is nearly 1-dimensional along the center line. In this sense, the selected ILIDS measurement points cover unburned, flame, and burned regions, and the selected measurement positions are adequate to investigate the atomization, evaporation, and combustion processes.

Figure 14 shows an example of droplet diameter distribution measurement using ILIDS. Each droplet is represented by an interference fringe and the fringe number accounts for the droplet diameter scaling.

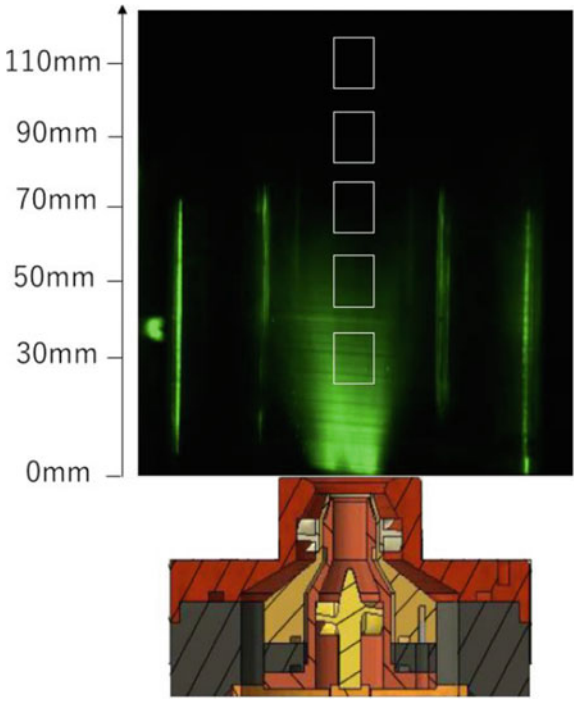

Fig. 12 Spray scattered image (fuel: Jet A1)

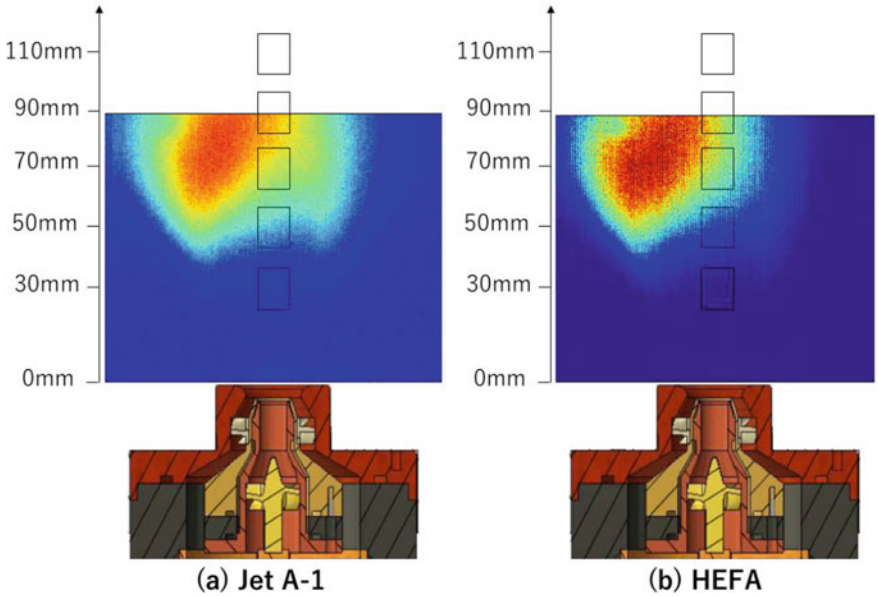

Fig. 13 Time-averaged image of CH* chemiluminescence

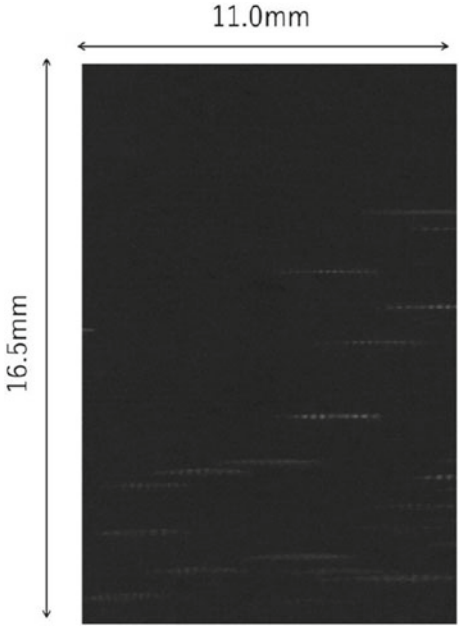

Fig. 14 Example of ILIDS measurement

Figure 15 shows droplet diameter distribution at 30 mm downstream from injector exit both for Jet A1 (a) and HEFA (b) fuels. The location is well upstream from a flame location indicated in Fig. 13 and atomization characteristics can be compared between the two fuels. Measured Sauter Mean Diameter indicated in Fig. 15 was slightly larger for cases using HEFA compared to Jet A1 experiments.

Figure 16 shows the change of Sauter Mean Diameter with distance from the injector exit. In the figure, calculated value using an empirical equation proposed by El-Shanawany and Lefebvre [15] for the two fuels are plotted. The equation is expressed as follows:

$$\frac{\mathrm{SMD}}{D_h} = \left(1 + \frac{1}{\mathrm{AFR}}\right)\left[0.33\left(\frac{\sigma_L}{\rho_A U_A^2 D_P}\right)^{0.6}\left(\frac{\rho_L}{\rho_A}\right)^{0.1} + 0.068\left(\frac{\mu_L^2}{\sigma_L \rho_L D_P}\right)^{0.5}\right]$$

where SMD is the Sauter Mean Diameter, D_h is the hydraulic diameter of injector exit, D_p is liquid film diameter, U_A is airflow velocity, ρ_L is liquid density, ρ_A is gas density, σ_L is surface tension of liquid, μ_L is viscosity coefficient of liquid, and AFR is mass air fuel ratio.

Figure 17 shows the change of estimated axial velocity with distance from injector exit. This estimation was made using the moving speed of drops in the measurement location.

From Figs. 16 and 17 it can be deducted that measured and estimated Sauter Mean Diameter immediately after the injection was slightly larger for HEFA compared to the case of Jet A1. This indicates that atomization characteristics are better for Jet A1

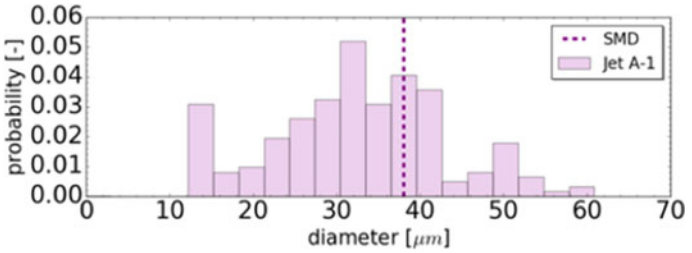

(a) Jet A1

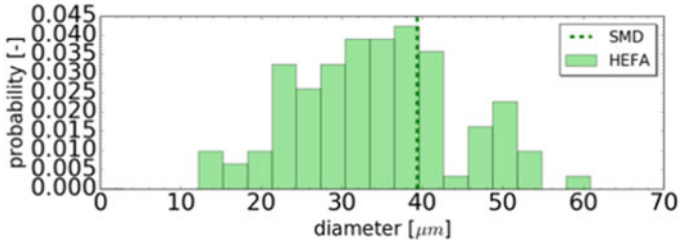

(b) HEFA

Fig. 15 Droplet diameter distribution at 30 mm downstream from injector exit. **a** Jet A1, **b** HEFA

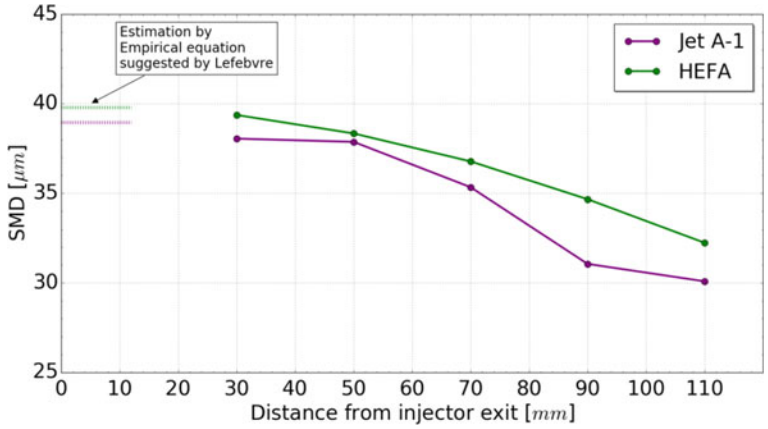

Fig. 16 Change of Sauter Mean Diameter with distance from injector exit

than HEFA. Table 6 shows a summary of the related properties used in the equation for SMD calculation. The slight difference in atomization characteristics comes from the difference of related properties used in the equation.

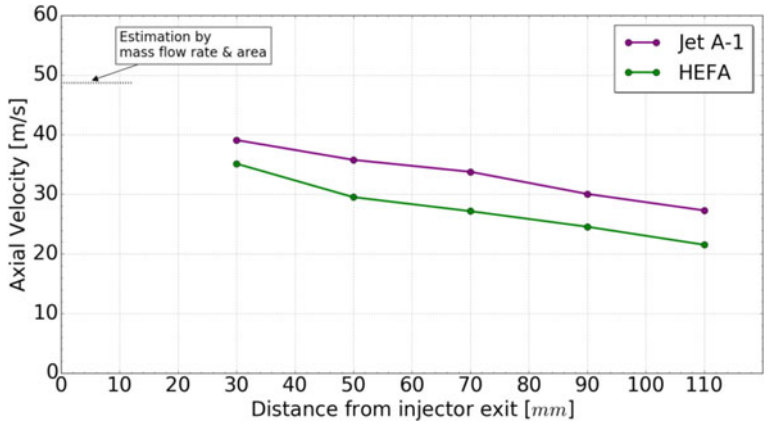

Fig. 17 Change of axial velocity with distance from injector exit

Table 6 Comparison of properties related to the equation by El-Shanawany and Lefebvre (taken from Table 1)

Properties	HEFA	Jet A1
Dynamic viscosity (mm^2/s) @15 °C	1.963	1.655
Surface tension (mN/m)	22.5	23.6
Density (g/cm^3) @15 °C	0.7554	0.7886

Atomization characteristics are an important factor in determining the combustion stability. Evaporation rate was measured from single droplet evaporation tests in high-temperature vessels. Figure 18 shows an example of back-lit image of an evaporating droplet. This single droplet evaporation test relies on the diameter (d) squared (d^2) law [16]. For the evaporation and combustion of single droplets, the square of the

Fig. 18 Appearance of droplet during evaporation testing

droplet diameter changes linearly with time. This constant of proportionality for the evaporation case is called the evaporation rate constant, K_v. This constant, after a short period of initial heat-up period, takes almost no change in value.

Figures 19 and 20 compare the time history of droplet diameter squared and instantaneous evaporation rate constant for Jet A1 and HEFA, respectively. For both fuels, the evaporation rate constant for most of the time takes nearly constant value except the initial and terminating periods. Average values from 40 to 80% of the time progressed were compared and Figs. 19 and 20 show a higher evaporation rate constant for HEFA than for Jet A1. This indicates that evaporation characteristics are better for HEFA than Jet A1 and HEFA is advantageous than Jet A1 in combustion stability point of view. This contrast might come from the difference in the fuel composition and further investigation may be necessary to understand the in-detail mechanism.

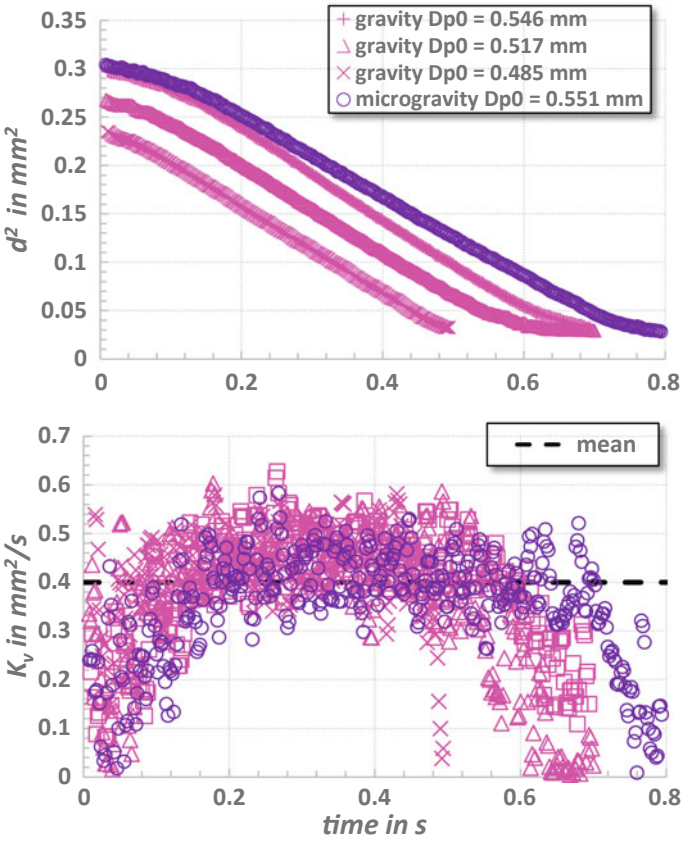

Fig. 19 Time history of droplet diameter squared and instantaneous evaporation rate constant (Jet A1)

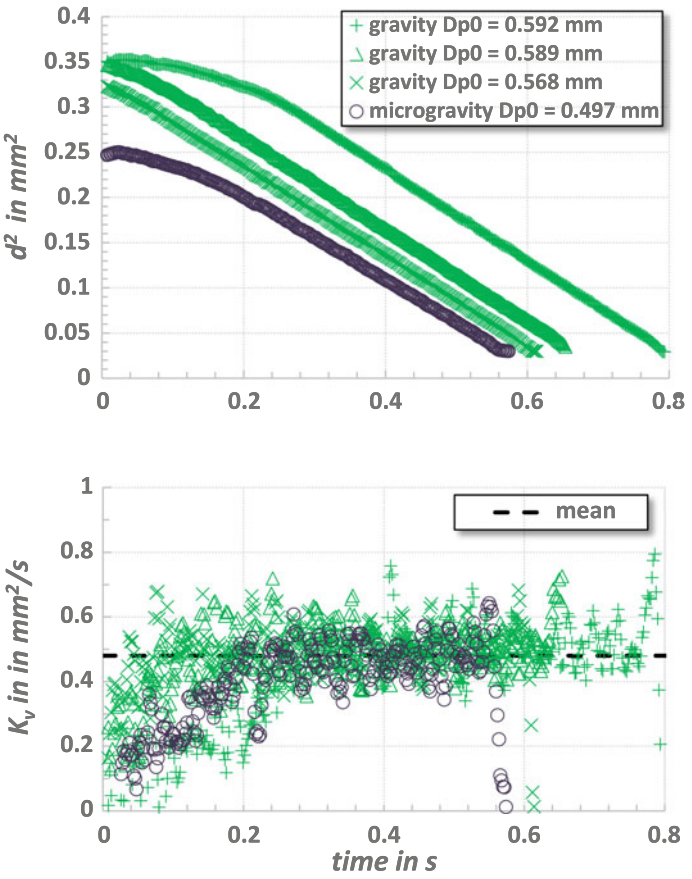

Fig. 20 Time history of droplet diameter squared and instantaneous evaporation rate constant (HEFA)

In addition, Figs. 19 and 20 show the evaporation of a HEFA and Jet A1 droplet at microgravity, respectively. Microgravity experiments are conducted by using the apparatus displayed in Fig. 3 under free-fall conditions. The dropping package can fall for 1.4 s in the 10 m high drop tower of the University of Tokyo (for more information, the authors refer to [17]). Microgravity experiments allow combustion and evaporation without the influence of, e.g., buoyancy effects. The influence of those effects increases with initial droplet size. Although the droplets used for the evaporation experiments are bigger than 0.5 mm in diameter, the gravity and microgravity data match and prove that evaporation data under normal gravity are reliable for the presented conditions.

High-temperature and high-pressure combustion testing at low equivalence ratio conditions was conducted to investigate the flame stability at those conditions. The experiments indicate, that the pressure fluctuation characteristics are clearly different

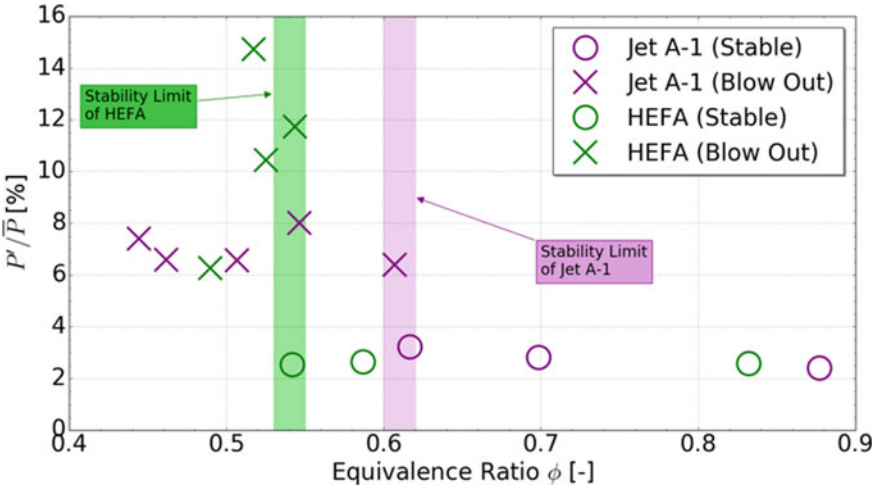

Fig. 21 Combustion stability in the case of high-temperature and high-pressure testing

between the stable combustion and blowout conditions. To compare the pressure fluctuation characteristics, a parameter P' showing the degree of pressure variation is defined as follows:

$$P' = 2\overline{|P_C - \overline{P}_C|}$$

Figure 21 shows the change of the parameter with equivalence ratio for the two fuel types. This figure clearly shows that for both fuels there exists a threshold of stability limit. For the blowout conditions, the pressure fluctuation is more intense than stable combustion conditions. Figure 21 shows that the onset of instability for HEFA as the fuel has a lower equivalence ratio than for Jet A1. In this context, the stable combustion region is wider for HEFA than Jet A1.

It was mentioned that blowout condition in lean combustion regime shows large pressure fluctuation with time than stable combustion condition. These pressure fluctuations are compared in the following.

Figures 22 and 23 show pressure oscillation measured (time history and frequency analysis) at a stable condition ($\varphi = 0.87$) for Jet A1 and HEFA, respectively.

Figures 24 and 25 show pressure oscillation measured (time history and frequency analysis) at a blowout condition ($\varphi = 0.52$) for Jet A1 and HEFA, respectively.

For the frequency analysis, Power Spectrum Density (PSD) applying Fast Fourier Transform (FFT) was plotted. For the stable combustion case, Figs. 22 and 23 show similar tendencies. Frequency analysis shows several peaks, which resemble both fuel cases. Helmholtz frequency (120 Hz) and axial-direction natural acoustic frequency (1170 Hz) are both observed in the figures.

For the blowout condition, pressure oscillation history and frequency analysis both shows different tendency comparing the two fuel cases. For Jet A1 shown in

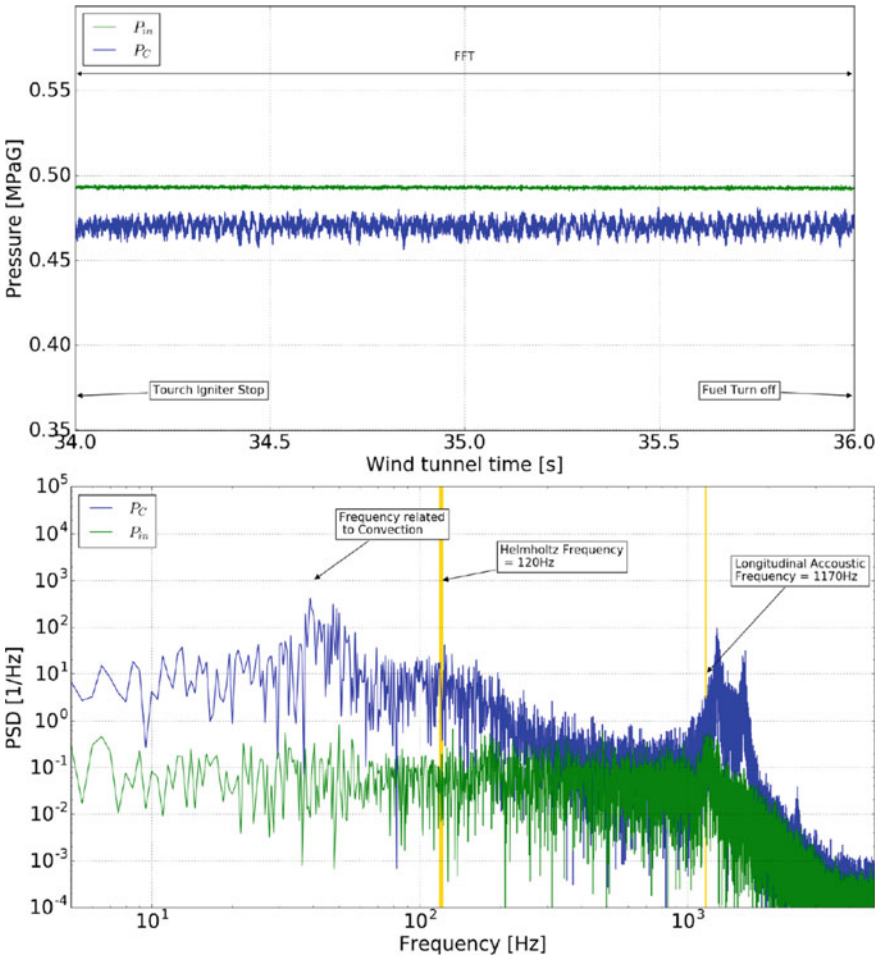

Fig. 22 Pressure oscillation measured (time history and frequency analysis; stable condition ($\varphi = 0.87$) and Jet A1 case)

Fig. 24, periodic vibration was observed before onset of blowout. This suggests that the combustion oscillation occurred was related to Helmholtz-type combustion oscillation. On the other hand, pressure history for HEFA fuel case did not show periodic vibration and was almost irregular with time as seen in Fig. 25. Frequency analysis also shows nearly no clear peak, especially in the low-frequency area. To further investigate this irregular flame oscillation, flame behavior is next compared to the two fuel cases.

Figures 26 and 27 show appearances of spray (Mie scattered image) and flame (CH* chemiluminescence) at unstable combustion conditions ($\varphi = 0.52$) for Jet A1 and HEFA, respectively.

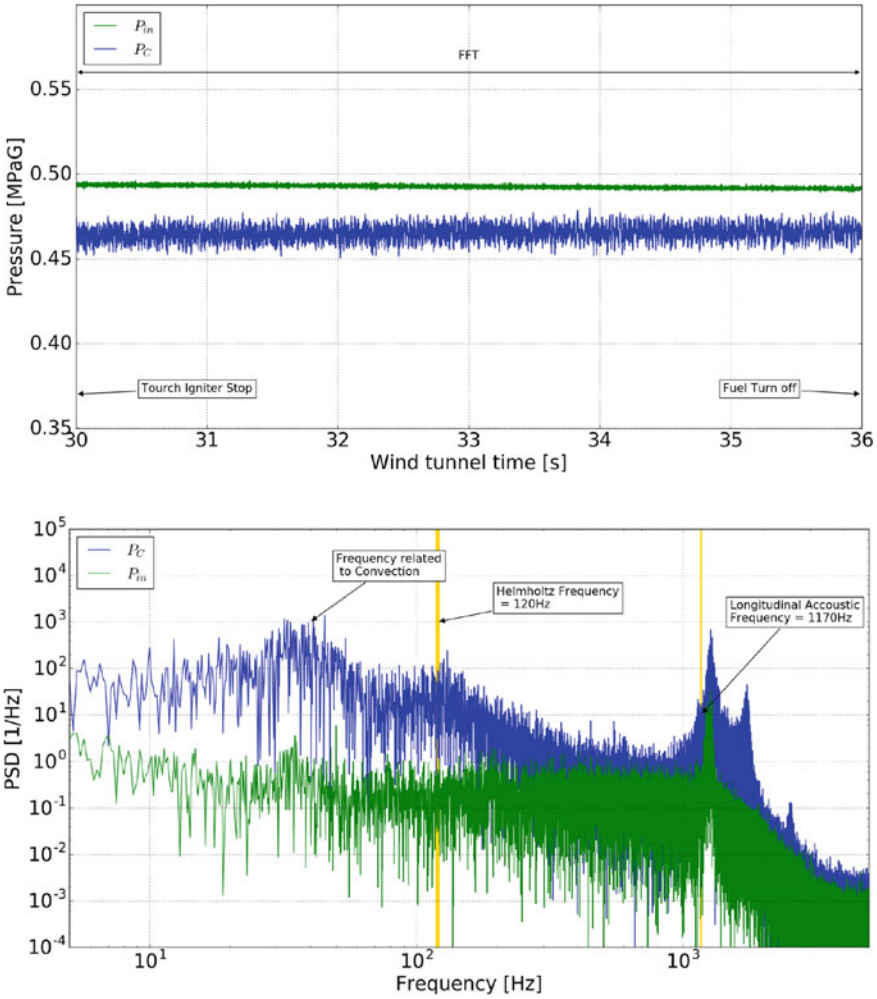

Fig. 23 Pressure oscillation measured (time history and frequency analysis; Stable condition ($\varphi = 0.87$) and HEFA case)

At first, flame appearance shown in Fig. 26 is investigated. Number 1 through 8 shows a flame image for almost 1 period of the periodic oscillation. During the (1) and (2) time period, as the combustion chamber pressure P_C decreases the pressure difference between P_C and incoming air pressure P_{in} increases, and the large pressure difference enhances air entrainment and incoming velocity. This suggests that large amount of fuel spray is introduced due to the large pressure difference. This is in accordance with the following images from (2) to (5) Mie scattered images. Furthermore, an increase in air velocity related to the atomization process might enhance the atomization characteristics. The change of the pressure difference and

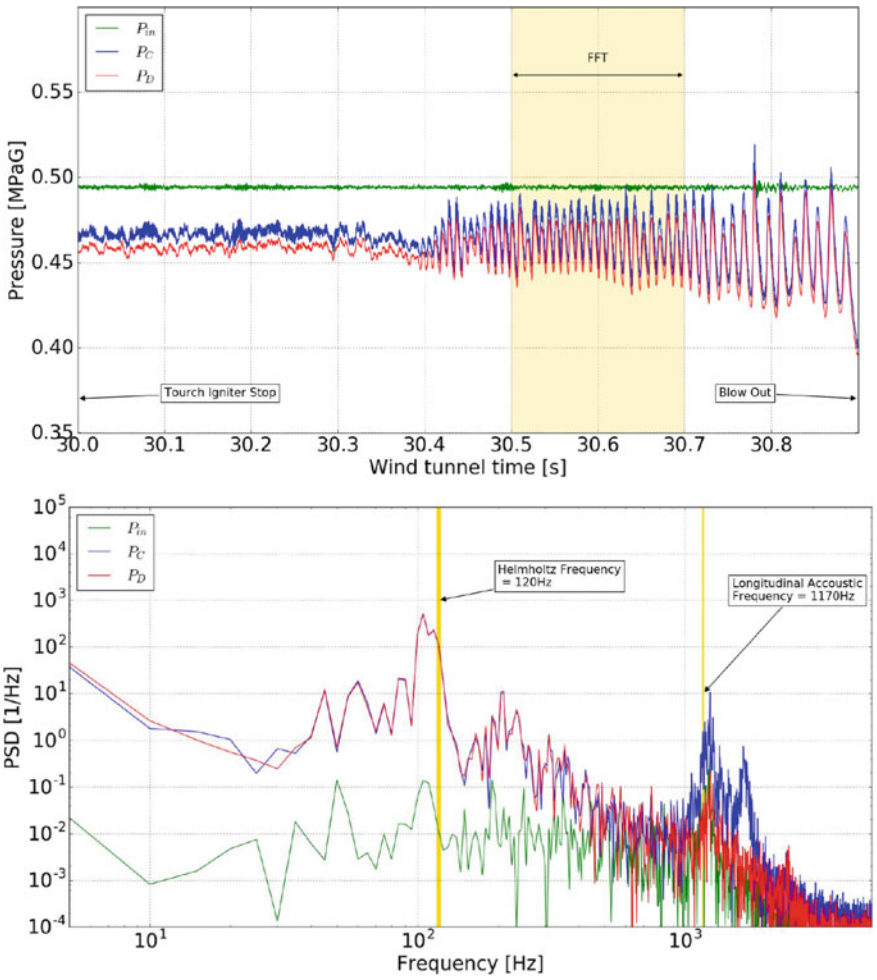

Fig. 24 Pressure oscillation measured (time history and frequency analysis; blow out condition ($\varphi = 0.52$) and Jet A1 case)

the change of the sprays in time has a time delay, and the delay suggests characteristic times for atomization and convection are apparent. CH^* chemiluminescence image from (2) to (7) shows combustion and heat release, thereby time variation of spray and of chemiluminescence also have a time delay. This delay would be related to the time delay due to spray evaporation and chemical reactions. CH^* chemiluminescence images of (5) and (6) are most prominent among the eight images, suggesting that heat release is most intense. In these time period, chamber pressure P_C takes highest value. Phases in variation of heat release and pressure are likely to close each other. Therefore, the oscillation seen in Fig. 24 might be related to the Rayleigh relationship. From these observations, in the case of Jet A1 fuel, the reason for the oscillation

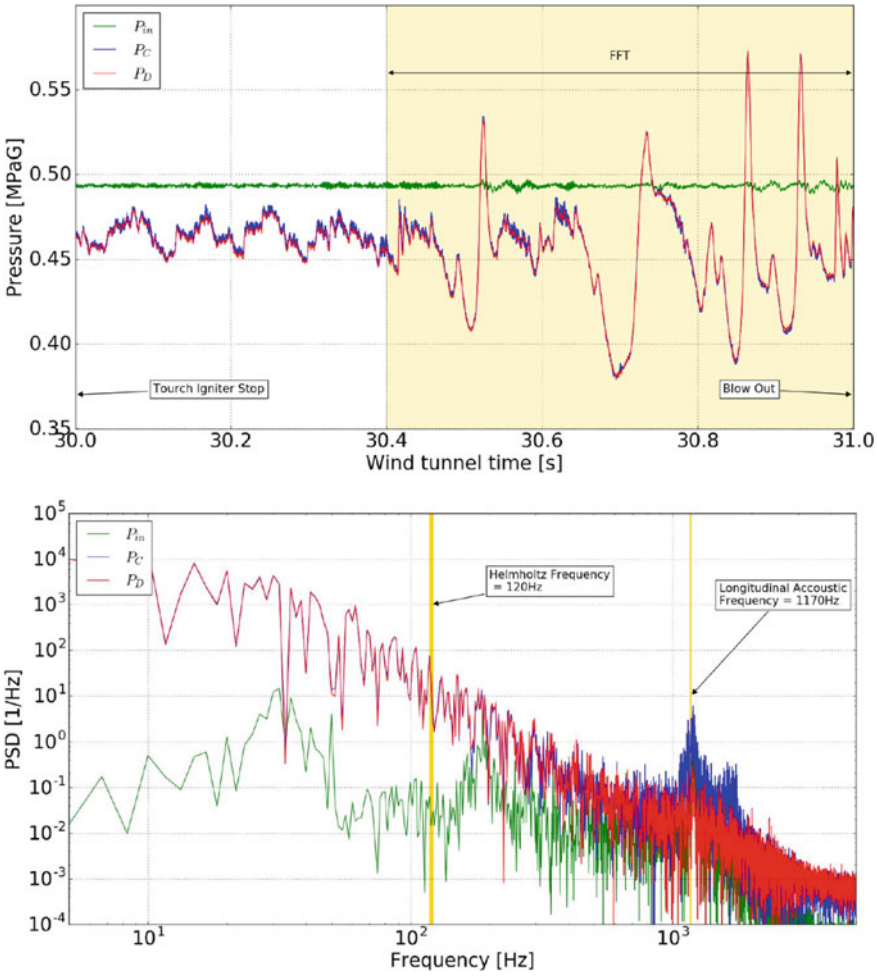

Fig. 25 Pressure oscillation measured (time history and frequency analysis; blow out condition ($\varphi = 0.52$) and HEFA case)

occurrence was the time delay between the pressure and heat release fluctuations was adequate for the excitation of the Helmholtz-type combustion oscillation.

Appearances of spray (Mie scattered image) and flame (CH^* chemiluminescence) at unstable combustion condition ($\varphi = 0.52$) for HEFA seen in Fig. 27 does not show similar causal relationships between spray and chemiluminescence as Jet A1 case seen in Fig. 26.

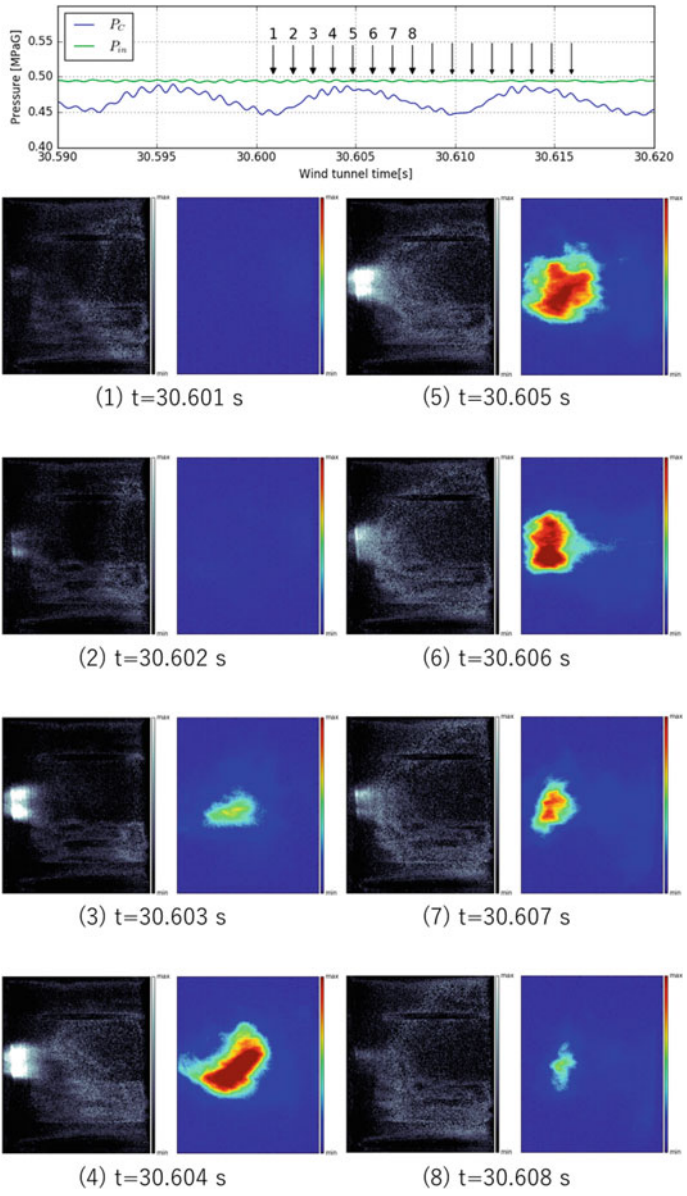

Fig. 26 Appearance of unstable combustion (blow out condition ($\varphi = 0.52$) and Jet A1 case)

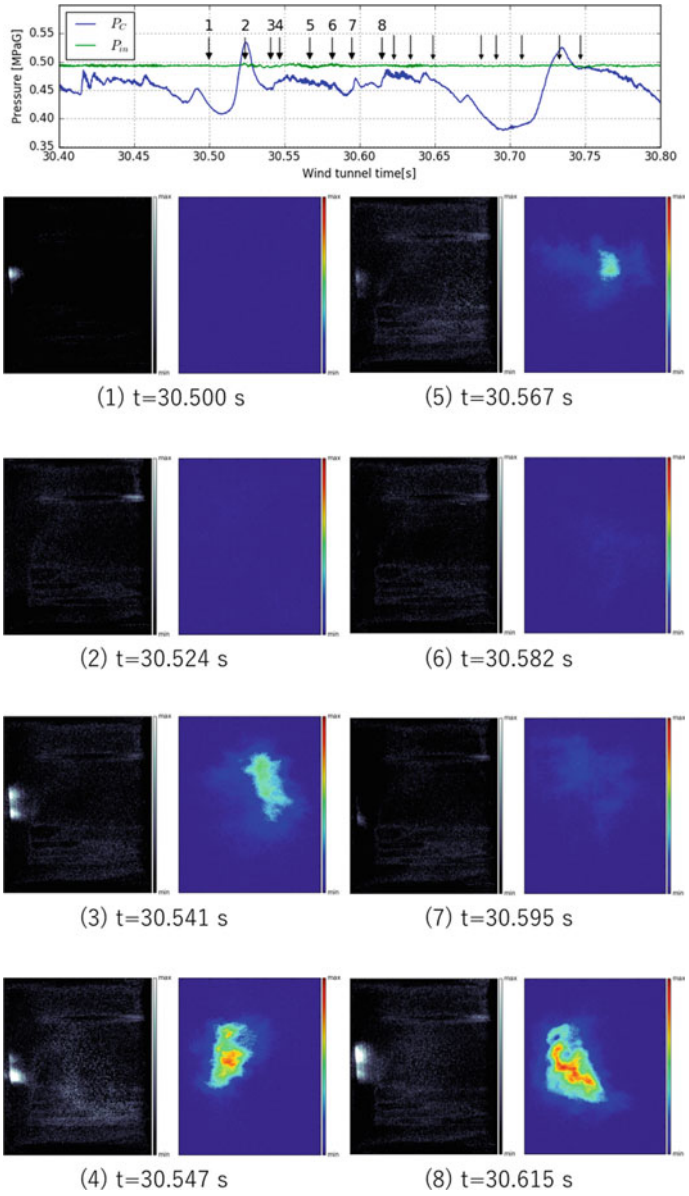

Fig. 27 Appearance of unstable combustion (blow out condition ($\varphi = 0.52$) and HEFA case)

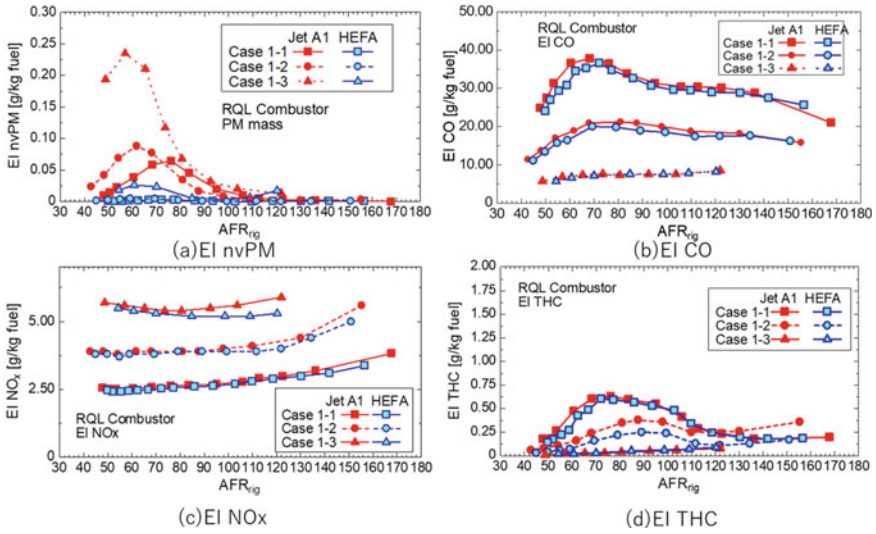

Fig. 28 Emission characteristics for RQL combustor testing (case 1)

3.2 Combustion Testing with RQL Combustor[1]

Combustion rig tests were conducted using two different combustors (case 1: rich burn quick quench lean burn, RQL, Combustor, and case 2: Concentric Lean Burn Combustor). The results obtained from RQL combustor are presented at first in this subsection.

Three inlet air conditions (cases 1-1, 1-2, and 1-3) shown in Table 5 were tested with total air/fuel ratios ranged from about 50 to 150. Jet A1 and HEFA were blended before supplying to the fuel nozzle through a T-junction when a mixture of the two fuel was tested.

Combustion tests with each having 100% HEFA and 100% Jet A1 supplied separately were conducted to investigate the effect of the fuel on the combustion behavior. Figure 28 shows the non-volatile PM (nvPM), NO_x, CO, and THC emission index (in g/kg fuel) as a function of the air/fuel ratio.

The result indicates that the nvPM emission index was greatly reduced with HEFA while other exhaust gas components were like each other.

NvPM emission for each fuel increases with the increase of load (pressure and temperature) intensity. EI CO decreases with the increase of load intensity for both fuels, approaching perfect combustion. EI NO_x increases with the increase of pressure and temperature for both fuels. EI THC decreases with the increase of load intensity for both fuels like EI CO, approaching perfect combustion.

[1] AIAA 2016-4953 [18] and AIAA2019-1772 [19]: reprinted with permission of American Institute of Aeronautics and Astronautics, Inc.

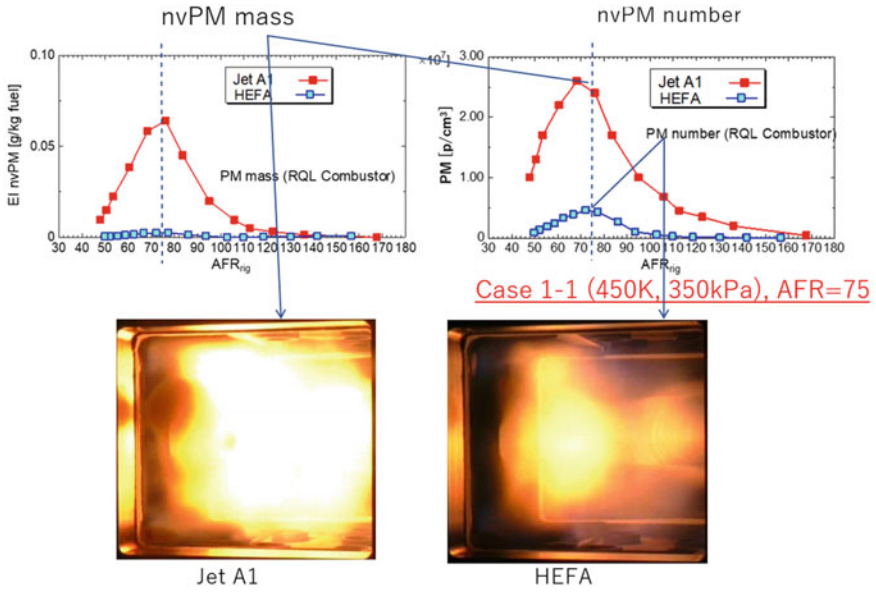

Fig. 29 Comparison of nvPM mass and number (case 1-1; RQL combustor)

Figure 29 shows mass and number of nvPM emission for case 1-1. It also shows that the maximum value of nvPM emission index appeared at the condition of air fuel ratio of approximately 75, wherein 96% reduction of nvPM mass emission index was observed when using HEFA instead of Jet A1, while the peak value of nvPM number with HEFA is about 18% of that with Jet A1. The reduction of nvPM mass with HEFA was more critical than the number of nvPM, indicating that large size nvPMs are decreased with HEFA than Jet A1 and the average size of nvPM with HEFA is smaller than that with Jet A1.

Figure 29 also compares the direct flame images at air fuel ratio of 75 with HEFA and Jet A1 images captured from outside of the pressure chamber by a usual digital camera without changing any conditions of the camera including the aperture. The images show that HEFA had less flame brightness than that from Jet A1 combustion; this is consistent with the above results of the reduced nvPM emission (both on mass and number) when using HEFA. Figure 30 shows spatial distribution of soot showing the KL factor determined using Hottel and Broughton two-color radiometry. KL factor in Jet A1 flame shows a region having large value of KL factor around luminous flame and on the other hand, KL factor in HEFA flame shows smaller value than Jet A1 case. Change of KL factor with the increase of AFR shows a similar tendency with nvPM mass and number.

In order to further examine the effect of the blending ratio of the two fuels to the exhaust gas emission index, the blending ratio of HEFA were changed in increments of 10%, keeping the air fuel ratio at 75. The result is shown in Fig. 31. The results show that both nvPM mass emission index and number density were reduced with

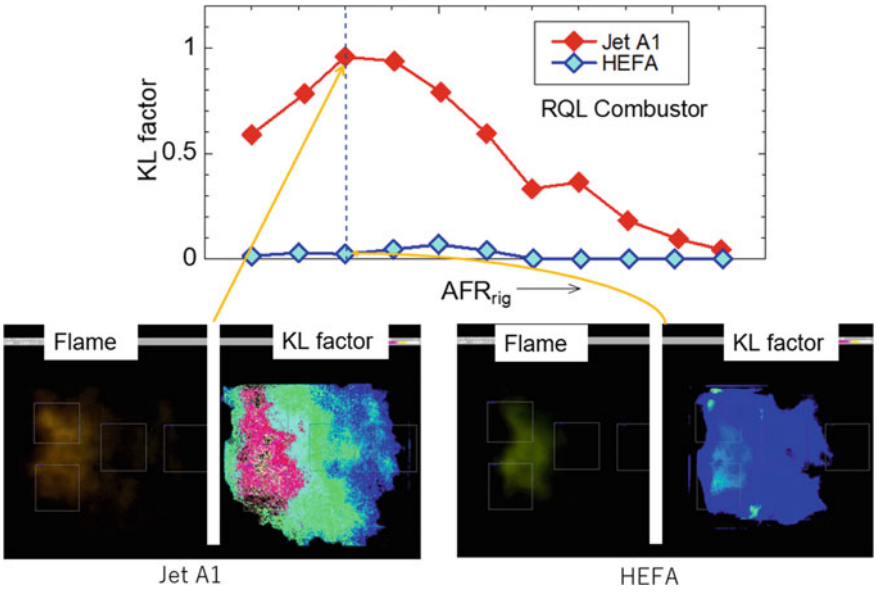

Fig. 30 KL factor taken from Hottel and Broughton two-color radiometry (RQL combustor)

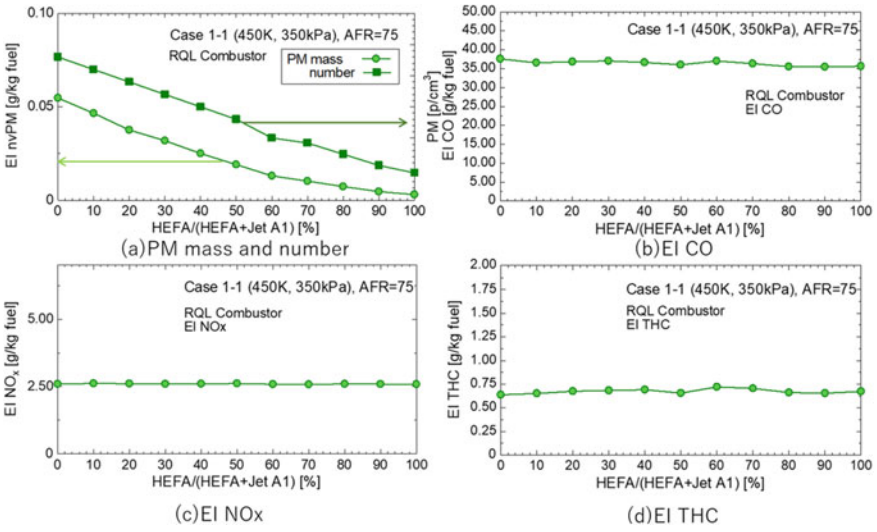

Fig. 31 Effect of fuel composition on emission characteristics (case 1-1; RQL combustor)

an increase in HEFA blend ratio while NO_x, CO and THC remained constant. The decrease rate of nvPM mass and number with an increase of HEFA content in mixture fuel look slightly different by each other. This difference in emission indices and soot distribution would be important for the different mechanisms of agglomeration and perhaps different impacts on environment (through cirrus formation), which requires further investigation.

3.3 Combustion Testing with Concentric Lean Burn Combustor[2]

The results obtained from concentric lean burn combustor are presented in this subsection.

Case 2-1 and cases 2-2 and 2-3 were different in fuel injection schedule. In case 2-1 only pilot fuel was injected, which represents a low load condition. Cases 2-2 and 2-3 had both pilot and main fuel injected and represents a high load condition.

Figure 32 compares the two different fuel injection schedules.

In the results of case 2-1 (pilot only), air fuel ratio was 100 and direct flame images of the condition with pure fuel (both Jet A1 and HEFA) were compared as shown in Fig. 32 (upper side). A blue flame was dominant with HEFA, while a yellow flame was dominant with Jet A1. In case 2-2, both pilot and main burner were fueled. In a previous study, a combustion instability was observed, and its phenomena were reported, when the same combustor and injector configuration were used [21]. As expected, in the present study with Jet A1 as fuel, combustion instability was observed at a pilot fuel ratio of up to 15% (case 2-3). Initially, the fuel injection condition without inducing instability was examined. No combustion instability was observed when the pilot fuel ratio was at 20% for both pure fuel cases (Jet A1 and HEFA). The bottom side of Fig. 32 shows a comparison of the direct flame images when the pilot fuel ratio was 20% and air fuel ratio was 35 (stable combustion condition). The results showed that both main and pilot flames are blue when HEFA was used, while the main flame was blue, and the pilot flame was yellow when Jet A1 was used as fuel.

In the case of no instability cases [Case 2-1 (pilot only) and 2-3 (pilot fuel ratio was 20%)], the emission indices were compared in Fig. 33, indicating that NO_x, THC, and CO emission were like each other. Non-volatile PM was much smaller than in case 2-1, with only the pilot burner operational. A similar tendency was also observed for the cases 1-1 through 1-3 with RQL combustor given earlier in this chapter.

Figure 34 shows a comparison of NO_x emission between the two fuels under the condition of both stable and instable combustion observed in the Jet A1 case (only pilot fuel ratio is different). Figure 34 also shows the stated pressure oscillation,

[2]AIAA 2018-1474 [20]: reprinted with permission of American Institute of Aeronautics and Astronautics, Inc.

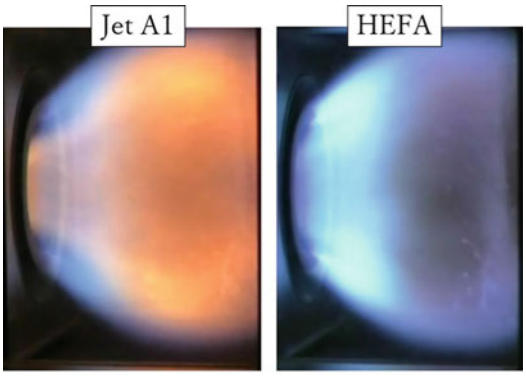

Case 2-1 Pilot only case (pilot burner only, AFR = 100)

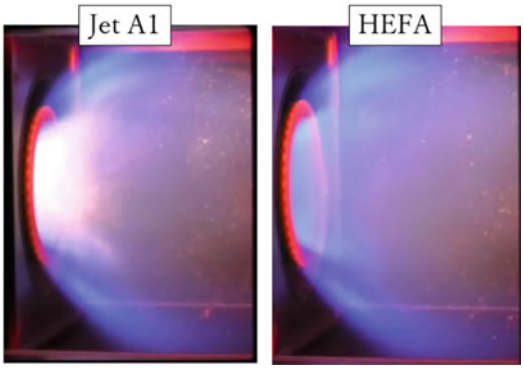

Case 2-2 Pilot and main burner case (AFR ~ 35)

Fig. 32 Comparison of the direct flame images (lean burn combustor cases 2-1 and 2-2)

as measured using a pressure transducer located on the liner wall at the condition where air fuel ratio was 40.7, pilot fuel ratio was 15% and Jet A1 was used as the fuel (top left side of the figure on the bottom). The upper figures on the bottom show time-dependent pressure oscillation while the lower show spectrum of oscillation. The figure shows a pressure oscillation of around 550 Hz using Jet A1 fuel. Right side at the bottom of Fig. 34 shows the same pressure oscillation as mentioned above (with Jet A1) at the condition when air fuel ratio was 38.5, pilot fuel ratio was 15% using HEFA as the fuel. In the HEFA test, no oscillation was observed under any condition as seen from the figure.

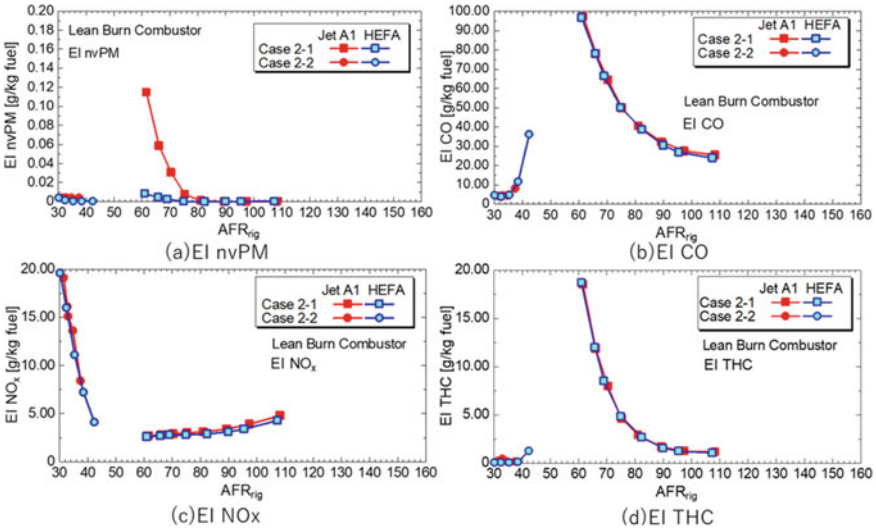

Fig. 33 Emission characteristics for lean burn combustor testing (cases 2-1 and 2-2)

3.4 Discussions

Combustion test cases in which spray and diffusion flame region are dominant, the effect of fuel change from Jet A1 to HEFA is remarkable especially in soot-formation phenomena. The results showed clear reduction of Emission Index (EI) nvPM and number density nvPM for HEFA and mixture fuels compared to pure Jet A1 and this is attributed largely to the reduced aromatic concentration [5]. This tendency was also verified through KL factor distribution taken from Hottel and Broughton two-color radiometry, which is related to soot concentration spatial distribution. Comparison between nvPM mass and number indices, it was suggested that HEFA fuel reduces PM mass but the rate of decrease in number nvPM was less than that in mass, indicating a large number of smaller particles formed. These might affect the ability to form early stage of cirrus cloud. Further, in-detail investigation is necessary.

The other combustion properties, EI of CO, NO_x and THC were almost unaffected by the fuel change. In case 2-3, an unstable condition exhibited when using Jet A1, but no visible instability occurred when using HEFA in the same condition. This might be from the slight differences in atomization behavior due to different properties, such as density and surface tension.

In the present combustor rig test, the fuel composition was well within the stable combustion regime with respect to the lean blowout. Fuel injector testing investigated those lean blowout conditions. The test results showed a slight wider stability regime obtained for HEFA than for Jet A1. This result is in accordance with the consideration given by Corporan and co-workers [22]. Edwards and co-workers [23] evaluated the effect of fuel properties on LBO in the same combustor and the same environment

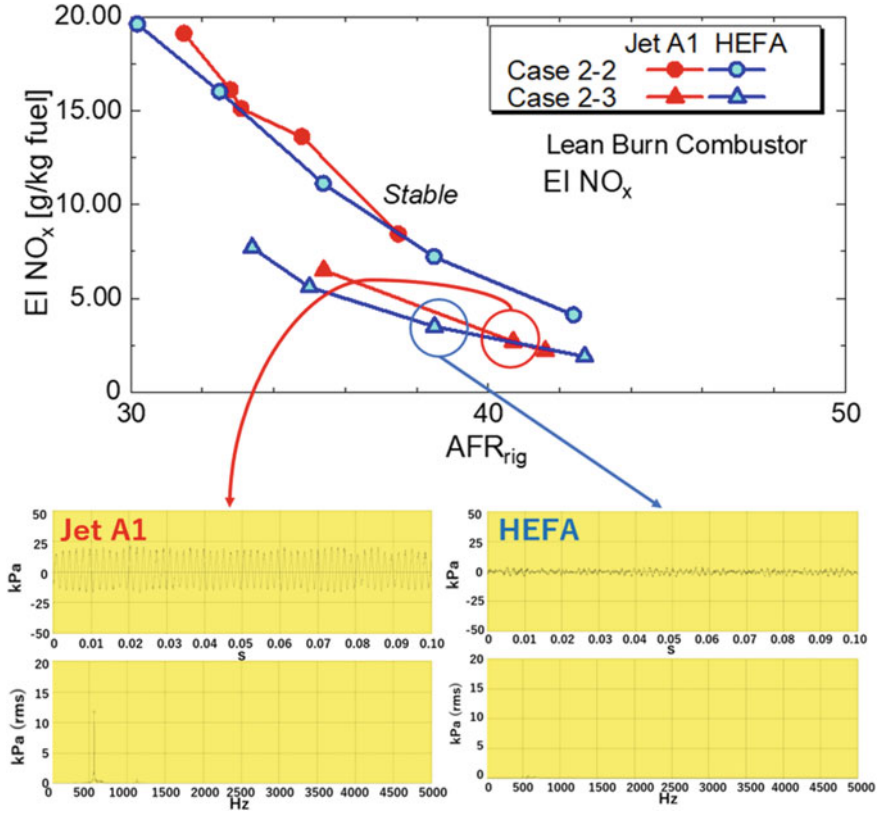

Fig. 34 Stable and unstable combustion in lean burn combustor (cases 2-2 and 2-3)

referencing a phenomenological model developed by Lefebvre [24] as follows:

$$\varphi_{\mathrm{LBO}} = \left[\frac{f_{pz}}{V_{pz}}\right]\left[\frac{\dot{m}_A}{P_3^{1.3}\exp(T_3/300)}\right]\left[\frac{D_0^2}{\lambda_{\mathrm{eff}}\mathrm{LCV}}\right]$$

The first term of the right side of the equation is a function of combustor design. The second term represents the operating conditions. The last term embodies the relevant fuel properties, D_0, λ, and LCV, the diameter of the fuel spray, the evaporation constant, and lower heating value for the fuel, respectively. If the experiments only changed fuels, the ratio φ_{LBO} becomes a ratio of the fuel properties. Ratio of properties utilizing the present results are

$(D_0|_{\mathrm{JetA}}/D_0|_{\mathrm{HEFA}}) = 0.97$ (From SMD in Figs. 15 and 16)
$(\lambda_{\mathrm{eff}}|_{\mathrm{JetA}}/\lambda_{\mathrm{eff}}|_{\mathrm{HEFA}}) = 0.85$ (From Evaporation constant, in Figs. 19 and 20)
$(\mathrm{LHV}|_{\mathrm{JetA}}/\mathrm{LHV}|_{\mathrm{HEFA}}) = 0.98$ (From Heat of Combustion in Table 1).

From these ratios, the ratio of φ_{LBO} from the above equation becomes 1.13. This is in accordance with the present results shown in Fig. 21.

In the previous report using the same combustor [21], a simple acoustic velocity coupling mechanism was proposed as the driving mechanism to generate heat release oscillations which were used to explain the observed oscillation. In the proposed mechanism, there were coupled features inducing the oscillation, including the path of "fuel atomization, evaporation, and mixing."

As explained by Lefebvre and Ballal [5], "the time between the injection of fuel and the region of maximum heat release represents the characteristic combustion time, which is obtained as the sum of the characteristic times for the fuel evaporation, mixing of fuel vapor with air and combustion products to reach a critical reaction temperature and chemical reaction. The system becomes prone to instabilities when the overall combustion time becomes equal to a characteristic acoustic time of the combustor."

Additional measurements of Sauter Mean Diameter indicated that atomization characteristics are slightly better for Jet A1 than HEFA. Evaporation characteristics were better for HEFA than Jet A1 and HEFA is advantageous than Jet A1 in combustion stability point of view. The autoignition characteristics of the conventional jet fuel and alternative jet fuel were investigated using a rapid compression machine by Allen and co-workers [25]. The result showed that alternative fuels ignited more readily than conventional fuels for all tested conditions. This suggests that higher chemical reactivity for HEFA than Jet A1. Overall, among the characteristic times, HEFA is advantageous for some aspects and disadvantageous for others than Jet A1. It was suggested that the slightly different physical properties (density and surface tension) might affect the liquid atomization characteristics for the two fuels. Other characteristics are also affected by the slight difference between physical and chemical properties and conditions. In the unstable combustion seen in lean burn combustor case, a slight difference in fuel properties changed the onset condition of instability.

By introducing HEFA and bio-derived fuels to aviation, the results showed carbon emission reduction that shifted towards carbon-neutrality. If the upper limit of alternative fuels in mixtures for aviation propulsion is increased, the contribution to reduce carbon emission would be enhanced. From these investigations, major issues associated with increasing the ratio of, e.g., HEFA in the fuel mixture above 50% would be the cause in swelling of O-rings, a different energy content due to different density, etc. These drawbacks seem technically solvable in the medium-term perspective. Other than lean blowout conditions, cold start and altitude ignition [26] might be important for the confirmation of wider use of these alternative fuels for aviation.

4 Conclusion

In this chapter, several important aspects of original aviation fuel (Jet A1) and an alternative aviation fuel (HEFA) were compared and investigated.

Chemical and physical property analysis and combustion rig test with two different combustor types were performed and investigated using both fuels and their blends.

The exhaust gas measurement data showed that the non-volatile PM mass reduced when using HEFA and its blends with Jet A1, which was also supported by the flame visualization studies.

Non-volatile particulate matter (nvPM) mass was reduced with HEFA only at pilot mode for the concentric lean burn burner, while NO_x, THC, and CO emissions were similar between the two fuels.

Combustion instabilities were observed with Jet A1 under certain conditions of pilot and main fuel injection mode for the concentric lean burn burner, while those were not observed with HEFA at any conditions within the present test conditions examined. Fuel changes may affect combustion instability characteristics.

Acknowledgements This work was in part supported by JSPS KAKENHI Grant Number 16H04586.

The authors thank Professor Ashwani K. Gupta of the University of Maryland for his comments and revisions.

References

1. National Academies of Sciences, Engineering, and Medicine (2016) Commercial aircraft propulsion and energy systems research: reducing global carbon emissions. The National Academies Press, Washington, DC. https://doi.org/10.17226/23490
2. ASTM D7566-18 (2018) Standard specification for aviation turbine fuels containing synthesized hydrocarbons. ASTM International, West Conshohocken, PA
3. Fukuyama Y, Fujiwara H, Okai K (2009) Alternative fuels and their impact on the turbofan engine design and performance under the realistic flight conditions. In: ACGT paper no. 51, Asian joint congress on gas turbines 2009 (ACGT 2009), Tokyo, Japan 2009 (ACGT2009-051)
4. Okai K, Fujiwara H, Hongoh M, Shimodaira K (2012) Application of a bio-fuel to a single sector combustor for an experimental small aero-engine. In: Asian joint congress on gas turbines 2012 (ACGT 2012), Shanghai, China, 2012 (ACGT 2012–2121)
5. Lefebvre AH, Ballal DR (2010) Gas turbine combustion: alternative fuels and emissions, 3rd edn. CRC Press, Taylor & Francis, New York
6. Mitsubishi-Hitachi Power Systems (2017) An activity of R&D and verification of bio fuel production—a pilot-scaled testing of throughflow production process (in Japanese). http://www.nedo.go.jp/content/100870869.pdf. Accessed 03 Sept 2018
7. Abe Y, Toba M, Mochizuki T, Yoshimura Y (2009) Oxidative degradation behaviour of fatty acid methyl ester in fish oil biodiesel and improvement of oxidation stability by partial hydrogeneration. J Jpn Pet Inst 52(6):307–315 (in Japanese)
8. Glover AR, Skippon SM, Boyle RD (1995) Interferometric laser imaging for droplet sizing: a method for droplet-size measurement in sparse spray systems. Appl Opt 34(36):8409
9. Shigeta Y, Hayashi K, Ichiyanagi M, Hishida K (2012) Measurement of droplet size, velocity and spatial distribution of mass flux in spray by combining focus and defocus imaging technique. Trans Jpn Soc Mech Eng Ser B 78(788):867–880
10. Maeda M, Kawaguchi T, Hishida K (2000) Novel interferometric measurement of size and velocity distributions of spherical particles in fluid flows. Meas Sci Technol 11:L13–L18

11. Nakaya S, Fujishima K, Tsue M, Kono M, Segewa D (2013) Effects of drop-let diameter on instantaneous burning rate of isolated fuel droplets in argon-rich or carbon dioxide-rich ambiences under microgravity. Proc Combust Inst 34(1):1601–1608
12. Hottel HC, Broughton FP (1932) Ind Eng Chem 4(2):166–174
13. Makida M, Yamada H, Shimodaira K (2014) Detailed research on rich-lean type single sector and full annular combustor for small aircraft engine. In: 29th congress of the international council of the aeronautical sciences (ICAS 2014), St. Petersburg, Russia (ICAS2014-0628)
14. Yamamoto T, Shimodaira K, Yoshida S, Kurosawa Y (2013) J Eng Gas Turb Power 135:031502
15. El-Shanawany MS, Lefebvre AH (1980) Airblast atomization: effect of linear scale on mean drop size. J Energy 4(4):184–189
16. Spalding DB (1953) The combustion of liquid fuels. Symp Combust 4(1):847–864
17. Ando S, Wu Y, Nakaya S, Tsue M (2020) Droplet combustion behavior of oxidatively degraded methyl laurate and methyl oleate microgravity. Combust Flame (in press)
18. Okai K, Fujiwara H, Makida M, Shimodaira K, Yamada H, Namakura M (2016) The effect of the fuel change from petroleum kerosene to HEFA alternative jet fuel on the emission of an RQL type gas turbine combustor. In: 14th international energy conversion engineering conference, AIAA propulsion and energy forum (AIAA 2016-4953)
19. Okai K, Fujiwara H, Makida M, Shimodaira K (2019) The effect of the fuel change from petroleum kerosene to HEFA alternative jet fuel on the number of nvPM emission of an RQL gas turbine combustor. In: AIAA aerospace science meeting, AIAA SciTech Forum (AIAA 2019-1772)
20. Okai K, Fujiwara H, Yoshida S, Yamamoto T, Shimodaira K (2018) The effect of the fuel change from petroleum kerosene to HEFA alternative jet fuel on the emission of a concentric lean-burn burner for gas turbine. In: AIAA aerospace science meeting, AIAA SciTech Forum (AIAA 2018-1474)
21. Tachibana A, Saito K, Yamamoto T, Makida M, Kitano T, Kurose R (2015) Experimental and numerical investigation of thermo-acoustic instability in a liquid-fuel aero-engine combustor at elevated pressure: validity of large-eddy simulation of spray combustion. Combust Flame 162:2621–2637
22. Corporan E, Edwards T, Stouffer S, Hendershott T, DeWitt M, Klingshirn C, West Z, Bruening C, Striebich R (2017) Impacts of fuel properties on combustor performance, operability, and emissions characteristics, 55th AIAA aerospace science meeting, Grapevine, Texas (AIAA 2017-0380)
23. Edwards T, Moses C, Dryer F, Evaluation of combustion performance of alternative aviation fuels. In: 46th AIAA/ASME/SAE/ASEE joint propulsion conference & exhibit, Nashville, Tennessee (AIAA 2010-7155)
24. Lefebvre AH (1985) Fuel effects on gas turbine combustion—ignition, stability and combustion efficiency. J Eng Gas Turbines Power 107:24–37
25. Allen C, Toulson E, Edwards T, Lee T (2013) Ignition behaviour and surrogate modelling of JP-8 and of camelina and tallow hydrotreated renewable jet fuel at low temperatures. Combust Flame 160(2):232–239
26. Heyne JS, Colket M, Gupta M, Jardines A, Moder J, Edwards JT, Roquemore WM, Li C, Rumizen M, Year 2 of the national jet fuels combustion program: moving towards a streamlined alternative jet fuels qualification and certification process. In: 55th AIAA aerospace science meeting, Grapevine, Texas (AIAA 2017-0145)

Aerothermal Technologies for Low Emissions Combustors

M. Brend, J. F. Carrotte, and J. J. McGuirk

1 Introduction and Background

For 40 years, improvements in aircraft and engine technology have led to significant reductions in fuel burn and emissions. However, the fleet of commercial aircraft/business jets is expected to double over the next 20 years [1]. Future growth is critically dependent on even lower emission propulsion systems to mitigate climate change effects and threats to human health. Specific targets supported by legislation were proposed in 2001 (ACARE 2020 [2]) and in Flightpath 2050 [3], which established a new datum (2000) and set targets of 75 and 90% reductions in CO_2 and NO_x see Fig. 1. The aviation industry has thus repeatedly committed to a strategy of stringent emissions reduction targets. Reflecting growing concern regarding the impact of particulate matter on human health, further targets are also likely. A recently developed measurement technique for non-volatile particulate matter (NVPM) emissions [4] enabled ICAO's Committee on Aviation Environmental Protection to introduce (Feb. 2019) a new regulatory particle mass and number measurement protocol (CAEP10).

For short and ultra-short haul aircraft, introduction of electrical/hybrid propulsion will help address these emissions reduction requirements. However, it is acknowledged that liquid fuels will be the fundamental energy source for larger/longer range aircraft for the foreseeable future. Reinforcing this, the Joint Press Release [5] by 7 CTOs from leading aerospace manufacturers emphasised that increased R + D effort is also essential for sustainable aviation fuels (SAFs) (exploiting recycled rather than fossil-based carbon) and for further advances in existing aircraft/engine technology.

M. Brend · J. F. Carrotte · J. J. McGuirk (✉)
Department of Aeronautical and Automotive Engineering, Loughborough University, Loughborough LE11 3TU, United Kingdom
e-mail: j.j.mcguirk@lboro.ac.uk

© Springer Nature Singapore Pte Ltd. 2021

A. De et al. (eds.), *Sustainable Development for Energy, Power, and Propulsion*, Green Energy and Technology,
https://doi.org/10.1007/978-981-15-5667-8_14

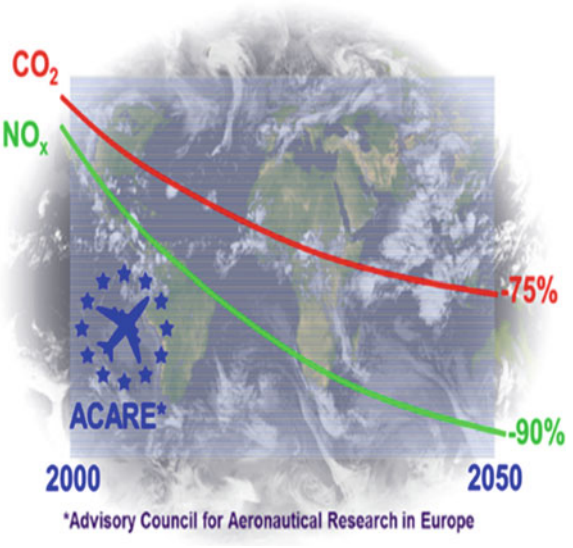

Fig. 1 Flightpath 2050 [3] emissions targets

Improvements must obviously be sought for the rich burn RQL design paradigm—the standard approach for the last 30+ years (Rich burn—Quick quench—Lean burn, (Mosier and Pierce [6])). However, the current preferred methodology to meet NO_x targets is development of lean burn combustion technology. Reduced CO_2 emission is achieved via increasing the thermal efficiency via higher operating pressure ratio (OPR). Unfortunately, since this increases combustor temperature, it also increases NO_x. This is exacerbated in RQL combustors where the FAR (fuel/air ratio) changes from a rich primary zone mixture (increased flame stability) to a lean mixture further downstream, passing through the stoichiometric state where flame temperature and NO_x production rate are highest. A different combustion concept is needed to reduce CO_2 and NO_x simultaneously. Mixture FAR must be maintained on the lean side of stoichiometric as far as possible, with stoichiometric regions being minimised. Several lean burn strategies have been proposed (Li et al. [7]); the basic concept being developed by most engine manufacturers (Lean Direct Injection—LDI) is based on:

(i) a larger effective area fuel injector—to pass up to 70% of compressor efflux air (2–3 times that in RQL systems) with no increase in combustor pressure drop,
(ii) multiple swirlers and at least two fuel injection locations per injector—typically a central pilot stage (for stability/ignition at low power), and a radially outboard main stage (optimised for low NO_x and medium/high power) (Lazik et al. [8]).

However, whilst the LDI concept is a promising route for NO_x reduction, integration of a high mass flow injector into the engine requires careful consideration if adverse consequences on the combustion system and upstream/downstream turbomachinery are to be avoided. Some lean burn integration issues which may require substantial change to combustion system aerothermal elements and the design process are:

(i) the established aerodynamic design for minimising total pressure loss at the compressor/combustor interface—the pre-diffuser/dump diffuser combination (Fishenden and Stevens [9], Klein [10])—may need alteration,
(ii) high quality airflow feed to all injector swirlers will be important,
(iii) spray formation and fuel/air mixing will be changed from RQL systems due to staged fuel delivery,
(iv) the combustor/turbine aerodynamic interface will change dramatically—lean burn combustors do not include primary/secondary dilution jets as in RQL designs, thus aerodynamic characteristics at combustor exit will be quite different—highly swirling flow and velocity/temperature/turbulence profiles upstream of turbine NGV will differ from conventional combustor practice,
(v) much less air is available for combustor wall/NGV cooling, more efficient cooling arrangements will be required (perhaps even cooled cooling air),
(vi) lean burn combustors are more prone to combustion-induced thermo-acoustic instabilities—more attention must be paid to acoustic characteristics of the combustor, in particular the fuel injector,
(vii) CFD methods developed for RQL systems need to be altered/validated for lean burn conditions.

A review by McGuirk [11] has discussed the aerodynamic challenges posed in aeroengine gas turbine combustion systems. The present paper describes research carried out at Loughborough University to extend this to include all aerothermal aspects of lean burn combustors.

2 Combustor/Turbomachinery Matching

2.1 Compressor/Combustor Interaction

Figure 2 indicates the relative size, shape, and flow split differences between rich burn and lean burn combustor architectures (left) and typical fuel injector geometries (right).

Proper aerodynamic matching of the compressor/combustor interface needs careful attention, with increased injector size/flow introducing increased compressor/combustor interactions. It will be shown below how the stronger circumferential variation of flow into (and static pressure on) the combustor head can feed upstream and may disturb compressor OGV/pre-diffuser flow, increasing losses, even possibly forcing the compressor off its design line. The deeper flame tube adversely affects system loss by increasing annulus flow turning within the dump region. Finally, an increased mismatch occurs between pre-diffuser exit height and injector inflow, introducing the risk of poor quality swirler air supply. The presence of a two-way interaction between compressor OGV wake flow, pre-diffuser flow, and the combustor in RQL systems is well known. Turbulence in the OGV wakes helps avoid pre-diffuser separation (Stevens et al. [12], Barker and Carrotte [13]) and high

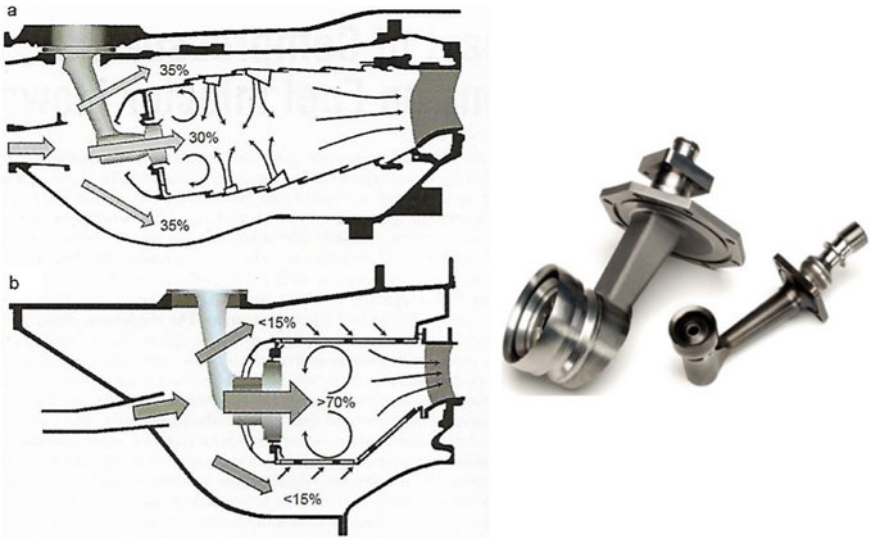

Fig. 2 **Left** a Rich burn, b Lean burn architecture and typical flow split. **Right** Comparison of lean and rich burn fuel injectors

static pressure on the pre-diffuser centreline at its exit plane caused by combustor blockage drives flow towards the walls, further stabilising pre-diffuser wall boundary layers (Klein [10]). It is essential that any experimental studies undertaken to investigate these aerodynamic aspects are at operating conditions as closely representative of the engine as possible. McGuirk [11] has outlined the technique developed at Loughborough to achieve this in a cost-effective, isothermal, atmospheric pressure, fully annular, test facility (full details in Denman [14]). A cross-section schematic of the rig is shown in Fig. 3 (top), with a Perspex combustor model being lowered into the rig in Fig. 3 (bottom). NB—the rig is vertically mounted with an under-floor plenum.

To ensure pre-diffuser inlet conditions match engine operating conditions, a bespoke 1½ stage compressor (IGV + rotor) is installed. This is designed to deliver pitch-averaged radial profiles of total pressure, axial velocity, and swirl angle expected at outlet from the final rotor stage of a multi-stage compressor (from CFD or industrial test rig data). OGV, pre-diffuser, dump diffuser, combustor, and inner/outer casing can be made comparable to engine geometry, although from cheaper/more convenient materials (Perspex, 3D printed rapid prototype material) as only atmospheric temperature/pressure (non-reacting flow) is involved in these tests. The flow is driven by a combination of rotor plus an external fan pumping air into the under-floor plenum. This is ideal to ease rig start-up and allows sufficiently high OGV chord-based Reynolds numbers to be achieved to avoid boundary layer transitional effects ($>2 \times 10^5$). Throttle valves in the downstream exhaust flange maintain correct mass flow splits into injector and flame tube inner/outer annuli. Several entry points for

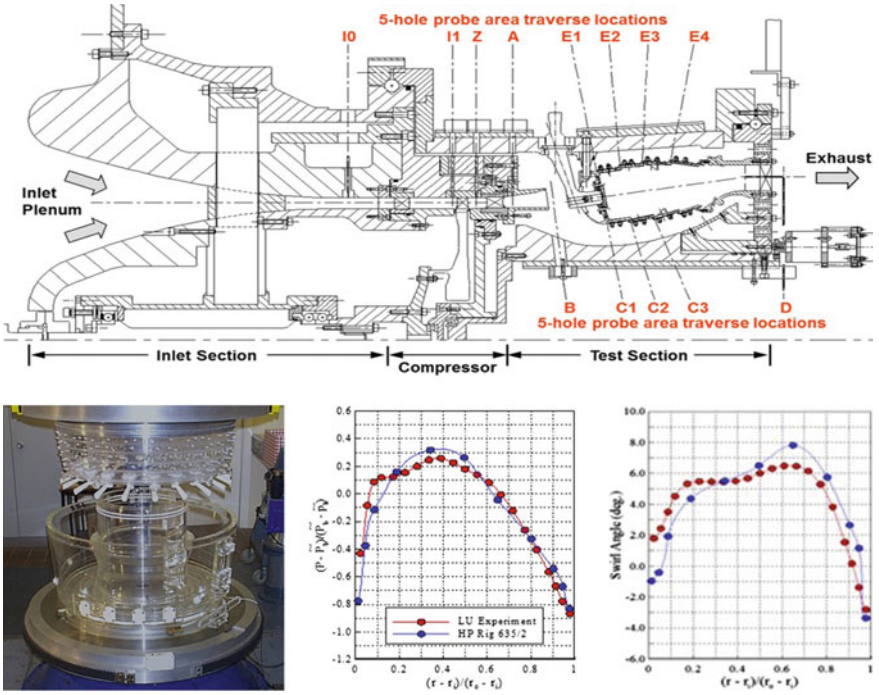

Fig. 3 **Top** Cross-section of fully annular combustion system rig with compressor. **Bottom** Perspex combustor and pre-diffuser exit data: total pressure, flow angle

pneumatic probe traverse are provided (Fig. 3) to allow measurement of total pressure profiles and complete mapping of losses throughout the combustion system. Adoption of this strategy means that the significantly increased cost/complexity of a high pressure multi-stage compressor is avoided. The success of this strategy is illustrated in Fig. 3 (bottom right). Comparison of Loughborough atmospheric rig data at pre-diffuser exit with measurements for the same OGV/pre-diffuser system from a high pressure multi-stage compressor rig at Rolls-Royce demonstrates excellent agreement.

Walker et al. [15, 16] have exploited this test facility to investigate compressor/diffuser/combustor aerodynamic interactions in lean module combustors using the annular test geometry shown in Fig. 4. The RQL design practice for pre-diffuser/dump diffuser systems, i.e. a 'dump gap' ratio $d/h = \sim 1.0$ (d = distance of pre-diffuser exit to combustor head, h = pre-diffuser exit height) has been adopted. This practice allows maximum pre-diffuser area ratio for a given length (hence minimised dump loss).

The question is: does this design rule remains optimum if flow into the injector is doubled? Figure 4 indicates that the simplified combustion system chosen captures the essential elements of a lean burn design—increased radial depth/increased percentage of compressor efflux entering the combustor cowl. Complex injector

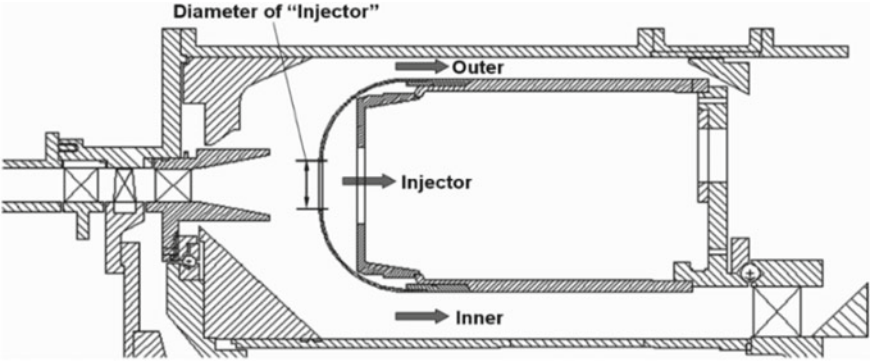

Test No.	'Injector' Diameter (mm)	Mass Flow Split, % (Inner/Cowl/Outer)
1	40.0	35/30/35
2	52.5	25/50/25
3	61.5	15/70/15

Fig. 4 **Top** Annular $d/h = 0.8$ test rig. **Bottom** Summary of test configurations

geometry was avoided and simulated in these experiments by the presence of 20 simple round holes (diameter D). Figure 4 also presents the test matrix studied; holes of increasing D were used to represent increasing injector effective area, with test runs for 30/50/70% of flow entering the combustor cowl; the remaining flow was equally split between inner/outer annuli.

All tests were carried out with $d/h = 0.8$; measurements first examined the upstream extent of the potential field due to the high combustor cowl impingement pressure between injectors. Figure 5 (top) illustrates results at rotor exit via measured pitch wise averaged mean axial velocity radial profiles. These indicate that at 30 and 50% injector flow rotor exit conditions change only marginally. However, for the 70% flow condition, the rotor flow has clearly been altered, showing a strong flow deficit at rotor tip.

The outer wall rotor exit static pressure data in Fig. 5 indicate that at 50% only small variations occur in measured pressure over a circumferential distance of two combustor sectors. These are due to the upstream potential field of flow impingement on OGV leading edges (eight OGVs per combustor sector). A totally different shape emerges for 70% cowl flow—low pressure in-line with injectors and high pressure in between (OGV-induced fluctuations still visible). The cowl flow-induced variation is ~5% of rotor total pressure rise, more than sufficient to force the rotor to move up and down its characteristic, an obviously adverse effect. A further cause for concern was that high mass flow injectors at the standard dump gap remove the stabilising property of combustor blockage (higher static pressure on pre-diffuser exit centreline, which drives flow towards pre-diffuser walls, delaying separation). Figure 5 (bottom right)) displays pre-diffuser exit static pressure profiles for $d/h = 0.8$ for the various

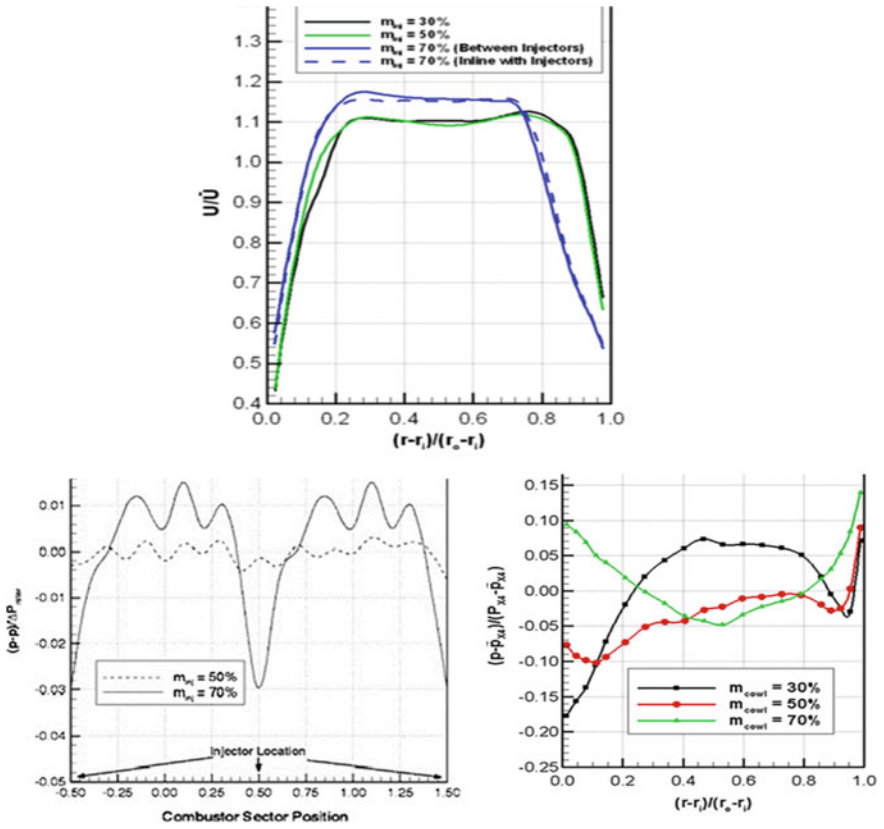

Fig. 5 **Top** Pitch-averaged mean axial velocity radial profiles at rotor exit. **Bottom left** Rotor exit static pressure circumferential profiles. **Bottom right** Radial profiles of pitch-averaged static pressure at pre-diffuser exit

cowl flow rates. At 30%, the profile has a distinctive '*n*' shape indicating a positive blockage effect. As cowl flow increases, the profile gradually changes, and at 70%, a '*u*' shape is seen (pressure lower in the centre than the walls), which is detrimental to end wall boundary layers remaining attached. Walker et al. [15] present further measurements which confirm that at 70% flow and a $d/h = 0.8$, there is clear evidence of a worsening of pre-diffuser exit profiles—the inner wall boundary layer is close to separation, the OGV loss coefficient has risen, and system total pressure loss (rotor to combustor feed annuli) has also increased by almost 20% [15].

It is clear that RQL dump gap design rules do not apply to high mass flow lean module combustors. Increasing the dump gap is the obvious solution to avoid rotor forcing, and this was studied by Walker et al. [16]. Their measurements showed that increasing dump gap to 1.2 or 1.6 removes the undesirable rotor forcing. However, increasing d/h further weakens the upstream combustor blockage effect that creates

the boundary layer stabilising '*n*' shaped static pressure profile at pre-diffuser exit—the '*u*' shaped profile persisted at higher *d*/*h* values. As a consequence, the flow quality within the pre-diffuser (already suspect in the inner wall boundary layer at $d/h = 0.8$) deteriorated further. At $d/h = 1.2$, the boundary layer was incipiently separated, and for 1.6, it was in very poor condition showing clear signs of separation. Thus, to operate in lean burn modules at increased dump gap, either the pre-diffuser area ratio must be reduced to remove separation or a method must be found to re-design the pre-diffuser to allow the same (or possibly increased) area ratio at the same pre-diffuser length without separation and without needing any combustor blockage stabilisation assistance. One novel technology developed at Loughborough to achieve this is the integrated OGV/pre-diffuser (IOGV) concept Walker et al. [17].

Barker and Carrotte [18] had noted that high turbulence levels/secondary flow at OGV exit exerted significant influence on end wall boundary layer growth and helped delay separation. A flow control approach to coupled OGV/pre-diffuser design was thus adopted in [17] to allow maximum area ratio whilst maintaining flow quality. First, a datum OGV geometry was designed from a purely compressor viewpoint (removal of exit swirl). This resulted (for a 30%, $d/h = 0.8$ condition) in an area ratio of 1.8. Then, an IOGV design was created by manipulation of the datum blade cross-section at a series of radial heights from the hub to introduce blade lean (circumferential cross-section movement) and sweep (axial movement). Small alterations were also made to trailing edge camber to reduce residual swirl. The modified spanwise aerodynamic loading induced secondary flows which drove fluid towards each end wall, off-loading the wall boundary layers. RANS CFD was used to vary lean, sweep, and camber until an optimum area ratio at the same axial length as the datum design was achieved. The area ratio was increased to 2.23 (IOGV) from 1.8 (Datum).

Figure 6 illustrates the two geometries created. Comparison of measured axial velocity contours and secondary flow vectors at OGV exit indicated relatively thin wakes but thick low momentum regions near the hub and tip for the datum design. In contrast, the IOGV geometry has near-wall regions that are thinner than in the datum case but a thicker and deeper wake in the central region. Since this region does not experience wall shear stresses, it is less prone to separation when flowing through the diffuser. The success of this IOGV approach is indicated best by comparison of measured axial velocity profiles at pre-diffuser exit (Fig. 6 (bottom right)). Notable improvement in the quality of the end wall boundary layers at pre-diffuser exit is evident. NB.-although the IOGV method development/validation was carried out in [17] for a 30% injector flow, the methodology is clearly also applicable to lean burn pre-diffuser design.

The second area of concern related to compressor/lean burn combustor interaction is the height mismatch between pre-diffuser exit and injector inlet. This has been studied by Ford [19], Ford et al. [20] and Williams et al. [21]. The extent of mismatch is illustrated in Fig. 7 (top left), which shows a typical pre-diffuser exit axial velocity contour map (over one combustor sector and for a compressor producing a hub-biased outlet profile), with the downstream injector cross-section superimposed. The central (pilot) injector passage is aligned with the pre-diffuser outlet flow, but the air feeding the main swirler (its outer passage in particular) has to negotiate a circuitous

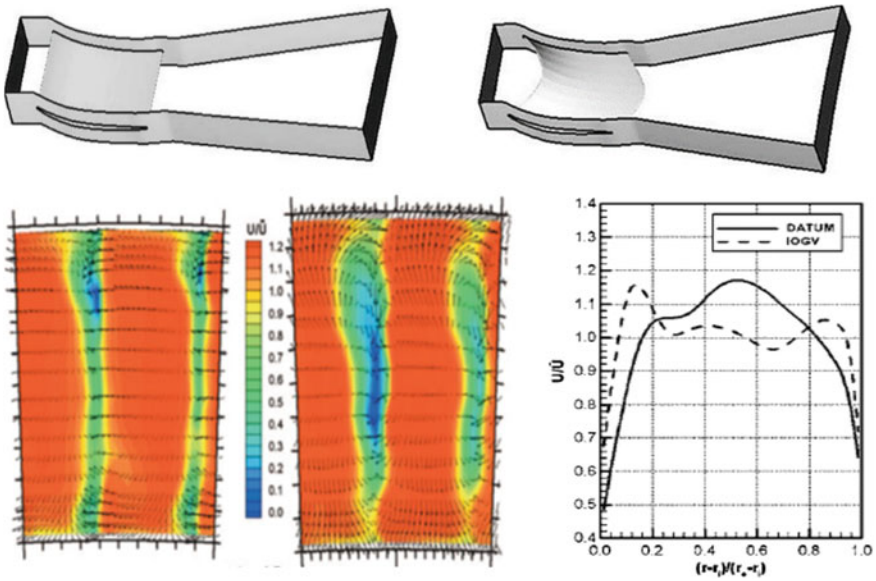

Fig. 6 **Top** Datum and IOGV geometries. **Bottom** Measured OGV exit axial velocity flow (left) datum (right) IOGV, pitch wise averaged axial velocity profiles

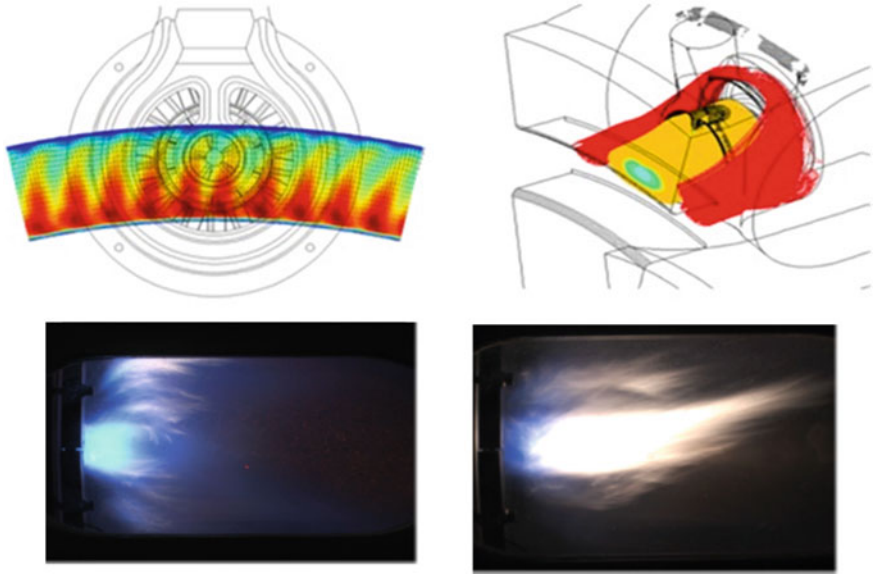

Fig. 7 **Top** Mismatch between pre-diffuser exit and injector (left), CFD deduced capture stream-tubes of various injector passages (right). **Bottom** Lean injector flame photos–plenum fed (left), with inlet flow simulation (right)

route, particularly to enter the top and bottom of the swirler. This will lead to non-uniformity in the velocity around the circumference of this swirler passage, which will have consequences for the fuel air ratio distribution inside the combustor. Details of the non-uniform feed were revealed in the CFD investigation of Ford et al. [20]. This showed that non-uniformity was exacerbated by the streamtube fraction of the pre-diffuser flow which feeds the outer swirler passages. Figure 7 (top right) illustrates that the outer swirler streamtube capture originates in two vertical 'pillars' of pre-diffuser exit flow. Since this flow has to undergo considerable re-distribution before entering the annular swirler entry area, it is highly unlikely to result in a uniform injector entry flow.

The impact of the height mismatch and the importance of employing engine representative inlet conditions in rig testing of lean burn injectors was underlined in the measurements of Williams et al. [21] shown in Fig. 7 (bottom). Whilst the test carried out did not exactly reproduce compressor/pre-diffuser conditions (no upstream rotor was included), a letterbox-shaped slot placed at the pre-diffuser exit location relative to the injector did reproduce the flow area mismatch. Combusting flow was investigated using Jet A1 fuel at an intermediate pressure of 5 bar and air temperature of 650 K. Figure 7 (bottom) shows two flame images taken with plenum-fed inlet (left) and letter-box inlet conditions (right)—a large difference in flame structure results.

The extent of injector non-uniformity was quantified in the measurements of Ford et al. [20] in the non-reacting fully annular facility of (Fig. 3). A single hot-wire was used to measure the flow on the exit plane of the main outer swirling passage resulting when fed by the inlet flow arrangement of Fig. 7 (top left), see Fig. 8 (left). Note that the swirl introduced causes the flow to rotate ~45° between entry and exit from the swirler passage. Variations are seen which correspond to swirl vane wakes and also the bulk maldistribution caused by the 'pillar' feed arrangement. Radial averaging provides a better picture of the extent of variations due to these two effects (Fig. 8 (right)). Vane wakes produce variations of ~±5% of the mean, whereas the

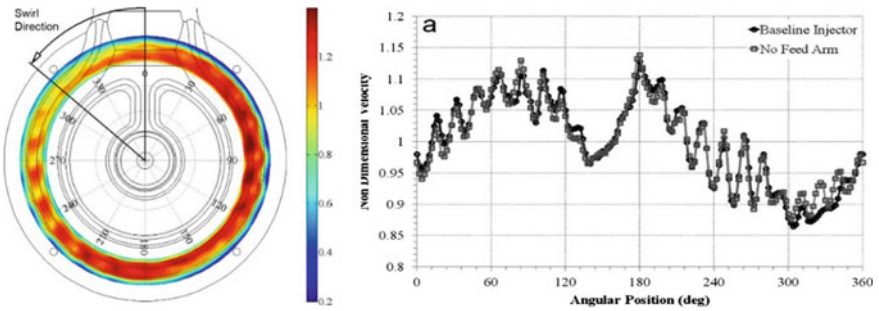

Fig. 8 **Left** Injector exit velocity contours (main outer passage, viewed looking downstream). **Right** Radially averaged circumferential distribution

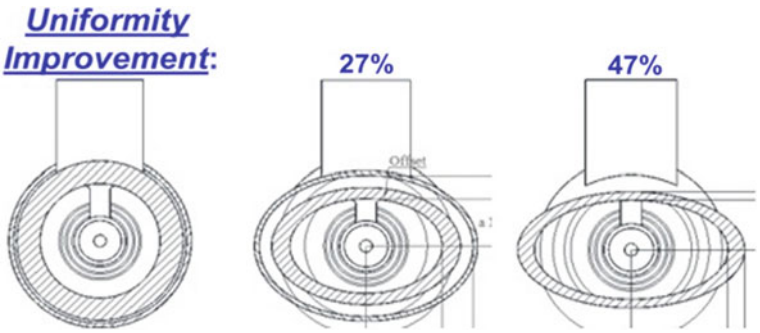

Fig. 9 Improvements in flow uniformity of outer swirler passage in lean burn fuel injector [19]

non-uniformities resulting from the maldistributed feed are around twice as large as this.

Finally, Ford [19] proposed injector technology modifications that would help reduce the non-uniformity; these take advantage of additive manufacturing techniques to alter the injector inlet to conform better to the capture streamtube shape (Fig. 9). Measurements in the same facility indicated significant improvements in uniformity with this technique compared to an axisymmetric design.

2.2 Combustor/Turbine Interaction

Knowledge of temperature traverse at combustor exit is a pre-requisite for HP turbine design since this is an important input into turbine cooling arrangements. Exit traverse is conventionally measured on high pressure combustor test rigs via the non-dimensional temperature: $T^* = (T - \overline{T})/(\overline{T} - T_{\text{ref}})$, where $\overline{T}$ is the temperature averaged over a combustor sector and T_{ref} is a reference temperature (temperature is usually extracted from gas analysis measurements). Combusting test rigs have obvious disadvantages—high operating costs and but data are typically taken with approximate injector inlet conditions (no compressor), which has been shown to be of some importance.

Cha et al. [22] and Dhopade et al. [23] have reported combined CFD and experimental investigations describing how an isothermal, atmospheric pressure facility (Fig. 3) can be used to deliver exit traverse data at reduced cost and including representative injector inlet conditions (NB—for reasons given below, this technique is only applicable to rich burn systems). Combustor/turbine interaction is normally handled using an 'interface plane' around one turbine NGV chord distance upstream of the NGV where flow/temperature distribution is only marginally influenced by the NGV potential field. Isothermal measurements (representative injector inlet flow but no NGV) are carried out by seeding injectors with CO_2 gas. This is sampled at the combustor interface plane into an IR gas analyser, which corrects for

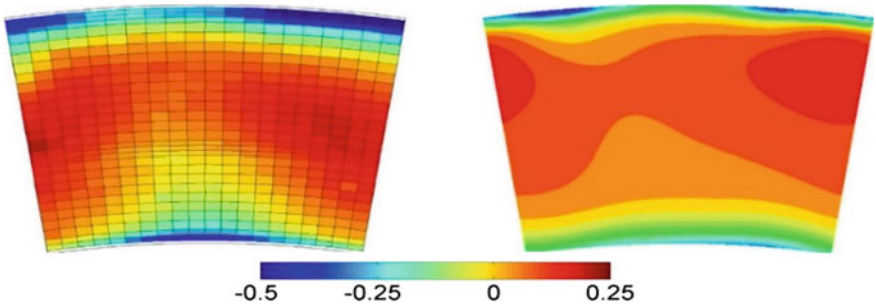

Fig. 10 Combustor interface plane contours: CO_2^* from isothermal rig (left), from RANS CFD (right)

atmospheric CO_2 levels. The equivalent to T^* defined using CO_2 mass fraction is $CO_2^* = (CO_2 - \overline{CO_2})/\overline{CO_2}$. Cha et al. [22] present a RANS CFD prediction (single sector) using conditions as in the measurements. Interface plane comparison between CFD and rig data showed good agreement (Fig. 10).

Further evidence that this technique produces useful exit traverse data was confirmed by comparing measurements made in industry on a high pressure combusting rig (different combustor geometry to [22]) with Loughborough rig isothermal data (Fig. 11), again showing good agreement. Cha et al. [22] analysed their CFD predictions to identify that the reason there is a good match between isothermal and combusting data is that the T^* (or CO_2^*) distribution on the interface plane is dominated by the high turbulent mixing of the dilution jets with only weak influence of density variations (NB—this is the reason that this practice is only relevant to RQL combustors since lean burn systems do not contain dilution jets).

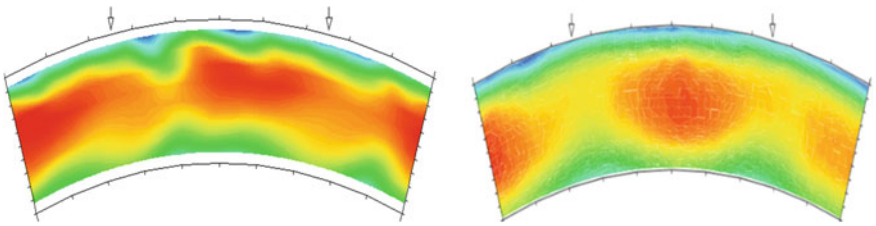

Fig. 11 Combustor interface contours: (left), T^* combusting, (right) CO_2^* isothermal

3 Combustor Cooling

3.1 Effusion Cooling

Reduction in cooling air for the combustor liner has prompted a search for more efficient cooling technologies. Manufacture of liner walls from single/double-skinned tiles, including combinations of impingement and effusion hole arrays, has received considerable attention. Choice of the optimum geometric arrangement requires rapid and accurate methods for testing/comparing heat transfer performance to assist design down select. Krawciw et al. [24] describe a technique for evaluation of adiabatic film cooling effectiveness of effusion cooled geometries. A continuous flow wind tunnel at ambient conditions (Fig. 12) supplies cross-flowing mainstream air (combustor side); coolant is delivered via a plenum arrangement and comprises an air/nitrogen mixture set by two flow controllers. Both mainstream and coolant flow are at ambient temperature, with cooling film/mainstream mixing quantified by mass transfer measurement.

Optical access to the test plate is via a plain float glass window. Adiabatic film effectiveness is measured using a pressure sensitive paint (PSP) technique; the paint is applied to the 'hot' side of the test plate and when illuminated with light (wavelength = 447.5 nm) emits light with an intensity proportional to the partial pressure of O_2 on the test plate, detected via a digital camera. After calibration, adiabatic effectiveness

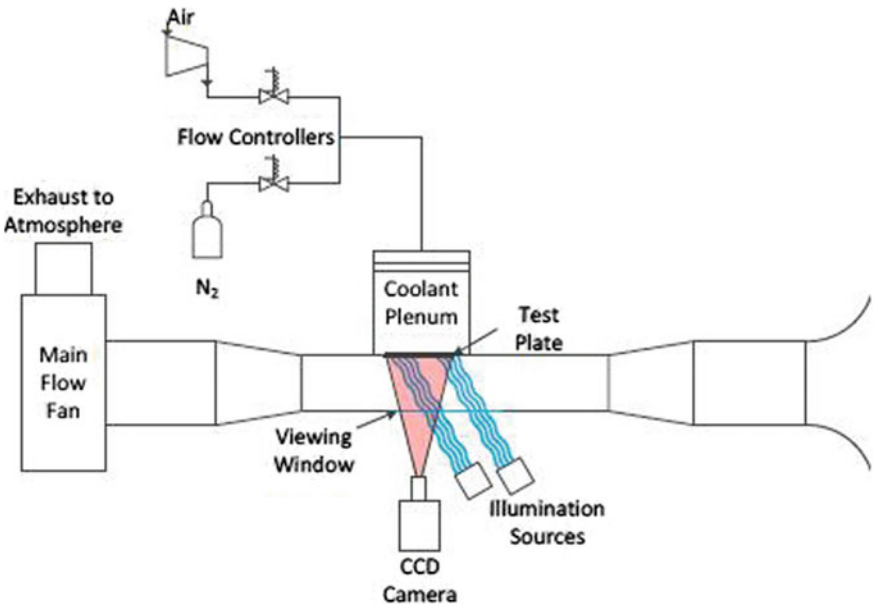

Fig. 12 Wind tunnel schematic for adiabatic film effectiveness measurements

is calculated using a heat-mass transfer analogy. Tests covered a range of coolant blowing ratios, with aerodynamic scaling used to match Re and blowing ratios of interest.

The effusion test plates in [24] (Fig. 13 (top)) were produced using a direct metal laser sintering process (DMLS) and consisted of cylindrical and fanned hole geometries. Hole diameters were scaled based on C_d values (evaluated by CFD and checked by flow testing) in order to ensure mass flow rate and pressure drop were consistent across all test plates. Surface maps of adiabatic film effectiveness are illustrated in Fig. 13 (middle), providing a clear indication of the effect of hole shape—fanned holes providing better surface coverage with higher effectiveness values. Blowing ratio effects are captured quantitatively as illustrated in Fig. 13 (bottom). The benefit of fanned holes was clearly demonstrated, and the blowing ratio above which no further improvement was obtained was identified—1.5 (cylindrical)/2.6 (fanned).

To complement experimental studies, work to establish the optimum computational approach for effusion cooling is also underway. Since the work of Bergeles et al. [25], it is known that RANS 2-equation statistical models are inadequate for film cooling, requiring an anisotropic eddy viscosity (enhanced in wall parallel directions)

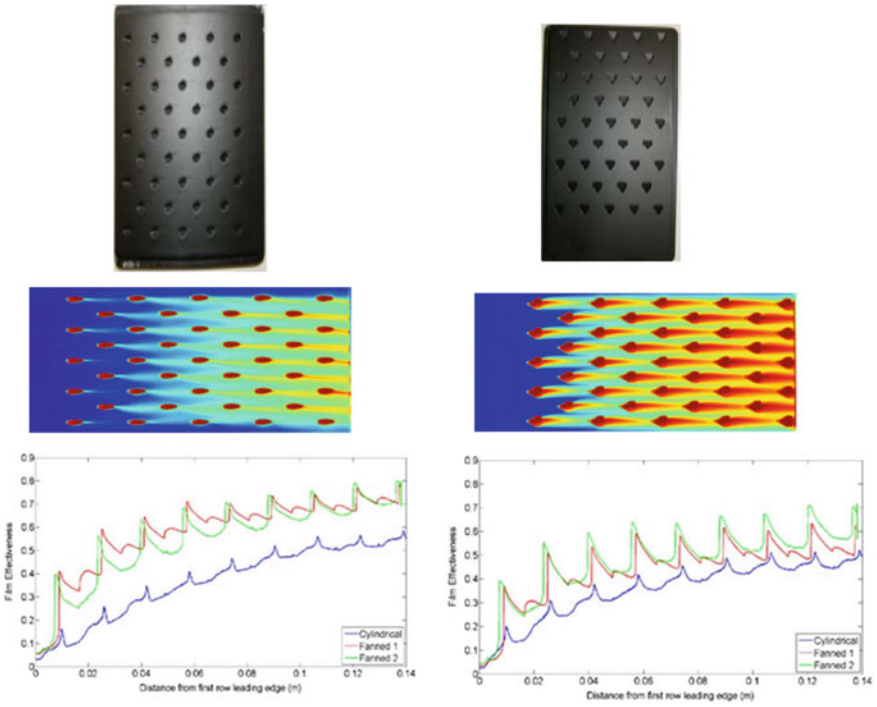

Fig. 13 **Top** Effusion test plates: left Cylindrical ($C_d = 0.62$), right Fanned hole ($C_d = 0.82$). **Middle** Adiabatic film effectiveness, blowing ratio = 3.8: left Cylindrical, right Fanned holes. **Bottom** Spanwise averaged effectiveness at blowing ratios 3.8 (left), 0.8 (right)

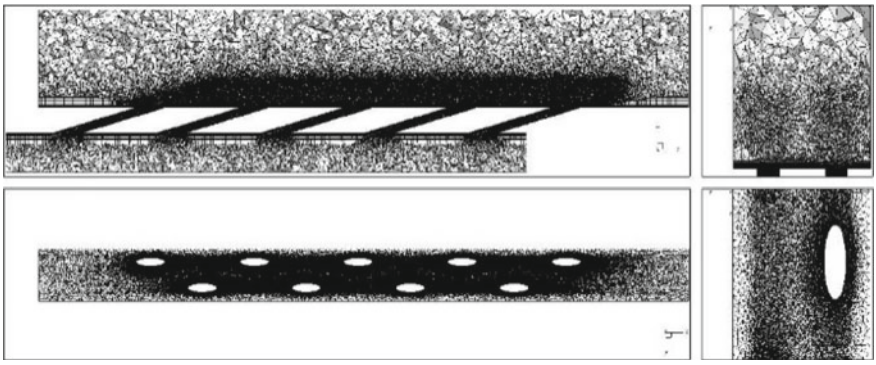

Fig. 14 Mesh for effusion flow test problem

as proposed by Li et al. [26] via an algebraic anisotropic Reynolds stress/heat flux model. Chen and Xia [27] have adopted a different, more general, approach, motivated by the fact that in a combustor environment film cooling takes place whilst surrounded by the highly unsteady motions of the internal combustor flow. For such highly unsteady flows, large eddy simulation (LES) is the preferred approach to turbulence rather than statistical RANS modelling (see Sect. 4.1). Thus, Chen and Xia [27] consider LES more appropriate for combustor wall effusion cooling. Since near-wall LES is inherently computationally expensive (due to the need to resolve all energetic eddy motions, which become smaller as the wall is approached), a hybrid RANS/LES methodology has been developed. RANS CFD is used up to a fixed wall distance ($\sim y^+ = 60$), with the switch between RANS and LES controlled by a blending function for the parameter ε (where $\varepsilon = 1$ implies LES solution). A smooth transition between RANS and LES is achieved, which is important for numerical stability. An unstructured grid of 18×10^6 cells was used in the simulation reported (Fig. 14). Two columns of holes (at fixed axial and spanwise pitch) with periodic side boundaries was adopted to represent the hole array used in the experiments of [24]. Grid refinement was used in shear layer and possible separation/reattachment regions (the blowing ratio (1.5) was relatively high.

Figure 15 presents a sample of the results. The top image represents an instantaneous temperature contour map on a plane through the first column of holes. The unsteadiness is well illustrated; separation occurs behind the first hole, and the coolant only fully attaches after the third row, with the coolant jet penetration settling down after five rows. The middle image shows predicted adiabatic effectiveness comparing experiment (top) with LES (bottom); the spanwise averaged effectiveness is in the bottom image and demonstrates a clear improvement in accuracy of LES over RANS.

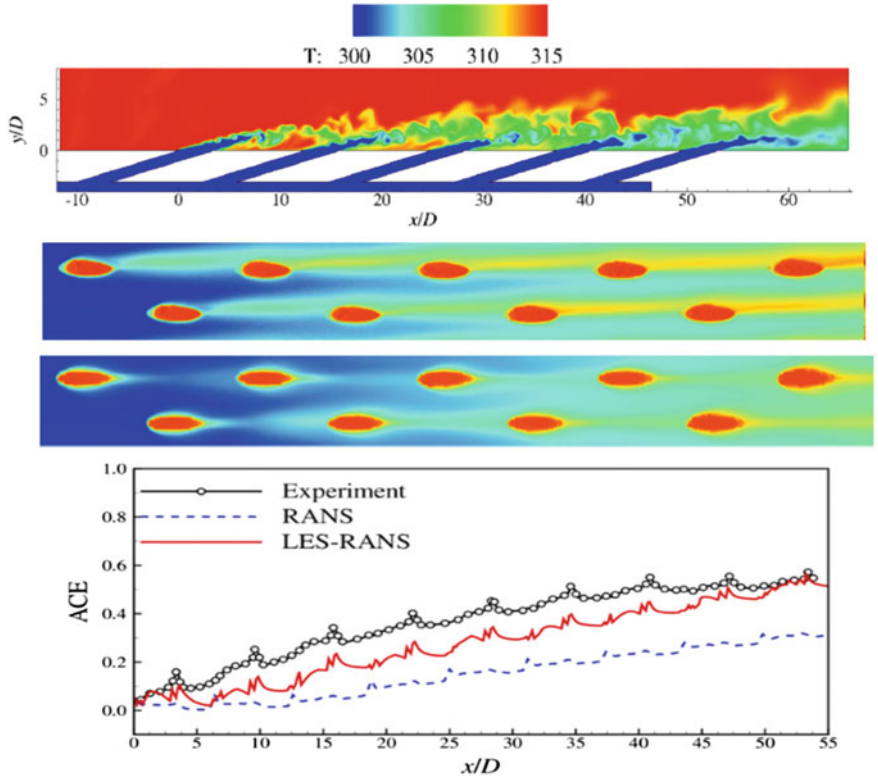

Fig. 15 **Top** Instantaneous temperature field. **Middle** Adiabatic effectiveness comparison expts. [24] (top) and hybrid LES (bottom). **Bottom** Comparison of spanwise averaged effectiveness

3.2 Cooled Cooling Air

The trend for increasing engine OPR is driven by reduced CO_2/fuel burn. It is of course accompanied by increased compressor exit temperature, which lowers its cooling effectiveness. Together with the reduced availability of cooling air that lean burn brings, the task of cooling the highly thermally loaded turbine is made considerably more difficult. One potential solution is a cooled cooling air (CCA) system in which some compressor air is diverted through a heat exchanger and cooled (by ~100 °C). An overview of the aerodynamic aspects of CCA has been provided by Walker et al. [28]. A sketch of a CCA concept is provided in Fig. 16, indicating the three extra components required: a low pressure (LP) system to deliver (cold) air from the by-pass duct, a heat exchanger (HX), and a high pressure (HP) system to deliver air from the combustion system to the HX and return this to the core engine for turbine cooling.

Focussing attention on LP/HP duct systems, which must be carefully integrated with existing components, Elango and Walker [29] and Spanelis et al. [30] have dealt

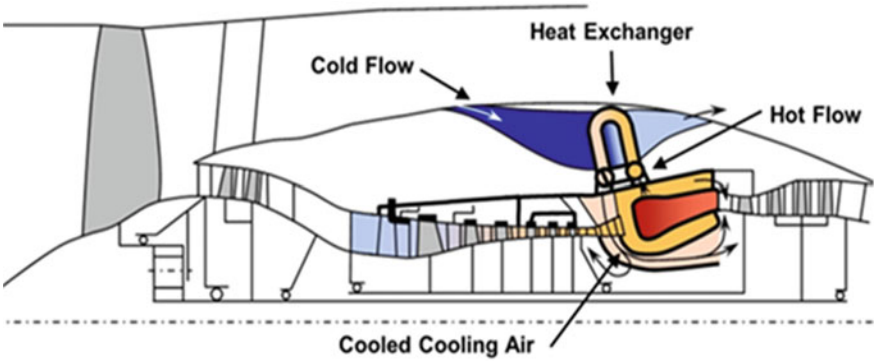

Fig. 16 Cooled cooling air (CCA) concept

first with the LP system. In [29], it was demonstrated that the simple by-pass duct flush off-take shown in Fig. 16 is not a viable solution. Low total pressure of the by-pass inner wall boundary layer is problematic, leading to separation when the flow encounters the diffusion necessary to reduce HX losses to an acceptable level. Spanelis et al. [30] have proposed a more attractive alternative which bleeds by-pass air through a total pressure fed scoop (Pitot) off-take located on the outer edge of the engine bifurcation strut.

Whilst the aerodynamic quality of this air is much better than in the flush off-take design, it still must be fed through curved diffusing S-ducts to reach HX entry. The design of a low loss version of such ducts avoiding separation is highly challenging. A final design with acceptable performance in terms of diffusion and flow uniformity (validated against data taken from an isothermal test rig at Loughborough University) was only identified in [30] after considerable RANS CFD optimisation, requiring use of a Reynolds stress turbulence model in order to take account of curvature effects.

For the HP system, bleed off-takes positioned on the combustion system outer casing are a relatively simple part of the design. More difficult is the duct system to return the cooled HP air from the HX outlet back to the core of the engine. To do this requires the cooled air to cross the main gas path into the rotor drive cavity inboard of the combustion system inner casing. This must be done with minimum aerodynamic disruption. Two proposed solutions to this problem are sketched in Fig. 17; the first method uses a simple transfer pipe located in the dump region (left), and the second effects the transfer via radial struts in the pre-diffuser (right). The risk of disturbing pre-diffuser or injector inlet flow has to be minimised (strong interaction of the simple transfer system is avoided by locating pipes in between injectors). To examine which concept can best be integrated into the combustion system, their aerodynamic performance was examined in the annular facility (Fig. 3), see Walker et al. [31]. Figure 18 shows measured pre-diffuser exit velocity contours with/without transfer pipe for the simple system.

Little change appears when the pipe is added, indicating that pipe blockage has not adversely affected the pre-diffuser flow (in fact if anything pipe blockage has had

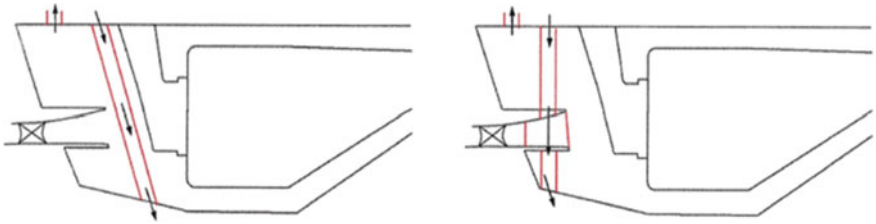

Fig. 17 Potential CCA routes across the main gas path

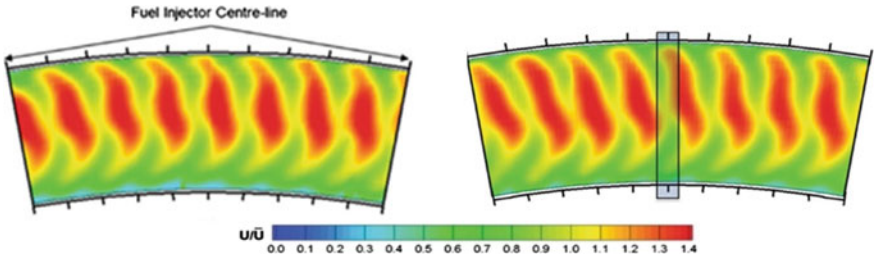

Fig. 18 Pre-diffuser exit axial velocity contours, clean (left), with transfer pipe (right)

a slightly beneficial effect on the lower wall boundary layer). Similar results were obtained when the total pressure field was measured in the immediate vicinity of the fuel injector; neither inner nor outer swirler flow was influenced. These results imply the apparently 'crude' simple transfer pipe solution is in fact an aerodynamically viable design. A similar investigation was undertaken for the radial strut design (a different OGV was used). After introduction of the strut, the pre-diffuser area ratio was lowered from 1.61 to 1.45 due flow area blocked by the strut. Figure 19 presents pre-diffuser exit measurements for clean and strutted geometries.

This time there are noticeable differences—the outer wall boundary layer is clearly closer to separation after addition of the strut. Also, the hub-biased shape of the velocity profile (with this OGV) has been exaggerated with the peak velocity close to the inner wall increasing in magnitude relative to the clean geometry.

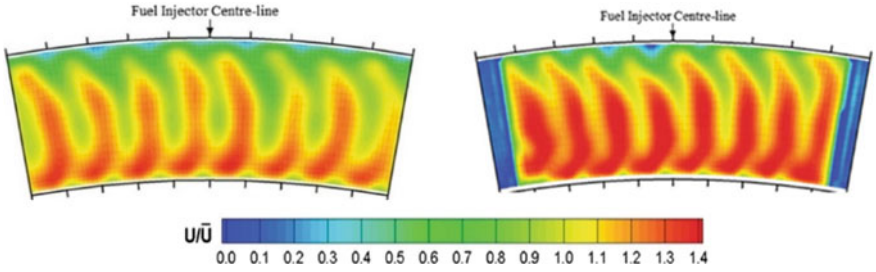

Fig. 19 Pre-diffuser exit axial velocity contours—clean (left), with struts (right)

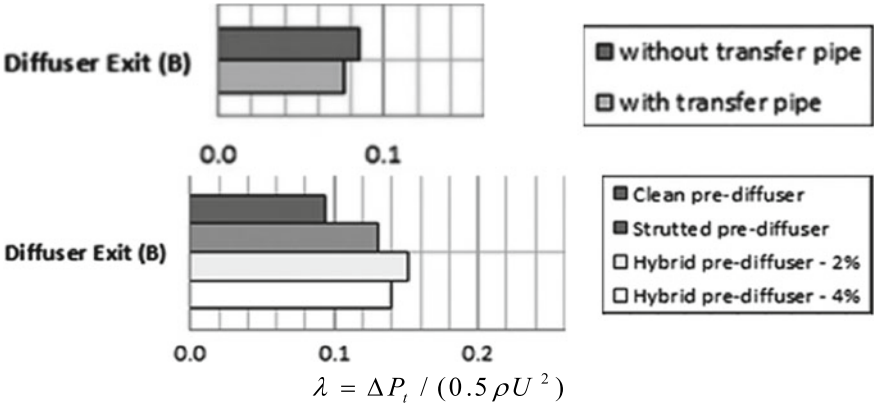

Fig. 20 Pre-diffuser loss coefficients (λ)

The reduction in pre-diffuser area ratio brought about by the strut has serious consequences. The dump loss is proportional to the square of the pre-diffuser exit velocity, so any area ratio reduction inevitably increases dump loss. Simply increasing the area ratio in the presence of the struts is aerodynamically risky since it is an acknowledged weakness of strutted pre-diffusers that the confluent boundary layers at the end wall/strut interface are particularly prone to separation. To avoid this and return the area ratio back to the clean value, a 'hybrid' diffuser design involving air bled from a slot in the outer wall (Walker et al. [32]) was explored in [31] with area ratio returned to 1.61 and various levels of bleed. Examination of the success of this and overall performance of all designs studied is provided in Fig. 20.

A larger pre-diffuser loss in the strutted design (due to increased wetted area) is revealed, and the inevitable increased dump loss of this approach has been noted above. The hybrid bled diffuser increases the pre-diffuser loss slightly (reduces at higher bleed), but it will certainly help the overall system loss performance as the dump loss has been reduced. The conclusion reached in [31] was that the 4% hybrid bled system was able to match the overall loss performance of the datum un-strutted design.

4 Fuel Injector Technology

4.1 High Swirl Injector Aerodynamics

The increasing number of swirlers used in a lean burn injector and the complexity of interacting high swirl flows means it is vital to have a good understanding of high swirl injector aerodynamics and to develop an appropriately validated CFD methodology. At Loughborough, experimental studies were first undertaken on the

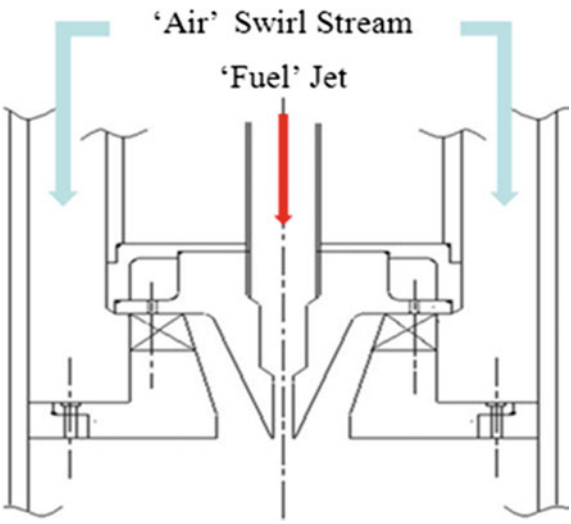

Fig. 21 Two stream model injector [33–35]

geometry in Fig. 21. Only isothermal flow was considered, and a two-stream design chosen with a central non-swirling jet representing fuel flow and an annular radially fed swirl stream representing air flow (Swirl No. 0.74). A series of experimental studies on this geometry have been reported: Midgely et al. [33], Spencer et al. [34], and Cheng et al. [35].

It was convenient to conduct measurements in a water flow tunnel and employ non-intrusive velocity (PIV) and scalar (PLIF) techniques. For the injector size chosen, matching typical Reynolds numbers of practical application meant velocities were a factor of ~15 lower than in an equivalent airflow. This reduces the range of dynamically important frequencies in the fluctuating turbulence field. For the maximum frame rate available with the PIV system (1 kHz), most of the energy-containing eddies could then be time-resolved. Rhodamine dye was added to the central jet flow to enable scalar mixing data to be collected. Optical arrangements allowing combined stereo-PIV/PLIF measurements in $x - r/r - \theta$ planes are shown in Fig. 22. Simultaneous time-resolved measurements of all velocity components and the fluctuating scalar were made, allowing all six Reynolds stress components and 3 turbulent scalar fluxes to be captured. The experimental data have been extensively exploited as CFD validation data to identify the predictive capability of both URANS (unsteady RANS) and large eddy simulation for highly swirling injector fluid mechanics. It became evident that injector flows were strongly influenced by unsteady phenomena such as vortex breakdown and only unsteady CFD was considered appropriate.

Figure 23 provides a comparison of URANS and LES predictions [35] of time-mean streamlines (superimposed on time-mean axial velocity contours) for this injector. Two cases were considered, with and without the central jet operational. Whilst the overall flow structure is similar, the shape of the recirculation regions and the number of internal streamlines inside these show notable differences between the two CFD methods.

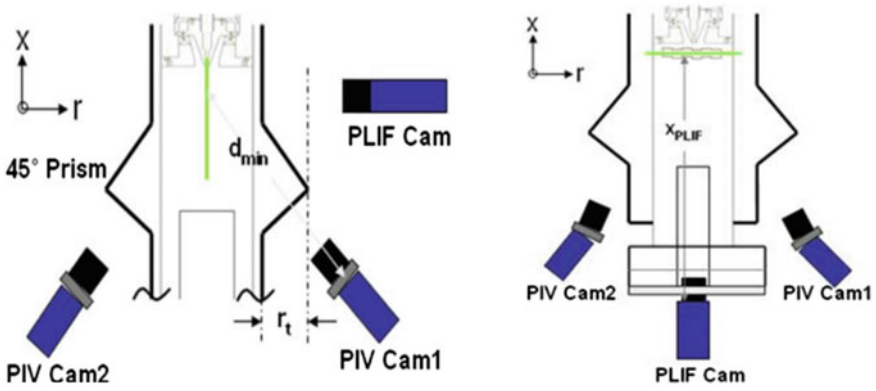

Fig. 22 PIV/PLIF set up for $x - r$ (left) and $r - \theta$ (right) plane views [35]

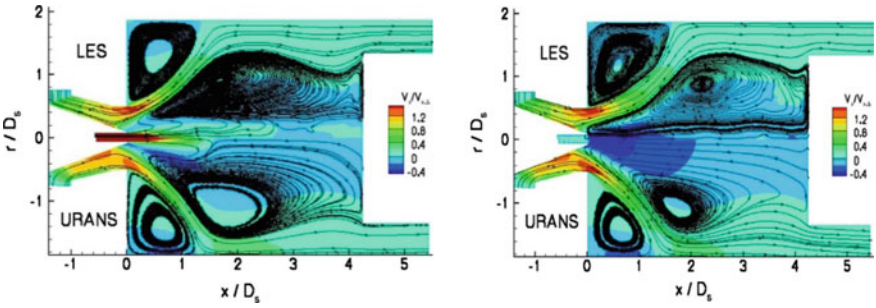

Fig. 23 URANS/LES predictions—mean velocity field: with (left) and without (right) central jet

Evidence of the importance of unsteady flow structures in high swirl flows is given in Fig. 24 (left). This shows a power spectral density (PSD) of the velocity fluctuations at a point on the inner edge of the swirler flow shear layer near at injector exit (frequency defined in terms of a non-dimensional Strouhal No. ($St = fD/U$). Whilst the broadband frequency shape of a highly turbulent flow is clearly visible, strong tonal components are also seen. Examination of videos of the flow shows these are caused by helical vortices which emanate from the swirler and propagate down the swirl shear layer, see Fig. 24 (right); this is clear evidence of highly energetic, unsteady vortex breakdown. LES captures these features in the spectrum well. The unsteady structures are revealed better via predicted two-point correlations, as shown in the cross-sectional snapshots of the helical vortices from the PIV and predicted by LES and URANS (Fig. 25). URANS and LES capture overall flow structure and unsteady features qualitatively the same, but the quantitative accuracy of LES for unsteady characteristics is superior.

The above example considered a relatively simple injector geometry, and the question arises whether the same aerodynamic characteristics and CFD performance

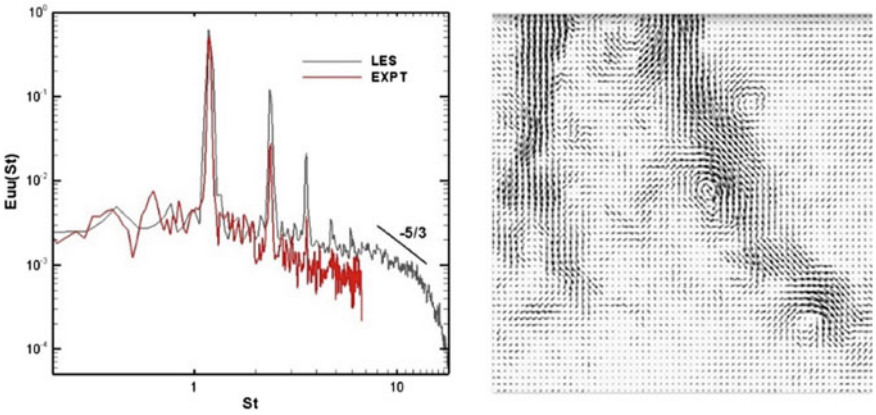

Fig. 24 PSD of axial fluctuation (left), instantaneous $x - r$ plane image (right)

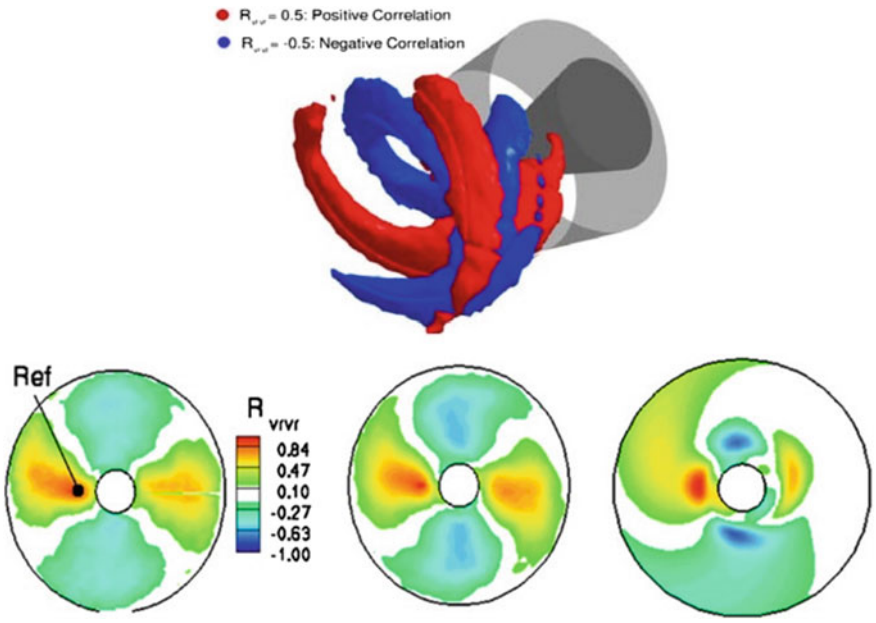

Fig. 25 **Top** Unsteady flow structures visualised using two-point correlations. **Bottom** Comparison of measured vs predicted two-point correlations. Left—Expts, Middle—LES, Right—URANS [35]

apply to industrially relevant injector geometries. Dianat et al. [36] have considered this for a rich burn geometry (containing three swirlers) see Fig. 26. Very similar results to those observed in the simple laboratory injector were obtained. Embedded helical instabilities are again seen, although now originating from the central rather

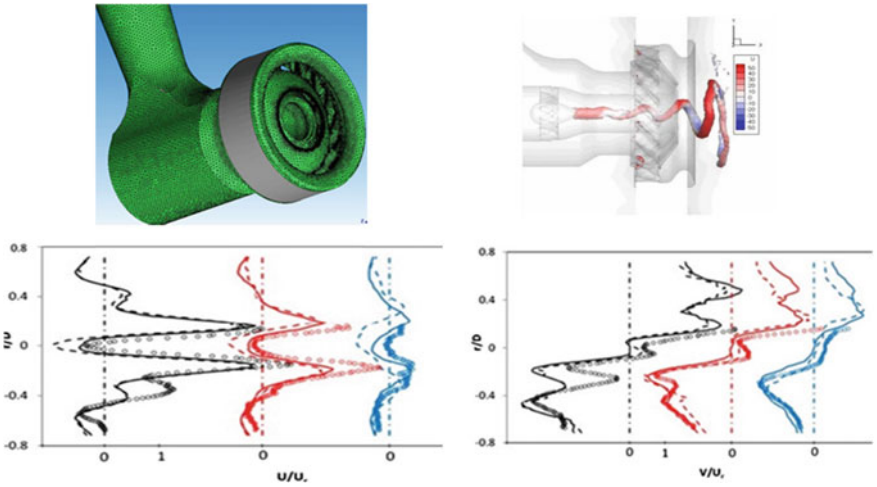

Fig. 26 Industrial rich burn geometry, LES vortex breakdown, and LES/PIV data comparison for axial (left) and radial (right) mean velocities [36]

than one of the annular swirlers. Further, the agreement between LES and PIV for the time-mean flow is of the same quality as in the simple geometry test case.

4.2 Injector Aeroacoustics

Given the increased probability of thermo-acoustic oscillations in lean burn combustors, it is important to pay attention to the acoustic characteristics of all combustor components. Up to 70% of the air passes through the injector, and this is the sole component establishing internal combustor flow patterns and conditions for fuel/air mixing. Hence, understanding the acoustic response of the injector is of prime importance. In CFD terms, both unsteadiness and compressibility must be considered for aeroacoustics. From evidence provided above, the detailed aerodynamics/mixing behaviour of high swirl injectors is better predicted by LES as opposed to a URANS approach. However, compressible LES is extremely expensive (very small tine-steps required since the speed of sound determines the time step from a maximum CFL condition). On the other hand, the fluctuating acoustic motions possess much larger spatial wavelength than the energetic turbulent eddies at the same frequency. There is therefore a distinct possibility that, whilst the acoustics and turbulence will interact, they are not strongly correlated. This suggests that if URANS can provide a reasonably accurate prediction of the aerodynamics, perhaps it is sufficient to accurately capture acoustic wave behaviour. This argument encouraged Gunasekaran and McGuirk [37] to explore a compressible URANS for acoustics prediction. Calculations of acoustic wave transmission/absorption by a simple round orifice in a duct

demonstrated good agreement with measurements of Rupp et al. [38] including accurate prediction of the linear and nonlinear behaviour occurring for high and low orifice pressure drops, respectively.

This approach was developed further by Su et al. [39] and applied to prediction of the acoustic impedance of orifices of different length/diameter ratios. Acoustic impedance is defined as the complex transfer function linking pressure fluctuation induced on the injector front face by an approaching acoustic wave (e.g. originating from fluctuating heat release) and resulting injector velocity/mass flow fluctuations. The complex impedance has a real part (resistance) which describes the velocity response in phase with the pressure fluctuation and an imaginary part (reactance) which describes the out-of-phase response (due to inertia of air mass within the injector passages). Together these components describe the amplitude gain and phase shift (time lag) between incoming pressure wave peak and the peak in injector mass flow disturbance. Figure 27 shows (left) the experimental setup—involving acoustic excitation using loudspeakers—used to generate measurement data suitable for validation. CFD results (right) for the in-phase resistive component of the orifice impedance were in excellent agreement with measured data (out-of-phase reactance also well predicted, see [39]).

The next step was to apply the method to injector impedance prediction. This was demonstrated for a lean burn injector by Treleaven et al. [40]. Figure 28 (left) illustrates the injector geometry, containing three swirlers: a central pilot passage and two mains air flow (inner/outer) swirler passages. In order to increase mixing, the two mains flow swirlers rotate in the opposite direction to the pilot flow swirler. The experimental setup to measure the impedance of the injector was as shown in Fig. 27 (left). The computational domain and mesh (~ 9 million cells) are indicated in Fig. 28 (right). It is important that correct acoustic (characteristic) boundary conditions are applied to faithfully reproduce the measurement conditions. The upstream plenum was treated as a large hemispherical space in the CFD with non-reflecting boundary conditions to allow injector transmitted acoustic waves to exit the domain without interference. The duct exit is an outlet boundary condition for mean flow but

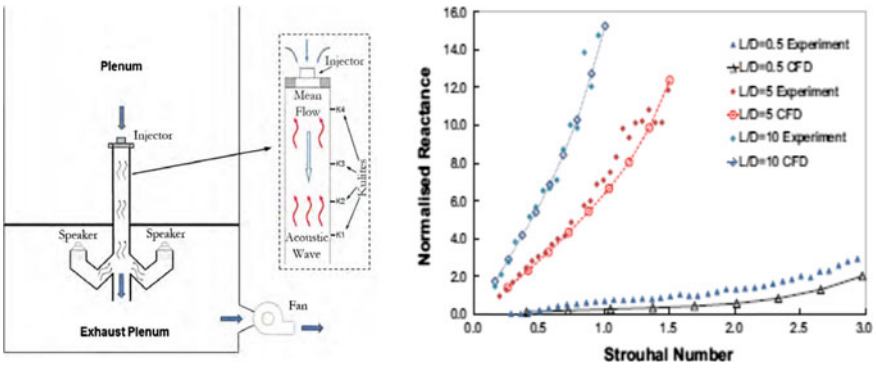

Fig. 27 Experimental setup (right), acoustic resistance prediction various L/D (right)

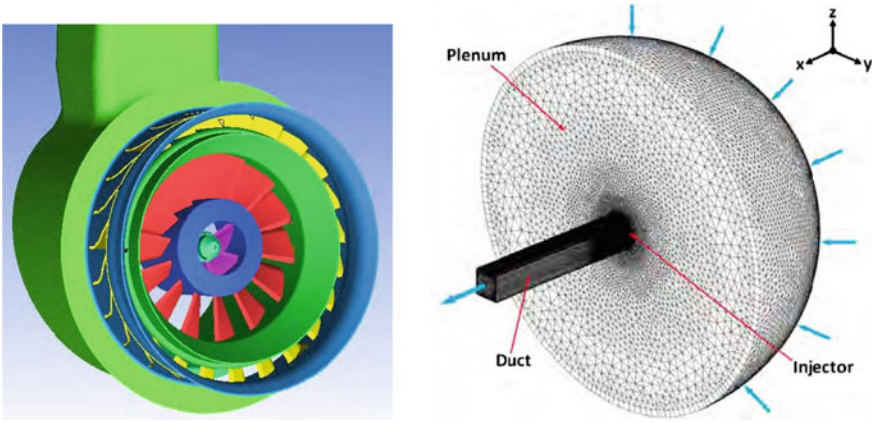

Fig. 28 Three swirler passage injector (left), computational domain and grid (right)

must allow specified frequency and amplitude incoming plane waves (representing loudspeaker excitation) and any waves reflected at the injector face to exit smoothly.

Predictions were conducted for a range of excitation frequencies from 250 to 550 Hz; the amplitude of the loudspeaker excitation wave entering was 300 Pa. A minimum of 12 acoustic cycles completed at each frequency was demonstrated as sufficient to ensure accuracy of calculated impedance values.

Figure 29 (left) displays comparison between URANS predicted impedance components and the measured properties, Fig. 29 (right) provides an instantaneous snapshot of the flowfield indicating the form of vortex breakdown for this injector geometry and the presence of swirler vane wakes, which will clearly influence mixing. Excellent agreement was obtained for the acoustic characteristics over the whole range of frequencies tested, including the roll-up of the resistance and roll-down of the reactance at high frequency. Two important conclusions emerged from this investigation: (i) compressible URANS is clearly an adequate CFD approach to

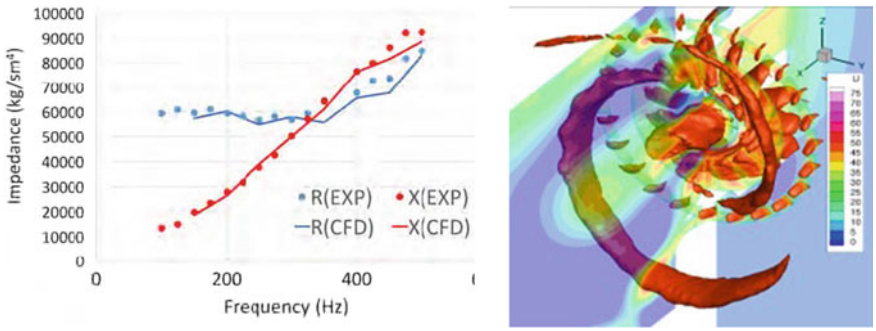

Fig. 29 Injector acoustic impedance (left) URANS predicted mean axial velocity field (right)

capture complex geometry injector acoustics, (ii) analysis of the flow field predictions showed that the acoustic perturbation promoted not just mass flow fluctuations through the injector but also swirl number variations. Clearly, both of these will influence unsteady flame dynamics under combusting conditions. Finally, the success of compressible URANS in this study encouraged the authors (see Treleaven et al. [41]) to explore the possibility of using the URANS predictions at injector exit as inlet boundary conditions for an incompressible LES combusting calculation starting at injector exit. This compared very favourably with a full compressible calculation, which would offer large computational savings for an LES calculation of the combustion process.

4.3 Injector Two-Phase Flow

Liquid fuel is introduced into a lean burn LDI-style injector typically via a simple pressure jet atomiser for the central pilot stream and a pre-filming surface for the main stream. Fuel issues from a slot onto a pre-filming surface over which an airstream passes, with air momentum used to atomise the fuel (usually sandwiched between two swirling streams). Whilst there have been several studies of film flow/atomisation behaviour on a planar surface (e.g. Bhayaraju et al. [42]), descriptions provided above indicate that in real injectors the film is exposed to non-uniform flow (e.g. discrete vane wakes). Barker and Carrotte [43] made measurements to establish the importance of such flow features on pre-filmer atomisation. Figure 30 (left) indicates the test geometry, with emphasis placed on the swirling air stream first in contact with the liquid fuel (issuing from a slot on the pre-filmer surface). Axial velocity profiles were measured in two planes upstream and two downstream of the slot for an azimuthal sector corresponding to two swirl vane passages (Fig. 30 (middle)). Contours at vane exit capture the vane wakes clearly and show hub-biased flow. Downstream the wakes spread and are stretched and transported azimuthally by the swirl. The liquid enters just after plane M3, and the wake flow migrates towards the pre-filmer surface. The liquid film is clearly exposed to localised regions of slow but

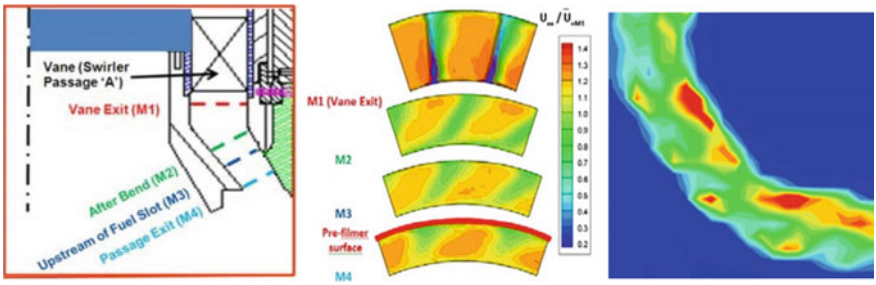

Fig. 30 Experimental geometry, velocity contours, fuel volume flux distribution

highly turbulent air, which are likely to produce localised variations in fuel velocity and thickness. To visualise this, phase doppler anemometry (PDA) measurements were made downstream of the injector over a single quadrant and are shown in Fig. 30 (right) (viewing the injector axially from downstream) in the form of contours of fuel volume flux. This clearly shows a non-uniform distribution with variations identified in [43] related to features of the aerodynamic field or variations in fuel flow from the slot which connects the upstream liquid supply system to the pre-filmer surface.

Film thickness development and its value at the end of the pre-filmer surface are important design features for atomisation. These were not captured in [43]; however, novel measurements which do allow this are contained in Brend et al. [44]. Their approach involves a line of sight ratiometric fluorescence technique based on the emission reabsorption laser induced fluorescence (ERLIF) concept of Hidrovo and Hart [45]. This eliminates difficulties associated with excitation non-uniformities and scatter from the pre-filmer surface. High fidelity measurements of spatially distributed film thickness and ligament statistics were obtained over a range of operating pressures in [44]. Importantly, measurements were carried out on a fully featured LDI pre-filming style injector with both air streams surrounding the pre-filmer included, see Fig. 31 (left). The method works by doping the liquid supplied to the fuel slot with two appropriately chosen fluorescent dyes. The dyes have different fluorescent emission/absorption spectra and are chosen such that the emission spectrum of the shorter wavelength dye is reabsorbed by the longer wavelength dye. This reabsorption of emitted light results in the linearity that enables recovery of thickness by evaluation of the ratio of fluorescent returns. Details on the technique, the special optical system designed for injector measurements, and the data analysis techniques used are available in [44]. Figure 31 (right) shows the linearity calibration carried out; film thicknesses expected in the experiment lay predominantly in the linear region shown.

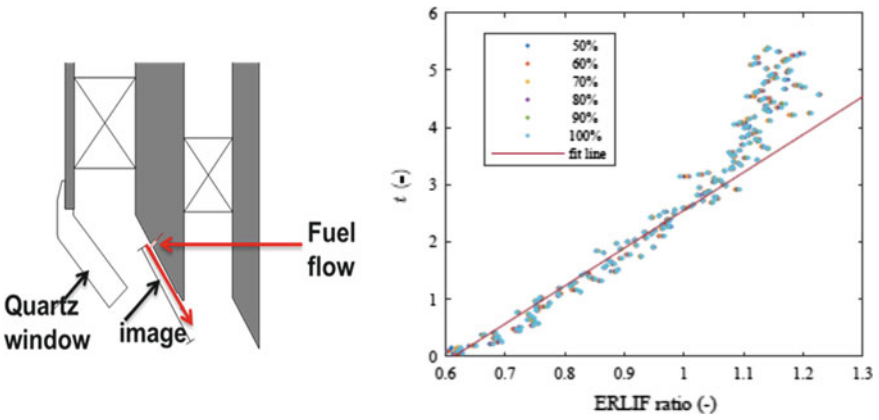

Fig. 31 Experimental arrangement (left), linearity of measurement technique (right)

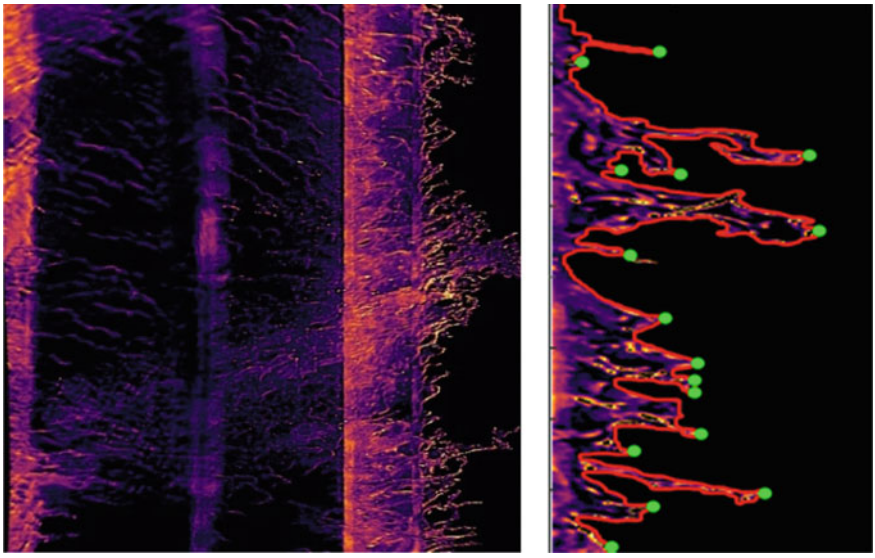

Fig. 32 Instantaneous image of film thickness $P = 3$ bar (left), example of instantaneous ligament detection process (right)

Figure 32 (left) presents an example of an instantaneous image of the evaluated film thickness as it develops from the slot over the pre-filmer surface (which contains a small step just before the pre-filmer edge) and also captures the initial formation of a liquid sheet from which ligaments grow and break up into droplets after the pre-filmer edge (the primary atomisation phase). Data analysis techniques were developed in [44] to identify the outer limit (perimeter) of the liquid sheet at the pre-filmer edge; peaks in this perimeter were extracted and used as a measure of the tips of ligaments—an example of a single instantaneous image of this process is illustrated in Fig. 32 (right).

Statistical analysis of this data allowed probability density functions (pdfs) of ligament properties to be evaluated. Figure 33 shows two examples of this, for the pdf of the ligament circumferential position (left) and of ligament axial length (right). It appears that the pressure has little effect on these distributions. Such data allow detailed understanding to be developed of the interaction between aerodynamics and liquid flow but also serve an important role for CFD models being developed of primary break-up (e.g. [46] for an example involving a liquid jet in crossflow). These CFD models are inevitably LES-based, but the same data analysis technique as used to extract the pdfs in Fig. 33 could be applied to the LES results, and then, such experimental measurements become excellent validation data.

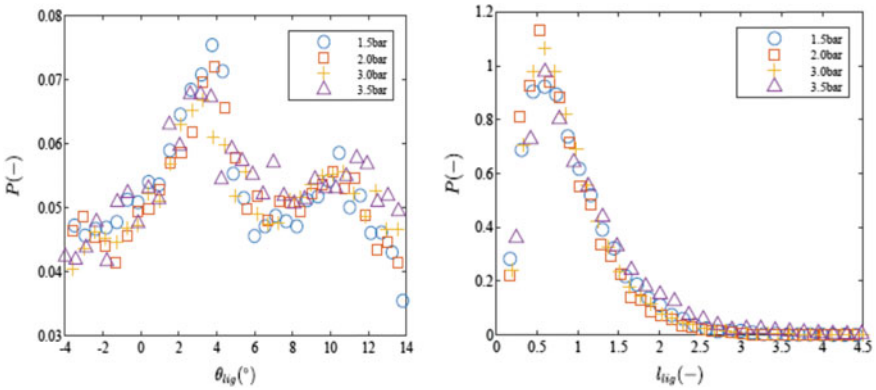

Fig. 33 Probability density function of ligament circumferential position (left). Probability density function of ligament length (right)

5 Future Developments—National Centre for Combustion and Aerothermal Technology

The next generation of gas turbines must continue to exploit new combustion technologies to deliver more efficient cycles and further reduce emissions. Any aerospace combustion system must undergo a rigorous development campaign to verify and validate its performance, culminating in (expensive) fully annular combustion or engine tests at high pressures and temperatures. However, sophisticated facilities that capture engine representative processes at affordable costs are now playing an increasingly crucial role. Prior to the prohibitively expensive high technology readiness level (TRL) validation tests, these facilities enable designs to be trialled, optimised, and developed. Examples have been provided above which demonstrate a range of affordable and cost-effective experiments which, when appropriately scaled and combined with high fidelity computations, adequately capture the complex aerothermal process that occurs within the high pressure and temperature engine environment. This cost-effective approach promotes understanding and helps identify promising new ideas. In addition, it promotes a multidisciplinary and integrated design methodology which accounts for the relevant processes and their interactions. This approach has been embedded within the recently opened National Centre for Combustion and Aerothermal Technology (NCCAT) at Loughborough University. The Centre provides access to a range of both reacting and non-reacting facilities that can capture the key aerothermal processes. Furthermore, as the boundaries between research, design, and development become increasingly blurred, NCCAT facilities will be able to support activities over a range of technology readiness levels, which helps align early research activities and ideas with future commercial goals to ensure the rapid pull-through of new technologies.

6 Summary and Conclusions

This paper has highlighted some of the complex aerothermal processes that must be considered in the design of a modern gas turbine combustion system. These range from fuel injector technology designed to generate highly swirling flows within which fuel is atomised and mixed, through to considerations of aero-acoustic phenomena, cooling systems, and how the combustion system integrates and interacts with the upstream and downstream turbomachinery components. The presented work also illustrates that the strategic use of isothermal, atmospheric pressure experimental facilities is an extremely cost-effective approach to identify promising ideas for future combustor aerothermal technologies. Unsteady, spatially resolved and temporally resolved measurements in well-chosen, industrially relevant test cases have also provided important validation data to improve and build confidence in appropriately chosen CFD techniques (RANS, URANS, and LES) for various aspects of the problems studied. A balanced combination of experimental and computational methods is the optimum approach for improving understanding and for development of new technological solutions. This approach is now being extended in activities being undertaken within the National Centre for Combustion and Aerothermal Technology (NCCAT).

Acknowledgements The material contained in this paper comprises research outcomes from projects undertaken within the Loughborough/Rolls-Royce UTC. We wish to express our thanks to all our Loughborough University and Rolls-Royce colleagues who participated in the research projects which produced these outcomes.

References

1. (2016) Raising ambition. Aerospace Technology Institute Technology Strategy and Portfolio Update
2. (2001) European aeronautics: a vision for 2020. ACARE Report
3. Flightpath 2050 (2011) Europe's vision for aviation, European Commission
4. Lobo P et al (2015) Measurement of aircraft engine non-volatile PM emissions: results of the aviation particle regulatory instrumentation campaign (A-PRIDE 4). Aerosol Sci Technol 49(7):472–484
5. CTO's co-operate to drive the sustainability of aviation. Joint Industry Statement, Paris Airshow, Le Bourget, 18 June 2019
6. Mosier SA, Pierce RM (1980) Advanced combustion systems for stationary gas turbine engines, vol 1. In: Review and preliminary evaluation, US Environmental Protection Agency Report No. EPA-600/7-80-0171
7. Li Y et al (2017) Review of modern low emissions combustion technologies for aero gas turbine engines. Prog Aerosp Sci 94:12–45
8. Lazik W, Doerr T, Bake S, vd Bank R, Rackwitz L (2008) Development of lean-burn low-NOx combustion technology at Rolls-Royce Deutschland. ASME paper GT2008-51115, ASME Turbo Expo, Berlin, Germany, June 2008
9. Fishenden CR, Stevens SJ (1977) Performance of annular combustor dump diffusers. J Aircr 14:60–67

10. Klein A (1995) Characteristics of combustor diffusers. Prog Aero Sci 31:171–271
11. McGuirk JJ (2014) The aerodynamic challenges of aeroengine gas-turbine combustion systems. Aeronaut J 118(1204):557–599
12. Stevens SJ, Harasgama SP, Wray AP (1984) The influence of blade wakes on combustor shortened pre-diffusers. AIAA J Aircr 21(9):641–648
13. Barker AG, Carrotte JF (2001) Influence of compressor exit conditions on combustor annular diffusers, part 1: diffuser performance. ASME J Prop Power 17(3):678–686
14. Denman PA (2002) Aerodynamic evaluation of a double annular combustion system. ASME paper GT2002-30465, ASME Turbo Expo, Amsterdam, The Netherlands, June 2002
15. Walker AD, Carrotte JF, McGuirk JJ (2008) Compressor/diffuser/combustor aerodynamic interactions in lean module combustors. ASME J Eng Gas Turbines Power 130:011504-01–011504-08
16. Walker AD, Carrotte JF, McGuirk JJ (2009) The influence of dump gap on external combustor aerodynamics at high fuel injector flow rates. ASME J Eng Gas Turbines Power 131:031506-01–031506-10
17. Walker AD, Carrotte JF, McGuirk JJ (2006) Enhanced external aerodynamic performance of a generic combustor using an integrated OGV/pre-diffuser technique. ASME paper GT2006-90184, ASME Turbo Expo, Barcelona, Spain, May 2006
18. Barker AG, Carrotte JF (2001) The influence of compressor exit conditions on combustor annular diffusers—part 1: diffuser performance. ASME J Propul Power 17:678–686
19. Ford CL (2013) Novel lean burn injector designs for improved flow uniformity. PhD Thesis, Loughborough University, Loughborough, UK
20. Ford CL, Carrotte JF, Walker AD (2012) The impact pf compressor exit conditions on fuel injector flows. ASME J Eng Gas Turbines Power 134:111505-1–111504-9
21. Williams MA, Carrotte JF, Moran AJ, Walker AD (2018) Impact of upstream boundary conditions on fuel injector performance in a low TRL reacting flow experimental facility. ASME paper GT2018-75621, ASME Turbo Expo, Oslo, Norway, June 2018
22. Cha CM, Hong S, Ireland PT, Denman P, Savarianandam V (2012) Experimental and numerical investigation of combustor-turbine interaction using an isothermal non-reacting tracer. ASME J Eng Gas Turbines Power 134:081501-1–081501-18
23. Dhopade P, Denman P, Ireland P, Ravikanti M (2017) Experimental and numerical investigation of the effect of compressor OGV profile on combustor exit measurements using an isothermal non-reacting tracer. In: Proceedings of 12th European conference on turbomachinery fluid dynamics and thermodynamics, Stockholm, Sweden, April 2017, Paper ETC2017-247
24. Krawciw J, Martin D, Denman P (2015) Measurement and prediction of adiabatic film effectiveness of combustor representative effusion arrays. ASME paper GT2015-743210, ASME Turbo Expo, Montreal, Canada, June 2015
25. Bergeles G, Gosman AD, Launder BE (1978) The turbulent jet in a cross stream at low injection rates: a 3-dimensional numerical treatment. Num Heat Trans 1:217–242
26. Li X, Qin Y, Ren J, Jiang H (2014) Algebraic anisotropic turbulence modelling of compound angled film cooling validated by particle image velocimetry and pressure sensitive paint measurements. ASME J Heat Transf 136:032201-1–0322011-18
27. Chen X, Xia H (2017) A hybrid LES-RANS validation of effusion cooling array measurements. In: Proceedings of 23rd international symposium on air breathing engines (ISABE), Manchester, UK, September 2017
28. Walker AD, Koli B, Spanelis A, Beecroft PA (2017) Aerodynamic design of a cooled cooling air system for an aero gas turbine. In: Proceedings of 23rd international symposium on air breathing engines (ISABE), Manchester, UK, September 2017, Paper ISABE-2017-21302
29. Elango P, Walker AD (2016) An investigation of flush off-takes for use in a cooled cooling air system. In: Proceedings of the royal aeronautical society applied aerodynamics conference, Bristol, UK, July 2016
30. Spanelis A, Walker AD, Beecroft P (2017) The aerodynamic design of the low pressure air delivery ducts for a cooled cooling air system. ASME paper GT2017-63959, ASME Turbo Expo, Charlotte, NC, USA, June 2017

31. Walker AD, Koli B, Guo L, Beecroft P, Zedda M (2017) Impact of a cooled cooling air system on the aerodynamics of a gas turbine combustion system. ASME J Eng Gas Turbines Power 139:051504-1–051504-13
32. Walker AD, Denman PA, McGuirk JJ (2004) Experimental and computational study of hybrid diffusers for gas turbine combustors. ASME J Eng Gas Turbines Power 126:717–725
33. Midgley K, Spencer A, McGuirk JJ (2005) Unsteady flow structures in radial swirler fed fuel injectors. ASME J Eng Gas Turbines Power 127:755–764
34. Spencer A, McGuirk JJ, Midgley K (2005) Vortex breakdown in swirling fuel injector flows. ASME J Eng Gas Turbines Power 130:021503-1–021503-8
35. Cheng L, Dianat M, Spencer A, McGuirk JJ (2012) Validation of LES predictions of scalar mixing in high swirl fuel injector flows. Flow Turb Comb 18:146–168
36. Dianat M, McGuirk JJ, Fokeer S, Spencer A (2014) LES of unsteady vortex dynamics in complex geometry gas-turbine fuel injectors. In: Proceedings of 10th engineering turbulence modelling and measurements conference, Marbella, Spain, September 2014
37. Gunasekaran B, McGuirk JJ (2011) Mildly-compressible pressure-based CFD methodology for acoustic propagation and absorption prediction. ASME paper GT2011-45316, ASME Turbo Expo, Vancouver, Canada June 2011
38. Rupp J, Carrotte JF, Spencer A (2010) Interaction between the acoustic pressure fluctuations and the unsteady flow-field through circular holes. ASME J Eng Gas Turbines Power 132:06150-1–06150-9
39. Su J, Rupp J, Garmory A, Carrotte JF (2015) Measurements and computational fluid dynamics predictions of the acoustic impedances of orifices. J Sound Vib 352:174–191
40. Treleaven NCW, Su J, Garmory A, Page GJ (2017) The response to incident acoustic waves of the flow field produced by a multi-passage lean burn aero-engine fuel injector. ASME paper GT2017-64527, ASME Turbo Expo 2017, Charlotte, NV, USA
41. Treleaven NCW, Su J, Garmory A, Page GJ (2019) An efficient method to reproduce the effects of acoustic forcing in gas turbine fuel injectors in incompressible simulations. Flow Turbul Combust 103:417–437
42. Bhayaraju U, Hassa C (2009) Planar liquid sheet breakup of pre-filming and no-pre-filming atomisers at elevated pressure. Atomisation Sprays 19:1147–1169
43. Barker AG, Carrotte JF (2014) The impact of representative aerodynamics flow fields on liquid fuel atomisation in modern gas turbine fuel injectors. ASME paper GT2014-26927, ASME Turbo Expo 2014, Duessseldorf, Germany
44. Brend MA, Barker AG, Carrotte JF (2019) Measurements of fuel thickness for pre-filming atomisers at elevated pressure. Int J Multi Phase Flow 129
45. Hidrovo CH, Hart DP (2001) Emission reabsorption laser induced fluorescence (ERLIF) film thickness measurement. Meas Sci Technol 12:467–477
46. Xiao F, Dianat M, McGuirk JJ (2013) Large eddy simulation of liquid jet primary breakup in air crossflow. AIAA J 51:2878–2893

Cluster Analysis of Turbulent Premixed Combustion Using On-the-fly Flame Particle Tracking

Madwaraj Hatwar, Ashwin S. Nayak, Himanshu L. Dave, Utkarsh Aggarwal, and Swetaprovo Chaudhuri

Nomenclature

Da	Damköhler number
ρ	Density of the mixture
ϕ	Equivalence ratio
U	Fluid velocity
Ω	Kinematic restoration term
η	Kolmogorov length scale
τ_η	Kolmogorov time scale
Le	Lewis number
$\tau_{F,L}$	Lifetime of flame particle
n	Local vector normal to an isoscalar surface
S_d	Local flame displacement speed
D	Mass diffusivity
Y_k	Mass fraction of kth species
κ	Mean curvature of flame surface
$\langle U \rangle$	Mean fluid velocity
X^F	Position vector of the flame particle
$\dot{\omega}$	Production/consumption rate of species
Re_λ	Reynolds number based on Taylor micro-scale
u_{rms}	RMS value of the fluctuating velocity
ψ	Scalar field (temperature or species mass fractions)
t	Simulation time

M. Hatwar · A. S. Nayak · H. L. Dave · U. Aggarwal · S. Chaudhuri (✉)
Department of Aerospace Engineering, Indian Institute of Science, C. V. Raman Avenue, Bangalore, India
e-mail: schaudhuri@utias.utoronto.ca

S. Chaudhuri
University of Toronto Institute for Aerospace Studies, Toronto, Canada

© Springer Nature Singapore Pte Ltd. 2021

A. De et al. (eds.), *Sustainable Development for Energy, Power, and Propulsion*, Green Energy and Technology,
https://doi.org/10.1007/978-981-15-5667-8_15

K_T Tangential strain rate
δ_L Thermal flame thickness
Re_T Turbulent Reynolds number

1 Introduction

Turbulent premixed and partially premixed flames are utilized in many practical engineering devices ranging from spark-ignition (SI) engines and industrial gas burners (land-based) to gas turbine engines (aero-based), to realize clean combustion with lower emissions [1–4]. Due to the stringent restrictions on NO_x and emissions of other pollutants, reliance on premixed combustion has increased in the recent years and efforts to comprehensively understand turbulent premixed flames have gained significant interest. Thermonuclear combustion preceding a Supernova Ia is also known to be strikingly similar to premixed combustion involving chemical reactions in a turbulent flow field [5, 6]. With the significant advances in high-performance computing, computationally intensive simulations of turbulent combustion with detailed transport and chemistry have become feasible. This has helped gain better insights into the underlying multi-scale, multi-physics and nonlinear phenomena [7, 8] of turbulence–flame interaction.

To understand turbulent premixed flames, various studies [9, 10] have primarily investigated the Eulerian fields and their statistics conditioned on the flame surfaces, at particular time instants. While these described global characteristics satisfactorily, it may not comprehensively describe localized phenomena such as the local annihilation of flames, formation of pockets and flame islands. In non-reacting turbulence, the Lagrangian approaches [11] have garnered significant interest while investigating mixing and dispersion problems. Taking cue from these developments, it seems worthwhile to explore Lagrangian approaches to understand mixing processes within the flames, study flame element dispersion [12], investigate flame propagation and local-to-global flame extinction among many other problems, while also providing inputs for the modeling of turbulent premixed flames [13].

Lagrangian fluid particle tracking methods [11, 14–16] developed for non-reacting turbulence could be directly used in reacting turbulent flows. However, their direct application in premixed turbulent combustion may not be helpful due to the very short residence times that a fluid particle would spend within the premixed flame. This can be attributed to the thin width of the premixed flame, its self-propagation, and the large acceleration that a fluid particle would experience due to heat release from combustion. Due to significant variations in properties from the unburnt and burnt side of the flames, a fluid particle moving through the flame would encounter inhomogeneous turbulence and the statistics thereof would be highly non-uniform.

A premixed flame can be considered as an ensemble of propagating isoscalar surfaces. In [17], Pope argues that certain phenomena are better described in terms of propagating surfaces and provide a detailed mathematical framework for studying evolution of such surfaces in turbulence. Following this, the flame particle tracking

(FPT) technique was developed in [18], where flame particles are defined as mathematical points on isoscalar surfaces, isotherms in particular. These flame particles co-move with their resident surfaces with a local flame displacement speed, relative to the local fluid velocity, along the local normal to the isoscalar surface. Such an approach enables tracing the paths of these flame particles (i.e., surface points on reactive isoscalar surfaces) and thereby studying variation of flame–flow properties at these spatio-temporally evolving locations on surfaces which are representatives of the premixed flame. FPT has since proven useful in providing insights into localized phenomena within premixed flames interacting with turbulence [12, 19, 20].

Previously, the FPT algorithm was implemented in a pre-computed reacting flow of a turbulent premixed flame, using triangle–ray intersection method [21] combined with numerical integration. A brief review of this implementation is presented here. Flame particles are usually distributed uniformly on the isoscalar surfaces at the start of the FPT simulation. The isoscalar surfaces are computationally represented as a mesh of triangles and are obtained using the marching cubes algorithm. Interpolation schemes are used to obtain relevant properties, such as fluid velocity, from the DNS grid points to the flame particle location. From their current positions, the displacement exclusively due to fluid velocity is drawn. From the tip of this displacement vector, a ray is shot along the positive and negative direction of the local normal. The direction of the ray corresponds to the local surface normal defined at the starting position of the flame particle. The ray is allowed to intersect with the face(s) of a triangle on the surface mesh at the next time step. The final point of intersection, obtained by a corrective step [18] and a thresholding criterion, is the location of that particular flame particle at the next time step. For further details, readers can refer to [18].

The FPT algorithm operates in the post-processing stage after performing the DNS simulations. To accurately track the flame particles, the Eulerian field variables must be saved on one or more storage media at time intervals which are sufficiently smaller than the smallest relevant time scales, usually the Kolmogorov time scale. As the turbulent Reynolds number increases, the requirement for finer time intervals and finer grids poses severe computational challenges. The FPT algorithm, therefore in its current form, can become extremely demanding for storage space. Secondly, the existing implementation uses an interpreted programming language which is time intensive. This "two-step" approach also requires various interfaces between the data output from the solver, which is written in the compiled language, and the post-processing application, i.e., FPT, thus requiring careful handling of the data and additional scripts. All these issues can be effectively circumvented by integrating the FPT algorithm with the DNS solver. The proposed new implementation would not make use of marching cubes and ray–face intersection algorithm, which are the backbone of the existing FPT methodology [18], but will instead be based on standard numerical integration algorithms to compute the flame particle trajectories permitting better accuracy, stability along with scalability and computational efficiency. We refer to this integrated implementation of FPT within the DNS as "on-the-fly" FPT. In this study, we demonstrate, possibly for the first time, the implementation of on-the-fly FPT and illustrate its use in understanding the dynamics of annihilation of isoscalar surfaces within premixed flames. From the past works, we expect that flame

particles cluster preferentially in trailing regions of the surface at different times. Such clustering precedes flame annihilation and therefore is an important feature of the turbulent flame dynamics.

The remaining paper is organized as follows: First, we describe the details of the DNS solver, the governing equations it solves, different computational aspects of on-the-fly FPT algorithm and its implementation. Following this, we describe the clustering algorithm used in understanding the flame annihilation dynamics. Finally, we present the results and discussion concerning the implementation of the algorithm and the results from the investigation of flame annihilation dynamics.

2 Computational Techniques

2.1 Solver

The direct numerical simulations (DNS) of the turbulent premixed flames were performed using the Pencil Code—a highly modular, highly scalable, open-source finite difference solver for weakly compressible flows for solving the governing equations in the non-conservative form [22]. It utilizes a sixth-order accurate explicit, central, finite difference scheme for evaluating spatial derivatives and a third-order accurate Runge–Kutta time integration scheme as proposed by Williamson [23], referred to as RK3-2N. In this paper, a statistically planar turbulent premixed flame is simulated within a cuboid in an inflow–outflow configuration. Navier–Stokes Characteristic Boundary Conditions (NSCBC) were used in the direction of the flow (X-direction), and periodic boundary conditions were used in the other two directions (i.e., Y and Z directions). A premixture of H_2-air is used as the reactant and a detailed H_2-air reaction mechanism with nine species and 19 reactions developed in [24] was incorporated into the chemistry solver developed by Babkovskaia et al. [25].

2.2 Governing Equations

The governing equations solved in the Pencil Code [22] are presented below. The continuity equation is

$$\frac{D\left(\ln \rho\right)}{Dt} = -\boldsymbol{\nabla} \cdot \boldsymbol{U} \tag{1}$$

where $D/Dt = \partial/\partial t + \boldsymbol{U} \cdot \boldsymbol{\nabla}$ is the material derivative, ρ is the density and $\boldsymbol{U}$ is the fluid velocity. The momentum equation is

$$\frac{D\boldsymbol{U}}{Dt} = \frac{1}{\rho}\left(-\boldsymbol{\nabla} P + \boldsymbol{F}_{\mathrm{vs}}\right) \tag{2}$$

where P is pressure,

$$\boldsymbol{F}_{\mathrm{vs}} = \nabla \cdot (2\rho\nu\boldsymbol{S}) \tag{3}$$

is the viscous force, where $S_{ij} = -\frac{1}{3}\nabla \cdot \boldsymbol{U}\delta_{ij} + \frac{1}{2}\left[\partial U_i/\partial x_j + \partial U_j/\partial x_i\right]$ is the traceless rate of strain tensor. The equation for the mass fraction of each species is

$$\rho\frac{DY_k}{Dt} = \nabla \cdot \boldsymbol{J}_k + \dot{\omega}_k \tag{4}$$

where Y_k is mass fraction, $\boldsymbol{J_k}$ is the diffusive flux, $\dot{\omega}$ is the reaction rate and subscript k refers to the species number k. Since detailed reaction mechanism of [24] is considered here, nine such species equations (Eq. 4) are solved in addition to the one continuity (Eq. 1) and three momentum equations (Eq. 2). Furthermore, the energy equation

$$\left(c_p - \frac{R}{m}\right)\frac{D\left(\ln T\right)}{Dt} = \sum_{k=1}^{N_s}\frac{DY_k}{Dt}\left(\frac{R}{m_k} - \frac{h_k}{T}\right) - \frac{R}{m}\nabla \cdot \boldsymbol{U} + \frac{2\nu\boldsymbol{S}^2}{T} - \frac{\nabla \cdot \boldsymbol{q}}{\rho T} \tag{5}$$

was solved. Here, T is the temperature, c_p is the constant pressure specific heat capacity, R is the universal gas constant, h is the enthalpy, m is the molar mass and $\boldsymbol{q}$ is the heat flux. The ideal gas equation connects pressure and temperature as follows

$$P = \frac{\rho RT}{m} \tag{6}$$

2.3 Governing Equations for Flame Particles

Flame particles are surface points, co-moving with a given isoscalar surface within the premixed flame. Therefore, flame particles are identified by their initial position $\boldsymbol{X}$ and the isovalue ψ_0 of the reactive scalar ψ (say, T or Y_k) that is conserved along the trajectory or time history of a given flame particle. These two conditions can be combined as $\boldsymbol{X}_0^F = \boldsymbol{X}^F\,(t = 0, \psi = \psi_0)$. Flame particles are advected along the resultant of the local fluid velocity vector $\boldsymbol{U}$ and the local flame displacement speed S_d along the local normal vector $\boldsymbol{n}$. The kinematic equation governing the position of a flame particle and the constraint of scalar conservation are described below by Eqs. 7 and 8, respectively [17, 18]:

$$\begin{aligned}\frac{\partial}{\partial t}\boldsymbol{X}^F\left(t, X_0^F\right) &= \boldsymbol{V}^F\left(t, \boldsymbol{X}_0^F\right)\\ &= \boldsymbol{U}^F\left(t, \boldsymbol{X}_0^F\right) + S_d^F\left(t, \boldsymbol{X}_0^F\right)\boldsymbol{n}^F\left(t, \boldsymbol{X}_0^F\right)\end{aligned} \tag{7}$$

$$\frac{\partial\psi}{\partial t} + \boldsymbol{V}^F \cdot \nabla\psi = 0 \tag{8}$$

where $\boldsymbol{X}^F\left(t, \boldsymbol{X}_0^F\right)$ represents the spatial location of flame particle at time t, defined on isoscalar surface of ψ with isovalue ψ_0, with initial position as $\boldsymbol{X}_0^F$. All the quantities mentioned with a superscript "F" are evaluated at the flame particle location and, therefore, are Lagrangian quantities. They are obtained from the corresponding Eulerian fields by interpolation, say $\boldsymbol{U}^F\left(t, \boldsymbol{X}_0^F\right) = \boldsymbol{U}\left[\boldsymbol{X}^F\left(t, \boldsymbol{X}_0^F\right), t\right]$. Here, $\boldsymbol{U}(\boldsymbol{x}, t)$ represent Eulerian velocity field in space and time. For other parameters, identical procedure is adopted. $\boldsymbol{V}^F$ is the resultant velocity of flame particle; S_d^F is the flame displacement speed and $\boldsymbol{n}^F$ is the normal to the isoscalar surface at the flame particle. S_d and $\boldsymbol{n}$ are computed using the following equations:

$$S_d = -\frac{1}{|\nabla\psi|}\frac{D\psi}{Dt} \tag{9}$$

$$\boldsymbol{n} = \frac{\nabla\psi}{|\nabla\psi|} \tag{10}$$

where $\psi(\boldsymbol{x}, t)$ is the scalar field. In this paper, we study flame particles defined on surfaces of constant mass fraction of H_2. Therefore, Y_{H_2} remains constant along the trajectory of a given flame particle. The flame particles are uniformly initialized on the surfaces. The on-the-fly FPT implementation allows particle initialization on a smooth or wrinkled surface at the initial or at any intermediate time of the DNS simulation, respectively. For such surfaces, the substantial derivative in Eq. 9 is observed to be the right-hand side of the species transport equation for H_2, i.e., Eq. 4. Hence, the displacement flame speed and the normal vector are calculated as,

$$S_d = -\frac{1}{\rho|\nabla Y_{H_2}|}(\nabla(\rho D\nabla Y_{H_2}) + \dot{\omega}_{H_2}) \tag{11}$$

$$\boldsymbol{n}^F = \frac{\nabla Y_{H_2}}{|\nabla Y_{H_2}|} \tag{12}$$

In the solver, Eqs. 11 and 12 which explicitly appear within Eq. 7 are evaluated only within the flame region defined by a temperature range of 312–2500 K. Equations 11 and 12 are solved at the grid points. From these points, relevant properties are interpolated to the flame particle positions. For interpolation, quadratic spline interpolation scheme is used which utilizes the values at 27 grid points in the neighborhood of $\boldsymbol{X}^F\left(t, \boldsymbol{X}_0^F\right)$. Equation 7, governing the motion of a flame particle, is integrated in time using a third-order accurate Runge–Kutta scheme (RK3-2N) [23] to compute the trajectories of the flame particles. The method makes efficient use of memory registers requiring only two sets of the variables to be held in memory. Accordingly, the position vector at "$n+1$"th time step maybe obtained from the position at "n"th time step by an iterative procedure, Hence, the updated particle positions are third-order accurate in both time and space.

Table 1 List of coefficients of Williamson's RK3-2N scheme

c_1	c_2	c_3	α_1	α_2	α_3	β_1	β_2	β_3
0	4/9	15/32	0	−5/9	−153/128	1/3	15/16	8/15

$$d\boldsymbol{X}_i^F = \alpha_i d\boldsymbol{X}_{i-1}^F + \delta t \left(c_i H\left(\boldsymbol{X}_{i-1}^F, t_{i-1}\right)\right)$$
$$\boldsymbol{X}_i^F = \boldsymbol{X}_{i-1}^F + \beta_i d\boldsymbol{X}_i^F$$

with $i = 1, 2$ and 3 represent the three sub-steps of the RK3-2N integration scheme and H is evaluated as the right-hand side of the ordinary differential equation Eq. 7. The coefficients, α, β and c above are listed in Table 1.

2.4 Cluster Analysis

Cluster analysis deals with grouping of objects into clusters such that the objects in the same group have similar property and are different from objects in other groups. It is often employed in grouping, decision making, machine learning in data mining, document retrieval, image segmentation and pattern classification and various other fields to determine natural groups of objects based on certain similarity features and criteria [26]. As the surfaces and the resident flame particles interact with the turbulence, eventually, they are found to preferentially agglomerate in the trailing edges of the surface, on which they are defined (i.e., regions toward the products), before annihilation. Particles are considered annihilated when the corresponding flame surface in the neighborhood of a flame particle no longer exists. Therefore, studying the clustering phenomena may help in investigating the flame annihilation dynamics. Later, in the paper, a more formal definition of flame annihilation will be introduced. Here, we utilize cluster analysis on the flame particles to study the dynamics of flame annihilation and explore if a simple statistical measure like ensemble average could emerge as its suitable representative to describe the annihilation process of that cluster.

Cluster analysis is useful toward reduced-order modeling (ROM) [27]. Model order reduction is a technique to reduce the computational complexity of mathematical models in numerical simulations. Model order is reduced either by reducing the degree of freedom or the state-space dimensions. This reduced order model is an approximation for the original model at best but could be computationally very efficient. In terms of turbulent premixed flames, reduced order of flame particles needs to resolve important localized phenomena at different regions of the flame, occurring at different times. Cluster models could be useful in capturing the important physical phenomena of the flame surface with very few points without sacrificing the fidelity of localized dynamics and reduce computational cost.

In this study, a k-medoids clustering approach proposed by Kaufman [28] is used, which segregates the particles into k number of clusters based on reference points called medoids, which is the most centrally located point in a cluster. We use the partitioning around medoids (PAM) [29] algorithm which minimizes the distance between the non-medoid o and the medoid m data points. The algorithm initially selects k points as initial medoids, and each point is assigned to a cluster with the closest medoid [28]. The algorithm then swaps medoid m and a random non-medoid point o from that particular cluster and computes the distances between points and their medoid. This step is undone if the distance increases. This is iteratively done till we get the minimum average distance between the points and their medoid.

3 Results and Discussions

Direct numerical simulations were conducted using the Pencil Code as mentioned earlier. The parameters of the simulation are listed in Table 2. "Case 1" refers to the case where the turbulence has not yet strongly interacted with the flame, and hence, there are no flame annihilation events. Therefore, this could be used to validate "on-the-fly FPT" algorithm. "Case 2" refers to later time where the turbulence has substantially interacted with the flame surface. The data obtained from this case are used to study the flame annihilation events.

3.1 Validation

Validation of the on-the-fly flame particle tracking is done by obtaining a time series of the "isoscalar" value at all the flame particle positions. By definition, the flame particles must always remain attached to the isoscalar surface before annihilation. Thus, theoretically, the scalar value is a conserved quantity for the lifetime of a flame particle. This has been expressed mathematically in Eq. 8. Any deviation from the initial value can originate from errors like numerical integration or interpolation, or physical phenomena like the annihilation of local surface due to self-propagation or extinction when the scalar value ceases to exist in the neighborhood of the flame particle. In the present study, the flame particles were defined on constant mass fraction surfaces of H_2. To initialize flame particles on arbitrarily wrinkled isosurfaces, marching cubes algorithm was used. After defining particles using this sub-routine, the flame particle co-ordinates were imported into the solver. After initialization, the particle tracking module is "switched on" and the flame particles are tracked in space and time. The validation was done for low turbulence intensity case when the isoscalar surfaces are not highly wrinkled. Since the surface is not strongly wrinkled, no flame annihilation events are expected; hence, there is no physical mechanism by which the isoscalar value at the flame particle position can change with respect to the initial value. This can help in assessing the numerical accuracy of the algorithm.

Table 2 List of simulation parameters

Parameters	Case 1	Case 2
Grid	960 × 240 × 240	960 × 240 × 240
Domain, $L_x \times L_y \times L_z$ (cm^3)	1.918 × 0.48 × 0.48	1.918 × 0.48 × 0.48
Grid size, Δ_{DNS} (μm)	20	20
Inlet temperature, T_{in} (K)	310	310
Inlet pressure, P_{in} (atm)	1.0	1.0
Equivalence ratio (ϕ)	0.81	0.81
Mean fluid velocity, $\langle U \rangle$ (cm/s)	1137	1216
rms value of fluctuating velocity, u'_{rms} (cm/s)	656	627
Time step (μs)	0.01	0.01
Scalar isosurface	5 Y_{H_2} isosurfaces	5 Y_{H_2} isosurfaces
Scalar values	0.0022, 0.005, 0.0110, 0.0189, and 0.0225	0.0022, 0.005, 0.0110, 0.0189, and 0.0225
Number of particles used	5000	5000
Lewis number, Le	0.84	0.84
Kolmogorov length scale, η (μm)	14	14
Kolmogorov time scale, τ_η (μs)	8.83	9.62
Turbulence Reynolds number, Re_T	352.73	310.56
Damköhler number, Da	0.85	1.27
Taylor micro-scale Reynolds number, Re_λ	89	85
Thermal flame thickness, δ_L (cm)	0.0361	0.0361
Simulation time (τ_η)	7.93	50.42

Figure 1 shows the time histories of the Y_{H_2} at particle positions for 100 sampled particles embedded initially on five different constant Y_{H_2} surfaces—0.0022, 0.0050, 0.0110, 0.0189 and 0.0225. The value of Y_{H_2} was normalized from 0 to 1 using the following definition of a progress variable c.

$$c = \frac{Y_{H_2,u} - Y_{H_2}}{Y_{H_2,u} - Y_{H_2,b}} \tag{13}$$

where the subscripts u and b defines unburnt and burnt sides, respectively. The value of c is 0 when Y_{H_2} is at the unburnt side and 1 when Y_{H_2} is at the burnt side. The value of Y_{H_2} at the unburnt side is 0.0229 and that at the burnt side is 0.0006. The values of c corresponding to the chosen scalar values (see Table 2) are 0.93, 0.80, 0.53,

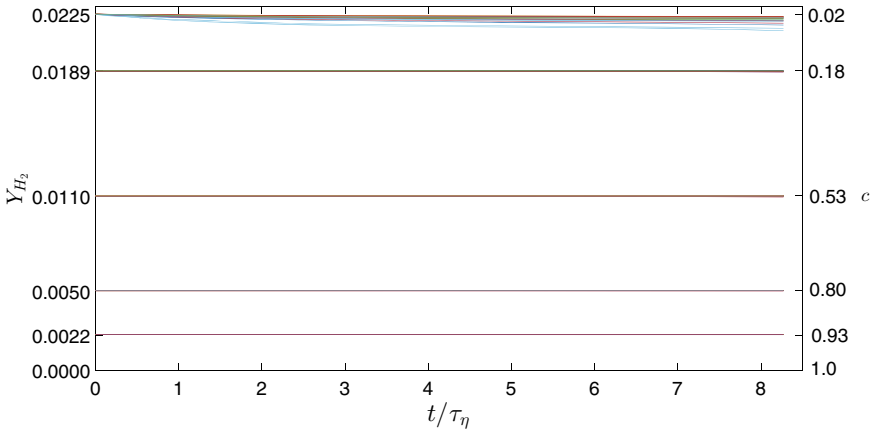

Fig. 1 Variation of Y_{H_2} at particle positions in time for 100 randomly selected particles

0.18 and 0.02 for Y_{H_2} values 0.0022, 0.005, 0.011, 0.0189, and 0.0225, respectively. The flame particles on each of these surfaces are evolved for over $7.93\tau_\eta$ for this validation exercise.

Figure 2 shows the percentage deviation of isovalue of Y_{H_2} at the end of validation exercise. The difference is computed with respect to the initial value. The deviations are less than 0.2% for majority of the particles. The maximum deviation is less than 2%. Therefore, the accuracy of on-the-fly FPT algorithm is validated. On interaction with turbulence, flame surfaces stretch and fold leading to surface annihilation. Following flame surface annihilation, flame particles should also annihilate. This is why

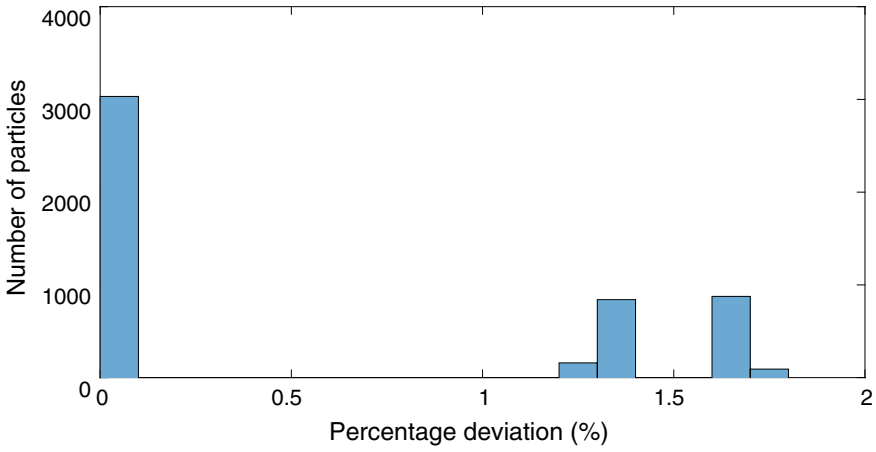

Fig. 2 Percentage deviation of Y_{H_2} for the 5000 particles from initial value after 7.93 Kolmogorov time scales

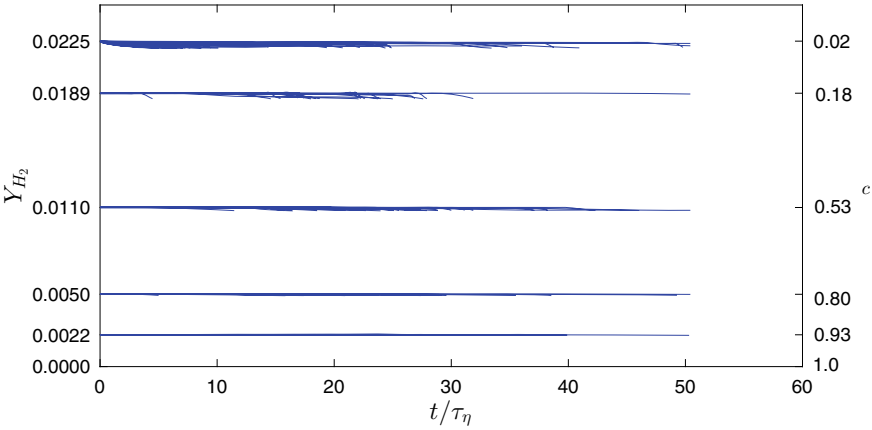

Fig. 3 Variation of Y_{H_2} at particle positions with time for 100 randomly selected particles by considering particle annihilation

the validation exercise had to be performed in a weak turbulence case for a limited time. To identify the flame particle annihilation criteria, the time series of the scalar value is used. Simultaneous to surface annihilation, the isoscalar surface on which the flame particle is defined ceases to exist. Other surfaces identified by different isovalues now occupy these flame particle locations. This causes a sharp change in the scalar value at the flame particle locations. Figure 3 shows the time series of the Y_{H_2} at flame particle locations. Also, clearly visible in the figure is the small change in the Y_{H_2} value as time progresses. This is because a particle is considered annihilated when the scalar value is found to deviate beyond a threshold of 2% from its original state and is ceased from tracking.

3.2 Flame Particle Trajectories

The trajectories of the flame particles are shown in Fig. 4. It can be observed that the particles cluster as time progresses. Figure 5 shows the particle trajectories colored with the magnitude of the particle velocity $|\boldsymbol{V}^F|$, while Fig. 6 shows the probability density function (pdf) of $|\boldsymbol{V}^F|$ at three different times. These plots clearly show the particle velocity increasing with time. However, the change in velocity during particle annihilation is rather gradual. Figure 7, shows the variation of mean curvature of the flame evaluated using Eq. 14. Figure 8 shows the probability distribution function (PDF) of mean curvature evaluated at the flame particle locations. In the present paper, positive (negative) value of κ indicate that the surface at those point is convex (concave) to the unburnt reactants. The PDF clearly shows that large, negatively curved surfaces, or in other words, highly concave surfaces are more common than convex surfaces as flame particles evolve in time. This observation obtained with

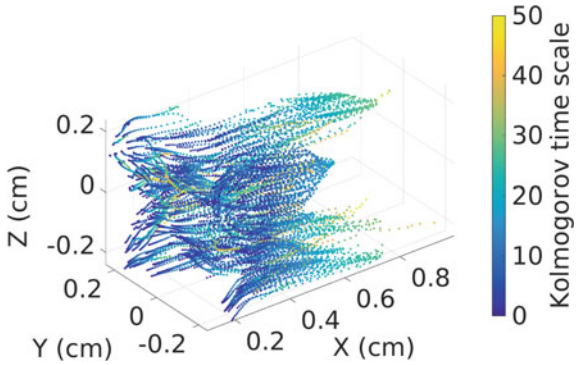

Fig. 4 Trajectory of flame particles with time

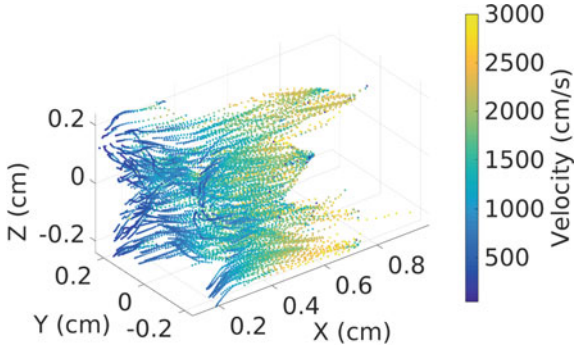

Fig. 5 Velocity of flame particles over its trajectory

on-the-fly FPT agrees with those obtained by the post-processing based FPT method in [18, 19]

$$\kappa = -\nabla \cdot \left(\frac{\nabla Y_{H_2}}{|\nabla Y_{H_2}|} \right) \tag{14}$$

It is found that the magnitude of mean curvature along the particle trajectories increases with time, while κ at these points remains negative. This suggests that as time progresses the flame particles progressively cluster in the concave regions of the flame surface. These concave regions are usually in the trailing sections of the isoscalar surface.

Figures 9, 10, 11 and 12 show the variations of tangential strain rate K_T, flame displacement speed S_d, mean curvature κ and $|\nabla Y_{H_2}|$ at the particle positions, respectively. The parameters are plotted against t/τ_{FL} which is the ratio of physical time (t) to the lifetime of the flame particle (τ_{FL}). Since different regions of flame annihilate at different times, a definition of normalized times seems more appropriate [19]. The term t/τ_{FL} is a normalized parameter from 0 to 1, between the time of particle initialization to its annihilation. However, as shown later, we will revert to analysis in physical times when clusters of flame particles are analyzed instead of the full ensemble.

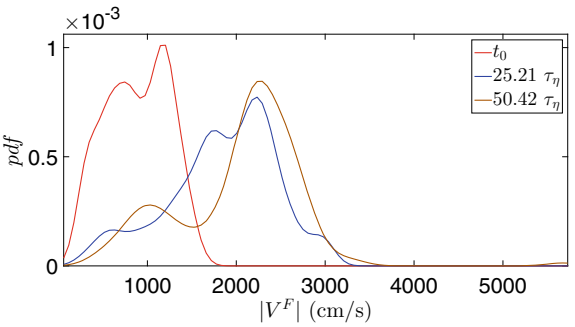

Fig. 6 PDF of velocity of flame particles

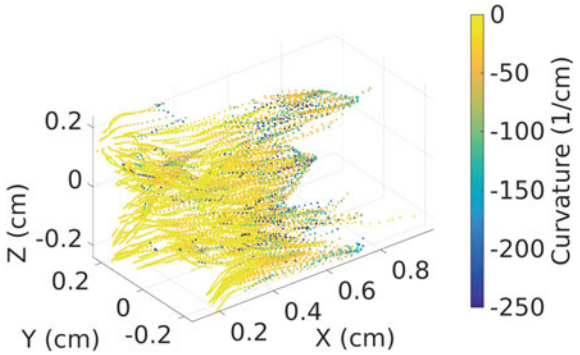

Fig. 7 Mean curvature of the surface at the flame particle locations

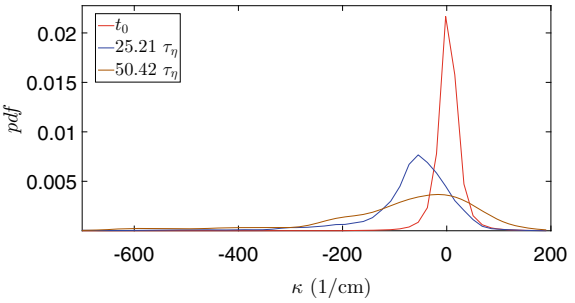

Fig. 8 PDF of mean curvature of the surface at the flame particle locations

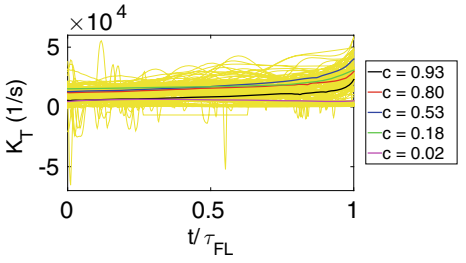

Fig. 9 Variation of tangential strain rate at the particle positions with time

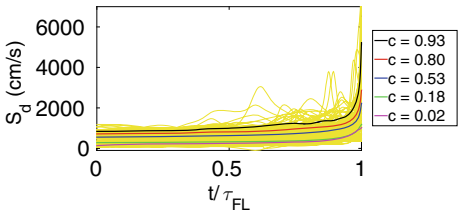

Fig. 10 Variation of logarithm of flame displacement speed at the particle positions with time

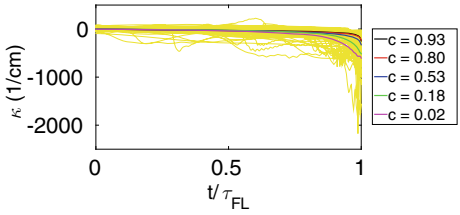

Fig. 11 Variation of mean curvature at the particle positions with time

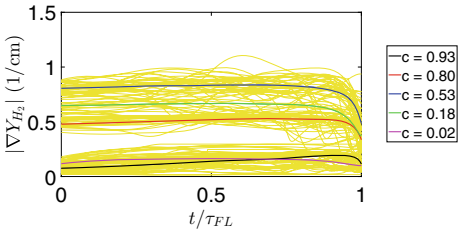

Fig. 12 Variation of $|\nabla Y_{\mathrm{H}_2}|$ at the particle positions with time

From Figs. 9 and 10, we can see that K_T and S_d increase significantly before particle annihilation. The variation of the ensemble average of the parameters is indicated using the thick lines of different colors corresponding to different surfaces. Figure 11 shows the formation of negatively curved regions with large curvature near the end of flame particle lifetimes. Figure 12 shows the magnitude of scalar gradient of H_2 mass fraction which tends to vanish as particles annihilate. When the flame surface is locally annihilated, the local scalar property tends to homogenize which results in the value of $|\nabla Y_{\mathrm{H}_2}|$ to decrease sharply. The trends of increasing flame displacement speed, tangential strain rate and increasing concavity of surface at flame particle locations were also observed using FPT [19]. The variation of S_d with κ is shown in Fig. 13. The points represent the values at the particle positions, and the solid line represents the ensemble averages. Apparently, one could attempt to explain the increase of S_d with κ using pure curvature effects [30], discussed below. For stationary spherical flames with the reactants entering from a point source at the center, non-dimensional mass flux and non-dimensional curvature are given by:

$$\tilde{f}_u = \left(1 + \frac{1}{2}\tilde{\nabla} \cdot \boldsymbol{n}\right)^{-2} \tag{15}$$

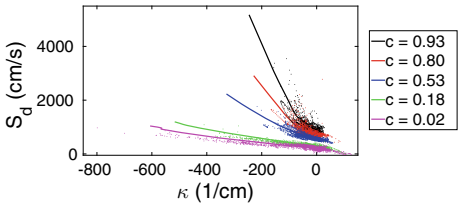

Fig. 13 Variation of S_d with κ

$$\tilde{f_u} \simeq (1 - \tilde{\nabla} \cdot \boldsymbol{n}) \tag{16}$$

$$\tilde{\kappa} = \tilde{\nabla} \cdot \boldsymbol{n} \tag{17}$$

$\tilde{\kappa}$ is $\delta_L \kappa$ and $\tilde{\nabla}$ is $\delta_L \nabla$, where δ_L is the planar laminar flame thickness. The reader is encouraged to refer [31] for a new development on this topic.

Equation 15 is the non-dimensional mass flux, and Eq. 16 is its linearized form. Equation 17 is the non-dimensional curvature. The increase in concavity of flame surface at the particle locations results in an increase in the mass flux which increases the S_d to large values.

3.3 Kinematic Restoration

Kinematic restoration is a dissipation mechanism of fluctuations on a flame surface leading to smoothing of wrinkles on individual flame branches. This is affected by self-propagation of the flame which causes flame wrinkle destruction. Kinematic restoration of a flame surface can be quantified by the term given [32] by

$$\Omega = -s_L^0(\kappa\sigma + \nabla^2 G) \tag{18}$$

where Ω is the kinematic restoration term, s_L^0 is the burning velocity of the planar laminar flame, κ is the mean curvature, G is the isoscalar surface which in our case is constant mass fraction surface of H_2, i.e., $G = Y_{H_2}$ and $\sigma = |\nabla G|$.

The kinematic restoration term was calculated for all the particles at different time instants as shown in Fig. 14. Since the flame was not initially perturbed heavily, the value of Ω is small as observed in 14a. As the flame surface wrinkles with time, Ω changes. Figure 14a shows the value of Ω at the initial time instant. Figure 14b shows the flame surface which has undergone wrinkling due to turbulence–flame interaction. The value of Ω has increased significantly at the negatively curved regions. This is shown in Fig. 14c and d where an increased population of particles are experiencing very high values of Ω. Figure 14e and f shows further increase in the high Ω values carried by the flame particles. We can see that very high Ω values are experienced by particles which cluster in the negatively curved regions. These particles undergo annihilation either due to formation of flame islands or kinematic restoration due to

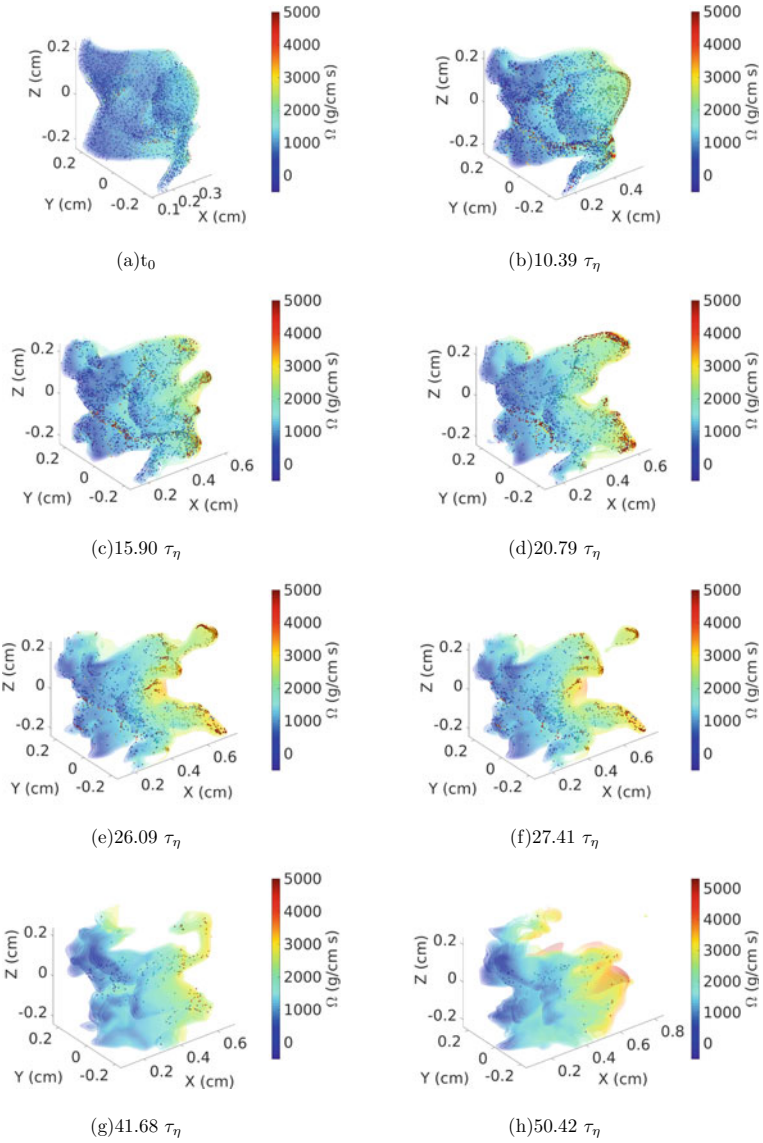

(a)t_0 (b)10.39 τ_η

(c)15.90 τ_η (d)20.79 τ_η

(e)26.09 τ_η (f)27.41 τ_η

(g)41.68 τ_η (h)50.42 τ_η

Fig. 14 Variation of kinematic restoration term on the flame surface

high Ω values. The tendency of the particles to form flame islands increases with increasing Ω, which eventually reduces the number of particles with very high Ω values. This is shown in Fig. 14g. The value of Ω at the surviving particle positions increases with time due to the continuous wrinkling of flame surface. These particles again undergo annihilation as described above. This is shown in Fig. 14h where very few particles have survived flame particle annihilation. Mathematically, the initial increase in Ω value can be explained by the increase in the magnitude of κ in the concave regions, without a very significant change in the value of σ and $\nabla^2 Y_{H_2}$ with increase in flame surface wrinkling. As the surface wrinkles too much, negatively curved regions undergo local flame annihilation, i.e., flame particles with very high negative curvature values, and hence, flame particle/surfaces with high Ω values are annihilated resulting in flame wrinkle destruction. This decreases the proportion of particles which have high Ω values, and the surface is smoothened. The smoothened flame surface further undergoes wrinkling due to turbulence resulting in an increase in the value of Ω at the particle locations.

3.4 Cluster Analysis

Apart from the implementation of on-the-fly FPT, one of the major contributions of this work is cluster analysis of the flame particles to elucidate the aggregated yet localized dynamics of flame particles on turbulent premixed flames. To that end, here, a partitional clustering algorithm k-medoids, mentioned in Sect. 2.4, was used to segregate the particles into nine separate groups on each of the isosurfaces. The isoscalar surfaces on which the particles are defined are plotted at different time intervals in Fig. 15.

Figure 15a corresponds to initial time t_0. At t_0, particles are uniformly initialized on the five isoscalar surfaces. The formation of clusters can be seen in Fig. 15d–f at the trailing regions where number density of particles is large. Figure 15d and e also shows that elongated channels filled with unburned gas, called the unburned mixture finger (UMF) [33], develop on the flame surface. The regions with high number density of flame particles undergo flame surface annihilation due to processes like island formation on self-intersection of flame with itself and due to kinematic restoration. Figure 15f shows the formation of a flame island in the trailing regions of the flame where flame particles have clustered. The detached island behaves like an inwardly propagating spherical flame by consuming the trapped reactants and propagating normal to the flame surface leading to a loss of flame surface and flame particles. The UMF which is prominent in Fig. 15d and e and the flame island shown in Fig. 15f have disappeared in Fig. 15g. The disappearance of the UMF is characterized by large negative curvature resulting in high flame displacement speed. Figure 15g shows the formation of another trailing region just before it is detached from the flame surface to form a flame island as shown in 15h. Figure 15i shows the final fate of the particles.

The average distance between the particles and their medoids is calculated for each group of particles. Since the particles are uniformly distributed initially, the

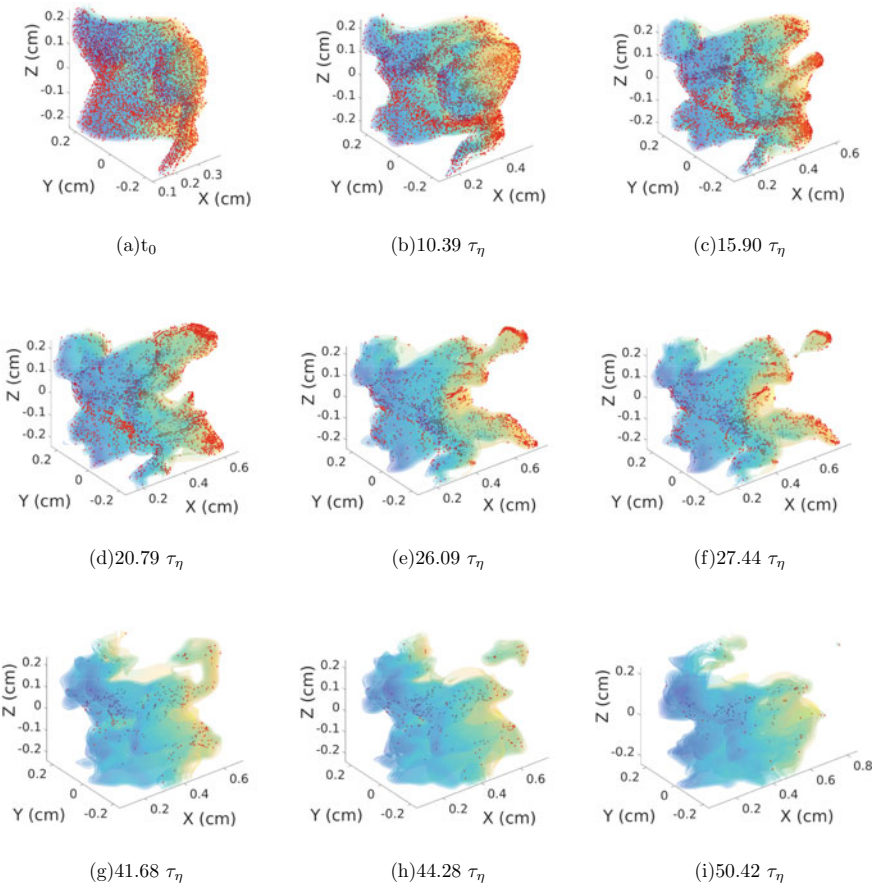

(a)t_0 (b)10.39 τ_η (c)15.90 τ_η

(d)20.79 τ_η (e)26.09 τ_η (f)27.44 τ_η

(g)41.68 τ_η (h)44.28 τ_η (i)50.42 τ_η

Fig. 15 Flame surface with particles at various time steps

average distances are approximately equal. The distance changes with the wrinkling of the flame surface. Particles are considered to be clustered if the value of average distance in a particular group of particles is significantly less than the initial value. The particles cluster on different surfaces of constant Y_{H_2} at different times. Figure 16 shows the clusters formed at the same region of the flame on different constant Y_{H_2} isosurfaces at different times.

The flame properties like displacement flame speed, tangential strain rate, mean curvature of the flame surface, hydrogen mass fraction gradient, kinematic restoration and temperature were calculated on the clustered particles for each surface of constant Y_{H_2}. The mean values of these properties are calculated and compared with the overall trend of the clusters shown in Fig. 16.

Figure 17 shows the variation of the different parameters on the cluster formed on the isosurface, $c = 0.02$ which is shown in Fig. 16. In Figs. 17, 17, 18, 19, 20,

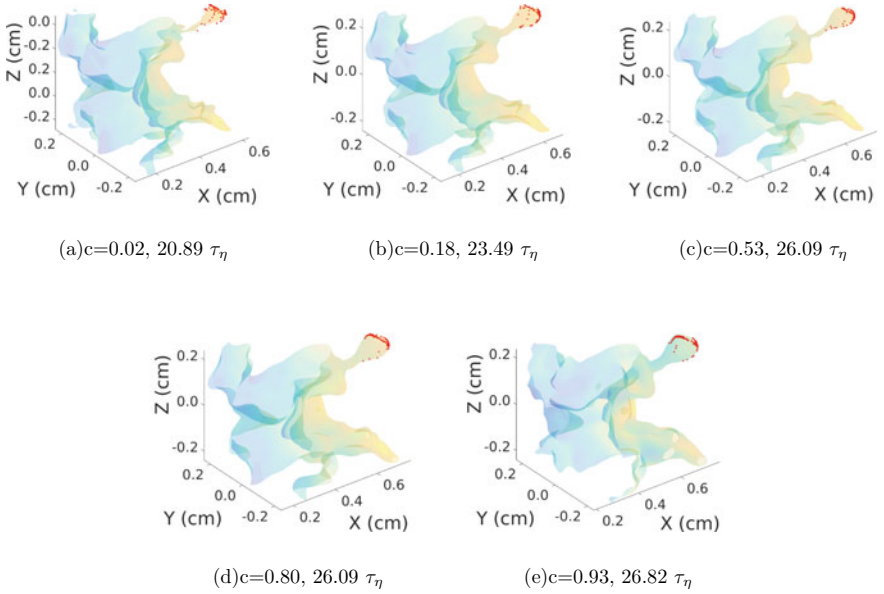

(a)c=0.02, 20.89 τ_η (b)c=0.18, 23.49 τ_η (c)c=0.53, 26.09 τ_η

(d)c=0.80, 26.09 τ_η (e)c=0.93, 26.82 τ_η

Fig. 16 Flame particle clusters at various time steps on different isoscalar surfaces

and 21 the teal colored curves represent the time history of different properties conditioned on flame particles belonging to the particular cluster, while the black lines represents the variation of that property averaged only over that cluster. As shown in Fig. 17a the value of displacement flame speed on the clustered particles increases at the end of flame particle lifetime as expected. Figure 17b shows the variation of tangential strain rate on the clustered particles. The value of K_T generally tends to increase at the end of flame particle lifetime but here the cluster is annihilated before we can see any notable difference for this particular isosurface. From Fig. 17c we can see that the magnitude of flame curvature on the clustered particles increase in the concave regions signifying wrinkling of the flame surface and attains very high values before annihilation. Figure 17d shows the variation of $|\nabla Y_{H_2}|$ with time. Since the initial value is less due to the high c value, the decrease in its value is not significant. Figure 17e shows the variation of kinematic restoration term on the clustered particles. The value of Ω increases with the wrinkling of the flame surface. The increase is significant at the end of the flame particle lifetime when the particles form a flame island. Figure 17f shows the variation of temperature on the clustered particles. The temperature at this region is very close to ambient temperature because of its proximity to the unburnt region. The notable point is that, most flame particles follow similar trends in variation of the properties which is reflected in the averaged property variation.

Figure 18 shows the variation of the parameters on the cluster formed on the isosurface, $c = 0.18$ which is shown in Fig. 16b. Figure 18a is the variation of displace-

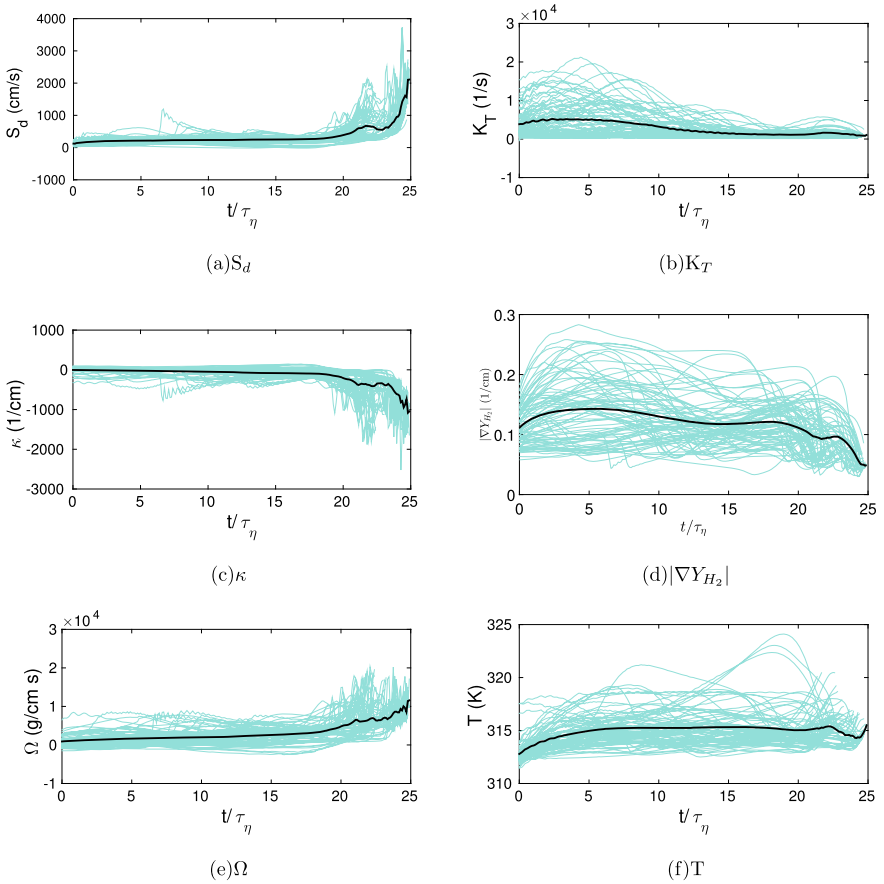

Fig. 17 Variation of properties on the clustered particles on the isosurface, $c = 0.02$

ment flame speed which increases to very high values just before particle annihilation. Figure 18b is the variation of tangential strain rate which increases at the end of flame particles' lifetime. Figure 18d is the variation of curvature of the flame surface which reaches high negative values at the end of its lifetime. Figure 18d shows the variation of $|\nabla Y_{H_2}|$ on the clustered particles with time. Since the value of c is not near the extreme values, the decrease in the value of $|\nabla Y_{H_2}|$ at the end of particle lifetime is significant. Figure 18e shows the variation of Ω on the clustered particles. The value of Ω increases with time which helps in flame particle annihilation. Figure 18f shows the variation of temperature on the clustered particles.

Similarly, Figs. 19, 20 and 21 show the variation of the parameters on the cluster formed on the isosurfaces, $c = 0.53$, $c = 0.80$ and $c = 0.93$ which are shown in Fig. 16c, d and e, respectively. The variation of properties on the clustered particles seen in Figs. 19, 20 and 21 is similar to the variations seen in Figs. 17 and 18.

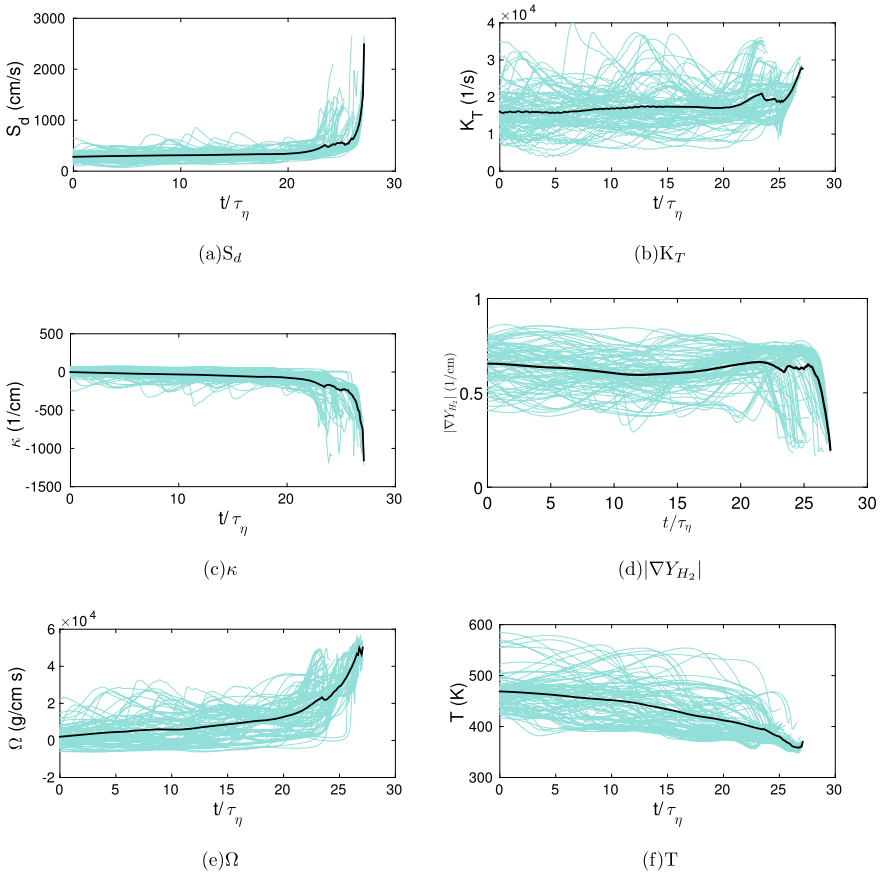

Fig. 18 Variation of properties on the clustered particles on the isosurface, $c = 0.18$

The cluster analysis results presented here could be useful to perform reduced-order modeling where a group of particles can be simplified into a single particle. To perform reduced-order modeling, the particles should execute similar behavior. This can be verified by considering the properties of the clustered particles and analyze their behavior for similarities. We can observe from Figs. 17, 18, 19, 20 and 21 that particles in a particular cluster behave in a very similar way, and the lifetime of the particles in the cluster is nearly equal. Thus, we can use physical time scale to describe the evolution of particles belonging to a given cluster, with time. This is not possible for an entire surface as particles in the different regions annihilate at different times which required us to use the normalized time scale t/τ_{FL} to describe an entire surface. Hence, the entire cluster can be reduced to a single point (need not be an actual flame particle) which is considered to represent the entire cluster, where the physical properties of this point is obtained by averaging over the cluster.

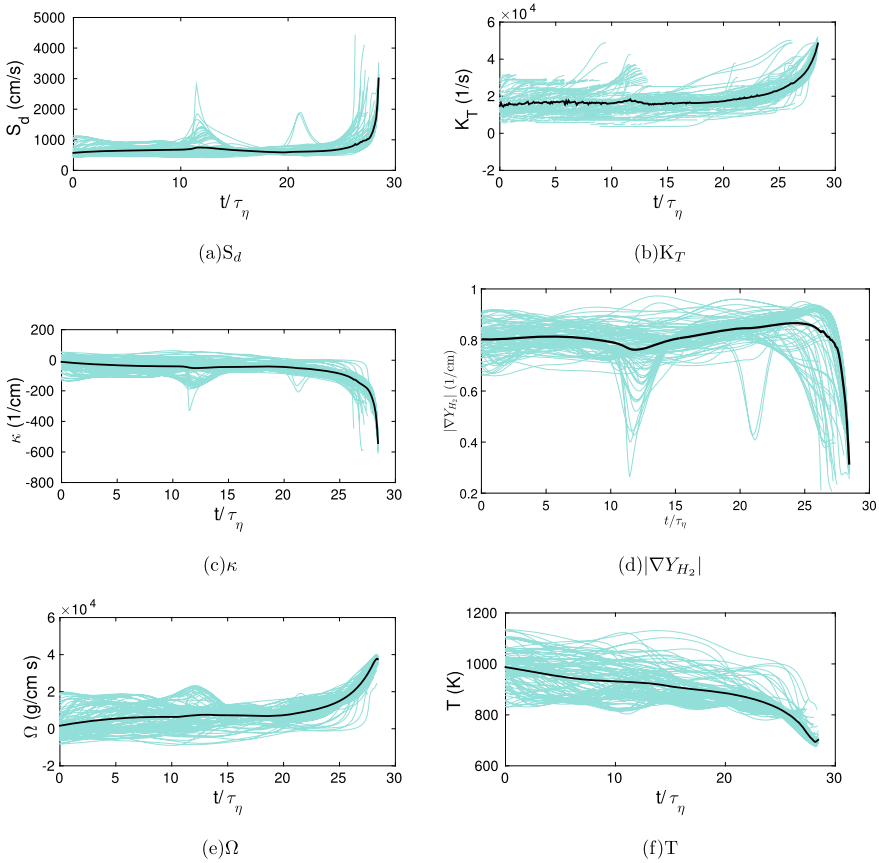

Fig. 19 Variation of properties on the clustered particles on the isosurface, $c = 0.53$

4 Conclusion

DNS of H_2-air premixed combustion is performed with detailed H_2-air reaction mechanism consisting of nine species and twenty-one reactions. "On-the-fly FPT" is used to track flame particles distributed on five different constant mass fraction surfaces of H_2. The surfaces wrinkle on interaction with turbulence causing the flame particles to preferentially cluster in different negatively curved trailing regions of the flame surface. As the wrinkling of the flame surface increases, the flame tries to smooth out the wrinkles by kinematic restoration, i.e., propagation of the flame surface normal to itself. In such situations, kinematic restoration may lead to intersection of multiple flame branch which results in flame wrinkle destruction. Kinematic restoration of the flame surface is quantified at different times. The wrinkling of flame surfaces also increases the tangential strain rate, leading to increase in negative value of the curvature resulting in a very high magnitude of local flame displacement speed.

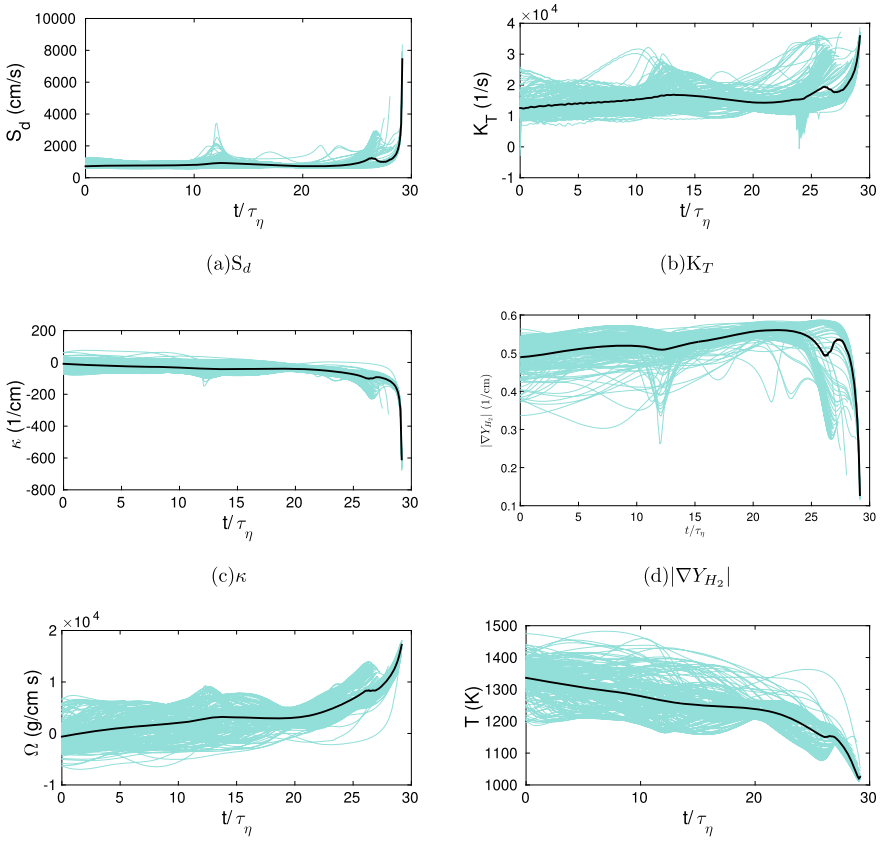

Fig. 20 Variation of properties on the clustered particles on the isosurface, $c = 0.80$

These effects culminate in local annihilation of flame surface and the resident flame particles, by forming islands or by kinematic restoration.

Cluster analysis of the particles was done using a k-medoids clustering approach which employed a partitioning around medoids (PAM) algorithm where the particles were segregated into different groups. The average distance between the particles with its medoid was calculated to identify the particle clusters. The results showed that the particles cluster at the negatively curved regions. These regions have the highest tendency for local flame annihilation. The cluster analysis performed could be applied to reduced-order modeling where the clusters on each isosurface are reduced to corresponding individual points, based on their similar physical properties. This could ensure that the computational costs are reduced without missing out on critical yet localized physical phenomena.

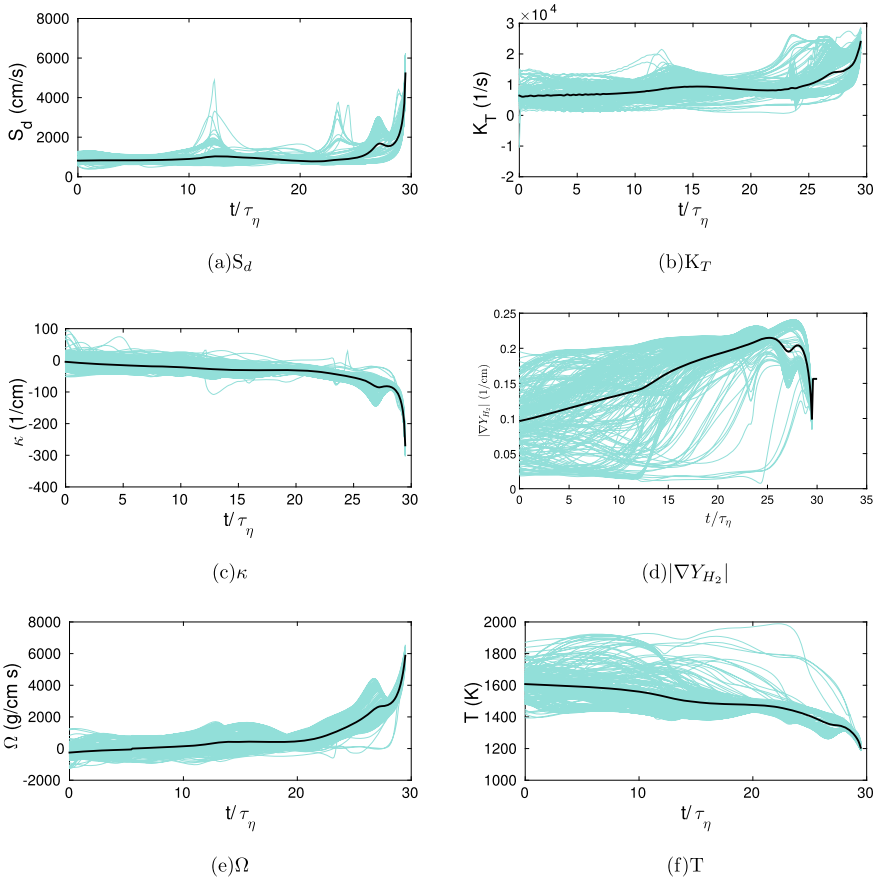

Fig. 21 Variation of properties on the clustered particles on the isosurface, $c = 0.93$

Acknowledgements Support of the Supercomputer Education and Research Center, IISc toward usage of the Cray XC-40: Sahasrat for performing the DNS reported in this paper, is gratefully acknowledged.

References

1. Lieuwen T (2012) Unsteady combustor physics. Cambridge University Press, Cambridge
2. Driscoll J (2008) Turbulent premixed combustion: flamelet structure and its effect on turbulent burning velocities. Prog Energy Combust Sci 34(1):91–134
3. Swaminathan N, Bray KNC (2011) Turbulent premixed flames. Cambridge University Press, Cambridge
4. Gore J, Zhan N (1996) No$_x$ emission and major species concentrations in partially premixed laminar methane/air co-flow jet flames. Combust Flame 105(3):414–418, IN1, 419–427

5. Khokhlov A (1995) Propagation of turbulent flames in supernovae. Astrophys J 449:695
6. Oran E (2005) Astrophysical combustion. Proc Combust Inst 30(2):1823–1840
7. Poinsot T (1996) Using direct numerical simulations to understand premixed turbulent combustion. In: Symposium (international) on combustion, vol 26. Elsevier, pp 219–232
8. Pitsch H (2006) Large-eddy simulation of turbulent combustion. Annu Rev Fluid Mech 38:453–482
9. Chen J, Echekki T, Kollmann W (1999) The mechanism of two-dimensional pocket formation in lean premixed methane-air flames with implications to turbulent combustion. Combust Flame 116(1):15–48
10. Echekki T, Chen J (1996) Unsteady strain rate and curvature effects in turbulent premixed methane-air flames. Combust Flame 106(1–2):184–190, IN1–IN4, 191–202
11. Salazar J, Collins L (2009) Two-particle dispersion in isotropic turbulent flows. Annu Rev Fluid Mech 41:405–432
12. Chaudhuri S (2015) Pair dispersion of turbulent premixed flame elements. Phys Rev E 91(2):021001
13. Pope S (1994) Lagrangian pdf methods for turbulent flows. Annu Rev Fluid Mech 26(1):23–63
14. Girimaji S, Pope S (1992) Propagating surfaces in isotropic turbulence. J Fluid Mech 234:247–277
15. Toschi F, Bodenschatz E (2009) Lagrangian properties of particles in turbulence. Annu Rev Fluid Mech 41:375–404
16. Yeung P (2002) Lagrangian investigations of turbulence. Annu Rev Fluid Mech 34(1):115–142
17. Pope S (1988) The evolution of surfaces in turbulence. Int J Eng Sci 26(5):445–469
18. Chaudhuri S (2015) Life of flame particles embedded in premixed flames interacting with near isotropic turbulence. Proc Combust Inst 35(2):1305–1312
19. Uranakara H, Chaudhuri S, Dave H, Arias P, Im H (2016) A flame particle tracking analysis of turbulence-chemistry interaction in hydrogen-air premixed flames. Combust Flame 163:220–240
20. Uranakara H, Chaudhuri S, Lakshmisha KN (2017) On the extinction of igniting kernels in near-isotropic turbulence. Proc Combust Inst 36(2):1793–1800
21. Möller T, Trumbore B (2005) Fast, minimum storage ray/triangle intersection. In: ACM SIGGRAPH 2005 courses. ACM, p 7
22. http://pencil-code.nordita.org/ (2013)
23. Williamson J (1980) Low-storage Runge-Kutta schemes. J Comput Phys 35(1):48–56
24. Li J, Zhao Z, Kazakov A, Dryer F (2004) An updated comprehensive kinetic model of hydrogen combustion. Int J Chem Kinet 36(10):566–575
25. Babkovskaia N, Haugen N, Brandenburg A (2011) A high-order public domain code for direct numerical simulations of turbulent combustion. J Comput Phys 230(1):1–12
26. Jain A, Murty M, Flynn P (1999) Data clustering: a review. ACM Comput Surv (CSUR) 31(3):264–323
27. Lucia D, Beran P, Silva W (2004) Reduced-order modeling: new approaches for computational physics. Prog Aerosp Sci 40(1):51–117
28. Kaufman L (1987) Clustering by means of medoids. Statistical data analysis based on the L1-norm and related methods
29. Kaufman L, Rousseeuw PJ (1990) Partitioning around medoids (program pam). Finding groups in data: an introduction to cluster analysis, pp 68–125
30. Law CK (2010) Combustion physics. Cambridge University Press, Cambridge
31. Dave H, Swetaprovo C (2020) Evolution of local flame displacement speeds in turbulence. J Fluid Mech 884(A46):1–47
32. Wenzel H, Peters N (2005) Scaling of production, kinematic restoration, and dissipation of the mean flame surface area. Combust Sci Technol 177(5–6):1095–1107
33. Lipatnikov A, Chomiak J, Sabelnikov V, Nishiki S, Hasegawa T (2015) Unburned mixture fingers in premixed turbulent flames. Proc Combust Inst 35(2):1401–1408

Starting Characteristics of a Micro Gas Turbine Engine at Different Loading Conditions

T. Chandra Sekar, Ramraj H. Sundararaj, Rajat Arora, and Abhijit Kushari

Nomenclature

A	Area
CG	Centralized power generation
C-D	Convergent divergent
C_{pc}	Specific heat at constant pressure cold side
C_{ph}	Specific heat at constant pressure hot side
DG	Distributed power generation
ECU	Electronic control unit
EGT	Exhaust gas temperature
J	Polar moment of Inertia
L-1	Test configuration 1
L-2-I	Test configuration 2 (Trail 1)
L-2-II	Test configuration 2 (Trial 2)
M	Mach number
N	Angular speed (Revolutions per minute)
N1	Convergent nozzle 1
N2	Convergent nozzle 2
N-L	No load
P	Static pressure
P_t	Total pressure
T	Static temperature
T_t	Total temperature
w	Power
TET	Turbine entry temperature

T. C. Sekar · R. H. Sundararaj · R. Arora · A. Kushari (✉)
Department of Aerospace Engineering, Indian Institute of Technology Kanpur, Kanpur, India
e-mail: akushari@iitk.ac.in

© Springer Nature Singapore Pte Ltd. 2021

A. De et al. (eds.), *Sustainable Development for Energy, Power, and Propulsion*, Green Energy and Technology,
https://doi.org/10.1007/978-981-15-5667-8_16

$\dot{v}$	Flow rate (cc/min)
$\dot{V}$	Volume flow rate (m^3/s)
π_c	Compressor pressure ratio
π_t	Turbine pressure ratio
$\dot{m}_a$	Mass flow rate of air
$\dot{m}_f$	Mass flow rate of fuel
ω	Angular velocity
η_c	Isentropic efficiency compressor
η_t	Isentropic efficiency turbine
γ_c	Ratio of specific heat cold side
γ_t	Ratio of specific heat hot side

Subscript

3	Compressor exit
4	Turbine inlet
5	Turbine exit
6	Nozzle exit
a	Ambient conditions
e	Exit
f	Fuel
i	Initial
red	Reduced

1 Introduction

Gas turbines inherently have a high thrust-to-weight ratio, making them an efficient propulsive device for aircraft. Gas turbines also offer a more efficient alternative for electric power generation. They can be used with a wide range of fuels, have lower emissions, a smaller footprint and better reliability. Gas turbine-based power plants require fewer secondary systems for their smooth operation, making them easier to start/stop. The response of a gas turbine to load changes is faster as compared to conventional power plants. These qualities combined makes a gas turbine-based distributed power generation (DG) and supply system, a more lucrative option compared to other sources of power generation. However, a DG system is associated with other technical issues such as voltage/current transients [1] and frequency control [2]. Re-synchronization issues may arise with small gas turbine units because of their lower rotor inertia [3].

Understanding the transient operation of a gas turbine during starting or load changes is important, since the components may encounter instabilities (surge, higher

combustion chamber temperatures, etc.) which may result in catastrophic failure of the gas turbine engine. A power generation gas turbine has several operating regimes such as load increase/decrease as decided by operator, response to load rejection, trip and over/under frequency events [4]. All the events are transient in nature. Information on transient characteristics would help decide the engine response and, in turn, help design the control system for adapting the power plant to the above mentioned events.

Consider the starting process of a gas turbine in a power plant. The speed of the engine rotor has to be increased from zero to the synchronization speed and then to its full speed under no-load condition [4]. After the full speed is achieved, the load is increased (to full load or a value as selected by user) by connecting the generator to the grid. All these steps are to be carried out while keeping in consideration the critical parameters such as stress, temperature, combustion instability, compressor stall and surge. The major factors involved in transient analysis for a gas turbine used in power plant are shaft speed (rotor speed), heat soak and volume packing [4].

One of the early works in this direction was by Agarwal and Yunis [5], in which a general model to estimate starting characteristics of a gas turbine engine was proposed. The model was capable of predicting minimum starting torque requirements and startup time at any ambient temperature and altitude condition. A general model for prediction of transient performance of a gas turbine was proposed by Pilidis and Maccallum [6], and the method was applied to various configurations including single-spool and multi-spool configurations without including the influence of thermal effects. The model developed by Ganji et al. [7] has the capability to predict the transient behavior of the engine, when the C-D nozzle area is changed with time, keeping the throat area constant. There was a sharp increase in thrust with increase in nozzle area. However, there are no other effects as the nozzle was chocked. The work by Asgari et al. [8] showed that models based on Simulink and NARX (nonlinear autoregressive exogenous model) are capable of satisfactory predictions, with the experimental data (taken during gas turbine normal operation) used for model training and validation. The energy density of the fuel was found to have a noticeable effect on the rotor over-speed [9]; hence, it must be considered when designing the fuel control system.

In the present work, experiments have been carried out on a micro turbojet engine fitted with a convergent nozzle. Various thermodynamic and structural dynamic parameters were measured at different locations, using which different parameters related to gas turbine performance were estimated. The gas turbine was tested at three different loading conditions. The loading on the gas turbine was simulated by reducing the nozzle exit area. The control logic used for gas turbine operation remains unaltered for all test conditions. The difference in steady-state operation between the no-load and first load condition is compared. Also, the starting characteristics for the three differently loaded conditions are compared to garner a better understanding of the transient process involved.

2 Experimental Setup and Instrumentation

Following conventional nomenclature, Station 2 is the inlet of the engine, Station 3 is after the compressor, Station 4 is after the combustion chamber and Station 5 is after the turbine. Station 6 is usually used for the mixer; however, in this setup, it is used to denote the exit of the jet pipe or the start of the nozzle.

2.1 Single-Spool Turbojet Engine

The baseline engine comprises a single-stage centrifugal compressor mechanically coupled and driven by a single-stage axial flow turbine. The assembly consisting of the compressor, turbine and interconnecting shaft is referred to as "rotor" in the ensuing discussions. Between the compressor and turbine is a reverse flow-type combustion chamber. A bell mouth intake is present upstream of the compressor for flow conditioning at inlet. Following the turbine exit duct, there is a nozzle of very short length. The engine is equipped with an electric motor, located outside the engine upstream of the intake. The electric motor rotates the rotor during engine starting, providing the necessary speed, and thus the inlet air mass flow rate for combustion of the fuel. A fuel pump along with two valves provides the starting and main fuel for the engine. The flow rate of fuel is controlled by means of altering the pump voltage.

The engine control system consists of an electronic control unit (ECU) and a control box. The control box consists of a switch and throttle knob. The switch has three positions, depending on the required operation in the start/stop sequence. The throttle knob is used for increasing/decreasing rotor speed and hence engine thrust/power output. Based on the throttle setting by the user, the ECU regulates the fuel flow rate accelerating/decelerating the rotor to the required speed. A picture of the engine, taken during testing, is shown in Fig. 1. A sectional view of the engine showing the components and measurements locations is shown in Fig. 2.

2.2 Pressure Measurements

Three total pressure ports are provided at stations 3–5, circumferentially distributed 120° apart along the circumference of the engine. The total pressure ports at Station 3 are interconnected, giving a circumferentially averaged total pressure (P_{t3}). Station 3 also has three static pressure ports, which are circumferentially averaged, for measurement of compressor exit static pressure (P_{s3}). The total pressure ports at Station 4 are not circumferentially averaged, but taken individually. This is because the pressures are not uniform, and circumferential averaging will lead to cross flow

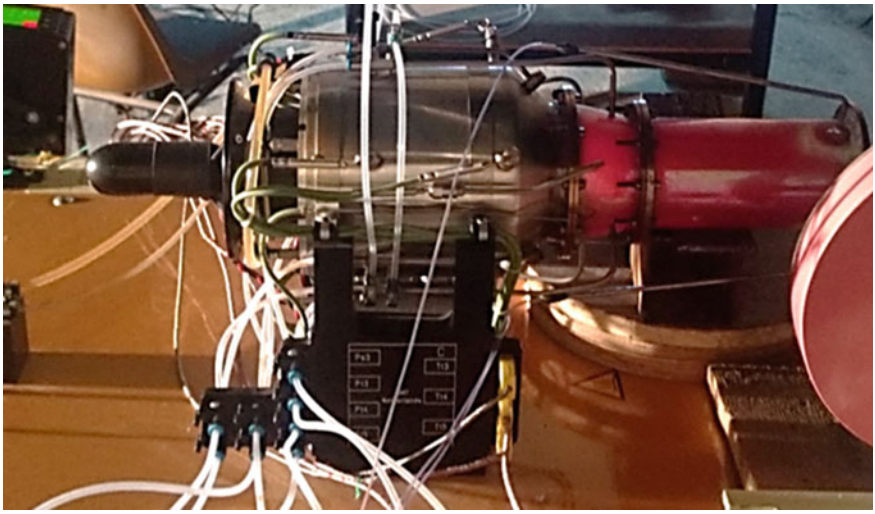

Fig. 1 Picture of the engine fitted with jet pipe

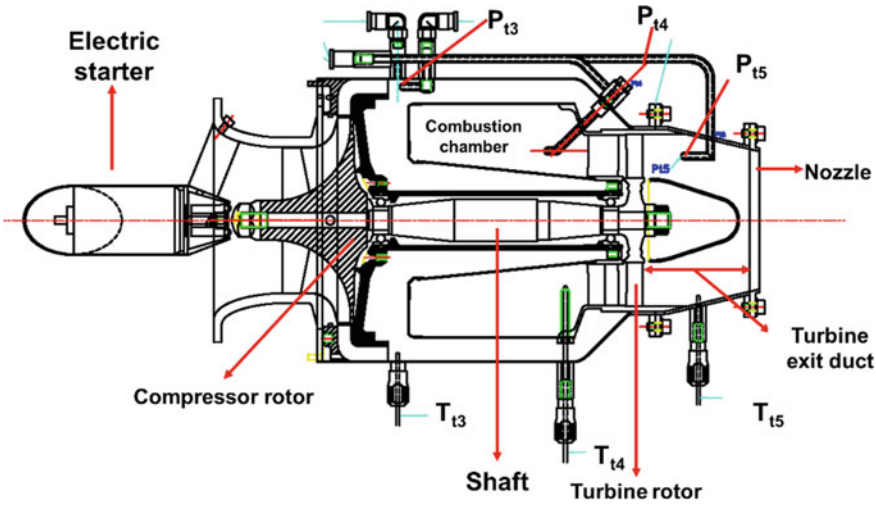

Fig. 2 Sectional view of the engine showing various components and measurements

between the ports. Similarly, the total pressure ports at Station 5 are not circumferentially averaged, but taken individually. Additionally, three static pressure ports are present at Station 6, the exit of the jet pipe, just ahead of the nozzle N1.

2.3 Temperature Measurements

At every station, there are three thermocouples installed. Similar to the pressure ports, the thermocouples are installed 120° apart along the circumference of the engine. K-type thermocouples are used at all stations. In addition to this, a thermocouple is installed in the turbine exit duct, for measurement of exhaust gas temperature (EGT). This measurement is directly read by the ECU and serves as a control parameter during start/stop sequences.

2.4 Other Measurements

The engine is equipped with a speed sensor to measure the rotor speed (N) and a turbine flow meter to measure the fuel flow rate $\left(\dot{v}_f\right)$. These measurements are also directly read by the ECU and serve as control parameters during start/stop sequence.

2.5 Data Acquisition

The pressure ports are connected to a 16-port pressure scanner for pressure measurement. The data from the pressure scanner, thermocouples, ECU (N, throttle setting) and fuel flow meter are recorded in real time during experiment using a computer-based data acquisition system from National Instruments (NI®). The data from ECU and fuel flow meter are sampled once every one second. The data from each port in pressure scanner is read 100 times a second, and average of these samples is recorded at end of second. Details pertaining to all the measurements are given in Table 1, and the ambient conditions during engine testing are given in Table 2.

2.6 Simulating Loading on Engine

The loading condition on the engine is simulated by reducing the exit area of the nozzle, as shown in Fig. 3. The engine is fitted with a constant area jet pipe. The exit area of the jet pipe is designated as "A_i" and the test condition is referred as no-load (N-L) test case. A circular converging nozzle (N1) with ~20% area reduction (i.e., $A_e \approx 0.8\,A_i$) is attached at the exit of jet pipe, as shown in Fig. 3. In this configuration, the nozzle exit area is ~20% less than that of N-L case, and the engine is considered to be under loading condition. This configuration is referred as load-1 (L-1) test case. Further, a second circular converging nozzle (N2) is attached at the exit of N1, to reduce area by ~38% (i.e., $A_e \approx 0.6\,A_i$). In this configuration, the

Table 1 Measurement type and measurement locations

Station #	Station name	Parameter	# Measurements
3	Compressor exit/combustor inlet	Static pressure (P_{s3})	03 (120° apart) (averaged)
		Total pressure (P_{t3})	03 (120° apart) (averaged)
		Temperature (T_{t3})	03 (120° apart)
4	Combustor exit/turbine inlet	Total pressure (P_{t4})	03 (120° apart)
		Temperature (T_{t4})	03 (120° apart)
5	Turbine exit/nozzle inlet	Total pressure (P_{t5})	03 (120° apart)
		Temperature (T_{t5})	03 (120° apart)
		Exhaust gas temperature (EGT)	01 (ECU)
–	Rotor	Engine speed (N)	01 (ECU)
6	Exhaust/nozzle	Static pressure (P_{s6})	03 (120° apart)
a	Ambient	Temperature (T_a)	01 (Ambient)
		Pressure (P_a)	
–	Fuel flow meter	Fuel flow rate ($\dot{\mathbf{v}}_\mathbf{f}$)	01 (Turbine flow meter)

Table 2 Ambient conditions

Parameter	Value
Flight Mach number (M)	0
Ambient Temperature (T_a)	20 °C
Flight altitude	126 m above sea level

nozzle exit area is ~38% less than that of N-L case, and this configuration is referred as load-2 (L-2) test case. The last configuration (L-2) was tested twice. During the second test with L-2 configuration (Test 4), to enable a smooth start, the initial fuel pump voltage was reduced by 12.5%. All test cases are shown in Table 3.

2.7 Experimental Procedure

Routine checks are carried out before the start of every experiment, ensuring that all systems are working satisfactorily. Following this, continuous data recording is started until the end of the test. After the data acquisition is started, the starting sequence is activated using the control box, for the engine to start. After the engine starts successfully and reaches idle operating speed, the throttle knob is used to increase speed. The rotor speed (N) is increased from 30,000 rpm to 83,000 rpm in required steps. Auto shutdown switch setting is used to stop the engine and initiate auto cool down procedure after the tests. For all the test conditions, the measurements, control system and control logic were unchanged.

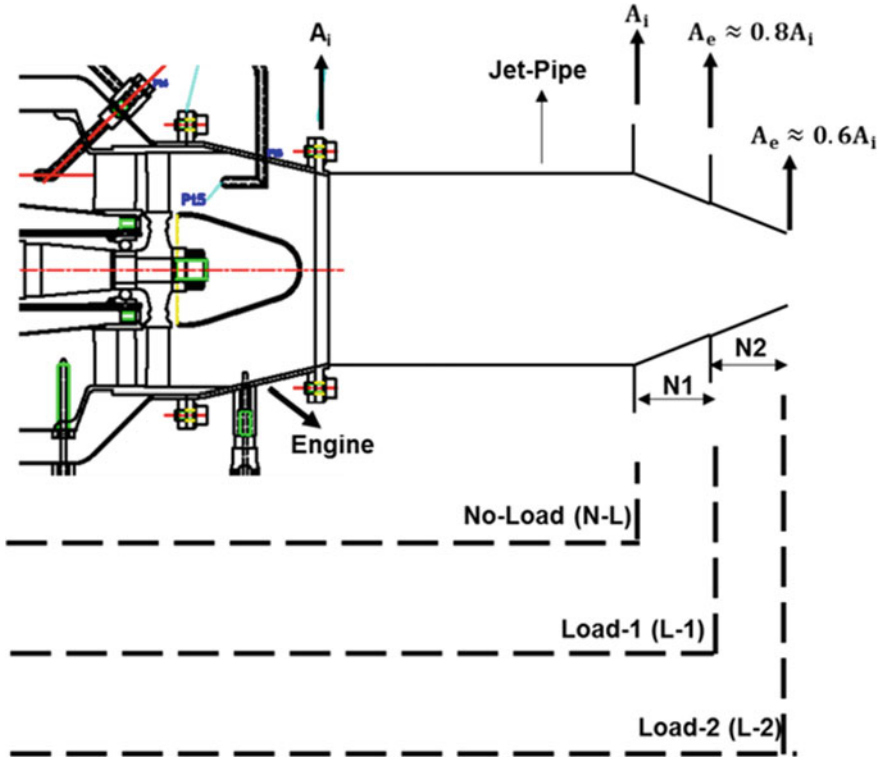

Fig. 3 Schematic diagram showing the configurations used for simulating different loading conditions on the engine

Table 3 Test matrix

Test #	Test condition	Area reduction (%)	Case name
Test 1	Base engine	0	No-Load (N-L)
Test 2	Base engine + N1	20.72	Load-1 (L-1)
Test 3	Base engine + N1 + N2	37.68	Load-2 (L-2-I)
Test 4	Base engine + N1 + N2	37.68	Load-2 (L-2-II)

2.8 Engine Starting Procedure

For easy inference, all the events have been indicated using numerals in Fig. 4. It shows the behavior of rotor speed (N) during the starting process.

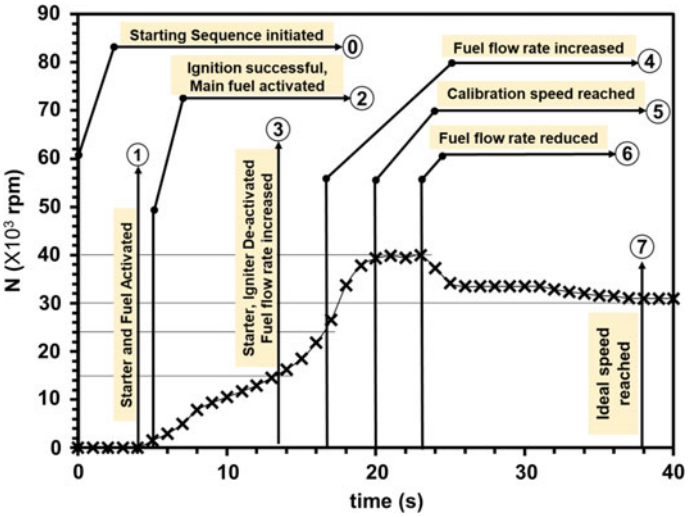

Fig. 4 Behavior of rotor speed (N) along with various events associated with the engine starting sequence

The starting sequence is initiated by setting the control switch to "run" position. After the starting sequence is initiated (event-0), an electric glow plug (used for ignition) is activated. After 5 s (from event-0), the electric starter is activated (event-1). As the rotor speed (N) reaches 3,000 rpm, the fuel pump is activated injecting the starting fuel required for ignition. Successful ignition is when there is a 5 °C temperature rise in EGT. After ignition is successful (event-2), fuel through main fuel line is started, and the power to the starter motor is increased to 100% of rated value. As $N \rightarrow$ 15,000 rpm, the igniter, electric starter and starting fuel are deactivated. Simultaneously, fuel flow rate through the main fuel line is increased (event-3). As $N \rightarrow$ 24,000 rpm, the fuel flow rate is further increased (event-4). This new fuel flow rate increases N to 40,000 rpm (event-5). This speed is maintained for 2–3 s allowing for control system calibration, following which the fuel flow rate is reduced (event-6) to decrease the rotor speed to the idle value of 30,000 rpm (event-7).

3 Results and Discussion

3.1 Steady-State Operation of the Engine

For the first two test configurations (N-L and L-1), the engine start sequence was successful, and the rotor speed (N) was increased gradually to 83,000 rpm to simulate different power/thrust settings. The engine performance for these two tests is represented on a compressor map, shown in Fig. 5. The X-axis corresponds to corrected

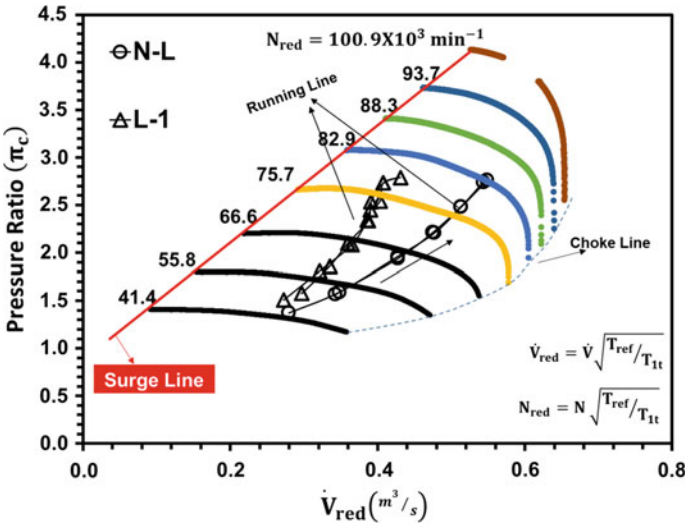

Fig. 5 Compressor map showing running line for both N-L and L-1 test cases

volumetric air flow rate $\left(\dot{V}_{\text{red}}\right)$, and the Y-axis corresponds to compressor pressure ratio (π_c). The continuous lines of varying color represent lines of constant reduced shaft speed (N_{red}). The volumetric air flow rate is estimated from the measured values of compressor pressure ratio $\left(\pi_c = \frac{P_{t3}}{P_a}\right)$ and shaft speed (N). The locus of all the steady-state operating points is referred to as "running-line" for the engine. These steady-state operating points are plotted in real time, as the experiment proceeds, allowing the controller to monitor engine performance in real time.

For the N-L test case, which serves as the baseline, upon increasing throttle, the operating point of the compressor shifts toward higher π_c and higher $\dot{V}_{\text{red}}$, as is expected. For $N_{\text{red}} \cong 42,000$ rpm, the operating point is closer to choke line, and as N is increased, the operating point moves to the center of region bounded by the surge and choke lines. When the throttle is decreased back to idle, the points perfectly retrace the running line. During engine operation with load (L-1), at lower rotor speed (42,000 rpm), the equilibrium operating points are closer to the N-L test case. As N increases, the operating point shifts away from the running line for N-L test case and moves toward the surge line. Based on the observed trend during experiments, for higher values of N ($N > 83,000$ rpm), the running line is expected to move closer to the surge line or even cross the surge line. Owing to this, the engine was not operated at higher speeds and limited to a maximum of 80,000 rpm for the L-1 test case. This shift in the running line for L-1 compared to N-L is due to a mass flow rate reduction caused by the smaller exit area presented by L-1 compared to N-L.

In addition to shifting the running line toward the surge line, turbine inlet temperatures (T_{t4}) are higher when operating at L-1. This is illustrated in Fig. 6, along with fuel flow rate and equivalence ratio. At lower speeds, fuel flow rate T_{t4} and equivalence ratio are fairly similar for both the test cases. At higher speeds, the difference

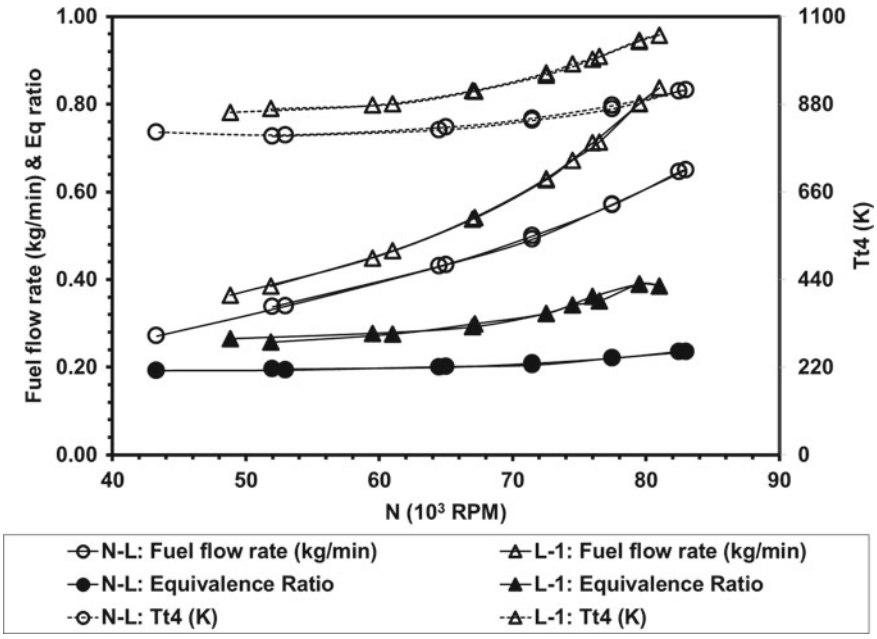

Fig. 6 Variation of fuel flow rate, equivalence ratio and T_{t4} with rotor speed (N) for both N-L and L-1 test cases

between the two cases becomes larger. Higher T_{t4} is required to provide adequate energy to the turbine, allowing it to accelerate the rotor to the required speed. This additional energy is required since the air flow rate through the engine has reduced. The additional energy is provided by increasing the fuel flow rate, which in turn provides higher temperatures, allowing the turbine to extract more energy from a flow that has reduced mass, to meet the compressor's demand.

Consider the behavior of compressor pressure ratio $\left(\pi_c = \frac{P_{t3}}{P_a}\right)$ and turbine pressure ratio $\left(\pi_t = \frac{P_{t4}}{P_{t5}}\right)$ with rotor speed (N), shown in Fig. 7. The compressor map shown in Fig. 5 shows that when operating on a constant speed line, compressor pressure ratio increases when air flow rate is reduced. During compressor testing and characterization, this is usually done by reducing the compressor exit area or throttling the compressor [10]. A similar effect occurs when running engine at L-1 test condition. When operating the engine at the same speed for both test cases, there is an increase in compressor pressure ratio for L-1 as compared to N-L. However, when throttled, the turbine pressure ratio and air flow rate decrease, as depicted in any standard turbine characteristic map [10]. The effect of throttling on compressor and turbine performance leads to the difference in pressure ratio between the two test conditions, as shown in Fig. 7. This difference in compressor pressure ratio is lower compared to the difference in turbine pressure ratio between the two test conditions.

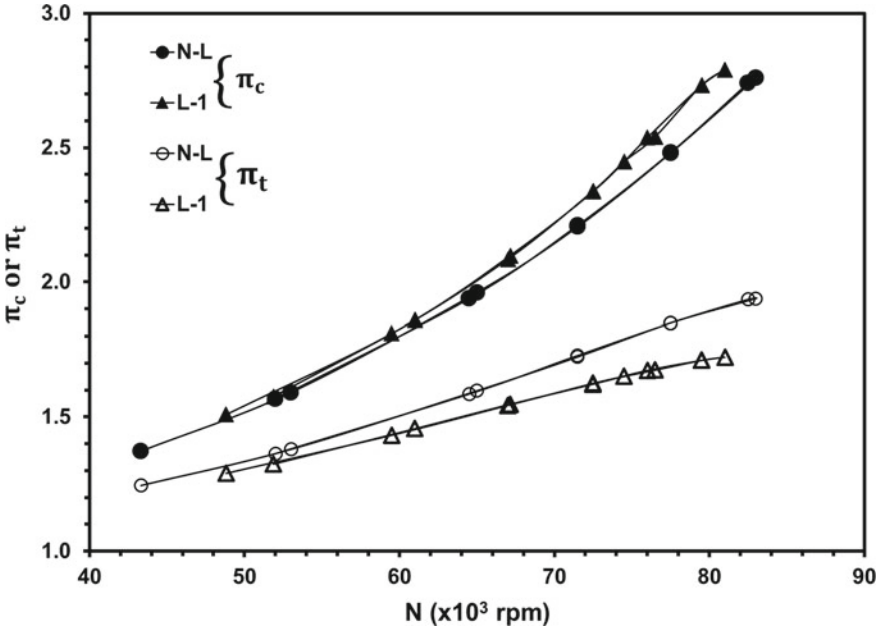

Fig. 7 Behavior of compressor pressure ratio (π_c) and turbine pressure ratio (π_t) with rotor speed (N) for both N-L and L-1 test cases

$$w_t = \eta_t\left(\dot{m}_a + \dot{m}_f\right)C_{ph}T_{t4}\left(1 - \left(\frac{P_{t4}}{P_{t5}}\right)^{\frac{1-\gamma_h}{\gamma_h}}\right) \tag{1}$$

$$w_c = \frac{\dot{m}_a C_{pc} T_a}{\eta_c}\left(\left(\frac{P_{t3}}{P_a}\right)^{\frac{\gamma_c - 1}{\gamma_c}} - 1\right) \tag{2}$$

From Fig. 7, between the two test conditions at a given N, the value of π_c increases while the mass flow rate reduces. Hence, at a given N, the power required by the compressor (w_c) remains constant for both test conditions. However, at a given N, the value of π_t and air mass flow rate decreases between the two test conditions. This will result in a lower w_t than what is required to accelerate the rotor to the required speed, if the value of T_{t4} (TET) is maintained constant. To overcome this deficit, $\dot{v}_f$ is higher for L-1 compared to N-L resulting in a higher TET which is required to compensate for the reduction in turbine pressure ratio (π_t) and engine air mass flow rate.

3.2 Transient Operation During Engine Starting

Transient operation during engine starting procedure is discussed here to better understand the effect of loading conditions when the engine is started. A total of three configurations are studied in this section. The first configuration is the no-load configuration, referred to as N-L. There is no area reduction for this case. The no-load case (N-L) serves as the baseline, against which the other cases are compared. The second case is the first loading condition, referred to as L-1. The exit area is reduced by attaching nozzle N1 to the jet pipe. The third case is the second loading condition, referred to as L-2. The exit area is further reduced by attaching nozzle N2 to the jet pipe.

The engine was unable to start and reach a stable speed when operated at L-2. With a further reduction in area, the air mass flow rate is bound to have decreased even further than it did at L-1. However, the fuel flow rate during the initial phase of the starting procedure (Event 0–Event 3) remained fairly constant. This could have led to incomplete combustion owing to the fuel–air ratio being richer than what is desirable. This would have led to reduced acceleration rates for the rotor, resulting in a failed start. Based on this preliminary analysis, another attempt was made to start the engine at L-2. To facilitate better combustion, the fuel pump voltage was reduced, thus reducing the initial amount of starting fuel that is supplied to the engine. This is the fourth case, where the engine configuration is same as L-2, but with a reduced fuel pump voltage at engine start.

For both experiments at L-2, the engine starting sequence was forcefully interrupted owing to the continuous increase in TET, preventing critical damage to the hot parts of the engine. In order to understand the reasons for the failed start, we consider the behavior of various parameters during the starting phase of the engine (Figs. 8 and 9).

Various events related to starting procedure were explained earlier in Fig. 4, and the corresponding events are shown using numerals in all figures in this section. To further elucidate the starting procedure, we consider rotor speed, fuel flow rate and TET for N-L case. Here, more emphasis is given to the behavior of TET, since it is a critical parameter which reached higher values leading to an interrupted start for higher loading conditions. After the starting sequence is initiated (event-0) and the rotor starts spinning (event-1), the starting fuel is injected and fuel is ignited (event-2). There is an increase in TET, shown as event-2 in Fig. 10. After this, the starter motor speed increases to 15,000 rpm (event-3) and the value of TET increases to ~650 °C shown as event-3 in the figures. This rise in TET is caused due to the fuel flow addition from the main fuel line. After the starter motor and igniter are deactivated, $\dot{v}_f$ is increased (event-3). After this increase in $\dot{v}_f$, TET increases to 730 °C and remains a constant for a short duration. This is the peak value of TET during the starting process. However, N continues to increase reaching 24,000 rpm. After $\dot{v}_f$ is further increased (event-4), the value of TET starts to decrease, and N further increases to 40,000 rpm. This rotor speed, 40,000 rpm, is called “calibration

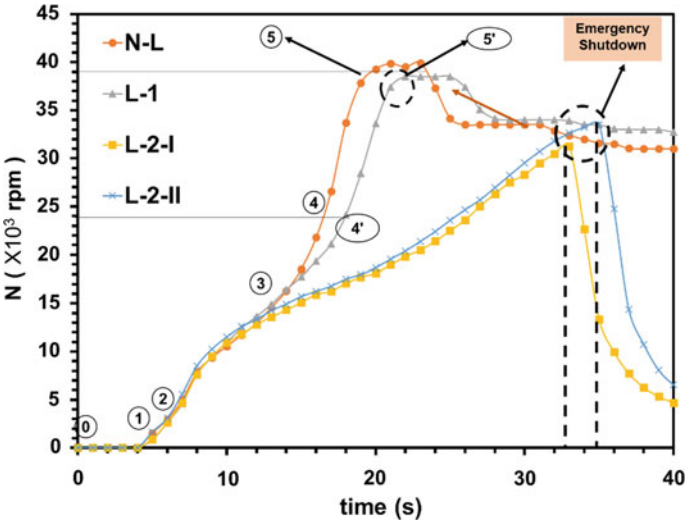

Fig. 8 Behavior of rotor speed (N) during starting process of the engine for all the test cases N-L, L-1 and L-2

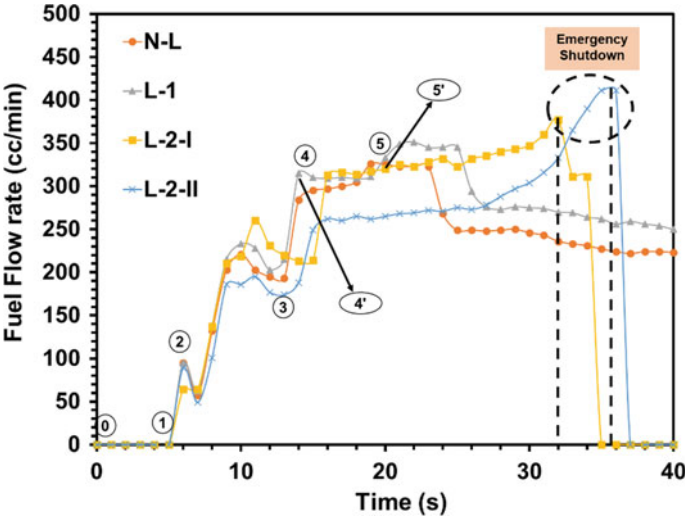

Fig. 9 Variation of fuel flow rate during starting process of the engine for all the test cases N-L, L-1 and L-2

speed." The control system is calibrated at this speed. After N reaches a value of 40,000 rpm, $\dot{v}_f$ is reduced, decreasing N to the idle speed of 30,000 rpm.

Comparing the transient performance of L-1 with N-L, the behavior of N and TET is similar up to event-3 (i.e., $N = 15{,}000$ rpm). After the electric starter is

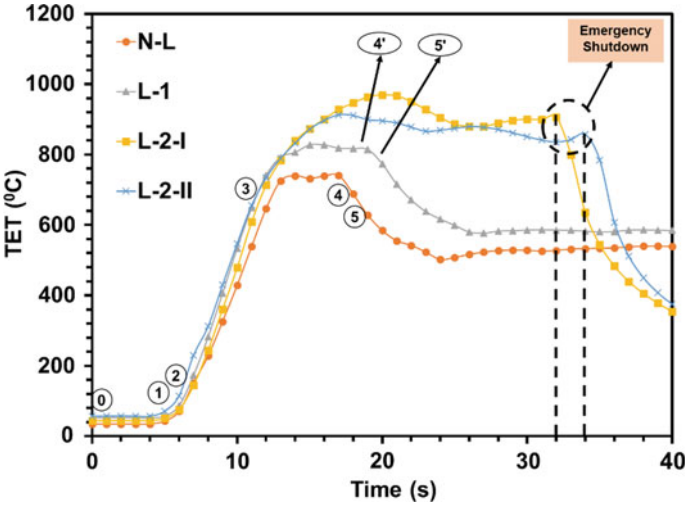

Fig. 10 Behavior of turbine entry temperature (TET) during starting process of the engine for all test cases N-L, L-1 and L-2

disengaged (event-3), the rate of increase of N is higher for N-L (event-4) compared to L-1 (event-4′), and the value of TET is higher by ~80 °C for L-1 (event-4) compared to N-L (event-4′). Hence, engine takes longer to reach $N = 24{,}000$ rpm for L-1. With increase in $\dot{v}_f$ at $N = 24{,}000$ rpm, the rate of increase of N is lower for L-1, until the rotor speed reaches 40,000 rpm (event-5 and event-5′). Also, the decrease in value of TET is approximately same for both cases. Between event-5 and event-6, $\dot{v}_f$ is ~6% higher for L-1 compared to N-L. This increased $\dot{v}_f$ is the reason for a higher TET for L-1. In summary, the peak value of TET (event-3) is higher by ~80 °C for L-1 compared to that N-L, and the startup sequence is delayed by approximately 2 s.

Comparing L-2 with N-L, the behavior of N and TET is same until 15,000 rpm (event-3). After the electric starter is disengaged (event-3), the rate of increase in N is lower for L-2 as compared to the previous two cases. TET increases to ~1000 °C at N ~ 20,000 rpm. Further on in the starting procedure, the value of TET decreases to 900 °C as $N \rightarrow 30{,}000$ rpm. At this instant, the emergency stop switch is activated to stop the engine. A second attempt was made with reduced starting pump voltage (reduce the amount of starting fuel). The behavior of N and TET for second attempt is same as that of first attempt.

As can be observed from Fig. 9, for L-2, $\dot{v}_f$ is increasing continuously exceeding the peak value for N-L and L-1 after the electric starter is deactivated (event-3). This continuous increase in $\dot{v}_f$ is enforced by the ECU in an attempt to achieve a rotor speed of 40,000 rpm as required by its algorithm for calibration of the control system. After event-2, $\dot{v}_f$ is ~16% lower for the second attempt with L-2 (Test-4) compared to the first attempt (Test-3). This is due to the reduction in the initial fuel pump voltage.

For L-2, the value of TET crossed the safe operation limits before the rotor could reach the required speed (N). In an attempt to reach the required N, the ECU continuously increased fuel flow rate. The starting procedure was aborted when it became apparent that the rotor will not reach the required calibration speed of 40,000 rpm and also because TET was higher than before. Further stressing the engine and pushing it to reach the required calibration speed could have resulted in undesirable damage to the core components.

To further understand the reasons for the behavior of N and TET, the acceleration/deceleration of the rotor $\left(\frac{dN}{dt}\right)$ and net shaft power (w_{net}) are considered. The value of $\frac{dN}{dt}$ is computed from the measured values of N using Eq. 3. The net shaft power (w_{net}) is given by Eq. 4, where w_t is the power from turbine (Eq. 1) and w_c is the power required by the compressor (Eq. 2). The acceleration/deceleration $\left(\frac{dN}{dt}\right)$ and net power available w_{net} are related by Eq. 5, where J is the polar moment of inertia of the rotor and ω is angular speed of rotor. In Eq. 5, since the term J is a constant for the rotor, the quantity $N\frac{dN}{dt}$ is used as a measure of w_{net}.

$$\left.\frac{dN}{dt}\right|_{t=t} = \frac{N_t - N_{t-1}}{1} \tag{3}$$

$$w_{net} = w_t - w_c \tag{4}$$

$$w_{net} = J\omega\frac{d\omega}{dt} \quad \text{where, } \omega = \frac{2\pi N}{60} \tag{5}$$

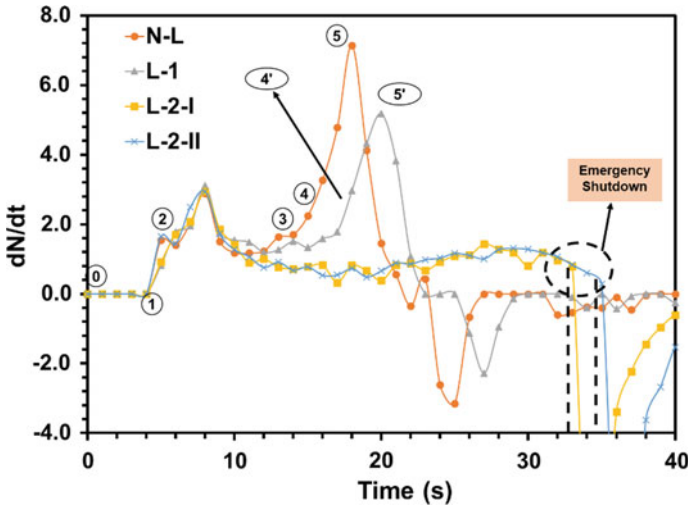

Fig. 11 Behavior of $\frac{dN}{dt}$ during starting process of the engine for all test cases

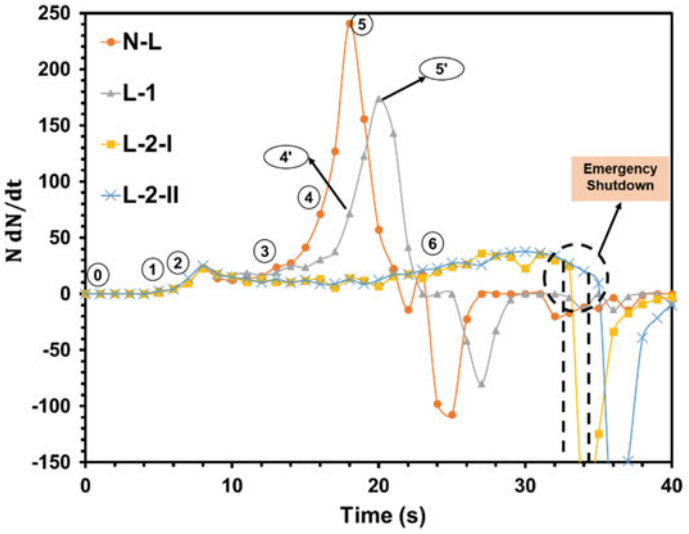

Fig. 12 Behavior of $N\frac{dN}{dt}$ during starting process of the engine for all test cases

Figure 11 shows the behavior of $\frac{dN}{dt}$, and Fig. 12 shows the behavior of $N\frac{dN}{dt}$ during starting sequence of the engine. After the starting sequence is initiated (at $t = 0$ s) and electric starter is activated (at $t = 5$ s), $\frac{dN}{dt} > 0$ and the value of both $\frac{dN}{dt}$ and $N\frac{dN}{dt}$ increase with time for the first 4 s and then decrease for the next two seconds. This reduction in $N\frac{dN}{dt}$ and $\frac{dN}{dt}$ at $t = 8$ s is attributed to the w_{net} given by Eq. 4. In this phase, the electric starter continues governing the acceleration and speed of the rotor. Even after the fuel is ignited (event-2), ($w_{net} < 0$) and the starter motor continue to provide the power to drive the rotor. The net power available $\left(N\frac{dN}{dt}\right)$ to accelerate the rotor has decreased, reducing the magnitude of $\frac{dN}{dt}$. However, $\frac{dN}{dt} > 0$, due to the additional effort of the start motor, which causes the value of N to rise. For 10 s $< t <$ 14 s, magnitude of $N\frac{dN}{dt}$ remains constant and the value of N is increasing. Since $N\frac{dN}{dt}$ is constant and N is increasing, the value of $\frac{dN}{dt}$ is decreasing as governed by Eq. 5.

As $N \rightarrow$ 15,000 rpm ($t \rightarrow$ 14 s), the electric starter is deactivated (event-3), and the acceleration (speed) of the rotor is governed by w_{net} according to Eq. 5. For 14 s $< t <$ 18 s, the magnitude of $N\frac{dN}{dt}$ is increasing which increases the magnitude of $\frac{dN}{dt}$. This increase in $N\frac{dN}{dt}$ is caused by an increase in $\dot{v}_f$, which allows sufficient energy to be available for the turbine to accelerate the rotor. For 18 s $< t <$ 22 s, the magnitude of $N\frac{dN}{dt}$ is decreasing reducing $\frac{dN}{dt}$. During this phase, N stabilizes at 40,000 rpm (calibration speed). For 22 s $< t <$ 35 s, $N\frac{dN}{dt}$ is negative which results in a negative $\frac{dN}{dt}$ reducing N to 30,000 rpm. The reduction in $\dot{v}_f$ is the reason for $N\frac{dN}{dt} < 0$. On reducing $\dot{v}_f$, the value of TET decreases which decreases w_t resulting in $w_{net} < 0$.

The behavior of both $N\frac{dN}{dt}$ and $\frac{dN}{dt}$ for L-1 is qualitatively similar to that for N-L. However, the following quantitative differences are to be observed. First, the peak value of both $N\frac{dN}{dt}$ and $\frac{dN}{dt}$ is less for L-1 compared to that for N-L. Second, between event-3 and event-5, the rate of increase in $N\frac{dN}{dt}$ is less for L-1 compared to that for N-L. The magnitude of $\frac{dN}{dt}$ remains constant for 2 s after the electric starter is deactivated (event-3), although the magnitude of $N\frac{dN}{dt}$ starts to rise. This suggests that under loading condition (L-1), there is a delay in transition after the electric starter is deactivated. This transition delay of approximately 2 s is observed in other parameters like N, resulting in an overall delay in the starting process. Similarly for L-2, after the electric starter is deactivated (event-3), the magnitude of $\frac{dN}{dt}$ is decreasing, and the magnitude of $N\frac{dN}{dt}$ remains constant. The magnitude of $N\frac{dN}{dt}$ starts to increase at $t = 20$ s. This decrease in magnitude of $\frac{dN}{dt}$ (after event-3) may be attributed to the reduced magnitude of $N\frac{dN}{dt}$ at that speed. Hence, for L-2 test case, it may be concluded that the engine failed to attain the required magnitude of $N\frac{dN}{dt}$ for accelerating the rotor to the desired speed (event-5) which resulted in a failed start.

To understand the reasons for the prolonged starting sequence (2 s) for L-1 and failed start for L-2, the performance of the compressor and turbine is considered. Figure 13 shows the behavior of compressor pressure ratio $\left(\pi_c = \frac{P_{t3}}{P_a}\right)$, and Fig. 14 shows the behavior of turbine pressure ratio $\left(\pi_t = \frac{P_{t4}}{P_{t5}}\right)$ during the starting process for all test cases.

Consider N-L test case. After the electric starter is activated, π_c and π_t start increasing along with N. The increase in π_c and π_t is rapid for $N > 15{,}000$ rpm, and π_c reaches a peak value of 1.3 and π_t a peak value of 1.2 at $N = 40{,}000$ rpm. As

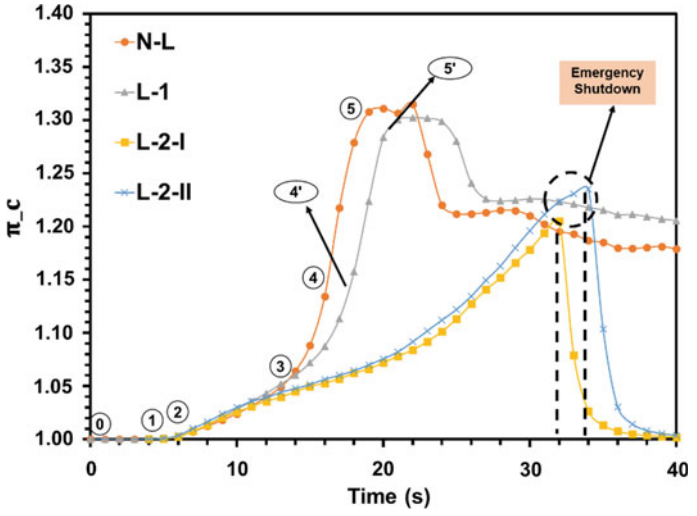

Fig. 13 Behavior of compressor pressure ratio (π_c) during starting process of the engine for all test cases

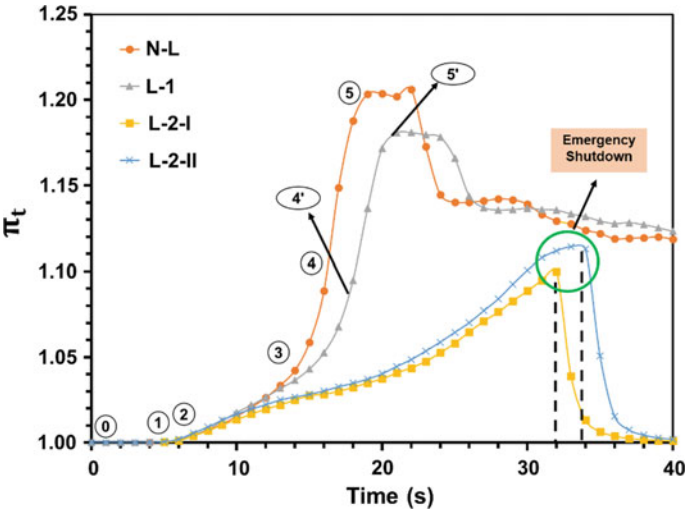

Fig. 14 Behavior of turbine pressure ratio (π_t) during starting process of the engine for all test cases

$N \rightarrow$ 30,000 rpm, π_c decreases to 1.17 and π_t decreases to 1.12. The behavior of both π_c and π_t for L-1 is qualitatively same as that for N-L However; the following quantitative differences are to be observed. Firstly, the rate of increase of both π_c and π_t is less, for L-1, delaying the peak value by 2 s. Second, π_c reaches a peak value of 1.3, which is same as that of N-L, and π_t reaches a peak value of 1.18 which is less than the value for N-L.

The delayed rate of increase in π_c and π_t (starting sequence) has been explained earlier in Fig. 11. The effect of reduced π_t has been explained earlier in Fig. 7. However, for completeness, it is reiterated here. This reduction in π_t (event-5′) would decrease w_t (Eq. 1) if TET is maintained same as that for N-L. Since, π_c is same as that for L-l, the w_c required remains the same. Hence, w_t required would also be the same to achieve the desired behavior. In order to compensate for the reduction in π_t, the TET is increased by having higher $\dot{v}_f$ Fig. 9 compared to N-L.

From Fig. 9, it can be observed that the variation of $\dot{v}_f$ is same up to event-4 for both N-L and L-1. After event-5, $\dot{v}_f$ is higher for L-1 compared to N-L, and thereafter, $\dot{v}_f$ remains higher for L-1 compared to N-L as N is reduced to its ideal value. The behavior of π_c with N is shown in Fig. 15, and behavior of π_t with N is shown in Fig. 16.

From Fig. 15, it can be observed that after event-3 at any given N, the value of π_c is same for both N-L and L-1. From Fig. 16, it can be observed that after event-3 at any given N, the value of π_t is less for L-1 compared to N-L. From this, it may be asserted that for L-1, there is no effect on the performance of compressor, whereas there is an reduction in turbine pressure ratio. This reduction in π_t for L-1 is compensated by an increase in TET.

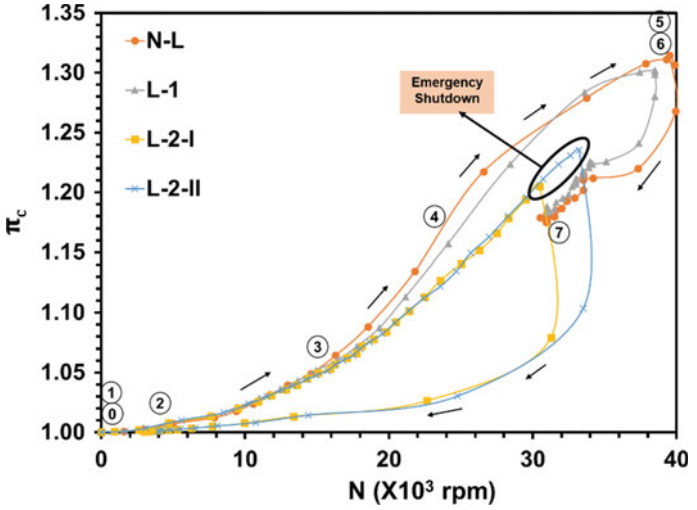

Fig. 15 Behavior of compressor pressure ratio (π_c) with N during starting sequence for all test cases

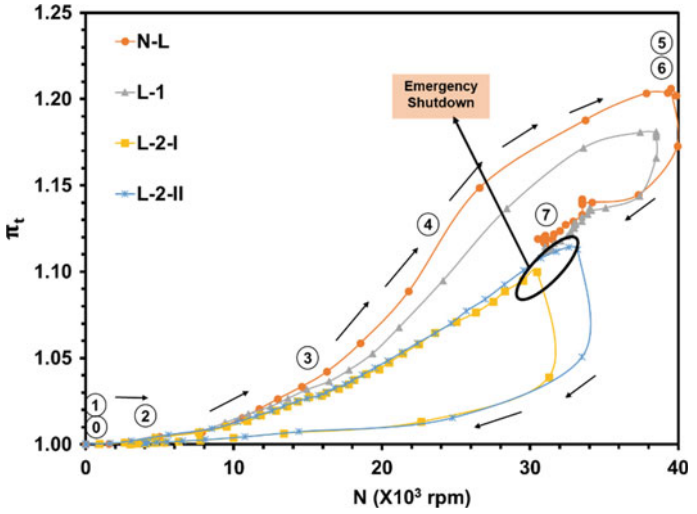

Fig. 16 Behavior of turbine pressure ratio (π_t) with N during starting sequence for all test cases

Consider the first attempt (Test-3) of L-2 configuration. After the electric starter is deactivated (event-3), the rate of increase of both π_c and π_t is small compared to that for N-L and L-1. Both π_c and π_t do not reach the peak values as for N-L and L-1. From Figs. 15 and 16, it can be observed that after event-3 as at any given N,

the value of both π_c and π_t is less compared to both N-L and L-1. Although TET is higher for L-2 test case, it could not compensate for this reduction in π_t as happened earlier in case L-1.

In summary, the value π_t for a given N is less or L-1 and L-2 compared to N-L. This decrease in the value of π_t reduces the power available for acceleration of the rotor. The ECU tries to compensate for this deficit by increasing $\dot{v}_f$ (increasing the TET), which was successful for L-1 but failed for L-2 (as the TET exceeded its operation limits before the rotor could reach the desired speed). A second attempt (Test-4) was made to start the engine by reducing the flow rate at its starting, which showed similar behavior as that of the first attempt.

4 Summary

Experiments have been carried out on a micro-turbojet engine for three different loading conditions, namely no-load (N-L), load-1 (L-1) and load-2 (L-2). For the first two loading conditions (N-L and L-1), the engine started successfully and the power/thrust level of the engine was increased by increasing the rotor speed (N). Pressure and temperature at various locations in the engine along with rotor speed (N) and fuel flow rate were measured during the entire operation of the engine. The time taken for starting procedure for L-1 condition was 2 s more compared to N-L. The prolonged starting time for L-1 is attributed to the reduced turbine pressure ratio (π_t) which is due to the rise in pressure at turbine exit due to the reduction in nozzle exit area. The compressor operation was found to shift closer to the surge line at higher rotor speeds for L-1. This resulted in lesser flow rates of air for L-1 compared to N-L. The fuel flow rate required to achieve a given rotor speed is higher for L-1. As a result, the equivalence ratio and turbine entry temperature (TET) are higher for L-1 compared to N-L at any given rotor speed. This increase in flow rate of fuel for L-1 at any rotor speed (N) is due to the reduction in the turbine pressure ratio (for L-1) as a result of the decrease in nozzle exit area and the compressor pressure ratio being same for N-L and L-1. The turbine entry temperature was required to be increased to compensate for the reduction in turbine pressure ratio to produce the power required to run the compressor.

For L-2 test case, the engine failed to start. Before the rotor could reach the speed as set in the control system, the temperatures in the combustion chamber reached the upper limit. The engine was forced to stop by activating the emergency shutdown switch. Due to the increased load, resulting in a lower air flow rate through the engine, the rotor speed was unable to gain enough momentum to accelerate and reach the required speed. To enable the rotor to reach the required speed for a successful start, the ECU pumps more fuel. The side effect of this is an increase in TET, reaching values that were close to the maximum limits of operation.

Acknowledgements This work was sponsored by Aeronautical Development Agency, India.

References

1. Martin J (2009) Distributed vs. centralized electricity generation: are we witnessing a change of paradigm? An introduction to distributed generation. http://www.vernimmen.net/ftp/An_introduction_to_distributed_generation.pdf
2. Chuvychin V, Sauhats A, Strelkovs V (2008) Problems of frequency control in the power system with massive penetration of distributed generation. Power Syst Oper Control 8:19–23. https://doi.org/10.1109/FarEastCon.2018.8602504
3. Ivanovich VN, Valeryevna CM (2018) Transient stability problems of electric power systems with distributed generation. In: International multi-conference on industrial engineering and modern technologies (FarEastCon), Vladivostok, 3–4 Oct 2018, pp 1–6. https://doi.org/10.1109/fareastcon.2018.8602504
4. Gülen S (2019) Transient operation. In: Gas turbines for electric power generation. Cambridge University Press, Cambridge, pp 549–592. https://doi.org/10.1017/9781108241625.020
5. Agrawal RK, Yunis M (1982) A Generalized mathematical model to estimate gas turbine starting characteristics. J Eng Power 104(1):194–201. https://doi.org/10.1115/1.3227249
6. Pilidis P, Maccallum NRL (1985) A general program for the prediction of the transient performance of gas turbines. ASME. Turbo expo: power for land, sea, and air, Volume 1: aircraft engine; marine; turbomachinery; microturbines and small turbomachinery: V001T03A053. https://doi.org/10.1115/85-gt-209
7. Ganji AR, Khadem M, Khandani SMH (1993) Transient dynamics of gas turbine engines. ASME. Turbo expo: power for land, sea, and air, Volume 3C: General: V03CT17A014. https://doi.org/10.1115/93-gt-353
8. Asgari H, Venturini M, Chen X, Sainudiin R, (2014) Modeling and simulation of the transient behavior of an industrial power plant gas turbine. J Eng Gas Turbines Power ASME 136(6):061601-061601-10. https://doi.org/10.1115/1.4026215
9. Singh V, Axelsson Lars-Uno, Visser W P J, (2016) Transient performance analysis of an industrial gas turbine operating on low-calorific fuels. J Eng Gas Turbines Power ASME 139(5):051401-051401-7. https://doi.org/10.1115/1.4034942
10. Cohen H, Rogers GFC, Saravanamuttoo HIH (1996) Gas turbine theory, 4th edn. Addison Wesley Longman Limited, England

Transport Processes in Energy Systems

Transported PDF Modeling of Jet-in-Hot-Coflow Flames

Ashoke De, Gerasimos Sarras, and Dirk Roekaerts

1 Background

The need to avoid pollutant emissions has resulted in the development of new combustion techniques. These techniques include high-temperature air combustion (HiTAC), flameless oxidation combustion (FLOX), and moderate and intense low-oxygen dilution (MILD) combustion which falls under the category of 'clean combustion techniques.' One of the features of MILD combustion is the high re-circulation ratio. The hot gas re-circulation serves the combustion process in two ways; first, it raises the reactant temperature, providing the heat needed for stable ignition. Secondly, it reduces the oxygen concentration of the mixture which reduces the flame temperature and the thermal NO_x emissions. Other features of the MILD combustion include flat temperature field, low turbulence fluctuations, smooth radiation flux, and barely visible and audible flame [1–8].

Dally et al. [9] of the Adelaide University designed a jet-in-hot-coflow burner and carried out experiments producing detailed profiles of major as well as minor species. The experiments performed on this burner provided a comprehensive database that has been used in the present study. Various numerical studies [10–18] have also been carried out using these databases to evaluate the performance of different turbulence and combustion models.

There have been various RANS-based modeling studies carried out in the context of the Adelaide burner, most notable among them being the ones carried out by

A. De (✉)
Department of Aerospace Engineering, Indian Institute of Technology Kanpur, Kanpur 208016, India
e-mail: ashoke@iitk.ac.in

G. Sarras · D. Roekaerts
Department of Process and Energy, Delft University of Technology, Leeghwaterstraat 44, 2628 CA Delft, The Netherlands

© Springer Nature Singapore Pte Ltd. 2021

A. De et al. (eds.), *Sustainable Development for Energy, Power, and Propulsion*, Green Energy and Technology,
https://doi.org/10.1007/978-981-15-5667-8_17

Christo and Dally [10, 11]. The major finding was the fact that the SKE turbulence model with a modified dissipation constant ($C_{\varepsilon 1} = 1.6$) produces the best agreement with the experimental results. Other notable RANS-based modeling studies include the ones carried out by Frassoldati et al. [12], Mardani et al. [13, 14], and Aminian et al. [15]. All of these studies made use of the EDC combustion model in combination with DRM 22 [19], GRI 2.11 [20], and KEE-58 [21] chemical mechanisms to study the flame structure and the effects of molecular diffusion on flame characteristics in the MILD regime. Kim et al. [16] simulated the JHC flames using the conditional moment closure (CMC) with the primary goal of understanding the flame structure and NO formation in the MILD regime. Ihme et al. [17, 18] studied the JHC flames using LES with the flamelet/progress variable (FPV) approach. They considered the burner as a three-stream mixing problem by introducing an additional conserved scalar to identify flamelets of different mixture compositions and showed that the coflow mixture composition could only inadequately be represented by one mixture fraction.

From the above review, it is evident that a major problem while modeling these flames is the nonlinear interaction between fluid mixing and finite rate chemistry in the MILD regime. The transported probability density function (PDF) method is suited to handle this problem. It allows us to include the effects of turbulence–chemistry interaction in the Reynolds-averaged Navier–Stokes (RANS) framework [22].

The objective of this work is to explore the predictive capability of flamelet-generated manifold (FGM) chemistry [23] in a RANS/PDF framework. The FGM has been successfully applied to simulations of various combustion systems [23–27]. In all these cases, a mixture fraction and a progress variable were adequate to create the table. This study is the first attempt to extend the FGM with a second mixture fraction to account for coflow inhomogeneity and air entrainment in predicting JHC flames in the MILD combustion regime. The numerical predictions obtained using this model are compared with experimental databases.

2 Tabulated Chemistry Construction[1]

2.1 Coflow Representation

In the following, the tabulated chemistry model is presented for describing a three-mixing problem. The chemistry data have been tabulated using the FGM approach. The FGM is based on laminar diffusion flamelets between the fuel ($CH_4 + H_2$) and the coflow (a mixture of combustion products and air). Since the coflow composition and temperature vary in space (Fig. 1), flamelets with different coflow compositions and temperatures are required. The mean temperature and mass fractions have

[1]This section is reproduced from Sarras et al. [27].

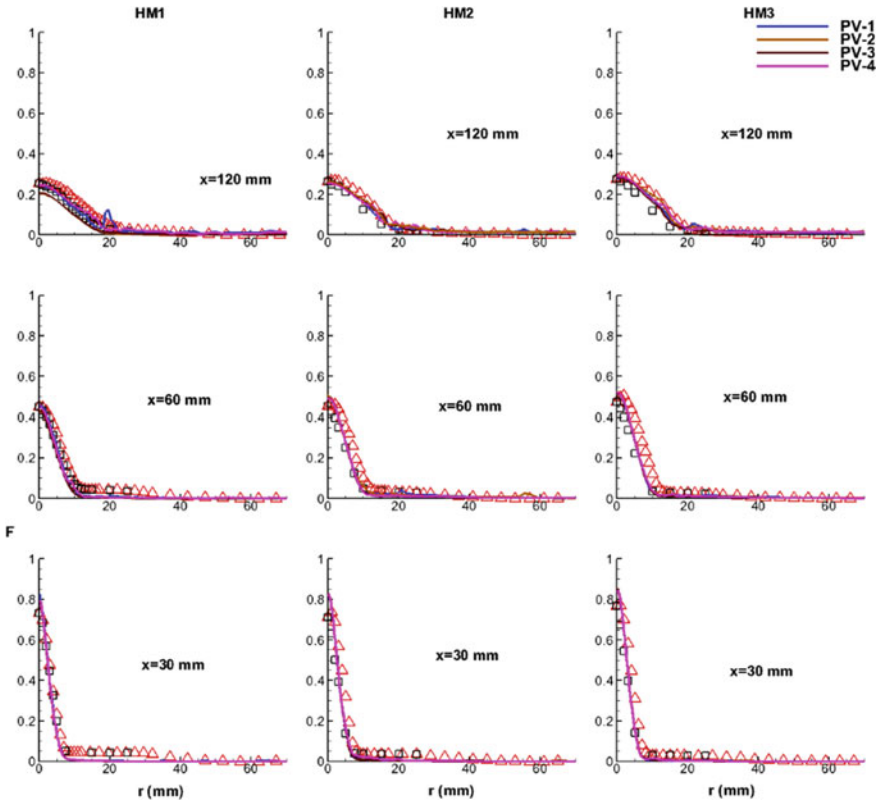

Fig. 1 Radial profiles of mean mixture fraction (F) using different PVs: (triangle $0 \leq r \leq 70$ and squares $-25 \leq r \leq 0$) symbols are measurements and lines are predictions

been measured along the radial direction of the coflow at $x = 4$ mm above the jet nozzle as shown in Fig. 1. Following the approach of Ihme and See [17], a second mixture fraction Z_2 is introduced, which will quantify the mixing between a coflow representative and the surrounding air and, at the same time, can be used to describe the variation in the coflow composition based on oxygen concentration. The coflow representative is defined at the radial position $r = r_{\text{rep}}$ such that:

$Y_{O_2}(r_{\text{rep}}) = \min(Y_{O_2}(r))$. For every point in the radial direction, we define:

$$Z_2(r) = \frac{Y_{O_2}(r) - Y_{O_2}(r_{\text{rep}})}{Y_{O_2}(r_{\text{air}}) - Y_{O_2}(r_{\text{rep}})} \tag{1}$$

The coflow representative is given by $Z_2 = 0$, and the cold ambient air is provided by $Z_2 = 1$. In this approach, the enthalpy deficit (Δh) relative to the adiabatic mixing is assumed strictly correlated with Z_2. To take into account that the enthalpy deficit is not a unique function of Z_2 and to allow independent fluctuations of Z_2 and Δh,

it would be necessary to consider Δh as an extra independent variable. Assuming chemical equilibrium at the coflow inlet, the full composition is entirely determined from Z_2. With this definition, the composition and temperature at the coflow inlet are functions of Z_2

$$\begin{aligned} Y_i(r) &= Y_i(Z_2(r)), \\ T(r) &= T(Z_2(r)). \end{aligned} \tag{2}$$

2.2 3D Manifold Construction

The FGM method is based on laminar flamelets. A flamelet is the solution of a low Mach number formulation of the one-dimensional Navier–Stokes equations supplemented with species and enthalpy equations, including detailed chemistry. The detailed chemistry model presently employed is the GRI 3.0 [20] reaction mechanism. Since the auto-ignition is the primary stabilization mechanism for the JHC [10] flames, unsteady effects should be included. Non-premixed unsteady laminar flamelets are formulated and solved in physical space and time with the CHEM1D code [28, 29]. Preferential diffusion effects are included using the mixture average approach. The initial condition for the unsteady flamelet solution is given by a pure mixing solution of the above boundary value problem. The oxidizer composition is a function of the second mixture fraction $Y_i^{\text{ox}} = (1 - Z_2)Y_i^{\text{rep}} + Z_2 Y_i^{\text{air}}$.

FGM tables have been constructed for a set of values of the second mixture fraction with corresponding enthalpy deficit levels. First, the values for the second mixture fraction have been chosen which correspond to a particular radial location, and these values are needed to represent accurately the enthalpy deficit range of the coflow. For each Z_2 value, a FGM table is constructed from a non-premixed igniting flamelet between fuel and the coflow composition at Z_2 with the corresponding enthalpy deficit, according to Fig. 1. A moderate strain rate $a = 100\,\text{s}^{-1}$ is used in all the flamelet calculations. For each of the coflow compositions, the solution is stored at successive time instances. These solution files form the base of the 2D-FGM construction. A total of ten 2D-FGMs are obtained.

The first step in the 2D-FGM construction consists of defining a suitable progress variable Y. In any given flamelet (i.e., fixed Z_2 value), the progress variable must be a monotonic function of time at each physical position. Since the first mixture fraction is a monotonically increasing function of the spatial coordinate [25], this requirement can also be stated in terms of the first mixture fraction instead of the spatial position. The reaction progress variable in this work is defined by

$$Y = \sum_i \frac{Y_i}{M_i}, \tag{3}$$

where Y_i is the mass fraction of CO_2, CO, H_2, H_2O, or CH_4 and M_i denotes the molar mass of the considered species. Then, the 2D-FGM is simply obtained by transforming the dependence on the spatial coordinate into a dependence on the first mixture fraction and time into dependence on the reaction progress variable

$$\phi(x, t; Z_2) \rightarrow \phi_{\mathrm{FGM}}(Z_1, Y; Z_2) \tag{4}$$

where ϕ stands for any thermochemical variable. In practice, this transformation is obtained by sorting and relabeling the data in each flamelet such that all dependent variables are stored as a function of the mixture fraction Z_1 and the scaled progress variable c. The scaled progress variable is defined by

$$c = \frac{Y - Y_{\min}(Z_1)}{Y_{\max}(Z_1) - Y_{\min}(Z_1)}, \quad c \in [0, 1] \tag{5}$$

The minimum $Y_{\min}$ and maximum $Y_{\max}$ values of the unscaled progress variable are also stored.

The 3D-FGM is obtained by combining the 10 different 2D-FGMs. Then, every local thermochemical state can be described by using the three independent variables Z_1, Z_2, Y,

$$\phi = \phi(Z_1, Y; Z_2). \tag{6}$$

The computer program FLAME [30] developed at the TU Delft has been used to optimize the tabulation of the 3D-FGM. In the FLAME code, the physical range of the four independent variables is mapped onto a cube $[0, 1]^3$ to facilitate adaptive grid refinement. The grid refinement automatically detects regions in composition space (Z_1, Z_2, Y) with large gradients of the dependent variables and inserts grid points as necessary to resolve the gradients. The adaptive tabulation uses linear interpolation between any two 2D-FGMs (Z_2 direction) and within each 2D-FGM ($Z_1 - Y$ plane). For consistency, the density is not interpolated but is recalculated based on the interpolated temperature and composition. In addition to the relevant thermochemical variables, the source term of the progress variable is stored in the table,

$$S_Y(Z_1, Z_2, Y) = \frac{\dot{\omega}_Y}{\rho}. \tag{7}$$

However, special care has to be taken for the source term at the boundary $Y = Y_{\max}(Z_1, Z_2)$ which corresponds to the steady-state flamelet solution. In the steady state, we have

$$\frac{\partial \rho u Y_{\max}}{\partial t} - \frac{\partial}{\partial x}\left(\frac{\lambda}{c_p}\frac{\partial \rho Y_{\max}}{\partial x}\right) + \rho G Y_{\max} - \rho S_{Y_{\max}} = 0 \tag{8}$$

and hence, in general $S_{Y_{\max}} \neq 0$. Without any further measures, this leads to the occurrence of $Y > Y_{\max}(Z_1, Z_2)$. To avoid this problem, we set $S_{Y_{\max}} = 0$ which holds in chemical equilibrium as obtained in a steady flamelet with a strain rate $a \to 0$.

3 PDF Formulation with 3D-FGM Table

The details of the in-house PDFD code and the PDF method can be found in Refs. [31–33]. Here, we only describe the modifications that have been made to use the 3D-FGM in the PDFD simulations. Every Monte Carlo particle carries two mixture fractions Z_1, Z_2 and a reaction progress variable Y. This means that every particle now evolves in composition space according to the general equation:

$$\mathrm{d}\phi_\alpha^* = \theta_{\alpha,\mathrm{mix}}^* \mathrm{d}t + S_\alpha\left(\vec{\phi}\right)\mathrm{d}t \tag{9}$$

where $\vec{\phi} \equiv (Z_1, Z_2, Y)$ and $\alpha = 1, 2, 3$. Also, $\theta_{\alpha,mix}$ represents the chosen micro-mixing model and $S_\alpha\left(\vec{\phi}\right)$ the chemical source term of the progress variable. The mixture fractions are not affected by chemical reactions, and their values only change according to the chosen micro-mixing model. Radiative heat losses are not included here. The evolution of the reaction progress variable is split into a micro-mixing step and a reaction step. Micro-mixing is performed first, and then the reaction step is mainly based on an explicit Euler scheme:

$$\mathrm{d}Y = S_Y(\phi) \cdot \mathrm{d}t \tag{10}$$

where S_Y is the source term and t is the time step. A Runge–Kutta method [32] is implemented to accurately advance the progress variable changes due to the highly nonlinear source terms. In all the igniting flamelets, the source term is a very smooth function of the progress variable, and hence the gradients are small. The boundary conditions for the reaction progress variable at any radial position at the inlet are given by

$$Y = Y_{\min}(0, Z_2(r) = \mathrm{const}) \tag{11}$$

The local composition is given by the two mixture fractions and the reaction progress variable. All other scalar variables (temperature, species mass fractions, density, etc.) are retrieved from the lookup table.

4 Simulation Details

A detailed description of the burner geometry can be referred from Dally et al. [9, 10]. In the context of the numerical setup, a very similar numerical setup, explained above, with a few changes has been used to model the methane–hydrogen JHC flames in the Adelaide burner. Three different flames with different oxygen contents in the hot coflow have been simulated, namely HM1 (3% O_2), HM2 (6% O_2), and HM3 (9% O_2). The Reynolds number has been kept constant at Re = 10,000 for all three flames.

A 2D axisymmetric grid has been used in the simulations. As the central fuel jet protrudes 4 mm at the jet exit, the computational domain starts 4 mm downstream of the jet exit and extends for 300 mm in the axial direction and 80 mm in the radial direction. The grid consists of 200 × 120 cells in the axial and radial direction, respectively (stretched in both directions). At the end of the computational domain, in the axial direction, the boundary condition is set to outflow. For the fuel jet inlet, the velocity profiles are used from a detailed separate simulation, whereas at the hot and cold coflow inlets, the velocity boundary conditions are set to 3.2 m/s and 3.3 m/s, respectively. As per the previous studies, the solution is very sensitive to the turbulent quantities at the inlet; therefore, the turbulent intensities at the hot and cold coflow have been set to 5%, while it is set to 7% at the fuel jet inlet as per the published results [8, 12].

The flamelet-generated manifold for the methane–hydrogen combustion is based on the GRI 3.0 [20] chemical mechanism with 53 species and 325 chemical reactions. The radial profiles of the temperature and species mass fraction with experimental values at $x = 4$ mm have been used to create the FGM tables. The FGM table resolution is set to $Z \times Y = 201 \times 201$ points with equidistant spacing.

The PDF transport equation was solved using the Lagrangian Monte Carlo approach initialized with approximately 20 particles per cell. The effect of micro-mixing models is also studied with a mixing constant $C_\phi = 2$. The Reynolds number has been kept constant at Re = 10,000. The results obtained are compared with the respective experimental database, and the profiles of mean temperature, mean mixture fraction, and major species are reported.

5 Results and Assessment[2]

In this section, the simulation results are presented for three flames, i.e., HM1, HM2, and HM3. The profiles of mean temperature, mean mixture fraction, and major species are reported and are compared with the respective experimental database.

[2]Some portion of this section is reproduced from De et al. [8].

5.1 *Effect of Progress Variable*

Initially, we have considered a different linear combination of PV to test the sensitivity of the PV in predictions. The mixing model is kept constant for all the simulation, and that is IEM. The considered combination is defined as:

$$\mathrm{PV1} = \mathrm{CO_2} + \mathrm{H_2O} + \mathrm{H_2}$$

$$\mathrm{PV2} = \mathrm{CO} + \mathrm{CO_2} + \mathrm{H_2O}$$

$$\mathrm{PV3} = \mathrm{CO} + \mathrm{CO_2} + \mathrm{H_2O} + \mathrm{H_2}$$

$$\mathrm{PV4} = \mathrm{CO} + \mathrm{CO_2} + \mathrm{H_2O} + \mathrm{H_2} + \mathrm{CH_4}$$

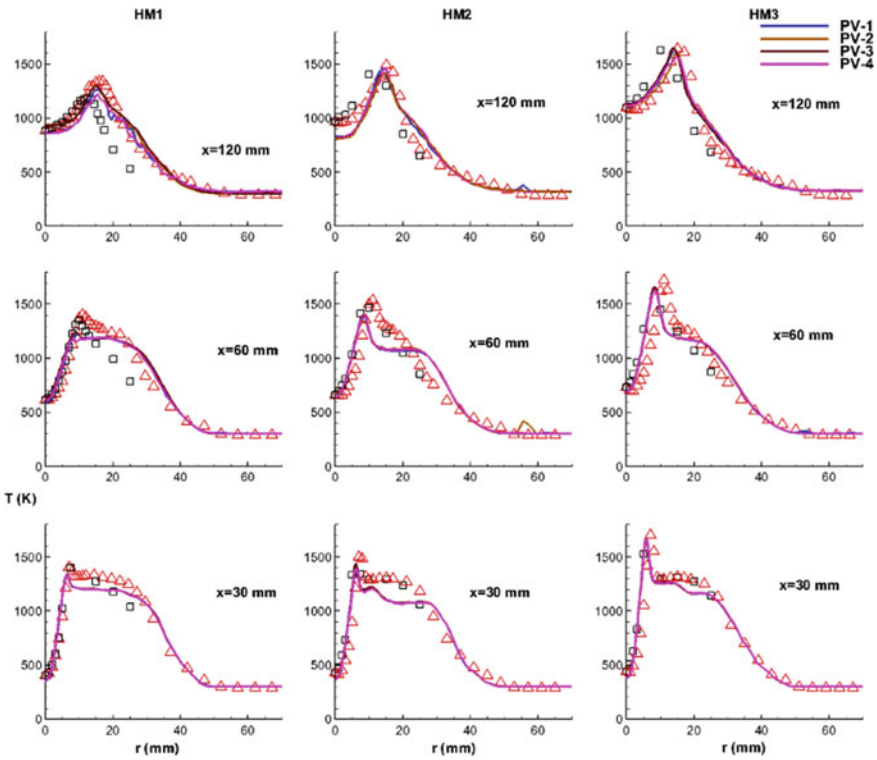

Fig. 2 Radial profiles of mean temperature using different PVs: Symbols are measurements and lines are predictions (legends are the same as Fig. 1)

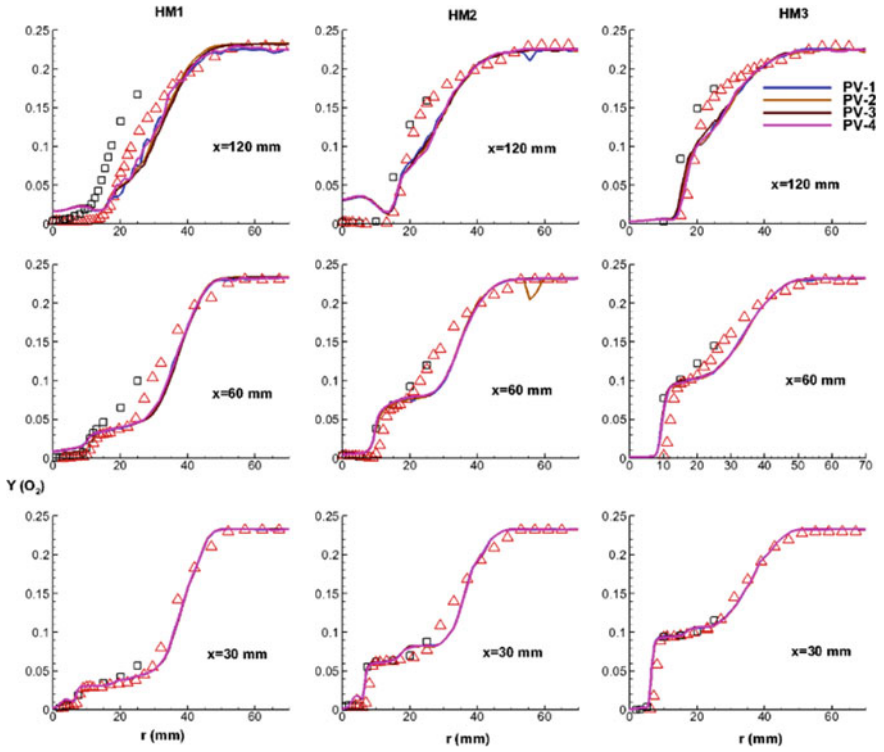

Fig. 3 Radial profiles of mean O_2 using different PVs: Symbols are measurements and lines are predictions (legends are the same as Fig. 1)

Figures 1, 2, and 3 depict the radial profiles of mean mixture fraction, temperature, and one major species (O_2) using different PVs. As observed from the figures, the predictions are not sensitive to the different combinations of PV, thereby not showing any significant differences in results.

This means the linear combination of major species is good enough for the predictions of these flames. Hence, the rest of the results are reported with PV3 only, which is precisely the same as reported in the published work by Ihme et al. [18] to make an assessment of our predictions.

5.2 Effect of Mixing Models and PDF Models

In this section, using the PV3 definition, a detailed analysis is carried out. Two critical parameters are varied here are: (a) mixing models: IEM, CD, EMST, and (b) PDF models: scalar composition PDF and joint velocity-scalar composition PDF.

Figure 4 shows the profiles of the mean mixture fraction obtained for HM1 flame. As observed, all the models capture the profiles accurately, and no significant differences are observed among these predictions except the CD model. Some discrepancies can be observed in the mean temperature profiles as depicted in Fig. 4. The predictions are similar for HM2 and HM3 flames. For HM1 flame, the centerline temperature profiles are overpredicted; however, the predictions are improved along with the shear layer. Among the transported PDF models, the LPDF-EMST predictions are better compared to the LPDF-IEM and LPDF-CD predictions, especially for HM1 flame. No significant differences are observed using only the scalar composition PDF method, as represented using '*Sc*' in all the plots. The peak temperature predictions are reasonably well, while some discrepancies are observed at the outer shear layer, especially the case with lower O_2 concentration, i.e., HM1 flame. Even though the LPDF-CD predictions are consistently poor in all three flames, we can observe an improvement in the predictions as the oxygen content in the coflow increases. As the oxygen content in the hot coflow increases from 3% (by mass) in HM1 to 6% in HM2 and to 9% in HM3 flames, the reaction rate improves due to which the models are able to predict the flames with better accuracy and a clear improvement in the temperature predictions, obtained using all the models.

Figure 5 depicts the profiles of mean CH_4 and H_2 mass fraction obtained for HM1 flame. Near the jet exit, the peak of CH_4 is overpredicted by all the models, but the mean H_2 profiles are found to be good. Major discrepancies can be observed in O_2 predictions for all three flames, as shown in Figs. 6, 7, and 8. In this case, the dominance of scalar composition PDF is observed at the downstream locations. Even after providing better boundary conditions for oxygen (obtained from $x = 4$ mm measurements) for all three flames, the evolution of O_2 could not be captured accurately. This discrepancy is primarily due to the handling of reaction rate in modeling (turbulence–chemistry interaction) and cannot be quantified unless we look at the velocity statistics in the domain, and this remains another drawback of this burner as it does not provide any velocity data. Among the LPDF models, there are no substantial differences observed between IEM and EMST predictions for all three flames, but as we move to HM2 and HM3, we observe the predictions appear to be in better shape, especially, for HM3 flame. For all three flames, LPDF-CD predictions show substantial differences from the other two models [8].

The profiles of mean CO_2 and H_2O mass fraction obtained for HM1, HM2, and HM3 flames are shown in Figs. 9, 10, and 11. All the models adequately capture the profiles near the jet exit area, but the centerline profiles are consistently overpredicted. Discrepancies can be observed for the predictions away from the jet exit at $x = 120$ mm location. The profiles of mean H_2O mass fraction exhibit a completely different picture from that of CO_2 profiles. As the oxygen content increases in the coflow from HM1 to HM3 flames, the extent of under-prediction at the centerline also increases. Previous studies all reported similar behavior where they have looked at the impact of chemical kinetics; however, the present study includes fairly detailed chemistry. Thus, we can assert that the chemical mechanism is not primarily responsible for the predictions obtained herein. However, it should be noted that the turbulent timescale is the dominant factor along the centerline, which supersedes the scalar

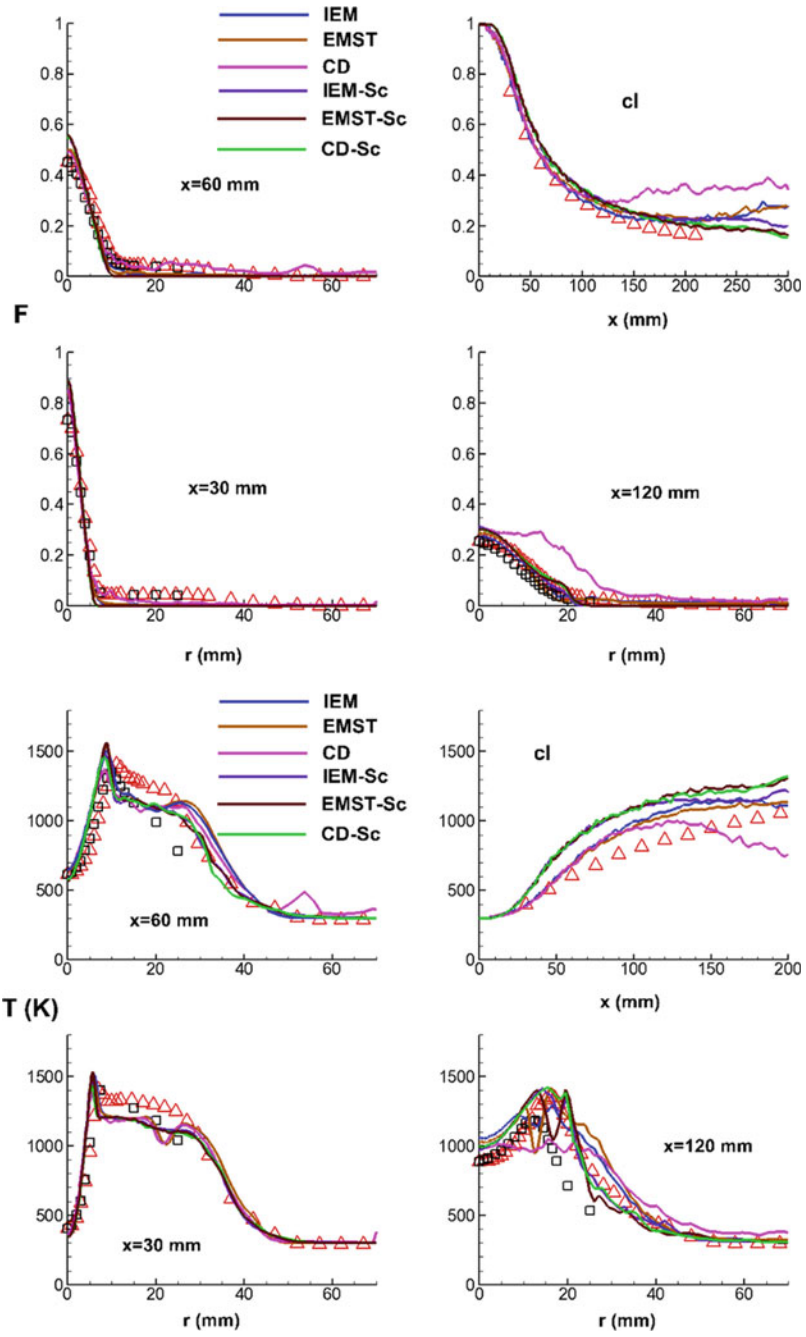

Fig. 4 Profiles of mean mixture fraction and temperature for HM1 flame (legends are the same as Fig. 1). '*Sc*' stands for scalar composition PDF

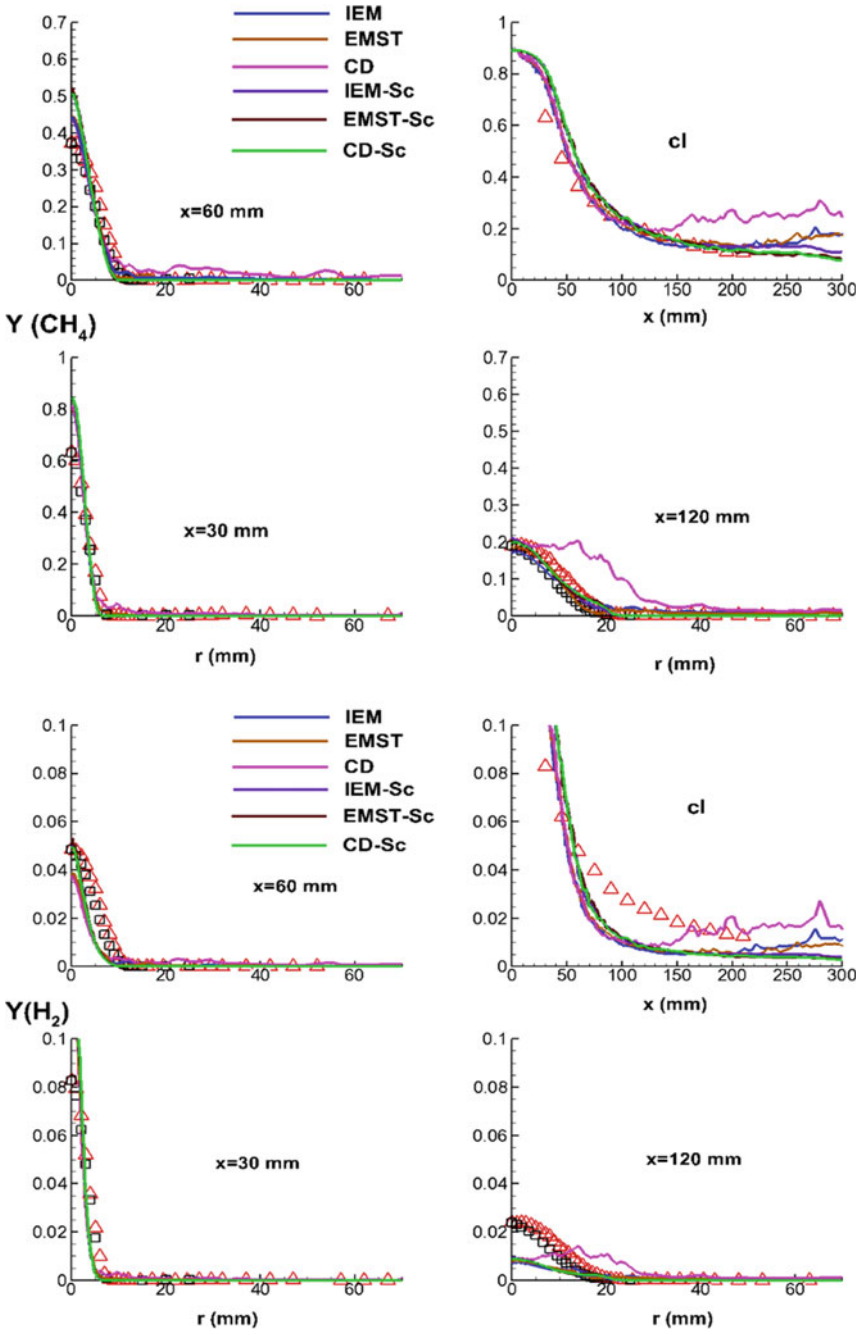

Fig. 5 Profiles of mean CH_4 and H_2 for HM1 flame (legends are the same as Fig. 1)

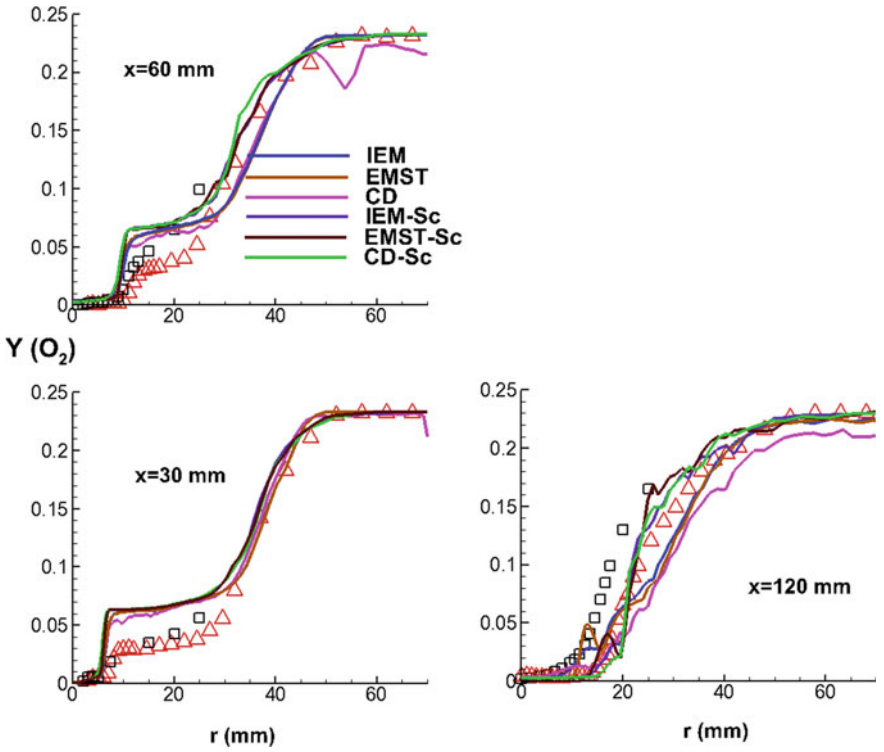

Fig. 6 Profiles of mean O_2 for HM1 flame (legends are the same as Fig. 1)

dissipation timescale, and hence the combustible mixture dissipates quickly as the species are not allowed to stay for a longer duration in this region to complete reaction. This is one of the major reasons behind the discrepancies observed in species profiles along the centerline, especially the O_2 profiles and temperature, in turn, affecting the CO and H_2O profiles. This slow chemistry increases the chemical timescales and, in turn, reduces the Damkohler number, and all the combustion models are unable to capture the flame characteristics in this low Damkohler number range, which has significantly affected the species predictions.

To better understand the model behavior, it is worthwhile to look at the predictions of minor species like OH and CO. Major discrepancies can be observed in Figs. 12, 13, and 14 depicting OH and CO profiles, respectively. Looking at the radial profiles of OH obtained for HM2 and HM3 flames, it can be seen here that the predictions are in better shape compared to those obtained for HM1 flame as the oxidation of O_2 into OH is sufficiently captured. The CO profiles are significantly under-predicted in the shear layer between fuel jet and hot coflow for HM2 and HM3 flames. The CO profiles are better in HM3 compared to those obtained in the HM2 flame owing to the better performance of combustion models due to improved reaction rates and oxygen contents in the coflow. While comparing all the models, it has been observed that the

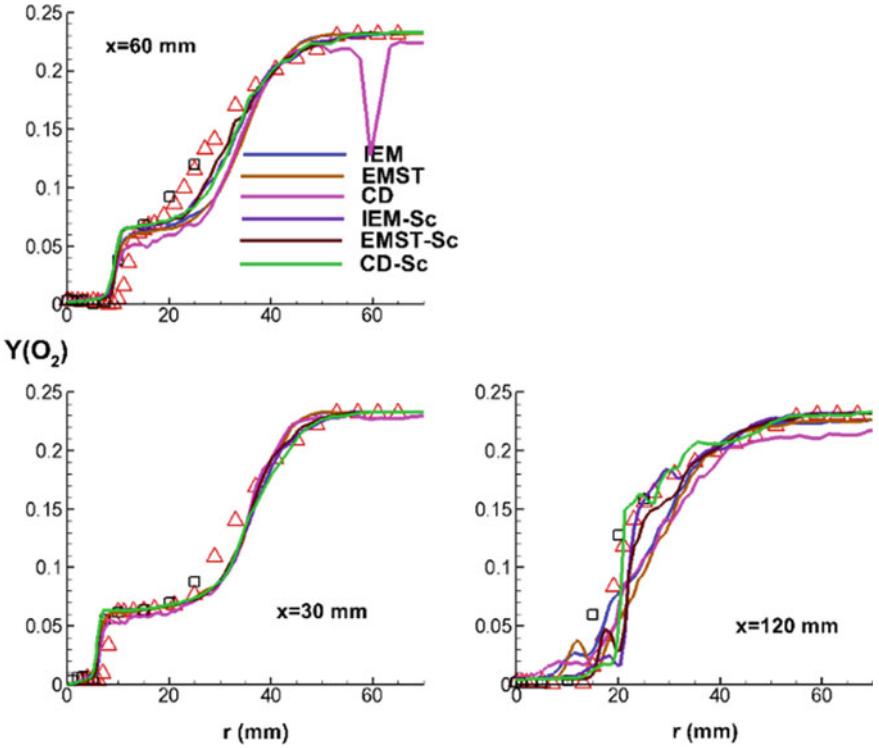

Fig. 7 Profiles of mean O_2 for HM2 flame (legends are the same as Fig. 1)

differences between EMST and IEM predictions are small and better compared to the CD predictions, which show considerable deviation from the two. It can be noted that the CO → CO_2 conversion is significantly affecting the proper predictions of CO_2, whereas OH → H_2O conversion is not significantly affecting the H_2O predictions. These phenomena are strongly coupled between turbulence–chemistry interaction models and chemical mechanism which needs further investigation [8].

The discrepancies observed, so far, with the finite rate chemistry-based models arise due to multiple reasons. Slower reaction rates in JHC flames, compared to standard combustion processes, make it more challenging for modeling. Despite having the chemical source terms in closed form, the transported PDF models cannot also be precisely accurate as the major source of errors in these models comes from the inaccuracies of the micro-mixing closures. The predictions in the shear layer are primarily affected due to mixing between the hot coflow and the fuel jet. This mixing between the streams, due to turbulence and species gradients, emphasizes the role of micro-mixing here. In case of IEM model [34], the composition of all the scalars relaxes toward the mean composition at the same rate whereas in case of CD mixing model, a number of particles in a cell are randomly selected and their individual compositions are moved toward the mean composition [35]. Therefore,

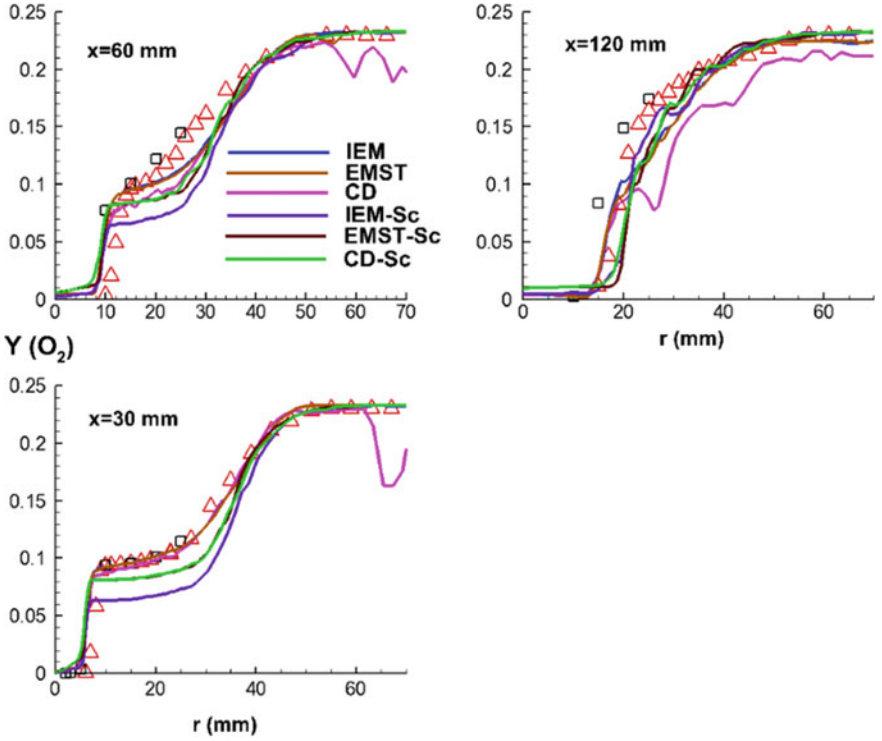

Fig. 8 Profiles of mean O_2 for HM3 flame (legends are the same as Fig. 1)

both of these mixing models are missing the effect of localness in the flow field which is a potential source of errors for the discrepancies observed in the predictions obtained through these models. However, on the contrary, the EMST model [36] takes into account the effects of local mixing among the particles in the composition space, thereby making it more accurate compared to the CD and the IEM models. Since, in the case of the CD mixing model, the particles, in a cell, are selected randomly, CD formulation is missing the effects of localness in the composition space, which is the main reason behind the differences observed between EMST and CD predictions. Another potential source of errors may arise from the 'notional particles' used in Lagrangian PDF approach: one due to particle tracking scheme and another one due to Monte Carlo methods. The mean density of particles in physical space should remain proportional to the local mean fluid density all the times, and this can be satisfied as long as the particle systems evolve consistently with the Eulerian equation systems. Therefore, the accuracy of the particle tracking scheme may induce some errors. The second source of discrepancies in the LPDF predictions is the numerical errors associated with the Monte Carlo methods, e.g., statistical errors and bias errors. Statistical errors are the random errors, whereas bias errors are deterministic errors, and both of them are strongly dependent on the

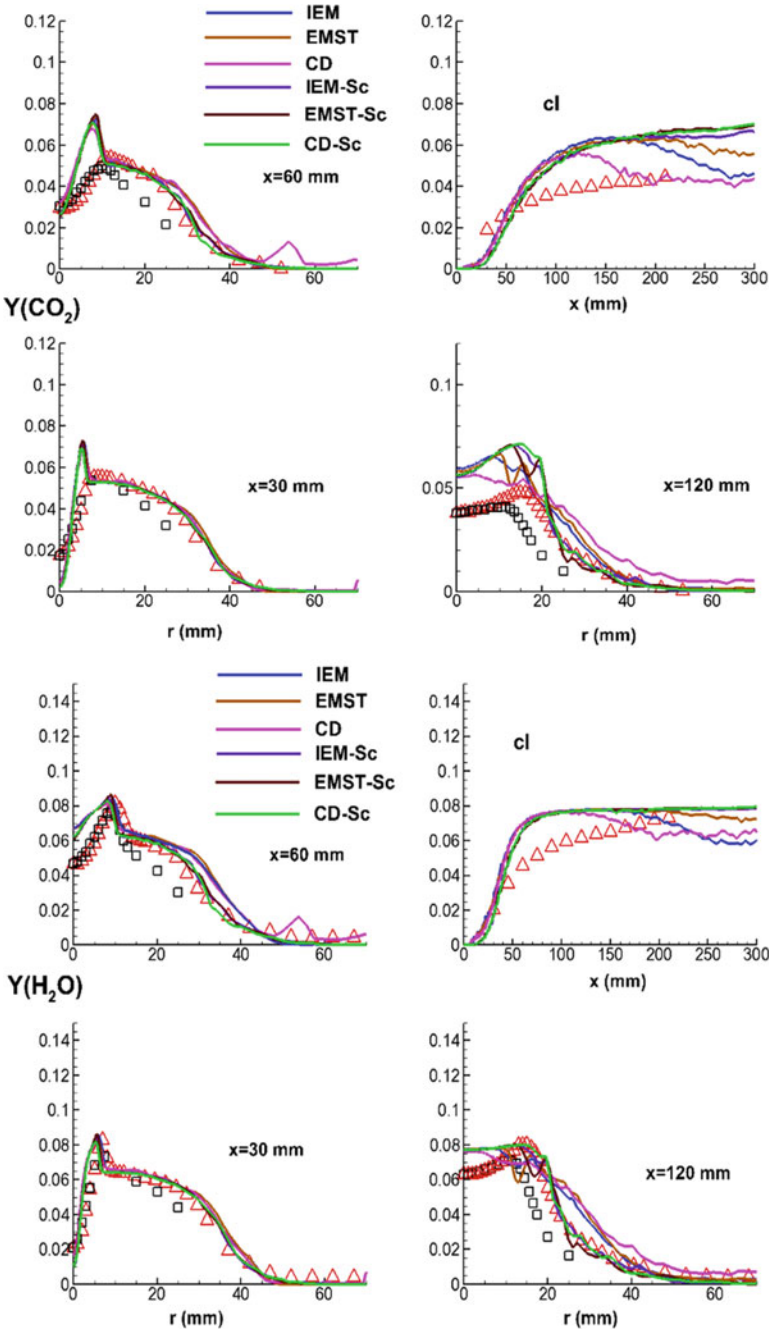

Fig. 9 Profiles of mean CO_2 and H_2O for HM1 flame (legends are the same as Fig. 1)

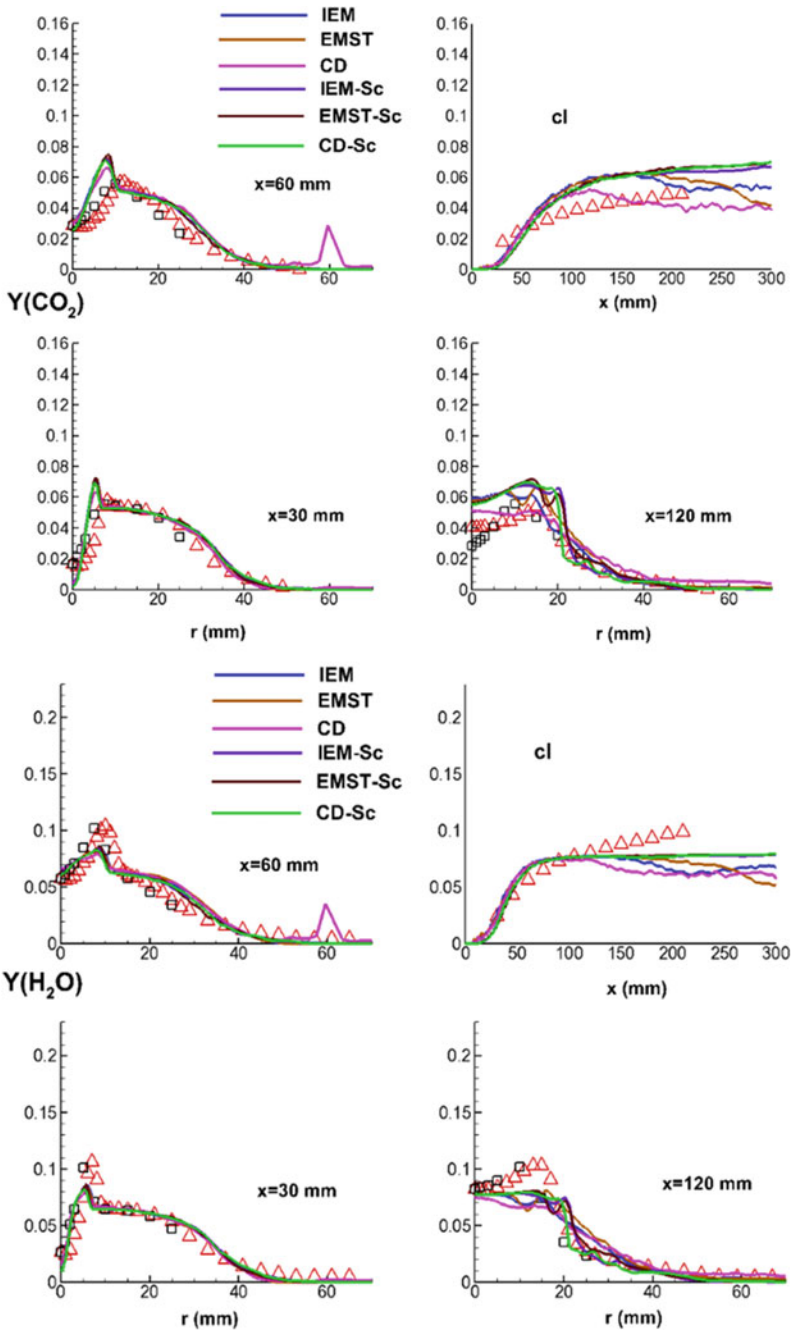

Fig. 10 Profiles of mean CO_2 and H_2O for HM2 flame (legends are the same as Fig. 1)

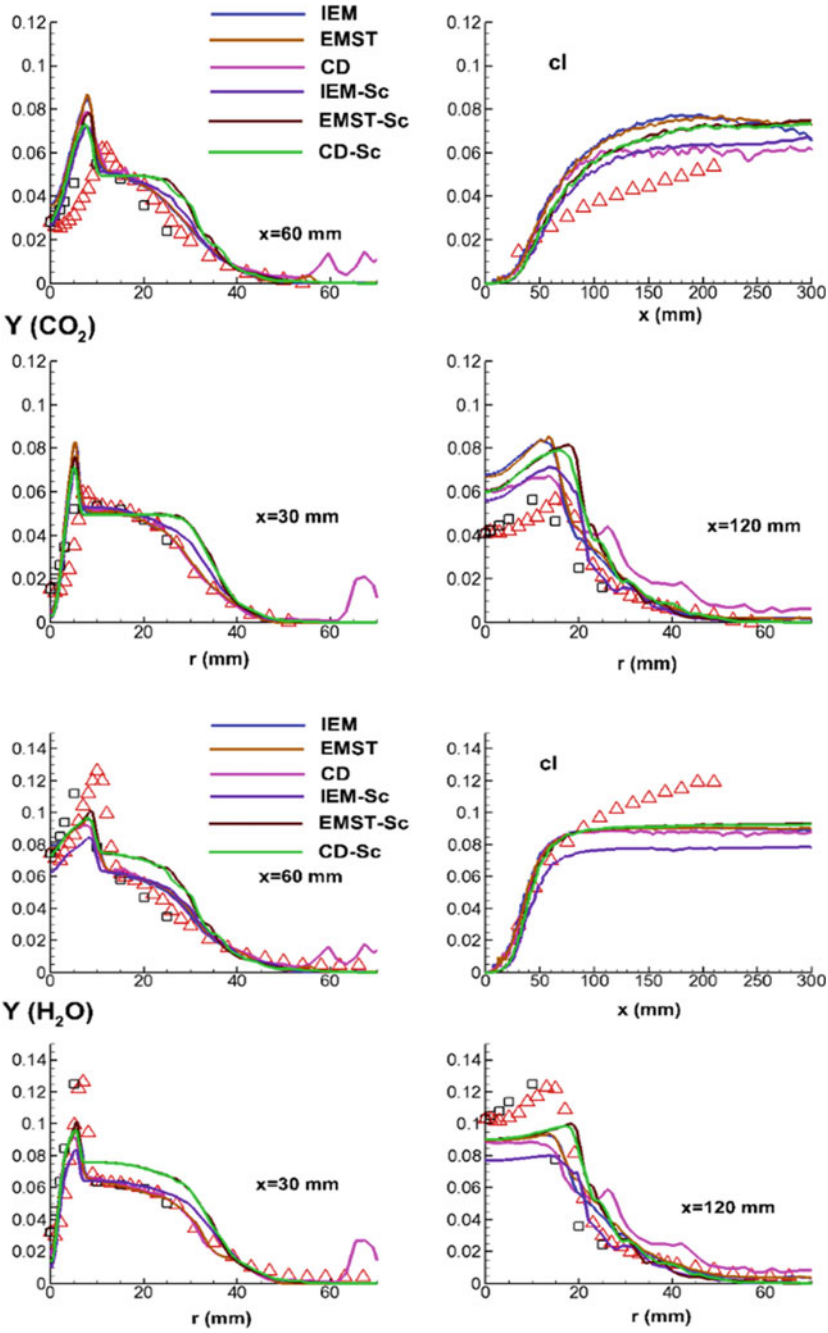

Fig. 11 Profiles of mean CO_2 and H_2O for HM3 flame (legends are the same as Fig. 1)

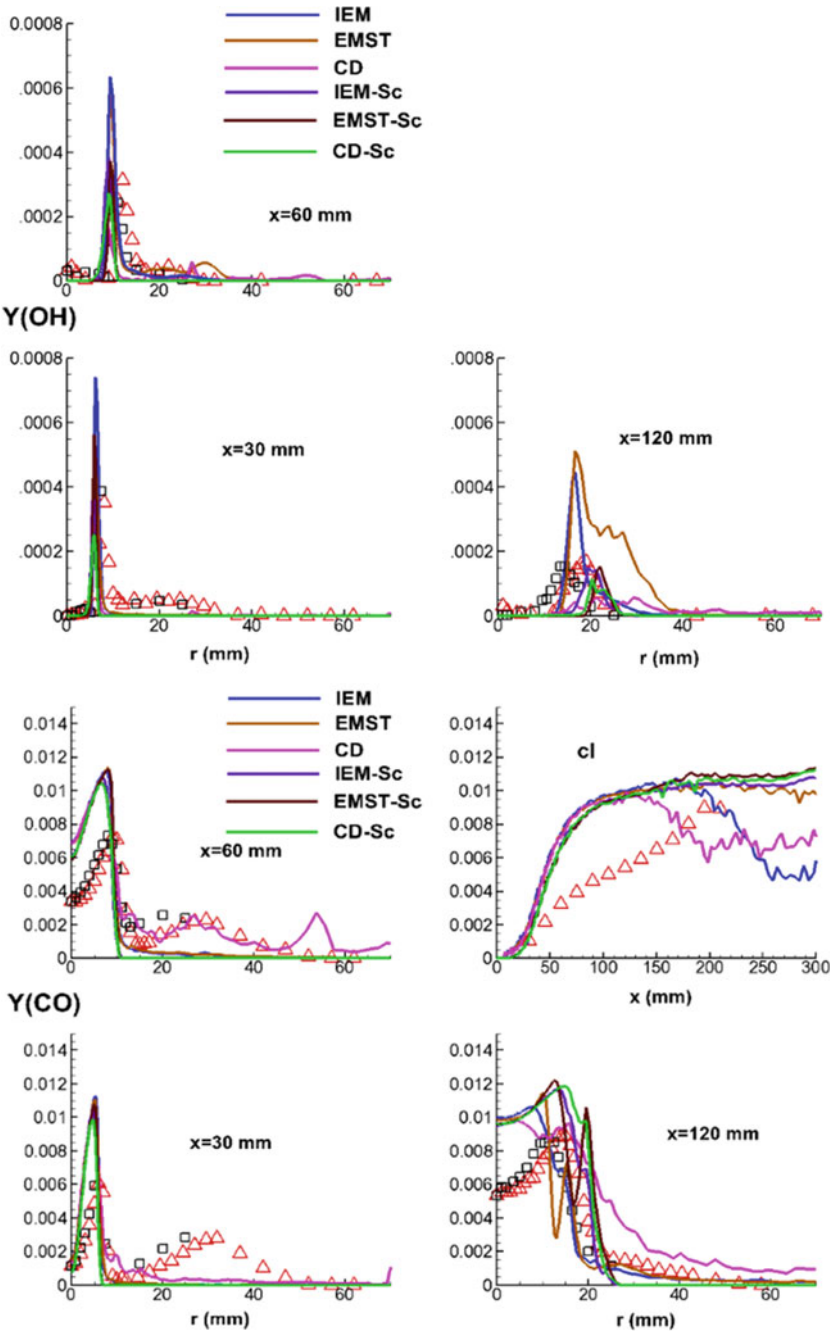

Fig. 12 Profiles of mean OH and CO for HM1 flame (legends are the same as Fig. 1)

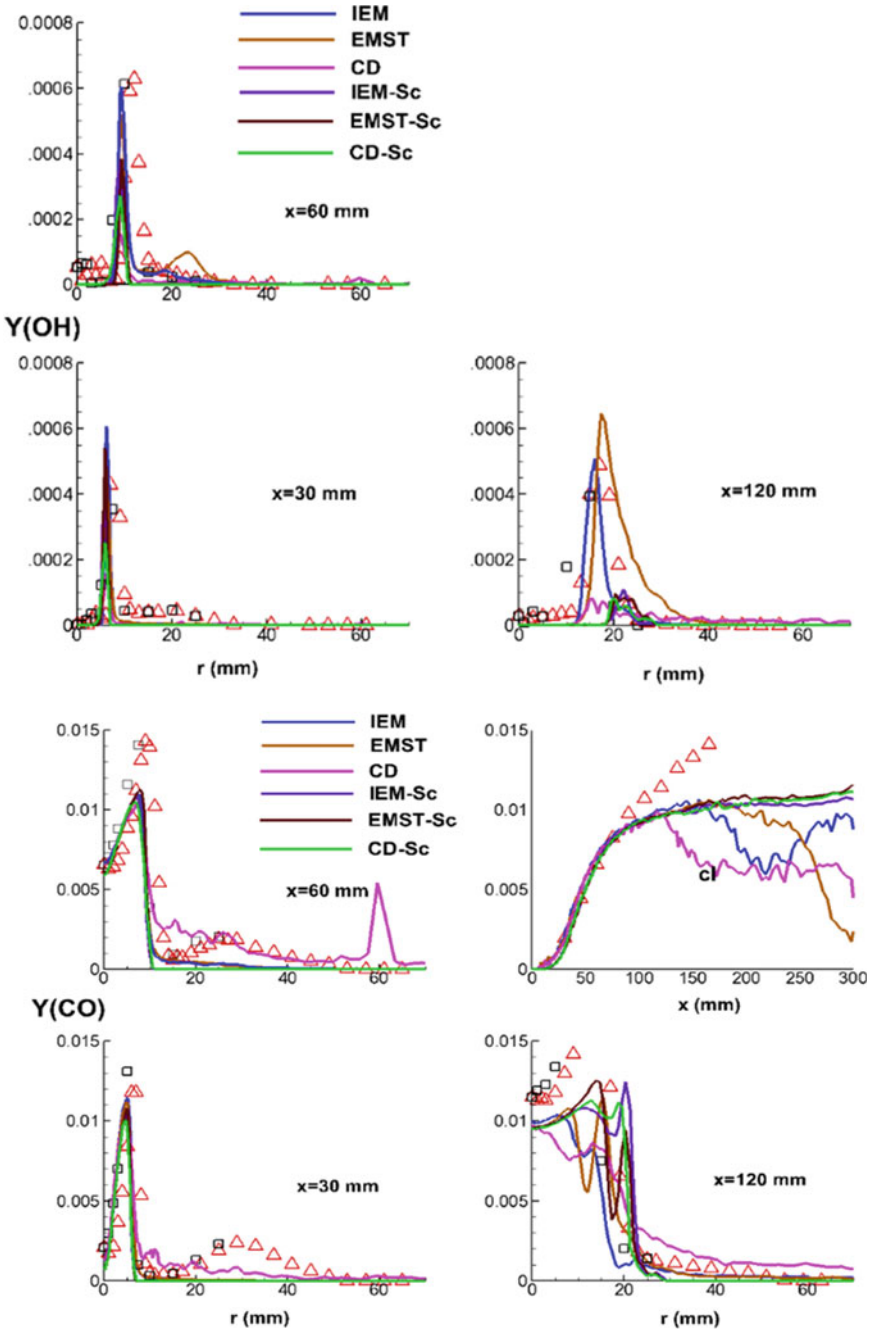

Fig. 13 Profiles of mean OH and CO for HM2 flame (legends are the same as Fig. 1)

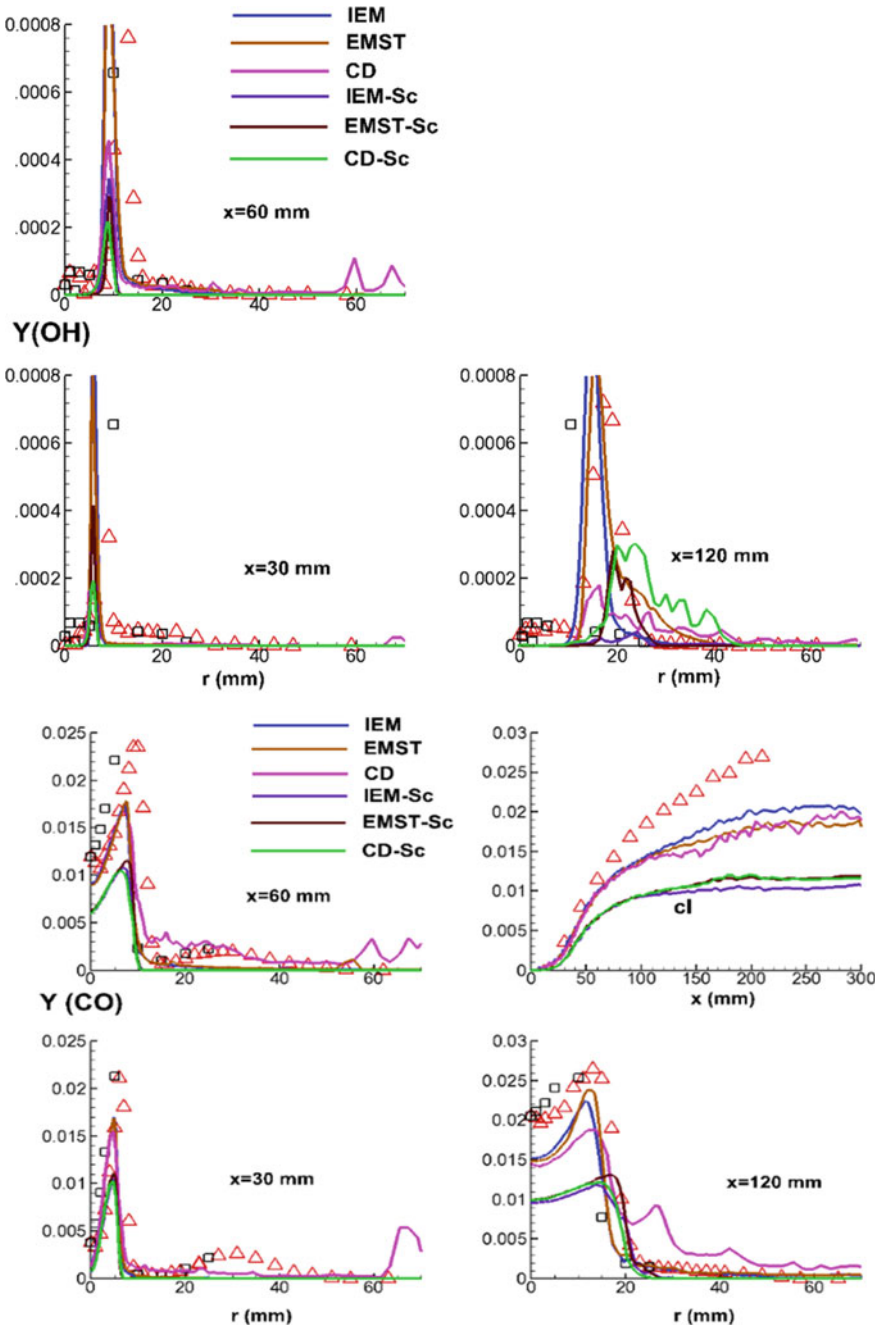

Fig. 14 Profiles of mean OH and CO for HM3 flame (legends are the same as Fig. 1)

number of particles used per cell. Statistical errors are not present in the present simulations; however, the bias errors, which arise from the mean quantities, are not completely reduced by averaging [8, 21].

In the JHC flames, the initiation of reaction is delayed, and overall reaction rates are lower than the conventional flames with lower temperatures and NO_x emissions. For the HM1 flame, there is 3% oxygen in the coflow, which is too much dilution for a JHC flame, and hence the HM1 flame forms a very crude case for studying the combustion models. Thus, comparing all the flames spread over a wide range of $O_{2\%}$ (3–9) at the end, it is evident that predictions improve as the oxygen content of the coflow increases, the reaction rate also increases, which, in turn, increases the Damkohler number. Therefore, we can say that we obtain better results at high Damkohler numbers irrespective of the chosen turbulence–chemistry interaction models. Overall, the mean predictions obtained through transported PDF-based models are in good agreement with some discrepancies observed mostly in the shear layer between the fuel jet and the hot coflow.

6 Conclusion

The performance of hybrid RANS/PDF method including tabulated chemical kinetics to predict the JHC flames is reported. A 3D-FGM table based on two mixture fractions and a reaction progress variable has been constructed to account for the inhomogeneity of the coflow and the entrainment of the ambient air. Igniting counterflow diffusion flamelets are created for different coflow compositions quantified by the second mixture fraction. To assess the predictive capability of the 3D tabulated chemistry manifold, Adelaide JHC flames have been considered for varying degrees of parameters. Comparison between predicted measurements is found to be in good agreement. It can be inferred from the present simulations that the 3D-FGM-based tabulated chemistry has the potential to predict JHC flame combustion with greater accuracy, and the sensitivity of current methodology needs further investigation for betterment.

Acknowledgements The first author would like to thank the Science and Engineering Research Board (SERB), India, for providing financial support. Further, the first author would also like to acknowledge the IITK Computer Center (www.iitk.ac.in/cc) for providing support to perform the computation work, data analysis, and article preparation.

References

1. Oldenhof E, Tummers M, van Veen EH, Roekaerts DJEM (2010) Ignition kernel formation and lift-off behavior of jet-in-hot-coflow flames. Combust Flame 157:1167–1178
2. Oldenhof E, Tummers MJ, van Veen EH, Roekaerts DJEM (2010) Role of entrainment in the stabilization of jet-in-hot-coflow flames. Combust Flame 157(6):1167–1178

3. Oldenhof E, Tummers MJ, van Veen EH, Roekaerts DJEM (2012) Transient response of the Delft jet-in-hot coflow flames. Combust Flame 159(2):697–706
4. De A, Oldenhof E, Sathiah P, Roekaerts D (2011) Numerical simulation of Delft-Jet-in-Hot-Coflow (DJHC) flames using Eddy Dissipation Concept (EDC) model for turbulence-chemistry interaction. Flow Turbul Combust 87(4):537–567
5. De A, Dongre A, Yadav R (2013) Numerical investigation of Delft-Jet-in-Hot-Coflow (DJHC) burner using Probability Density Function (PDF) transport modelling. In: ASME Turbo Expo, San Antonio, TX, 2012, ASME paper GT2013-95390
6. Bhaya R, De A, Yadav R (2014) Large Eddy Simulation of MILD combustion using PDF based turbulence-chemistry interaction models. Combust Sci Technol 186:1138–1165
7. Dongre A, De A, Yadav R (2014) Numerical investigation of MILD combustion using multi-environment Eulerian probability density function modeling. Int J Spray Combust Dyn 6(4):357–386
8. De A, Dongre A (2015) Assessment of turbulence-chemistry interaction models in MILD combustion regime. Flow Turbul Combust 94:439–478
9. Dally BB, Karpetis AN, Barlow RS (2002) Structure of turbulent non-premixed jet flames in a diluted hot coflow. Proc Combust Inst 29:1147–1154
10. Christo FC, Dally BB (2005) Modeling turbulent reacting jets issuing into a hot and diluted coflow. Combust Flame 142(1–2):117–129
11. Christo FC, Dally BB (2004) Application of transport PDF approach for modeling MILD combustion. In: 15th Australasian fluid mechanics conference, Sydney, Australia, 13–17 Dec
12. Frassoldati AF, Sharma P, Cuoci A, Faravelli T, Rangi E (2010) Kinetic and fluid dynamics modeling of methane/hydrogen jet flames in diluted coflow. Appl Therm Eng 30:376–383
13. Mardani A, Tabejamaat S, Ghamari M (2010) Numerical study of influence of molecular diffusion in the Mild combustion regime. Combust Theory Model 14(5):747–774
14. Mardani A, Tabejamaat S, Ghamari M (2011) Numerical study of effect of turbulence on rate of reactions in the MILD combustion regime. Combust Theory Model 15(6):753–772
15. Aminian J, Galletti C, Shahhosseini S, Tognotti L (2012) Numerical investigation of a MILD combustion burner: analysis of mixing field, chemical kinetics, and turbulence-chemistry interaction. Flow Turbul Combust 88:597–623
16. Kim SH, Huh KY, Dally BB (2005) Conditional moment closure modeling of turbulent non-premixed combustion in diluted hot coflow. Proc Combust Inst 30:751–757
17. Ihme M, See YC (2011) LES flamelet modeling of three-stream MILD combustor: analysis of flame sensitivity to scalar inflow conditions. Proc Combust Inst 33:1309–1317
18. Ihme M, Zhang J, He G, Dally BB (2012) LES of a Jet-in-Hot-Coflow burner operating in the oxygen-diluted combustion regime. Flow Turbul Combust 89:449–464
19. Kazakov A, Frenklach M (1994) Reduced reaction sets based on GRI-MECH 1.2. http://www.me.berkeley.edu/drm/
20. Bowman CT, Hanson RK, Davidson DF, Gardiner WC Jr, Lissianski V, Smith GP, Golde DM, Frenklach M, Goldenberg M (1999) GRI Mech. http://www.me.berkeley.edu/gri_mech/
21. Bilger RW, Starner SH, Kee RJ (1990) On reduced mechanisms for methane-air combustion in non-premixed flames. Combust Flame 80:135–149
22. Haworth DC (2010) Progress in probability density function methods for turbulent reacting flows. Prog Energy Combust Sci 36:168–259
23. van Oijen JA, Lammers FA, de Goey LPH (2001) Modelling of complex premixed premixed burner systems using flamelet-generated manifolds. Combust Flame 127(3):2124–2134
24. Vreman AW, Albrecht BA, van Oijen JA, de Goey LPH, Bastiaans RJM (2008) Premixed and nonpremixed generated manifolds in large eddy simulation of Sandia flame D and F. Combust Flame 153:394–416
25. Ramaekers WJS, van Oijen JA, de Goey LPH (2010) A priori testing of flamelet generated manifolds for turbulent partially premixed methane/air flames. Flow Turbul Combust 84:439–458
26. Bekdemir C, Somers LMT, de Goey LPH, Tillou J, Angelberger C (2013) Predicting diesel combustion characteristics with large-eddy simulations including tabulated chemical kinetics. Proc Combust Inst 34:3067–3074

27. Sarras G, Mahmoudi Y, Arteaga Mendez LD, van Veen EH, Tummers MJ, Roekaerts DJEM (2014) Modeling of turbulent natural gas and biogas flames of the Delft Jet-in-Hot-Coflow burner: effects of coflow temperature, fuel temperature and fuel composition on the flame lift-off height. Flow Turbul Combust 93(4):607–635
28. CHEM1D. A one-dimensional laminar flame code. Eindhoven University of Technology. https://www.tue.nl/combustion/chem1d
29. an Oijen JA, de Goey LPH (2002) Modelling of premixed counterflow flames using the flamelet-generated manifold method. Combust Thoery Model 6:463–478
30. Peeters TWJ (1995) Numerical modeling of turbulent natural-gas diffusion flames. PhD thesis, Technische Universiteit Delft
31. Naud B, Jiménez C, Roekaerts D (2006) A consistent hybrid PDF method: implementation details and application to the simulation of a bluff-body stabilised flame. Prog Comput Fluid Dyn 6:147–157
32. Naud B, Merci B, Roekaerts D (2010) Generalised Langevin model in correspondence with a chosen standard scalar-flux second-moment closure. Flow Turbul Combust 85:363–382
33. Merci B, Naud B, Roekaerts D (2009) Joint scalar versus joint velocity-scalar PDF simulations of bluff-body stabilized flames with REDIM. Flow Turbul Combust 82(2):185–209
34. Dopazo C, O'Brien EE (1974) Functional formulation of non-isothermal turbulent reactive flows. Phys Fluids 17:1968–7195
35. Curl RL (1963) Dispersed phase mixing: 1. Theory and effects in simple reactors. AIChE J 9:175–181
36. Subramaniam S A mixing model for turbulent reactive flows based on Euclidean minimum spanning trees. Combustion and Flame 115(4):487–514

CFD Simulation of Soot Dynamics in the Exhaust System of an Engine to Meet Particulate Standards of 2020 and Beyond

P. S. Rajagopal, Ashish Magar, Janki Shinde, Madhukar M. Rao, and Akshai K. Runchal

1 Introduction

Soot particles are formed due to pyrolysis of hydrocarbons (breaking up at high pressure or temperature), nucleation, and later coagulation/agglomeration of the carbon compounds [4, 5]. Low molecular weight hydrocarbons are treated with acetylene-based soot inception (formation) method, whereas high molecular weight HC (such as kerosene and jet fuels) are treated as PAH (Polycyclic Aromatic Hydrocarbon) based method [5]. However, these methods are only to be considered if formation of soot is to be modeled.

Soot dynamics consists of various phenomenon, most important are nucleation, coagulation/aggregation, and oxidation (other important phenomenon are condensation, rounding, sintering, etc.). Coagulation is handled as described by Smoluchowski (similar to aerosols). Initially smaller particles are assumed to coagulate to form a spherical particle. However, after reaching a primary particle diameter (25–30 nm, [36]), the particles start to form large chain-like structures and are described by fractal dimension (Df). Nucleation of soot particles is transition of gas-phase carbon molecule clusters to solid phase. Various methods of modeling include chemical kinetics to form a cluster of carbon dimer (nC2) from base hydrocarbons such as acetylene and pyrene [5, 24]; using empirical relations in the form of kernels [11]; and rate constants varying with temperature [4]. Similar work has been done for oxidation.

P. S. Rajagopal (✉) · J. Shinde · M. M. Rao · A. K. Runchal
ACRi Infotech Pvt. Ltd., Bangalore, Karnataka, India
e-mail: rajagopal@cfdvrinstitute.org; rajagopal@acricfd.com

A. K. Runchal
e-mail: runchal@cfdvrinstitute.org

A. Magar
CFDVRi, Mount View Complex, McLeod Ganj, Dharamsala, Himachal Pradesh 176219, India

© Springer Nature Singapore Pte Ltd. 2021

A. De et al. (eds.), *Sustainable Development for Energy, Power, and Propulsion*, Green Energy and Technology,
https://doi.org/10.1007/978-981-15-5667-8_18

Challenges are faced in modeling of different interaction phenomenon of soot particles, as they involve non-spherical geometries, rather than during inception. Method of Moments (MOM) and its variants have been used widely, for obtaining averaged values of particles rather than the complete distribution. This may have been a reason to overlook complications in modeling fractal geometries. Used moments methods are, Conditional- Quadrature Method of Moments (CQMOM) [32, 35, 34], MOM-Interpolative Closure (MOMIC) [34], Multi-Moment Sectional Method [42], along with conventional MOM [2]. Computational study done in Rodrigues et al. [32] compares combustion and soot generation by semi-empirical, Hybrid method of moments (HMOM) and CQMOM in an experimental combustor. Semi-empirical methods assume spherical soot particles, and the rate expressions for inception, nucleation, and oxidation are taken as from Salenbauch et al. [34]. HMOM and CQMOM used bivariate density functions, for volume and surface-area of particles [23]. Experimentally and numerically investigated size of primary soot particles in an ethylene flame at different height above burner (HAB). Study confirmed soot aggregates formed have non-spherical shape, composed of spherical primary soot particles. Salenbauch et al. [34] numerically investigated two types of flames using various methods (sectional, two equations, and MOMIC) and successfully validated the nucleation rates available in the literature and proposed two more sets providing a better fit to experimental data.

Experimental investigations involve sampling of soot particles at tailpipe and dilution tunnel [15, 28] in case of vehicle engines, and thermophoretic plates in case of flames [3]. Soot particles in experimental findings are characterized in terms of mobility diameter (dm) [5, 19, 20, 24]. Study in [28] aimed towards establishing a relation between particle mass and mobility diameter of soot particles from diesel engine exhaust. Mass size distribution was obtained using different measurement techniques [switch-mode power supply (SMPS), micro-orifice uniform deposit impactor (MOUDI)] for various engine loads [19]. Discusses measurements from oil aerosols, flame soot particles, and two types of diesel engine exhausts. Number distributions are obtained in terms of mobility and aerodynamic diameters [15]. Briefly describe that the soot particle distributions closely fit into a log-normal form (for various fractal sizes). This study has been confirmed for exhausts from both diesel and gasoline type of engines, and for different loading conditions. This trend can also be observed in the experimental findings of Park et al. [6], Commodo et al. [28]. Discusses size distribution for a range of equivalence ratios of ethylene/air mixture. Mixtures where combustion is clean produce very fine soot particles, whereas a richer fuel mixture produces larger particles, and shows a bimodal distribution. Numerical simulation of soot particle filter (diesel particulate filters, DPF) was done by Maricq and Xu [19]. Exhaust gas containing soot particles was forced to pass through porous walls of the channels. Behavior of monodisperse soot particles of size 100, 200, 500 nm, and 2 μm were studied individually.

One disadvantage of porous particulate filter is that they get clogged by soot after regular use. This reduces their performance and also increases backpressure. This required periodic cleaning or removal of soot by high-temperature oxidation using catalysts.

Thermophoresis is the phenomenon of suspended particles experiencing a force due to thermal gradients. Exhaust gases come into the exhaust system at very high temperatures. If the pipe walls are maintained at ambient temperature, the temperature gradient can cause the soot particles to move towards the cooler wall and deposit, removing dangerous soot particles from the exhaust gas.

Thermophoretically active plate precipitators and deposition to them were investigated experimentally by Tsai and Lu [39], Messerer et al. [21], Shi and Harrison [37] under conditions relevant to engine operations. While Shi and Harrison [37] considered a fluidized bed that was activated by thermophoresis, Messerer et al. [21] studied deposition onto plate precipitators. Two plates maintained at different temperatures were kept separated by a narrow gap leading to high-temperature gradient. Exhaust gas carrying soot was sent through the gap under different temperature gradient, plate separation, and exhaust gas velocities.

In this study, deposition of soot onto plate precipitators is numerically investigated for conditions reported in Messerer et al. [21]. The particle size range is divided into a number of size classes, and a transport equation is solved for each particle size, with the coagulation of fractal particles modeled with the birth and death integral terms. The partial-integro-differential equation is handled through a sectional method [30].

2 Aerosol Transport and Dynamics Model

The dynamics and transport of aerosols is mathematically described by the Aerosol General Dynamics Equation (GDE) [12, 41]

$$\begin{aligned}\frac{\partial n(d_p,r,t)}{\partial t} + \nabla .[Un(d_p,r,t)] &= \nabla .\{D(r,t)\nabla n(d_p,r,t)\} \\ &+ \frac{1}{2}\int_0^{d_p} K(d_p', d_p - d_p')\, n(d_p', r, t)\, n(d_p - d_p', r, t)\, d(d_p') \\ &- n(d_p,r,t)\int_0^{\infty} K(d_p, d_p')\, n(d_p', r, t)\, d(d_p') \\ &+ S(d_p,r,t) - \lambda n(d_p,r,t) - \nabla .[U_{\text{drift}} n(d_p,r,t)] \end{aligned} \quad (1)$$

where d_p and $d_p^{'}$ are particle diameters; $n\ (d_p,\ r,\ t)$ is the spatially (r) and temporally (t) varying number concentration distribution function for particle diameter d_p; U is the gas-phase velocity; D is the particle diffusivity; K is the collision frequency between particles of different sizes; S is the source term arising from nucleation and direct emission; λ is the decay rate of the species; U_{drift} is the total drift velocity of the aerosol particles due to various mechanisms like gravitational settling, thermophoresis, turbophoresis, etc.

In the above equation, terms on the left-hand side include the temporal change in number distribution function and convective transport. The first term on the right side of the equation accounts for the diffusive transport of aerosol particles under the flow conditions. Coagulation terms appear as integrals in the GDE. The first integral in the GDE represents the rate of formation of new particles of a particular size due to collision of two particles of smaller sizes. The second integral represents the rate of depletion due to particles of a particular size combining with another particle.

The particle diffusivity used in the above equation is also a function of particle size and is given by

$$D = \frac{k_b T C_c}{3\pi \mu_g d_p} \tag{2}$$

where k_b is the Boltzmann constant, T is the temperature, μ_g is the gas viscosity, and C_c is the Cunningham slip factor [7, 8]

$$C_c = 1 + \mathrm{Kn} * (2.514 + 0.8 * \exp(-0.55/\mathrm{Kn})) \tag{3}$$

where Kn, Knudsen number, is the ratio of the mean free path of the gas particles (λ) to the particle diameter (d_p) and is given as

$$Kn = \frac{2\lambda}{d_p} \tag{4}$$

2.1 Coagulation

Aerosol particles undergo collision and coalesce to form bigger particles, with the conservation of mass. The frequency with which particles collide, the coagulation kernel, depends on the sizes of the particles and the forces and phenomena which cause their movement. Some of the mechanism which affects the collision frequency include Brownian motion, gravitational settling of particles, laminar and turbulent diffusion, laminar and turbulent shear, electric charge.

The Knudsen number, which is the ratio of molecular free path of the particle to the particle radius, characterizes the different regimes of interest, namely the continuum regime (Kn $\ll$ 1), free molecular regime (Kn $\gg$ 1), and the transition regime (Kn $\approx$ 1). The current study falls in the transition regime, and the Fuchs kernel [13, 17] was used to obtain the collision frequencies.

$$K_{ij} = \frac{2\pi \left(D_i + D_j\right)\left(d_{c,i} + d_{c,j}\right)}{\frac{d_{c,i}+d_{c,j}}{d_{c,i}+d_{c,j}+2\sqrt{\delta_{m,i}^2+\delta_{m,j}^2}} + \frac{8\left(D_i+D_j\right)}{\left(d_{c,i}+d_{c,j}\right)\sqrt{\bar{v}_{pi}^{-2}+\bar{v}_{pj}^{-2}}}} \tag{5}$$

$$\bar{v}_{pi} = \sqrt{\frac{8k_b T}{m_i \pi}} \tag{6}$$

$$\delta_{m,i} = \frac{1}{3d_{m,,i}\lambda_i}\left[\left(d_{m,i} + \lambda_i\right)^3 - \left(d_{m,i}^2 + \lambda_i^2\right)^{\frac{3}{2}}\right] - d_{m,i} \tag{7}$$

$$\lambda_i = \frac{8D_i}{\pi v_{pi}} \tag{8}$$

$$d_{c,i} = d_s N_i^{3/D_f} \tag{9}$$

$$N_i = \frac{v_i}{v_s} \tag{10}$$

$$d_{m,i} = \max\left\{\frac{d_{c,i}}{\ln\left(\frac{d_{c,i}}{d_s}\right)+1}, d_s\left(\frac{D_f}{2}\right)^{0.7}, d_{A,i}\right\} \tag{11}$$

$$d_{A,i} = d_s * \left\{\max\left[N_i^{\frac{2}{3}}, \min\left(1 + \frac{2}{3}(N_i - 1), \frac{1}{3}D_f N_i^{2/D_f}\right)\right]\right\}^{-1/2} \tag{12}$$

where d_{pi} and d_{pj} are particle diameters; d_{ci} and d_{cj} is the particle collision diameter; d_{ci} and d_{cj} is the particle mobility diameter; $d_{A,i}$ and $d_{A,j}$ is the particle area equivalent diameter; D_i and D_j are particle diffusivities; D_f is the fractal dimension; v_{pi} and v_{pj} are thermal velocity of air molecules of same size as the aerosol particles; $\delta_{m,i}$ and $\delta_{m,j}$ are distance from particle surface to continuum/free molecular regime dividing surface; λ_i is particle mean free path; N_i is the number of spherules in an aggregate; m_i is the mass of particle i.

The presence of the integral terms that couple number concentration of various size classes makes the GDE a partial integro-differential equation. The aerosol particle size range is divided into a finite number of discrete, zero-width nodes. The integral terms in the GDE are then converted into a summation over the finite number of particle sizes following [30]. When two particles combine, the new particle formed often has a size that falls between the discretized zero-width nodes. The new particle is then assigned to the nodes on either side using a mass conserving splitting factor [30].

In this work, the particle size classes were uniformly distributed in the logarithmic space.

Validation of the ANSWER CFD code's coagulation module [31] was carried out by comparison against the results from the published NGDE code [30].

2.2 Gravitational Settling

Aerosol particles experience the downward force of gravity under simultaneous counter drag. This force is proportional to the particle mass, so the bigger particles experience a larger force. The gravitational settling velocity v_g is given by [14, 27]

$$v_g = g\tau \tag{13}$$

where τ is relaxation time,

$$\tau = \frac{C_c \rho_g d_p^2}{18\mu_g} \tag{14}$$

and ρ_g is gas density.

Only gravitational settling was used as a part of drift flux term in this study. Additionally, source terms for the cases considered here are imposed log-normal distribution with defined properties.

2.3 Thermophoresis

The settling velocity vg of aerosol particles due to gravity is function of particle size and is given by Talbot et al. [38], Guha [14], Overholt et al. [27]

$$u_{\text{th}} = \frac{K_{\text{th}} \nu}{T_g} \frac{\mathrm{d}T}{\mathrm{d}x} \tag{15}$$

where, τ is relaxation time,

$$K_{\text{th}} = \frac{2C_s(\alpha + C_t K_n)C_n}{(1 + 3C_m K_n)(1 + 2\alpha + 2C_s K_n)} \tag{16}$$

where K_{th} is the thermophoretic coefficient, and the constants C_s (thermal slip coefficient) = 1.147, C_t (temperature jump coefficient) = 2.18, and C_m (momentum exchange coefficient) = 1.146 [27, 38].

For a 2D laminar flow in a rectangular channel of height H and length L, with an inlet average velocity of u_{av}, the efficiency of deposition is given by Tsai and Lu [39]

$$E = \frac{u_{\text{th}} L}{u_{\text{av}} H} \tag{17}$$

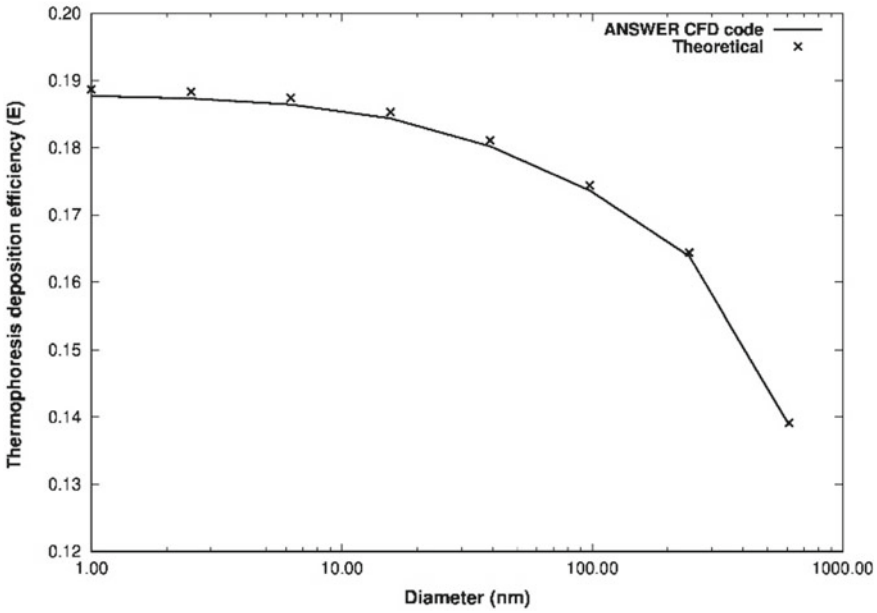

Fig. 1 Deposition efficiency of thermophoresis of particles for laminar flow in a 2D duct

The thermophoresis model in ANSWER CFD code was benchmarked against the above analytical solution (Eq. 17) and the comparison of thermophoretic deposition efficiency is shown in Fig. 1. The ANSWER CFD predictions were seen to match well with the analytical solution.

3 Results and Discussion

The experiments carried out by Tsai and Lu [39] showed that plate precipitator design with two flat plates where one plate is heated and the other is cooled allows for collection of particles on the cooled plate at high efficiency. The experiments [39] were performed in a rectangular duct, where the top plate was heated by a hot water bath kept at a particular temperature, while the lower plate kept at ambient temperature, to obtain the required temperature gradient. Air at constant flow rate was passed through the region between the plates. The flow and temperature profile become fully developed very quickly. Polydisperse aerosol was generated and passed through an electrostatic classifier to generate monodisperse aerosol of specific sizes. Two different materials were used to generate the aerosol, namely sodium chloride (NaCl) and Sodium Fluorescein. Thermophoretic deposition efficiency was measured for eight different aerosol particle diameters ranging from 0.04 to 0.5 μm at two different temperature gradients. Since Brownian diffusion and gravitational settling

are important for particles in this size, a separate set of experiments was performed for every size with top and bottom plates kept at the same temperature, thereby eliminating thermophoresis. This was used to compute the deposition efficiency of thermophoresis alone.

Tsai and Lu [39] also found that the experimental results matched the thermophoretic velocity proposed by Talbot et al. [38] better than that proposed by Derjaguin and Yalamov [9, 10].

CFD simulations were carried out using the 3D finite volume code ANSWER [1, 29, 33, 40].

To simulate the conditions of this experiment, a 3D rectangular duct of length 7.1 cm, width 3 cm, and height (gap between plates) of 0.38 mm was meshed with a uniform structured grid. The air inflow velocity was 58.4 cm/s. The Prandtl number for air was taken to be 0.7. The simulations were carried for eight particle diameters, namely 0.04, 0.06, 0.08, 0.1, 0.2, 0.3, 0.4, and 0.5 μm.

To compare the results of the CFD simulations with the experimental data, the plots in Fig. 4a, b in Tsai and Lu [39] were digitized and the data extracted.

Figure 2 shows the comparison of thermophoretic deposition efficiency from the results of the ANSWER CFD simulations with the experimental results of Tsai and Lu [39] for sodium fluorescein particles. The deposition efficiencies match the experimental data well at both temperature gradients, namely 526.3 and 878.96 °C/cm, beyond 0.08 μm.

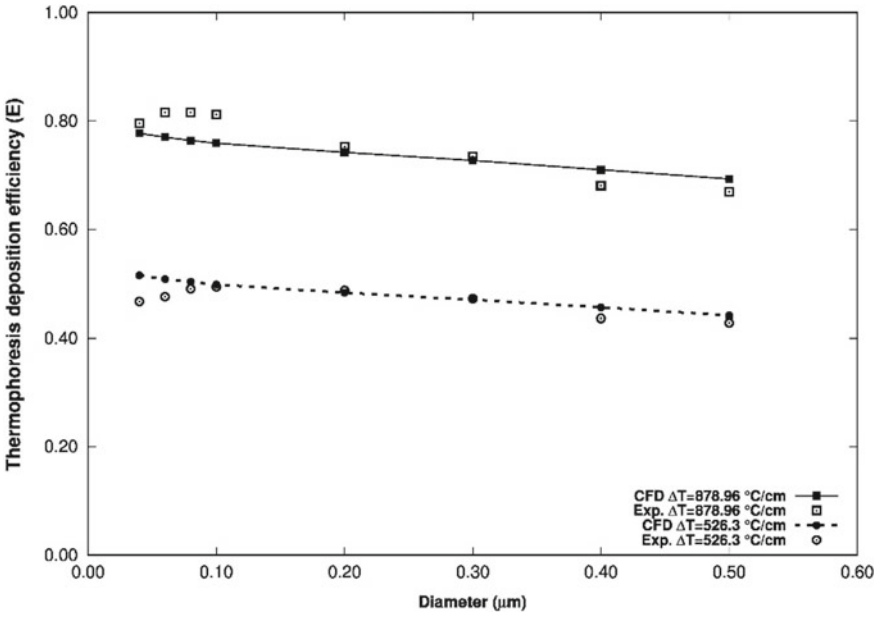

Fig. 2 Comparison of deposition efficiency of thermophoresis of sodium fluorescein particles in laminar flow in a 3D duct with [39]

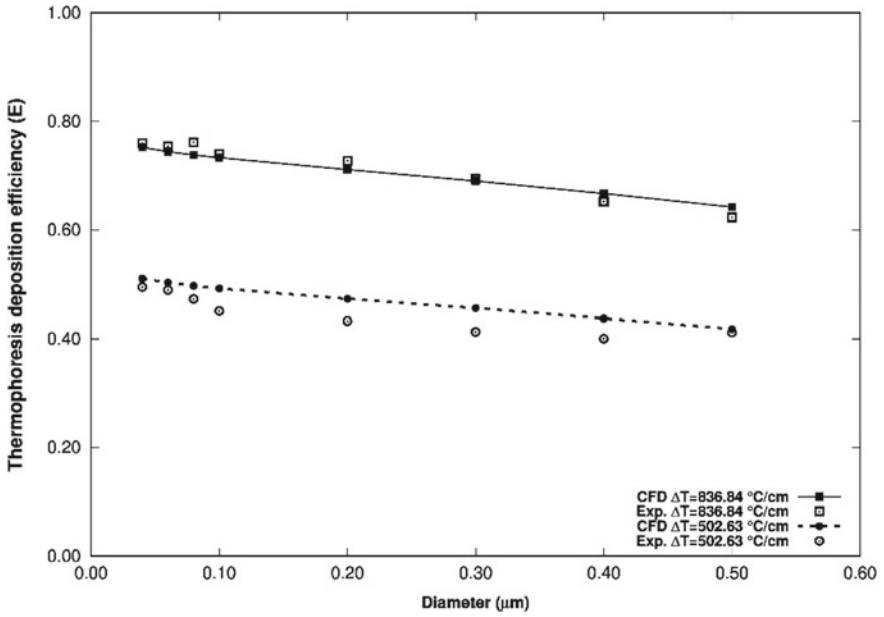

Fig. 3 Comparison of deposition efficiency of thermophoresis of sodium chloride particles in laminar flow in a 3D duct with [39]

Figure 3 shows the comparison of thermophoretic deposition efficiency from the results of the ANSWER CFD simulations with the experimental results of Tsai and Lu [39] for sodium chloride particles. The deposition efficiencies match the experimental data very well at the higher temperature gradients of 836.84 °C/cm. The ANSWER CFD code slightly over-estimates the deposition efficiency at the lower temperature gradient of 502.63 °C/cm.

With the validity of the thermophoretic velocity equation proposed by Talbot et al. [38] verified by the above results, the ANSWER CFD code's aerosol module was applied for the problem of soot deposition in plate precipitators under conditions relevant to modern diesel engine exhaust systems [21]. Here, dynamics of soot transport and deposition in a plate precipitator were experimentally studied as a method to remove soot particles from exhaust gases.

In this experiment, two plates separated by a narrow gap were maintained at different temperatures. When soot laden exhaust gas flowed through the gap between the plates, a temperature gradient was setup in the gas, driving soot particles towards the cooler lower plate due to thermophoresis.

A variety of conditions were considered and soot size distributions were measured experimentally near the inlet and the outlet [21].

The experimental setup in Messerer et al. [21] had wide plates separated by a narrow gap. The setup can be mimicked in numerical simulations by using a 3D grid

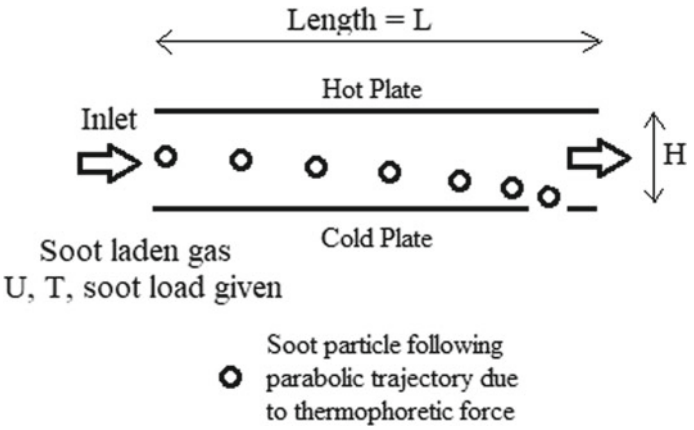

Fig. 4 Computational domain for case 1

and applying periodic boundary conditions for the direction perpendicular page. This is equivalent to doing a 2D simulations, which was the choice made in this study.

The inlet gas was a 50–50 mixture of argon and air [21]. The fluid properties for the gas in the simulation were set to the average value of those for argon and air at the average of upper and lower wall temperatures in each simulation.

Figure 4 shows the schematic of the problem studied in this work.

The exhaust gas enters the plate gap carrying soot particles. As the particles move along with the exhaust gas, they also experience a thermophoretic drift velocity towards the bottom cooler plate. Some fraction of the particles are deposited on to the plate. The Reynolds number based on the gap between the plate precipitators for the different cases varied between 247 and 271, so the flow was always considered to be laminar.

The gap between the plates is varied between 0.45 and 1.45 mm in the experiments [21]. The temperature difference between the plates was varied between 19 and 113 K, which resulted in a thermal gradient between the plates from 1300 to 23,000 K/m.

The inlet temperature was always uniform and set to the lower wall temperature. The temperature reaches the fully developed profile very quickly (Fig. 4), while the flow was not seen to be fully developed (Fig. 5) in most scenarios considered.

Figure 5 shows the particle size distribution at the outlet and Fig. 6 shows the average size distribution in the domain after 2 h for the same case.

In the experiments in Messerer et al. [21], soot generated from a spark discharge was diluted with a carrier gas and allowed to flow between the plates at high velocities and thermal gradients. This generated a log-normal distribution of aerosol particles [21].

A log-normal distribution is given by Lee et al. [18], Otto et al. [26].

$$n(v,t) = \frac{N_0}{3\ln\sigma\sqrt{2\pi}} \exp\left\{\frac{-\ln^2(v/v_m)}{18\ln^2\sigma}\right\}\frac{1}{v} \tag{19}$$

Fig. 5 Temperature contours in flow between parallel plate with heated top plate

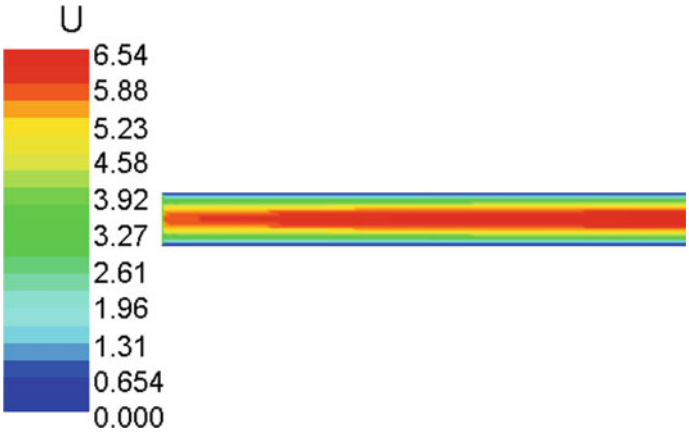

Fig. 6 Axial velocity contours in flow between parallel plates

where $n(v)$ is the number of particles of volume v, N_0 is the total number concentration of particles at the inlet in ($/m^3$), v_m is the mean particle volume of the distribution. Following the data reported in Messerer et al. [21], the inlet total number (N_0) was taken to be $10^7/cm^3$, the geometric standard deviation, σ, was set to 1.67, for all simulations in this work, and the mean of the distribution was fixed at a diameter of 85 nm. The particle size range of 20–300 nm was divided into 16 size classes spaced uniformly in logarithmic space.

Soot particles are known to become fractal beyond a certain size [16] and this can significantly affect the coagulation rate. In Messerer et al. [21], the aerosol is reported as being generated by the Palas GFG1000 soot generator. Following experimental data reported for the same soot generator in Orihuela et al. [25], the fractal dimension for aerosol particles in the case study was set to 2.05.

The aerosol size distribution was reported in [31] for two different temperature gradients for the same flow speed of 11 m/s. Figure 7 shows a comparison between ANSWER CFD results and experimental data from Messerer et al. [21] for the soot size distribution at the outlet. In this case, the inlet velocity was set to 7.7 m/s for the 70 K temperature difference case and to 8.5 m/s for the 105 K temperature difference case, following the values reported in Messerer et al. [21]. The experimental data was digitized and plotted for comparison. It is seen in the experiments that the peak of the distribution has reduced (due to deposition on the lower plate), the shape of the distribution and location of its peak has not shifted much. This indicates all sizes of soot particles undergo deposition at nearly the same rates.

ANSWER is able to reasonably capture the reduction in peak and the shape of the distribution for the lower value of thermal gradient. For the higher thermal gradient scenario, the CFD results show a shift of the peak of the distribution to the right, indicating more lower sized particles were deposited than were larger-sized particles.

Figure 8 shows a comparison of experimentally measured and CFD computed deposition efficiency (fraction of incoming soot deposited on to the wall) for different temperature gradient and channel heights. In this case, the inlet velocity profile was uniform with a magnitude of 4 m/s. CFD simulations captured the deposition efficiency well at $h = 0.9$ mm and $\Delta T = 110$ K and $h = 0.45$ mm and $\Delta T = 105$ K. However, for the case of $h = 0.45$ mm and $\Delta T = 70$ K, the CFD results predict very high deposition efficiencies of close to 100%, whereas the experimental data

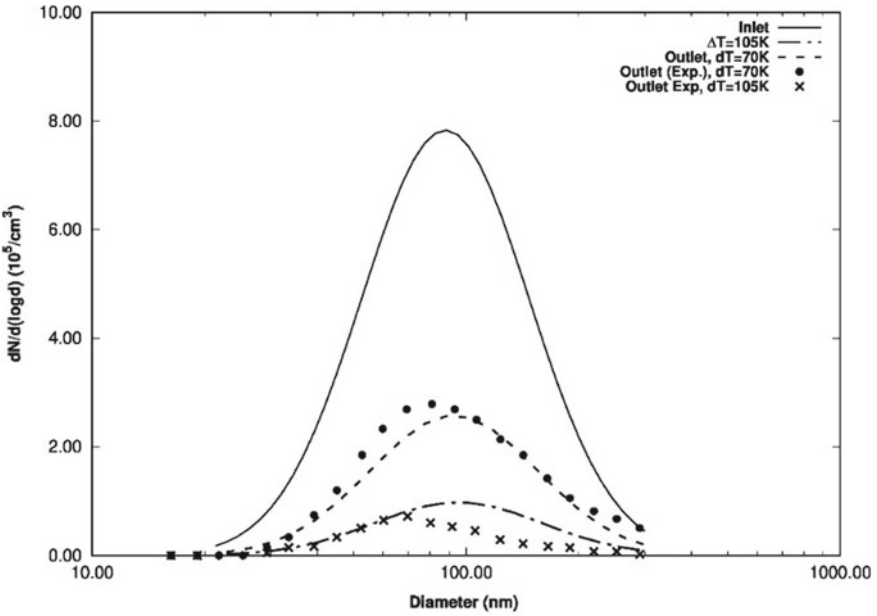

Fig. 7 Comparison of CFD and experimental soot size distribution at outlet for d$T = 70$ K and d$T = 105$ K

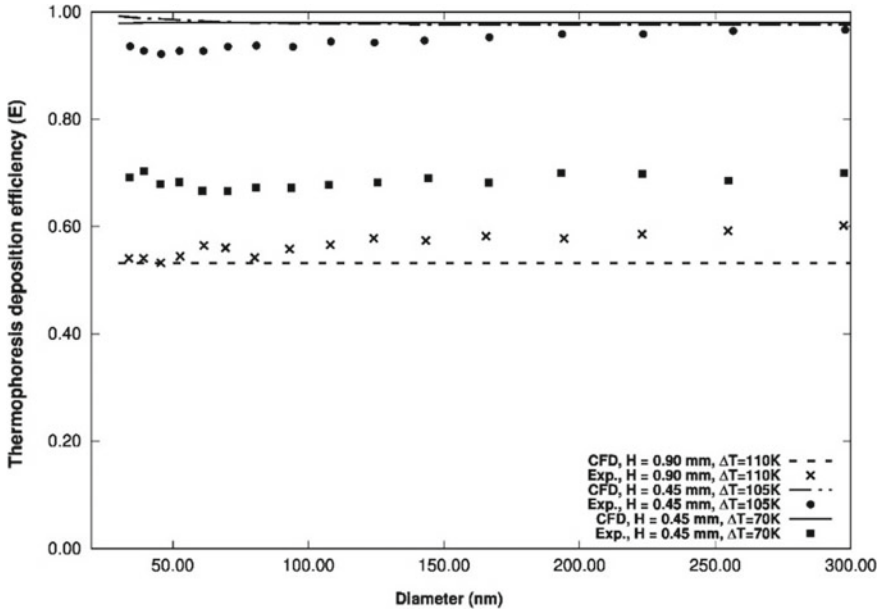

Fig. 8 Comparison of CFD and experimental deposition efficiencies at different thermal gradients

reported in Messerer et al. [21] show deposition efficiencies of around 70% over the range of particle sizes considered.

Figure 9 shows the average deposition efficiencies (over the range of sizes 34–300 nm) for different values of temperature gradient between the plates, at different flow speeds. It can be seen from the experimental data and the theoretical curve in Fig. 8 that for $h = 0.45$ mm and $\Delta T = 70$ K at flow speed of 4 m/s, the deposition efficiencies will be close to 100%. Therefore, the CFD prediction for $h = 0.45$ mm and $\Delta T = 70$ K in Fig. 8 matches the theoretical curve. The discrepancy may be explained if the experimental curve in Fig. 8 for $h = 0.45$ mm and $\Delta T = 70$ K was for inlet velocity 6 or 8 m/s, and not for 4 m/s as reported in Messerer et al. [21].

Figure 10 shows the contours of particle concentration for different sizes. It is clearly seen that the lowest size particles are deposited in a greater fraction due to higher thermophoretic force.

4 Conclusions

A computational model was developed for modeling particle transport and dynamics, incorporating models for coagulation and various deposition mechanisms such as gravitational settling, thermophoresis. The models were validated against analytical solutions.

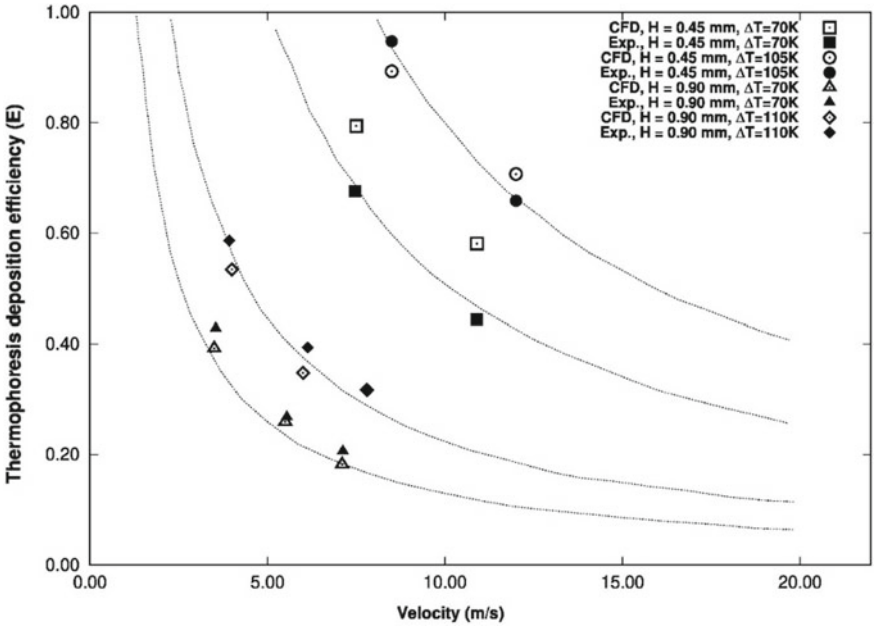

Fig. 9 Comparison of average deposition efficiencies over all sizes for inflow velocities at different values of temperature gradients

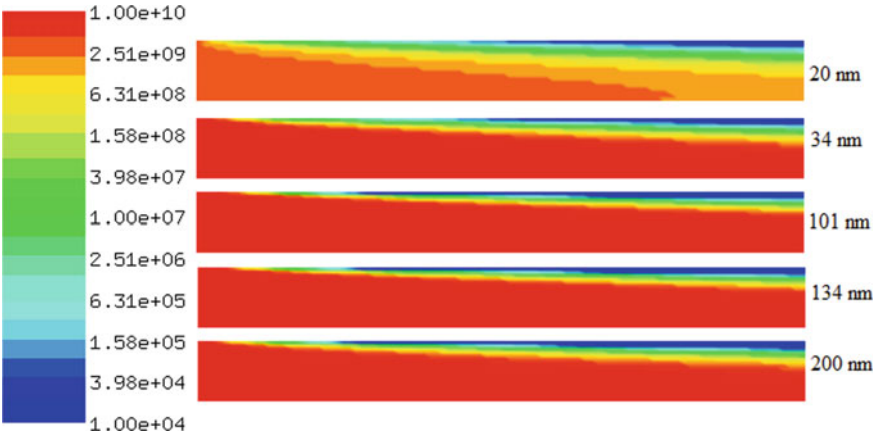

Fig. 10 Contours of soot particle concentration in plate precipitator for various particle sizes

The model was then used to study soot transport and deposition, a problem which has direct relevance to removing soot from vehicle exhaust systems and enabling vehicles to meet emission norms of 2020 and beyond.

CFD results were compared to experimental measurements of soot size distribution and deposition efficiency in a plate precipitator setup.

1. The ANSWER CFD code was able to capture very well the deposition efficiencies for sodium chloride and sodium fluorescein particles under conditions reported in [39]. There is some difference between the CFD and experimental results of sodium fluorescein particles at low particle sizes.
2. The ANSWER CFD model applied to the problem of soot deposition by thermophoresis in a plate precipitator [21] under conditions relevant to diesel engine exhaust systems. The ANSWER model was able to capture the outlet size distribution of soot particles in a plate precipitator fairly well at low- and high-temperature gradients. There is a shift in the peak of the distribution in the CFD results, which is not seen in the experimental data.
3. The ANSWER CFD model was able to match well the deposition efficiencies reported in [21] for sizes ranging from 34 to 300 nm for different temperature gradient conditions.
4. There is a discrepancy in the CFD and experimental results for plate gap of 0.45 mm and $\Delta T = 70$ K at 4 m/s inlet flow velocity. Considering other data reported in Messerer et al. [21] and the theoretical curve of deposition efficiencies, the discrepancy can be explained if the experimental data reported in Messerer et al. [21] was for inflow velocity of 6 or 8 m/s and not 4 m/s.

References

1. ACRi (2016) ANSWER® and CFDStudio® "Keyword Commands", Version 6.43.0
2. Akridis P, Rigopoulos S (2017) Modelling of soot formation in laminar diffusion flames using a comprehensive CFD-PBE model with detailed gas-phase chemistry. Combust Theor Model 21(1):35–48
3. Bensaid S, Marchisio DL, Fino D (2010) Numerical simulation of soot filtration and combustion within diesel particulate filters. Chem Eng Sci 65(1):357–363
4. Botero ML, Eaves N, Dreyer JA, Sheng Y, Akroyd J, Yang W, Kraft M (2018) Experimental and numerical study of the evolution of soot primary particles in a diffusion flame. Proc Combust Inst 37:2047–2055
5. Chong ST, Raman V, Mueller ME, Selvaraj P, Im HG (2018) Effect of soot model, moment method, and chemical kinetics on soot formation in a model aircraft combustor. Proc Combust Inst 37:1065–1074
6. Commodo M, De Falco G, Minutolo P, D'Anna A (2018) Structure and size of soot nanoparticles in laminar premixed flames at different equivalence ratios. Fuel 216:456–462
7. Cunningham E (1910) On the velocity of steady fall of spherical particles through fluid medium. Proc R Soc Lond Ser A Containing Pap Math Phys Charact 83(563):357–365
8. Davies CN (ed) (1966) Aerosol science, vol 1102. Academic Press, London
9. Derjaguin BV, Yalamov Y (1965) Theory of thermophoresis of large aerosol particles. J Colloid Sci 20(6):555–570
10. Derjaguin BV, Yalamov Y (1966) Authors' reply to Brock's discussion remarks on the theory of thermophoresis of large aerosol particles (1a). J Colloid Interface Sci 21:256–258
11. Franzelli B, Vié A, Darabiha N (2018) A three-equation model for the prediction of soot emissions in LES of gas turbines. Proc Combust Inst 37:5411–5419

12. Friedlander SK (2000) Smoke, dust, and haze: fundamentals of aerosol dynamics, 2nd edn. Oxford University Press, New York
13. Fuchs NA (1964) The mechanics of aerosols 1964. Pagamon, New York
14. Guha A (2008) Transport and deposition of particles in turbulent and laminar flow. Annu Rev Fluid Mech 40:311–341
15. Harris SJ, Maricq MM (2001) Signature size distributions for diesel and gasoline engine exhaust particulate matter. J Aerosol Sci 32(6):749–764
16. Ismail BIA (2004) The heat transfer and the soot deposition characteristics in diesel engine exhaust gas recirculation system cooling devices. Doctoral dissertation
17. Jacobson MZ (2005) Fundamentals of atmospheric modeling. Cambridge University Press
18. Lee KW, Chen J, Gieseke JA (1984) Log-normally preserving size distribution for Brownian coagulation in the free-molecule regime. Aerosol Sci Technol 3(1):53–62
19. Maricq MM, Xu N (2004) The effective density and fractal dimension of soot particles from premixed flames and motor vehicle exhaust. J Aerosol Sci 35(10):1251–1274
20. Maricq MM, Chase RE, Podsiadlik DH, Vogt R (1999) Vehicle exhaust particle size distributions: a comparison of tailpipe and dilution tunnel measurements (No. 1999-01-1461). SAE Technical Paper
21. Messerer A, Niessner R, Pöschl U (2003) Thermophoretic deposition of soot aerosol particles under experimental conditions relevant for modern diesel engine exhaust gas systems. J Aerosol Sci 34(8):1009–1021
22. Di Natale F, La Motta F, Carotenuto C, Tammaro M, Lancia A (2018) Condensational growth assisted Venturi scrubber for soot particles emissions control. Fuel Process Technol 175:76–89
23. Ni P, Bai L, Wang X, Li R (2018) Characteristics of evolution of in-cylinder soot particle size and number density in a diesel engine. Fuel 228:215–225
24. Ong JC (2017) Development of Lagrangian soot tracking method for the study of soot morphology in diesel spray combustion. Doctoral dissertation, University of Nottingham
25. Orihuela MP, Gómez-Martín A, Miceli P, Becerra JA, Chacartegui R, Fino D (2018) Experimental measurement of the filtration efficiency and pressure drop of wall-flow diesel particulate filters (DPF) made of biomorphic Silicon Carbide using laboratory generated particles. Appl Therm Eng 131:41–53
26. Otto E, Fissan H, Park SH, Lee KW (1999) The log-normal size distribution theory of Brownian aerosol coagulation for the entire particle size range: part II—analytical solution using Dahneke's coagulation kernel. J Aerosol Sci 30(1):17–34
27. Overholt KJ, Floyd JE, Ezekoye OA (2016) Computational modeling and validation of aerosol deposition in ventilation ducts. Fire Technol 52(1):149–166
28. Park K, Cao F, Kittelson DB, McMurry PH (2003) Relationship between particle mass and mobility for diesel exhaust particles. Environ Sci Technol 37(3):577–583
29. Patankar S (1980) Numerical heat transfer and fluid flow. CRC Press
30. Prakash A, Bapat AP, Zachariah MR (2003) A simple numerical algorithm and software for solution of nucleation, surface growth, and coagulation problems. Aerosol Sci Technol 37(11):892–898
31. Rajagopal PS, Joshi M, Shinde J, Anand S, Runchal AK, Sapra BK, Mayya YS, Rao MM (2018) Numerical modeling of aerosol transport and dynamics. In: Energy for propulsion. Springer, Singapore, pp 345–364
32. Rodrigues P, Franzelli B, Vicquelin R, Gicquel O, Darabiha N (2018) Coupling an LES approach and a soot sectional model for the study of sooting turbulent non-premixed flames. Combust Flame 190:477–499
33. Runchal AK (1987) CONDIF: a modified central-difference scheme for convective flows. Int J Numer Meth Eng 24(8):1593–1608
34. Salenbauch S, Sirignano M, Marchisio DL, Pollack M, D'Anna A, Hasse C (2017) Detailed particle nucleation modeling in a sooting ethylene flame using a Conditional Quadrature Method of Moments (CQMOM). Proc Combust Inst 36(1):771–779
35. Salenbauch S, Sirignano M, Pollack M, D'Anna A, Hasse C (2018) Detailed modeling of soot particle formation and comparison to optical diagnostics and size distribution measurements in premixed flames using a method of moments. Fuel 222:287–293

36. Schiener MA, Lindstedt RP (2018) Joint-scalar transported PDF modelling of soot in a turbulent non-premixed natural gas flame. Combust Theory Model 1–42
37. Shi JP, Harrison RM (2001) Study of a water-cooled fluidized bed for diesel particle agglomeration. Powder Technol 115(2):146–156
38. Talbot LRKRWDR, Cheng RK, Schefer RW, Willis DR (1980) Thermophoresis of particles in a heated boundary layer. J Fluid Mech 101(4):737–758
39. Tsai CJ, Lu HC (1995) Design and evaluation of a plate-to-plate thermophoretic precipitator. Aerosol Sci Technol 22(2):172–180
40. Versteeg HK, Malalasekera W (2007) An introduction to computational fluid dynamics: the finite volume method. Pearson Education
41. Williams MMR (1990) Nuclear aerosol behavior during reactor accidents. Prog Nucl Energy 23(2):101–108
42. Yang S, Mueller ME (2018) A multi-moment sectional method (MMSM) for tracking the soot number density function. Proc Combust Inst 37:1041–1048

Polydisperse Spray Modeling Using Eulerian Method

Sourav Sarkar, Joydeep Munshi, Achintya Mukhopadhyay, and Swarnendu Sen

Nomenclature

B_M	Splading mass transfer number
C_D	Coefficient of drag
c_{pg}	Specific heat of gas
D	Diameter of droplet
$D_{i,m}$	Mass diffusivity of the ith species in gas phase
D_P	Diameter of the pth size class
h_d^p	Enthalpy of the pth size class
K	Wave number
K_e	Evaporation constant
k_g	Thermal conductivity of gas phase
L	Axial length of channel
L_v	Latent heat of vaporization
$m^{(p)}$	Concentration of the pth size class
$\left[\dot{m}_p\right]$	Mass transfer rate of a droplet
n	Number density of droplets

S. Sarkar · A. Mukhopadhyay · S. Sen (✉)
Department of Mechanical Engineering, Jadavpur University, Kolkata 700032, India
e-mail: sen.swarnendu@gmail.com

S. Sarkar
e-mail: souravsarkar.iitm@gmail.com

A. Mukhopadhyay
e-mail: achintya.mukho@gmail.com

J. Munshi
Department of Mechanical Engineering and Mechanics, Lehigh University, 19 Memorial Drive, West Bethlehem, USA
e-mail: jom317@lehigh.edu

© Springer Nature Singapore Pte Ltd. 2021

A. De et al. (eds.), *Sustainable Development for Energy, Power, and Propulsion*, Green Energy and Technology,
https://doi.org/10.1007/978-981-15-5667-8_19

S^m	Mass source to continuous phase
S^{mom}	Momentum source to continuous phase
S^{enth}	Enthalpy source to continuous phase
Sc	Schmidt number
Sh_C	Corrected Sherwood number
T_g	Gas temperature
T_l	Liquid phase temperature
t	Time
u_d^p	Velocity of the pth size class
u_g	Gas phase velocity
x	Axial distance along channel
Y_i	Mass fraction of the ith species
ρ_l	Density of liquid phase
ρ_g	Density of gas phase

1 Introduction

Modeling of polydisperse evaporating spray convected by a gaseous phase is a point of interest in different engineering fields including chemical, environmental and biomedical engineering. The liquid jet or spray injected into a cross-flowing gas stream has found a wide application in different fields including propulsive systems, heat exchangers, agricultural sprayer. The crossflow situation is often encountered in agricultural field where chemicals are applied to the crops by flat-fan nozzles mounted on boom sprayers [1, 2]. Liquid fuel is injected as spray into a gaseous crossflow in the afterburners of air-breathing engines like gas turbines, and ramjet and scramjet combustors [3, 4]. Study of fuel spray in crossflow is significant because it determines the performance of whole device—like combustion efficiency, overall power and pollutant formation. A lot of analytical and experimental works [5–10] have been carried out on the jets in crossflow to investigate different associated phenomena like liquid breakup, flow field characteristics, droplet movement and two-phase interaction.

Spray transport is strongly influenced by the kinematic and thermal conditions of the carrier phase. The condition of the gas phase directly affects the evaporation process and also the drag experienced by individual droplets. Hence, it is necessary to have a full understanding of the physics of sprays in order to accurately predict not only the distribution of the droplets and their behavior, but also the dynamics of the gas phase, that is, the characteristics of the combined two-phase flow. The interaction of droplets or particles with various flow structures has been widely studied in the literature [11, 12]. In order to handle the complexities of the physics, often LES or DNS is used to model the spray—turbulence interaction [13] Madabhushi [14] developed a model for liquid jet atomization in a subsonic crossflow for numerical simulation. Despande et al. [15] have numerically studied the hollow cone spray

exposed to a cross-flowing stream of air using Lagrangian–Eulerian approach in OpenFOAM solver. Salewski et al. [16] performed large eddy simulation (LES) for single-phase and multiphase jets in crossflow. Bai et al. [17] developed a three-dimensional model for droplet dispersion in turbulent crossflow.

These studies provide almost an accurate simulation of the complex physics involved, but they are computationally expensive. Moreover, it is also difficult to interpret the results of parametric variation in such complex modeling approaches. A rather simplified canonical geometry can be adopted for interpreting the effects of different parameters such as droplet size distribution, carrier phase velocity and ambient temperature. The process of grouping of non-evaporating particles in an oscillating gas flow field is numerically studied by Katoshevski et al. [18] based on a simple 1D model. In their study, they consider only one-way coupling between dispersed phase and the carrier gas phase. A nonzero relaxation time of particles is identified as the most important cause for grouping and trapping of particles in an oscillating gas flow field. The study of the response of particles in an oscillating flow field using a 1D modeling was further extended by Sazhin et al. [19]. They predicted the equation of motion of Stokesian particles using an analytical approach in some limiting condition. The study further considers behavior of non-Stokesian particles in an oscillating flow field by calculating the particle trajectories by numerical solution. Droplet grouping in an oscillating flow field in the presence of evaporation has been investigated by Katoshevski et al. [20]. It was found that droplet dispersion due to an oscillating flow significantly differs from non-evaporation situation. Particle clustering phenomenon due to particle—vortex interaction in a mixing layer has also been reported in the literature [21, 22].

In most of the numerical study, Eulerian and Lagrangian formulations have been used for the gas and liquid phases, respectively. However, modeling of droplets using Lagrangian approach is computationally expensive for complex configuration. An alternative approach which is known as Eulerian–Eulerian formulation is developed in recent time to reduce the computation cost. In Eulerian–Eulerian formulation, both gas phase and dispersed droplet phase are treated in an Eulerian framework. The Eulerian multi-fluid model, developed by Greenberg [23], is derived from William's kinetic equation. In this approach, the entire range of droplet size is divided into several sections or classes and each class is treated as a separate fluid [24]. Continuity, momentum and energy equations are solved for each of the classes. Moreover, these classes can exchange mass and momentum with other classes and the continuous phase as well, which is represented mathematically through corresponding source terms in their individual governing equations. Marchisio et al. [25] introduced quadrature method of moments (QMOM) for solving population balance equation for modeling of polydisperse phase. Vie et al. [26] developed a new model called coupled size-velocity moment (CSVM) model that considers size-velocity correlations by the transport of an additional size-velocity moment for each space dimension.

2 Model Description

According to multi-fluid approach, it is assumed that each droplet class possesses a unique velocity. The set of droplets in one class can be seen as a "fluid" for which conservation equations are valid. The classes exchange mass, momentum and heat. It is assumed that the profile of n in a given section is a function of the droplet diameter only.

Hence,

$$n(t, x, D) = m^{(p)}(t, x)\kappa_D^{(p)}(D) \quad \forall D \in \left[D_p, D_{p+1}\right] \tag{1}$$

where $n(t, x, D)$ is the number density of droplet of diameter D and $m^{(p)}$ is the concentration of droplets in the pth class, given by:

$$m^{(p)}(t, x) = \int_{D_p}^{D_{p+1}} \rho_l D^3 n(t, x, D) \mathrm{d}D \tag{2}$$

$\kappa_D^{(p)}$ is a size distribution function and is approximated by a piecewise constant function, given by

$$\kappa_D^{(p)} = \frac{4}{\left(D_{p+1}^4 - D_p^4\right)} \tag{3}$$

Conservation equations of pth class

$$\partial_t m^{(p)} + \partial_x \left(m^{(p)} u_d^{(p)}\right) = -\left(E_1^{(p)} + E_2^{(p)}\right) m^{(p)} + E_1^{(p+1)} m^{(p+1)} \tag{4}$$

$$\begin{aligned} \partial_t \left(m^{(p)} u_d^{(p)}\right) + \partial_x \left(m^{(p)} u_d^{(p)} u_d^{(p)}\right) = &-\left(E_1^{(p)} + E_1^{(p)}\right) m^{(p)} u_d^{(p)} \\ &+ E_1^{(p+1)} m^{(p+1)} u_d^{(p+1)} + m^{(p)} F_d^{(p)} \end{aligned} \tag{5}$$

$$\begin{aligned} \partial_t \left(m^{(p)} h_d^{(p)}\right) + \partial_x \left(m^{(p)} u_d^{(p)} h_d^{(p)}\right) = &-\left(E_1^{(p)} + E_1^{(p)}\right) m^{(p)} h_d^{(p)} \\ &+ E_1^{(p+1)} m^{(p+1)} h_d^{(p+1)} + m^{(p)} Q_d^{(p)} \end{aligned} \tag{6}$$

where the averaged velocity $\left(u_d^p\right)$ and enthalpy $\left(h_d^p\right)$ in the pth class are defined as:

$$u_d^p(t, x) = \frac{1}{m^{(p)}} \int_{D_p}^{D_{p+1}} u_d(t, x, D) n \, D^3 \, \mathrm{d}D \tag{7}$$

$$h_d^p(t,x) = \frac{1}{m^{(p)}} \int_{D_p}^{D_{p+1}} h_d(t,x,D) n\, D^3 \,\mathrm{d}D \tag{8}$$

External Forces and Heat Exchange Terms
The external forces $\left(F_d^p\right)$ and heat exchange $\left(Q_d^p\right)$ terms are given by:

$$F_d^p(t,x) = \frac{1}{m^{(p)}} \int_{D_p}^{D_{p+1}} \rho_l F_d(t,x,S) n\, D^3 \,\mathrm{d}D \tag{9}$$

$$Q_d^p(t,x) = \frac{1}{m^{(p)}} \int_{D_p}^{D_{p+1}} \rho_l E_d(t,x,S) n\, D^3 \,\mathrm{d}D \tag{10}$$

Evaporation Terms
Regarding the evaporation term, an integration by part is conducted to separate the exchange terms between successive classes, given by:

$$E_1^{(p)} = \frac{2\, D_p^2}{\left(D_{p+1}^4 - D_p^4\right)} K_e \tag{11}$$

$$E_2^{(p)} = \frac{3\left(D_{p+1}^2 - D_p^2\right)}{\left(D_{p+1}^4 - D_p^4\right)} K_e \tag{12}$$

where $E_1^{(p)}$ and $E_2^{(p)}$ are interpreted as the exchange terms between successive class and the exchange terms with the gaseous phase. K_e is the evaporation constant which has been described in Evaporation Modeling section.

The corresponding source terms in the gas phase equations are

$$S^m = \sum_{i=1}^{N} -E_2^{(p)} m^{(p)} \tag{13}$$

$$S^{\mathrm{mom}} = \sum_{i=1}^{N} -E_2^{(p)} m^{(p)} u_d^{(p)} + \sum_{i=1}^{N} m^{(p)} F^{(p)} \tag{14}$$

$$S^{\mathrm{enth}} = \sum_{i=1}^{N} -E_2^{(p)} m^{(p)} h_d^{(p)} + \sum_{i=1}^{N} m^{(p)} E^{(p)} \tag{15}$$

where S^m, S^{mom} and S^{enth} are mass, momentum and enthalpy exchange term to the gaseous phase, respectively.

Often in studies related to spray behavior, a two-way coupling between the dispersed phase and the carrier gas phase is avoided, the assumption being valid for a low volume fraction of the dispersed phase. Moreover, solving governing equations for both the dispersed phase and the carrier gas phase is also computationally expensive. The computation of water vapor mass fraction is important in the present case as it strongly influences the evaporation process. In the present work, only continuous phase species transport is solved with the appropriate source terms.

$$\rho_g \partial_t(Y_i) + \rho_g u_g \partial_x(Y_i) = \rho_g D \partial_{xx} Y_i + S^m \tag{16}$$

Droplet Model Spray Equation Closure

The terms in the spray governing equations need proper closure in order to capture physical phenomena like drag, heat transfer and evaporation. The classical models used for closure are based on the isolated droplet assumption. The droplet models used in the present study are provided herewith.

Drag Force Modeling

The force experienced by the droplets per unit mass can contain different terms which will consider different effects such as gravity and buoyancy effects, drag force, virtual mass effect, Basset force and lift force. In the present study, only drag force is considered as ρ_g/ρ_l is of the order of 10^{-2} to 10^{-3}. Furthermore to simplify the problem gravity is neglected. The general expression of drag force (F_d) is given as

$$F_d = \frac{1}{2}\rho_g C_D\left(\pi D^2\right)\left(u_g - u\right)\left|u_g - u\right| \tag{17}$$

where C_D is the drag coefficient. In the present case, the droplets are considered as spherical and a Reynolds number defined based on the droplet diameter and the relative speed between the gas and the liquid phase is used to predict the value of C_D.

$$\text{Re}_p = \frac{\rho_g D}{\mu_g}\left|u_g - u\right| \tag{18}$$

The flow over a spherical particle can be classified into two regimes. The first regime is called the Stokes flow regime where C_D varies inversely with Reynolds number. The drag coefficient within the Stokes regime, for low relative velocity ($\text{Re}_p < 1$) is given by the Stokes law

$$C_D = \frac{24}{\text{Re}_p}, \quad \text{Re}_p < 1. \tag{19}$$

The variation of drag coefficient for non-Stokesian flow (which is the second classification) is modeled as:

$$C_D = \frac{24}{\mathrm{Re}_p}\left(1 + \frac{\mathrm{Re}_p^{2/3}}{6}\right), \quad \mathrm{Re}_p < 1000 \tag{20}$$

Evaporation Modeling

The size evolution rate of the droplets is one of the important closure relations to capture the evaporation process. The evaporation constant is defined as the rate of change of surface area of the droplet and is expressed as:

$$K_e = -d_t\left(\pi D^2\right) \tag{21}$$

The mass transfer rate from a droplet can be calculated using the following relation

$$\left[\dot{m}_p\right] = -d_t\left(\pi \frac{\rho_l D^3}{6}\right) = \frac{1}{4}\rho_l D K_e \tag{22}$$

where m_p is the mass of the droplet.

The mass transfer from a single droplet is modeled using the following expression

$$\left[\dot{m}_p\right] = \pi D \rho_g D_{i,m} \mathrm{Sh}_C \tag{23}$$

$D_{i,m}$ is the diffusion coefficient of vapor with the bulk. With unity Lewis number assumption, it can be modified as

$$\left[\dot{m}_p\right] = \pi D \frac{k_g}{c_{pg}} \mathrm{Sh}_C \tag{24}$$

where Sh_C is corrected Sherwood number. In quiescent ambient condition, Sherwood number is equal to 2. Sherwood number is modified in a convective situation by Spalding mass transfer number (B_M). The following relationship is adopted for calculating Sherwood number in convective situation from the work of Ranz-Marshall [27], Miller et al. [28] and Sazhin et al. [29].

$$\mathrm{Sh}_C = 2\left(1 + 0.3\,\mathrm{Sc}^{\frac{1}{3}}\right)\ln(1 + B_M) \tag{25}$$

where

$$B_M = \frac{Y_{i,S} - Y_{i,\infty}}{\left(1 - Y_{i,S}\right)} \tag{26}$$

with $Y_{i,S}$ being the vapor mass fraction at the surface of droplet and $Y_{i,\infty}$ is the vapor mass fraction in the bulk gas. The mass fraction of vapor at the droplet surface is

evaluated by assuming the partial pressure of vapor at the interface to be equal to the saturated vapor pressure p_{sat} at droplet temperature.

Hence, final expression for mass transfer used in the present study can be expressed as:

$$\left[\dot{m}_p\right] = 2\pi D \frac{k_g}{c_{pg}} \ln(1 + B_M)\left(1 + 0.3\,\mathrm{Re}^{\frac{1}{2}}\mathrm{Sc}^{\frac{1}{3}}\right) \tag{27}$$

Heat Transfer Modeling

Heat transferred from the gas to the liquid droplets consists of two mechanisms, one the sensible heating of the liquid core while other being the latent heat for vaporization of the droplets.

$$\begin{aligned} Q_g &= Q_{\text{evap}} + Q_{\text{sens}} \\ Q_{\text{sens}} &= Q_g - Q_{\text{evap}} = \pi D k_g \left[\mathrm{Nu}_C\left(T_g - T_l\right) - \mathrm{Sh}_C \frac{L_v}{C_{pg}}\right] \end{aligned} \tag{28}$$

In quiescent ambient condition, the value of Nusselt number is equal to 2. In a convective situation, Nu_c can be modified by the Spalding mass transfer in the following way [29].

$$\mathrm{Nu}_C = 2\left(1 + 0.3\,\mathrm{Re}^{\frac{1}{2}}\,\mathrm{Pr}^{\frac{1}{3}}\right)\ln(1 + B_M) \tag{29}$$

So, the final expression used in the present study for droplet heat transfer closure is given as (with the assumption of unity Lewis number):

$$\begin{aligned} Q_{\text{sens}} &= Q_g - Q_{\text{evap}} \\ &= 2\pi k_g D \ln(1 + B_M)\left[\frac{\left(T_g - T_l\right)}{B_M} - \frac{L_v}{C_{pg}}\right]\left(1 + 0.3\,\mathrm{Re}^{\frac{1}{2}}\,\mathrm{Pr}^{\frac{1}{3}}\right) \end{aligned} \tag{30}$$

3 One-Dimensional Transport of Evaporating Polydisperse Sprays

Firstly, one-dimensional transport of evaporating polydisperse water droplets has been studied. Proper heat and mass transfer sub-models are considered for the heating and evaporation of droplets in a convective situation. The effect of injection velocity on the spray transport process is numerically studied. The effect of the evaporation constant on droplet number density is also investigated. Sprays often flow through

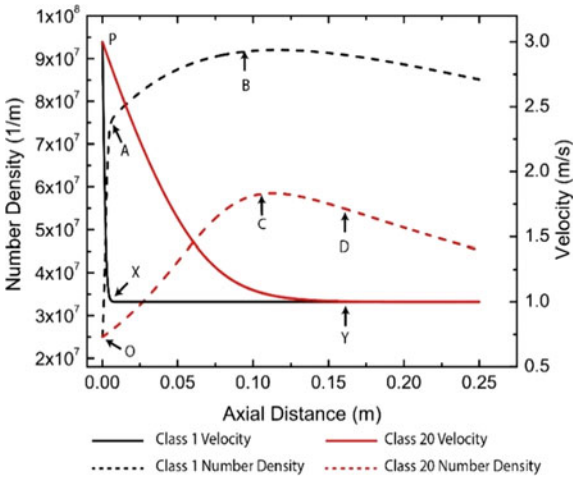

Fig. 1 Variation of number density and velocity along the channel length

a varying temperature field which strongly influences evaporation process. The one-dimensional transport of polydisperse water spray in a linearly varying temperature field is studied. The response of droplets' different size classes in an oscillating flow field is investigated.

A 1D channel of axial length 0.25 m is considered. A grid- and time step-independent study is performed for selecting the appropriate grid size and time step size which are 10^{-4} m and 10^{-6} s, respectively. A class independence study is also required in the present formulation as the size is chosen as an internal variable. The droplet distribution considered in the present study has minimum and maximum diameter of 15 μm and 115 μm, respectively. A total of 20 equally spaced size classes of droplets was found to be appropriate for class-independent solution. A top hat distribution of number density $2.5 \times 10^7 \mathrm{m}^{-1}$ is assumed at the inlet for each size class of the droplets. Figure 1 represents the number density and velocity variation of largest droplet class (class 20, which has droplet diameters in the range of $110 - 115\,\mu\mathrm{m}$) and smallest droplet class (class 1, which has droplet diameters in the range of $15 - 20\,\mu\mathrm{m}$) for spray injection velocity 3 m/s, carrier phase velocity 1 m/s and inlet temperature 303 K. The smallest class responds rapidly and attains the carrier gas velocity at point *X*. Due to higher inertia, the largest size class of the droplets attains the carrier phase velocity at a much later distance along the channel length (point *Y*). The number density for the smallest class increases sharply from *O* up to the point *A*. The main reason for number density increment between *O* and *A* is the deceleration of the droplets caused by the drag due to velocity difference with carrier phase. Evaporation of the droplets from immediately higher size class (class 2) to the smallest class is also an additional mechanism of this increment. An illustration of these mechanisms is provided in Fig. 2. After reaching the point *A*, the number density slowly increases and reaches a maximum at *B*. Evaporation of the droplets from the next higher size class to the lower class is only responsible

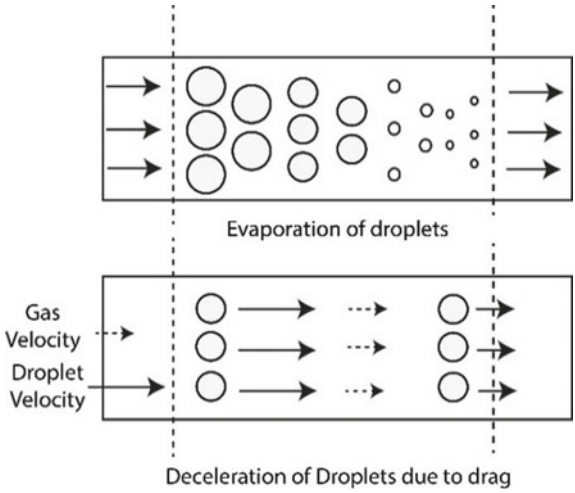

Fig. 2 Illustration of droplet transport mechanism

for this number density increment as the relative velocity between the lowest class and the carrier phase becomes negligible. Further downstream, the number density starts to decrease as evaporation from the lowest class to the gaseous phase becomes significant than the evaporation of the droplets from next higher size class. In the largest class, the number density increases gradually until it reaches a maximum at point *C*. The drag force is responsible for this increment as evaporation from a higher size class is absent for the largest class. The number density starts to decrease and reaches the point *D* as the evaporation from largest class to previous class (class 19) and to the carrier phase dominates than the deceleration due to drag. After reaching *D*, the evaporation from the largest class to the previous class (class 19) and to the carrier phase is only mechanism that causes decrement of number density.

Figures 3, 4 and 5 represent the variation of number density, velocity and temperature along the channel length for classes 1, 5, 10, 15 and 20. These results will give a better understanding of the transport mechanism of intermediate size classes. After reaching the maximum, the number density decrement rate is the highest for class 5 and the lowest for class 15 among classes 5, 10 and 15 (Fig. 3). It can be deduced that the evaporation to the continuous phase and to the successive class dominates for the lower droplet size classes than the evaporation from a higher class to that class. Similarly, evaporation from a comparatively higher class is significant for higher classes and comparable to the next lower size class and the continuous phase.

It is clearly evident from Fig. 4 that different size classes attain the gas velocity at different lengths along the channel due to inertia. For isothermal inlet condition of the droplet and the gas phase, the droplet size class temperature will decrease due to evaporative heat loss till it attains the dew point temperature which is 291 K (Fig. 5). It is also observed that different size classes attain the dew point temperature at different axial distances due to thermal inertia.

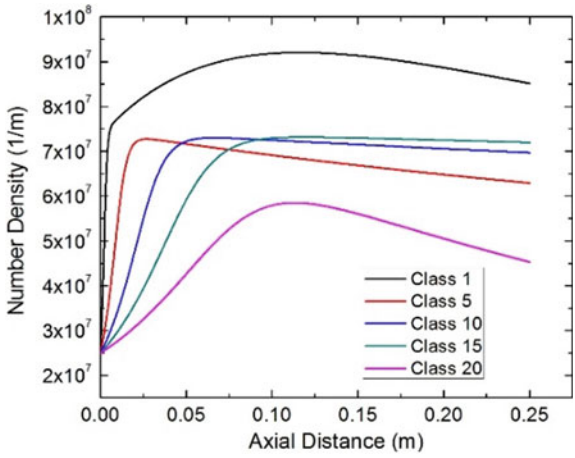

Fig. 3 Variation of number density along the channel length

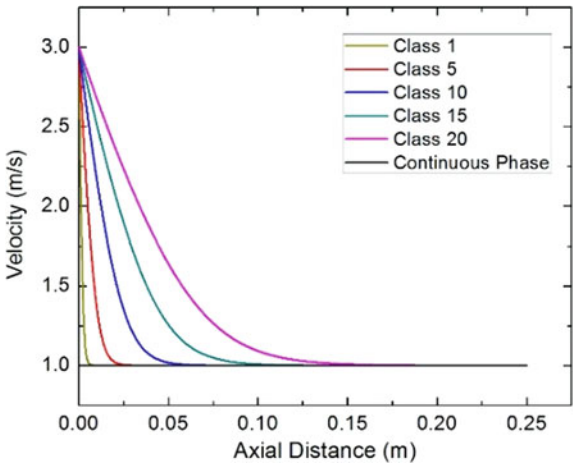

Fig. 4 Variation of velocity along the channel length

The effect of injection spray velocity on the number density and the droplet class velocity are presented in the Figs. 6 and 7 respectively for different spray injection velocities. Number density increases rapidly for higher injection velocity due to higher relative velocity with the gas phase. The number density for the largest class reaches the maximum latest along the channel for an injection velocity of 5 m/s as it is the last one to attain the carrier phase velocity.

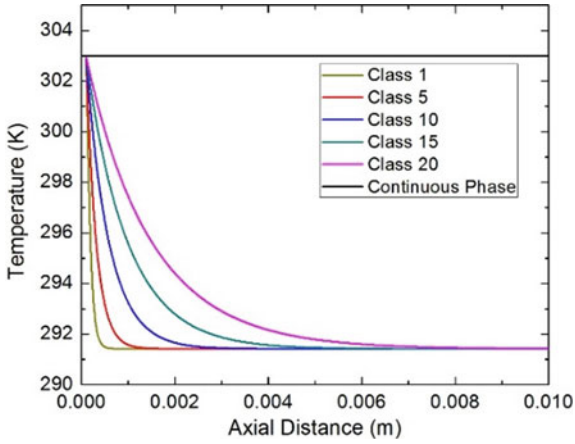

Fig. 5 Variation of temperature along the channel length

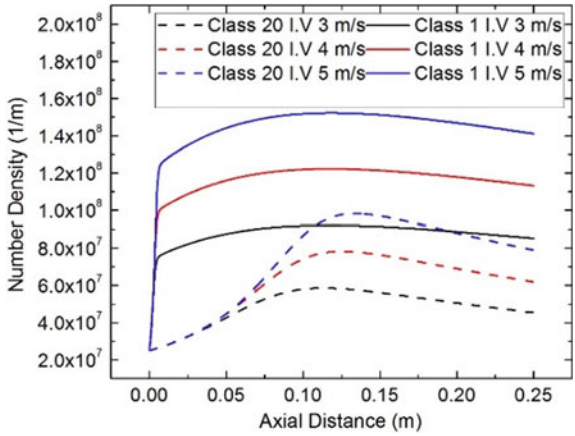

Fig. 6 Variation of number density along the channel length

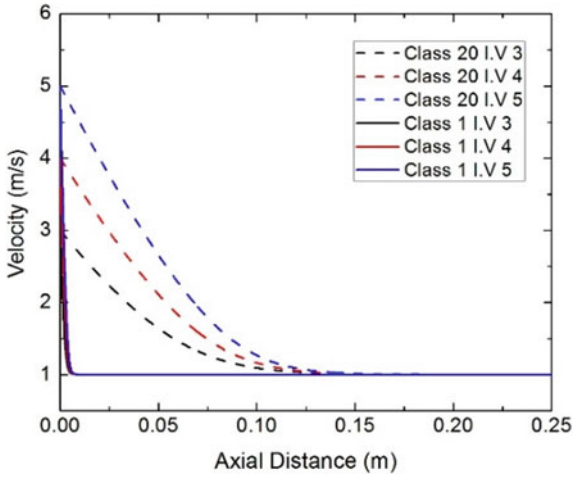

Fig. 7 Variation of velocity along the channel length

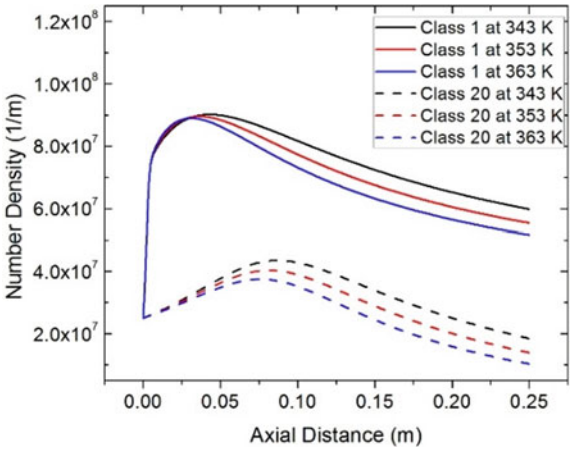

Fig. 8 Variation of number density and velocity along the channel length

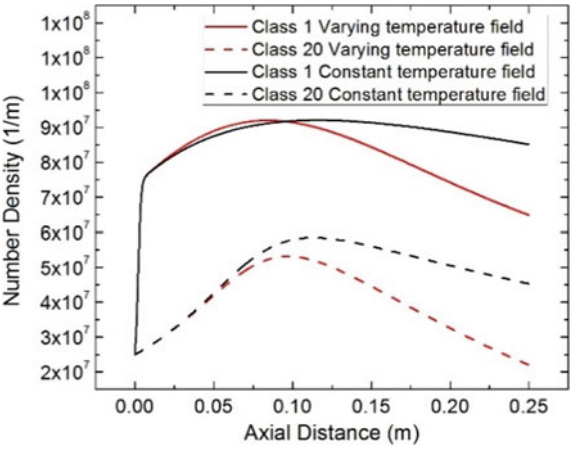

Fig. 9 Variation of number density and velocity along the channel length

The effect of carrier phase temperature is presented in Fig. 8 for different carrier phase temperatures of 343, 353 and 363 K. The carrier phase gas temperature significantly influences the evaporation constant. It is observed that the number density starts to drop earlier in higher ambient temperature due to enhanced evaporation.

The behavior of the spray is studied in a linearly varying temperature field and compared with that for an isothermal case (having temperature of 303 K) in Fig. 9. Temperature field is expressed by the function

$$T = T_a + \frac{T_b - T_a}{L} x$$

where $T_a = 303$ K, $T_b = 363$ K and $L = 0.25$ m. The rate of change of number density along the channel length is found to be higher in a varying temperature field due to enhanced evaporation.

In order to study the effect of flow field oscillations, a spatially varying velocity field is expressed by the function

$$V = V_a + V_b \sin Kx$$

where $V_a = 1$ m/s, $V_b = 0.5, K = 50,100,$ and $200\,\mathrm{m}^{-1}$ is considered. The variation of number density and droplet class velocity is presented in Figs. 10, 11, 12, 13, 14 and 15 for different wave numbers. It is observed that smallest size droplet class

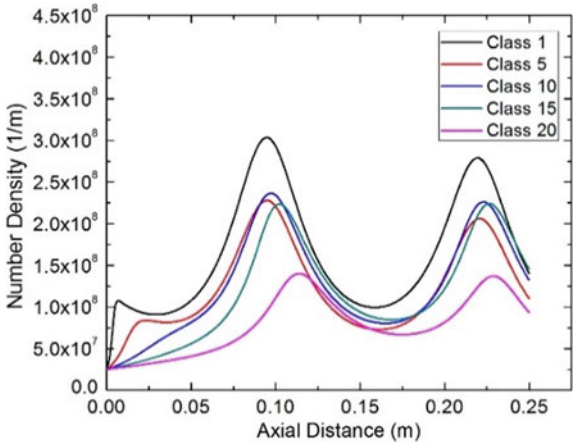

Fig. 10 Variation of number density and velocity along the channel length

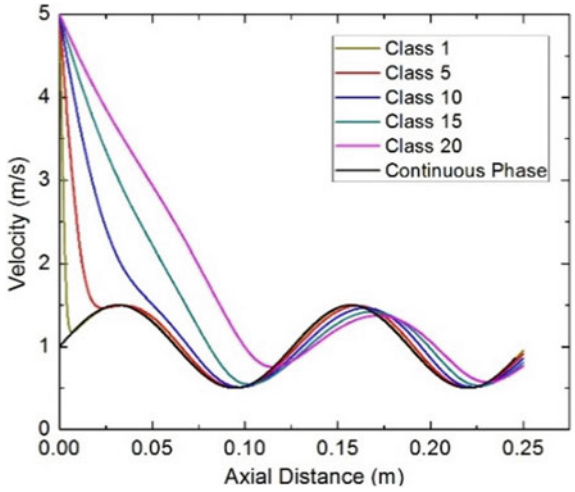

Fig. 11 Variation of velocity along the channel length

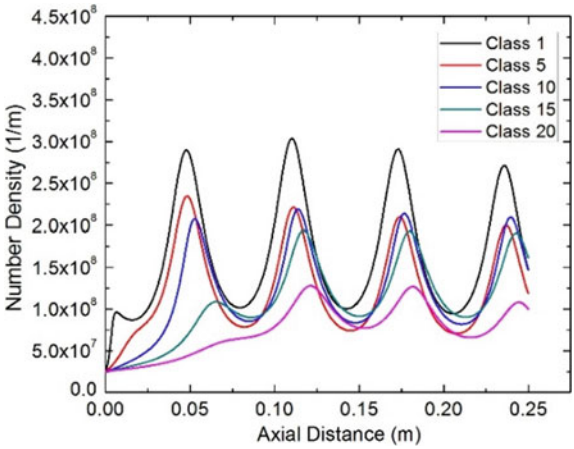

Fig. 12 Variation of number density along the channel length

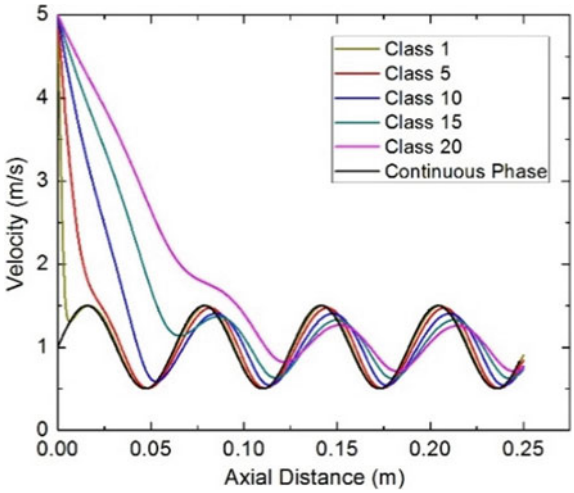

Fig. 13 Variation of velocity along the channel length

synchronizes almost instantaneously with the carrier phase. A delayed response is observed for larger size class droplets. A stable grouping is observed for smaller droplet size class due to small response time. A phase lag with the carrier phase velocity is observed for larger size classes. For high wave number, it is observed that number density peak initially increases due to evaporation from comparatively larger size class and then starts to decrease due to evaporation to the carrier phase.

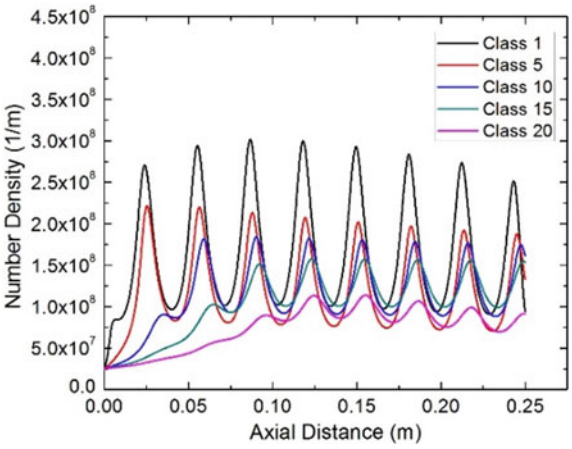

Fig. 14 Variation of number density along the channel length

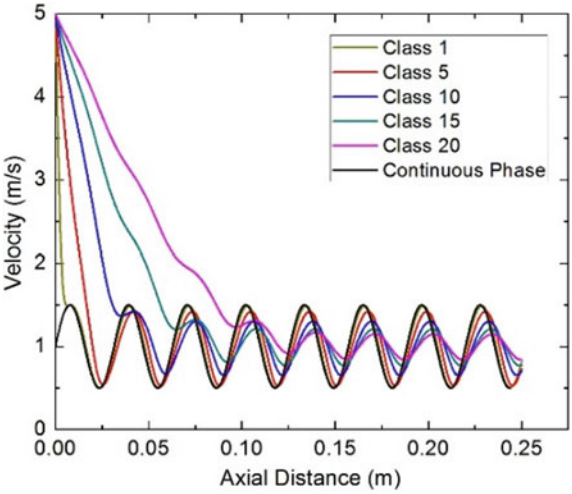

Fig. 15 Variation of velocity along the channel length

4 Two-Dimensional Transport of Evaporating Polydisperse Spray in Gaseous Crossflow

Numerical simulation of polydisperse evaporating fuel spray in a gaseous crossflow situation using an Eulerian multi-fluid method is presented in this section. The trajectories of droplets in crossflow have been validated with analytical results. The effect of evaporation constant has been studied considering different size classes. Injection velocity at spray inlet has been varied for a chosen evaporation constant in order to understand the effect of drag on accumulation and dispersion of different droplet classes.

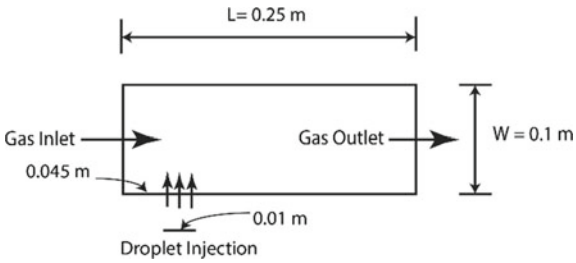

Fig. 16 Schematic of the configuration

A 0.25-m-long and 0.1-m-wide 2D channel is used in the simulation to describe the flow behavior of droplets as shown in Fig. 16. A first-order upwinding scheme has been used to discretize the governing equations. The grid size and time step chosen for simulation are 10^{-4} m and 10^{-5} s, respectively, after performing a grid-independent and time-independent study. In the present simulation, a total of 10 equal size classes of droplets are considered with a minimum diameter of 15 μm to maximum of 115 μm. Carrier gas phase velocity chosen for this problem is 0.5 m/s. Injection velocity is varied between 1 and 3 m/s.

A droplet distribution which fits with Rosin–Rammler distribution with spread parameter 3.5 and number mean diameter of 45 μm is subjected at the spray inlet. Trajectory predicted by Eulerian multi-fluid method is validated against the analytical solution as shown in Fig. 17. The analytical solution shown in Fig. 17 represents the envelope of overall droplet trajectories. The numerical solution shows that the contour of normalized droplet number density in the crossflow situation is in excellent agreement with the analytical counterpart.

Figure 18 shows normalized (with respect to the inlet value) number density contour for the lowest size class (class 1), class 5 and the highest size class (class 10).

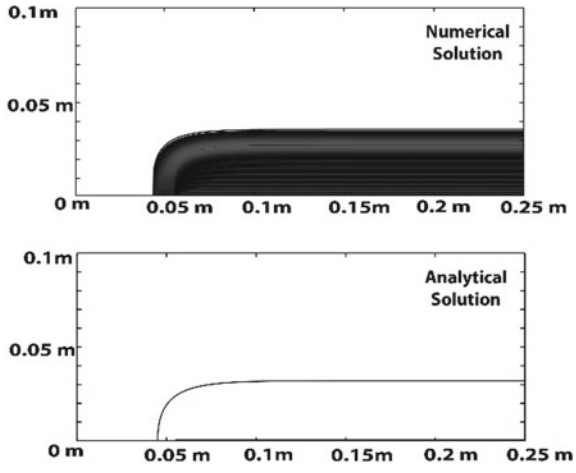

Fig. 17 Validation of droplet trajectories with analytical result

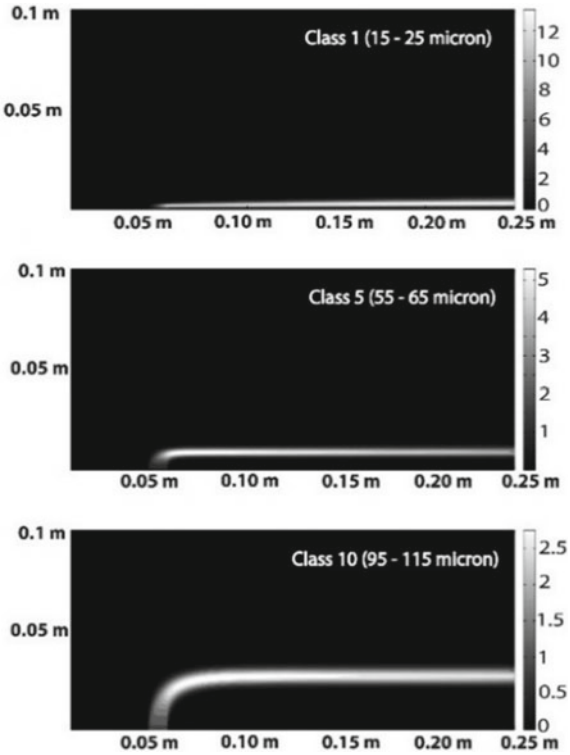

Fig. 18 Distribution of normalized number density for different classes

As expected intuitively, it can be seen the lowest size class starts following the continuous phase flow earliest because of its low inertia, whereas, due to highest inertia, the largest class penetrated to a maximum depth and then followed gas phase flow. A competition between droplet inertia and drag due to interaction between droplet and continuous phases gives rise to the different trajectories as observed. Finally, dispersion of the droplets from its mean position can be compared for different classes. From Fig. 18, it can be observed qualitatively that with increase in droplet size, the spread of the droplets across its mean position has increased, giving highest spread for the largest class (class 10).

After being validated, effect of variation of evaporation constant has been studied as shown in Fig. 19. Effect of evaporation is clearly visible for higher evaporation constant. Once the droplets balance themselves out from the competition of inertia and drag in the continuous phase flow field, evaporation effect starts dominating. Change in droplet number density due to evaporation is observed in Fig. 4. For evaporation constant 10^{-9}, Fig. 20 shows change in the droplet distribution at different locations downstream to the spray inlet. Reduction in number mean diameter at downstream locations can be observed which can be explained by the evaporation of the droplets. Although there is overall evaporation taking place, smaller size droplets, due to much higher surface area, have a higher evaporation rate. However, at the

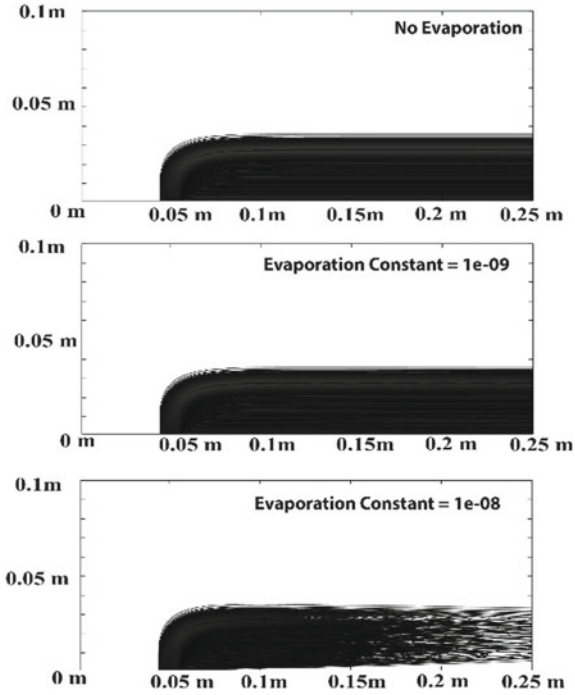

Fig. 19 Number density contour for different values of evaporation constant

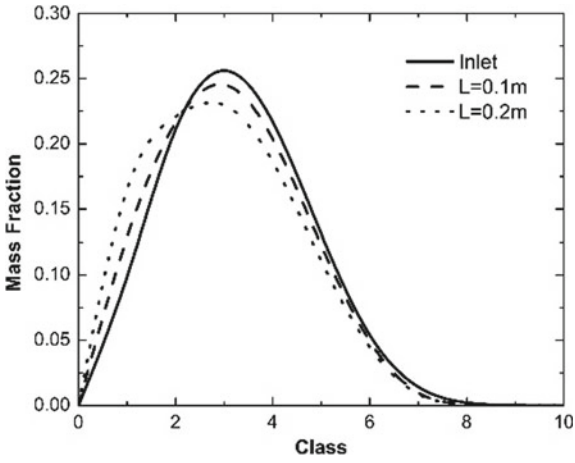

Fig. 20 Droplet distributions at different positions

same time, for a certain class, droplets are also entering from the higher size class giving rise to the number of droplets for the class. Finally, there exists an optimization between droplets evaporating from a class and droplets evaporating to the class, giving a reduction in number mean diameter of the overall distribution of the droplets.

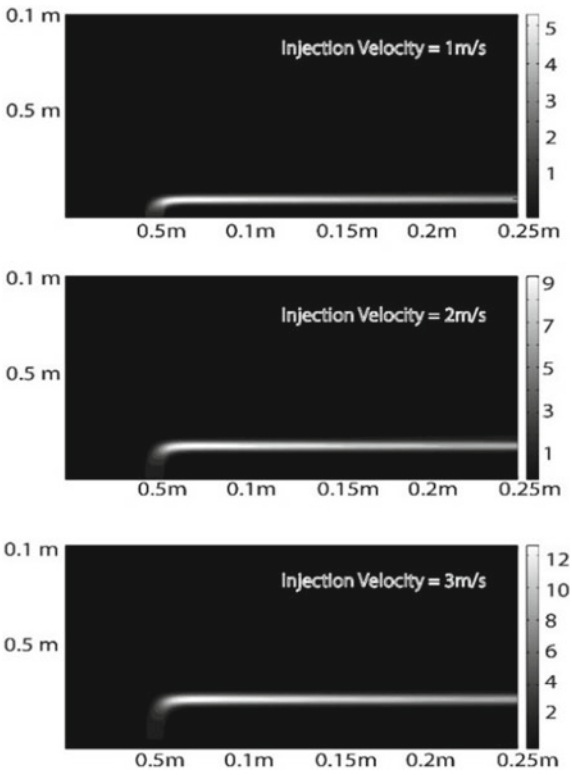

Fig. 21 Effect of injection velocity on normalized number density

Figure 21 shows a variation of injection velocity for evaporation constant 10^{-9} m^2/s. Injection velocities from nozzles in actual combustors are not always specific and can vary over a range. Thus, it is reasonable to understand the effect of injection velocity on droplet dispersion in a crossflow situation. With increase in velocity, as expected, increase in penetration length and droplet accumulation is observed. Figure 21 shows normalized number density for class 5 droplets. Increase in the droplet accumulation is significant with increase in inlet velocity. This is due to higher inertia in case of higher velocity, which leads to high accumulation of droplets.

5 Summary

The behavior of evaporating polydisperse sprays is numerically studied using an Eulerian multi-fluid approach. The classical models for drag, heat and mass transfer for a droplet are used for simulation. One-dimensional transport in a channel of length 0.25 m with 20 size classes of equal range is considered in the present study.

Four mechanisms are identified that influence the polydisperse spray transport

1. Deceleration of the droplets due to drag
2. Evaporation from a size class to the carrier gas phase
3. Evaporation from a size class to the immediately lower size class
4. Evaporation to a size class from the immediately higher size class.

Mechanism 3 is not applicable for the smallest size class, while mechanism 4 is not applicable for the largest size class. The effect of injection velocity on the number density variation is studied, and contribution of mechanism 1 is highlighted. The effect of carrier phase temperature is investigated, and it is found that the temperature field strongly influences the evaporation process. The clustering phenomenon of different size class droplets is studied in the presence of an oscillating flow field. It is found that the smaller droplets accumulate more than the larger droplets.

The behavior of evaporating polydisperse sprays in crossflow configuration is numerically studied using an Eulerian multi-fluid approach. A size-based droplet segregation is observed. It is found that droplet distribution strongly depends on evaporation constant. Injection velocity strongly influences the penetration depth of the spray regardless of the size class.

References

1. Ghosh S, Hunt JCR (1998) Spray jets in a cross flow. J Fluid Mech 365:109–136
2. Philips JC, Miller PCH (1999) Field and wind tunnel measurements of the airborne spray volume downwind of single flat-fan nozzles. J Agri Eng Res 72:161–170
3. Lefebvre AH (1989) Atomization sprays. Hemisphere
4. Karagozian AR (2010) Transverse jets and their control. Prog Ener Combust Sci 36:531–553
5. Wu PK, Kirkendall KA, Fuller RP, Nejad AS (1997) Breakup processes of liquid jets in subsonic crossflow. J Propul Power 13:64–73
6. Zhang L, Yang V (2017) Flow dynamics and mixing of a transverse jet in crossflow—part II: oscillating crossflow. ASME J Eng Gas Turbines Power 139(8):082602
7. Schetz A, Kush EA, Joshi PB (1980) Wave phenomena in liquid jet breakup in a supersonic crossflow. AIAA J 18:774–778
8. Inamura T, Nagai N (1997) Spray characteristics of liquid jet traversing subsonic airstreams. J Propul Power 13:250–256
9. Tambe S, Jeng SM, Mongia H, Hsiao G (2005) Liquid jets in subsonic crossflow. In: 43rd AIAA aerospace sciences meeting and exhibit. American Institute of Aeronautics and Astronautics
10. Sallam K, Ng C, Sankarakrishnan R, Aalburg C, Lee K (2006) Breakup of turbulent and non-turbulent liquid jets in gaseous crossflows. In: 44th AIAA aerospace sciences meeting and exhibit. American Institute of Aeronautics and Astronautics
11. Kaplanski F, Sazhin SS, Rudi Y (2005) Particle dynamics and mixing in an oscillating viscous pair. Proc Est Acad Sci 11:140–153
12. Sazhin SS, Kaplanski F, Feng G, Heikal MR, Bowen PJ (2001) A fuel spray induced vortex ring. Fuel 80:1871–1883
13. Mashayek F, Pandya RVR (2003) Analytical description of particle/droplet-laden turbulent flows. Prog Ener Combust Sci 29:329–378
14. Madabhushi RK (2003) A model for numerical simulation of breakup of a liquid jet in crossflow. Atomization Sprays 13:413–424

15. Deshpande S, Gao J, Trujillo MF (2011) Characteristics of hollow cone sprays in crossflow. Atomization Sprays 21:349–361
16. Salewski M, Stankovic D, Fuchs L (2007) A comparison of single and multiphase jets in a crossflow using large eddy simulations. J Eng Gas Turbines Power 129:61–68
17. Bai B, Sun H, Zhang H, Liu L (2011) Numerical study on turbulent mixing of spray droplets in crossflow. J Propul Power 27:132–143
18. Katoshevski D, Dodin Z, Ziskind G (2005) Aerosol clustering in oscillating flows: mathematical analysis. Atomization Sprays 15:401–412
19. Sazhin S, Shakked T, Sobolev V, Katoshevski D (2008) Particle grouping in oscillating flows. Eur J Mech B Fluids 27:131–149
20. Katoshevski D, Shakked T, Sazhin SS, Crua C, Heikal MR (2008) Grouping and trapping of evaporating droplets in an oscillating gas flow. Int J Heat Fluid Flow 29:415–426
21. Yang X, Thomas NH, Guo LJ (2000) Particle dispersion in organized vortex structures within turbulent free shear flows. Chem Eng Sci 55:1305–1324
22. Wen F, Kamalu N, Chung JN, Crowe CT, Troutt TR (1992) Particle dispersion by vortex structures in plane mixing layers. J Fluids Eng 114:657–666
23. Greenberg JB, Silverman I, Tambour Y (1993) On the origins of spray sectional conservation equations. Combust Flame 93:90–96
24. Laurent F, Massot M (2001) Multi-fluid modelling of laminar polydisperse spray flames: origin, assumptions and comparison of sectional and sampling methods. Combust Theor Model 5:537–572
25. Marchisio DL, Fox RO (2005) Solution of population balance equations using the direct quadrature method of moments. J Aerosol Sci 36:43–73
26. Vié A, Laurent F, Massot M (2013) Size-velocity correlations in hybrid high order moment/multi-fluid methods for polydisperse evaporating sprays: modeling and numerical issues. J Comput Phys 237:177–210
27. Ranz WE, Marshall WRJ (1952) Evaporation from drops, part I and part II. Chem Eng Prog 48:173–180
28. Miller RS, Harstad K, Bellan J (1998) Evaluation of equilibrium and non-equilibrium evaporation models for many-droplet gas-liquid flow simulations. Int J Multiph Flow 24:1025–1055
29. Sazhin SS (2006) Advanced models of fuel droplet heating and evaporation. Prog Ener Combust Sci 32:162–214

Sustainable Energy Technologies

Future Aviation Biofuel, Efficiency and Climate Change

G. Abdulkareem-Alsultan, N. Asikin-Mijan, and Y. H. Taufiq-Yap

1 Introduction

Concerns about the environmental effects of fossil fuel use and the depletion of oil reserves have lead to the development of renewable energy source to replace fossil fuels [1]. For the aviation sector, fuel is a major source of expenditure. The fuel used to power air transport is petroleum-based, and such fuels must meet stricter quality requirements than those used to power motor vehicles for road use. Jet fuel is designed uniquely to provide power to the gas-turbine engines, and this will be discussed as a primary subject in the present work. A report produced by the US Department of Energy's (DOE's) Bioenergy Technologies Office [2] points out that four gallons of crude oil are needed to generate just one barrel of jet fuel. As a whole, the global aviation sector uses around 1.5–1.7 billion barrels (47.25–53.55 billion gallons) of traditional jet fuel each year [3, 4]. Key issues such as the price of crude oil, national security, environmental effects and issues of sustainability mean that it is highly challenging to implement a plan for the long term and to create an effective budget for operational costs. Sustainable biofuels produced around the world are a viable alternative that can be used to address such issues. What's more, biomass-derived jet fuels (bio-jet fuels) can serve as a replacement for petroleum jet fuel. The

G. Abdulkareem-Alsultan (✉)
Department of Chemical and Environmental Engineering, Faculty of Engineering, Universiti Putra Malaysia, 43400 UPM Serdang, Selangor, Malaysia
e-mail: kreem.alsultan@yahoo.com

N. Asikin-Mijan
Department of Chemical Sciences, Faculty of Science and Technology, Universiti Kebangsaan Malaysia, 43600 UKM Bangi, Selangor Darul Ehsan, Malaysia

Y. H. Taufiq-Yap (✉)
Chancellery Office, Universiti Malaysia Sabah, 88400 Kota Kinabalu, Sabah, Malaysia
e-mail: taufiq@upm.edu.my

© Springer Nature Singapore Pte Ltd. 2021

A. De et al. (eds.), *Sustainable Development for Energy, Power, and Propulsion*, Green Energy and Technology,
https://doi.org/10.1007/978-981-15-5667-8_20

Intergovernmental Panel on Climate Change state that the annual CO_2 emissions saw a rise of 80% between 1970 and 2004, which may be explained through the speed at which CO_2 replacements are growing. When compared to the growth of the previous period from 1970 to 1994 (0.43 $GtCO_2$-eq per year) [4] and the period of 1995–2004 (0.92 $GtCO_2$-eq per year) saw a growth of almost double. The key source of CO_2 emissions is power generation and transport. In 2009, the usage of petroleum-derived jet fuel has contributed to 64% of the total anthropogenic CO_2 emissions [5]. Hence, in order to lower the harmful emission, the production of newly alternative jet fuel energy sources which is more cleaner and environmental friendly is necessary. This is aligned with the predictions by the International Energy Agency indicate that utilization of biofuels will contribute to approximately 27% of the total fuels used within the transport industry by 2050, and that they will serve to replace diesel and jet fuel [6]. The present research will thus concentrate on exploring how bio-jet fuel can be produced. In recent times, bio-jet fuel has become a topic of interest, with the International Air Transport Association (IATA) describing the strategy as having a great deal of potential to decrease the CO_2 emissions produced by the aviation industry. Furthermore, it is anticipated that bio-jet fuel will lead to partial fuel dependence throughout the aviation industry. Fossil jet fuel will be described and discussed in the subsequent section in order to go on to discuss bio-jet fuel.

1.1 Jet Fuel Specifications

To be able to provide a definition of target compositions, it is important that there are criteria that new jet fuels must meet, most of which relate to the required performance characteristics. These criteria are as follows: The fuel must have a suitable minimum energy density according to mass, must have the highest possible allowable freeze point temperature and maximum allowable deposits when subject to standard heating tests, they must possess maximum allowable viscosity, as well as highest allowable sulphur and aromatics content, they must be able to withstand the greatest allowable wear when subjected to standardized test, they must be of maximum acidity and mercaptan concentration, have the lowest possible aromatics content, must have the least electrically conductivity and the minimum allowable flash point [7]. In terms of certifying jet fuel, there are three standards that must be met: ASTM D1655 [8], International Air Transport Association Guidance Material (Kerosene Type) [8], and the United Kingdom Ministry of Defence, Defence Standard (Def Stan) 91–9. The ASTM Specification D7566 (Standard Specification for Aviation Turbine Fuel Containing Synthesized Hydrocarbons), has a specific focus on alternative types of jet fuel, and it outlines key fuel properties and requirements that must be met in order to manage the creation of a renewable energy source ensure the safety of air transport [9]. Other fuel standards may also need to be met, with Table 1 outlining the key requirements for two typical jet fuels used in both military and commercial aviation. A high flash point is crucial for jet fuel, since fire-hazard is a point of major concern.

Table 1 Summary of common documents used in the US regarding specification and recommended practices for handling jet fuel [9]

Organization	Document	Title
Jet Fuel Production Specification[a]		
ASTM	D-1655	Standard Specification for Aviation Turbine Fuels
ASTM	D-7566	Standard Specification for Aviation Turbine Fuel Containing Synthesized Hydrocarbons
UK Ministry of Defence	DEFSTAN 91-91	Turbine Fuel, Aviation Kerosine Type, Jet A1
Supply Chain Recommended Practices		
API	API 1543	Documentation, Monitoring and Laboratory Testing of Aviation Fuel During Shipment from Refinery to Airport
API	API 1540	Design, Construction, Operation and Maintenance of Aviation Fuelling Facilities (Model code of safe practice Part 7)
EI/HM 50	EI/HM	Guideline for the Cleaning of Tanks and Lines for Marine Tank Vessels Carrying Petroleum and Refined Products
A4A	ATA 103	Standards for Jet Fuel Quality Control at Airports
IATA	IATA Fuel Quality Pool	Control of Fuel Quality and Fuelling Safety Standards
JIG	JIG Sections 1–4	Guidelines for Aviation Fuel Quality Control and Operating Procedures for Joint Into-Plane Fuelling Services
API	API 1595	Design, Construction, Operation, Maintenance, and Inspection of Aviation Pre-Airfield Storage Terminals
EI	EI 1530	Quality Assurance Requirements for the Manufacture, Storage and Distribution of Aviation Fuels to Airport
ICAO	Doc 9977, AN/489	Manual on Civil Aviation Jet Fuel Supply
SAE Aerospace	SAE-AS 6401	Storage, Handling and Distribution of Jet Fuels at Airports

[a]There are other country or region-specific aviation fuel specifications, but this study focuses on ASTM and DEFSTAN 91-91 since these are the most common in the USA

The key fuel properties tend to be very alike for various standards, however, some variations can be noted. D7566, for example, is an expansion of D1655 but includes fuel specifications that must be met by the SPK blendstocks. What's more, jet fuel requires effective cold flow properties to be present, including the lowered freezing

point, since this ensures that fuel will be usable and transportable at high altitude [10].

2 Renewable Resources

When producing bio-jet fuels, renewable feedstocks are more effective source. These sources have the key benefits as follows: They are sustainable, allow for the recycling of carbon dioxide, are renewable, use eco-friendly technology and have a lesser reliance on petroleum supplying nations [11]. Non-food energy crops, waste wood, municipal and sewage wastes, forest residues, algae and halophytes tend to be preferred types of feedstocks. Below, one can see a description of some of the key features of various renewable feedstocks.

2.1 Camelina

One type of non-food energy crop is camelina, which contains a high level of oil around 30–40%. It is also a plant that can grow with less fertilizers being used [12]. There are a number of benefits to Camelina, including that is able to grow in infertile soil or marginal land [13] and will not be affected by diseases and pests [8]. It is possible to cultivate camelina in such a way that it can serve as an alternative for wheat and cereals, with little effort being needed for its growth [12]. After extraction of the oil, the remaining is suitable to feed the animals. Camelina oil is inexpensive ($0.40–$0.70/gal) and 200 gallons of it were produced in USA in 2012. It can be cultivated as a rotational crop, meaning it may be able to resolve issues pertaining to monocropping and this can aid farmers in making extra profits [14]. Without this, the continuous monocropping could lead to a decline in the yield and ruin the soil.

2.2 Jatropha

Jatropha is also a nonedible energy crop that thrives on marginal land and thus has no interference with food plants. The jatropha plant is not affected by drought or pests. In fact, it is even able to grow in unproductive soil in poor climatic settings. It also has a quick growth rate [15]. It can permanently produce high oil yields [16]. The plant is able to keep producing yield for four decades if it is provided with a small amount of moisture [15]. It is not possible to use the remaining edible parts, as they are poisonous. However, the remaining part contains high levels of N, K and P and thus could be applied as organic manure [16]. At the moment, jatropha cultivation is primarily in countries in South Africa, South East Asia and Central and South America. Jatropha seed production is largely determined by location, varieties and

management practices, with available information from plantations indicating that irrigation leads to better crop growth for this particular plant.

2.3 Algae

Algae is also a viable solution to combat the growing lack of fuel, since they are high in lipids, have a high absorption rate of carbon dioxide, require only small amounts of land and they grow very quickly [17]. A key advantage of algae is that they have no interference with crop cultivation because no land or water is needed for its cultivation, and this eliminates food-fuel competition [18]. Algae is able to generate vast quantities of lipids and carbohydrates through the use of sunlight, wastewater and carbon dioxide which means it is vital for wastewater treatment. The biomass that is still present after the algal oil has been removed can be used to feed animals, to make bioplastic. It is also possible to further process the dried biomass to produce energy. To make fuels, microalgae are commonly used, primarily due to its simple cultivation requirements and ability to be harvested throughout the year [19]. Algae, as opposed to alternative energy plants, can generate 30 times more yields per acre and is able to produce various biofuels [20, 21].

2.4 Wastes

Different types of waste can be used as reliable feedstock sources to produce biofuels. Waste originating from animals and plants (including foodstuffs, wood stuffs, animal waste, paper waste, forest residues, household wastes, industrial and agricultural wastes and municipal wastes) are able to be converted to biofuel in a variety of ways [15]. Such resource is inexpensive and readily accessible. They are a benefit to waste management technology and do not produce anything harmful in the process. Since sewage and municipal wastes are highly available and contain a high amount of lipids, they can be more beneficial [22]. Using waste products to create biofuels can combat various issues including issues with land, labour and fertilization [23].

2.5 Halophytes

Halophytes are types of grass that cultivate in saltwater, which is a typical for plant growth [15]. They tend to grow in tropical and subtropical areas, in locations such as coastlines, marshes, island lakes, deserts and the ocean. The key advantage of halophytes feedstock is their lack of interference with agricultural plants in terms of competing for water supply or land [24].

3 Production Technology Overview of Bio-aviation Fuel

Particularly, the biomass resources could be converted to bio-jet fuel via several process, including chemo-catalytic, thermo-chemical and bio-chemical conversions. The process of transforming biomass to bio-aviation fuel typically requires a number of related steps such as the creation of an intermediate state, adapting carbon chain length to create precursors to bio-jet fuel and conducting hydro-processing. This section will give an overview the bio-jet fuel creation process through the use of lipids and lignocellulosic biomass, with pilot tests also being outlined.

4 Main Reaction Involve in Production of Bio-jet Fuel

There are several reactions involved in production of bio-jet fuel we will summarize them in this section

4.1 Hydrogenolysis

The process of hydrogenolysis actually removes oxygen from oxygen-containing compounds. What's more, a complex reactive is usually part of the deoxygenation process. During these reactions, unsaturated TG bonds are able to be converted into saturated bonds if subjected to high H_2 pressure using a reliable catalyst. Subsequently, the saturated TGs bonds may be transformed again into fatty acids using intermediate 'di' and 'mono' glycerides [25]. As a result, C-C bonds are created and glycerol compounds are broken down to create propane and free fatty acids [26].

4.2 Deoxygenation

Deoxygenation (DO) is a process elimination of oxygen bonded species in the form of carboxyl group from triglycerides and fatty acid derivatives via decarboxylation and decarbonylation reaction. In decarboxylation, the production of a deoxygenated fuel involves removal of the carboxyl group in the fatty acid structure via CO_2, while decarbonylation involves carbonyl group (CO) and water rejection, thereby producing a linear hydrocarbon possessing one carbon less than the original fatty acid chain.

4.3 Hydrodeoxygenation

The hydrodeoxygenation (HDO) route is an upcoming and viable means of producing bio-jet fuel from triglycerides and fatty acid derivatives using an appropriate catalyst within a high H_2 pressure condition [27]. Hydrodeoxygenation itself is an exothermic reaction that results in the production of *n*-alkanes that have the exact amount of carbons as the relevant fatty acids. During the process, water is also eliminated in the form of a by-product [28].

Overall, the most economical route for converting the triglycerides and fatty acid derivatives to bio-jet fuel is via deoxygenation process. This is because the bio-jet fuel could be produced under H_2-free atmospheric condition. In contrast, the production of bio-jet fuel via hydrodeoxygenation process is unattractive since it involved the high consumption of H_2 gaseous under high pressure. Both of these processes will produce high quality of hydrocarbon and fungible with petroleum-derived fuel. It has been reported that the viscosity and cloud points of the linear paraffins produced in the deoxygenation process tend to be greater and this causes poor cold flow features [29]. Thus, to be in line with the jet fuel specifications, the normal paraffins created as a result of the deoxygenation reaction must be both hydrocracked and hydro-isomerized, since this will make the alkanes lighter (from C_5 to C_{15}) which will ultimately enhance the cold-flow features and choice of products use to produce bio-jet fuel.

5 Deoxygenation Catalyst Features

A common feature of catalysts is the ability to crack the reactant and ultimately speed up the reaction (i.e., ion exchange). The catalyst must also be the same at the beginning and end of the process. For this reason, catalysts are often used throughout process industries and research to ensure the most efficient product distribution and as a means of enhancing product selectivity [30]. Important features of catalysts include pore structure and volume, surface area and acidity, since these can largely impact the ability to crack the reactant, as well as product selectivity [31]. Zeolites and alumina-based catalysts have been widely applied in catalytic deoxygenation of triglycerides and fatty acid derivatives for biofuel production. Zeolites are structured in the form of crystalline aluminosilicate sieves which have open pores and the capacity to enable ion exchange. What's more, zeolites are made up of various SiO_2/Al_2O_3 ratios determined by the acidic features and shape selectivity. SiO_2/Al_2O_3 ratio tends to determine how reactive the zeolite of triglycerides-based oils will be and the extent to which this will affect the final product [32]. It was stated by Sharuddin et al. that alumina serves as an amorphous acid catalyst that can enclose Brønsted acid sites and ionizable hydrogen atoms, as well as combining Lewis acid sites with an electron site that will accommodate it. These features have lead to alumina-based catalysts being most commonly use when upgrading oil into a fuel [33].

It is evident that zeolite catalysts have a bigger surface area than Al_2O_3, which is beneficial for promoting the deoxygenation activity. When adapting the zeolite activity, metal elements like Ni and Mo have often been employed, with Co, Ni, Pd and Pt being commonly used to adapt the activity of Al_2O_3. The surface area of the modified zeolite varies between 85.6 and 711.5 m^2/g, and Al_2O_3 has a surface area varying from 148 to 222 m^2/g. Sudhakara et al. point out that modified Ni-ZSM has a greater performance as a result of the bigger surface area and higher level of acidity than modified Ni-Al [31]. Furthermore, it has been revealed by Galadima et al. that Al_2O_3 modified using metals performs less effectively as a result of the low surface area and problems with stability [27]. Such stability problems tend to be related to sintering and agglomeration of the metal particles which lower the catalyst's active surface area. What's more, the light alkanes have a high conversion rate due to the high surface area and strong catalyst acidity (C_5 to C_{15}) and this makes it a suitable option for bio-jet fuel production [27].

Additionally, the zeolite and Al_2O_3 catalysts' activity is largely determined by the pore size and pore volume, both of which significantly impact product selectivity [26]. Both pore size and pore volume of zeolite-based catalyst range between 3–90 A° and 0.10–0.73 cm^3/g, compared to the pore size and volume of Al_2O_3-based catalysts which vary from 7.0–75 A° and 0.21–0.63 cm^3/g, respectively. Pure zeolite ZSM-5 is much more effective than metal modified zeolite (Ni-ZSM-5) since nickel particles are vulnerable to sintering and agglomeration in the process of reduction [31]. Inside the ring formation of zeolite catalysts, the pore volume and sizes vary greatly and can be restricted by any cation within the system. The main reason for this variation in zeolitic pore structure is the exchange of exchangeable cations location, which tends to be situated close to the pore openings [12]. Furthermore, the pore size and volume of pure Al_2O_3 exceed those of metal modified Al_2O_3 given the extra metals that are integrated, and this can cause a partial blockage in catalytic channels. What's more, there can be an excessive number of metal particles.

Eventhough, zeolite and alumina-based offer greater deoxygenation activity, but the catalyst rapidly deactivated due to coke deposits. This is due to the existence of large Bronsted acidic sites (strong acidic sites) on those catalysts. It have been discovered by several researchers that the deoxygenation activity particularly enhanced by the existence of rich weak and medium acidic sites (Lewis acid) [34]. Evinced by Asikin-Mijan and co-worker in deoxygenation of triglycerides over NiO-CaO/SiO_2-Al_2O_3 under H_2-free atmospheric condition, which found catalyst with large distribution of weak and medium acidic sites offers highest % of hydrocarbon fractions with greater *n*-(C_{15}+C_{17}) [34]. Interestingly, the use of carbon support in deoxygenation reaction is effectively beneficial for increasing the deoxygenation activity and product selectivity. This is due to their amphoteric properties, surface functionalities and greater surface area [35].

6 Factors Impacting the Deoxygenation Process

The key measurement when assessing how effective the deoxygenation process is the number of bio-jet fuel hydrocarbons in the output product. The rate of bio-jet fuel production can affect by multiple factors, however, research into such factors is relatively limited to date [36]. There has been research relating to three key factors which have been found to impact the bio-jet fuel content, namely reaction temperature, feedstock and reaction atmosphere.

6.1 Feedstocks

The choice of feedstock greatly impacts the deoxygenation procedure. To produce bio-jet fuel, feedstocks emanating from plant-based oils, like vegetable oil, animal fats, used cooking oil (UCO) and palm oil, are the most frequently used. Nonetheless, as previously stated, such oils are sought after in edible markets and this makes alternative, nonedible oils (like jatropha and algal oils) and waste oil more beneficial [37, 38]. There also seems to be controversy related to applying saturated fatty acids and unsaturated fatty acids as types of feedstocks.

If nonedible oil sources are used, then the conduction of an ecofining process is crucial to synthesize the hydrocarbons [39]. This process can withstand high levels of free fatty acid, which enables the more inexpensive, nonedible oils become the source of feedstocks. A distinct feature here is the fatty acid concentration, with the source possessing more elevated levels of saturated fats (such as palm and tallow oils) not needing so much hydrogen. On the other hand, when employing soybean and rapeseed oils for the deoxygenation process, extra hydrogen must be used to combat the higher olefin content. For all cases, the feedstocks must be washed in advance to remove salt and solids prior to starting the concentration process [39, 40].

Snåre et al. [41] made comparisons between the outputs produced when different natural catalysts are used for the DO process and found a lower conversion rate for diunsaturated linoleic acid than monounsaturated oleic acid and methyl oleate. They reasoned that the presence of unsaturated fatty acids meant that extra hydrogenation had to be added in order to transform these acids into monounsaturated fatty acids prior to being transformed into the relevant hydrocarbons. Moreover, the unsaturated hydrocarbons lead to adsorption on the catalyst surface, ultimately causing the catalyst to deactivate and heightening the chances of cracking and coking reactions taking place [35].

According to other research, feedstocks with less unsaturated fatty acid content do not require much hydrogen in the process [42], since the unsaturated fatty acids can limit the selectivity to *n*-alkane [43]. It has thus been found that the deoxygenation of fatty acid can lead to *n*-alkane selectivity at a rate of 86%, whereas that of fatty acid esters leads to a lower selectivity of only 40%. The reason for this is thought to be that fatty acid deoxygenation has a higher decarboxylation rate than fatty acid ester

deoxygenation. Since the deoxygenation process is more robust, a lower bio-jet fuel cloud point is created. However, this also causes a change in the yield from longer molecular weight fuel to lower molecular weight fuels. Nonetheless, through the ecofining process, changes can be made to operating conditions to enable different feedstock to be used, and for sporadic alternations to be made to the requirements of the fuel properties standard [39].

6.2 Reaction Atmosphere

Much research has explored the yield variations in the reaction atmosphere, especially as far as the presence of hydrogen is concerned [44]. Rozmysłowicz et al. [45] explored the impacts that hydrogen has on the reaction process and the yield output of the relevant hydrocarbons in lauric acid deoxygenation. They employed a semibatch reactor, to make the yield comparisons of hydrocarbons through deoxygenation over Pd/C catalysts in an inert setting and a hydrogen-rich setting. It was revealed in this study that the inert setting was optimal for the first 100 min and yielded a much higher amount of desired hydrocarbons than the hydrogen-rich setting. The reason given for this was the development of intermediates in the hydrogen-rich setting, since these went on to transform into the relevant hydrocarbons. However, following this initial period of time, there was a much higher conversion rate of deoxygenation when hydrogen was used. The reactive route of the two processes serves as the key variation between the two processes. The presence of hydrogen causes hydroxylation to occur, and an absence of hydrogen (an inert setting) enables decarboxylation and decarbonylation.

Subsequent research which explored the impacts of hydrogen in the reaction atmosphere showed that adding a small proportion of hydrogen to an inert setting can generate a significantly higher concentration of hydrocarbons that either the completely inert setting or hydrogen-rich setting being used in isolation. Comparisons between the deoxygenation of oleic acid over Pd/C in different conditions were made by Snåre et al. They found hydrogen to heighten the conversion rate as opposed to an inert setting. Furthermore, Lestari et al. [46] examined the impact of hydrogen on the deoxygenation of stearic acid and palmitic acid during the reaction process, and Madsen et al. [47] investigated the use of diluted and concentrated stearic acid. The use of smaller amount of hydrogen during the reactive process was found to generate a higher yield, as well as lesser amounts of unwanted unsaturated hydrocarbons. Furthermore, it also allowed the desired saturated hydrocarbons to be created. What's more, a small amount of hydrogen was found to lower the coke formation, stopping the catalyst from deactivating, which occurred in the inert setting. The adding of little amount of hydrogen thus appeared to stabilize the catalytic activity of Pd/C catalysts through the preventing of coke formation [47].

It was found by Pattanaik and Misra [35], who reviewed various studies into the impact of the reaction atmosphere on deoxygenation, revealed that the deoxygenation routes vary according to the reaction atmosphere. In an environment, that is, high in

hydrogen, reaction pathways remain alike regardless of which feedstock is used. Yet, in a setting that is inert, there are big differences in the reaction routes and product selectivity when fatty acids, esters and triglyceride feeds are used. The conversion rates for fatty acids and esters are low, and the catalysts for these are less stable as a result of cracking. For this reason, a H_2+Ar environment is favourable for such feedstocks.

6.3 Reaction Temperature

Particularly, high % of bio-jet fuel production could be achieved at temperature reaction range from 250 to 360 °C [35]. Snare et al. [41] investigated the impacts of reaction temperature on deoxygenation of oleic acid from 300 to 360 °C, with a noted conversion rate of 78% at 300 °C and further rise to 93% at both 330 and 360 °C reaction temperature. The impacts of diluted dodecanoic acid deoxygenation within the same temperature range was explored by Bernas et al. [48], who identified a rise in the undecane to undene conversion rate of 10% at 300 °C to 60% at 360 °C. Further research explored the speeds at which diluted stearic acid would convert at 270 and at 330 °C, with less time also being needed for a 100% conversion to the desired hydrocarbons [49]. What's more, it was also revealed that there was an increase in rate at which diluted ethyl stearate was converted into desired hydrocarbon in the deoxygenation process, when conducted through a semibatch reaction, was also found to rise from 40% at 300 °C to 100% at 360 °C [50]. It was documented by the researchers here that this increase was primarily due to 70–40% rise in selectivity of *n*-heptadecane from within the same temperature range. This, thus, suggest diesel-like hydrocarbons become less selective under high temperatures.

Furthermore, there has also been a reported change in yield of diesel when changes are made to the reaction temperature of deoxygenation tall oil fatty acid (TOFA) over Pd/C catalyst from 300 to 350 °C [51]. Findings of the research in question indicate that the selectivity of diesel fuel was reduced when the reaction temperature increased, with only a very light coke formation of Pd/C catalysts being identified when the highest reaction temperature of 350 °C was set. This change primarily impacts the selectivity of the hydrocarbons, and thus produces higher *n*-heptadecane yields than *n*-heptadecene at 300 °C, as well as lower yields at higher reaction temperatures of 350 °C [40].

The extent to which reaction temperatures impact the decarboxylation of oleic acid in settings void of hydrogen has also been investigated by Na et al. [52] using temperatures varying from 350 to 400 °C. A conversion in excess of 98% was found at 400 °C using three different hydrotalcite catalysts. It was also found that, when lower temperatures were applied, the saponification of oleic acid and MgO (catalyst) caused solid products to build up that impacted the conversion rate. When deoxygenating the oleic in a hydrogenated setting, there was found to be an increase in temperature that caused a rise in the conversion rate [47], thus indicating that the reaction temperature is not caused by the catalyst choice or reaction atmosphere. The increase in reaction

temperature often leads to a heightened deoxygenation conversion rate whilst simultaneously lowering the deoxygenation selectivity. It was revealed by Pattanaik and Misra [35] that this was predominantly due to the higher thermal decomposition rate at higher temperatures, as well as additional aromatic products being synthesized. To address this, it is crucial to employ a balanced approach using an optimal temperature range. This approach must lead to high and effective conversion rates with suitable deoxygenation selectivity. The temperature was also not found to impact the deoxygenation reaction pathway, which is instead determined by the catalyst.

7 Bio-jet Fuel Production Challenges

Despite alternative bio-jet fuel being necessary, a number of challenges must be addressed, the first of which is the pricing differences between bio and traditional jet fuels. Moreover, issues of sustainability and finance relating to fuel commercialization must be considered [53]. Other concerns include economic issues, environmental concerns such as land-water usage, greenhouse gas emissions (GHG), particulate emissions and fuel-food competition. Sustainability serves as a key obstacle and is largely reliant upon feedstock availability and the choice of fuel production method. Socio-economic and environmental effects will also need to be addressed.

7.1 Environmental Issues

A key issues to address are the environmental impacts of fuel production. In 2005, the aviation sector contributed to 2.5% of man-made carbon dioxide production, which, by 2050, is predicted to rise to 4.7%. The increasing bio-jet fuel demand will lead to deforestation problems, impacting soil fertility and biodiversity and heightening atmospheric CO_2. Food scarcity will result from the use of agricultural land to grow the necessary crops, and soil ruination and water pollution will result from fertilizer and insecticide use. It is crucial that the fuel produced does not compromise human health [15].

7.2 Production Issues

Two key obstacles to bio-jet fuel production are the process cost and feedstock flexibility. Despite the ongoing projects exploring the use of algae as feedstock, this still generates various issues. For example, the selection of beneficial algal species and lipid extraction is complicated. To produce bio-jet fuel using the algae feedstock, funding is required. Moreover, there will be a need for optimization and receiving of necessary certifications [54]. Furthermore, it is crucial that the most suitable catalyst

and process design are chosen by the alternative fuel producers. The production process very much depends upon the feedstock, and must be both efficient and effective [54].

7.3 Distribution Issues

In terms of the supply process, product quality and blending capacity to ensure optimal functioning are major issues. Hydrotreated renewable jet (HRJ) and biomass-to-liquid (BTL) fuel production currently generate costs varying from 0.80 to $2.00/L, three times the cost of petroleum-based jet fuels [55]. Other issues to address in this category include marketing regulations and specifications for the fuels, fuel infrastructure, selection of feedstock, storing the fuel and by-products [21]. If the present cost of bio-jet fuel production is not lowered, it will not be a viable option [56]. Involvement of investors and biomass suppliers is a further essential matter [57].

7.4 Feedstock Availability and Sustainability

For bio-jet fuel production, the most preferable feedstock are those that are the most cost-effective feedstock, those which require a minimal water supply, minimal fertilizers, but still produces a good output and does not compete with food plants [15]. The key issues pertaining to feedstock are availability, price and large-scale applications [58]. The biggest challenges relating to algae culture are upholding the necessary temperature and providing energy [59]. In order to test the fuels in aircraft, vast amounts of fuel need to be produced. In the process of producing aviation biofuels, selected feedstocks must cause the least possible effects to land use and water intake. There is limited availability of biomass feedstock for the production of bio-jet fuel at present because of the heightened competition and fuel specifications [60].

7.5 Compatibility with Traditional Fuel

It is important that bio-jet fuels can do the same job as traditional jet fuels. Unlike traditional jet fuels; bio-jet fuels have to be void of any sulphur and aromatics, must possess a low freezing point and a high autoignition temperature. It will be challenging to separate bio-jet fuel at bigger airports and this could cause issues for some airlines. Other issues include the use of renewable energy sources in the commercial aircraft industry, problems with certifications, engine and quality testing processes and how to use the fuel in airplanes [7]. It is crucial that the produced fuel

can withstand various operational circumstances, performs well and is safe. Thermal stability and storage stability must also be addressed, with low temperature features, combustion characteristics and the inclusion of any small impurities (such as metals) being other matters of concern [61].

8 Future Outlook and Suggestions

Currently, the Defence Logistics Agency Energy (DLA Energy) focuses on two key areas. These are the market scale production of biofuels and the certifications of them. They have done this by creating partnerships with manufacturers and government agencies [62]. By commercializing bio-jet fuels, this can impact land, water and food resources, as well as the economy and overall society. Factors impeding research into this topic include a lack to initiative in place to asses sustainable feedstock production and distribution and an absence of cost-effective technologies to produce the fuels. It is crucial that the production process for bio-jet fuel does not generate an issue of food–fuel competition, does not have environmental impacts and can remain sustainable at a bearable cost. In terms of feedstock, the use of nonedible oils, algae and biomass all have potential, with algae able to be applied as a raw material in areas such as Australia, Arabia, north-west Africa and USA deserts [15]. To enhance the production process, innovative production technologies can be implemented and local feedstock can be used. Also important will be engagement from local government and other relevant agencies and industries, as well as long term policies since this will be a gateway to increased job openings, as well as ensuring that fuel production processes are sustainable.

9 Conclusion

Scientists have been focusing ever more on selecting sustainable fuel alternatives with the aim of creating more viable and environmentally methods of addressing the worldwide fuel demand. Bio-jet fuel has been a focal topic given its distinct fuel features, environmental friendliness, biodegradability, energy stability and associated costs. Furthermore, research has shown that bio-jet fuel is more beneficial than conventional fuel in safeguarding the environment. Bio-jet fuel is much possesses a greater heating value and better exhaust emission of specific pollutants.

Despite the cost of bio-jet fuel production being a matter of controversy, the cost itself is generally determined by the chosen synthesis process. Research has shown that removing an oxygenated, bonded compound using the deoxygenation method in an inert setting is much more economically friendly than using hydrodeoxygenation. The higher expense of hydrodeoxygenation is mainly a result of using hydrogen gas to conduct the process. Pyrolysis is less expensive; however, the hydrocarbon product is made up predominantly of light fractions.

Zeolite, silica-based catalyst offers greater deoxygenation activity, due to their higher surface area and excellent pore properties. But their high strong acidic sites facilitated side reaction such as cracking and oligomerization, hence, affect the catalyst stability. Interestingly, deoxygenation activity could be enhanced by tuning the acidic sites to weak and medium acidity. Utilization of carbon-based catalysts is also beneficial for deoxygenation activity, because carbon material is amphoteric in nature, surface functionalities and greater surface area [35].

Reaction temperature and atmospheres, as well as feedstock choices, are operational factors that must be considered when producing bio-jet fuel using a deoxygenation process. The deoxygeation process in the H_2+Ar setting had been found to favour fatty acids and esters as feedstocks. Research evidence shows that using triglycerides as feedstock is beneficial because they possess higher conversion rates in hydrogen-free settings. The most effective deoxygenation reactions can be ensured by using lower content unsaturated fatty acid feedstocks rather than high content unsaturated fatty acid feedstock (for example, ester). In terms of temperature, it is crucial to establish a balance between the selectivity of fuel-range hydrocarbons and the feedstock conversion rate. What's more, nonedible oils, including waste cooking oil is beneficial for various reasons, firstly due to the fact that it lowers the production cost, and secondly, as it may soon be able to serve as an alternative to edible oil-based green diesels.

References

1. Dibenedetto A, Angelini A, Stufano P (2014) Use of carbon dioxide as feedstock for chemicals and fuels: homogeneous and heterogeneous catalysis. J Chem Technol Biotechnol 89:334–353
2. Rosa L, D'Odorico P (2019) The water-energy-food nexus of unconventional oil and gas extraction in the Vaca Muerta Play, Argentina. J Clean Prod 207:743–750
3. Peeters P, Higham J, Kutzner D et al (2016) Are technology myths stalling aviation climate policy? Transp Res Part D Transp Environ 44:30–42
4. Singh J, Sharma SK, Srivastava R (2019) AHP-Entropy based priority assessment of factors to reduce aviation fuel consumption. Int J Syst Assur Eng Manage 10:212–227
5. Kim J-K, Park JY, Yim ES et al (2015) Bio-jet fuel production technologies for GHG reduction in aviation sector. Trans Korean Hydrogen New Energy Soc 26:609–628
6. Vo PK (2014) Canola derived biodiesel as blending agent for petroleum based fuels
7. Warren KA (2008) World jet fuel specification
8. Iakovlieva A (2013) Traditional and alternative jet fuels: problems of quality standardization. J Pet Environ Biotechnol 04:3–7
9. Wang WC, Tao L (2016) Bio-jet fuel conversion technologies. Renew Sustain Energy Rev 53:801–822
10. Wei CY, Chiu PY, Hou PN et al (2017) The value of 99mTc ECD SPECT with statistical image analysis on enhancing the early diagnosis of primary progressive aphasia. Clin Nucl Med 42:e117–e120
11. Bozell JJ (2011) The use of renewable production of chemicals and materials—a brief overview of concepts. Point
12. Abdulkareem-Alsultan G, Asikin-Mijan N, Lee HV, Rashid Umer, Islam Aminul, Taufiq-Yap YH, Alsultan GA et al (2019) A review on thermal conversion of plant oil (edible and inedible) into green fuel using carbon-based nanocatalys. Catalysts 9:1–25

13. Scott D, Peeters P, Gössling S (2010) Can tourism deliver its "aspirational" greenhouse gas emission reduction targets? J Sustain Tour 18:393–408
14. Bayu S (2011) Intercomparability of isotropic and anisotropic solar radiation models for different climatic zones of India. Environ Prog 30:925–932
15. Kandaramath Hari T, Yaakob Z, Binitha NN (2015) Aviation biofuel from renewable resources: routes, opportunities and challenges. Renew Sustain Energy Rev 42:1234–1244
16. van der Hagen TR (2012) The application of bio jet fuels until 2050 Scenarios for future developments. 1–61
17. Singh A, Nigam PS, Murphy JD (2011) Mechanism and challenges in commercialisation of algal biofuels. Bioresour Technol 102:26–34
18. Bailis R, Broekhoff D, Lee CM (2016) Greener Skies? Supply and sustainability of carbon credits and alternative fuels for international aviation. 64
19. Mahesh R, Naira VR, Maiti SK (2019) Bioresource Technology Concomitant production of fatty acid methyl ester (biodiesel) and exopolysaccharides using efficient harvesting technology in flat panel photobioreactor with special sparging system via Scenedesmus abundans. Bioresour Technol 278:231–241
20. Hong TD, Soerawidjaja TH, Reksowardojo IK et al (2013) A study on developing aviation biofuel for the tropics: production process—experimental and theoretical evaluation of their blends with fossil kerosene. Chem Eng Process Process Intensif 74:124–130
21. Skrzyńska E, Matyja M (2011) Comparison of the physicochemical properties of select natural fats and their methyl esters. Chemik 65:930–935
22. Alsultan GA, Asikin-Mijan N, Lee HVV et al (2017) Deoxygenation of waste cooking to renewable diesel over walnut shell-derived nanorode activated carbon supported CaO-La_2O_3 catalyst. Energy Convers Manage 151:311–323
23. Abdulkareem-alsultan G, Asikin-Mijan N, Mansir N et al (2018) Pyro-lytic de-oxygenation of waste cooking oil for green diesel production over Ag_2O_3-La_2O_3/AC nano-catalyst. J Anal Appl Pyrolysis 137:171–184
24. Eshel A, Oren I, Alekperov C et al (2011) Biomass production by desert halophytes: alleviating the pressure on the scarce resources of arable soil and fresh water. Eur J Plant Sci Biotechnol 5:48–53
25. Grosjean R, Delacroix S, Gouget G et al (2017) High pressures pathway toward boron-based nanostructured solids. Dalt Trans 47:7634–7639
26. Vásquez MC, Silva EE, Castillo EF (2017) Hydrotreatment of vegetable oils: a review of the technologies and its developments for jet biofuel production. Biomass Bioenergy 105:197–206
27. Galadima A, Muraza O (2015) Catalytic upgrading of vegetable oils into jet fuels range hydrocarbons using heterogeneous catalysts: a review. J Ind Eng Chem 29:12–23
28. Silva LN, Fortes ICP, de Sousa FP, Pasa VMD (2016) Biokerosene and green diesel from macauba oils via catalytic deoxygenation over Pd/C. Fuel 164:329–338
29. Li X, Luo X, Jin Y et al (2017) Heterogeneous sulfur-free hydrodeoxygenation catalysts for selectively upgrading the renewable bio-oils to second generation biofuels. Renew Sustain Energy Rev 82:1–36
30. Akhtar J, Saidina Amin N, Al-Salem SM et al (2012) Review of biomass pyrolysis oil properties and upgrading research. Renew Sustain Energy Rev 16:4044–4098
31. Reddy Yenumala S, Maity SK, Shee D (2016) Hydrodeoxygenation of karanja oil over supported nickel catalysts: influence of support and nickel loading. Catal Sci Technol 6:3156
32. Tang Q, Zheng YY, Wang T et al (2017) Biorefineries for biofuel upgrading: a critical review. Renew Sustain Energy Rev 58:520–594
33. Anuar Sharuddin SD, Abnisa F, Wan Daud WMA, Aroua MK (2016) A review on pyrolysis of plastic wastes. Energy Convers Manage 115:308–326
34. Asikin-Mijan N, Lee HV, Marliza TS, Taufiq-Yap YH (2018) Pyrolytic-deoxygenation of triglycerides model compound and non-edible oil to hydrocarbons over SiO_2-Al_2O_3 supported NiO-CaO catalysts. J Anal Appl Pyrolysis 129:221–230
35. Pattanaik BP, Misra RD (2017) Effect of reaction pathway and operating parameters on the deoxygenation of vegetable oils to produce diesel range hydrocarbon fuels: a review. Renew Sustain Energy Rev 73:545–557

36. Hermida L, Zuhairi A, Rahman A (2015) Deoxygenation of fatty acid to produce diesel-like hydrocarbons: a review of process conditions, reaction kinetics and mechanism. Renew Sustain Energy Rev 42:1223–1233
37. David E, Kopač J, Technologies I et al (2019) Upgrading the characteristics of the bio-oil obtained from rapeseed oil cake pyrolysis through the catalytic treatment of its vapors. J Anal Appl Pyrolysis 141:104638
38. Duman G, Okutucu C, Ucar S et al (2011) The slow and fast pyrolysis of cherry seed. Bioresour Technol 102:1869–1878
39. Kalnes TN, Marker T, Shonnard DR, Koers KP (2008) Green diesel production by hydrorefining renewable feedstocks. BIOFUELS Technol
40. Li S, Wang Y, Dong S et al (2009) Biodiesel production from Eruca Sativa Gars vegetable oil and motor, emissions properties. Renew Energy 34:1871–1876
41. Snåre M, Kubic I, Murzin DY (2006) Heterogeneous catalytic deoxygenation of stearic acid for production of biodiesel. 5708–5715
42. Kubic I, Ma P, Chichova D et al (2008) Catalytic deoxygenation of unsaturated renewable feedstocks for production of diesel fuel hydrocarbons. Fuel 87:933–945
43. Meller E, Green U, Aizenshtat Z, Sasson Y (2014) Catalytic deoxygenation of castor oil over Pd/C for the production of cost effective biofuel. Fuel 133:89–95
44. Popov S, Kumar S (2015) Rapid hydrothermal deoxygenation of oleic acid over activated carbon in a continuous flow process. Energy Fuels 29:3377–3384
45. Yeh TM, Hockstad RL, Linic S, Savage PE (2015) Hydrothermal decarboxylation of unsaturated fatty acids over PtSnx/C catalysts. Fuel 156:219–224
46. Lestari S, Mäki-Arvela P, Simakova I et al (2009) Catalytic deoxygenation of stearic acid and palmitic acid in semibatch mode. Catal Lett 130:48–51
47. Madsen AT, Rozmyszłowicz B, Simakova IL et al (2011) Step changes and deactivation behavior in the continuous decarboxylation of stearic acid. Ind Eng Chem Res 50:11049–11058
48. Bernas H, Eränen K, Simakova I et al (2010) Deoxygenation of dodecanoic acid under inert atmosphere. Fuel 89:2033–2039
49. Lestari S, Simakova I, Tokarev A et al (2008) Synthesis of biodiesel via deoxygenation of stearic acid over supported Pd/C catalyst. Catal Lett 122:247–251
50. Snåre M, Eränen K (2005) Hydrocarbons for diesel fuel via decarboxylation of vegetable oils 106:197–200
51. Mäki-Arvela P, Rozmysłowicz B, Lestari S et al (2011) Catalytic deoxygenation of tall oil fatty acid over palladium supported on mesoporous carbon. Energy Fuels 25:2815–2825
52. Shu Q, Gao J, Nawaz Z et al (2010) Synthesis of biodiesel from waste vegetable oil with large amounts of free fatty acids using a carbon-based solid acid catalyst. Appl Energy 87:2589–2596
53. Nair S, Paulose H (2014) Emergence of green business models: the case of algae biofuel for aviation. Energy Policy 65:175–184
54. Carlson LS, Lee MY, Oje CAE, Xu A (2010) Algae to alkanes. Scholarly Commons
55. Hunt AJ, Sin EHK, Marriott R, Clark JH (2010) Generation, capture, and utilization of industrial carbon dioxide. Chemsuschem 3:306–322
56. O'Connell A, Kousoulidou M, Lonza L, Weindorf W (2019) Considerations on GHG emissions and energy balances of promising aviation biofuel pathways. Renew Sustain Energy Rev 101:504–515
57. Deboni TL, Simioni FJ, Brand MA, Lopes GP (2019) Evolution of the quality of forest biomass for energy generation in a cogeneration plant. Renew Energy 135:1291–1302
58. Mueller-Langer F, Tzimas E, Kaltschmitt M, Peteves S (2007) Techno-economic assessment of hydrogen production processes for the hydrogen economy for the short and medium term. Int J Hydrogen Energy 32:3797–3810
59. Usher PK, Ross AB, Camargo-Valero MA et al (2014) An overview of the potential environmental impacts of large-scale microalgae cultivation. Biofuels 5:331–349
60. Baral NR, Kavvada O, Mendez-Perez D et al (2019) Techno-economic analysis and life-cycle greenhouse gas mitigation cost of five routes to bio-jet fuel blendstocks. Energy Environ Sci 12:807–824

61. Gil MV, Rubiera F (2019) Springer Book. Elsevier
62. Truong NTT, Boontawan A (2017) Development of bio-jet fuel production using palm kernel oil and ethanol. Int J Chem Eng Appl 8:153–161

A Review of Modern Hydrogen Combustor Injection Technologies for the Aerospace Sector

Pierre F. Ghali, Huanrong Lei, and Bhupendra Khandelwal

Nomenclature

AGP	Air guiding panel
APU	Auxiliary power unit
CFD	Computational fluid dynamics
DLN	Dry-Low NO_x
H_2	Dihydrogen
K	Kelvin
LDI	Lean Direct Injection
LES	Large-Eddy Simulation
m	Meters
mm	Millimeters
NO	Nitric oxide
NO_2	Nitrogen dioxide
NO_x	Nitrogen oxides
O_2	Dioxygen
ppm	Parts per million
RANS	Reynolds-Averaged Navier–Stokes
RDE	Rotating Detonation Engine
RL	Rich-Lean
y_{crit}	Critical micromix injection height
λ	Air/fuel ratio
λ_{rich}	Excess air ratio in the rich stage (Rich-Lean combustor)

P. F. Ghali · H. Lei
University of Sheffield, Sheffield, South Yorkshire S10 2TN, United Kingdom

B. Khandelwal (✉)
Mechanical Engineering Department, The University of Alabama, Tuscaloosa, Alabama, USA
e-mail: bhupendra.khandelwal@gmail.com

© Springer Nature Singapore Pte Ltd. 2021

A. De et al. (eds.), *Sustainable Development for Energy, Power, and Propulsion*, Green Energy and Technology,
https://doi.org/10.1007/978-981-15-5667-8_21

Φ Equivalence ratio

1 Introduction

The fuel and energy crisis anticipated in the next few decades is pushing the transportation sector towards more viable alternatives. The objectives for the fuel that will replace fossil fuels are twofold: first, it needs to be readily available in ample quantities; second, its combustion should produce as little harmful emissions as possible. Governments worldwide are working towards reducing smoke, carbon, and nitrous oxide emissions, which are characteristic of hydrocarbon-based fuel combustion. There are several possibilities such as nuclear, renewable energies like solar or wind power, all of which can—at first glance—replace hydrocarbon fuels. However, another alternative is hydrogen. Though it is relatively difficult to store and handle compared to its fossil fuel equivalents, hydrogen is more readily available, produces less harmful emissions, and has higher specific energy than Jet-A and other comparable hydrocarbon-based fuels. Furthermore, it has wider flammability limits allowing leaner combustion to take place, thereby lowering the production of harmful chemicals. This makes hydrogen a strong candidate for the aerospace sector—specifically, gas turbines (land-based and airborne). One of the greatest challenges today is to harness hydrogen's energy in compact, efficient combustors without creating harmful NO_x emissions, all while delivering satisfactory performance.

Integrating hydrogen into the energy sector is an endeavor with many aspects, ranging from the production of hydrogen, safely storing it, and injecting it at the combustion point, to safety mechanisms and procedures to use in case of emergency. Many of these aspects are addressed in Benson et al.'s work [1]. The present work, however, focuses on the implementation of hydrogen in gas turbine injector technology. Particular design approaches explored include premixed and non-premixed injectors, such as rotating detonation engines (RDE), Rich-Lean (RL), Lean-Direct Injection (LDI), and micromix injection systems. For each technology, metrics analyzed include temperature distributions as given by numerical or experimental results, as well as NO_x emissions.

2 Premixed Systems

Premixed combustors mix fuel and oxidizer before diffusing the flammable mixture into the combustion chamber. Various designs based around premixed combustion exist. These designs simplify combustor geometries, which offer a benefit from an application perspective (e.g., cheaper production costs or lower gas turbine weight). Because the mixture is already mixed at the point of ignition, there are typically

no hotspots forming, which contributes to the low nitrogen oxide emissions from premixed systems. Non-premixed injectors do not have this advantage.

Anderson [2] investigated how a premixed hydrogen combustor compared to its hydrocarbon-fueled counterpart. Injecting hydrogen into an indirectly-heated airstream, the mixture then passes through the flameholder, consisting of a hexagonal perforated plate with a cross-sectional blockage ratio of 92%. Downstream, a gas probe was used to draw a sample to send to an analyzer. The large blockage ratio on the flameholder was used to "prevent propagation of the hydrogen flame front upstream" [2].

As part of this study, different inlet mixture temperatures and combustor pressures were used as boundary conditions. The author reports that the strongest effect on emission was from a variation in equivalence ratio. In fact, for an inlet temperature of 600 K, the nitric oxide emissions varied from 0.007 to 0.07 g kg^{-1} of equivalent propane for equivalence ratios of $\Phi = 0.3$ and $\Phi = 0.4$, respectively. For the 700 K inlet temperature, NO_x emissions varied from 0.004 to 0.006 g kg^{-1} of equivalent propane, corresponding to $\Phi = 0.23$ and $\Phi = 0.26$.

In terms of concentrations, the measured values were too low to be accurate for flame temperatures below 1300 K; the maximum measured was 1.2 ppmv for a flame temperature of nearly 1700 K [2]. This generally agrees with well-stirred reactor predictions.

In addition to being a low-emission combustion system, the burner investigated by Anderson is very efficient. The lean blowout limit did not yield a combustion efficiency below 85% for inlet mixture temperatures between 600 and 700 K. Equivalence ratios tending towards 0.35–0.43 corresponded to efficiencies of 97–101%. The efficiency exceeding unity may have been due to the radiation corrections applied to the thermocouple, as well as the effects of the effective wire diameter and the emissivity associated with the instrumentation. Even taking into account a variation of 3–4%, this premixed combustor remains a strong performer.

Cappelletti and Martelli conducted a study on premixed combustors fed purely with hydrogen fuel, as opposed to methane/hydrogen syngas or hydrogen diluted with nitrogen [3]. The design was derived from an existing gas turbine Dry-Low-NO_x design, typically used with hydrocarbon-based fuels. The authors investigated the derivative design from both simulation and experimental perspective. First, the purpose of the simulation was to evaluate the complex flame shape, as well as estimate NO_x production based on the NNH formation path, as well as analyze elements that cannot be easily captured from the experimental environment. In terms of flame geometry, there is a strong general agreement between the numerical and experimental methods. The figure below depicts both cases (Fig. 1).

Because the laminar flamelet model is too slow to properly represent nitric oxide formation, three postprocessing methods were used to evaluate NO_x emissions: a thermal method, the NNH formation path, and GRI-Mech 3.0. Experimentally, under the nominal premixing configuration without the lit pilot flame, the combustor generated 6–17 ppm @15% O_2; under the low-premixing configuration with the pilot flame switched on, the burner formed 15–38 ppm @15% O_2. The latter result is attributed to the pilot flame. The emissions results are Table 1.

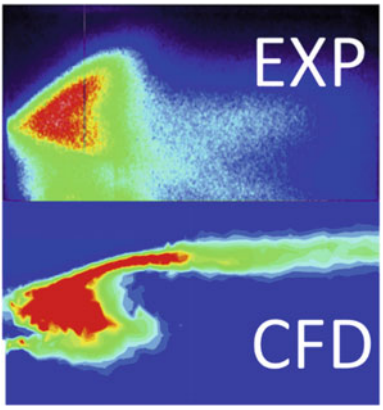

Fig. 1 Comparison between the experimental OH* imaging case and the numerical premix-C rate field. Figure reproduced from [3]

Table 1 Emissions from experimental and numerical methods

Method	ppm NO@15% O_2
Experimental	38.00
Pure thermal postprocessor	9.59
Decoupled only thermal way	6.32
Decoupled all ways	41.00

Note that the three rows below the experimental method represent numerical approaches. Reproduced from [3]

Completely decoupling the postprocessor allows for CFD to yield a relatively accurate estimation of NO emissions, though slightly conservative. The difference across these values illustrates that NO is formed through other paths in addition to the thermal one. The authors note that though premixing has been used historically, in the specific case of hydrogen combustion, the NO_x formation is primarily due to the NNH path, with the Zeldovich mechanism accounting for roughly 20% of the nitrogen oxides formation. Generally, careful integration of this premixed burner into design allows for staying at the lower end of the NO_x emission spectrum.

Using a simple premixed combustor, Cam et al. investigated the effect of equivalence ratio on the combustor temperature profile and on NO_x emissions [4]. The authors used numerical methods and compared their results to existing literature and to experimental results. Based on their CFD results, they calculated the emission performance of the combustor design. The geometry and their most salient emissions results are depicted in the following Figs. 2, 3, and 4.

The authors established that as the equivalence ratio decreased, the centerline temperature decreased, and the location for most chemical reactions moved downstream. Also, the maximum NO_x formation was identified at an equivalence ratio of 0.9, though the peak temperature was found to be highest at $\Phi = 1.1$. The reason for

Fig. 2 Premixed combustor geometry. Figure reproduced from [4]

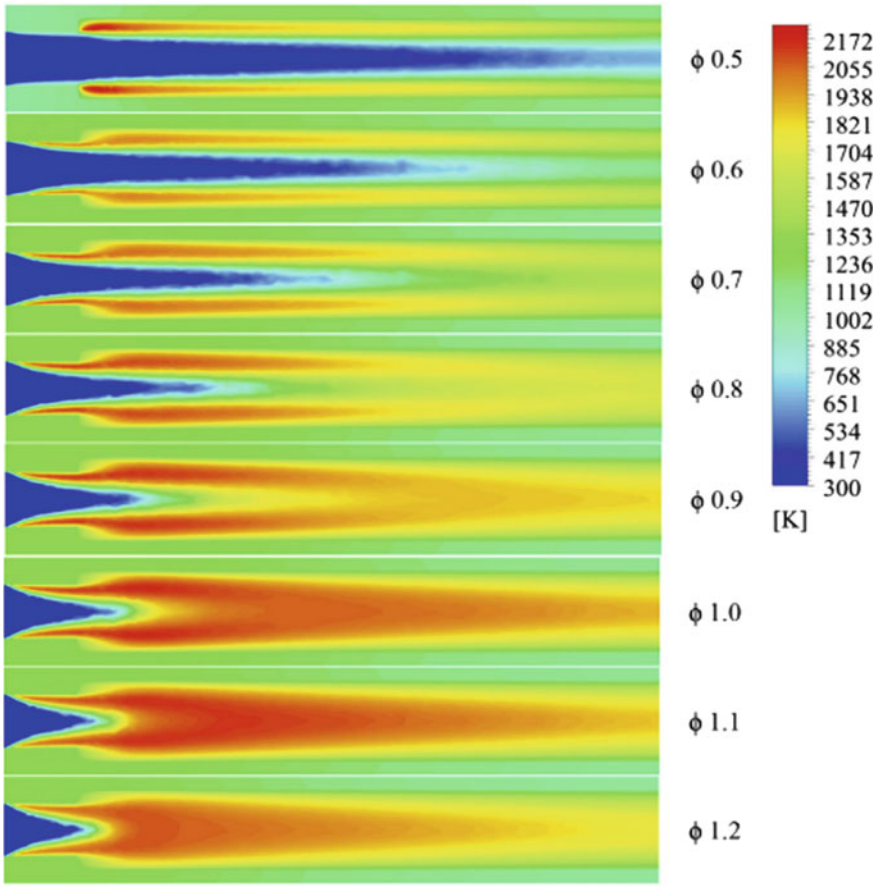

Fig. 3 Temperature profile associated with the premixed combustion. Figure reproduced from [4]

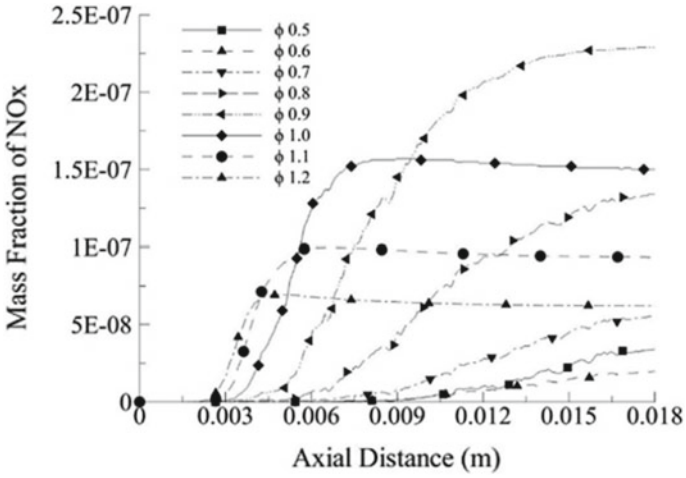

Fig. 4 NO_x mass fraction at various distances from the inlet in the burner. This plot is taken along the centerline of the burner. Figure reproduced from [4]

this apparent discrepancy is that the heat loss to the environment will be greater—assuming a fixed thermal power input. Therefore, increasing equivalence ratio will reduce overall thermal energy imparted to the flow and thereby overall performance, with respect to a bigger picture of the combustor in a gas turbine.

Finally, the authors showed that near the inlet, there is a significant difference in wall temperature values between the authors' simulation, simulation data available in the literature, and experimental results. However, because the general trends in the validation figure generally agree [4], this simulation was considered to be valid.

Marek et al. conducted an investigation on diffusion flame combustion systems via the creation of the Lean-Direct Injection burner [5]. Lean-Direct Injection consists of injecting hydrogen from two points into a perforated cylinder through which air flows. Between both walls of the flameholder, air and hydrogen mix, and the resulting mixture is ignited downstream. An example of a single ring of the injector assembly is depicted in the following Fig. 5.

The complete injector assembly is comprised of three concentric rings, with the centermost one having a single injector, the middle ring having seven injectors, and the outermost ring having seventeen injectors. This design was reproduced with different injection hole patterns. This allowed the comparison of different patterns with respect to total pressure drop and pollutant emissions via the effect of the patterns on the flame.

Consistent with other premixed systems, Lean-Direct Injection technology performed well on the emissions front. Injector configuration C4's emissions performed the best compared to the other options. In fact, for equivalence ratios below roughly 0.3, the burner with the C4 injector formed less than 10 ppm of NO_x. Below $\Phi = 0.18$, less than 1 ppm of nitrous oxides formed; however, this equivalence ratio corresponds to a combustor exit temperature of less than 1200 K. Although such

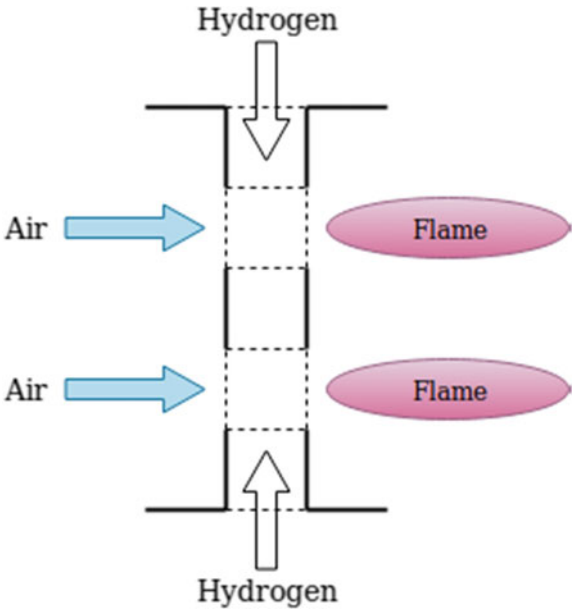

Fig. 5 Lean-direct injection injector assembly, based on [5]

emissions levels are sought after, this particular point may not be desirable because the exit temperature is too low for the required gas turbine performance. Though a just balance must be struck between higher combustion temperatures and emissions, this is an aspect that will vary according to the application associated with the injector.

Beyond emissions, each injector performed differently in terms of affecting the overall combustor pressure loss. Despite earning the lowest emissions rank out of each injector, C4 had a pressure loss of 25%, which is the maximum. The emissions performance thus was achieved at the cost of the efficiency of the burner. Injector patterns NASA N1 (6.350 cm liner) and C2 achieved the highest efficiency, with a pressure loss of 4%.

Despite their excellent performance along the lines of emissions and general thermal output, premixed combustors have some dangers associated with their operation: flashback and autoignition. By keeping hydrogen and air separate until the mixing and combustion point in the combustor, the risk of flashback is mitigated. This separation of fuel and oxidizer also limits the possibility of autoignition. Indeed, by having hydrogen and oxygen mixed within flammability limits, two of three ingredients for autoignition are present, with the last being the mixture reaching autoignition temperature. Non-premixed systems are inherently free of this risk. This risk is taken into consideration during the design of combustors, which is typically reflected by a high premixed mixture injection velocity into the combustion chamber to offset the high hydrogen flame speed.

3 Rotating Detonation Engines

Rotating detonation engines (RDE) are an improvement upon the pulse detonation engine, derived from the pulse jet. Their design is generally simpler than some other propulsion systems, making them cheap to produce, and easy to implement. To date, Frolov et al. have conducted research regarding integrating hydrogen combustion in an RDE design; so far, an annular combustor has successfully been designed, manufactured, and tested [6]. The authors found that increasing the gap in the annulus would decrease the number of detonation waves and their stability, but could also reduce pressure losses.

Further efforts have been focused on applying computational methods to RDEs, as well as working on various characteristics relating to RDE operation, such as relighting it and integrating variable-geometry inlets to optimize performance in varying conditions [7, 8].

Despite the significant progress, there are still issues at this point in the development of RDE technology. Stability is one of the major problems; Anand et al. focused their efforts on determining some of the fundamental instabilities of RDE systems [9]. They identified chaotic instability, a periodic waxing and waning of peak detonation wave pressures, sudden transient mode switching in the combustor, and the occurrence of pulse detonations within the continuous detonation combustor as the four principal instabilities. More investigation is required to develop hydrogen-powered RDE propulsion past these issues.

Though significant efforts have been made to make RDE technology commonplace in the aerospace sector, there is to date little literature available concerning RDE systems' emissions. The authors speculate that—based on [8]—increasing the equivalence ratio past the stoichiometric point would increase the detonation wave stability; however, NO_x production is immediately tied to the mixture's equivalence ratio (via the peak temperature). This leads the authors to believe that at its *current development stage*, rotating detonation engines are not a viable alternative propulsion system for the future *in terms of* NO_x *emissions*.

4 Rich-Lean Injectors

Rich-Lean (RL) is a technology that provides dual-mode operation capability to combustors. Rich-lean burners are indeed capable of burning fuel in a diffusive flame, or in a rich-lean configuration where the diffusive airflow is replaced by a lean mixture. Designs typically consist a first stage where hydrogen is burned in ratios in excess of stoichiometric conditions. The resulting mixture is then fed into a second stage containing excess air, where the unburnt fuel can be ignited. Heat transfer from the rich stage to the lean one facilitates pollutant emission control since it affects the ability of nitric oxide formation via the thermal path.

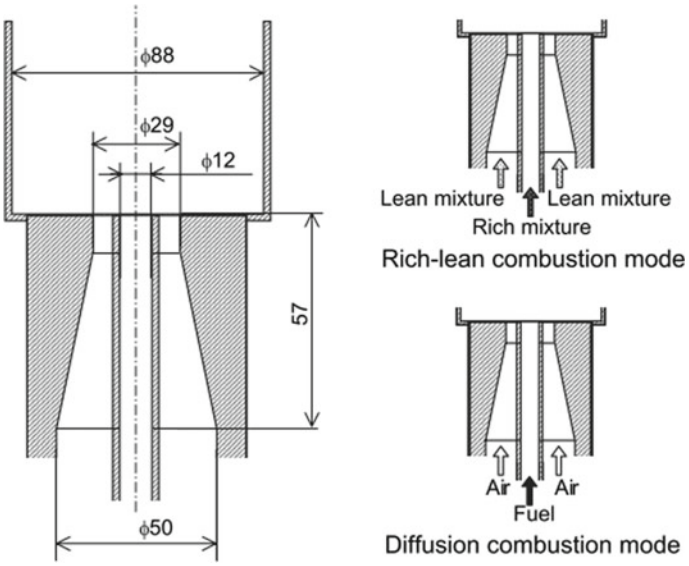

Fig. 6 Rich-lean combustor geometry used by Shudo et al. Figure reproduced from [10]

Shudo et al. studied the reduction of NO_x in hydrogen-fueled gas turbines that use rich-lean burners [10]. To that end, they use a coaxial burner that could operate in two modes: rich-lean and diffusion. Under the former, lean mixture would be injected through a nozzle surrounding a rich mixture fed through an axial nozzle; with both rich and lean mixtures meeting and being burnt. Under the latter operating mode, air would be supplied in the nozzle surrounding the central line, which fed fuel to the burner, in a manner typical of diffusion flame based combustors. The geometry used is depicted in Fig. 6.

Through their study, the authors found that H_2 combustion—even under an equivalence ratio above unity—will not result in prompt NO formation (since there is no carbon atom supplied by the fuel) [10, 11]. However, the peak flame temperature may contribute to increasing NO_x via the thermal formation mechanism. Nevertheless, compared to hydrocarbon-fueled rich-lean burners and "classic" diffusion flame burners, hydrogen rich-lean burners emit much less NO_x. Shudo et al.'s salient results are summarized in the following Figs. 7 and 8.

Figure 7 compares NO_2 values from rich-lean combustors to a baseline represented by an index of 1. This baseline corresponds to equivalent methane or hydrogen diffusion flame. Notice that for all rich side equivalence ratios, the hydrogen rich-lean combustor generates about half as much nitrogen dioxide as the combustor running in the diffusive flame mode. For an overall stoichiometric equivalence ratio, the Rich-Lean combustor will generate up to 75% lower NO_2 compared to a diffusion flame, which is a significant improvement in terms of emissions.

Figure 8 demonstrates that increasing the overall equivalence ratio of an RL burner will decrease the NO_2/NO_x ratio. Because NO_2 is more harmful than NO,

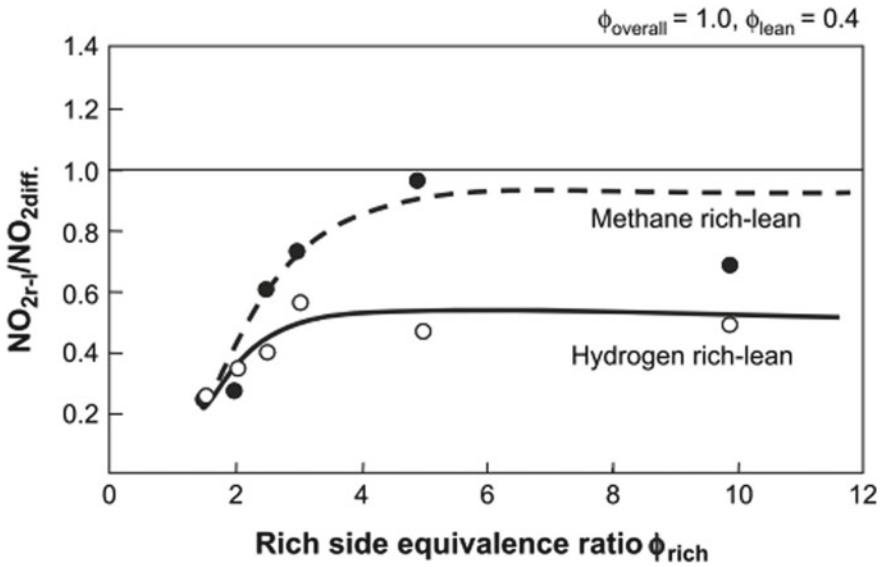

Fig. 7 NO_2 emission as a function of rich stage equivalence ratio. Figure reproduced from [10]

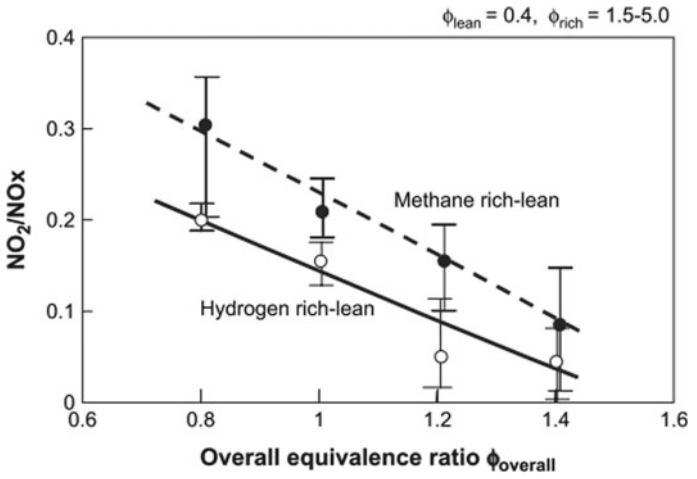

Fig. 8 Ratio of NO_2 to NO_x for hydrogen rich-lean burners. Figure reproduced from [10]

increasing Φ will reduce harmful pollutant emissions. Paired with the information from the preceding figure, a combustor design point with low NO_2 emissions and a small NO_2/NO_x ratio can be achieved for a lower rich side Φ and a higher overall combustor Φ. Overall, the hydrogen RL burner performed better than the methane one over a range of different equivalence ratios, further establishing that hydrogen is a viable option as far as combustor thermal and ecological performance is concerned.

Table 2 Comparison between Jet-A-powered APU, methane RL, and hydrogen RL combustor NO_2/NO_x ratios

Fuel type	NO_2/NO_x ratio
Jet-A (source 1)	0.421
Jet-A (source 2)	0.366
Methane (Rich-Lean)	0.320
Hydrogen (Rich-Lean)	0.200

Note the Jet-A figures were taken at the lowest APU load and the RL combustor figures at their lowest equivalence ratio, corresponding to the highest NO_2/NO_x ratio [10, 12]

To position RL combustion technology within the existing combustor designs, Khandelwal et al. investigated gas turbine vibrations and emissions for various fuels [12]. The NO_2/NO_x ratio was calculated at the lowest load for several fuels, including Jet-A from two different sources. These were then compared to the RL combustor results from Shudo et al. the results are tabulated below.

From Table 2, RL combustors perform better than conventional diffusion combustors at low loads. Because NO_2 is more harmful to the environment than NO, hydrogen-based Rich-Lean combustors yield a lower negative impact on the environment.

Bolaños et al. also investigated Rich-Lean combustor technology. Their work focused on a combustor operating under gas turbine conditions [13]. This combustor's geometry consisted of two sequential stages, as opposed to Shudo et al.'s parallel stages. First, in the rich stage, the mixture was burnt until the complete expenditure of the air, which was the limiting reactant. The combustion products and excess fuel from the rich stage were then injected into an oxidizer-rich environment comprising the lean stage, where lower-temperature combustion occurred. The experimental apparatus also included a gas probe as well as equipment for a chemiluminescence study.

This arrangement allowed for a careful study of the flame through chemiluminescence and of NO_x in the combustor's performance for different pre-conversion rates, or excess air ratios (also known as the fuel/air ratio), in the rich stage. These conversion rates are denoted by λ_{rich}. Because the rich stage is characterized by air being the limiting reactant, λ_{rich} correspondingly is less than unity. Conversely, in the lean stage, the air-fuel ratio is greater than unity.

The more important results from this study show that without pre-conversion, the NO_x emissions reached up to 165 ppm; by burning increasingly *lean* mixtures in the rich stage, the NO_x emissions decreased down to approximately 23 ppm. This is consistent with Shudo et al.'s result, further validating Bolaños et al.'s experimental data and experience with knowledge pertaining to the nitrous oxides thermal formation path. Compared to premixed systems, Rich-Lean injectors and combustors fared worse. Yet, Bolaños et al. identified several key features to address in order to reduce NO_x emissions: the reduction of amount of hydrogen injected in the lean stage, better mixing to enhance heat transfer (thereby eliminating hotspots), and self-dilution via pre-conversion, which causes cooler combustion products from the rich stage to

lower the peak temperatures in the lean stage. Implementing these factors helps in reducing the emission of harmful chemicals and may bring Rich-Lean technology closer to premixed systems' performance.

5 Diffusive Mixing

Diffusion flames are made of surfaces of local combustion where the mixture of fuel and oxidizer are within flammability limits. Combustors using diffusion flames have been used since the dawn of the jet age. In modern gas turbines, diffusion remains a reliable and efficient way of increasing the fluid's internal energy.

Gobbato et al. studied a design where air from the compressor flows along a perforated annulus surrounding the combustion chamber; the air is then reversed in direction and fed back into the combustion chamber, where it is mixed and ignited [14]. The computational domain associated with the geometrical arrangement is depicted in Fig. 9.

The authors conducted a two-phase study, with a computational fluid dynamics simulation comprising the first phase, and an experiment constituting the second phase. The results from both phases were then compared to establish whether numerical and experimental results agreed.

Experimentally, this combustor produced a maximum flame temperature of roughly 880 K at approximately 790 mm from the top of the combustor. Generally, there was a spread of 20 K at least and 80 K at most across the four rows. The associated CFD model did not reflect this temperature disparity very well along the axial direction. However, both the experimental and CFD temperature profiles agree at the combustor exit cross-section. These results are summed up in the following Fig. 10.

The authors identified a possible reason for the CFD results being consistently lower than experimental ones: using a one-step kinetic model yields a faster reaction in the simulation environment than in real life. Therefore, the reaction does not extend as far out radially, in turn leaving the liner walls (where the thermocouples are placed) cooler [14]. Solely based on the temperature profile provided by the experiment, however, it can be established that the peak temperature in the combustor will not exceed 880 K, thereby producing a reduced amount of NO_x.

Weiland et al. propose a different design where the diffusive injector idea is scaled down such that a whole circular array of injectors can be integrated into the combustor [15]. Their individual injector design is depicted below (Fig. 11).

This air and fuel injector arrangement allows—under low-pressure conditions—for the flame associated with each individual injector to form one large diffusion flame 1 cm downstream of the injector plate's face. The large, common diffusion flame lends itself towards lower emissions. Furthermore, injecting nitrogen to dilute the fuel stream allows for a reduction in peak temperature, which translates to reduced NO_x emissions. Paired with residence time reduction via airspeed increase and a lower combustor pressure, a reduction of several ppm can be achieved. In terms of

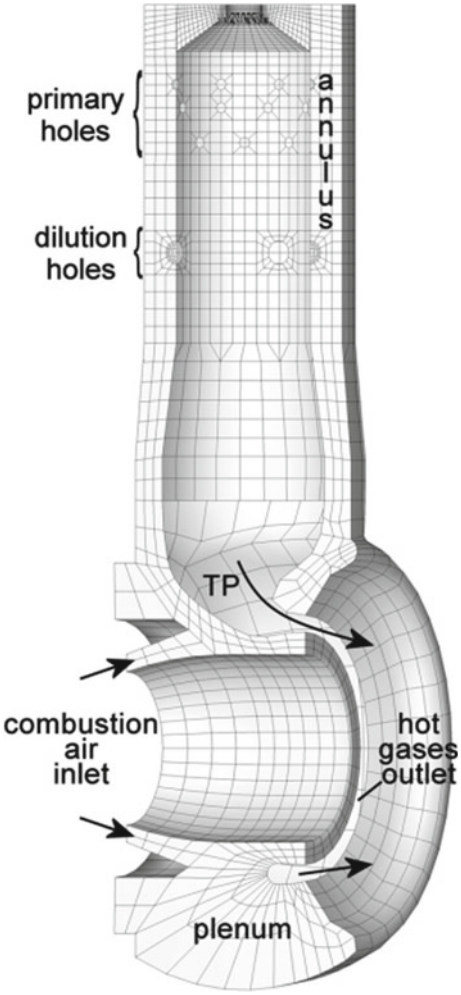

Fig. 9 Computational domain and mesh for Gobbato et al.'s diffusion flame combustor. Figure reproduced from [14]

nitrous oxide emissions, there were several observations made by the authors. First, reducing the combustion equivalence ratio yielded a reduction in corrected NO_x at 15% O_2. Next, reducing the pressure in the combustor also reduced nitrous oxide formation. Pairing both of these trends, the authors found that for an equivalence ratio of 0.7 and a burner pressure of 16 atm, the NO_x emissions were of roughly 6 ppm, whereas for an equivalence ratio of 0.5 and a burner pressure of 4 atm, the resultant emissions were down to 1–2 ppm. Residence time did not affect these results as much as previously anticipated. Weiland et al. note that despite the low NO_x emissions, premixed systems still perform better (roughly 3 ppm) [16]. However, their work clearly demonstrates that diffusion flame-based combustors are capable of at least matching the emissions performance of premixed systems while avoiding flashback potential and other downsides of premixed systems.

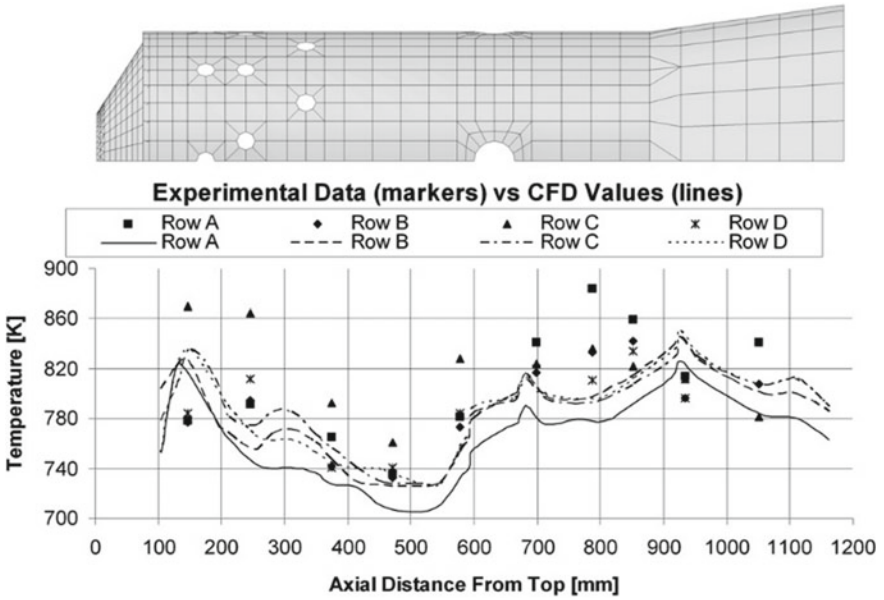

Fig. 10 Experimental and numerical temperature data for each row. The four rows run down the length of the combustor, and are at 90°-interval angles around the cross-section of the combustor. Figure reproduced from [14]

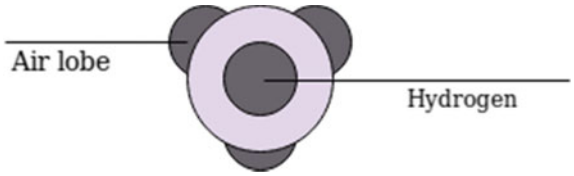

Fig. 11 Three air lobes surround each hydrogen injectors. This geometry is arranged in concentric circular arrays on the flameholder. The combustion creates a diffusion flame above each air/fuel injector. Based on [15]

6 Micromix Injection

Micromixing is proposed as an alternative of premixed combustor systems. There exist several variations of the micromix injector principle. Those include inverse micromixing and the Dry-Low-NO_x approach.

Micromixing is defined as injecting fuel into an oxidizer stream via an impinging jet. It is heavily based on research on "jet-in-cross-flow"-types of problems. The purpose of micromixing is to approach premixed systems' NO_x performance using diffusion flames while avoiding the risks of autoignition and flashback. The following figure illustrates the geometrical setup of a micromix injector (Fig. 12).

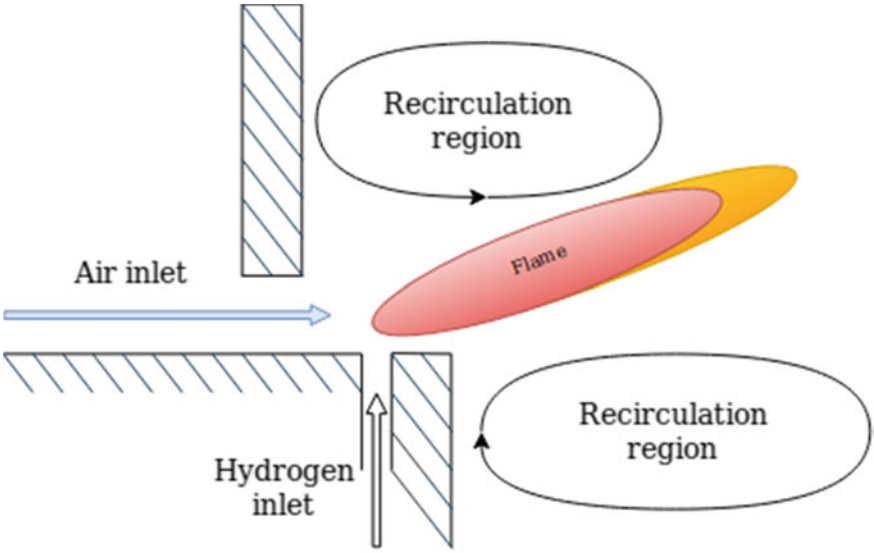

Fig. 12 Micromix injector general geometrical layout. Based on [17]

Currently, micromixing is used both for industrial gas turbines and microturbine applications [18]. There are several factors affecting the mixing capabilities of micromix combustors. These factors include the injection point of hydrogen with respect to the backward-facing step, the injection height of the impinging jet flow, and the combustion region's wall geometry. The injection height of hydrogen immediately affects mixing capabilities: too high an injection speed will prevent the fuel from properly mixing with the oxidizer, causing local stoichiometric conditions which harm emissions. The backward-facing step and combustion region wall geometry directly influence the shape of the recirculating vortices that given the flame its shape—in turn, affecting the uniformity of the temperature profile.

Lee et al. investigated micromix technology, focusing on a flashback-resistant injector [19]. Using closely-space mixing cups, the authors were able to achieve good mixing in a small space, which translated into low NO_x emissions. Three "cup" variations were studied: the S1F3, R1, and R3. The S1F3 cup, previously reported on by Lee et al., uses only radial air inlets offset from the center, thereby introducing a rotational motion in the combustor and increasing mixing [19, 20]. Additionally, there is no taper in the longitudinal direction for the S1F3 cup—the cross-section does not change in size, and fuel is injected in alternating air slots. The R-line cups pair axial-radial air inlets with a diverging cross-section and radial-inflow fuel from a single-point in the axial direction.

The authors conducted a computational fluid dynamics simulation for all three cups—S1F3, R1 with and without swirler. Additionally, an experiment was conducted where the cups were attached to a dilution module, an igniter module, and a quartz liner. The apparatus was then inserted into a pressure vessel where a gas

analyzer was used to measure—among others—NO_x and NO emissions. The salient results are that the S1F3 cup is capable of operating at both a higher and lower adiabatic flame temperature than R-line cups. This affords operational flexibility, under the right conditions (since there is a variation in operating pressure between the data points for lowest and highest adiabatic flame temperature). More importantly, however, is that the S1F3 cup is capable of reaching emissions below 3 ppm, thereby exceeding premixed systems' performance—up to a minimum of 0.3 ppm. This is a considerably low pollutant emission figure. Finally, the authors note that better results may be achieved with further tailoring and optimization of "mixing length, fuel injection type, and adjustment of the final injection layers" [19].

Khandelwal et al. investigated micromix combustors, also working with geometries featuring backsteps [21]. For their analysis, they conducted a computational fluid dynamics simulation on a circular combustor featuring four injectors arranged radially. For the first case, they simulated the injection of hydrogen through each injector, with the oxidizing and diluting air coming from upstream of the radial injectors. In the second case, they changed two of the four injectors to provide air instead of hydrogen. These two cases are illustrated in the following Fig. 13.

Khandelwal et al.'s findings included that introducing air injectors opposite of the hydrogen injectors increased hotspot formation (depicted by higher peak temperatures in Case 2 at $Z = 0$); however, mixing was also enhanced, thereby increasing heat transfer from combustion products to excess air downstream of the injectors. The enhanced mixing earlier in the combustor allowed for its overall length to be halved; because NO_x formation depends on residence time, the combustor generally improved in terms of pollutant emissions performance in the second case as compared to the first.

Kusterer et al. explored the impact of the momentum flux ratio of the impinging jet flow used in micromix combustion [18]. Their findings stipulate that lifted flames were a manifestation of excessive moment flux ratio and tended to increase NO_x production significantly. To avoid this situation, a lower critical injection height was

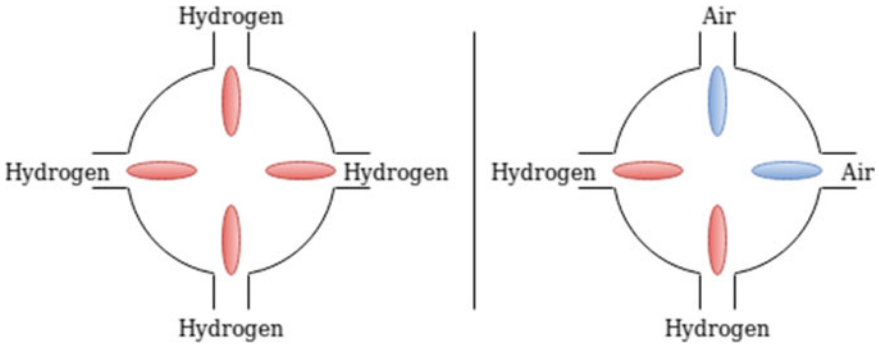

Fig. 13 Longitudinal cut of the micromix combustor. The left case, case (a), reflects having all four injectors supplying fuel, whereas the right case, case (b), corresponds to having two fuel injectors and two air injectors facing each other. Based on [21]

required, which could be achieved via a reduction in the hydrogen injection density or velocity. Alternately, an increase in density or velocity of the airstream impinged on by the hydrogen could alleviate this issue of "over-injecting" hydrogen. Thus, to mitigate the production of harmful emissions, careful design of the injectors and its associated operational parameters like air-guiding panel size, air, and hydrogen mass flow rates, is necessary. With that in mind, the authors identified the critical momentum flux ratio of 1:1 beyond which NO_x formation increased significantly. Additionally, increasing the size of the air-guiding panel, and thus making more air available for the dilution of hot combustion products, reduced the formation of nitrous oxides. In accordance with the thermal formation path of NO_x, the authors found that increasing the equivalence ratio increased the formation of NO_x. Overall, at the critical momentum flux ratio of 1:1, the nitrous oxides formed were at most of 7 ppm dry NO_x at 15% O_2 for the 80% AGP surface area (compared to the reference area) for fixed exit velocity.

The inclusion of a cold flow increased mixing with hot combustion products, thereby further lowering maximum combustion temperatures and thus reducing NO_x production. Micromix performance in terms of emissions metrics is in the range of 1–3 ppm for equivalence ratios of $\Phi = 0.16$–0.36, as reported by Kusterer et al. [18]. This is an improvement over premixed systems, which tend to reach minimal emissions of 3 ppm.

Current research efforts are focusing on harnessing numerical methods to further explore technology. Agarwal et al. investigated the general design space tied to micromix injectors [22]. The authors explored the relationship between various design parameters of micromix injectors and their effect on performance and emissions. The authors found that the recirculation zones determine the flame shape and size, thereby providing the designer with a tool to reduce NO_x-rich regions. Agarwal et al. also concluded that further NO_x reductions could be achieved by further studying the offset distance between the hydrogen and air feeds. Babazzi et al. found in their paper that moderately accurate emissions prediction via numerical methods was achievable using reactor networks, though using higher-fidelity dedicated analysis software would be advisable for final emissions quantification [23]. Also in the vein of further exploring the micromix design space, Ben Abdallah et al. report on the effects of various simulation setup parameters and the sensitivity of the simulation results to the value those parameters have [24]. Parameters investigated include turbulence and its interaction with chemistry, the sensitivity to thermal boundaries, and assessing thermoacoustic instabilities. In essence, Ben Abdallah et al.'s work identifies the key design and simulation parameters that affect the performance of single and arrayed micromix injection systems. Thus, the current efforts are moving towards the optimization of micromix injector geometry, which may translate into a future reduction of nitrous oxide pollutant formation.

A geometrical variation of conventional micromixing, inverse micromixing consists of "reversing the air and fuel supply roles" from baseline micromixing. Specifically, two air jets are impinged into a flow of hydrogen; the mixture is then burned. This version of the micromix injector was investigated by Hendrick et al. [25]. The geometrical arrangement of this type of injector is depicted in Fig. 14.

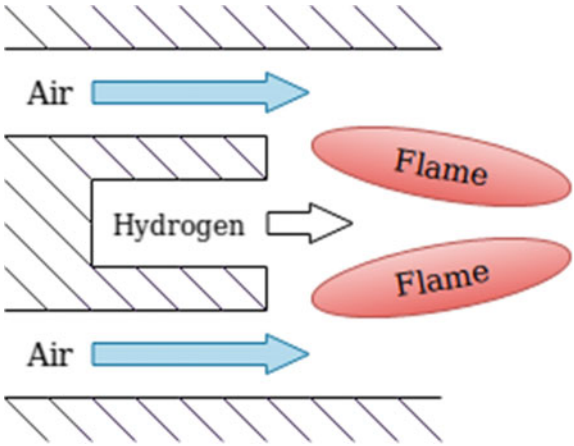

Fig. 14 Inverse micromix injector geometrical layout. Based on [25]

The authors did not identify emission performance directly; however, they reported on burning efficiency instead.

The authors identified two situations of interest: the first, where no preheat conditions were used, and the second, where preheat conditions of 690 K were used. They found that without preheat, for air-fuel ratios of 6 and below ($\Phi = 0.16$ and above), the burning efficiency was of quasi-100%. This was an improvement over the combustor investigated by Funke et al. [26], which had its efficiency drop significantly for air-fuel ratios beyond 4 ($\Phi = 0.25$ and below), characteristic of lean blowout. Using a preheat of 690 K greatly improved burner efficiency, with Funke et al.'s burner maintaining a quasi-100% efficiency up to an air-fuel ratio of 7 before sharply decreasing ($\Phi = 0.14$ and below). Though these numbers do not directly reflect a NO_x formation amount in ppm, they still provide a sense of the efficiency of the burner which could be used to establish a comparison point with other existing hydrogen combustors. Based on these numbers, it is reasonable to conclude that the inverse micromix burner is capable of leaner operation, which can translate into a reduction in nitrous oxide emissions during operation. Future efforts for the inverse micromix injector project include further exploration of geometry effects on performance, test general endurance testing of the microcombustor, and establish emission performance based on direct gas exhaust analysis [25].

The other variation, the Dry-Low-NO_x micromix injector technology is a recent improvement over the "baseline" micromix combustion principle [17, 27]. Specifically, it aims to reduce NO_x formation "by miniaturizing the reaction zone through the creation of multiple micro-flamelets with a typical size of 30–40 mm in length" [28]. Haj Ayed et al. found that, first and foremost, Dry-Low-NO_x micromix combustors needed to be designed from the beginning; retrofitting existing hydrocarbon combustors is not a viable solution [27].

In terms of performance, NO_x emissions depend on two dominant factors. The first is fuel injection height. If the injection height y exceeds the value of y_{crit}, which corresponds to the upper recirculation vortex's shear layer, the hydrogen will burn

under rich conditions and produce significantly more harmful emissions than if it is injected below that critical height [17, 27]. The second dominant factor is the combustor geometry. Increasing the gap between the Air-Guiding Panel (AGP) and the lower surface reduces nitric oxide formation throughout the combustor, though at the cost of flame stability. The recirculation vortices' strength and location are mostly influenced by the blockage ratio of the injector array. Additionally, using the lateral cold-air stream helps reduce the mixture combustion temperature, thereby lowering nitric oxide production [17]. These parameters allow for the Dry-Low-NO_x burner to perform well in terms of emissions. Increasing the energy density of hydrogen while maintaining the equivalence ratio of combustion lowers the overall NO_x formation by several ppm. These benefits are much less clear at lower equivalence ratios, where the DLN combustor generally performs well, generating only 1.7 ppm at equivalence ratios between 0.22 and 0.32 [17].

Clearly, Dry-Low-NO_x technology is capable of bringing low emissions while providing adequate performance with high energy density hydrogen fuels. This kind of performance rivals that of premixed systems.

Like Ben Abdallah for the general micromix technology, Striegan et al. focused their research efforts on establishing the impact of simulation setup parameters on Dry-Low-NO_x development [29]. Their findings include the importance and effects of including wall heating within the setup and enabling heat transfer within the combustion model. Taking into account the heat transfer between the flame and the combustor walls causes the hydrogen jet to accelerate and impinge further into the incoming airstream, thereby increasing flame temperature and thus NO_x emissions. This is an aspect of numerical methods that should be taken into account when evaluating general thermal and emissions performance for micromix combustors.

Finally, Funke et al. have pushed the envelope of the Dry-Low-NO_x technology by validating that the combustion mechanism by Hawkes et al. performs the best in estimating the performance of a micromix DLN systems [30]. The authors found that the Hawkes-based DARS-CFD combustion model performed better than other models (e.g., Li et al. Frassoldati et al. hybrid eddy break-up model), providing more accurate data. This research is directly contributing towards achieving the future goals of Dry-Low-NO_x technology, namely increasing energy density, reducing peak flame temperatures, and ensuring a more uniform temperature profile exists at the combustor's exit [27]. These improvements will certainly bring DLN technology towards even better performance.

7 Summary

Comparing various hydrogen burner injection technologies is difficult when emissions are reported in so many different ways. However, the bottom line is that non-premixed systems and premixed systems are reaching the same level of roughly

3 ppm of NO_x emitted. Some technologies, like micromix injections and Dry-Low-NO_x, are capable of breaching that floor and reaching emission levels of less than 2 ppm.

Looking at the bigger picture, these are emission levels that may or may not be achieved depending on the type of system the injector is implemented in. For instance, land-based gas turbines used for power generation are likely to run at lower emission levels around the clock, whereas aircraft of any size will undoubtedly require throttle variations that will bring the actual emissions towards and away from the optimal minimum.

Nevertheless, for now, hydrogen injection and combustor technology are showing significant improvement over existing emissions performance from fossil fuel combustors. Hopefully, society will continue to develop hydrogen technology—especially for the aerospace sector—so that the next generations may have a cleaner future.

References

1. Benson C, Ingram J, Battersby P, Mba D, Sethi V, Rolt A (2019) An analysis of civil aviation industry safety needs for the introduction of liquid hydrogen propulsion technology. In: Proceeding of ASME turbo expo 2019 turbomach. technology conference & expo, pp 1–11
2. Anderson DN (1976) Emissions of oxides of nitrogen from an experimental premixed-hydrogen burner. Lewis Research Center, Cleveland, OH
3. Cappelletti A, Martelli F (2017) Investigation of a pure hydrogen fueled gas turbine burner. Int J Hydrogen Energy 42(15):11
4. Cam O, Yilmaz H, Tangoz S, Yilmaz I (2017) A numerical study on combustion and emission characteristics of premixed hydrogen air flames. Int J Hydrogen Energy 42(40):25801–25811
5. Marek CJ, Smith TD, Kundu K (2005) Low-emission hydrogen combustors for gas turbines using lean direct injection. In: NASA Technical Memorandum, pp 1–27
6. Frolov SM, Aksenov VS, Ivanov VS, Shamshin IO (2015) Large-scale hydrogen-air continuous detonation combustor. Int J Hydrogen Energy 40(3):1616–1623
7. Jourdaine N, Tsuboi N, Ozawa K, Kojima T, Koichi Hayashi A (2019) Three-dimensional numerical thrust performance analysis of hydrogen fuel mixture rotating detonation engine with aerospike nozzle. Proc Combust Inst 37(3):3443–3451
8. Zhou S, Ma H, Li S, Zhou C, Liu D (2018) Experimental study of a hydrogen-air rotating detonation engine with variable air-inlet slot. Int J Hydrogen Energy 43(24):11253–11262
9. Anand V, George AS, Driscoll R, Gutmark E (2015) Characterization of instabilities in a rotating detonation combustor. Int J Hydrogen Energy 40(46):16649–16659
10. Shudo T, Omori K, Hiyama O (2008) NO_x reduction and NO_2 emission characteristics in rich-lean combustion of hydrogen. Int J Hydrogen Energy 33(17):4689–4693
11. Shahed SM, Newhall HK (1971) Kinetics of nitric oxide formation in propane-air and hydrogen-air-diluent flames. Combust Flame 17(2):131–137
12. Khandelwal B, Roy S, Lord C, Blakey S (2014) Comparison of vibrations and emissions of conventional jet fuel with stressed 100% SPK and fully formulated synthetic jet fuel. Aerospace 1(2):52–66
13. Bolaños F, Winkler D, Piringer F, Griffin T, Bombach R, Mantzaras J (2013) Study of a rich/lean staged combustion concept for hydrogen at gas turbine relevant conditions. In: Proceedings of the ASME turbo expo 2013 power land, sea air, pp 1–9
14. Gobbato P, Masi M, Toffolo A, Lazzaretto A (2011) Numerical simulation of a hydrogen fuelled gas turbine combustor. Int J Hydrogen Energy 36(13):7993–8002

15. Weiland NT, Sidwell TG, Strakey PA (2011) Testing of a hydrogen dilute diffusion array injector at gas turbine conditions. Combust Fuels Emiss Parts A B 2:1239–1247
16. Weiland NT, Sidwell TG, Strakey PA (2013) Testing of a hydrogen diffusion flame array injector at gas turbine conditions. Combust Sci Technol 185(7):1132–1150
17. Haj Ayed A, Kusterer K, Funke HH-W, Keinz J, Striegan C, Bohn D (2015) Improvement study for the dry-low-NO_x hydrogen micromix combustion technology. Propuls Power Res 4(3):132–140
18. Funke HH-W et al (2012) Numerical and experimental characterization of low NO_x micromix combustion principle for industrial hydrogen gas turbine applications. In: Proceedings of the ASME turbo expo 2012 power land, sea air, p 1069
19. Lee H, Hernandez S, McDonnell V, Steinthorsson E, Mansour A, Hollon B (2009) Development of flashback resistant low-emission micro-mixing fuel injector for 100% hydrogen and syngas fuels. In: Proceedings of the ASME turbo expo 2009 power land, sea air, pp 411–419
20. Hernandez SR, Wang Q, McDonell V, Mansour A, Steinthorsson E, Hollon B (2008) Micro-mixing fuel injectors for low emissions hydrogen combustion. In: Proceedings of the ASME turbo expo 2008 power land, sea air, no x, pp 1–11
21. Khandelwal B, Li Y, Murthy P, Sethi V, Singh R (2011) Implication of different fuel injector configurations for hydrogen fuelled micromix combustors. In: Proceedings of the asme turbo expo 2011 power land, sea air, pp 293–298
22. Agarwal P, Sun X, Gauthier PQ, Sethi V (2019) Injector design space exploration for an ultra-low NO_x hydrogen micromix combustion system. In: Proceedings of the ASME turbo expo 2019 turbomach. Technology conferences expo, pp 1–13
23. Babazzi G, Agarwal P, McClure J, Sethi V, Gauthier PQ (2019) NO_x emissions predictions for a hydrogen micromix combustion system. In: Proceedings of the ASME turbo expo 2019 turbomach. Technology conferences Expo
24. Ben Abdallah R, Sethi V, Gauthier PQ, Rolt AM, Abbott D (2018) A detailed analytical study of hydrogen reaction in a novel micromix combustion system. In: Proceedings of the ASME turbo expo 2018, p 11
25. Robinson AE, Funke HH-W, Wagemakers R, Grossen J, Bosschaerts W, Hendrick P (2009) Numerical and experimental investigation of a micromix combustor for a hydrogen fuelled [micro sign]-scale gas turbine. In: Proceedings of the ASME turbo expo 2009 power land, sea air, pp 253–261
26. Funke HH-W, Rönna U, Robinson AE (2008) Development and testing of a 10 kW diffusive micromix combustor for hydrogen-fuelled u-scale gas turbines. In: Proceedings of the ASME turbo expo 2008 power land, sea air, pp 1–8
27. Haj Ayed A, Kusterer K, Funke HHW, Keinz J, Bohn D (2017) CFD based exploration of the dry-low-NO_x hydrogen micromix combustion technology at increased energy densities. Propuls Power Res 6(1):15–24
28. Funke HHW, Beckmann N, Keinz J, Abanteriba S (2018) Comparison of numerical combustion models for hydrogen and hydrogen-rich syngas applied for dry-low-NO_x-micromix-combustion. J Eng Gas Turbines Power 140(8):081504
29. Striegan C et al (2017) Numerical combustion and heat transfer simulations and validation for a hydrogen fueled 'micromix' test combustor in industrial gas turbine applications. In: Proceedings of the ASME turbo expo 2017 power land, sea air, pp 1–10
30. Funke HHW, Beckmann N, Abanteriba S (2019) An overview on dry low NO_x micromix combustor development for hydrogen-rich gas turbine applications. Int J Hydrogen Energy 44(13):6978–6990

Aerodynamic Behavior of Rear-Tubercle Horizontal Axis Wind Turbine Blade

Ryoichi S. Amano

1 Introduction

Wind turbines are used in most renewable energy systems, including aerodynamics, wake studies, and self-healing of aerodynamic components such as for the exploration of the vortex wakes [1], a simulation of the flow on a wind turbine blades [2], a turbine blade design [3], and self-healing of the turbine blades [4]. The aerodynamic behavior of wind turbines is discussed by Vermeer et al. [5]. In this chapter, building and testing of the airfoil designs are discussed, along with fixing of a current problem that has been found with the column that holds the wind turbine.

Focus on the details of an airfoil design along with the turbine column to reach a steady speed that matches the resident frequency of the support column is discussed. The current column oscillates under resonance frequency during testing. This issue was successfully fixed by adding a collar and two support bars to the column. This builds on the original idea to only add one support bar that was welded to the column. This change was made to avoid welding to the column and the base of the column, which would result in a permanent change. To prove that the current design does reduce vibration, preliminary baseline testing was done. This approach is then followed by experimenting with the same setup as initial testing to see if the supports were, in fact, an improvement [6].

Additional improvements to the wind turbine column are the creation of motor attachment plates and a new turbine blade hub. The motor attachment plates were created to handle the new motor that is operated while running the tests. The plates have been designed to snuggly hold the motor while also minimizing the cost to

R. S. Amano (✉)
Department of Mechanical Engineering, University of Wisconsin-Milwaukee, Milwaukee, WI 53211, USA
e-mail: amano@uwm.edu

© Springer Nature Singapore Pte Ltd. 2021

A. De et al. (eds.), *Sustainable Development for Energy, Power, and Propulsion*, Green Energy and Technology,
https://doi.org/10.1007/978-981-15-5667-8_22

make it. This arrangement not only decreases the cost to build the part but also has less impact on airflow characteristics, making testing more accurate. The new hub allows the new motor for using in the measurements.

2 Experimental Setup

2.1 Test Facility

The wind tunnel laboratory is used to experiment with the current work. As in Fig. 1, it has eight layers of screens with hexagonal-shaped cells in the inlet section to reduce large-scale turbulence. The first section is the contraction section which has an inlet area of about 9.3 m^2. Then, the test section comes with dimensions of 1.2 m $\times$ 1.2 m $\times$ 2.43 m and the cross-sectional area of 1.4 m^2. It has polycarbonate walls to provide a smooth surface, hence eliminate the boundary layer effect as much as possible. The final section is the diffuser section which ends up with six-blade suction fan, which is of 1.83 m rotor diameter attached to 25.4 kW motor controlled by a variable frequency drive (VFD) to obtain different wind speeds.

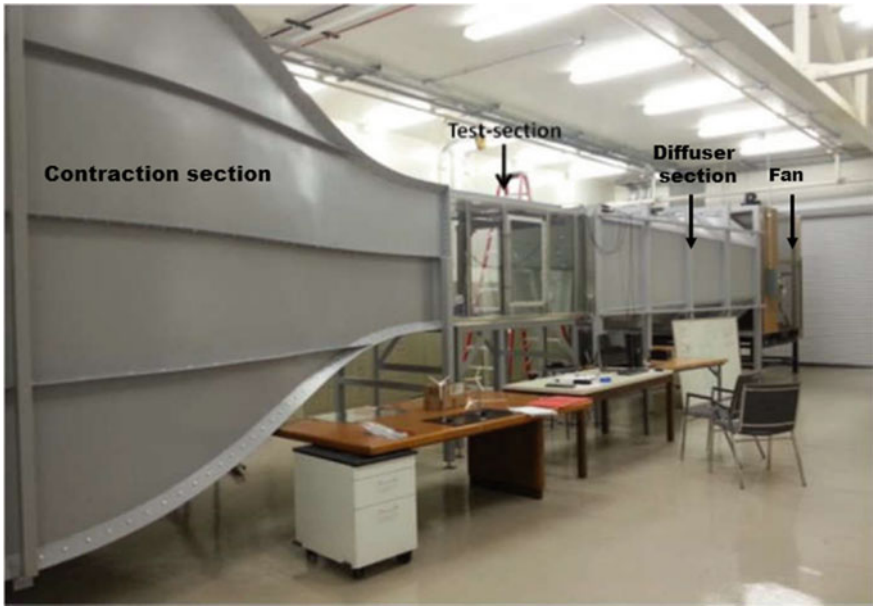

Fig. 1 Wind tunnel for the testing of wind turbine blade performance

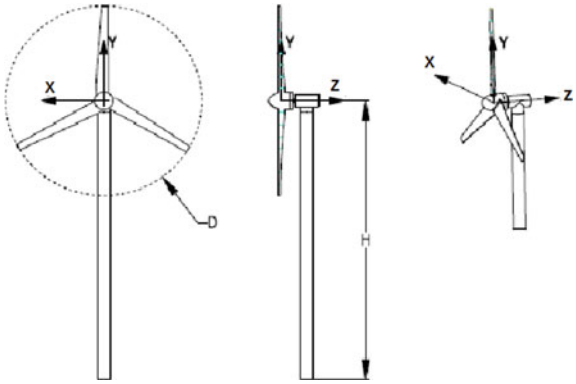

Fig. 2 Model wind turbine design

2.2 Model Wind Turbine at UWM Lab

The design of the model used in this work is demonstrated in Fig. 2. This model was built by Ibrahim et al. [7]. It is a small-scale three-blade model of 20.3 cm rotor diameter made from ABS plastic. Its tower is made from 12.7-mm-diameter steel rod with a hub height of 30.5 cm.

2.3 Hot Wire Probe and Anemometry

The Dantec Model 55P61 miniature wire probe is used in this work for velocity measurement. A three-axis traverse system mounted on the top panel is used to position the probe upon command. It is a dual-sensor, cross-wire-type probe designed to measure the axial and vertical velocities. The probe wires are aligned such that they are in the same plane of the mean flow, with the plane of the sensors parallel to the probe axis.

The 55P61 has two platinum-plated tungsten, 5 mm diameter, wires welded to the probe at 45° to each other and can measure velocity components within a ±45° cone. The range of velocity that can be measured by the probe is from 0.05 m/s to 500 m/s.

Two Dantec 54T30 miniature constant temperature anemometers (CTAs) are used. They can provide a 0–5 V analog output voltage based on the characteristics of the probe. The offset voltage on each wire was approximately 1.3 V at zero velocity.

3 Aerofoil Design

The airfoil construction does not just carry the weight and forces caused by the wing itself but also loads caused by the varying wind speed. Generally, a tubular construction of concrete or steel is used. Since we are building a smaller scale, aluminum was used. In the process of designing the structure, investigation of both designs showed problems of loss of stability.

A few changes were made to meet the challenge of having the best support under any given velocity within our range of 5–12 m/s. The design consists of two stands with the shape of the letter "L" bolted to a 6.35 mm plate between them. The L stands are 26.67 cm apart connected by a 1.27-cm-diameter steel rod. The stands are 58.42 cm tall and 16.51 cm wide, located vertically on the aluminum plate. The airfoil is mounted on a rotating rod that gives the ability to adjust the angle of attack. The result is a two-stand structure design.

A finite element analysis (FEA) was performed in Creo Parametric on the structure. An FEA-based design begins with the selection of the material type, 6061 aluminum, how accurate the results should be, and the direction and magnitude of the applied load. Reliable results of finite element data were achieved by creating 3D parts of the structure, followed by meshing with higher-order elements to produce more accurate results.

3.1 NACA 4412 Airfoil

Figure 3 shows a typical NACA 4412. The four-digit number is used to describe the geometry of the airfoils' profile. The following definitions explain the system further:

- First digit: Maximum camber in percent chord
- Second digit: Location of the maximum camber along the chord line (from leading edge)
- Third and fourth digits: Maximum thickness in percent chord.

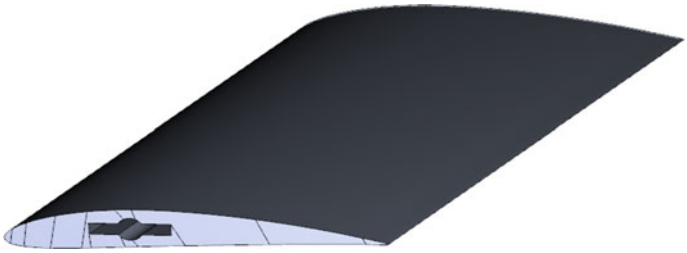

Fig. 3 NACA 4412

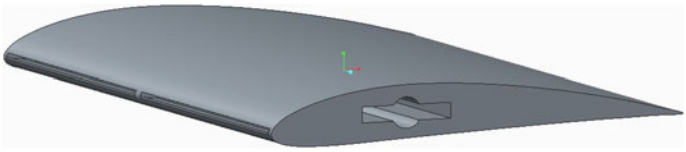

Fig. 4 NACA 4412 slotted

The design has a chord length of 7 in, giving the following dimensions by using the airfoil tools website:

- Max camber: 0.28 in. (4% × 7 in.)
- Location of max camber: 2.8 in. (0.4 × 7 in.)
- Max thickness: 0.84 in. (12% × 7 in.)

After the dimensioning of the airfoil was complete, a model was created in Creo Parametric 2.0 as shown in Fig. 3. To mount the airfoil to the structure, a key slot was made for a rod assembly to be inserted. The 0.5-in. diameter rod has two cross-members along its axis. The airfoil will slide onto the rod assembly and be tightened in place with a nut on each end. This design will disallow any movement from the airfoil while being tested.

3.2 Slotted Airfoil

In an attempt to understand how a simple change in geometric features might affect the aerodynamics of the NACA 4412 airfoil, a slotted front-edge design was chosen. This is a modified version of the NACA 4412 with small inlets on the front edge of the airfoil. The design was adopted from previous semesters of research at UWM. The inlets allow for airstreams to be split upon initial contact with the airfoil with some airstreams flowing above and below the airfoil as well as through the slots. Figure 4 shows a CAD model of the slotted hole blade created in Creo Parametric 2.0.

3.3 Tubercle Airfoil

Similar to the slotted airfoil, the tubercle design concept has been adopted from past semesters of research. There are several variations from which this design is based: biomimetic—humpback whales and saw blades. The concept of design used for this blade is based on the biomimetic approach. The tubercles, in theory, are believed to help separate the streamlines, reducing turbulent flow, which ultimately reduces drag. In nature, it has been discovered that Humpback Whales can maneuver with

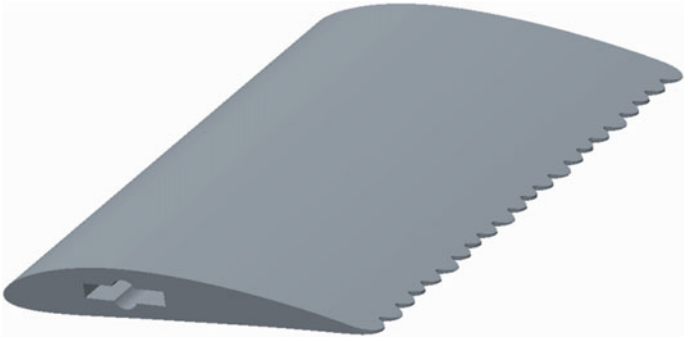

Fig. 5 Tubercle blade design

incredible movements when considering their immense size. The tubercles have been identified to help minimize stalling and increase lift forces, sometimes up to 16%.

Another theorized benefit for the tubercle design is it reduces acoustic energy or noise. Since noise can be defined as energy, it would be advantageous to minimize the noise developed. Siemens currently produces tubercle add-ons for pre-assembled wind turbines. The add-ons work on the same premise of our design, though they allow for a cost-effective alternative for companies to use. Siemens has outlined that about 1db equates to 2–4% of the annual energy production [8]. With improved noise characteristics, the wind turbine would be much more efficient and strengthen consumer outlook toward noisy wind turbines. In this project, the analysis undertaken was limited to the flow characteristics, and acoustic analysis has been omitted.

Figure 5 shows a CAD model of tubercle turbine blade design created in Creo Parametric 2.0. Here, the tubercle is applied to the trailing edge side.

4 Simulation Technology

The computational method should be carefully selected due to its accuracy totally based on the selection [9]. The simulation technique of turbulence prediction is based on the large-eddy simulation [10]. The domain of all three setups was chosen to resemble the wind tunnel in the UWM USR building. The wind tunnel test section has a 1.2192 m $\times$ 1.2192 m cross-section with a length of 2 m. Assemblies of the blades and structure were imported into the program together to run a simulation as close to the actual test setup as possible. Doing this allows for easy comparison between CFD results and actual results acquired from wind tunnel testing.

The CFD tests were run at wind speeds of 5, 8, and 12 m/s. A zero-degree angle of attack was chosen as this research will be a baseline for future testing of these airfoil designs.

5 NACA 4412 CFD Analysis

5.1 Velocity

Increasing the velocity shows similar wake regions early in the iteration process for all three speeds. These velocity profiles are a good visualization of the turbulence occurring behind the 4412 airfoils in the baseline case of a zero-degree angle of attack.

The velocity contours are shown in Fig. 6a through 6c for different approaching velocity, 5 m/s, 8 m/s, and 12 m/s, respectively. As the velocity increases, the eddy appearing close to the trailing edge moves toward the blade surface on the suction side.

5.2 Pressure

Pressure contours are shown in Fig. 7a–c for three different approaching velocities, 5, 8, and 12 m/s. The pressure is similarly distributed at all three wind speeds. The low pressure at the top of the blade and higher pressure below show a pressure gradient providing the lift force. As the pressure increases at each wind speed, so does the lift force at the point. The pressure drop from the leading to the trailing edges of the blade is the source of drag.

5.3 Slotted-Blade CFD Analysis

5.3.1 Velocity

The velocity contours for the flows over the slotted turbine blade are shown in Fig. 8a through 8c for different approaching velocity, 5 m/s, 8 m/s, and 12 m/s, respectively. As the velocity increases, the eddy appearing close to the trailing edge moves toward the blade surface on the suction side.

The velocity profiles of the slotted airfoil give a visualization of the flow moving through the slot at the leading edge. Lower velocity through the slot implies a pressure increase.

5.3.2 Pressure

Pressure contours for the flows over the slotted turbine blades are shown in Figs. 9a–c for three different approaching velocities, 5, 8, and 12 m/s. The pressure is similarly distributed at all three wind speeds. The low pressure at the top of the blade and higher

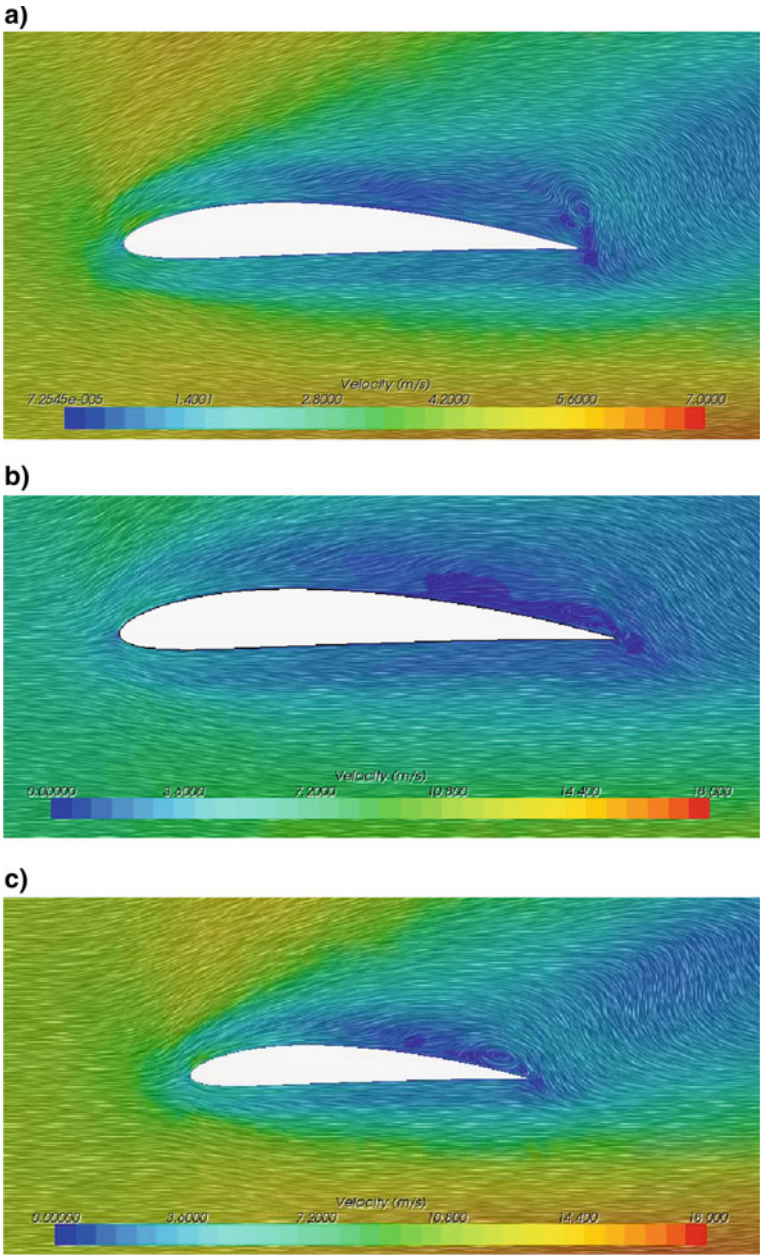

Fig. 6 **a** 4412 velocity profile at 5 m/s. **b** 4412 velocity profile at 8 m/s. **c** 4412 velocity profile at 12 m/s

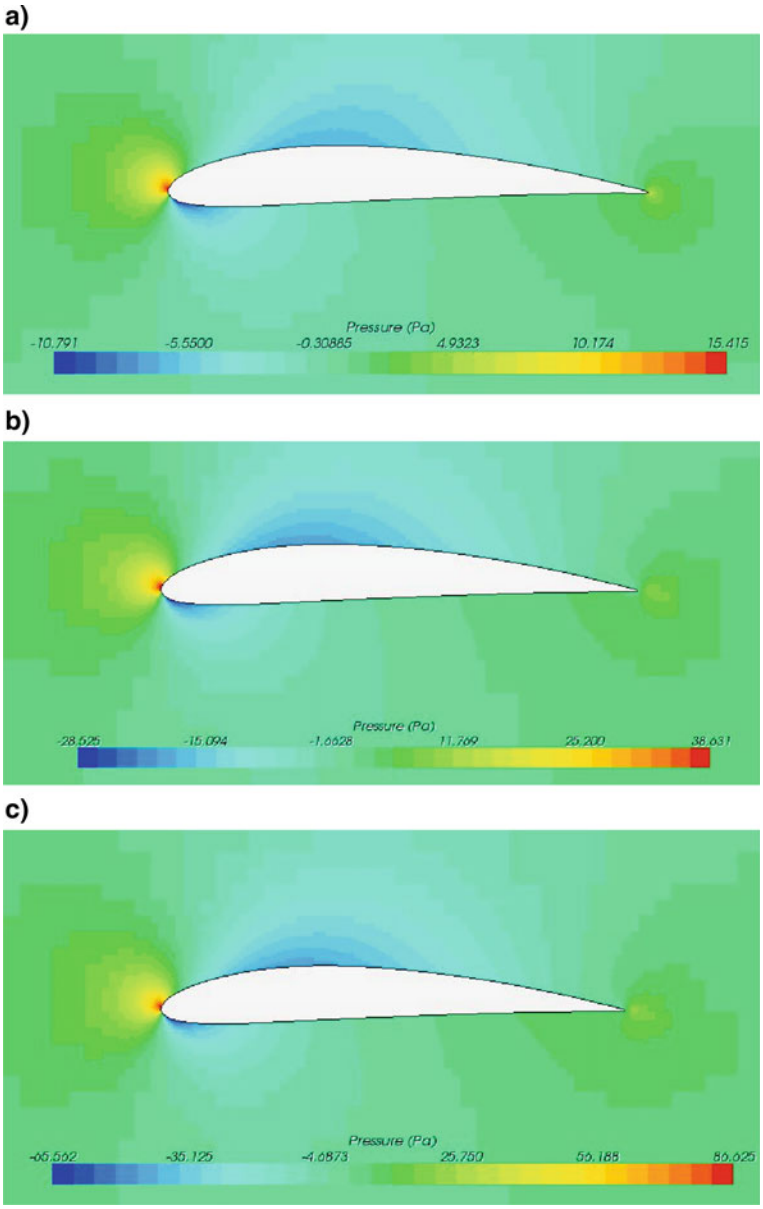

Fig. 7 **a** 4412 pressure distribution at 5 m/s. **b** 4412 pressure distribution at 8 m/s. **c** 4412 pressure distribution at 12 m/s

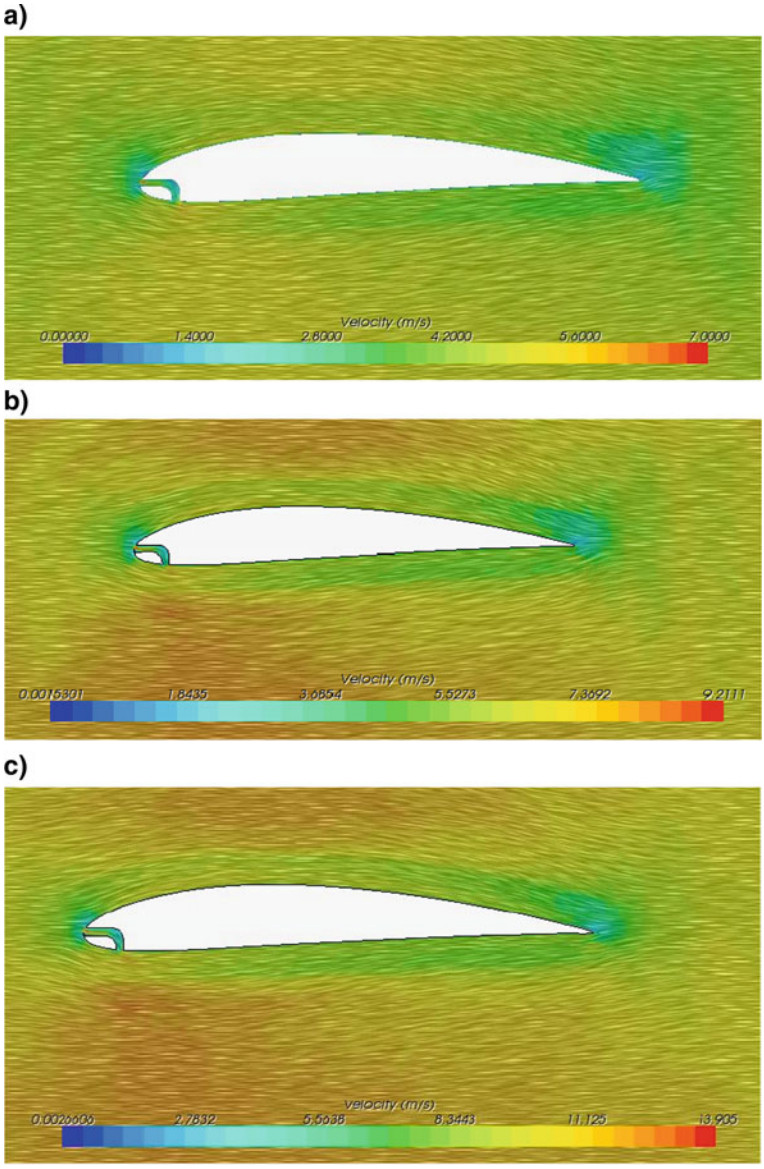

Fig. 8 **a** Slotted velocity profile at 5 m/s. **b** Slotted velocity profile at 8 m/s. **c** Slotted velocity profile at 12 m/s

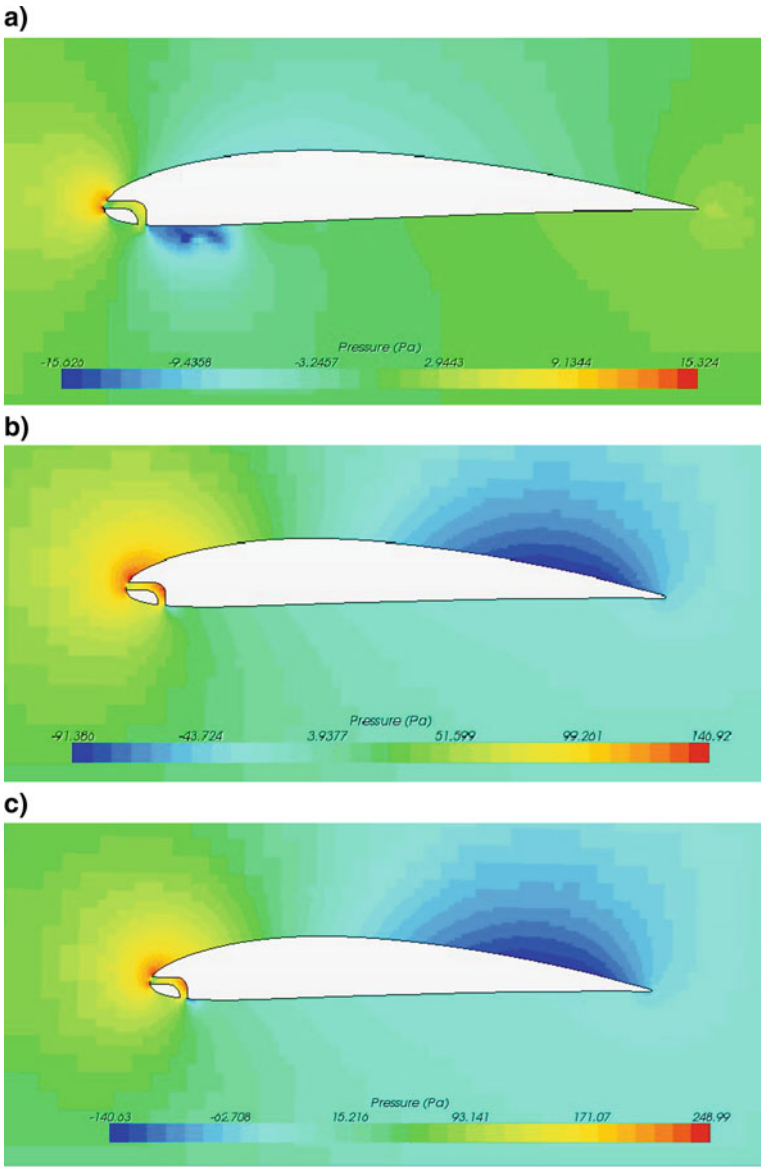

Fig. 9 **a** Slotted pressure distribution at 5 m/s. **b** Slotted pressure distribution at 8 m/s. **c** Slotted pressure distribution at 12 m/s

pressure below show a pressure gradient providing the lift force. As the pressure increases at each wind speed, so does the lift force at the point. The pressure drop from the leading to the trailing edges of the blade is the source of drag.

The pressure distributions for the slotted blade show the low-pressure sections on the top edge of the blade moving more toward the rear. This will produce greater lift at the rear of the blade than the front. The pressure differential from front to rear of the blade implies a larger drag force than the standard 4412 design. This slot geometry proves to have worse characteristics than expected as the pressure is high at the entrance versus the exit. High pressure exiting the slot would improve the blade lift force.

6 Tubercle-Blade CFD Analysis

The velocity contours for the flow with 5 m/s over a tubercle blade design are shown in Fig. 10a, b. The pressure contours for the same case are shown in Fig. 10c, d.

From the Fig. 10a through 10d, it is clear that the velocity is higher along to the top edge meaning higher pressure must be present along the bottom edge, adhering to Bernoulli's principle. The two figures below show the pressure distribution and verify Bernoulli's principle with lower pressure on the top surface.

The velocity contours for the flow with 8 m/s over the tubercle turbine blade are shown in Fig. 11a, b.

As we increased the wind velocity to 8 m/s, the blade had a much more profound interaction with the airstreams as apparent in Fig. 11a. From Fig. 11b, you can see that velocity is slightly higher along the tubercles as oppose to further from the tubercles. From this image, it is clear to see some impact the tubercles pose on airflow characteristics.

The velocity contours for the flow with 12 m/s over the tubercle turbine blade are shown in Figs. 12a, b.

Increasing the wind velocity to 12 m/s, the effects are much more apparent. From Fig. 12a, the point of separation along the blade body is in the last third of the blade body. Similarly, as the 8 m/s analysis, the tubercles seem to induce a slightly higher area of velocity, meaning less pressure immediately after the blade.

The pressure contours with the flow of 12 m/s are shown in Fig. 12c, d.

From Figs. 12b through 12d, it is apparent to see the high-pressure region along the leading edge of the blade and the low-pressure region along the trailing edge of the blade.

7 Experimental Results for Rotating Blades

Figure 13 shows the winglet turbine blades to compare with the other designs of the turbine blades as mentioned in the preceding section.

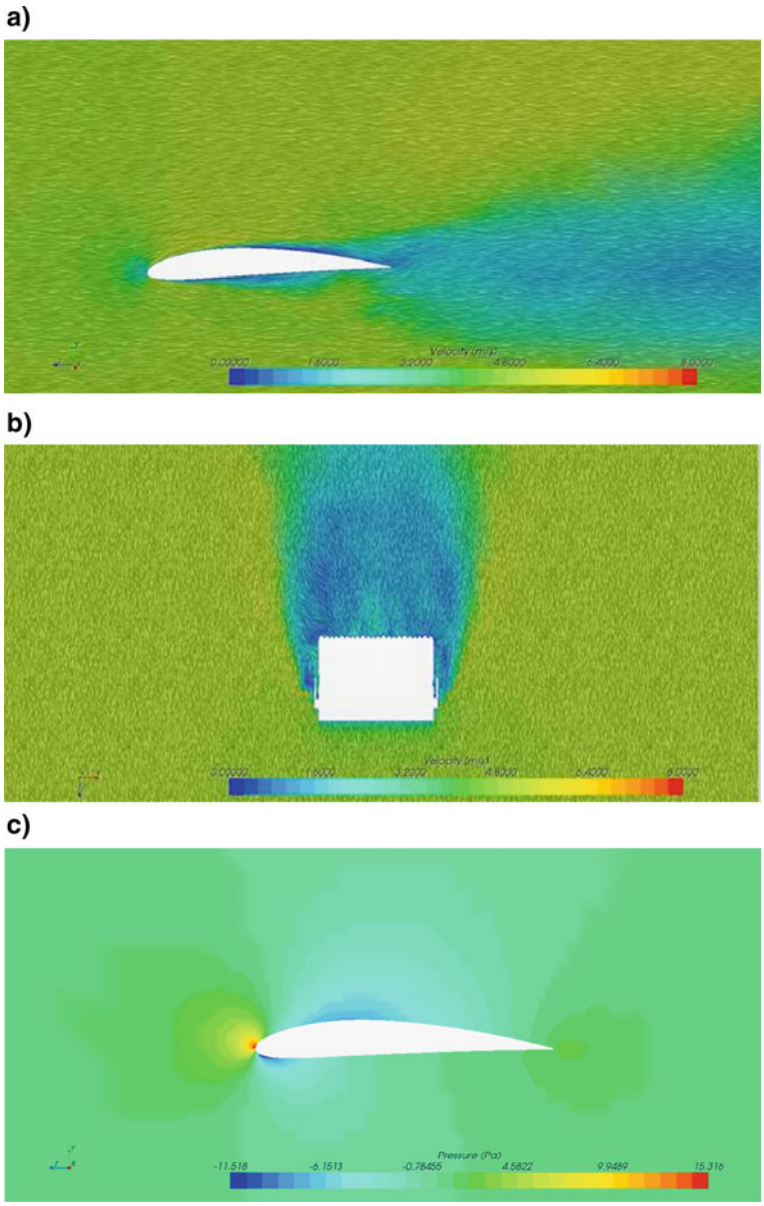

Fig. 10 **a** Tubercle velocity vertical profile at 5 m/s. **b** Tubercle velocity horizontal profile at 5 m/s. **c** Pressure vertical profile at 5 m/s. **d** Pressure horizontal profile at 5 m/s

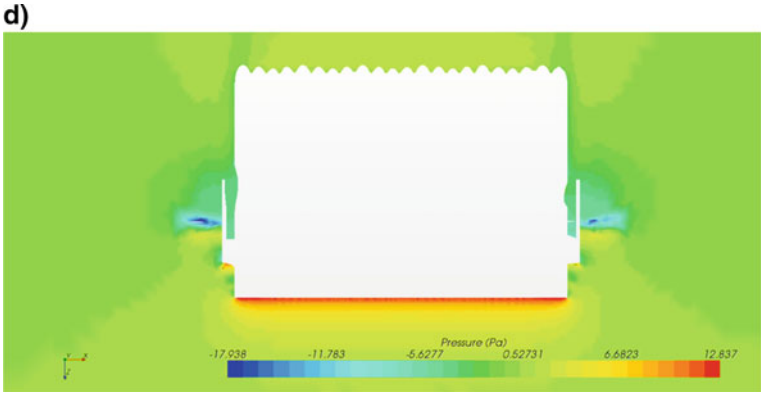

Fig. 10 (continued)

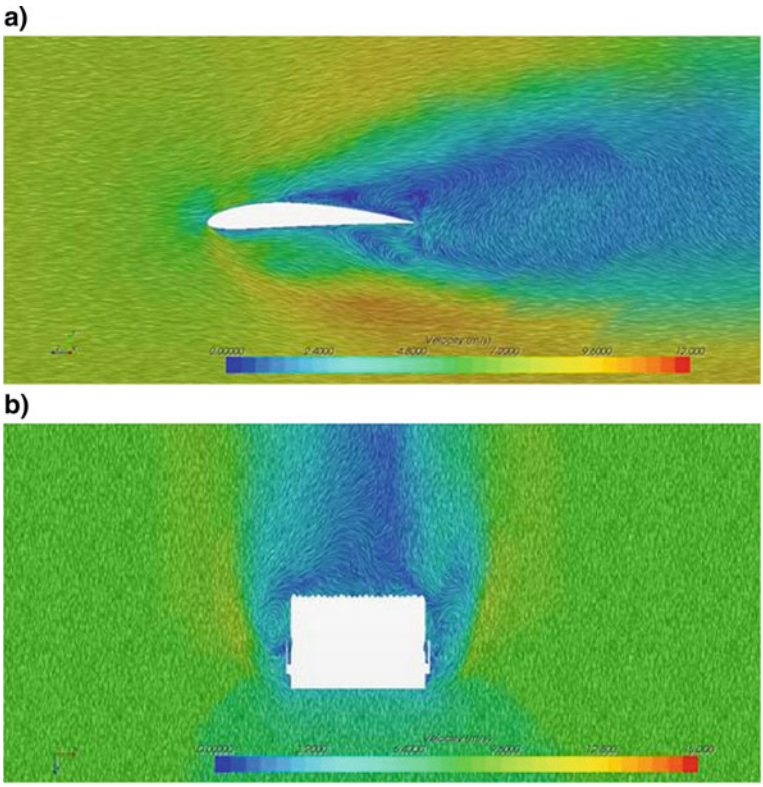

Fig. 11 **a** Tubercle velocity vertical profile at 8 m/s. **b** Tubercle velocity horizontal profile at 8 m/s

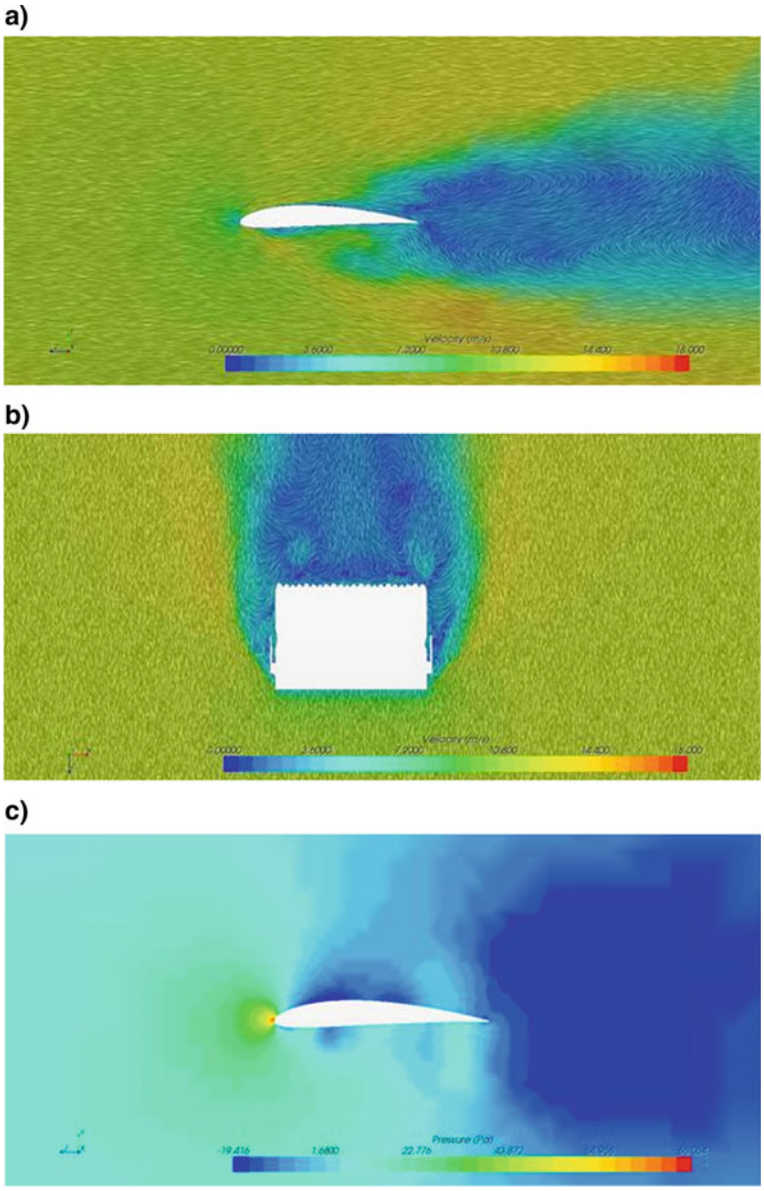

Fig. 12 **a** Tubercle velocity vertical profile at 12 m/s. **b** Tubercle velocity horizontal profile at 12 m/s. **c** Pressure vertical profile at 12 m/s. **d** Pressure horizontal profile at 12 m/s

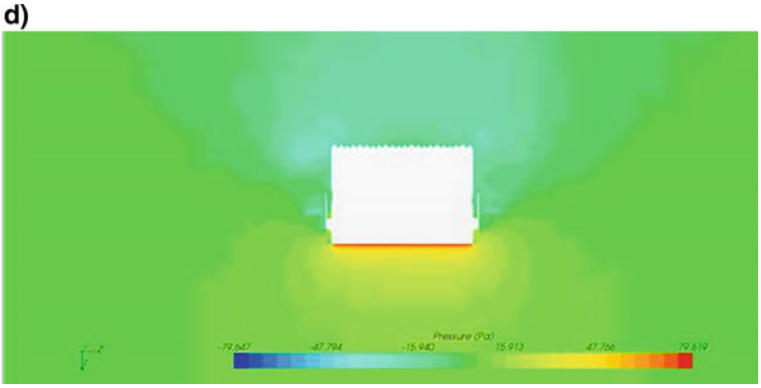

Fig. 12 (continued)

Fig. 13 Blades with winglet

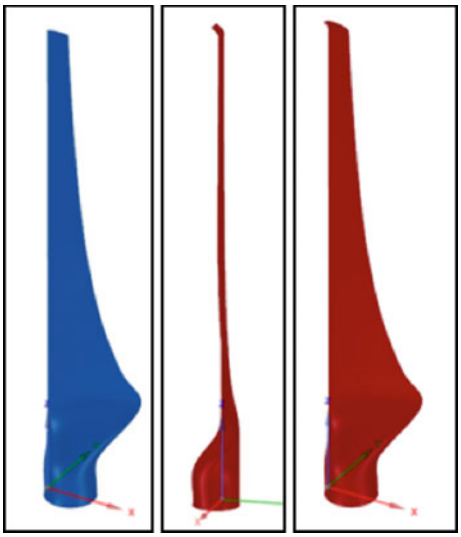

Figure 14 shows the power performance with all the rotating turbine blades. For most of the wind speed range, the slotted turbine performs the best among all. The winglet turbine blade shows the second superior performance in the production of power. However, the straight baseline design of turbine blade performs nearly the same as the winglet turbine blades in the wind speed range less than 11 m/s. It was found that the tubercle turbine blade shows the lowest among all the turbine blades.

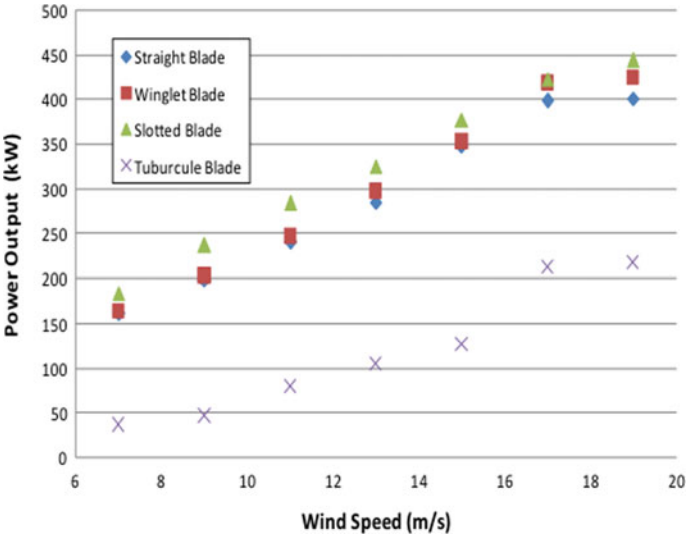

Fig. 14 Comparison of the results with different designs of the turbine blades (rotating case)

8 Conclusions

Through this investigation, the following findings emerged.

1. The slotted turbine blades demonstrated the best power performance gains among all the turbine blades examined here. This observation is mainly supported by the fact that the slotted blade allowed for the wind to enter the blade body, which contributed to added momentum for the lift force inside the blade body.
2. The tubercle wind turbine blade showed the lowest performance when compared to the blade designs examined here.
3. Winglet wind turbine performed just as well as the straight turbine blade with a slight superiority in power gains for the wind speed above 11 m/s.

References

1. Massouh F, Dobrev I (2007) Exploration of the vortex wake behind of wind turbine rotor. J Phys Conf Ser 75:012036
2. Jackson RS, Amano RS (2017) Experimental study and simulation of a small-scale horizontal-axis wind turbine. Trans ASME J Energy Resour Technol 139(5):051207
3. Beyhaghi S, Amano RS (2017) Investigation of flow over a wind turbine blade airfoil using a hybrid detached eddy simulation–algebraic stress turbulence model. Trans ASME J. Energy Resour Technol 139(5):051204

4. Arun Kumar Koralagundi Matt, Saman Beyhaghi, Ryoichi S. Amano, Jie Guo (2017) Self-Healing of Wind Turbine Blades Using Microscale Vascular Vessels, J. Energy Resour. Technol 139(5):051208
5. Vermeer LJ, Sorensen JN, Crespo A (2003) Wind turbine wake aerodynamics. Prog Aerosp Sci 39:467–510
6. Ibrahim M, Alsultan A, Shen S, Amano RS (2015) Advances in horizontal axis wind turbine blade designs: introduction of slots and tubercle. Trans ASME J Energy Resour Technol 137
7. Ibrahim AS (2015) Advances in horizontal axis wind turbine blade de-signs: introduction of slots and tubercle. ASME Trans J. Energy Resour Technol 137: 051205-1
8. Siemens (2019, September) Wind turbine technology. https://www.siemens.co.uk/education/pool/whats-new/a4siemens-lessonv1.pdf
9. Amano RS, Arakawa H, Suga K (2014) Turbulent heat transfer in a two-pass cooling channel by several wall turbulence models. Int J Heat Mass Trans (Impact Factor) 77: 406–418
10. Hattori, H., Umehara, T., and Nagano, Y (2013) Comparative Study of DNS, LES and Hybrid LES/RANS of Turbulent Boundary Layer with Heat Transfer Over 2d Hill, Flow, Turbulence and Combustion, 90: 491–510

Methanol-Based Economy: A Way Forward to Hydrogen

Naveen Kumar, Mukul Tomar, Ankit Sonthalia, Sidharth, Parvesh Kumar, Harveer S. Pali, and Dushyant Mishra

1 Introduction

The problem pertaining to the depletion of fossil fuels has been felt for a long time. The transportation and power sectors are heavily dependent upon petroleum-derived fuels for the last many decades. However, concern about long-term availability of these fuels coupled with environmental degradation has triggered extensive research in the area of alternative fuels [1–3]. Although the use of renewable energy sources has risen a lot in recent years, fossil fuels will remain the primary source of supply for the enormous demand in the future. It is due to the unavailability of cheaper, economic, and easier availability of alternative energies. However, the dependence on fossil fuels which is currently 81% will only slightly be reduced to 79% in the future, which deflect a negligible decrease in the consumption rate [4]. At present, it

N. Kumar (✉) · M. Tomar · A. Sonthalia · Sidharth · P. Kumar · D. Mishra
Centre for Advanced Studies and Research in Automotive Engineering, Delhi Technological University, Bawana Road, Delhi 110042, India
e-mail: naveenkumardce@gmail.com

A. Sonthalia
Department of Automobile Engineering, SRM IST, NCR Campus, Ghaziabad Uttar Pradesh, 201204, India

Sidharth
Department of Mechanical and Automation Engineering, Maharaja Agrasen Institute of Technology, Delhi, India

P. Kumar
Department of Mechanical Engineering, Vaagdevi College of Engineering, Warangal 506005, India

H. S. Pali
Department of Mechanical Engineering, National Institute of Technology Srinagar, Srinagar, India

© Springer Nature Singapore Pte Ltd. 2021

A. De et al. (eds.), *Sustainable Development for Energy, Power, and Propulsion*, Green Energy and Technology,
https://doi.org/10.1007/978-981-15-5667-8_23

is predicted that the world is at its peak rate of fossil fuels production and consumption, which is causing unprecedented perturbation in the prices [5, 6]. The USA is the largest consumer of energy, which will be surpassed by China in the next ten years. According to the International Energy Agency (IEA, 2017) report, China would become the largest consumer of the energy sources, and its demand will keep on increases up to the year 2040. China is followed up by a rapidly growing nation like India and the Association of Southeast Asian Nations. The International Energy Economics Japan (IEEJ, 2018) forecasted that the consumption of India and Association of Southeast Asian Nation would become equal to China by 2050 [7].

In the second half of 2014, crude oil prices reported a sudden hike due to an abrupt increase in demand and reached to $112/barrel which led to an energy crisis and deceleration in the growth of China and Europe. However, the crude oil prices decrease very sharply afterwards and shrank as low as $30.80/barrel in January 2016. As soon as the crude oil prices recovered after 2017, researchers again focused on alternative energy sources. Therefore, natural gas was placed among the top alternatives by reducing the dependency on crude oil. Hence, investment in natural gas production was increased from the year 2017, and it is forecasted that the production of natural gas will rise 1.7 times from 2016 to 2050 [7, 8]. USA and Canada are also focusing on the natural gas utilization, which results in increasing the rate for production in China and India as well [9]. Japan and Korea are the biggest importers of natural gas. However, besides the interest in natural gas and other renewable energy sources is rising, coal production is also assumed to be increased to 9.1 Gt in 2050, which was 7.3 Gt in 2016. Due to the increase in power generation, the consumption of steam coal would increase and will result in more production. The production of steam coal is assumed to rise to 7.4 Gt in 2050, which is 1.4 times of 5.5 Gt in 2016 (IEEJ, 2018). However, a slight decline in coking coal will be noticed. On the other hand, nuclear power generation was assumed cheapest and environment-friendly some years back. But the changes in public opinion, continuous increase in construction cost, higher maintenance, and accidents occurrence recently forced many countries to shut down their nuclear power plants. This results in an enhancement in renewable energy such as wind energy and solar photovoltaic.

According to the 2019 survey report of "World energy insight brief," it is assumed that the global consumption of primary energy will reach to 19.3 Gtoe in 2050, which was 13.8 Gtoe in 2016. This remarkable growth in energy consumption will lead to an increase in the capital in transportation, development, and power generation. The energy-related investments are divided into two categories, Organization for Economic Co-operation and Development (OECD) and non-OECD. Both the stakes are different from each other and both will grow continuously. However, the non-OECD investment will grow at a faster rate. It is forecasted that the investment of $82.3 trillion will be required in energy-related sectors for 34 years from 2017 to 2050 (IEEJ, 2018). Out of that $31.2 trillion, which is more than 40% will be invested for fossil fuels. This includes the investment on oil ($16.9 trillion), natural gas ($13.2 trillion), and coal ($1.9 trillion). The investment in power generation will be $34.4 trillion, which is more than 42% of the total expenditure. This investment includes transmission and distribution, thermal, nuclear, and renewable power

generation. The investment of $13 trillion will be needed for renewable power generation, which includes wind, solar photovoltaic, hydro, and other power generation. Also, $15.2 trillion must be invested for improvement of efficiency and technology improvement. Of the total investment, around $1.3 trillion will be assigned for technologies advancement (World energy insight brief, 2019). The combustion of all these energy sources emits harmful emissions like particulate matters (PM), carbon dioxides (CO_2), oxides of nitrogen (NO_X), etc.

Hence, this investment will be allotted to reduce the emissions by advancing the technologies and for the research of new renewable fuels [10]. These harmful emissions are a threat to human health, especially for children and old age peoples. According to the World Health Organization (WHO) report, every year, 3 million peoples are suffering to the point of death due to alarming air pollution rate [11, 12]. The air pollution generated from the combustion of fossil fuels directly affects the health of young children. This may cause diseases like respiratory illness, adverse birth outcomes, behavioral development, impairment of cognitive and childhood cancer [13]. These impacts would aggravate in the near future. The developing countries use more fossil fuels to fulfil their energy requirement, which impacts the immune of the human body. It is found that nearly 80% of air pollution is caused by the combustion of fossil fuels (like coal, petroleum oils, etc.) from transportation, power generation, and industry sectors. The increasing pollution level is depleting the environment by introducing NO_X and PM as major elements into the atmosphere. In the USA, CO_2 contributes a major share of 81% to greenhouse gases, and the majority of this comes from the excessive increase of vehicles on the roads [14]. Therefore, many experts have seen the major challenge and excellent opportunity in the transition to low carbon and cleaner energy economy.

2 Hydrogen Economy

In the world, petroleum, natural gas, and coal are highly dominant for fulfilling the energy demands. Also, nuclear energy and hydropower plants are used in many parts of the world to generate electricity. Beyond all these energy sources, hydrogen has evolved as a candidate for making one self-reliant [15]. The main benefits of the hydrogen economy are [16–19]:

- Air pollution: Health problems in cities are caused by particulate matter, ozone, and acid rain. The introduction of fuel cell cars to hydrogen can drastically reduce emissions of nitrogen oxides (NO_X) and sulphur dioxide (SO_2), as well as noise, also responsible for stress and health.
- Reduction of polluting emissions: Hydrogen emits nearly zero-emission when burnt. It can be a great solution for the reduction of greenhouse gas (especially CO_2) emissions in the case of transport, as well as for the improvement of local air quality.

- Energy efficiency: Hydrogen allows for improved performance at end-use of energy. However, when combined with fuel cells, it helps in attaining maximum efficiency. Hydrogen usage in fuel cells is the most efficient way to convert chemical energy into electrical energy. Hydrogen and the fuel cell make it possible to double fuel the efficiency of the internal combustion engine.
- Energy independence and security of supply: Hydrogen can be produced from domestic renewable sources such as wind, solar, or geothermal. It can also be produced from coal—primary source plus abundant and better distributed than oil—with carbon capture and sequestration.
- Economy and employment: Hydrogen and fuel cell industry offers goods and high value-added services. The investment in these sectors can lead to multiplier effects in the improvement of the economy. It also helps in generating more jobs in the country.

2.1 Challenges of the Hydrogen Economy

There are many hurdles to adoption of hydrogen economy [20]. The environmental balance of hydrogen depends on its production mechanism. The production from fossil fuels [21] is the most economical method. However, this does not solve the problem of greenhouse gas emissions [22–24]. Centralized production from coal and natural gas with carbon capture and sequestration [25–27] can be a great solution for the production of large quantities of hydrogen economically and without carbon emissions. However, it requires an excellent infrastructure and investment.

Apart from these challenges, storage [28, 29] and purity [30] are other issues related to hydrogen. Since hydrogen needs highly pressurized cylinders for their storage [31, 32] making it very difficult to use hydrogen as a fuel (Hord, 1978)which is not a problem with fossil-derived fuels [31–33]. Apart from this, for most of the typical applications like fuel cells, hydrogen of purity, 99.97% is desired [30, 34]. This requires sophisticated technologies for producing so much pure hydrogen. Moreover, hydrogen is highly flammable (Mirzaei, 2008) and when coming in the presence of air explosion can take place [35]. Therefore, safety is a major concern with hydrogen.

Transportation of hydrogen from one place to another requires a lot of investment. Special containers are required for transporting hydrogen through road and rail lines [36]. Moreover, for transporting it through pipelines, expensive treatments are needed to be undertaken on the pipeline for making it useful for hydrogen.

2.2 Transition from Hydrogen to Methanol Economy

Hydrogen being a very potential source also carries a lot of challenges. Therefore, the methanol economy is coming into the limelight since last few years. There are

several benefits of the methanol economy over hydrogen economy [37–39]. These include easy availability of natural gas and coal for producing methanol. Moreover, biomasses obtained from municipal waste-based routes are also available for producing methanol [40–42].

Apart from these benefits, storage of methanol is not so difficult. Its price is also very competitive to petroleum fuels. Moreover, the burning of methanol is very clean. Even the CO_2 recovery and utilization during both production and application stage of methanol reduce its greenhouse gases footprint [43]. Apart from that higher latent heat of vaporization of methanol increases its suitability in an engine. Also, several studies have shown that methanol burning removes the heat from the engine by quenching the engine cylinder.

The methanol burning is a cleaner process, producing almost zero SO_X and NO_X emissions [44–48]. Apart from the usage of methanol in SI engines, dimethyl ether, which is the gaseous version of methanol has been successfully tested in CI engines [49–51]. Also, methanol finds its applications in gas stoves and boilers [52, 53] and gas turbines [54], thereby reducing the dependence on fossil fuels and also helps in achieving the reduction of emissions in the environment. The usage of methanol most importantly reduces the reliance on fossil fuels and thus saves the country's foreign exchange. Among other applications, alike to hydrogen, methanol is used in fuel cells [55, 56] giving similar efficiencies and application areas with fewer issues and investments.

3 Methanol Production

Methanol is produced from many carbon-containing feedstocks such as syngas, coal, natural gas, CO_2, and biomass. Different processes for converting raw materials into methanol are shown in Fig. 1. Transformation of CO_2 to methanol is the most promising solution which significantly reduces the CO_2 emission. Due to surplus availability and immense reservoirs of coal, especially in countries like China and USA, it is excessively used for methanol production. However, due to the dreadful increase of CO_2 level and other harmful pollutants in the atmosphere, coal is not favoured feedstock. Moreover, the amount of carbon dioxide released during the combustion of coal is comparably higher than petro-diesel and natural gas. The transition towards renewable sources such as biomass can only provide a little two-thirds of feedstock for methanol production. Despite easier availability, the biomass alone cannot address the increasing demand for methanol in the nearer future. Therefore, new methods are in need to develop the large scale production of methanol.

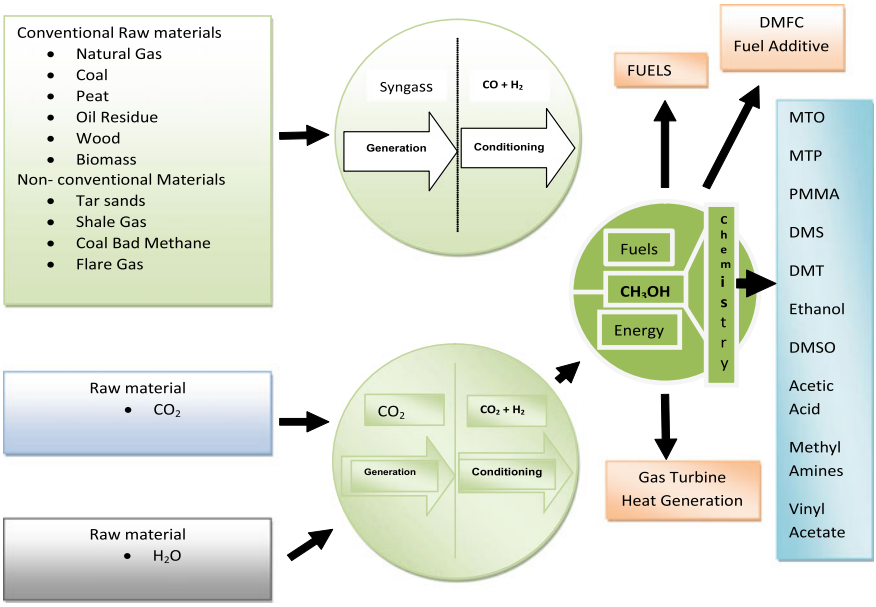

Fig. 1 Methanol production processes using different feedstocks

3.1 Methanol from Natural Gas

Presently, 90% of methanol is produced through natural gas. It is a simple and straightforward technique which involves three basic processes. In the first process, synthesis gas is produced by steam reforming, as shown in Eq. (1). During the reaction, the parameters such as temperature and pressure are kept around in the range of (810–1100 °C, 18–30 bar) [57]. At times, the carbon monoxide generated during the water shift reaction reacts with steam to produce carbon dioxide and excess hydrogen. Therefore, parameters such as the steam to methane proportion, pressure, and temperature of the reaction ratio significantly affect the reaction. Increase in the temperature of the reaction accelerates the production of syngas. Also, the carbon monoxide and water vapour reaction become less effective at the higher temperature. However, for the successful continuation of the process, there is a requirement of a large amount of heat. This heat can be provided easily by burning the methane itself. The required ratio for the generation of hydrogen to CO ratio should be not more 2. However, in this process, it is nearly 3, which is considerably higher. Therefore, modifications are made in the steam reformer exit gas to resolve this prevalent issue [58, 59].

It is observed in the previous studies that partial oxidation of methane yields in the release of an enormous amount of heat and steam reformation cycle of methane requires higher heat energy. Majority of present-day plants make use of both the process, to achieve a neutral thermodynamic reaction. The amalgamation of both

the cycles is known as autothermal reforming of the steam (Eq. 2). This combined-cycle provides flexibility to operate in a single reactor, thereby saving the manufacturing cost and also reducing the process complexities. However, due to unalike optimized conditions for both the processes, it is desirable to carry out the reactions in different reactors. The process continues in systematic order: firstly, the reformation of methane takes place at high temperature in the primary reactor. Later, the partial oxidation of products is carried out in the secondary reactor. The oxidation process requires an excess supply of air or additional oxygen-producing set-up. However, using pure air for partial oxidation process results in the formation of nitrogen along with the syngas. The nitrogen acts as an obstacle in the path of methanol synthesis and is required to be extracted out. Therefore, the modern-day plants usually prefer oxygen supply over pure air [60].

As discussed above, the composition of syngas required for methanol production should have a stoichiometric ratio of 2. Reactant such as methane can easily react with deficient oxygen with or without the presence of catalyst yielding hydrogen and CO with ideal S ratio of 2 (Eq. 5) [61]. However, at times, the carbon monoxide and hydrogen formed may be oxidized to CO_2 and water, bringing about losses in product gases required for methanol generation. Therefore, it is a matter of concern as the heat produced during exothermic oxidation processes is wasted if there is no immediate requirement [62].

$$CH_4 + H_2O \rightleftharpoons CO + 3H_2 \tag{1}$$

$$CH_4 + 2O_2 \rightarrow CO_2 + 2H_2O \tag{2}$$

$$CO_2 + H_2 \rightleftharpoons CO + H_2O \tag{3}$$

$$CH_4 + \frac{1}{2}O_2 \rightarrow CO + 2H_2 \tag{4}$$

$$CO + \frac{1}{2}O_2 \rightleftarrows CO_2 \tag{6}$$

$$H_2 + \frac{1}{2}O_2 \rightleftarrows H_2O \tag{7}$$

Syngas is characterized by stoichiometric number as shown Eq. (5)

$$\text{Stoichiometric Number (S)} = \frac{\text{moles } H_2 - \text{moles } CO_2}{\text{moles } CO_2 + \text{moles } CO} \tag{5}$$

In an ideal condition, stoichiometric number (S) should keep a value of 2. This value takes into consideration the presence of CO_2 converted that consumes hydrogen via the reverse water gas shift reaction as shown in Eq. (6).

$$CO_2 + 3H_2 \rightleftharpoons CH_3OH + H_2O \quad (6)$$

Conversion of syngas into crude oil occurs at a pressure of 50–100 bar and temperature of 200–300 °C. Main reactions for methanol synthesis as shown from Eq. (7)–(10) [Klier 1982].

Hydrogenation of CO

$$CO + 2H_2 \rightleftharpoons CH_3OH \quad (7)$$

$$CO + H_2 \rightleftharpoons CH_2O \quad (8)$$

$$CH_2O + H_2 \rightleftharpoons CH_3OH \quad (9)$$

Hydrogenation of CO_2

$$CO_2 + 3H_2 \rightleftharpoons CH_3OH + H_2O \quad (10)$$

In the first part of process, conversion of CO_2 into the CO and later conversion of synthesis gases subjected to thermodynamic equilibrium. Reactions from Eqs. 7–10 are strongly exothermic. CO and H_2 are fed into converter at a maintained ratio from 1:3 to 1:5. WGS is used to improve the H_2 content. Superior heat management is required to handle synthesis gas in liquid phase methanol process. To minimize the by-product formation and maximize the yield of methanol, many solid catalysts are employed from the last few decades.

3.2 Methanol from Biomass

Biomass, such as wood, agricultural products, solid waste, landfill gas, biofuels, are a suitable feedstock for methanol production. It is a renewable and sustainable source which uses sunlight to recycle the carbon dioxide of atmosphere into fresh oxygen. The heat energy released during the burning of biomass can be utilized for the production of liquid biofuels or generation of biogas. In the early '90s, methanol was produced using the process of destructive distillation. The process involves the decomposition of wood at a higher temperature, i.e., 400–600 °C in the absence of air. However, due to complications in the process, this method is not practiced these days. Presently, the commonly used methanol techniques are liquification, gasification, pyrolysis, and process hybridization [63–65]. Generally, the gasification process is used for the processing of solid feedstocks such as wood and cellulosic materials into syngas. The conversion process of animal waste biomass into syngas is carried out in two steps, firstly converting the biomass to biogas, followed by the process of the reformation [66, 67].

It is necessary to reduce the moisture content to not more than 15–20% during the process of gasification. Therefore, the initial process involves drying and pulverization of feedstock, followed by mixing oxygen and water at high pressure in the gasifier. To sustain the gasification process, heat energy is required. This fraction of heat energy is produced by burning some part of biomass only in the presence of oxygen. Later, the reactants CO_2 and water react with the remaining biomass in the absence of oxygen to yield hydrogen and CO. Hence, no external supply of heat is required for the process of gasification; biomass itself acts as the heating fuel. There are a wide variety of technical complications faced during the single-step partial oxidation process of syngas production—the reason due to which biomass gasification is accomplished in two steps. In the first stage, the pyrolysis of dried biomass is carried out in the presence of insufficient oxygen. During this process, the incomplete combustion of biomass takes place at a temperature limit of 400–600 °C to obtain pyrolyzed gas. The gas comprises of different compounds such as hydrogen, carbon monoxide, water, carbon dioxide, and volatile tar. In the second stage, the residue, charcoal left over after the pyrolysis is allowed to react with oxygen to form carbon monoxide. The temperature during this process is maintained in the range of 1300–1500 °C. Later, the syngas obtained is filtered and sends forward for methanol production [68].

It is observed that the gasification process can only be continued if there is a constant supply of heat energy. This heat is generated by burning some part of biomass, hence resulting in wastage of feedstock required for methanol conversion. Therefore, renewable sources such as solar power and nuclear energy can be a probable solution. In one of the previously published research, [69] the solar energy was utilized for the purpose and drying and heat energy generation inside the gasifier. The biomass was allowed to disperse in a tank of molten salt, and concentrated solar energy was used as a heat generation medium during the experiment. The energy stored in the molten salt helps in the production of syngas from biomass without any disturbance, thus reducing the overall energy requirement.

However, everything in this nature has its pros and cons. Methanol production using biomass conversion also faces similar issues as are experienced in using coal as feedstock. The higher carbon dioxide to carbon monoxide ratio and lower hydrogen to carbon ratio are some of the critical issues. As discussed in the earlier section, the composition of syngas plays a significant role in methanol production. Due to the use of CO_2 and losses present at different stages, the desired quantity is not obtained; therefore, S ratio close to 2, necessary for methanol production is not achieved [70, 71]. The modern-day plant uses hybridization process, i.e., mixing of syngas produced from natural gas and biogas, to get rid of these severe problems. This is because the syngas produced from natural gas has hydrogen to CO ratio equal or close to 3.

Similarly, syngas from biogas has low H2/C ratio [72, 73]. Therefore, the hybrid plant is viable choices for methanol production as it provides flexibility to adjust the hydrogen to carbon monoxide ratio. Moreover, in hybrid plants, the CO_2 required for the reformation of natural gas can be obtained from biomass reformation. Hence, reducing the harmful emissions of CO_2 emitted during production. This overall

process of no net output of carbon dioxide is termed as Hynol process [74–76]. Methanol can also be synthesized using hydrogen generated from coke oven gas. It contains about 66% of hydrogen which can be easily mixed with biomass, but due to limited availability of non-renewable sources, coke oven gas is not a preferable choice. The utilization of renewable sources for hydrogen production is a sustainable approach as it will contribute to reducing the carbon footprints of methanol production.

As discussed above, methanol can be generated from a wide variety of sources. However, the biggest challenge is the quantity of methanol produced. Due to the transition towards alternative sources, the demand for methanol would increase in the nearer future. This escalating demand requires sustainable feedstocks and cheap and economical methods of production. The utilization of food crops will also give rise to severe concerns about fuel vs. food debate [77]. The non-edible food crops can be the targets for feedstock and therefore should be cultivated extensively. However, researchers are in progress to grow advance species of trees and grasses for methanol production.

Moreover, an ample quantity of resources such as land, water, fertilizers, and proper temperature and time is required for these hybrid crops productions. Therefore, the search for new and advanced resources must not create hindrance in the path of food crops. Also, the excessive use of fertilizers and water resources would result in degradation of land soil and will also give rise to groundwater pollution [78]. One of the major hindrances in the roadway of methanol production is high carbon footprints, which cannot be neglected [79, 80]. Taking into consideration all the above-mentioned factors, renewable resources such as biomass alone can only bridge up to the 20% requirement of energy. Therefore, to maintain a proper balance between energy supply and demand, other sustainable resources are required to be explored.

3.3 Methanol from CO_2

After burning any compound containing carbon, water, and CO_2 is formed. The biggest problem today is to reverse this process. After the death of a plant, it becomes fossil fuel in millions of years. The biomass collected in the plant can also be converted into fuel and other products. But, this resource is not enough to meet human needs. So, a technology that can efficiently process CO_2 in a short time must be developed. One of these approaches is catalytic hydrogenation of CO_2 to DME/methanol which can further be converted to other products. The conversion of hydrogen and CO_2 to methanol has been known since the early twentieth century. In the 1920s CO_2 was obtained as a by-product of the fermentation process from methanol producing plants. In the conversion process, copper and zinc were used, as well as their oxides. These catalysts are similar to those used currently for producing methanol. The CO in the syngas is first converted to CO_2 and H_2 and the CO_2 is further hydrogenated to get methanol [81–83]. Many researchers reported

technological progress in the production of methanol from hydrogen and CO_2 [84–87]. It was also revealed that investments in a plant for the synthesis of methanol from CO_2 and hydrogen are similar to investments based on syngas. But, the only problem is the scaling of the plant due to the less availability and cost of CO_2 and H2, as well as energy sources. Various sources, such as fossil fuel power plants and various industries, such as aluminium smelters, cement plants, etc. produce CO_2 that can be trapped and cleaned. Natural resources such as geothermal and natural gas also contain a lot of CO_2. Finally, CO_2 can also be separated from the air to get methanol and other products. Currently, fossil syngas is used to produce hydrogen, which releases a large amount of CO_2 into the atmosphere, and causes an increase in global warming. In addition, due to the decrease in fossil fuel quantities, several other sources of hydrogen production should be used. The best way for the future is to separate the water by electrolysis.

4 Comparison of Storage of Methanol and Hydrogen

Hydrogen storage is a major problem, which should be cost-effective, safe, and easy to use. The energy density per unit volume of hydrogen is lower than that of liquid fuel at the same pressure, since hydrogen is lightweight and therefore,] causes a storage problem. Compared to petrol, hydrogen requires 3000 times more space under normal conditions. Hence, for commercially using hydrogen, it is necessary to compress, liquefy, or absorb on the material [88]. Hydrogen economy depends upon storage of hydrogen. Here are some of the storage methods: storage in an insulated container of high pressure in a liquefied or compressed form, chemical storage of hydrogen in the materials that absorb it and its easy release if necessary [89].

Presently, the most preferable method for the internal combustion engine and automobiles operating on fuel cells is to store hydrogen in the form of compressed gas. Small hydrogen cylinders can readily store the same amount of hydrogen. Over the years, studies have been carried out on pressure vessels such as cylinders capable of withstanding pressures of up to 700 bar, consisting of compounds reinforced with light carbon fibre. Despite this, the hydrogen energy density at 700 bar is almost 4.5 times (by volume) lower than that of petrol. Therefore, a cylinder capable of carrying a larger quantity of hydrogen is required. Besides, fuel tanks of any shape can be used based on the free space in the vehicle, while the shape of a cylinder with compressed hydrogen is fixed in the form of a cylinder. Therefore, more attention should be paid to the integration of the hydrogen cylinder into the vehicle. The energy requirement for hydrogen compression is nearly 15% of the energy [90].

Similar to petrol or diesel, methanol can also be supplied from gas stations. Consumers will not feel any changes, except that instead of oil, they fill their tanks with another liquid. In existing or newly developed gas stations, the installation of methanol storage tanks and distribution pumps is similar to the installation of petrol or diesel. Since 1980, gas stations for methanol cars have been built in California. Most vehicles are flexible fuel vehicles (FFVs), which means that any mixture of

methanol and petrol can be used for their work, while some can only be used with pure methanol. Methanol fuel pumps have also been installed in other parts of the USA and some in Canada. The cost of converting existing methanol delivery points is fairly low.

The double-walled underground tank used for diesel or gasoline is easy to clean and can be used to store methanol. Only new methanol compatible hoses and metering pumps will be required. The conversion cost is almost 20,000 US dollars and takes about a week to be set up [91]. This means that by investing $3 billion, nearly one-fourth of the existing fuels stations can also provide methanol [92–94]. Compared to hydrogen infrastructure, which requires special equipment to manage low temperature and high pressure, methanol filling stations require less capital. Moreover, hydrogen delivery technology is still in its early stages and is not reliable as are liquid fuels. Another issue is the regulatory standards which disallow the installation of a hydrogen gas station within 25 metres of the gas pump and hence restricts the installation of hydrogen filling stations. In cities, space is already limited, so it is not very feasible to install new gas stations that contain the only hydrogen. Moreover, transporting hydrogen at extremely low temperature or high pressure from the production centre to the distribution centre is very expensive compared to methanol.

5 Methanol Use as a Fuel

Methanol is the most potent fuel for both SI and CI engines; however, the production of methanol requires further research. In the early 1970s, due to higher perturbation in the price of conventional fuels, methanol is introduced in the fuel market as an alternative fuel. Many researcher/scientists are strenuous to find the fuel economy and solution for sustainable production of methanol. Though, the lower calorific value and lesser stoichiometric air/fuel ratio of methanol compared to CI and SI engine are few challenges essentials to be addressed.

Comparison of different fuel properties of methanol with diesel, gasoline, and ethanol is shown in Table 1.

5.1 Methanol Use as an SI Engine Fuel

This section focuses on the influence of methanol and its different blends of gasoline on SI engines. Wang et al. [95] evaluated the chemical and octane sensitive effects of methanol on SI engine. The experimental investigations depicted that pure methanol on the engine operation at a higher compression ratio as compared to gasoline. High octane number assists the fuel–air mixture entering into the cylinder to compress at a minor range of volume. Better atomization enhances the characteristics of the combustion of the methanol. The aspects such as sulphur-free fuel, lower emissions, high octane number, immense availability, etc. make it a best potential

Table 1 Comparison of fuel properties diesel, gasoline, biodiesel, ethanol, and methanol [95, 96, 116]

Fuel property	Diesel	Gasoline	Biodiesel	Ethanol	Methanol
Formula	$C_{10–26}$	$C_{5–12}$	various	C_2H_5OH	CH_3OH
Oxygen content (mass%)	0	0	10	34.8	50
Density (kg/m^3 at 20 °C)	834	740	850	790	790
Viscosity at 40 °C (mPa s)	2.9	0.29	7.8	1.1	0.59
Stoichiometric air/fuel ratio	14.5	14.6		9	6.45
Lower calorific value (MJ/kg)	43	44	39	26	19
Higher calorific value (MJ/kg)	45.8	46.6	44	28.5	22.5
Freezing point at 1 bar (°C)	−40	−57	–	−80	−97.7
Boiling point at 1 bar (°C)	175–360	30–220	262–359	78.4	64.5
Flash point (°C)	55	−45	166	13	11
Autoignition temperature (°C)	220–260	228–470	363	422	463.8
Research octane number (RON)	<0	80–98	–	108	107
Motor octane number (MON)	<0	81–84	–	92	92
Cetane number	40–55	0–10	47–52	6	<5
Specific heat (20 °C) (kJ/kg K)	1.9	2.3	–	–	2.55
Heat of vaporization (MJ/kg)	270	310	300	910	1109

substitute for gasoline fuel. Literature exposes that capability to operate with leaner mixtures, higher compression ratio (CR) and latent heat of evaporation attached with the methanol-fuelled engine can provide up to 10–20% rise in thermal efficiency for the SI engines. Celik et al. [96] investigated the performance and emission characteristics of single-cylinder SI engine at different compression ratios (CR), i.e., 6:1, 8:1, and 10:1 using methanol and gasoline. The research revealed that gasoline fuel exposed, knocking above 6:1 compression ratio. However, methanol runs smoothly on all range of compression ratios. Additionally, a considerable decrease in CO, CO_2, and NO_x emissions was also observed. However, entire replacement fuel is not possible due to lower calorific value and the formation of formaldehyde and high NO_x emissions. Many researchers also used methanol as an extender in gasoline engines [97]. The amalgamation of methanol in gasoline and light alcohols in the form of binary/ternary blends is a promising approach which can reduce the shortcomings related to the usage of neat methanol in SI engine. Table 2. shows limitations associated to the use of neat methanol as SI engine fuel. The engine power and BTE were also found to increase with methanol fuel. Li et al. [98] investigated that optimization of the ignition timing of the methanol-fuelled SI engine showed improved in heat release rate, cylinder pressure, and BSFC. Investigations indicated that a significant change in the performance, combustion, and emission characteristics of direct injection SI methanol engine. A comprehensive work of literature showed some extreme feature of methanol. Yanju et al. [99] investigated on Gasoline Direct Injection Engine using the blends (%v/v) of gasoline and methanol. These binary blends of

Table 2 Merits and demerits of using neat methanol in an SI engine [97–99]

Merits	Demerits
Minimizing the unwanted issues of knocking phenomenon. Methanol also provides flexibility to work at higher compression ratio, resulting in improved efficiency in SI engines	Indigent self-ignition properties resulting in long ignition delay
Exhaust emissions are soot free, therefore providing cleaner (soot-free) combustion	Mixing quality with conventional fuel is poor, resulting in difficulties of cold starting of engine
Improved fuel economy, flexibility of operating at lean mixtures and reduced harmful emissions of NO_x, HC and CO	Corrosion of engine parts on longer-term usage
Higher latent heat of vaporization imparts lower combustion temperature and results in lower NO_x emissions	Evaporation in fuel lines (vapour locks)
Higher volatility providing better fuel distribution of air–fuel mixtures among the cylinders	Poor oxidation stability and degradation of oil lubrication properties resulting from low viscosity

gasoline and methanol significantly enhanced the in-cylinder pressure, heat release rate (HRR), rate of pressure rise, and CHR as compared to neat gasoline.

5.2 Methanol Use as a CI Engine Fuel

Diesel engines are the most efficient engines for heavy-duty applications such as industrial, transportation, and power sector. It shows a fundamental role in driving the economy of the developing nations [100]. However, diesel fuel is the biggest cause of harmful pollutants such as smoke, soot, and NO_x into the atmosphere. The introduction of stringent emission norms (Euro VI) is compelling to explore a potential alternative fuel which can sustainably exchange diesel fuel and also facilitates in preserving the existing CI engines. Physical and chemical properties of methanol have attracted the attention of the entire research fraternity due to its distinctive merits. Emissions of NO_x along with soot particles reduce drastically in the combustion of methanol concerning the combustion of diesel [101]. Besides this the higher volatility and vapour pressure of methanol endorses its usage as CI engine fuel. Heavy-duty CI engines have the leverage to run efficiently in cold weather condition, thus providing an appropriate solution for cold starting. The methanol powered CI engines are even now in practice in different parts of the world, especially in the USA [102]. In the early '90s, a heavy-duty diesel engine 6V-92TA (retrofitted by Detroit Diesel Corporation) to run on neat alcohol [103]. Methanol is used as fuel to run its public transportation system in Detroit (USA), also known as "motor city." Environmental Protection Agency (EPA) and the California Air Resource Board (CARB) certified as the low emission heavy-duty diesel engine in the year 1992. The

methanol engine can provide a great hike in reducing the hazardous issues of climate changes and acid rain in compare to diesel fuel. However, diesel engines have certain hurdles in the use of neat methanol.

The lower cetane number of methanol resulting in longer ignition delay and other abiding issues such as higher maintenance cost due to corrosion of engine parts and issues with fuel system are some of the deficiencies which restrict its usage as neat methanol fuel. Therefore Methanol in the form of blends (binary/ternary), fumigation, and derivate DME (Dimethyl ether) are some of the approaches which can widespread the use of methanol in CI engines [104]. Methanol containing an immense quantity of oxygen content and high enthalpy of vaporization can be used as a blend with diesel, i.e., 85% methanol and 15% diesel or other proportions.

Many experimental studies were conducted in the past on diesel-methanol blends. Canakci et al. [97] investigated the performance, combustion and emission characteristic of CI engine fuelled with methanol-diesel blends. Four blends containing 0, 5, 10, and 15% methanol were tested. The analysis was conducted at three different injection pressures like 180, 200, and 220 bar. The results showed improvement in peak cylinder pressure, HRR, combustion efficiency as the injection pressure increases. Also, emissions such as unburnt hydrocarbon (UBHC) and CO were also reduced considerably.

Dimethyl ether (DME) is also a potential route for the best alternative of diesel fuel. It is derivative of methanol and it can be achieved from the dehydrogenation of methanol. It is non-toxic, non-corrosive, non-explosive, and non-carcinogenic nature. Due to these favourable properties, DME is the most desirable choice of CI engine [105]. Remarkably, the properties of DME such as cetane index, low boiling point motivated to the fuel economy to investigate its assets for the diesel engines. DME fuelled engines are very common in many parts of the world mainly in Europe [106]. Volvo, a Swedish luxury vehicle company is currently focusing on utilizing the applications of DME in their vehicles. Also, other leading automobile industries like "Isuzu" are working on fuel injection systems to transform their engines compatible with DME. Denmark is already running its public transport buses on DME fuelled engine [107]. The DME powered CI engines not only provide improved performance and emissions but also produces less noise as compared to diesel. However, DME as an environmentally friendly fuel, but it possesses some inferior properties such as poor lubricity, low density, and viscosity.

5.3 Methanol Use as a Fuel Cell

Another fuel modification application of methanol is to develop the fuel cells. It is an electrochemical process which converts the chemical energy of the fuel/hydrogen into electricity in the presence of some suitable oxidant. Many issues are arising with the usage of conventional fuels that is forcing the fuel economy towards electric vehicles. The electric cars, unlike IC engines, take advantages of the fuel cells for its working. Hydrogen is the cleaner and eco-friendly fuel; however, the stability, higher

maintenance, and other undesirable handling issues make it challenging to be used for fuel applications. Therefore, to utilize the benefits of hydrogen as a fuel, it can be employed to drive the fuel cells [108]. Almost all the fuel cells currently being manufactured for electric vehicles operate primarily on the hydrogen fuel. A fuel cell is the best alternative which can reduce dependence on the millions of existing IC engines in the world [109]. It can provide higher efficiency and reduced emissions as compared to the diesel/gasoline.

Methanol can be potentially used as feedstock for hydrogen generation. The most popular and economical fuel cell functioning on hydrogen gas is Proton Exchange Membrane Fuel cell (PEMFC). In PEMFC, the hydrogen is generated externally and is then fed into the fuel cell. Therefore, the fuel cell can be used in large system applications [110]. However, methanol also has the flexibility to be fed directly for running the fuel cell systems known as Direct Methanol Fuel Cell (DMFC). In DMFC, methanol is internally reformed to generate hydrogen. It is a continuous generation process which uses an appropriate catalyst for converting methanol to hydrogen. The temperature range in which the fuel operates is 60–130 °C [111]. Therefore, the DMFC fuel cells are restricted to light-duty systems and can be potentially used for battery charging applications such as electric cars, forklift trucks, etc. The commonly used catalyst in DMFC fuel cell is ruthenium–platinum. It converts liquid methanol into hydrogen and making it suitable to be used as fuel. Zhang et al. [112] investigated the performance of DMFC by incorporating a methanol barrier known as methanol-resisting pervaporation film (PVF), a buffer cavity, and a water-resisting PVF. The anode controls the flow of methanol coming from the tank. The results showed a significant increase in the efficiency of the fuel cell. Also, the performance of the fuel cell showed no change over 400 h of continuous working.

6 Challenges of Methanol Economy

Methanol is internationally recognized and is rapidly gaining interest as a sustainable energy resource. It has vast advantages such as fuel for IC engines, fuel cells, etc. However, methanol use at commercial scale requires more flesh on the bones.

At present, a lot of research is going on in the field of alternative fuels to utilize the assets of the methanol economy. The previously published investigations proved that blending of methanol in an internal combustion engine (gasoline engine) is an attractive choice to cut down the price of gasoline fuel and reduce the harmful emissions. However, serious issues such as cold starting, the formation of a higher amount of formaldehyde were observed with the use of methanol. The problems were more common in cold weather areas. Therefore, due to lower volatility and calorific value as compared to petrol–diesel, the use of methanol in the form of blends with diesel and petrol would only be the viable solution according to future perspective [113].

Moreover, methanol is a polar molecule hydrocarbon due to which it is more corrosive as compared to gasoline. Therefore, extensive utilization of methanol in IC

engines requires engine modifications. Also, the methyl tert-butyl ether (MTBE) found in methanol contaminates the groundwater. The contaminated water has hazardous effects on the life of flora and fauna. Therefore, the filling stations are reducing over the past few years across the world due to the high installation cost of methanol [114]. More likely, the developed countries have boycotted the production of methanol to blend with gasoline.

In terms of cost-effectiveness, methanolm and gasoline are almost similar. The exhaustive literature showed that low-level blends are more cost-effective as compared to a high-level blend. The high-level blends required a separate distribution system because of its corrosive nature [3], which demands an extra cost of production and transportation. Therefore, high-level methanol blends are less attractive. Hence, as discussed in the above sections, methanol provides flexibility to obtain from a wide variety of sources [115]. Therefore, there is an urgent need to explore the cheap and economical method for its production and utilization on a large scale all around the globe.

7 Conclusion

The coal, crude oil, and natural gas obtained from fossil fuels still continue to hold the major sources of energy consumption worldwide. The rapid industrialization, higher living standards, etc. are depleting the energy resources in a manner that it cannot be replenished in the future. The increase in demand for energy and shortage in the supply would create an energy crisis in the nearer future. The non-renewable energy resources are minimal and will last only for the next 80–100 years. Therefore, there is an urgent need to explore the alternative energy resource which can fulfil the ever-growing demand for energy. Although hydrogen economy is seen as a major solution to human needs, it still is not a preferable choice. Many countries can not afford the cost for replacement of existing infrastructure for hydrogen storage. Apart from that, safety is another concern with hydrogen as any carelessness can cause fatal effects. Governments should take the vital initiative to explore the potentials of the methanol economy. The introduction of the methanol economy in the energy supply chain can significantly reduce the high crude oil imports and severe issues of greenhouse gases and climate change from the environment. Due to the cheaper and vast availability of methanol sources like coal, natural gas, and biomass, it can sustainably fill the hydrogen economy voids.

Moreover, less infrastructure and investment are required for storing and handling methanol. The storage of methanol is also simple, safe, and can be done with minor replacement in existing setups. Also, the harmful exhaust emissions such as SO_X and NO_X emissions are nearly zero during the burning of methanol. Therefore, it can be effortlessly used in a variety of setups, including SI engines, CI engines, fuel cells, etc. Hence, methanol can be used as a convenient energy storage substance and as a suitable feedstock for synthesizing hydrocarbons, and it is contemplated that the methanol economy shall proliferate in times to come.

References

1. Sommer A (2016) Burning fossil fuels: impact of climate change on health. Int J Health Serv 46:48–52. https://doi.org/10.1177/0020731415625253
2. Resitoglu IA, Altinisik K, Keskin A (2015) The pollutant emissions from diesel-engine vehicles and exhaust aftertreatment systems. Clean Techn Environ Policy 17:15–27. https://doi.org/10.1007/s10098-014-0793-9
3. Bae C, Kim J (2017) Alternative fuels for internal combustion engines. Proc Combust Inst 36:3389–3413. https://doi.org/10.1016/j.proci.2016.09.009
4. BP (2019) BP Energy Outlook 2019 edition The energy outlook explores the forces shaping the global energy transition out to 2040 and the key uncertainties surrounding that. BP Energy Outlook 2019, pp 1–134
5. Covert T, Greenstone M, Knittel CR (2016) Will we ever stop using fossil fuels? SSRN Electron J. https://doi.org/10.2139/ssrn.2720633
6. Daly H (1994) Fossil fuels. Appl Energy 47:101–121. https://doi.org/10.1016/0306261 9(94)90074-4
7. IEEJ (2018) Outlook (2050) https://eneken.ieej.or.jp/data/7570.pdf
8. Resources WE, Review C (2019) World energy insights brief
9. International Energy Agency (2017) Key world energy statistics. https://doi.org/10.1787/key_energ_stat-2017-en. Accessed 18 April 2019
10. Pearson RJ, Turner JWG (2012) Renewable fuels: an automotive perspective. Elsevier Ltd.
11. Tomar M, Kumar N (2019) Influence of nanoadditives on the performance and emission characteristics of a CI engine fuelled with diesel, biodiesel, and blends—a review. Energy sources part a recover. Util Environ Eff 1–18. https://doi.org/10.1080/15567036.2019.1623347
12. World Health Organization (2016) Ambient air pollution: a global assessment of exposure and burden of disease. https://apps.who.int/iris/bitstream/handle/10665/250141/9789241511353-eng.pdf?sequence=1. Accessed 18 April 2019
13. Epstein PR (2005) Climate change and human health. N Engl J Med 353:1433–1436. https://doi.org/10.1056/NEJMp058079
14. Schipper L, Saenger C, Sudardshan A (2011) Transport and carbon emissions in the United States: the long view. Energies 4:563–581. https://doi.org/10.3390/en4040563
15. Saeedmanesh A, Mac Kinnon MA, Brouwer J (2018) Hydrogen is essential for sustainability. Curr Opin Electrochem 12:166–181. https://doi.org/10.1016/j.coelec.2018.11.009
16. Abe JO, Popoola API, Ajenifuja E, Popoola OM (2019) Hydrogen energy, economy and storage: Review and recommendation. Int J Hydrogen Energy 44:15072–15086. https://doi.org/10.1016/j.ijhydene.2019.04.068
17. Alanne K, Cao S (2017) Zero-energy hydrogen economy (ZEH 2 E) for buildings and communities including personal mobility. Renew Sustain Energy Rev 71:697 711. https://doi.org/10.1016/j.rser.2016.12.098
18. Marbán G, Valdés-Solís T (2007) Towards the hydrogen economy? Int J Hydrogen Energy 32:1625–1637. https://doi.org/10.1016/j.ijhydene.2006.12.017
19. Moliner R, Lázaro MJ, Suelves I (2016) Analysis of the strategies for bridging the gap towards the Hydrogen Economy. Int J Hydrogen Energy 41:19500–19508. https://doi.org/10.1016/j.ijhydene.2016.06.202
20. Dou Y, Sun L, Ren J, Dong L (2017) Opportunities and future challenges in hydrogen economy for sustainable development. In: Hydrogen economy. Elsevier, pp 277–305
21. Gaudernack B (1998) Hydrogen production from fossil fuels. In: Hydrogen power: theoretical and engineering solutions. Springer Netherlands, Dordrecht, pp 75–89
22. Müller S, Stidl M, Pröll T, Rauch R, Hofbauer H (2011) Hydrogen from biomass: large-scale hydrogen production based on a dual fluidized bed steam gasification system. Biomass Convers Biorefinery 1:55–61. https://doi.org/10.1007/s13399-0110004-4

23. Granovskii M, Dincer I, Rosen M (2007) Greenhouse gas emissions reduction by use of wind and solar energies for hydrogen and electricity production: economic factors. Int J Hydrogen Energy 32:927–931. https://doi.org/10.1016/j.ijhydene.2006.09.029
24. Zacharias R, Visentin S, Bock S, Hacker V (2019) High-pressure hydrogen production with inherent sequestration of a pure carbon dioxide stream via fixed bed chemical looping. Int J Hydrogen Energy 44:7943–7957. https://doi.org/10.1016/j.ijhydene.2019.01.257
25. Blok K, Williams RH, Katofsky RE, Hendriks CA (1997) Hydrogen production from natural gas, sequestration of recovered CO_2 in depleted gas wells and enhanced natural gas recovery. Energy 22:161–168. https://doi.org/10.1016/S03605442(96)00136-3
26. Spath P, Amos W Hydrogen production from western coal including CO_2 sequestration and coalbed methane recovery: economics, CO_2 emissions, and energy balance. In: Advances in hydrogen energy. Kluwer Academic Publishers, Boston, pp 17–30
27. Voldsund M, Jordal K, Anantharaman R (2016) Hydrogen production with CO_2 capture. Int J Hydrogen Energy 41:4969–4992. https://doi.org/10.1016/j.ijhydene.2016.01.009
28. Mori D, Hirose K (2009) Recent challenges of hydrogen storage technologies for fuel cell vehicles. Int J Hydrogen Energy 34:4569–4574. https://doi.org/10.1016/j.ijhydene.2008.07.115
29. Schüth F (2009) Challenges in hydrogen storage. Eur Phys J Spec Top 176:155–166. https://doi.org/10.1140/epjst/e2009-01155-x
30. Yakabe H, Kurokawa H, Shirasaki Y, Yasuda I (2015) Operation of a palladium membrane reformer system for hydrogen production: the case of Tokyo Gas. In: Palladium membrane technology for hydrogen production, carbon capture and other applications. Elsevier, pp 303–318
31. Andersson J, Grönkvist S (2019) Large-scale storage of hydrogen. Int J Hydrogen Energy 44:11901–11919. https://doi.org/10.1016/j.ijhydene.2019.03.063
32. Bellosta von Colbe J, Ares J-R, Barale J, Baricco M, Buckley C, Capurso G, Gallandat N, Grant DM, Guzik MN, Jacob I, Jensen EH, Jensen T, Jepsen J, Klassen T, Lototskyy MV, Manickam K, Montone A, Puszkiel J, Sartori S, Sheppard DA, Stuart A, Walker G, Webb CJ, Yang H, Yartys V, Züttel A, Dornheim M (2019) Application of hydrides in hydrogen storage and compression: achievements, outlook and perspectives. Int J Hydrogen Energy 44:7780–7808. https://doi.org/10.1016/j.ijhydene.2019.01.104
33. Hord J (1978) Is hydrogen a safe fuel? Int J Hydrogen Energy 3:157–176. https://doi.org/10.1016/0360-3199(78)90016-2
34. Staffell I, Scamman D, Velazquez Abad A, Balcombe P, Dodds PE, Ekins P, Shah N, Ward KR (2019) The role of hydrogen and fuel cells in the global energy system. Energy Environ Sci 12:463–491. https://doi.org/10.1039/C8EE01157E
35. Mirzaei M (2008) Failure analysis of an exploded gas cylinder. Eng Fail Anal 15:820–834. https://doi.org/10.1016/j.engfailanal.2007.11.005
36. Pasupathi S, Gomez JCC, Su H, Reddy H, Bujlo P, Sita C (2016) Recent advances in high-temperature PEM fuel cells. Elsevier
37. Goeppert A, Olah GA, Surya Prakash GK (2018) Toward a sustainable carbon cycle. In: Green chemistry. Elsevier, pp 919–962
38. Iaquaniello G, Centi G, Salladini A, Palo E (2018) Methanol economy: environment, demand, and marketing with a focus on the waste-to-methanol process. In: Methanol, Elsevier, pp 595–612
39. Kumabe K, Fujimoto S, Yanagida T, Ogata M, Fukuda T, Yabe A, Minowa T (2008) Environmental and economic analysis of methanol production process via biomass gasification. Fuel 87:1422–1427. https://doi.org/10.1016/j.fuel.2007.06.008
40. Beenackers AACM, Van Swaaij WPM (1983) Methanol from wood, a state of the art review. In: Biomass Utilization. Springer US, Boston, MA, pp 585–609
41. Borgogna A, Salladini A, Spadacini L, Pitrelli A, Annesini MC, Iaquaniello G (2019) Methanol production from refuse derived fuel: influence of feedstock composition on process yield through gasification analysis. J Clean Prod. https://doi.org/10.1016/j.jclepro.2019.06.185

42. Holmgren KM, Andersson E, Berntsson T, Rydberg T (2014) Gasification-based methanol production from biomass in industrial clusters: characterisation of energy balances and greenhouse gas emissions. Energy 69:622–637. https://doi.org/10.1016/j.energy.2014.03.058
43. Pérez-Fortes M, Schöneberger JC, Boulamanti A, Tzimas E (2016) Methanol synthesis using captured CO_2 as raw material: techno-economic and environmental assessment. Appl Energy 161:718–732. https://doi.org/10.1016/j.apenergy.2015.07.067
44. Chudnovsky B, Livshits D, Baitel, S.: Burning Methanol and its blends attractive alternative for emission reduction. In: ASME 2016 power conference. ASME, p V001T03A001
45. Geng P, Zhang H, Yang S (2015) Experimental investigation on the combustion and particulate matter (PM) emissions from a port-fuel injection (PFI) gasoline engine fueled with methanol–ultralow sulfur gasoline blends. Fuel 145:221–227. https://doi.org/10.1016/j.fuel.2014.12.067
46. Hobson C, Márquez C (2018) Renewable methanol report
47. Sileghem L, Coppens A, Casier B, Vancoillie J, Verhelst S (2014) Performance and emissions of iso-stoichiometric ternary GEM blends on a production SI engine. Fuel 117 (A):286–293. https://doi.org/10.1016/j.fuel.2013.09.043
48. Yao C, Cheung CS, Cheng C, Wang Y (2007) Reduction of Smoke and NO x from Diesel Engines Using a Diesel/Methanol Compound Combustion System. Energy Fuels 21:686–691. https://doi.org/10.1021/ef0602731
49. Chen Y, Ma J, Han B, Zhang P, Hua H, Chen H, Su X (2018) Emissions of automobiles fueled with alternative fuels based on engine technology: a review. J Traffic Transp Eng (English Ed) 5:318–334. https://doi.org/10.1016/j.jtte.2018.05.001
50. Thomas G, Feng B, Veeraragavan A, Cleary MJ, Drinnan N (2014) Emissions from DME combustion in diesel engines and their implications on meeting future emission norms: A review. Fuel Process Technol 119:286–304. https://doi.org/10.1016/j.fuproc.2013.10.018
51. Ying W, Genbao L, Wei Z, Longbao Z (2008) Study on the application of DME/diesel blends in a diesel engine. Fuel Process Technol 89:1272–1280. https://doi.org/10.1016/j.fuproc.2008.05.023
52. Ebbeson B, Stokes CA, Stokes H (2002) Project Gaia: converting biomass to a clean liquid fuel for domestic use. Energy Sustain Dev 6:43–48. https://doi.org/10.1016/S0973-0826(08)60312-9
53. Ozier A, Charron D, Chung S, Sarma V, Dutta A, Jagoe K, Obueh J, Stokes H, Munangagwa CL, Johnson M, Olopade CO (2018) Building a consumer market for ethanol-methanol cooking fuel in Lagos, Nigeria. Energy Sustain Dev 46:65–70. https://doi.org/10.1016/j.esd.2018.06.007
54. Chudnovsky B, Reshef M, Talanker A (2017) Evaluation of methanol and light fuel oil blends firing at a 50 MW gas turbine. In: Volume 1: boilers and heat recovery steam generator; combustion turbines; energy water sustainability; fuels, combustion and material handling; heat exchangers, condensers, cooling systems, and balance-of-plant. ASME, p V001T04A002
55. Falcão DS, Oliveira VB, Rangel CM, Pinto AMFR (2014) Review on micro-direct methanol fuel cells. Renew Sustain Energy Rev 34:58–70. https://doi.org/10.1016/j.rser.2014.03.004
56. Simon Araya S, Grigoras IF, Zhou F, Andreasen SJ, Kær SK (2014) Performance and endurance of a high temperature PEM fuel cell operated on methanol reformate. Int J Hydrogen Energy 39:18343–18350. https://doi.org/10.1016/j.ijhydene.2014.09.007
57. Kochloefl K (1997) Steam reforming. In: Ertl G, Knozinger H, Weitkamp J (eds) Handbook of heterogeneous catalysis, vol 3. Wiley-VCH GmbH, Weinheim, p 1819
58. Subramani V, Sharma P, Zhang LLK (2009) Catalytic steam reforming technology for the production of hydrogen and syngas. Hydrogen and syngas production and purification technologies. Wiley
59. Rostrup-Nielsen J, Christiansen L (2011) Concepts in syngas manufacture. Imperial College Press, London
60. Hansen JB (1997) Methanol synthesis. In: Ertl G, Knözinger H, Weitkamp J (eds) Handbook of heterogeneous catalysis, vol 4. Wiley-VCH GmbH, Weinheim, p 1856
61. Choudhary TV, Choudhary VR (2008) Energy-efficient syngas production through catalytic oxy-methane reforming reactions. Angew Chemie Int Ed 47:1828–1847. https://doi.org/10.1002/anie.200701237

62. Olah GA, Goeppert APG, Surya Prakash GK (2009) Beyond oil and gas: the methanol economy. Wiley-VCH, Weinheim
63. Williams RH, Liu G, Kreutz TG, Larson ED (2011) Coal and biomass to fuels and power. Ann Rev Chem Biomol Eng 2:529–553. https://doi.org/10.1146/annurev-chembioeng-061010-114126
64. Bridgwater AV (1994) Catalysis in thermal biomass conversion. Appl Catal A Gen 116:5–47. https://doi.org/10.1016/0926-860X(94)80278-5
65. Bulushev DA, Ross JRH (2011) Catalysis for conversion of biomass to fuels via pyrolysis and gasification: a review. Catal Today 171:1–13. https://doi.org/10.1016/J.CATTOD.2011.02.005
66. Budzianowski WM (2016) A review of potential innovations for production, conditioning and utilization of biogas with multiple-criteria assessment. Renew Sustain Energy Rev 54:1148–1171. https://doi.org/10.1016/j.rser.2015.10.054
67. Sheets JP, Ge X, Li YF, Yu Z, Li Y (2016) Biological conversion of biogas to methanol using methanotrophs isolated from solid-state anaerobic digestate. Bioresour Technol 201:50–57. https://doi.org/10.1016/j.biortech.2015.11.035
68. Milne TA, Evans RJ, Abatzoglou N (1998) Biomass gasifier "Tars": their nature, formation, and conversion NREL/TP-570-25357
69. Adinberg R, Epstein M, Karni J (2004) Solar gasification of biomass: a molten salt pyrolysis study. J. Sol. Energy Eng. 126:850–857
70. Ribeiro AM, Santos JC, Rodrigues AE (2010) PSA design for stoichiometric adjustment of bio-syngas for methanol production and co-capture of carbon dioxide. Chem Eng J 163:355–363. https://doi.org/10.1016/J.CEJ.2010.08.015
71. Specht M, Band A, Baumgart F, Murray C, Gretz J (1999) Synthesis of methanol from biomass/CO_2 resources. In: Eliasson B, Riemer P, Wokaum A (eds) Greenhouse gas control technologies. Pergamon, Amsterdam, p 723
72. Borgwardt R (1998) Methanol production from biomass and natural gas as transportation fuel. Ind Eng Chem Prod Res Dev 37:3760–3767
73. Li H, Hong H, Jin H, Cai R (2010) Analysis of a feasible polygeneration system for power and methanol production taking natural gas and biomass as materials. Appl Energy 87:2846–2853. https://doi.org/10.1016/J.APENERGY.2009.07.001
74. Dong Y, Borgwardt RH (1998) Biomass reactivity in gasification by the hynol process. Energy Fuels 12:479–484. https://doi.org/10.1021/ef970127i
75. Dong Y, Steinberg M (1997) Hynol—An economical process for methanol production from biomass and natural gas with reduced CO_2 emission. Int J Hydrogen Energy 22:971–977. https://doi.org/10.1016/S0360-3199(96)00198-X
76. Lundgren J, Ekbom T, Hulteberg C, Larsson M, Grip C-E, Nilsson L, Tunå P (2013) Methanol production from steel-work off-gases and biomass based synthesis gas. Appl Energy 112:431–439. https://doi.org/10.1016/J.APENERGY.2013.03.010
77. Food and Agricultural Organization (2008) Soaring food prices: facts, perspectives, impacts and actions required. Presented at High level conference on world food security: the challenges of climate change and bioenergy. Food and agricultural Organization of the United Nations, Rome, 3–5 June 2008
78. Donner SD, Kucharik CJ, Corn-based ethanol production compromises goal of reducing nitrogen export by the Mississippi River. Proc Natl Acad Sci 105:4513–4518. https://doi.org/10.1073/pnas.0708300105
79. Fargione J,Hill J, Tilman D, Polasky S, Hawthorne P (2008) Land clearing and the biofuel carbon debt. Science 319:1235–1238. https://doi.org/10.1126/science.1152747
80. Searchinger T,Heimlich R, Houghton RA, Dong F, Elobeid A, Fabiosa J, Tokgoz S, Hayes D, Yu T-H (2008) Use of U.S. croplands for biofuels increases greenhouse gases through emissions from land-use change. Science 319:1238–1240. https://doi.org/10.1126/science.1151861
81. Hansen JB (1997) Methanol synthesis, in handbook of heterogeneous catalysis. In: Ertl G, Knozinger H, Weitkamp J (eds) Handbook of heterogeneous catalysis, vol 4. Wiley-VCH GmbH, Weinheim, Germany

82. Ostrovskii V (2002) Mechanisms of methanol synthesis from hydrogen and carbon oxides at Cu–Zn-containing catalysts in the context of some fundamental problems of heterogeneous catalysis. Catal Today 77:141–160. https://doi.org/10.1016/S09205861(02)00241-9
83. Rozovskii AY, Lin GI (2003) Fundamentals of methanol synthesis and decomposition. Top Catal 22:137–150. https://doi.org/10.1023/A:1023555415577
84. Goehna H, Koenig P (1994) Producing methanol from CO_2. CHEMTECH; (United States)
85. Saito M (1998) R&D activities in Japan on methanol synthesis from CO_2 and H2. Catal Surv Asia 2:175–184. https://doi.org/10.1023/A:1019082525994
86. Xiaoding X, Moulijn JA (1996) Mitigation of CO_2 by chemical conversion: plausible chemical reactions and promising products. Energy Fuels 10:305–325. https://doi.org/10.1021/ef9501511
87. Saito M, Murata K (2004) Development of high performance Cu/ZnO-based catalysts for methanol synthesis and the water-gas shift reaction. Catal Surv Asia 8:285–294. https://doi.org/10.1007/s10563-004-9119-y
88. Midilli A, Ay M, Dincer I, Rosen MA (2005) On hydrogen and hydrogen energy strategies: I: current status and needs. Renew Sustain Energy Rev 9:255–271. https://doi.org/10.1016/J.RSER.2004.05.003
89. Züttel A (2004) Hydrogen storage methods. Naturwissenschaften 91:157–172. https://doi.org/10.1007/s00114-004-0516-x
90. Bossel U, Eliasson B, Taylor G (2003) The future of the hydrogen economy: bright or bleak?
91. EA Engineering Science and Technology (1999) Methanol refueling station costs. https://afdc.energy.gov/files/pdfs/methfr.pdf. Accessed 28 April 2019
92. Basu A, Wainwright J (2001) DME as a power generation fuel: performance in gas turbines. Paper presented at 4th international petroleum conference and exhibition, New Delhi, India, 9–12 January
93. Dolan G (2002) In search of the perfect clean-fuel options. Hydrocarb Process 81:13–15
94. Ashley S (2005) On the road to fuel cell cars. Sci Am 292:50–57
95. Wang C, Li Y, Xu C, Badawy T, Sahu A, Jiang C (2019) Methanol as an octane booster for gasoline fuels. Fuel 248:76–84. https://doi.org/10.1016/J.FUEL.2019.02.128
96. Çelik M.B, Özdalyan B, Alkan F (2011) The use of pure methanol as fuel at high compression ratio in a single cylinder gasoline engine. Fuel 90:1591–1598. https://doi.org/10.1016/J.FUEL.2010.10.035
97. Canakci M, Ozsezen AN, Alptekin E, Eyidogan M (2013) Impact of alcohol–gasoline fuel blends on the exhaust emission of an SI engine. Renew Energy 52:111–117. https://doi.org/10.1016/J.RENENE.2012.09.062
98. Li J.; Gong C.-M.; Su Y.; Dou H.-L.; Liu X.-J.: Effect of injection and ignition timings on performance and emissions from a spark-ignition engine fueled with methanol. Fuel. 89, 3919–3925 (2010). doi:10.1016/J.FUEL.2010.06.038
99. Yanju W, Shenghua L, Hongsong L, Rui Y, Jie L, Ying W (2008) Effects of methanol/gasoline blends on a spark ignition engine performance and emissions. Energy Fuels 22:1254–1259. https://doi.org/10.1021/ef7003706
100. Huang Z, Lu H, Jiang D, Zeng K, Liu B, Zhang J, Wang X (2004) Combustion behaviors of a compression-ignition engine fuelled with diesel/methanol blends under various fuel delivery advance angles. Bioresour Technol 95:331–341. https://doi.org/10.1016/J.BIORTECH.2004.02.018
101. Huang ZH, Lu HB, Jiang DM, Zeng K, Liu B, Zhang JQ, Wang XB (2004) Engine performance and emissions of a compression ignition engine operating on the diesel-methanol blends. Proc Inst Mech Eng Part D J Automob Eng 218:435–447. https://doi.org/10.1243/095440704773599944
102. Li R, Wang Z, Ni P, Zhao Y, Li M, Li L (2014) Effects of cetane number improvers on the performance of diesel engine fuelled with methanol/biodiesel blend. Fuel 128:180–187. https://doi.org/10.1016/J.FUEL.2014.03.011
103. Chen H, Su X, He J, Xie B (2019) Investigation on combustion and emission characteristics of a common rail diesel engine fueled with diesel/n-pentanol/methanol blends. Energy 167:297–311. https://doi.org/10.1016/J.ENERGY.2018.10.199

104. Balki MK, Sayin C (2014) The effect of compression ratio on the performance, emissions and combustion of an SI (spark ignition) engine fueled with pure ethanol, methanol and unleaded gasoline. Energy 71:194–201. https://doi.org/10.1016/J.ENERGY.2014.04.074
105. Park SH, Lee CS (2014) Applicability of dimethyl ether (DME) in a compression ignition engine as an alternative fuel. Energy Convers Manag 86:848–863. https://doi.org/10.1016/J.ENCONMAN.2014.06.051
106. Kobayashi M, Eritate S, Kanzaki Y, Ito I (2006) Polymer electrolyte membrane and polymer electrolyte fuel cell. https://patentimages.storage.googleapis.com/7e/cf/81/49330b3a450edb/US20060029853A1.pdf
107. Hsueh K, Tsai L, Lai C, Peng Y (2012) Direct methanol fuel cells. In: Zhang J, Zhang L, Liu H, Sun A, Liu RS (eds) Electrochemical technologies for energy storage and conversion, vol 1 & 2. Wiley-VCH GmbH
108. Vijay Babu AR, Manoj KP, Srinivasa RG (2018) Parametric study of the proton exchange membrane fuel cell for investigation of enhanced performance used in fuel cell vehicles. Alexandria Eng J. 57:3953–3958. https://doi.org/10.1016/J.AEJ.2018.03.010
109. González-Espasandín Ó, Leo TJ, Raso MA, Navarro E (2019) Direct methanol fuel cell (DMFC) and H_2 proton exchange membrane fuel (PEMFC/H_2) cell performance under atmospheric flight conditions of unmanned aerial vehicles. Renew Energy 130:762–773. https://doi.org/10.1016/J.RENENE.2018.06.105
110. Wang J, Wang H, Fan Y (2018) Techno-economic challenges of fuel cell commercialization. Engineering 4:352–360. https://doi.org/10.1016/J.ENG.2018.05.007
111. Jenn A, Azevedo IML, Michalek JJ (2016) Alternative fuel vehicle adoption increases fleet gasoline consumption and greenhouse gas emissions under united states corporate average fuel economy policy and greenhouse gas emissions standards. Environ Sci Technol 50:2165–2174. https://doi.org/10.1021/acs.est.5b02842
112. Zhang F, Jiang J, Zhou Y, Xu J, Huang Q, Zou Z, Yang H A neat methanol fed passive DMFC with a new anode structure. Fuel Cells 17:315–320. https://doi.org/10.1002/fuce.201600221
113. Yang CJ, Jackson RB (2012) China's growing methanol economy and its implications for energy and the environment. Energy Policy. 41:878–884. https://doi.org/10.1016/j.enpol.2011.11.037
114. Huang P, Ju H, Tan S, Wang H, Zhao T (2015) The future of methanol fuel, vol 30. The Franke Institute for Humanities report, pp 7–45
115. Hamelinck CN, Faaij APC (2002) Future prospects for production of methanol and hydrogen from biomass. J Power Sources 111:1–22. https://doi.org/10.1016/S0378-7753(02)00220-3
116. Verhelst S, Turner JW, Sileghem L, Vancoillie J (2019) Methanol as a fuel for internal combustion engines. Prog Energy Combust Sci 70:43–88. https://doi.org/10.1016/J.PECS.2018.10.001